The Optimal Control of Power Electronic Embedded Networks in More Electric Aircraft

by David N. Dewar, MEng

Thesis submitted to The University of Nottingham

for the degree of Doctor of Philosophy, February 2021

The University of Nottingham

Contents

List of Figures

Abstract

With the advancement of power electronic technologies over recent decades, there has been an overall increase in the utilisation of distributed generation and power electronic embedded networks in a large sphere of applications. Probably one of the most prominent areas of utilisation of new power electronics embedded systems is the use in power networks onboard military and civilian aircraft. With environmental concerns and increased competition in the civil aviation sector, more aircraft manufactures are replacing and interfacing electrical alternatives over heavier, less efficient and costly pneumatic, hydraulic and mechanical systems. In these modern power systems, the increased proliferation of power electronic converters and distributed generation raises important issues in regards to the performance, stability and robustness between interfaced switching units. These phenomena, such as power electronic sub-system interactions, become even more prominent in micro-grid applications or other low voltage distribution systems where interfaced converters are in close proximity to one another. In More Electric Aircraft (MEA), these interfaced power electronic converters are connected to the same non-stiff low power AC grid, which further increases the interactive effects between converter sub-systems. If these effects are not properly taken into account, then external disturbances to the system at given operating conditions can result in degradation of the system performance, failure in meeting the operating requirements of the grid, or in the worst case, instability of the whole grid. With much research in the area of decreasing the size and weight of systems, there is much literature proposing optimisation methods which decrease the size of filters between interfacing converters. Whilst effectively decreasing the size of these systems, interactions between interfaced converters gets worse, and is often improperly accounted for.

The work presented in this thesis proposes a novel approach to the decentralisation and optimisation of converter controls on a power electronics embedded power network. In order to account for the interactive dynamics between sub-systems in the environment of reduced passive filter networks, all the system dynamics including the interactive terms are modelled globally. An optimal controller design approach based on the H_2 optimisation is proposed to synthesise and generate automatically the controller gains for each power electronic sub-system. H_2 optimisation is a powerful tool, which not only allows the submission, optimisation and development of closed loop controls for large dynamic systems, but offers the ability to the user to construct the controller for given structures. This enables the development of decentralised controllers for every sub-system with intrinsic knowledge of the closed loop dynamics of every other interconnect sub-system. It is shown through simulation and by experimental validation that this novel approach to grid control optimisation not only can improve overall dynamic performance of all sub-systems over

traditional methods of design, but can also intrinsically reduce or better yet mitigate against the interactive effects between all converters. In addition, this method of controller design will be shown to not only be scalable to expanding sizes of grids, but the Phase-locked loops (PLLs) integrated to grid connected devices can also be considered in the optimisation procedure. PLLs are widely known to further cause interactive behaviours between grid interfaced devices. Including this into the optimisation also has been validated experimentally to prevent interactions on the grid, and improve performance over traditional design methods. Adaptations to the controller are performed to ensure operation in variable frequency environments (as is common in MEA), as well as methods of single converter optimisation when interfacing to an unknown grid. Additionally some initial research towards an adaption of the H_2 controller to incorporate robustness as well as performance into the optimisation procedure is presented with mathematical concepts shown through simulation.

Acknowledgements

A PhD can not be successful without the immense amount of emotional and intellectual support a researcher gets from their academic supervisors, friends and loved ones. Throughout the four years of my PhD research, there have been highs and lows, ups and downs and if it were not for everyone who supported me through my work my research would not have got to the stage it is today.

I am so thankful for all the people around me, continuing to encourage and motivate me through this work, and all the academic support I got from my colleagues and friends. You have all been such a great help to me and I shall never forget how you helped me achieve my life goals.

I would like to give my biggest thanks to my supervisors Prof. Pericle Zanchetta, and Dr. Andrea Formentini for the huge amount of support they have provided me throughout my PhD. Their guidance has been key to my success over the past four years and I can not thank you enough for the help you have given me over the years. I would like to thank Dr. Shafiq Odhando and Dr. Luca Rovere for always assisting and helping me decipher all my hardware problems and questions and helping me the process through hardware diagnosis. I'd like to thank all the technicians John, Ian, Guy and Kevin for their assistance in constructing my rig. I'd love to thank my best friends Mr. Linglin Chen and Mr. Patrick Xie for always being someone I can talk my problems to, discuss ideas and debate research. Without their support, the PhD would have surely been a lot harder and more emotionally demanding. I'd like to thank all of my friends and the PEMC research group for whom I have always had delightful discussions with, and during my low times were able to always make me feel upbeat and determined to keep working. I'd like to thank Dr. Jaime Rohten, for whom I have collaborated with in publishing our joint works to journals and his continued support he gives me in helping me achieve my ambitions. I'd like to thank my parents Mr. Andrew Dewar, and Mrs. Liesbeth Dewar-Koopmans for always being at my side and for supporting my decision for pursuing a PhD. Finally, I'd love to thank my girlfriend Ms. Qian Zhang, who has always been my foundation, my meaning and my truest motivation for all my achievements. I would not be where I am today without you.

Chapter 1

Introduction

The world of aviation in recent years has experienced a rapid expansion in the number of planes in the sky, along with a rapid increase in the number of airlines operating these aircraft. Back in the 1970's, flying was only an affordable means of transport for the privileged few. Ticket prices were high and often nations had only one or two international airlines. In 1978, when the Airline Deregulation Act was introduced in the US, and similar legislation introduced in 1987 by the European Union, numerous low cost budget airlines such as EasyJet, Ryanair and Southwest Airlines entered the market allowing air transport to be affordable by all classes of society and thus fuelling competition with the old civil aviation giants such as British Airways, KLM and Lufthansa.

With the increased competition in the aviation sector comes the need where airlines need to reduce as much as possible the operating costs of their aircraft. Airlines look towards the purchase of more efficient aircraft, and this further sparks competition between aircraft manufactures such as Airbus and Boeing to produce larger and more efficient aircraft. In addition, there have been greater calls for airlines as well as governments from across the world to reduce global carbon emissions, with the ever increasing threat of global warming causing irreversible effects to our climate in the near future. The world as it is today cannot function without its capacity for aircraft and therefore, aircraft manufactures are under pressure both commercially and politically to develop new aircraft which are more efficient, releases fewer or no toxic emissions into the upper atmosphere, and being built using more sustainable materials to be of paramount performance.

More Electric Aircraft, or MEA as it shall be referred to hereafter, is an alternative approach to aircraft design by engineers and researchers across the world to, as the name suggests, utilise more electrical systems into the core aircraft design. Power electronics over recent years has advanced significantly; from improved switching device technologies, faster and more advanced control

hardware and newly discovered power electronic converter topologies. These recent advancements in power electronics technology have allowed heavy pneumatic, hydraulic and mechanical non-propulsive aircraft systems to be instead powered using smaller, lighter, more efficient and more reliable power electronic systems.

Research into MEA has only ever grown larger in recent years, and with new modern aircraft today, such as the Boeing 787 Dreamliner and Airbus A350, utilizing much of this new MEA technology and have shown across the board how efficient aircraft can be; with consumers, governments and industry now investing heavily into research and development of MEA.

The title of the study detailed in this thesis is 'The Optimal Control of Power Electronic Embedded Networks in More Electric Aircraft'. This thesis presents research investigating alternative methods of design and optimization for the aircraft micro-grid focusing on the control system aspect. As more traditionally powered systems are converted to electrical systems, the aircraft electrical grid will only expand to utilize these new loads, and as systems get larger, so does the overall weight and size of the system, as well as the increased complexity of their design. In brief, the research exploited in this thesis is the development of methods for the integrated design and optimization of the aircraft electrical grid. Today, engineers responsible for the design of the electrical distribution systems on aircraft, typically source individual power converter sub-systems directly from commercial manufactures. These particular converter systems are typically locally optimized without further knowledge of the performance of the wider electrical system which can lead to sub-system interactions, when two sub-systems are improperly interfaced. This could then lead to degradation of the performance of the global electrical system. The most common approach to mitigate against the sub-system cross interactions is placing electrical filters between bus and converter. However, these filters can contribute up to 25-40% of the total weight of the electrical system [10]. This thesis introduces and proposes novel approaches to global design and optimization of these electrical systems in order to mitigate, or in some cases eliminate, cross-interaction between sub-systems with reduced passive-filter size, as well as improving overall dynamic performance and decreasing overall size and cost of the aircraft electrical system.

This chapter presents in more depth the concept of MEA from the environmental and commercial standpoints which drives the research in this area, covering recent technological advances as-well as the ongoing challenges faced. Following this, an in-depth literature review of current works to date around the topic of this thesis 'The Optimal Control of Power Electronic Converters in Embedded Grid Networks' shall be presented, also looking at the future trends in which this area is leading towards, the accomplishments thus far in literature and practical applications in industry. Finally the outline of the thesis is discussed and explained.

1.1 The Concept of More Electric Aircraft

The More Electric Aircraft concept is not anything new or has sprung up in only recent years. In fact, the whole notion of developing fully electrically propulsed aircraft has been an idea for more than 30 years [11]. Electrification within different branches of transportation is nothing new, where many trains are now fully electrified where cars and trucks are on a upward trend to also become fully electrical within the next 30 years. Aircraft has, since the conception of fly-by-wire, aimed at further electrifying all systems on the aircraft, however even with technology further advancing with every plane generation, aircraft, in particular commercial and military aircraft, are far from becoming all electric. The main impeding factor as to why technology isn't allowing electrically propelled aircraft is largely down to energy capacity, and the required energy to travel as fast and as far as current day aircraft. Take as a brief example a modern full electric car. A Tesla Model S has a 85kWh battery which weighs approximately 540kg. That is almost one quarter of the cars total weight. However, the only main obstacle a car has is acceleration against the friction of the ground and air. An aircraft on the other hand not only has to oppose acceleration, which is up to speeds of 9 times that of a car, but also must contend with lift to a great altitude. Taking into consideration that aviation fuel can contain up to 43.71 MJ/kg, and a Lithium-Ion battery of approximately 0.9MJ/kg. With current technology and power demands on modern aircraft, it is vastly impracticable to consider a fully electric aircraft with current day battery technology.

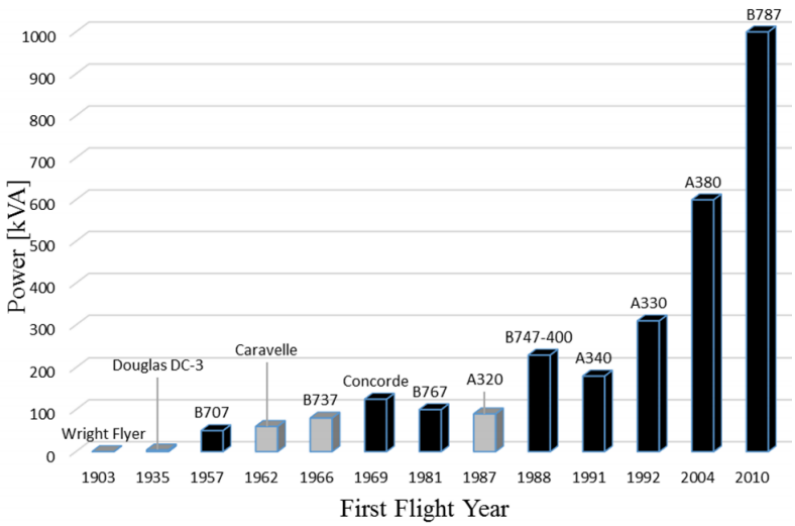

Figure 1.1: Evolution of electrical power demand of modern aircraft.
Grey for Short/Medium Range Aircraft, Black for Long Range Aircraft [1]

Therefore, this area of research with the intention of further electrification of aircraft is thus called More Electric Aircraft over Full Electric Aircraft, as for now the latter is not yet practical

to consider implementation.

The research area of MEA is the collaborative study into developing aircraft whereby all secondary power systems (also referred as non-propulsive power systems) are developed incorporating electrical technology over traditional power systems, for example, hydraulic, pneumatic or mechanical power [12]. The evolution and the further power demands of aircraft can be observed in Figure 1.1, where it can be seen that across all types of civil aircraft, electrical power demand is increasing for each new generation of aircraft.

Aircraft which have been categorised as MEA have been flying commercially since 2007, with the introduction of the Airbus A380, when it was brought to service by Singapore Airlines. It can be seen directly from Figure 1.1 the huge jump in the electrical power requirements upon the introduction of the A380. But, the Boeing 787 Dreamliner (B787) was seen as the moment where MEA technology was really starting to take off.

The B787 made a huge leap as compared to many other commercial aircraft at the time in the utilisation of electrified systems on aircraft. Figure 1.2 demonstrates clearly the increased utilisation and evolution of the aircraft electrical system in MEA.

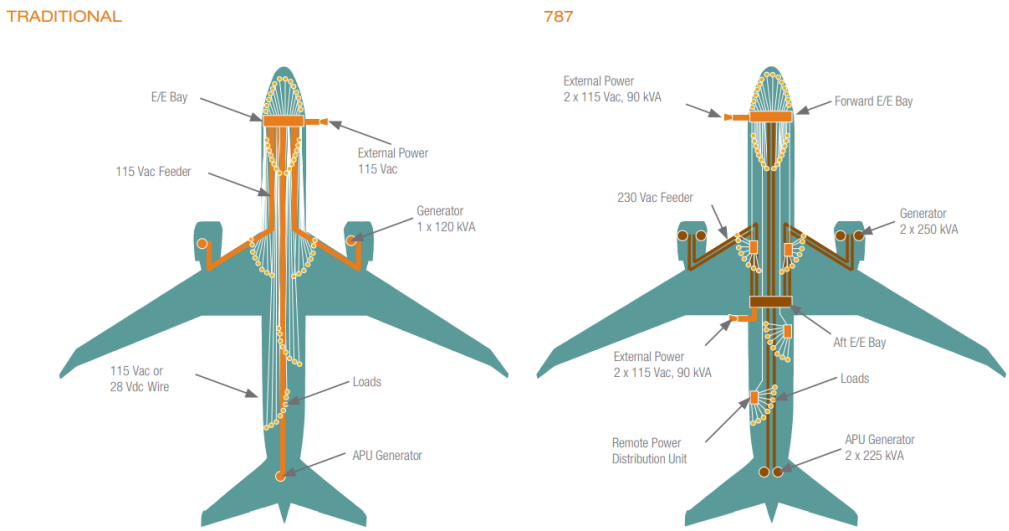

Figure 1.2: Aircraft Electrical System Comparison of Traditional vs MEA B787. Graphic from Boeing Corporation [2]

In general, traditional aircraft were constituted primarily of a single 115Vac grid, which was enough to power all electrical systems from aircraft avionics, lighting, and entertainment systems as small examples. However, a grand feature of the B787 is the fact that the engines are now completely bleed-less. What this means is that hot pressurised air is now no longer drawn from the engine, and therefore all forms of pneumatic power has been replaced with electrical alternatives.

To power all the additional loads which have now been replaced with electrical technology, many different DC grids (28V Auxiliary Power Unit (APU) , 270V), and AC grids (230Vac generator, 115Vac bus) can be now located on the MEA B787.

Additionally for the electrical system onboard aircraft, over many years since the inception of aircraft, the matter of the grid frequency has been debated. Back in the 1940's, standard aircraft had their grids set to a 240Hz, in order to keep the transformer and motor weights to a practical level. Additionally 240Hz was selected due to the availability of magnetic materials for the time [13]. From World War 2, the British army in 1943 started implementing 4-pole 12000rpm generators which typically generated the grid at 400Hz, and thus from here 400Hz became the standard frequency for the grid even to the current day. However, in order to generate a fixed grid frequency from the aircraft engines, mechanical couplings in order to ensure constant generator rotation are required, which are incredibly heavy devices [1]. These days, in an effort to further electrify the aircraft and to reduce the weight and improve the efficiency of aircraft, these mechanical couplings are removed and the grid operates at variable frequency. With power electronics typically lighter and cheaper to maintain that mechanical couplings, systems can be sourced by variable frequency input voltages and conditioned to output fixed frequency, or DC signals where required. Therefore, on today's modern MEA, variable frequency electrical grids are the norm, based on the rotational frequency of the jet engines, with these frequencies generally in the range of 360-800Hz [146].

Bleeding the engine was necessary in traditional aircraft in order to power all the pneumatic systems with hot compressed air, shown in Figure 1.3.

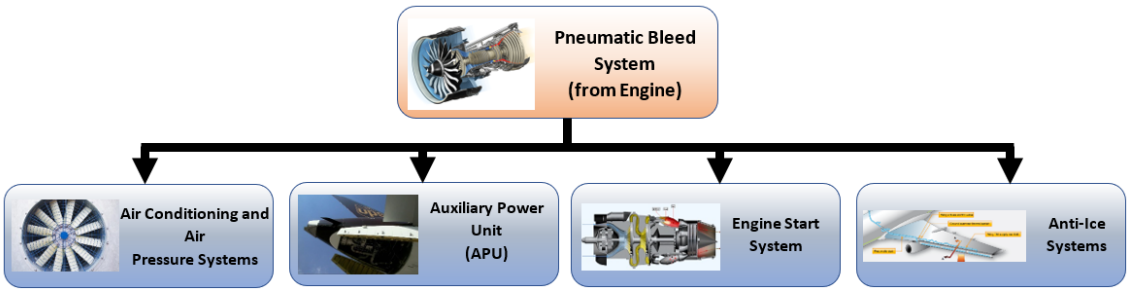

Figure 1.3: System Diagram of Pneumatic Systems on Traditional Aircraft

For traditional aircraft, the pneumatic power constitutes approximately 2%-3% of the maximum power produced by the jet engine [14]. This not only makes engine bleeding very inefficient for the engine, but also, all the piping and hydraulics incorporated to make all these subsystems functional adds considerable weight to the overall aircraft. If any of the hydraulic or pneumatic systems suffer malfunction, this can become a very costly repair, not only from the fact that such systems contain corrosive chemicals, which need to be carefully managed, but also is susceptible to grounding the

planes for long periods of time. On the contrary, power electronic based non-propulsive systems are well known to be easier and cheaper to maintain, as well as bringing additional benefits such as increased system efficiency, improved reliability and maintainability [15]. Therefore, manufacturers and customers alike are adopting these power electronic systems in order lower the complexity and the cost of system repair, increase aircraft reliability, reduce overall aircraft weight and improve aircraft efficiency. This does not only benefit the airlines, for if they can save money by implementing these technologies, the consumer will also benefit with cheaper airline tickets.

There have been several advancements in power electronics technology and the way we design these systems in recent years. From newly discovered power electronic circuit topologies, allowing for systems with greater efficiency or improved steady state performance for varying operating conditions [16], to the development of more efficient high switching frequency devices paving the way for greater power density of conventional power converters [17, 18], and to the advancement of modern day control systems, allowing for optimal performance for given system parameters and improvements in the dynamic performance of systems [19]. Such advancements come to great benefit when attempting to design aircraft electrical systems which need to have high power density, efficiency and reliability. It is therefore garnering huge interest in areas such as MEA in the development of lighter and more efficient aircraft. It can also be shown that it is proving popular with manufacturers.

In Figure 1.4 it is possible to see how since the inception of MEA the market for these types of aircraft have grown over a period of 12 years.

Prior to the A380 being in the mainstream market, the long-haul civil aircraft market share looked as shown in Figure 1.4a. The market of today (2019) is shown in Figure 1.4, where all the green segments detail MEA classified aircraft. With the B787 being only introduced 8 years ago into commercial service, 8% of current long-haul civil airliners currently in service are B787s.

Reflect on the fact that the A330, which was introduced 27 years ago currently holds 19%, and now after only 10 years in service the B787 is approaching half this number. This statistic alone is showing how new MEA aircraft are being adopted over older traditionally designed aircraft very rapidly. This is why, at this current period in time, research into MEA is at one of its fastest, and most accelerated phases.

This drive is not only from the fact that aircraft are in general becoming cheaper and easier to maintain as a result of MEA, but also from the fact of a large drive to reduce global carbon emissions. Globally in 2017 humans contributed a total of 37.1 billion tons of CO_2 into the upper atmosphere, of which 859m tons were generated through general aviation. This therefore puts aviation as contributing 2.3% of total carbon emissions globally, and 3% of the EU's total green house emissions [20]. To put this into perspective, a single person taking a return flight between

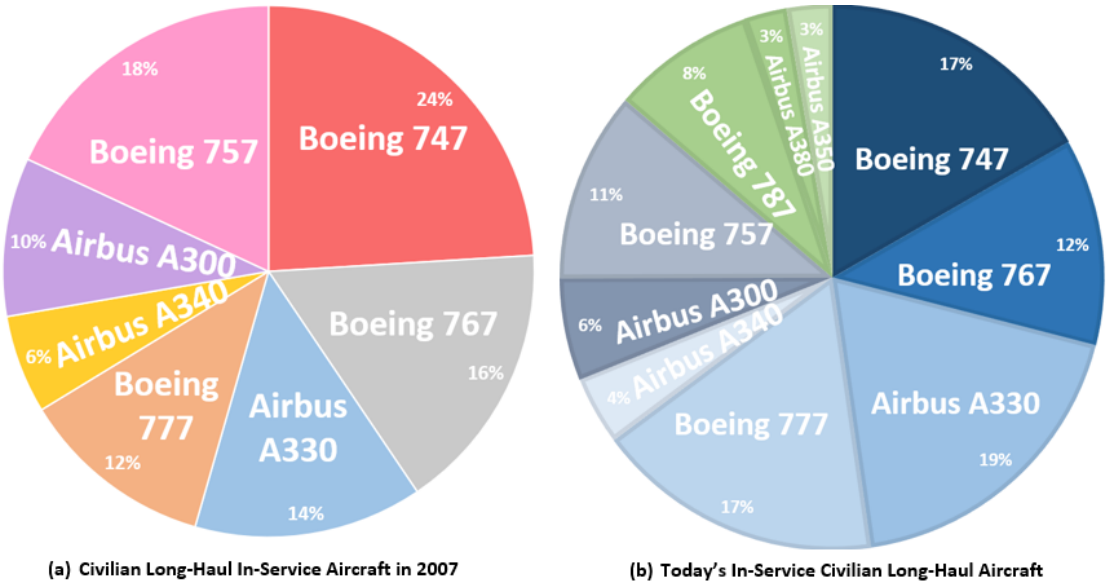

Figure 1.4: Long-haul in-service aircraft prior to (2007) and current day

In Figure (b) - Green Segments are new MEA Aircraft, Blue Segments Traditional (Non-MEA) Aircraft

(Data based on deliveries to customers for all sub-models of aircraft)

London and New York equates to roughly the same emissions produced by the average EU citizen heating their home for an entire year [21]. It has been projected that by 2020, total emissions produced by aviation alone will have increased by 70% when compared to 2005, and that by 2050, forecasts estimate an increase of 300-700% compared to the same year [3].

Figure 1.5, which is constructed using data from the International Civil Aviation Organisation (ICAO) shows the predictions of the total amount of CO_2 which will be emitted into the atmosphere up to the year 2050, where six possible future scenarios can take place. The scenarios (as indexed in the legend of Figure 1.5) shown are described in simple terms as:

1. No advancements to aviation technology conducted

2. Improvements in order to achieve currently targeted reduction of emission levels from aircraft, without technological improvement.

3. (Low Level Technological Improvements) A long with item 2, improvements made of 0.95% per annum to fuel burn technology targets for all new aircraft entering market after 2006 and prior to 2015. Then estimations of fuel burn improvement of 0.57% per annum between 2015 and 2036.

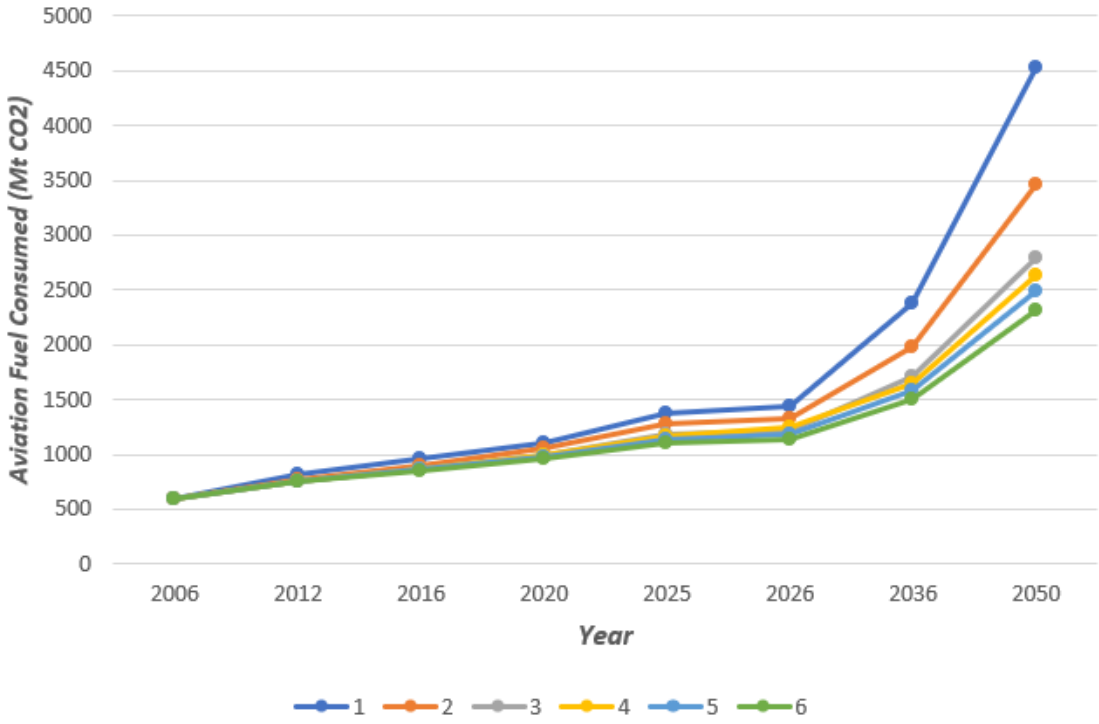

Figure 1.5: Predictions of total aviation fuel consumed by aircraft up to 2050 [3]

4. (Mid-level technological improvements) As with item 3, but a continual improvement of 0.95% per annum to fuel burn technology between 2006 and 2036.

5. (Advanced Technological Improvement) Fuel burn improvements of 1.16% per annum between the periods of 2006 and 2036.

6. (Optimal Technology Achieved) Realistically can improve to 1.5% per annum for the same period and other optimal technological advancements.

In order to reach these targets and improve the efficiency and fuel burn of civil aircraft, MEA research is continually always seeking ways to improve and make lighter and more efficient power electronic systems onboard aircraft. Currently, with the aircraft being introduced to the market today, it is looking as though with the continual research in this area that the expected targets could be reached. Again, looking at how the Boeing 787 has been a leap of technological advancement over previous generation aircraft, the following improvements have been reported by customers [22]:

1. 20% Lower fuel consumption per passanger when compared to similar size aircraft. Notably against the Boeing 767.

2. Increased range of up to 1000km when compared to other similar sized aircraft.

3. 25-30% less harmful NO_X gasses released into the atmosphere.

Therefore, with today's modern MEA, there has been significant improvement over traditional aircraft when it comes to the reduction of pollutants into the upper atmosphere and overall aircraft efficiency, with continuing advancements made each year towards the development of greener aircraft.

Today, one of the largest international collaborative partnerships being conducted in order to reach these targets is the EU's Clean Sky project. This project has even greater ambitious targets in regards to tackling the problem of More Electric Aircraft. A total of €5.6 billion has been given by the EU to fund all research with the ultimate task of developing aircraft and aircraft systems for the 2050 market with the following design targets [23]:

1. A 75% reduction in carbon dioxide CO_2 emissions of aircraft.
   (With an additional aim to reduce to 80% in the next research iteration 'Clean Sky 3')

2. A 90% reduction in mono-nitrogen oxide NO_X pollutants.

3. Reduce the noise pollution of aircraft by 65%

4. Improve the life cycle of aircraft by designing aircraft to be more recyclable.

Therefore, MEA research has a very broad spectrum across multiple disciplines in engineering. From material sciences attempting to achieve lighter and stronger composite materials for aircraft construction, to mechanical engineering to develop more efficient and quieter aircraft engines. A multidisciplined approach to the development of greener, lighter and more electric aircraft.

This thesis primarily focuses on the embedded power electronic systems located on the on-board the electrical distribution grid of the aircraft. At a time in aircraft design, where more traditional power systems are ever expanding incorporating new electrical alternative devices to traditional systems, these grids are only going to get larger, and in turn, more power electronic sub-systems which will be installed on aircraft [24]. Figure 1.6 shows a simplified power electronic distribution system on-board aircraft.

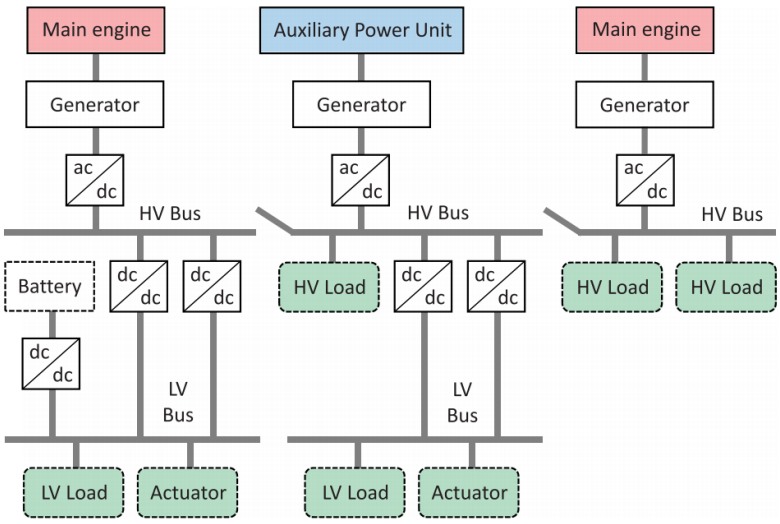

Figure 1.6: Simplified Power Electronic distribution diagram for a primarily DC based electrical system which has been proposed for MEA [4]

Each of the white blocks presented in this figure represent some power electronics used in power transfer or to condition three-phase grids to alternative voltage levels. With so many power electronic systems embedded close to one another interactions can be a common place phenomena [25, 26] which in-turn, if these systems are improperly designed, can lead to degradation of the performance and in the worst case instability [4, 27]. Therefore in addition to filtering out harmonics, these aforementioned filters can be increased in size to mitigate cross-interactive effects between sub-systems [28], but increasing the size of these components is counter-intuitive to efforts of decreasing the size and weights of these systems. There is therefore a need to develop distribution systems utilising reduced passive filters in order to reduce the overall weight of the electrical system, but also to develop a power electronic architecture which guarantees good performance and mitigates against the effects of interaction between sub-systems.

In the next section, the current research efforts performed in order to achieve such systems shall be reviewed, before defining the gap in current research, which this thesis hopes to address.

1.2 The Need for Integrated Optimal Design of the Aircraft Power Network

It has been quoted in articles that, with the recent advancement in computer aided design and simulation software, in recent decades research was largely focused on network simulations, and for the the next few years research will be largely focused on the integrated optimal design of these

aircraft power systems [29]. For the most part this is being held true where many optimisation studies, which have been conducted over recent years, have been focusing on the sizing of these electrical systems, especially in aspects of the filters, which, as previously mentioned contributes a large part of the total weight of the whole electrical system [30, 31, 32]. However, the majority of these studies deal with one general aspect of the converters stability under reduced filter environments; namely to reduce harmonics induced on the system which tend to increase as filters are reduced in size [33, 34]. Alternatively they also deal with the cases of instability of Constant Power Loads (CPL) due to the increase of interactive effects of grid connected power electronic devices in microgrids [35]. Additionally, whilst these studies are very beneficial towards the aim of reducing the overall size and weight of the electrical system, much of this research has been largely focused on single (grid-tied) converter applications. There has not been a vast amount of research published which focuses on the larger scale multi-converter network, and how these converters with reduced size output filters presents greater interactive effects to other sub-systems on the network [36]. This can be especially important for the case of systems augmented with a PLL controller, whose dynamics can be particularly sensitive to sub-system cross interactions [32, 37].

In recent years though, some research articles are attempting to address this problem. Some ideas proposed are the use of active damping controls in order to control the virtual impedance of individual converters to automatically adapt converters to grid resonances and suppress interaction. Such methods have been successfully implemented using control schemes such as Deadbeat controls [38] and using adaptive state-feedback control [39], where the control law $u = -Kx$ is adapted every sample time in order to keep the electrical system operating close to reference values under changing grid conditions. However many of the proposed schemes are themselves relatively sensitive to influences such as grid impedances and system parameter variation, which detriments the proposed methods efficacy [36].

1.2.1 Interaction Mitigation Approaches through Grid Impedance Analysis

Filters are not the fundamental reason as to why interactions are exhibited onto the grid. They are fundamentally implemented in order to reduce the switching harmonics exhibited by the power electronic devices, with the added benefit that the larger these filters are, the better are the effects of mitigation against transient behaviour between sub-systems. The phenomena is directly attributed to the fact that the grid is non-ideal, and to each grid-tied device, the grid is often presented as a non-ideal voltage source with very high impedance [40]. On the contrary, for systems supplying the grid, the grid is seen as a non-ideal load. Each converter on a grid is typically designed independently, which only adds further to the non-ideality at the point of common coupling (PCC)

between generator and grid tied devices to where instability of the whole grid system could occur.

Due to this phenomena a considerable amount of work has been conducted in recent years looking into the identification of converter impedances attached to a grid to identify when such system could be subject to instability from cross-interactive behaviour [41]. It is very well known in all branches of electronic or electrical engineering that if a sourcing impedance is larger than that of the loading impedance, mismatch will occur, and can cause undesired, sometimes unstable behaviour between subsystems [42]. Typically in the past, to measure the impedances of these three-phase systems, harmonic injections of the current or voltage are applied onto the network at the PCC. By supplying harmonic inputs of current on to the system, and measuring the resultant behaviour of the voltage (or vice versa by supplying harmonic inputs of voltage, and measuring resultant currents) a characteristic of either the input or output impedance of the converter for given frequencies can be evaluated [43, 44]. However, since the 2010's significant research had been applied in this area by transferring the analysis to the dq domain. The general methodology in the analysis is the same as was done in previous years, but the attained results are more direct and representative of the true converter impedance [45]. Of particular interest recently with these advances of impedance identification methods is the analysis of the PLL, and its contribution to the interactive effects between power electronic sub-systems. As was described in [46, 47] grid tied systems utilising PLLs for grid synchronisation, can often lead systems to instability; if the coupling dynamics from other systems is not accounted for, in addition to their effects to the intrinsic impedance of the subject converter. The reason as to why the PLL augmented to systems controlled in the dq reference frame inflicts interactive behaviours is due to that only the $q-$ axis component is utilised for phase tracking, where when the $q-$ axis being read as 0 on the PLL means the PLL is correctly synchronised to the grid. However, this tends to lead towards an asymmetric dq model for the global system, which then imposes cross-interactions with other subsystems, such a frequency coupling to come to effect [48]. Attempts were made as discussed in [37] to develop PLLs which can mitigate against these unwanted cross-coupling behaviour with largely little success. Largely down to the fact that these designs actuate only on the harmonics present on the system, and the cross-coupling effects of other sub-systems are not correctly accounted for in their design. Additionally it was found in [49] that the PLL exhibits a negative impedance characteristic onto the grid-tied converters when PLL bandwidths are too large; especially in the case of weak grids. This work was able to successfully predict, using grid impedance identification, when a given network would go unstable for a PLL controller of a given bandwidth. Although this work, and its derivatives [25, 50, 51], have enabled a simplified approach to the prediction of unstable grids due to the controls of individual converters, the fundamental problem, as was discussed in [37], has not fully been tackled. Namely, the fact that PLL controls

can still exhibit unwanted harmonic, and interactive behaviour through the cross-coupling effects between converters.

1.2.2 The Interactive Behaviours Between Interfaced Converters and the Attempts to Mitigate

It is evident there has been a major push in recent years for which impedance based stability analyses are being performed in order to characterise and predict the stability of non-linear systems. The areas in which the majority of this research is focusing on being renewable energy transmission and micro-grid networks.

With regards to the necessity of the filters between interfaced devices to mitigate interactions between sub-systems, work conducted in [52, 53] evaluated the true nature of the interactions with filter-less networks. Of course, if these filters contribute the most to the size and weight of the system, mitigation from the network would be ideal. However, it was shown in these studies the importance of these filters in not only dampening the interactive oscillations to dynamic system changes, but also to not detriment the power flow between interfaced devices. Additionally, in [54] studies were done using similar impedance based methods as was used for PLL stability, to evaluate and optimise the design of converters such that the stability is guaranteed. This work mostly aimed at studying the Nyquist plot of each converter and analysing the net encirclements of the critical point $(0, -1)$. It was then shown that stability between interfaced converters can be guaranteed if the number of clockwise and anti-clockwise encirclements from each of the converters at the critical point is equal. Typically, to do this, modification of the closed loop controllers is required to move the poles associated to the impedance transfer functions between these converters. Whilst not directly applicable to the MEA power system concept, many research articles have been published in recent years investigating the interactive effects of high power converter systems in close proximity in renewable energy applications, and developing ways to mitigate them [55, 56, 57, 58]. Again, primary focus of these studies has been towards the PLL, but it was observed in [55] that even an improper selection of the bandwidth of a single PLL can be enough to take the whole grid into instability. But in addition, if the current loops of the controller are set too slow for a single converter (whilst keeping the voltage control bandwidth 10x slower by convention) the same exact phenomena can be observed. This study again confirms that even if independently designed converters are stable, and with their PLLs correctly tuned, a single converter can cause the deterioration of the global system if all the dynamics are not taken into account [56]. An article back in 2004 did however initially investigate this phenomena beforehand and attempted to solve the issue of the cross interaction caused by the controller by use of selective decentralised controls

[59]. The method introduced here however is not the most intuitive as it searches many different controllers to find a set of controls for all sub-systems with the least Generalized Dynamic Relative Gain (GDRG). Then all the combinations of controllers are tested until the least interacting set can be identified. This is of-course not an elegant solution, but there have been a few papers published since that have looked into greater detail at decentralized control schemes to improve performance of the grid itself, and to overcome sub-system cross interactive effects [60, 61, 62]. However, like it was analysed in [59], to date, the approach of decentralised design of controllers has been largely focused still on guaranteeing global stability of the system based on localised measurements of each respective power converter and to actively damp the oscillations caused by the LCL filter at a local level [62]. Whilst the aforementioned methods can result in the reduction of sub-system interactions for the global micro-grid system, it can be shown in studies [55] and [60] that having independently designed systems which are all stable when interconnected together is not enough in the greater picture to guarantee global system stability. These studies discuss the need for each independent sub-system controller being designed with respect to the dynamics of all other sub-systems in order to improve overall system performance, robustness and greater mitigation against interactive behaviour. In other words, a global dynamic optimisation is required in order to attain the best performance against interactions. It is hoped therefore that the research presented in this thesis can address this issue.

To date, there has not been much research into decentralised control approaches for aircraft micro-grids [61] and today's solutions to mitigation of sub-system interactions look into the online control adaptations to situations; or using impedance analysis routines to ensure static controllers are stable for global operation. Therefore, this thesis wants to investigate this gap in research, and investigate novel methods by which a global control system can be designed, such that all dynamics of the micro-grid are taken into account, and closed loop controllers for each independent sub-system automatically designed with respect to the grid global dynamics. It is hoped that having controllers designed in this way, with full knowledge of all other closed loop dynamics of all exterior sub-systems, that this globally decentralised controller can actively mitigate against the sub-system interaction phenomena, and in addition bring no compromise to the global stability or the performance which can be attained by traditional means.

1.2.3 Controller Implementations Employed on Power Electronic Embedded Networks

From the literature analysed so far in this section, it is clear that there have been many approaches adopted in order to analyse the stability of power electronic embedded grid systems. Thus

far the methods range from performing impedance based Nyquist criterion stability analysis to check stability of interfaced systems; to developing controller design guidelines as to reduce the possibility of sub-system interaction based instability; or brute force methods of converter controller optimisation to achieve minimal interactions between sub-systems [59].

In this section, a small review will be undertaken analysing the work performed in the area of grid based control schemes so that a picture can be gained as to how to approach the control optimisation problem of interacting power electronic sub-systems.

Typically when investigating the literature about designing global control systems for micro-grid applications, three main topologies are discussed. This is either a centralised, distributed or a decentralised control structure [63, 5].

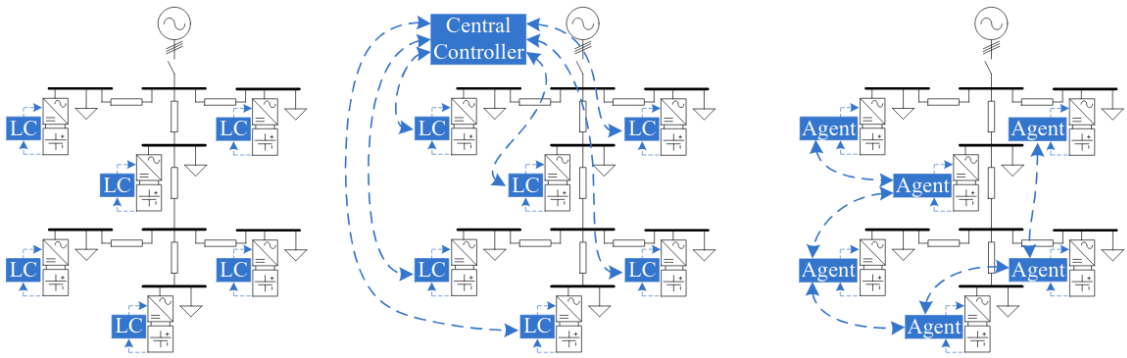

(a) Decentralised (b) Centralised (c) Distributed Multi-Agent

Figure 1.7: Representation of all the different control schemes utilised for micro-grid networks as presented in [5]

Centralised control schemes typically use a primary/ secondary structure of communication. A central master coordinates the actuations of the slave controllers. In addition, centralised controllers can be segmented into primary, secondary and tertiary controls; this configuration is often referred to as semi-decentralised. There are multiple benefits to this approach of control in that online intelligent algorithms can be employed to manage controls globally. In addition, global stability can more easily be guaranteed as all information of all converters is available in real time, and thus coordination of all sub-systems can be performed [64, 65]. However, there are many severe drawbacks for utilising centralised control structures. For one, communication between all the sub-systems is important for the proper operation of the control. This not only can add considerable weight and complexity of the overall system, but in addition can reduce the redundancy of the grid. Centralised controllers require the information of all systems at any given time for correct operation. So if point failure of one converter occurs, the rest of the control

system, and thus the grid could be compromised. In turn, with a vast amount of information being required to operate the central controller, scalability for ever growing electrical systems becomes a greater challenge. Not only do software adaptations need to be developed to incorporate new sub-systems, but also there is limitations of communication bandwidth which can limit the size of the system [64].

There are also decentralized controls, where each converter has its own independent controller dependant only on its local measurements (Figure 1.7a) or measurements from its local neighbourhood (distributed control) (Figure 1.7c). For many years, the problem of the development of a decentralised control scheme was considered a great mathematical challenge. Finding block-diagonal controllers by optimisation was considered to be an NP (non-deterministic polynomial-time)-Hard problem and because of this, it has had a great deal of research conducted over recent years [66]. Why decentralised control is of particular interest these days, is the strengths it has over the drawbacks of centralised control schemes. Namely, the single point of failure. Where a centralised controller is completely dependant on all the real-time signals of all converters, the decentralised approach is dependant only on local measurements, and does not require all systems to function for correct operational behaviour. This additionally brings up the scalability issue which occurs with centralised schemes. With independently operating controllers, the decentralised scheme in theory allows for the expandability of the power network. Bandwidth of communication protocols are no longer an issue, and the size of systems are therefore no longer limited [64]. The major drawback for decentralised control schemes being that, if one wishes to globally optimise all controls, still to this day it can be an incredibly hard computation task to conduct, with scaling up the system only increasing the complexity. Nonetheless, the advantages which has been attained by the decentralised approach, has led to a drive in research in the renewable and domestic energy sectors to decentralise the distribution grid [67, 68, 69]. In regards to the aviation sector, the fact of reduced required communication between sub-systems in decentralised configurations means that much of the cabling necessary for centralised control structures are eliminated, eliminating much undesired weight from the electrical network makes the decentralised controller approach highly desirable [70]. In addition, a study performed in [71, 72], where H_2 optimal controls are synthesised to develop both a centralized and a decentralised control for a given DC hybrid system and the performances compared. Both works concluded that such decentralised architectures are capable of delivering almost identical performance to that of the centralised counterparts if properly optimised. Additionally in terms of reliability of decentralised controllers it is reported that decentralised architectures can have the same reliability as that of centralised controllers, even when each independent controller is considered to be a less reliable form of control [64].

With decreased computational requirements on the controllers, due to them only requiring local

calculations, the reduced weight gained from eliminating cross-communications, non detrimental performance in closed loop and the greater possibility to scale up the electrical system under this scheme for expanded networks, decentralised control in today's literature is predominantly becoming the control architecture of choice for MEA power networks [73]. In fact, due to typical aircraft power networks being generally sourced by multiple parallel connected voltage source converters, decentralised control is starting to be widely adopted for systems which incorporate droop controllers [61, 73, 74, 75, 76, 77]. Since in general, the frequency is globally independent from the output power of the inverters, conventional droop controls can tend to skew the system frequency. Decentralisation methods have been shown to improve the power sharing capabilities between parallel interfaced converters, without interfering with the frequency of the global micro-grid [77].

Thus far, the reasons as to why decentralised control architectures are becoming a widely adopted approach to micro-grid controls have been analysed. Additionally some of the benefits that have been discovered by employing a decentralised approach to droop control in parallel sourced systems have been briefly investigated. However, whilst studies have predominantly shown that decentralised control offers numerous benefits over the centralised counter part, there has been little research as a whole investigating the use of decentralised control in the mitigation of sub-system interactions.

There are numerous methods that have been recently investigated regarding the design of decentralised controllers for micro-grid sub-systems. An increasingly popular method, which for a while has been utilised into DC grid setups, and more recently in more three-phase grid applications, is the use of decentralised Model Predictive Controls (MPC) [78, 79, 80]. With the improvement of micro-processors, MPC has been quickly adopted in recent years due to superior discrete performance over many other forms of control. Additionally MPC is very adaptive, and the controllers can be easily augmented such as in [79] to actively damp the harmonics due to input filters, where these elements can be simply augmented into the controller cost functions. However, whilst many of the MPC approaches could be considered decentralised in grid application as each control is dependant only on its local measurements, the approach of MPC for the application of interaction mitigation is not realisable, since to mitigate interactions on a AC based micro-grid, as has been previously mentioned, knowledge of the other converters on the network must be augmented into the controller design and optimised as such. This is not at all possible using popular methods such MPC, or other approaches such as back-stepping controls, where actuations are based on ensuring Lyapunov based criterion is kept given the current system conditions [81, 82, 83]. The problem is that in order to account for the closed loop dynamics of other converters for such control architectures, additional communication will need to be distributed

between neighbouring converters, thus increasing size and complexity, and moving away from a decentralised architecture to one that is referred to as distributed. Therefore, for many popular methods of decentralised control, the criteria of keeping the system fully decentralised is violated, due to the need of these control architectures requiring more information from other converters in order to mitigate interactions. Therefore, this means that micro-grid systems augmented in decentralised architectures are only optimal at the local converter level, instead of the global system level [27, 84].

In other words, a control design approach, which can fundamentally synthesise a globally decentralised control for a given micro-grid, where each decentralised control is designed based on the closed loop dynamics of all other sub-systems on the network, is what is required. This approach would therefore allow the automatic design of decentralised controllers, and in turn be designed with the knowledge of interactive effects of other systems to largely mitigate this phenomenon. Today, there is a popular control which is known as the H-infinity method for which this can be utilised. Coincidently, this is the control approach already discussed in [71, 72]. Although these methods have been around since they were introduced introduced by JC Doyle in [85], the approach has not at all been widely used as it has been, for the most part, a very computationally complex problem to solve. In general, systems which benefit most from decentralized architectures are for the most part large-scale systems, which make the optimisation problem of even greater complexity [86]. The daughter controllers stemming from H-infinity theory are the well known LQR/LQG controls. These controllers are indeed widely used across many power electronics applications as, given the system is of correct form, a convex solution to the control problem can always be found [87, 88, 89]. However, the LQR synthesis can not be constrained such that it delivers decentralised controls, and again can only offer a distributed or centralised solution to grid controls [27]. Typically again, when papers mention the term decentralized control using such controllers, they tend to be locally optimised systems and not truly globally decentralised controls [90]. In some situations, these controls are locally optimised converters, but use Kalman filters to estimate the behaviour of other interconnected converters, without the need of additional communication. But again, this type of LQG optimisation would not consider the interactive effects of other integrated sub-systems [91].

Recent papers reiterated the power that the H-infinity methods can provide for the global decentralisation for large-scale systems, and there have been a few studies which have utilised the power of this approach in order to develop globally decentralised controls for power networks [92, 93].

A first example can be found in [71]. In this work, a HVDC electrical system is partitioned into groups of poset-casual subsystems. Grouping sub-systems by poset-casualness and constraining the resultant controller K to decentralize around these groups, results in more tractable solutions

for the algorithms developed in [66, 92] to be solved, and thus more optimal solutions of control. However the fall back of this approach is that neighbour to neighbour communication is necessary to realise the optimal solution and therefore the network is distributed, not decentralized. In addition, work conducted in [94] uses a mixed approach of H_2/H_∞ in order to develop a decentralized control system for storage units supplying AC grids. What is novel in the approach here is that it is one of the few cases of work by which H-infinity methods have been utilised in order to decentralise the control with respect to the interconnection effects of other clusters of storage units. The controller synthesis algorithm depends on an iterative approach to locate the minimal convex solution to the H_∞ optimisation, and again iterating the feasibility of the control to expanding operating ranges. This results in the most optimal control solution for the largest region of operation. However, it is seen that the controller utilised here accounts only for uncertainty in the dynamics of other network clusters and doesn't seem to be employing the approaches devised in [92] for true global optimal behaviour. Nonetheless, the proposed approach was shown to counteract the interactive behaviours of the clusters when compared to PI controllers, and greater performance and larger operational range was attained. An H_∞ approach was also devised in [95] in the application of parallel islanded voltage source converters. In contrast to [94] however, the controller has been properly decentralized where controller K is constrained diagonally resulting in independent controls for each sub-system. The focus of this design is to enable the automatic controller design simultaneously along with the modelling of the system. For methods such as the ones discussed [71, 94], the need for network clusters or poset-casualness already restricts the form of controller which can be designed, limiting the ability to design a truly decentralized control [95]. It has been shown that utilising the H_∞ approach, one can simply model the system in state-space without concern of its structure, but instead impose the structure on the controller, as was shown in [92]. The drawback is that this approach becomes a non-convex optimisation, and thus for certain systems, only a sub-optimal solution may be found. The likelihood of not finding the optimal solution increases as system size grows. But compared to other solutions, its the only guaranteed procedure of achieving an optimal decentralised global controller.

1.2.4 Summary of the Literature Review

Fortunately in regards to the research presented in this thesis, much of the work into the design of decentralized control architectures primarily focus around DC micro-girds. This is because there is a huge push these days in renewable micro-grid networks, which are primarily interfaced with HVDC distribution systems [96]. To this day in literature, there is not much research into the decentralized control of aircraft electrical networks using global optimisation methods to attain

true decentralization [61].

From the literature review, it is clear that there is a clear gap in the research, not only toward the development of full globally decentralised controls in micro-grids for aerospace applications but more so in the AC networks incorporating grid-tied devices with PLLs. There have been numerous attempts at optimising the PLL with such works reported in [97, 98, 99, 100], but all these approaches only indirectly solve the issue of the PLL interactive dynamics on the rest of the network. They require the use of analytics to observe if the PLL is interacting and then adjustment and coordination of the tuning of the control accordingly to resolve the issue. To the authors knowledge, no literature has been reported as to directly optimising the PLL through decentralized control techniques, so that PLL dynamics are accounted for globally, and the interactive behaviour mitigated. In addition to this, due to the lack of research in the area of optimal decentralised controls in More Electric Aircraft applications, the optimisation by use of H-infinity methods of a DC/AC to AC/AC sub-system network would be a novelty in itself.

Therefore, the thesis addresses this aforementioned gap in research, and will provide methods of global decentralised optimisation of an AC sub-network of a MEA power system. In the approach to be presented, all dynamics of all the closed loop sub-systems on the grid are provided to the optimisation. With the controller constrained to a diagonal structure, each sub-system controllers on the network can be optimal in performance with respect to to all other sub-systems on the network, with no requirement of cross-converter communication. A completely decentralised control scheme. Additionally, the PLL will be augmented into the optimisation, and gains synthesised such that the PLL too becomes optimal with the rest of the grid, guaranteeing mitigation of the interactions which could arise from improper design. In addition, the drawback of this proposed design (as will be discussed in Chapter 7) is that this controller is ideal for static frequency operation. Whilst a constant 400Hz grid was common place in traditional civil aircraft, MEA generally adopts a variable frequency grid topology [101]. Augmentation and adaption of H-infinity based controls has been done before in some applications [102] to mitigate against un-modelled variable changes. However, since the proposed controller design is novel in its application, the adaptation to gain schedule the control for variable frequency applications is also novel in application, and is also therefore proposed as a solution to the original shortcomings of the design in this thesis.

1.3 The Novelty of the Work Presented

Grid optimisation is a large and complex topic for which all the research needed to carry out a full and complete power network optimisation is not feasible in the time for a PhD project, and this work can be branched out to many different areas. For example, global sizing and

component optimisations and EMC (Electro Magnetic Compatibility) optimisations, which are currently ongoing projects being conducted in the greater effort of power network global optimisation and are being performed in conjunction by both Virginia Tech, and G2E Lab Grenoble. The focus which this thesis is investigating is the analysis on global optimal control techniques on the grid, which to the knowledge of the reader as of writing this thesis is a new approach to power network control design.

This work focuses on the decentralised and global optimisation of a simplified aircraft embedded grid which paves a way for interaction mitigation of sub-systems under reduced passive filters. The work covers multiple areas of design, but the main novelties which are delivered in this thesis can be categorised as follows:

1. **Development of a globally optimal decentralised controller for hybrid DC/AC three-phase grids** (Chapter 3/4)
   There are many approaches of controller design for non-linear systems, and in these chapters many of the modern methods of design have ben employed to analyse how they can be interfaced into the optimisation of a global controller for a grid. This chapter showed all the complications that can occur across some of the methods and reasons as to why alternatives must be developed. Then the proposed approach of optimal decentralised control is proposed, whereby all grid dynamics are evaluated into an optimisation procedure and an output state-feedback controller decentralised for each individual interfaced subsystem is generated, whereby all power electronic sub-systems are optimal to one another and stable when interfaced with one another.

2. **Integration of PLL dynamics into a globally decentralised control architecture (Chapter 5)**
   As it has been presented through the literature review, the PLL is a big contributor to the detrimental effects of power electronic converter unstable interactions if improperly designed. With the benefits received from the proposed controller design, a PLL is also augmented into the decentralised optimisation procedure to guarantee stability of the PLL interfaced system as well as performance improvements dynamically over traditional methods.

3. **Developing a controller which is Scalable for easy expansion of optimised power networks (Chapter 6)**
   As a result from the first point, with all the system dynamics incorporated into a single optimisation, it will be shown how the proposed controller can not only improve the dynamic performance of all sub-systems on the network, but can also largely mitigate cross-interaction between converters. In some cases almost nullifying the transitional effects observed in

traditional control schemes. This chapter also presents the ease in which the proposed controller design can be extended and incorporate the dynamics of additional controllers onto the network. Showing how this method can be easily adapted for larger, greater scale power networks. In addition, this chapter also analyses how the well the proposed controller performs when subjugated to large parameter uncertainty, presenting very noticeable performance increase when compared to more traditional decentralised optimal control approaches.

4. **Optimal Controller Adaptation for Frequency Wild systems (Chapter 7)**
   MEA electrical systems are no longer static frequency but are now variable frequency electrical systems, and any controller must be augmented to take into account the full frequency range of operation of the grid. A gain scheduling adaptation to the controller synthesis is then proposed which guarantees stable and optimal performance across all operable grid frequencies and maintain the benefits of interaction mitigation even when subject to changing frequency.

5. **Region of Attraction Approximation for Optimally Controlled 3-phase converters with no simplification (Chapter 8)**
   Region of Attraction Approximation research on three-phase power converters to date has mainly focused on the simplification of the three-phase model using single phase analysis which is not accurate enough for full region of attraction approximation of the larger complex system. This thesis proposes a novel approach to the analysis of the ROA for three-phase systems with no simplification of the model, and thus providing more accurate measurements to the true controller stability region. This work is hoped to be used by researchers in the future to assist in the development of optimal controls with consideration to maximizing the stability regions of networks, as well as optimal performance.

These proposed designs have developed a way of decentralised optimal control for embedded grids, which guarantees stable and improved dynamic performance across static and variable frequency grid operations, whilst also mitigating cross-interactions between converters during transient disturbances.

1.4 Outline of the Thesis

Each of the chapters in this thesis details different aspects of the story to building up the novelties presented above. The thesis covers topics chapter by chapter as follows:

1. **Chapter 2** - A general understanding of the notional system under test in this thesis is presented, where the modelling and understanding to the operation of the simplified power

electronic grid is presented. The key equations derived in this chapter become essential for the controller design later on in the thesis.

2. **Chapter 3** - There are many approaches to the design of controller for non-linear systems. In this chapter, popular approaches to non-linear controller design, as well as popular linear controllers on non-linear systems are presented. It will be shown how when applied to grid applications, these popular methods incur problems during their design phase and how they cannot be utilised for this purpose in aircraft applications. This chapter slowly paves the way to the establishment of the proposed controller which is described in full in chapter 4.

3. **Chapter 4** - From the analysis of popular methods, the H_2 controller, a derivation of the H_∞ controller, is proposed as the controller of choice. This chapter goes in depth into the theory behind the synthesis of the H_2 optimal state-feedback controller, and the first initial design takes place on the simplified model presented in chapter 3. This proposed controller design was compared using a range of average and switching simulations before being experimentally validated on a custom built experimental rig.

4. **Chapter 5** - Proving the concept of the control using the simplest of examples, it is required to build and apply the controller for more practical scenarios. Phase-Locked Loops plays a vital role in grid connected converters, and are also shown to be a large cause of instability in systems when improperly designed. This chapter utilises the methods previously presented in chapter 4, to incorporate the PLL dynamics into the optimisation procedure to, in turn, optimise the PLL controller gains. A novel approach to the incorporation of PLLs into the controller optimisation is presented, which not only guarantees a fast and stable controller design, but also shows to improve performance when compared to traditional approaches of controller design. This chapter again presents simulative and experimental validation for the proposed design.

5. **Chapter 6** - Having scaled up the system to include the dynamics of the PLL into the optimisation procedure, in this chapter, the procedure to scale up the system to more complex converter networks will be investigated. As was discussed in the literature review, many approaches to decentralised control of converters have relied on continued cross-converter communication for optimal performance. This chapter presents how the proposed approach can remain completely decentralised with the rest of the network, whilst still maintaining optimal, robust performance, and in addition adheres to the redundancy requirements so important for aircraft. This chapter focuses on a three converter network, but paves directions for future designs for larger scale systems. The performance of this controller again has been

validated through use of simulation, and the grids susceptibility to parameter variations has been evaluated and compared with traditional optimal controls, presenting very interesting results.

6. **Chapter 7** All the following designs being shown to work from the previous two chapter calls for further adaptation for more realistic scenarios. With the previous designs the system operates at the notional aircraft grid frequency of 400Hz, however in MEA electrical generators provide variable frequency power. This chapter looks at an approach to gain-scheduling of the controller which allows for optimal performance across full operable frequency range, but also allows for fast transition of controller gains. It was shown to be very intuitive, and considering the non-convexity of the controller synthesis algorithm, was able to get very smooth operating controllers across all frequencies.

7. **Chapter 8** Finally, it is very important for any controller design to analyse how robust an applied controller is for the network. Region of attraction methods are the best way to visualise the stability of a complex system, however much research on higher order power electronic system analyse simplified models which are not very accurate representations of the regions. In this chapter, a review of commonly adopted procedures for Region of Attraction analysis is presented, and then applied to full order three-phase converter system with no simplifications. The approaches of approximation to all state-dimensions is presented, however due to time restrains of the project, only the theory is presented here, and experimental verification of the proofs discussed in this chapter have not been undergone, and therefore will be subject of future work.

8. **Chapter 9** Conclusive remarks of the project are given. Reiterating the main outcomes of the project work, and drawbacks to the proposed approaches. Future work for this project is discussed as well as other factors still to be analysed in regards to the performance of the proposed design.

1.5 Summary

More Electric Aircraft is a large area of research which over the years has been meeting its hard targets to improve the efficiency and decrease overall emissions for future aircraft. This work focuses primarily on the optimal controller design of power electronic embedded grids on-board More Electric Aircraft, such that reduced filter systems where greater interaction between converters is exhibited can be largely mitigated by optimal control methods. Whilst the work which will be

presented in this thesis uses a simplified form of a grid, it is seen fit for purpose as a proof of concept for controller design of a wider grid. In the preceding chapter, this area of research will be reviewed to ascertain the gaps of research in this field and to further refine the focus of research in this work.

Chapter 2

The Notional System

In order to conceptualise and put to practise the work and designs detailed in this thesis, a notional system from which the majority of the work will be applied to is developed. It is physically and financially problematic to develop and build a full scale embedded aircraft grid in the lab, whilst also being ultimately unnecessary as a proof of concept. Therefore, the majority of the work detailed in this thesis analyses a particular subsection found in the aircraft grid.

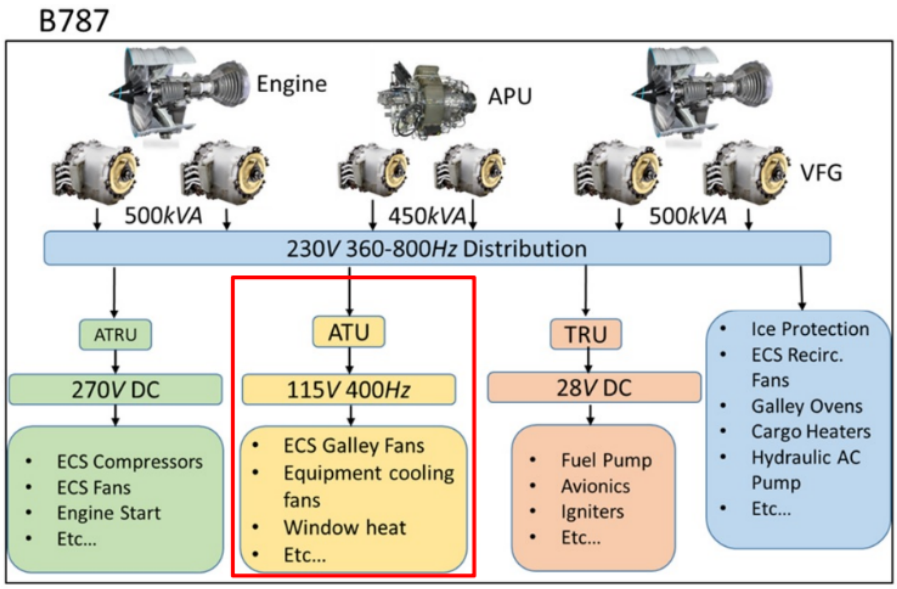

Figure 2.1: Simplified Boeing 787 Embedded Grid with Area of Focus in the Grid for work detailed in Thesis

Figure 2.1 depicts a simplified electrical diagram of the Boeing 787 which today as of writing is the most popular civil MEA. The MEA electrical grid is typically generated from two sources.

The vast majority of electrical power is generated directly from the turbine jet engines. Inside each of the jet engines, a gearbox configuration transfers the rotational energy of the engine via a variable speed shaft into two synchronous generators (SG). These in turn generate the 230Vac electrical grid which powers all the distribution grids on aircraft. This is shown in in Figure 2.2 to aid understanding.

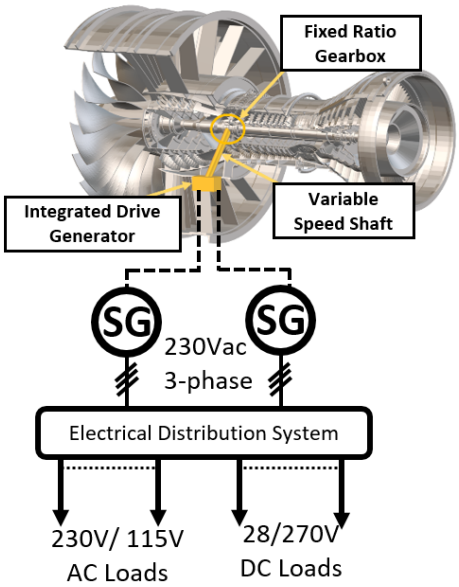

Figure 2.2: Grid Generation from Jet Turbine Engine

The distribution grid generated from the synchronous generators makes up the core of the aircraft electrical system from which all other sub-distributions utilize power from. For the research presented in this thesis, the sub-distribution of interest to which all designs will be carried out upon is the 115Vac 400Hz distribution gird. This sub-distribution was so selected due to it powering the crux of the essential flight systems on aircraft. The 115Vac also powers the majority of heating/ cooling systems, and many of the electromechanical drive systems. Systems such as 'All Electric Taxi' drives which are of particular research interest these days will also be driven from the 115Vac grid [103]. The large variety of critical and non-critical systems, and of varying types of loads makes this particular area of the aircraft grid a particularly interesting area to perform research for grid design and optimization.

In this chapter, the converters which are commonly interfaced in order to regulate the power flow shall be dynamically modelled such that advanced controls can be developed. It is important to note for simplification of the study in this chapter, and the subsequent chapters a simplified model of the aircraft grid involving two converters shall be utilised. This is in order to conceptualise the proposed controller design in a simpler more presentable manner. However, it is important to

investigate how our proposed designs also perform when in more grid like situations. It is in Chapter 6 where an expanded grid, more representable of an actual aircraft grid shall be investigated, utilising theory presented here and in subsequent chapters to show how well our designs perform in more grid-like scenarios.

2.1 Full Description of the Notional System

In order to provide a proof of concept for the novel approaches of optimized grid design in this thesis, a simplified notional system model of the 115Vac distribution system has been utilized.

This simplified grid model consist of two converters interfaced directly with one another. The Voltage Source Converter (VSI), which generates the 400Hz grid, and an Active Front End (AFE) which can be used to interface a range of DC loads to this sub-distribution grid. The notional system is depicted in Figure 2.3.

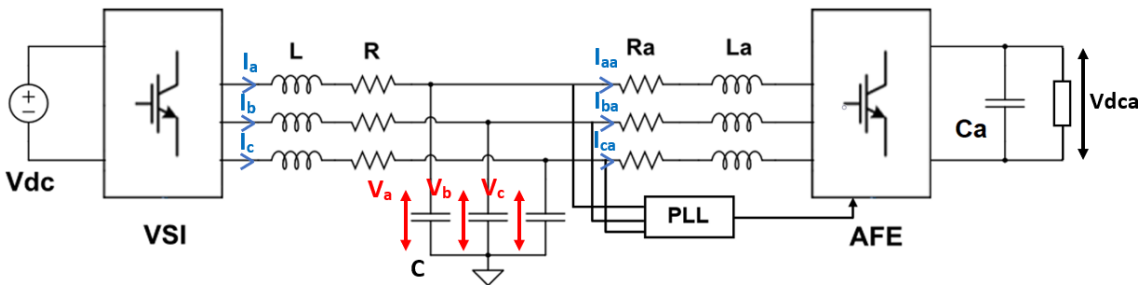

Figure 2.3: The Basic Notional System Under Investigation in this study

The VSI and AFE are both identical 2-level three-phase active rectifiers utilizing IGBT technology to interface the switching action in each leg.

The VSI is supplied directly from a fixed DC source (V_{dc}), which the VSI converts to generate the three-phase grid. The output of the VSI is directly connected to a three-phase LCR filter. Where L represents the filter inductance value, R the intrinsic resistance of the inductor and C the value of capacitance. The generated three-phase grid is then directly connected to the AFE via its input LR filter. In this case L_a and R_a represent the inductance value and the intrinsic resistance of said inductor respectively. The AFE functions as an active rectifier, converting the AC input power to DC, used to power DC loads. The DC-Link capacitor C_a is used to smooth the DC output voltage, filtering remaining AC components from the line. The load in the case study will take the form of either a standard resistive load, or a non-linear constant power load (CPL). In general the CPL load case will be analysed as it exaggerates the non-linear dynamics of the AFE , which is better for demonstrating the performance of proposed designs.

2.1.1 The Voltage Source Inverter

The circuit diagram of a standard Voltage Source Inverter is shown in Figure 2.4. The VSI is typically a DC/AC converter, which is fed by a fixed DC source. The output AC voltages are independent from the load and dependant only on the commutation of the switches S_1 to S_6. The output current waveforms and amplitudes are however dependant on the nature of the output load. The VSI converter for this study consists of a strict DC voltage source which feeds directly in the a 2-Level Three-Phase Insulated-Gate Bipolar Transistor (IGBT) bridge. The output of the bridge feeds into a three-phase LCR filter network, which thereafter outputs into the AC load, or in this case, the three-phase AC distribution bus.

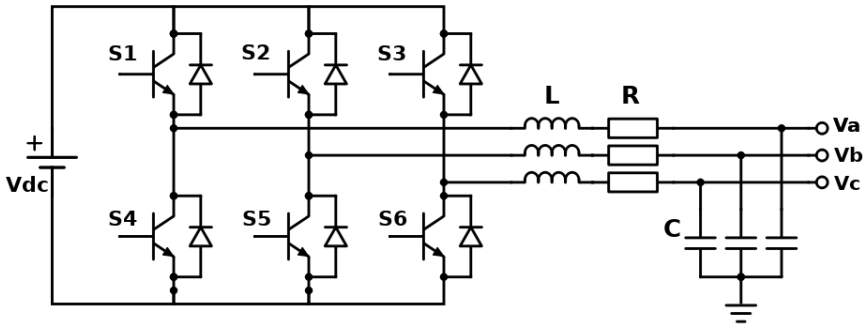

Figure 2.4: Voltage Source Inverter Circuit Diagram

Assuming, as it should be, the DC source voltage is fixed, an expression for the each of the phase voltages can be shown to be:

$$\begin{cases} V_a = \frac{1}{2}(1 + S_a)V_{dc} \\ V_b = \frac{1}{2}(1 + S_b)V_{dc} \\ V_c = \frac{1}{2}(1 + S_c)V_{dc} \end{cases} \tag{2.1}$$

The terms $S_{\langle a,b,c \rangle}$ are the continuous modulation signals applied to each leg. In general each modulation signal takes the form of either a sine or cosine function of the form:

$$\begin{cases} S_a = m_a \cos(\omega t - \alpha) \\ S_b = m_b \cos(\omega t - \alpha) \\ S_c = m_c \cos(\omega t - \alpha) \end{cases} \tag{2.2}$$

Where the term $m_{\langle a,b,c \rangle}$ is the modulation index, which in conventional use typically varies in the range of 0 to 1. If the modulation index varies, as it should do, in the range of 0 to 1, the

signal is termed in the 'linear modulation range', whilst values over 1 or less than 0 are referred to as the 'over modulation range'.

Assuming the converter is operating within the linear modulation range, where the appending value to a switch $S_{\langle a,b,c\rangle}$ is associated to the percentage time the switch is on for a given period T_s, e.g 0.8 = 80%.

From this, the valid switching functions to the phase voltages can be found to be as follows:

$$V_a = \frac{V_{dc}}{2}(S_1 + S_4) \quad V_b = \frac{V_{dc}}{2}(S_2 + S_5) \quad \frac{V_{dc}}{2}(S_3 + S_6) = V_c \tag{2.3}$$

Assuming that the system voltages are balanced, the phase-to-neutral voltage representation with switching functions can therefore be found to be:

$$\begin{cases} V_a = \frac{V_{dc}}{6}(2S_1 - S_2 - S_3) \\ V_b = \frac{V_{dc}}{6}(2S_2 - S_1 - S_3) \\ V_c = \frac{V_{dc}}{6}(2S_3 - S_2 - S_1) \end{cases} \tag{2.4}$$

Which is equivalently:

$$\begin{bmatrix} V_a \\ V_b \\ V_c \end{bmatrix} = \frac{V_{dc}}{6} \begin{bmatrix} 2 & -1 & -1 \\ -1 & 2 & -1 \\ -1 & -1 & 2 \end{bmatrix} \begin{bmatrix} S_1 \\ S_2 \\ S_3 \end{bmatrix} \tag{2.5}$$

DQ Equivalent Model

In a system, where voltages, currents and switching states are time-variant quantities across three alternative phases, it can prove to be difficult to perform steady-state analysis, and controller designs. There are common mathematical transformations which can be applied however which can transform a three-phase time varying system into two coupled DC systems which allow for easier analysis to be undertaken. This is known as a Clarke-Park Transformation, or commonly referred to as the DQ transform.

The first step in the DQ transformation, as the alternative name suggests, is the Clarke Transformation. The Clarke transform takes in the three-phase voltages, and converts them into two voltage values within the $\alpha\beta$-frame; hence the name, the $\alpha\beta$ transformation, which this is more commonly referred to as. Assuming balanced voltage conditions across each of the three phases outputted from the VSI, each phase is 120° out of phase from one another. These three-phase voltages can be easily mapped into two voltage quantities by performing the transformation in (2.6). This transformation is shown on the axis frames in Figure 2.5a, and in the time domain in Figure 2.5b.

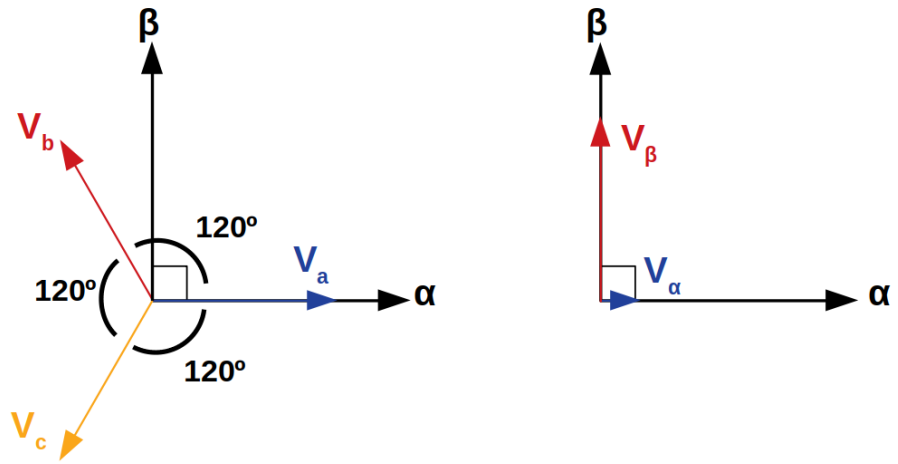

(a) Left hand figure representing Cartersian vector representation of balanced-three-phase voltages and right side depicting the equivalent point in the $\alpha\beta 0$ stationary domain

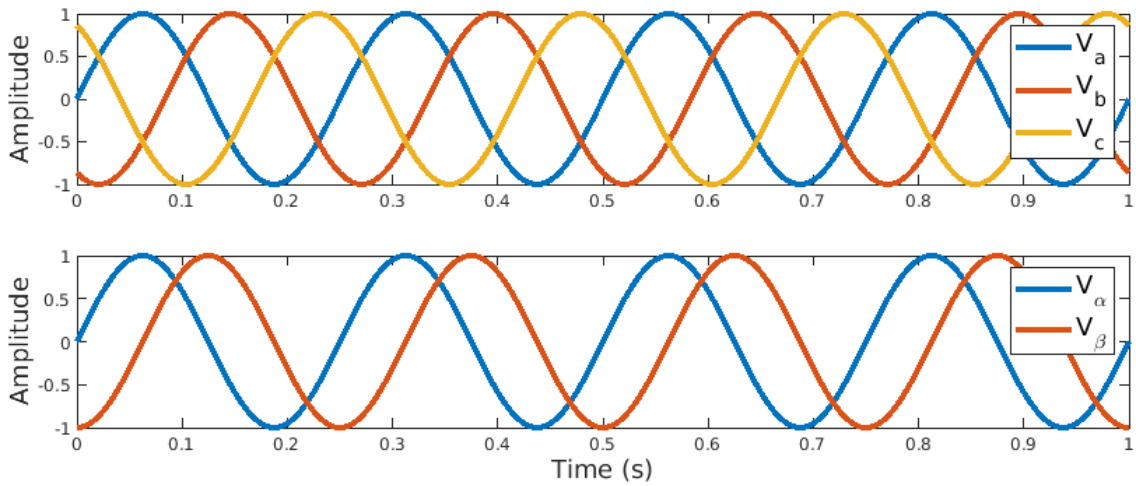

(b) Graphical abc-frame to $\alpha\beta$ frame representation

Figure 2.5: Representation of going from ABC to the $\alpha\beta$ domain

$$\begin{bmatrix} V_\alpha \\ V_\beta \end{bmatrix} = \frac{2}{3} \begin{bmatrix} 1 & -\frac{1}{2} & -\frac{1}{2} \\ 0 & \frac{\sqrt{3}}{2} & -\frac{\sqrt{3}}{2} \end{bmatrix} \begin{bmatrix} V_a \\ V_b \\ V_c \end{bmatrix} \tag{2.6}$$

The Clarke transformation has thus converted a three-phase system into two oscillating voltage reference points. Whilst it is simpler to analyse two rotating voltages instead of three, the $\alpha\beta$ voltages are still AC in nature, and thus more complex AC analysis would still have to be conducted on systems in this frame. However, the voltages V_α and V_β are each values on the α and β axes

respectively which can be resolved to single point values in the $\alpha\beta$ frame. Therefore, when analysing the $\alpha\beta$ voltages observed in Figure 2.5b, the points clearly rotate about the origin, whose radius is equal to that of the amplitude of the abc voltages, as shown in Figure 2.6, where ω is the grid angular frequency, and t the instantaneous time from initial start time $t_0 = 0s$.

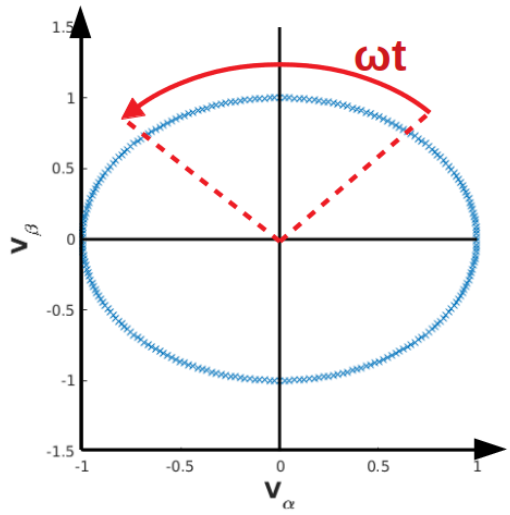

Figure 2.6: The $\alpha\beta$ resultant points over time circling around the origin at frequency ω

As the amplitude of the three-phase voltage remains unchanged, each point over time in the $\alpha\beta$ frame is equidistant from the origin. Therefore, relative to the origin, each $\alpha\beta$ point is changing only in angle θ. Thus came the idea of introducing a rotating reference frame, which rotates at the same rate of the phase voltages.

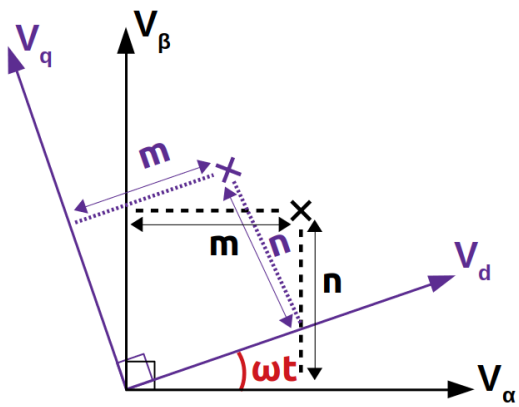

Figure 2.7: Axial depiction of the $\alpha\beta/dq$ transformation

The Park transformation, more widely known as the $\alpha\beta$ - DQ transform, does exactly this. As the phase of the grid changes, the angle of rotation for the dq reference frame also changes. One

can assume the $\alpha\beta$ frame in this case as the dq frame at zero angle. As the phase changes over time, the angle of rotation for the dq-frame changes equally. As the point moves through the $\alpha\beta$ frame, the point in the rotating dq frame remains constant, as if never having moved position. Therefore, for a full rotation of the phase voltages, the position in the dq-frame remains constant, at the axial dq voltages V_d and V_q. This is shown in the time domain in Figure 2.8.

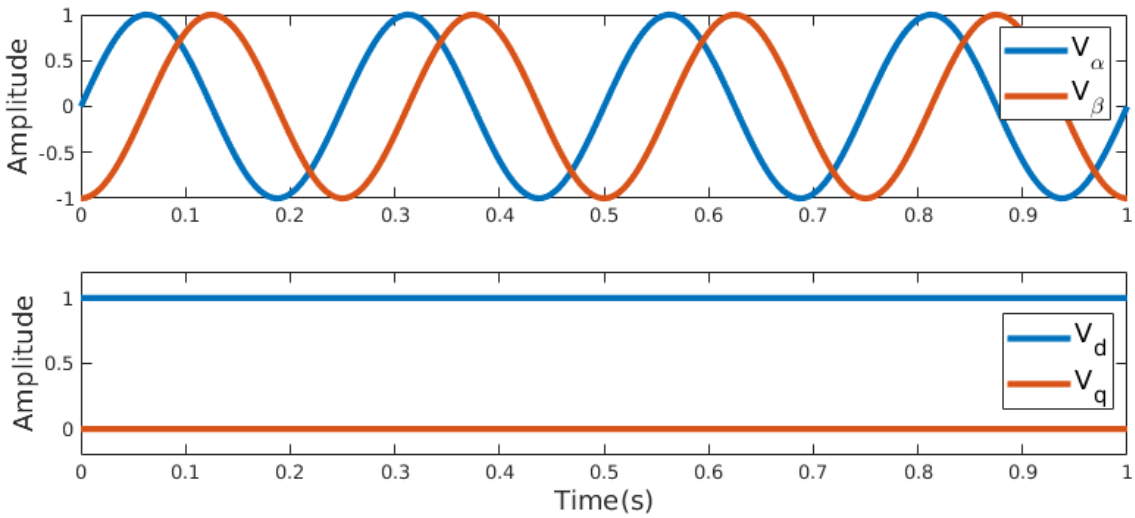

Figure 2.8: Time domain representation of $\alpha\beta$ to dq transformation

Thus, an alternating time variant three-phase AC signal, has now been transformed into two DC based voltage signals, which enables us to perform simpler DC based stability analysis and controller design on a complex 3-phase AC system. The mathematical transformation from $\alpha\beta$ frame to the dq-frame is defined in (2.7), where the direct abc-frame to dq-frame is shown in (2.8).

$$\begin{bmatrix} V_d \\ V_q \end{bmatrix} = \begin{bmatrix} \cos(\omega t) & \sin(\omega t) \\ -\sin(\omega t) & \cos(\omega t) \end{bmatrix} \begin{bmatrix} V_\alpha \\ V_\beta \end{bmatrix} \tag{2.7}$$

$$\begin{bmatrix} V_d \\ V_q \end{bmatrix} = \frac{2}{3} \begin{bmatrix} \cos(\omega t) & \cos(\omega t - \gamma) & \cos(\omega t + \gamma) \\ -\sin(\omega t) & -\sin(\omega t - \gamma) & -\sin(\omega t + \gamma) \end{bmatrix} \begin{bmatrix} V_a \\ V_b \\ V_c \end{bmatrix} \quad \gamma = \frac{2\pi}{3} \tag{2.8}$$

From Figure 2.8, it is clear how each axial term relates back to the three-phase voltages. The d-axis term V_d corresponds directly the peak voltage of the three-phase grid, and thus this value can be used to directly control grid voltage amplitudes. The q axis corresponds to the power factor (PF) between phases, where a value of 0 for V_q indicates the power factor is at unity, PF = 1.

In this thesis, since these dq voltages represent the voltages across the grid capacitors in the

dq frame, to distinguish from the soon to be discussed AFE dq frame, these dq voltages generated from the VSI shall from hereafter be referred to as V_{cd} and V_{cq} for the $d-$ and $q-$ axis voltages respectively.

Having now defined the process to perform a dq transformation on the grid voltages, the process in order to accurately model the VSI in terms of the newly defined DQ terms needs to be performed.

For this description, assume that T is the DQ transformation from the abc-frame:

$$T = \frac{2}{3}\begin{bmatrix} \cos(\omega t) & \cos(\omega t - \gamma) & \cos(\omega t + \gamma) \\ -\sin(\omega t) & -\sin(\omega t - \gamma) & -\sin(\omega t + \gamma) \end{bmatrix} \tag{2.9}$$

The description of the phase voltages in terms of the switching functions of the VSI was previously described in (2.5). Applying the DQ transform in (2.8), to this description develops a definition of the VSI dq voltages in terms of its dq modulation indexes.

$$T^{-1}V_{dq} = \frac{V_{dc}}{6}\begin{bmatrix} 2 & -1 & -1 \\ -1 & 2 & -1 \\ -1 & -1 & 2 \end{bmatrix} T^{-1}m_{dq} \tag{2.10}$$

Where:

$$V_{dq} = \begin{bmatrix} V_{cd} \\ V_{cq} \end{bmatrix} \qquad m_{dq} = \begin{bmatrix} m_d \\ m_q \end{bmatrix} = T\begin{bmatrix} S_1 \\ S_2 \end{bmatrix} \tag{2.11}$$

Following the methodology presented in [104], the switching functions as derived in (2.5), can be transformed into the DQ representations as follows, by process of pre-multiplication:

$$V_{dq} = \frac{V_{dc}}{6}2\begin{bmatrix} \cos(\omega t) & \cos(\omega t - \gamma) & \cos(\omega + \gamma) \\ -\sin(\omega t) & -\sin(\omega t - \gamma) & -\sin(\omega t + \gamma) \end{bmatrix} T^{-1}m_{dq} \tag{2.12}$$

$$V_{dq} = \frac{V_{dc}}{6}3TT^{-1}m_{dq} \tag{2.13}$$

and thus:

$$V_{dq} = \frac{V_{dc}}{2}m_{dq} \tag{2.14}$$

which defines the relationship between the VSI dq voltages to the modulation indexes. Following this, and referring back to Figure 2.4, the dq equivalent circuit can therefore be approximated.

Firstly, each of the phase voltages as a representation of the dynamics of each of their passive components can be shown to be:

$$\begin{bmatrix} V_a(t) \\ V_b(t) \\ V_c(t) \end{bmatrix} = R\begin{bmatrix} i_a(t) \\ i_b(t) \\ i_c(t) \end{bmatrix} + L\frac{d}{dt}\begin{bmatrix} i_a(t) \\ i_b(t) \\ i_c(t) \end{bmatrix} \tag{2.15}$$

Performing the Clarke-Park transformation on (2.15) results in the following representation:

$$TV_{abc} = TRi_{abc} + LT\Big[\frac{d}{dt}(i_{abc}(t))\Big] \tag{2.16}$$

$$T\begin{bmatrix} V_{an}(t) \\ V_{bn}(t) \\ V_{cn}(t) \end{bmatrix} = TR\begin{bmatrix} i_a(t) \\ i_b(t) \\ i_c(t) \end{bmatrix} + TL\left[\frac{d}{dt}\begin{bmatrix} i_a(t) \\ i_b(t) \\ i_c(t) \end{bmatrix}\right] \tag{2.17}$$

However, a differential term cannot be directly transformed in the same manner as the other terms. In order to approach this problem, first the dq transformation of the currents must be undertaken such that:

$$\frac{d}{dt}\begin{bmatrix} i_a(t) \\ i_b(t) \\ i_c(t) \end{bmatrix} = \frac{2}{3}\frac{d}{dt}\left[\begin{bmatrix} \cos(\omega t) & -\sin(\omega t) \\ \cos(\omega t - \gamma) & -sin(\omega t - \gamma) \\ \cos(\omega t + \gamma) & -sin(\omega t + \gamma) \end{bmatrix}\begin{bmatrix} i_{id}(t) \\ i_{iq}(t) \end{bmatrix}\right] \tag{2.18}$$

In the case for i_a (and also applicable to phases b and c), by use of the product rule, its derivative can be found to be:

$$\frac{di_a}{dt} = \frac{2}{3}\left[-\omega i_d(t)\sin(\theta) + \tfrac{di_d}{dt}\cos(\theta) - \omega i_q(t)\cos(\theta) + \tfrac{di_q}{dt}\sin(\theta)\right], \quad \theta = \omega t \tag{2.19}$$

Since:

$$\frac{d}{dt}\cos(\theta) = -\omega\sin(\theta) \tag{2.20}$$

$$\frac{d}{dx}\cos(\theta + \gamma) = -\omega\sin(\theta + \gamma) \tag{2.21}$$

a representation of the current differentials in dq-frame form is therefore:

$$T\left[\frac{d}{dt}\begin{bmatrix} i_a(t) \\ i_b(t) \\ i_c(t) \end{bmatrix}\right] = \frac{2\omega}{3}\begin{bmatrix} \cos(\theta) & -\sin(\theta) \\ \cos(\theta - \gamma) & -\sin(\theta - \gamma) \\ \cos(\theta + \gamma) & -\sin(\theta + \gamma) \end{bmatrix}\begin{bmatrix} -i_{iq}(t) \\ i_{id}(t) \end{bmatrix} + \frac{2}{3}\begin{bmatrix} \cos(\theta) & -\sin(\theta) \\ \cos(\theta - \gamma) & -\sin(\theta - \gamma) \\ \cos(\theta + \gamma) & -\sin(\theta + \gamma) \end{bmatrix}\begin{bmatrix} \frac{di_{id}}{dt} \\ \frac{di_{iq}}{dt} \end{bmatrix} \tag{2.22}$$

Substituting (2.22) back into (2.17) a full representation of the system in dq-frame form can be realised:

$$T\begin{bmatrix} V_{an}(t) \\ V_{bn}(t) \\ V_{cn}(t) \end{bmatrix} = TR\begin{bmatrix} i_a(t) \\ i_b(t) \\ i_c(t) \end{bmatrix} + \omega L\begin{bmatrix} -i_{iq}(t) \\ i_{id}(t) \end{bmatrix} + L\begin{bmatrix} \frac{di_d}{dt} \\ \frac{di_q}{dt} \end{bmatrix} \tag{2.23}$$

and thus the final derivation of the dq-frame form of the VSI phase voltages being:

$$\begin{bmatrix} V_{cd}(t) \\ V_{cq}(t) \end{bmatrix} = \begin{bmatrix} \frac{V_{dc}}{2}m_d \\ \frac{V_{dc}}{2}m_q \end{bmatrix} = R\begin{bmatrix} i_{id}(t) \\ i_{iq}(t) \end{bmatrix} + \omega L\begin{bmatrix} -i_{iq}(t) \\ i_{id}(t) \end{bmatrix} + L\begin{bmatrix} \frac{di_{id}}{dt} \\ \frac{di_{iq}}{dt} \end{bmatrix} \tag{2.24}$$

By following the exact same approach, the dq-frame representation of the VSI phase currents can also be derived.

The VSI phase currents are represented in (2.25), where it is assumed that the current from VSI output, $i_{\langle a,b,c\rangle}$, is entirely being drawn by the grid (or load), $i_{a_{\langle a,b,c\rangle}}$, and into the filter capacitor.

$$\begin{bmatrix} i_a(t) \\ i_b(t) \\ i_c(t) \end{bmatrix} = \begin{bmatrix} i_{a_a}(t) \\ i_{a_b}(t) \\ i_{a_c}(t) \end{bmatrix} + C\frac{d}{dt}\begin{bmatrix} V_{an} \\ V_{bn} \\ V_{cn} \end{bmatrix} \tag{2.25}$$

As has been done before when deriving the voltages, applying the dq transformation results in differential voltage terms across the capacitor which needs resolving separately.

$$T\begin{bmatrix} i_a(t) \\ i_b(t) \\ i_c(t) \end{bmatrix} = T\begin{bmatrix} i_{a_a}(t) \\ i_{a_b}(t) \\ i_{a_c}(t) \end{bmatrix} + TC\left[\frac{d}{dt}\begin{bmatrix} V_{an} \\ V_{bn} \\ V_{cn} \end{bmatrix}\right] \tag{2.26}$$

Following the methods presented in (2.18)-(2.24) on (2.26), the dq-frame representations of the VSI currents can be calculated to be:

$$\begin{bmatrix} I_{id}(t) \\ I_{iq}(t) \end{bmatrix} = \begin{bmatrix} I_{ad}(t) \\ I_{aq}(t) \end{bmatrix} + \omega C\begin{bmatrix} -V_{cq}(t) \\ V_{cd}(t) \end{bmatrix} + C\frac{d}{dt}\begin{bmatrix} V_{cd}(t) \\ V_{cq}(t) \end{bmatrix} \tag{2.27}$$

The equations defined in (2.24) and (2.27) are what derive the equivalent dq circuits which allows DC analysis methods to be conducted on the AC VSI system, and are shown in Figure 2.9, where the equivalent source voltages in the model are given by (2.14) [105].

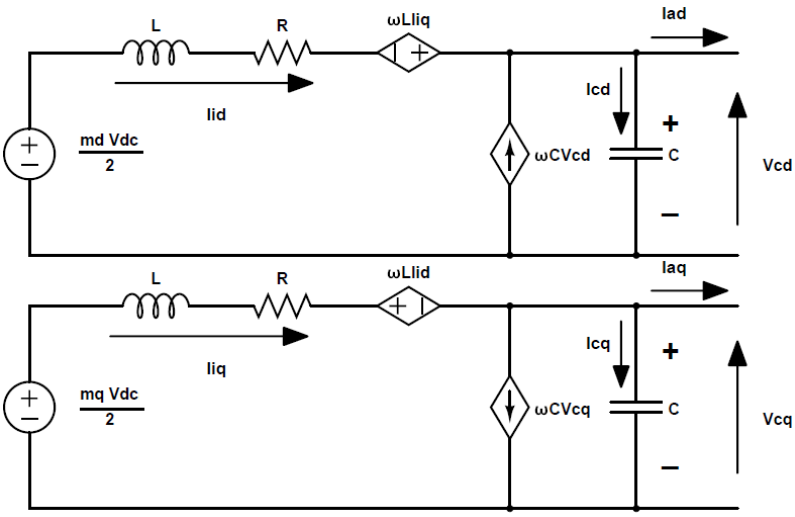

Figure 2.9: VSI dq-frame equivalent circuit

As previously stated, the equivalent dq model of the VSI comprises of two separate $d-$ and $q-$ frame DC circuits, which are coupled together through the inductor current $\omega L V_{c\langle d,q\rangle}$, and capacitor voltages $\omega V_{c\langle d,q\rangle}$.

The equations (2.24) and (2.27) constitute what are commonly known as 'state equations'. States of a system are generally comprised of the storage elements in the electric circuit, for instance in this case the capacitor and inductor. By making the current and voltage derivatives across the capacitor and inductor the subject in each of the state equations, the VSI dynamic equations can be found to be:

$$\begin{cases} \dot{I_{id}} = -\frac{R}{L} I_{id} - \frac{1}{L} V_{cd} + \omega L I_{iq} + \frac{m_d}{2L} V_{dc} \\ \dot{V_{cd}} = \frac{1}{C} I_{id} + \omega V_{cq} - \frac{1}{C} I_{ad} \\ \dot{I_{iq}} = -\omega I_{id} - \frac{R}{L} I_{iq} - \frac{1}{L} V_{cq} + \frac{m_q}{2L} V_{dc} \\ \dot{V_{cq}} = \frac{1}{C} I_{iq} - \omega V_{cd} - \frac{1}{C} I_{aq} \end{cases} \tag{2.28}$$

VSI Equilibrium Point Derivation

As previously discussed when deriving the dq transforms, it was shown the the $d-$ axis controls the amplitude of resultant three-phase waveforms and the $q-$ axis their power factor. With regards to generating and controlling a converter with the purpose of supplying an AC bus, control of the dq voltages are of paramount importance, as in general, grids are defined by their voltage characteristics, with output current dependant entirely on the types of load on the grid. Therefore, in standard operation of the VSI, the VSI will be controlled to operate at given reference dq voltages. Assuming both V_{cd} and V_{cq} are both operating at their reference values, equilibrium values for the dq currents, and modulation indexes can be formulated.

The system is considered to be at steady state, when all differential terms of the VSI state equations are 0.

$$\begin{cases} 0 = -\frac{R}{L} I_{id} - \frac{1}{L} V_{cd}^* + \omega I_{iq} + \frac{m_d}{2L} V_{dc} \\ 0 = \frac{1}{C} I_{id} + \omega V_{cq}^* - \frac{1}{C} I_{ad} \\ 0 = -\omega I_{id} - \frac{R}{L} I_{iq} - \frac{1}{L} V_{cq}^* + \frac{m_q}{2L} V_{dc} \\ 0 = \frac{1}{C} I_{iq} - \omega V_{cd}^* - \frac{1}{C} I_{aq} \end{cases} \tag{2.29}$$

Terms superscripted '*' are states at their reference or steady-state values. By simply solving (2.29), the dq currents I_{id} and I_{iq}, and the dq modulation indexes m_d and m_q can be found to be:

$$I_{id}^* = I_{ad} - \omega C V_{cq}^* \tag{2.30}$$

$$I_{iq}^* = \omega C V_{cd}^* + I_{aq} \tag{2.31}$$

$$m_d^* = \frac{2(-CLV_{cd}^*\omega^2 - I_{iq}^*\omega L + I_{id}^* R)}{V_{dc}} \tag{2.32}$$

$$m_q = \frac{2(I_{iq}^* R + I_{id}\omega L + CRV_{cd}^*\omega)}{V_{dc}} \tag{2.33}$$

Because we wish to operate the converter at unity power factor at all times for good power delivery, the above derivations assumes that V_{cq} is set strict to a reference of 0V. The terms I_{ad} and I_{aq} are independent of the VSI operating point, and are dependant on the AFE equilibrium point which is further discussed in Section 2.1.2.

2.1.2 The Active Front End Active Rectifier

The circuit diagram of the AFE is shown in Figure

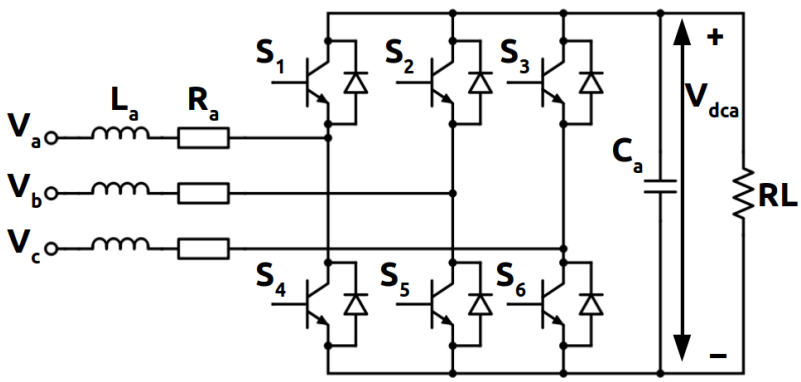

Figure 2.10: Active Front End Rectifier Circuit Diagram

Active Front End Converters draw three-phase current from the AC bus, and converts it by commutation of the switches S_1 to S_6 to DC. In this application, the AFE draws in the three-phase voltages via its input RL circuit whose inductance and intrinsic resistance are L_a and R_a respectively. The IGBT modules S_1 to S_6 are controlled in a manner to provide a DC voltage across the DC-Link capacitor C_a, and to the load. For all the work covered in this thesis, the load can constitute as either a standard resistive load, which will be referred to as R_L. The other is a Constant Power Load, or CPL, and will be referred to as P_l. As the name suggest, this load always requires a constant referenced power being delivered to it and is highly non-linear. AFE's are very commonly used to interface variable speed drives which are classic examples of CPL. A CPL is used in the case of this work due to the ability to exaggerate further the non-linear dynamics of the AFE, and emphasise greater the power of the proposed designs in this work.

Typically, it is assumed that the three-phase voltage source is balanced, and will thus take the form of the output voltages of the VSI.

$$V_a = V_{cd}^* \sin(\omega t) \tag{2.34}$$

$$V_b = V_{cd}^* \sin(\omega t - \gamma) \tag{2.35}$$

$$V_c = V_{cd}^* \sin(\omega t + \gamma) \tag{2.36}$$

Where as discussed in the previous section V_{cd}^* is the reference variable on the VSI to control the three-phase voltage amplitude and V_{cq} set to zero as discussed previously.

Due to the fact that the AFE is in technical terms the exact same core circuit, the switch definitions are exactly the same, replacing the DC source voltage with that of the DC-Link voltage V_{dc_a}.

Therefore, the relation between the phase voltage, switching duty cycle and the DC-Link voltage is:

$$\frac{V_{dc_a} p_{\langle a,b,c\rangle,n}}{2} = V_{\langle a,b,c\rangle,n} \tag{2.37}$$

Where the term p referrers to the the modulation indexes of the AFE.

As has been performed on the VSI, the AFE being intrinsically a three-phase system can too be transformed into the dq domain representation for easier DC based analysis to be performed.

Starting with the analysis of the phase voltages, these voltages can be defined as:

$$\begin{bmatrix} V_{an}(t) \\ V_{bn}(t) \\ V_{cn}(t) \end{bmatrix} = R_a \begin{bmatrix} i_{a_a}(t) \\ i_{a_b}(t) \\ i_{a_c}(t) \end{bmatrix} + L_a \left[\frac{d}{dt} \begin{bmatrix} i_{a_a}(t) \\ i_{a_b}(t) \\ i_{a_c}(t) \end{bmatrix} \right] \tag{2.38}$$

which is very similar in relation to that presented in (2.15). By following exact same procedure to that presented in (2.16) to (2.24), the dq form from the point of view of the phase voltages can be realised to be:

$$\begin{bmatrix} V_{cd}(t) \\ V_{cq}(t) \end{bmatrix} = R_a \begin{bmatrix} i_{ad}(t) \\ i_{aq}(t) \end{bmatrix} + \omega L_a \begin{bmatrix} -i_{aq}(t) \\ i_{ad}(t) \end{bmatrix} + L_a \begin{bmatrix} \frac{di_{ad}}{dt} \\ \frac{di_{aq}}{dt} \end{bmatrix} - \begin{bmatrix} \frac{V_{dc_a} p_d}{2} \\ \frac{V_{dc_a} p_q}{2} \end{bmatrix} \tag{2.39}$$

The terms defined in (2.39) thus give the state equations for the current derivatives across the inductor. However, the other storage element of the AFE is the capacitor C_a on the DC side. In order to develop the state equation for the AFE, an analysis needs to be performed on the DC current which is delivered by the converter. The total current I_O drawn from the converter must deliver current to both, the DC-Link capacitor, and the load, such that:

$$I_O = C_a \frac{dV_{dc_a}}{dt} + I_L \tag{2.40}$$

Where:

$$I_O = \frac{1}{2}\begin{bmatrix} p_a & p_b & p_c \end{bmatrix}\begin{bmatrix} i_{a_a} \\ i_{a_b} \\ i_{a_c} \end{bmatrix} \tag{2.41}$$

It follows that transforming the three-phase equations in (2.41) into the dq axis:

$$I_O = \frac{1}{2}\left[T^{-1}\begin{bmatrix} p_d \\ p_q \end{bmatrix}\right]^T T^{-1}\begin{bmatrix} I_{ad} \\ I_{aq} \end{bmatrix} \tag{2.42}$$

$$I_O = \frac{1}{2}\begin{bmatrix} p_d & p_q \end{bmatrix}\frac{3}{2}TT^{-1}\begin{bmatrix} I_{ad} \\ I_{aq} \end{bmatrix} \tag{2.43}$$

and therefore:

$$I_O = \frac{3}{4}(I_{ad}p_d + I_{aq}p_q) \tag{2.44}$$

Following on from (2.40), remember that this system can constitute of either a resistive load, R_L or a CPL. Dependant on the type of load, the load current I_L will alter.

Simply, for a resistive load I_L is simply:

$$I_L = \frac{V_{dc_a}}{R_L} \tag{2.45}$$

whilst on the other hand, for a CPL, I_L will be:

$$I_L = \frac{P_l}{V_{dc_a}} \tag{2.46}$$

so the two state-equations which can be formulated based on the type of load can be found to be:

Resistive Load Dynamic Equation:

$$C_a\frac{dV_{dc_a}}{dt} = \frac{3}{4}(I_{ad}p_d + I_{aq}p_q) - \frac{V_{dc_a}}{R_L} \tag{2.47}$$

Constant Power Load Dynamic Equation:

$$C_a\frac{dV_{dc_a}}{dt} = \frac{3}{4}(I_{ad}p_d + I_{aq}p_q) - \frac{P_l}{V_{dc_a}} \tag{2.48}$$

The transformations defined in (2.39) to (2.47) or (2.48) give rise to the equivalent circuit form:

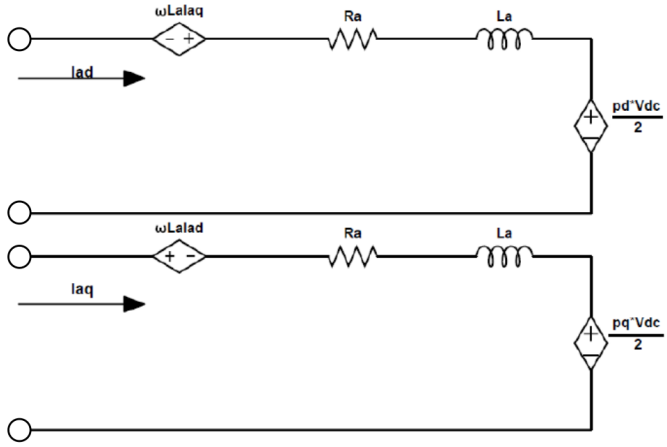

Figure 2.11: AFE DQ Equivalent Circuit

AFE Operating Equilibrium Point

As pointed out, and assuming the AFE is operating at given fixed reference values, the equilibrium points for the AFE can be defined. Again with the AFE, we wish to ensure that the output DC voltage is controlled to a fixed value $V^*_{dc_a}$. However, similarly to the AFE we need to ensure the AFE operates at unity power factor, to guarantee good power flow from the grid to load. In the VSI, this was achieved by directly controlling the q axis voltage, however the AFE only has dq currents which can be controlled. Again, the q axis current I_{aq} like the q axis voltage V_{cq} for the VSI can be controlled to a reference value of 0A to ensure unity power factor, and is thus assumed in the below equilibrium point approximations.

Again, by setting the differentials of each state equation in (2.39) and (2.47)-(2.48) to zero, and adopting the above assumptions, the equilibrium points for I_{ad} and the modulation indexes p_{dq} can be found to be:

Resistive Load Case:

$$\begin{cases} 0 = -\frac{R_a}{L_a} I_{ad} + \omega I_{aq} - \frac{1}{2L_a} V_{dc_a} p_d + \frac{V_{cd}}{L_a} \\ 0 = \frac{R_a}{L_a} I_{aq} - \omega I_{aq} - \frac{1}{2L_a} V_{dc_a} p_q + \frac{V_{cq}}{L_a} \\ 0 = \frac{3}{4C_a}(I_{ad} p_d + I_{aq} p_q) - \frac{1}{R_L C_a} \end{cases} \tag{2.49}$$

$$p^*_d = \frac{\sqrt{R_L} V^*_{cd} + \sigma}{\sqrt{R_L} V^*_{dc_a}} \qquad p^*_q = \frac{L_a \omega (\sqrt{R_L} V^*_{cd}) - \sigma}{\sqrt{R_L} R_a V^*_{dc_a}} \tag{2.50}$$

$$I^*_{ad} = \frac{\sqrt{R_L} V^*_{cd} - \sigma}{2\sqrt{R_L} R_a} \tag{2.51}$$

$$\sigma = \pm\sqrt{R_L V^{*2}_{cd} - \frac{8 R_a V^*_{dc_a}}{3}} \tag{2.52}$$

Constant Power Load Case:

$$\begin{cases} 0 = -\frac{R_a}{L_a} I_{ad} + \omega I_{aq} - \frac{1}{2L_a} V_{dc_a} p_d + \frac{V_{cd}}{L_a} \\ 0 = \frac{R_a}{L_a} I_{aq} - \omega I_{aq} - \frac{1}{2L_a} V_{dc_a} p_q + \frac{V_{cq}}{L_a} \\ 0 = \frac{3}{4C_a}(I_{ad} p_d + I_{aq} p_q) - \frac{P_l}{C_a V_{dc_a}} \end{cases} \tag{2.53}$$

$$p_d^* = \frac{V_{cd}^* + \sigma}{2R_a} \qquad p_q^* = -\frac{L_a \omega (V_{cd}^* - \sigma)}{R_a V_{dc_a}^*} \tag{2.54}$$

$$I_{ad}^* = \frac{V_{cd}^* - \sigma}{2R_a} \tag{2.55}$$

where:

$$\sigma = \pm\sqrt{V_{cd}^{*2} - \frac{8P_l R_a}{3}} \tag{2.56}$$

As it can be seen for each case, each of the equilibrium points has two possible values dependant on the sign of σ chosen. The selection of the ideal sign on σ is not a trivial matter. In either case, one of the points will result in a unrealistically high value in I_{ad}. Thus, the correct selection of σ is the value which results in the smallest I_{ad}^*. This point shall be used hereafter for all studies covered in this thesis.

2.2 System Linearisation and Feedback Control Concepts

For the system under investigation as shown in Figure 2.3, the VSI and AFE converters are to be interfaced together to form a simplified grid network. In order to ensure that these converters operate to the desired reference values V_{cd}, V_{cq}, I_{aq} and V_{dc_a} which are set by the user, a control system must be designed. Typically, such controllers which are implemented into the systems are 'linear controls'. This infers that generally, a given change to the system inputs would result in a proportional change to the system outputs. Such controllers can be implemented on systems whose behaviours can be termed 'linear time invariant'; for instance parameters of the system not changing their value over time. Whilst the VSI is a typical linear system; the AFE is considered not since it is interfaced with a non-linear load (the CPL for instance). As the VSI is directly interfaced to the AFE, the global grid system thus becomes a non-linear one. Therefore, if a global optimisation using linear based control systems is desired, the system must be converted into a linear, or 'linearised' form.

2.2.1 Linearisation of the Notional System

Generally, non-linear systems take the form:

$$\begin{cases} \dot{x}(t) = f(x(t), u(t)) \\ y(t) = g(x(t), u(t) \end{cases} \tag{2.57}$$

Where $y(t)$ is a function describing the system outputs in terms of the states and inputs.

Linearisation of a non-linear system is usually applied at the desired point of system operation, and thus results in a linear-dynamic approximation of the system around the local area around the operating point. In the previous section, the equilibrium points of the system were defined in (2.30)-(2.33) for the VSI, and (2.51)-(2.52) for the AFE. Looking at linearising around these operating points, the system equations in (2.57) becomes:

$$\begin{cases} 0 = f(x^*(t), u^*(t)) \\ y^*(t) = g(x^*(t), u^*(t)) \end{cases} \tag{2.58}$$

Assume now a small perturbation is applied to the system which shifts the system away from its natural steady state operating point. This perturbation can be reflected in the system equations as:

$$\begin{cases} \delta\dot{x}(t) = f(x^*(t) + \delta x_p(t), u^*(t) + \delta u_p(t)) \\ \delta y(t) = g(x^*(t) + \delta x_p(t), u^*(t) + \delta u_p(t)) \end{cases} \tag{2.59}$$

where x_p and u_p define the perturbations on the states and inputs respectively. It is desired that for even for these small perturbations away from the system steady state point we can still have relative accuracy on how this effects the behaviour of the system. To linearise the system accurately about its steady-state operating point, one can utilise a first order Taylor series approximation, such that:

$$\delta\dot{x}(t) = f(x^*(t), u^*(t)) + \left.\frac{\partial f}{\partial x}\right|_{x^*,u^*} \partial x(t) + \left.\frac{\partial f}{\partial u}\right|_{x^*,u^*} \partial u(t) \tag{2.60}$$

$$y^* + \delta y(t) = g(x^*(t), u^*(t)) + \left.\frac{\partial g}{\partial x}\right|_{x^*,u^*} \partial x(t) + \left.\frac{\partial g}{\partial u}\right|_{x^*,u^*} \partial u(t) \tag{2.61}$$

From equations (2.60) and (2.61), four linearised differentials have been obtained. For the term $\left.\frac{\partial f}{\partial x}\right|_{x^*,u^*} \partial x(t)$, this describes the dynamics of the system states in the linearised region around the system steady state operating point. The term $\left.\frac{\partial f}{\partial u}\right|_{x^*,u^*} \partial u(t)$ defines the approximated linear

change which occurs to the dynamic equations with regards to the input. Then $\left.\frac{\partial g}{\partial x}\right|_{x^*,u^*} \partial x(t)$ defines how perturbations to the states influence the system output in the linear region, and finally $\left.\frac{\partial g}{\partial u}\right|_{x^*,u^*} \partial u(t)$ defines how any external disturbances to the system can influence the system in the linearised region. Each of these terms can be solved by performing the Jacobi method on each of the system state equations [106]. This results in what is commonly known as the state-space matrices which take the form:

$$\begin{aligned} \dot{x} &= Ax + Bu \\ y &= Cx + Du \end{aligned} \tag{2.62}$$

where:

$$\begin{aligned} A &= \left.\frac{\partial f}{\partial x}\right|_{x^*,u^*} \partial x(t), \qquad B = \left.\frac{\partial f}{\partial u}\right|_{x^*,u^*} \partial u(t) \\ C &= \left.\frac{\partial g}{\partial x}\right|_{x^*,u^*} \partial x(t), \qquad D = \left.\frac{\partial g}{\partial u}\right|_{x^*,u^*} \partial u(t) \end{aligned} \tag{2.63}$$

It must however be noted that the state-space matrix will only be an accurate description of the non-linear system for the majority of cases to only very small perturbations to the system states; any perturbation that is too large a change may fall out the accuracy of the linearised model. Hence, this system description is also commonly known as the small-signal model.

Linearisation of the Non-linear AFE Model

Assuming the system is operating at the referenced DC voltage $V^*_{dc_a}$, and the q-axis current is controlled to a value I^*_{aq}, and thus is operating at the equilibrium point resulting from equations (2.54) and (2.55), applying the above methodology results in the perturbed system [104]:

Resistive Load:

$$\begin{cases} \dot{\delta I_{ad}} = -\frac{R_a}{L_a}\delta I_{ad} + \omega\delta I_{aq} - \frac{\delta V_{dc_a} p^*_d}{2L_a} - \frac{V^*_{dc_a}\delta p_d}{2L_a} + \frac{1}{L_a}\delta V_{cd} \\ \dot{\delta I_{aq}} = \omega\delta I_{ad} - \frac{R_a}{L_a}\delta I_{aq} - \frac{\delta V_{dc_a} p^*_q}{2L_a} - \frac{V^*_{dc_a}\delta p_q}{2L_a} + \frac{1}{L_a}\delta V_{cq} \\ \dot{\delta V_{dc_a}} = \frac{3}{4C_a}(\delta I_{ad}p^*_d + I^*_{ad}\delta p_d + \delta I_{aq}p^*_q + I^*_{aq}\delta p_d) - \frac{1}{R_L C_a}\delta V_{dc_a} \end{cases} \tag{2.64}$$

Constant Power Load:

$$\begin{cases} \dot{\delta I_{ad}} = -\frac{R_a}{L_a}\delta I_{ad} + \omega\delta I_{aq} - \frac{\delta V_{dc_a} p^*_d}{2L_a} - \frac{V^*_{dc_a}\delta p_d}{2L_a} + \frac{1}{L_a}\delta V_{cd} \\ \dot{\delta I_{aq}} = \omega\delta I_{ad} - \frac{R_a}{L_a}\delta I_{aq} - \frac{\delta V_{dc_a} p^*_q}{2L_a} - \frac{V^*_{dc_a}\delta p_q}{2L_a} + \frac{1}{L_a}\delta V_{cq} \\ \dot{\delta V_{dc_a}} = \frac{3}{4C_a}(\delta I_{ad}p^*_d + I^*_{ad}\delta p_d + \delta I_{aq}p^*_q + I^*_{aq}\delta p_d) - \frac{P_l}{C_a V^{*2}_{dc_a}}\delta V_{dc_a} \end{cases} \tag{2.65}$$

Therefore, writing down the linearised state-space matrices in the form presented in (2.62) and (2.63) results in the definitions:

Resistive Load **Constant Power Load**

$$A_R = \begin{bmatrix} -\frac{R_a}{L_a} & \omega & \frac{p_d^*}{2L_a} \\ -\omega & -\frac{R_a}{L_a} & -\frac{p_q^*}{2L_a} \\ \frac{3p_d^*}{4C_a} & \frac{3p_q^*}{4C_a} & -\frac{1}{R_L C_a} \end{bmatrix} \qquad A_C = \begin{bmatrix} -\frac{R_a}{L_a} & \omega & \frac{p_d^*}{2L_a} \\ -\omega & -\frac{R_a}{L_a} & -\frac{p_q^*}{2L_a} \\ \frac{3p_d^*}{4C_a} & \frac{3p_q^*}{4C_a} & \frac{P_l}{C_a V_{dc_a}^{*2}} \end{bmatrix} \tag{2.66}$$

$$B_{afe} = \begin{bmatrix} -\frac{V_{dc_a}^*}{2L_a} & 0 \\ 0 & -\frac{V_{dc_a}^*}{2L_a} \\ \frac{3I_{ad}^*}{4C_a} & \frac{3I_{aq}^*}{4C_a} \end{bmatrix} \tag{2.67}$$

$$C = \begin{bmatrix} 0 & 1 & 0 \\ 0 & 0 & 1 \end{bmatrix} \tag{2.68}$$

$$x = \begin{bmatrix} I_{ad} \\ I_{aq} \\ V_{dc_a} \end{bmatrix} \qquad u = \begin{bmatrix} p_d \\ p_q \end{bmatrix} \tag{2.69}$$

In general, the disturbance matrix D is often neglected in the modelling procedure to aid in the analysis and design of the system, as has been done in this example.

Global Model System Linearisation

With the VSI and AFE directly interconnected together through the AC bus, these systems can be considered a single 'global' system. As can also be seen by the VSI and AFE state equations in (2.28) and (2.53) respectively that one another's dynamic equations are dependant on states of the other. The complete state equation model for the full VSI + AFE global system is shown in (2.70)

$$\begin{cases} \dot{I_{id}} = -\frac{R}{L} I_{id} + \omega I_{iq} - \frac{1}{L} V_{cd} - \frac{m_d}{2L} V_{dc} \\ \dot{V_{cd}} = \frac{1}{C} I_{id} + \omega V_{cq} - \frac{1}{C} I_{ad} \\ \dot{I_{iq}} = -\omega I_{id} - \frac{R}{L} I_{iq} - \frac{1}{L} V_{cq} + \frac{m_q}{2L} V_{dc} \\ \dot{V_{cq}} = \frac{1}{C} I_{iq} - \omega V_{cd} - \frac{1}{C} I_{aq} \\ \dot{I_{ad}} = \frac{1}{L_a} V_{cd} - \frac{R_a}{L_a} I_{ad} + \omega I_{aq} - \frac{p_q}{2L_a} V_{dc_a} \\ \dot{I_{aq}} = \frac{1}{L_a} V_{cq} - \omega I_{ad} - \frac{R_a}{L_a} I_{aq} - \frac{p_q}{2L_a} V_{dc_a} \\ \dot{V_{dc_a}} = \frac{3}{4C_a}(I_{ad} p_d + I_{aq} p_q) - \frac{I_L}{C_a} \end{cases} \tag{2.70}$$

Where I_L is load dependant, taking the expression (2.45) or (2.46) for either resistive or CPL respectively. Whilst the VSI is a linear system and therefore wouldn't require linearisation on its

own the global model with the inclusion of the non-linear AFE model, the global system becomes non-linear and thus the VSI model must also be linearised inclusively. Therefore the global state matrix A from (2.62) can be found to be:

$$A_G = \begin{bmatrix} -\frac{R}{L} & -\frac{1}{L} & \omega & 0 & 0 & 0 & 0 \\ \frac{1}{C} & 0 & 0 & \omega & -\frac{1}{C} & 0 & 0 \\ -\omega & 0 & -\frac{R}{L} & -\frac{1}{L} & 0 & 0 & 0 \\ 0 & -\omega & \frac{1}{C} & 0 & 0 & -\frac{1}{C} & 0 \\ 0 & \frac{1}{L_a} & 0 & 0 & -\frac{R_a}{L_a} & \omega & -\frac{p_d^*}{2L_a} \\ 0 & 0 & 0 & \frac{1}{L_a} & -\omega & -\frac{R_a}{L_a} & -\frac{p_q^*}{2L_a} \\ 0 & 0 & 0 & 0 & \frac{3p_d}{4C_a} & \frac{3p_q}{4C_a} & \eta \end{bmatrix} \tag{2.71}$$

where for the resistive case:

$$\eta = -\frac{1}{R_L C_a} \tag{2.72}$$

and for the constant power load case:

$$\eta = \frac{P_l}{C_a V_{dc_a}^{*2}} \tag{2.73}$$

The input matrix B for the global model can thus be defined as:

$$B_G = \begin{bmatrix} B_{vsi} & \mathbf{0} \\ \mathbf{0} & B_{afe} \end{bmatrix} \tag{2.74}$$

where bold $\mathbf{0}$ terms define zero matrices of appropriate size and B_{afe} is defined in (2.67) and B_{vsi} can be found to be:

$$B_{vsi} = \begin{bmatrix} \frac{V_{dc}}{2L_a} & 0 \\ 0 & 0 \\ 0 & \frac{V_{dc}}{2L_a} \\ 0 & 0 \end{bmatrix} \tag{2.75}$$

2.2.2 The Theory behind State-Feedback Control

As stated previously, states of an electrical system are in general variables associated to the to storage elements of the circuit, i.e, capacitors and inductors. A powerful feature of these variables however ever are the fact that they allow predictions to the future state of the dynamic system given certain input conditions. By developing system models based on the dynamics of these variables, it allows the development of controllers, whereby dictation of given command inputs can ensure

that the future state values are controlled to and held to specific reference values commanded by the engineer.

The Proportional State-Feedback Controller

For systems involving multiple inputs and multiple outputs, or MIMO systems, linearised state-space state-feedback controller design approaches are very commonly employed. Typically, the state-feedback control system is of the form shown in Figure 2.12.

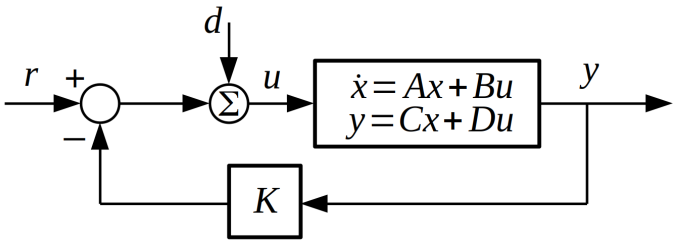

Figure 2.12: State-Feedback Control Block Diagram for State-Space Dynamic System

The terms r refers to the user defined reference inputs, and d represents the external disturbances to the system, and K is the state-feedback controller. The state-space block in Figure 2.12 can be expanded further to form the state-space closed loop block diagram as shown in Figure 2.13.

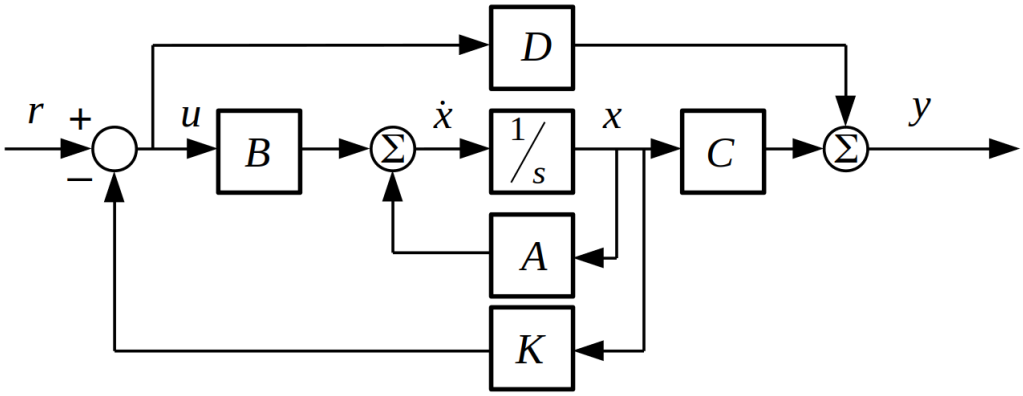

Figure 2.13: Full State-Space Block Diagram

For simplicity, as carried out earlier, when designing the controller K, the disturbances characterised in D are generally set to zero. The goal of this system is to match the output y to the given references r and to hold at these values even in events such as transients. It is assumed in the following descriptions that all the states in x are all measurable. Therefore, all the states at any given time t provides all the information required to predict the position of the system in a future time step. Then, for a time invariant system such as our global system, the control law can be

defined as:

$$u = -Kx \tag{2.76}$$

Where the negative sign indicates the negative feedback of the control, which is essential requirement for closed-loop system stability. Following the derivation of (2.76), and substituting into the state-space equation defined in (2.62), the derivation of the closed-loop dynamic equation can be found to be:

$$\dot{x_{cl}} = (A - BK)x \tag{2.77}$$

Stability is paramount to the control system design, and thus the controller K must ensure that all the eigenvalues of the closed loop representation all have negative real parts, or also refereed to as negative poles. So to check the stability criterion and analyse the eigenvalues of the system, one needs only to find the determinant of the state-matrix.

For **open-loop stability**, this can be found be solving:

$$det(I\lambda - A) = 0 \tag{2.78}$$

and for the **closed-loop stability**:

$$det(I\lambda - [A - BK]) = 0 \tag{2.79}$$

where λ is the eigenvalue and pole of the system, which to ensure stability, especially so in the closed-loop case, must all contain negative real parts.

The reference signals r depicted in Figures 2.12 and 2.13 have been briefly discussed throughout this chapter, and are the values which define the desired peak AC voltages, the grid power factor, the AFE power factor and the desired DC-Link voltage. In this order, the reference matrix r is thus defined as:

$$r = \begin{bmatrix} V_{cd}^* \\ V_{cq}^* \\ I_{aq}^* \\ V_{dc_a}^* \end{bmatrix} \tag{2.80}$$

Additionally, as previously described, the control input in order to shift the states to the desired values, set by r, are the modulation indexes, and thus in the global model the inputs u are defined as:

$$u = \begin{bmatrix} m_d \\ m_q \\ p_d \\ p_q \end{bmatrix} \tag{2.81}$$

Integral Control Action in State-Feedback Systems

The methodology of state-feedback control which has been discussed up to here is only a 'proportional' state-feedback controller and thus does not guarantee the zero steady state error of y to the reference r. In order to ensure that there is zero steady state error between reference and output, an integral action must be introduced.

When defining the error between the reference inputs and the system outputs, it can be characterised as:

$$\dot{\zeta}(t) = r(t) - y(t) \tag{2.82}$$

$$u = -Kx + K_I\zeta(t) \tag{2.83}$$

Where K_I is the state-feedback control acting on the integral of the error between reference and output.

By performing the Laplace transform on (2.82) the following can be received:

$$s\zeta(s) = R(S) - Y(S) = E(S) \tag{2.84}$$

$$\zeta(s) = \frac{E(s)}{s} \tag{2.85}$$

This indicates that the states characterised by ζ introduces an open-loop pole at s=0. This indicates that the state error characterised in ζ is having an integral action applied (integrals in Laplace form are $\frac{1}{s}$, as shown in (2.85)). Therefore, the state equations characterised in ζ shall from henceforth be referred to as integral states. Additionally in this thesis, ζ may also be referred to as x_i when integral states are explicitly mentioned.

The control law with integral actions defined in (2.83) can be written in state-space form as:

$$u(t) = -\begin{bmatrix} K & K_I \end{bmatrix} \begin{bmatrix} x(t) \\ \zeta(t) \end{bmatrix} \tag{2.86}$$

The resultant block diagram incorporating the integral action and state-feedback control can be observed in Figure 2.14.

The resultant closed loop state-space equation can then be yielded as:

$$\begin{bmatrix} \dot{x(t)} \\ \dot{\zeta(t)} \end{bmatrix} = \begin{bmatrix} A - BK & BK_I \\ -C & 0 \end{bmatrix} \begin{bmatrix} x(t) \\ \zeta(t) \end{bmatrix} + \begin{bmatrix} 0 \\ 1 \end{bmatrix} r \tag{2.87}$$

$$y(t) = \begin{bmatrix} C & 0 \end{bmatrix} \begin{bmatrix} x(t) \\ \zeta(t) \end{bmatrix} \tag{2.88}$$

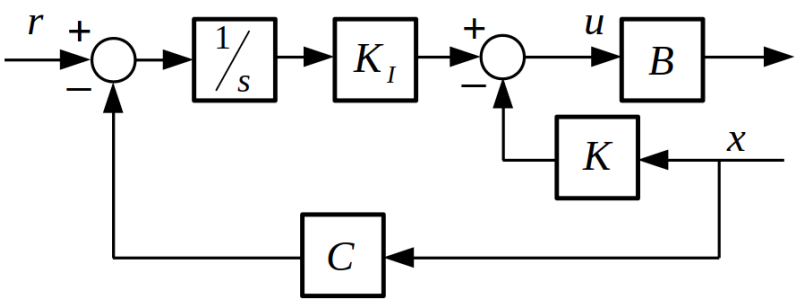

Figure 2.14: State-Space Block Diagram with Integrator Adaptation

The closed loop A matrix defined in (2.87) is comprised as follows:

$$\begin{bmatrix} A - BK & BK_I \\ -C & \mathbf{0} \end{bmatrix} = \begin{bmatrix} A & \mathbf{0} \\ -C & \mathbf{0} \end{bmatrix} - \begin{bmatrix} B \\ \mathbf{0} \end{bmatrix} \begin{bmatrix} K & -K_I \end{bmatrix} \tag{2.89}$$

This therefore provides the A and B matrix forms, by which any controller design for the state-space system must be augmented to, if one wishes to implement integral states into the system. The state-matrix A in this case is defined by $\tilde{A}$ as:

$$\tilde{A} = \begin{bmatrix} A & 0 \\ -C & 0 \end{bmatrix} \tag{2.90}$$

With the references of interest already defined in (2.80), and noting each individual integral state as follows:

$$\dot{\zeta} = \begin{bmatrix} \chi \dot{V}_{cd} \\ \chi \dot{V}_{cq} \\ \chi \dot{I}_{aq} \\ \chi \dot{V}_{dc_a} \end{bmatrix} = r - \begin{bmatrix} V_{cd} \\ V_{cq} \\ I_{aq} \\ V_{dc_a} \end{bmatrix} \tag{2.91}$$

The open-loop state-space equation can be derived in the form:

$$\dot{\tilde{x}} = \tilde{A}\tilde{x} + \tilde{B}u \tag{2.92}$$

where:

$$\tilde{x} = \begin{bmatrix} I_{id} & V_{cd} & I_{iq} & V_{cq} & I_{ad} & I_{aq} & V_{dc_a} & \chi V_{cd} & \chi V_{cq} & \chi I_{aq} & \chi V_{dc_a} \end{bmatrix}^T \tag{2.93}$$

and $\tilde{A}$ and $\tilde{B}$ represented the integral state augmented A and B matrices as derived in (2.89), and are of full form:

$$\tilde{A} = \begin{bmatrix} -\frac{R}{L} & -\frac{1}{L} & \omega & 0 & 0 & 0 & 0 & 0 & 0 & 0 & 0 \\ \frac{1}{C} & 0 & 0 & \omega & -\frac{1}{C} & 0 & 0 & 0 & 0 & 0 & 0 \\ -\omega & 0 & -\frac{R}{L} & -\frac{1}{L} & 0 & 0 & 0 & 0 & 0 & 0 & 0 \\ 0 & -\omega & \frac{1}{C} & 0 & 0 & -\frac{1}{C} & 0 & 0 & 0 & 0 & 0 \\ 0 & \frac{1}{L_a} & 0 & 0 & -\frac{R_a}{L_a} & \omega & -\frac{p_d^*}{2L_a} & 0 & 0 & 0 & 0 \\ 0 & 0 & 0 & \frac{1}{L_a} & -\omega & -\frac{R_a}{L_a} & -\frac{p_q^*}{2L_a} & 0 & 0 & 0 & 0 \\ 0 & 0 & 0 & 0 & \frac{3p_d}{4C_a} & \frac{3p_q}{4C_a} & \eta & 0 & 0 & 0 & 0 \\ 0 & -1 & 0 & 0 & 0 & 0 & 0 & 0 & 0 & 0 & 0 \\ 0 & 0 & 0 & -1 & 0 & 0 & 0 & 0 & 0 & 0 & 0 \\ 0 & 0 & 0 & 0 & 0 & -1 & 0 & 0 & 0 & 0 & 0 \\ 0 & 0 & 0 & 0 & 0 & 0 & -1 & 0 & 0 & 0 & 0 \end{bmatrix} \tag{2.94}$$

$$\tilde{B} = \begin{bmatrix} B_{vsi} & 0 \\ 0 & B_{afe} \\ \mathbf{0} & \mathbf{0} \\ \mathbf{0} & \mathbf{0} \\ \mathbf{0} & \mathbf{0} \\ \mathbf{0} & \mathbf{0} \end{bmatrix} \tag{2.95}$$

With this, the linearised notional system in state-space form has been derived, for which the work presented across Chapters 4 and 5 will be based upon. For more information about the augmentation of integral states, please refer to [107].

2.3 Summary

This chapter fundamentally provides the principle modelling techniques for the notional embedded grid system comprised of a AC bus generating VSI converter, which has an AFE directly connected to it. This system forms a simplified embedded grid system which provides an easy to understand, and easy to utilise platform in order to conduct the research presented in this thesis. The following is a short summary of all that is comprised in this chapter:

1. **The Electrical Characterisation and DQ Modelling**

   The electrical system model was realised by analysis of the switching states of each of the power electronic converters and three-phase equations for each were hence derived. Although, it is widely known the development of controllers in three-phase AC systems are naturally hard to develop controls for and thus the DQ Frame transformation was

introduced. Mathematical and pictorial derivations were developed, and applied to the electrical three-phase model, and was shown that the DQ frame equivalent model of the notional system consisted of two coupled DC equivalent networks, for which simpler, and more well understood linear based controls can be applied to.

2. **System Linearisation and Steady-State Equilibrium Points**
   Having defied the DQ equivalent models of the AC electrical system, it was then easy to derive the state equations which compose dynamic equations direct from the storage elements of the grid, being from the capacitor and inductor voltage and current dynamics respectively. By setting the state-differentials equal to zero, as it would be in steady state condition, it becomes very easy to derive all the necessary equilibrium points of the system. However, it was shown that careful consideration must be made when selecting the steady-state equilibrium position of the AFE. It was shown that the AFE naturally has one equilibrium at much higher values of I_{ad} (possibly 100's of amps) as opposed to the alternate point. Therefore, the point which results in the lesser of the two I^*_{ad} points must be selected for the study hereafter. The methodology of generating the state-space matrices was then shown, by developing partial differentials of the states x and inputs u on the state, and output equation derivations, with the derivations of these state-matrices being essential to the optimal controller design later in the study.

3. **The Concept of State-Feedback Control** An brief introduction behind the theory of state-feedback control was introduced, discussing firstly the formulation of the closed loop controller in the state-space domain, accurately portraying the implementation of such controllers to this system. This is essential in understanding how to grasp the basic concepts of the presented research. Following this, the adaptation of integral states to the state-space model was shown, implemented, and redefined in the state-equations, such that zero steady-state error can be achieved for these controllers when operating at equilibrium.

Chapter 3

Non-linear and Optimal Control Methods

The basic method of state-feedback control introduced in Chapter 2 requires linearisation of the global non-linear system. Therefore, any design based off the linearisation of the system at a given operating point is only valid for small signal deviations for where the linearised model is accurate. However, what if there is a large signal disturbance inflicted? Then the robustness and stability of the whole global system is then brought to question.

However, there are methods which do exist which can extend the region of validity of the linearised model. Most notable of all methods being gain scheduled control. This is where the controller changes according to the current operating condition of the system. When the system moves away from the linearised operating region of one control, a new controller is selected which was designed closer to the current operating point. In essence constantly moving the point of linearisation of the system to match that of the current time. While this method does sound like a simple solution to overcoming this region of validity problem, it is not the most elegant of solutions. For one, a many number of controllers will have to be designed across all the possible situations which the system may encounter. This can result in the need for costly hardware with a great memory capacity to be implemented. Additionally, is has been shown across many studies that gain scheduled control can in-fact impact of the dynamic performance of the system, as the gain scheduled approach can only deal with generally slower dynamic change in order switch control in a non-abrupt manner. Therefore, not the most elegant approach to solving this issue.

This chapter first investigates the common methods of non-linear control from recent literature which have been applied to non-linear systems and power converter applications. It was however discovered that many commonly used non-linear control approaches cannot be applied to applications

such as the one studied in this thesis, and will be fully explained. Following this, an investigation into modern optimal control strategies from recent literature will be investigated, applied and analysed, where finally the desired approach to non-linear system optimisation and control will be selected, discussed, and thoroughly analysed before being fully incorporated into the design procedure of our system.

3.1 Approaches of Non-linear Control

Non-linear control is a subclass of control theory investigating the design of controllers, and the stability analysis of non-linear dynamic systems, including time variant systems.

There are many well understood and easy to implement methods of linear controller design, where many powerful tools exist such as Laplace transforms, Bode and Nyquist plots, to name a few, which can be used to easily design linear control systems to specific design requirements. The general simplicity and the powerful tools available in linear controller design are reasons as to why non-linear dynamic systems are often linearised around an operating point, and linear controllers applied.

However, for reasons stated previously, such linear controls only work within a given region of validity which is not ideal in the terms of large signal disturbances. All real-world dynamic systems are intrinsically non-linear, and therefore a large research effort in recent years has been applied, discovering new methods of non-linear controls. Many of these controllers are being adopted widely across the research community and is slowly becoming common place in industry.

3.1.1 Feedback Linearisation

Feedback Linearisation is often considered among one of the most important approaches to the design of non-linear controllers. The main objective in this approach is to algebraically manipulate the non-linear dynamic system into that of a linear system by which linear control techniques can then be applied. Again, this is a linearisation of a non-linear dynamic system; wouldn't this pose the same issue in that linearised systems only have a certain finite validity region? In general to this approach, the answer is no. The feedback linearisation approach enables the use of a static linear feedback control to be implemented, on non-liner coordinate transformed dynamic system which is based on a differential geometric analysis of the full dynamic system. This means that the non-linearities are ever present still within the feedback-linearised form of the model [108].

General Theory of Classical Feedback Linearisation

Let us consider first a typical non-linear dynamic system of the form:

$$\begin{cases} \dot{x} = f(x) + g(x)u \\ y = h(x) \end{cases} \tag{3.1}$$

where $x = [x_1, \ldots, x_n]^T \in \Re^n$, $u = [u_1, \ldots, u_m]^T \in \Re^m$, and $y = [y_1, \ldots, y_j]^T \in \Re^j$ are the state, input and output vectors respectively; $f(x)$ and $g(x)$ are differentiable vector fields, and $h(x)$ define smooth functions all in the set $D \subseteq R^n$. Such a system can be visualised as that in Figure 3.1.

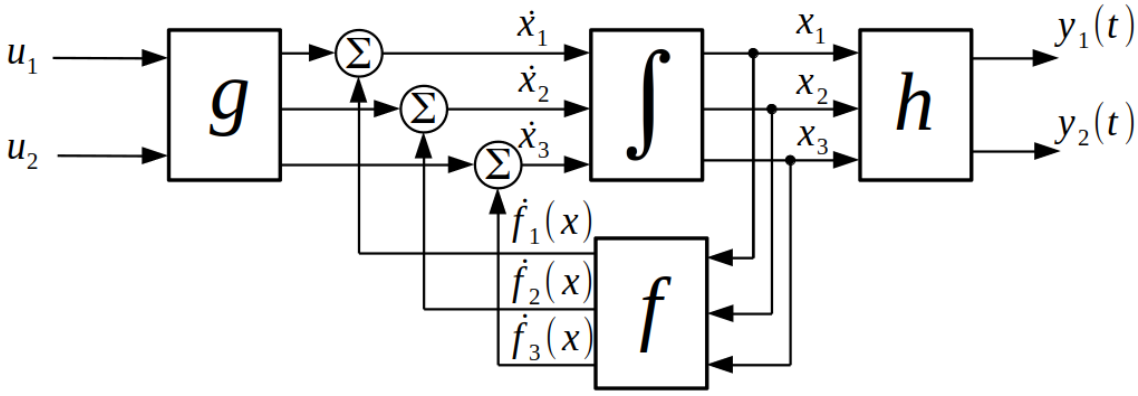

Figure 3.1: Open-loop representation of the Feedback-Linearised model

The aim is to develop a feedback control law on (3.1) of the form:

$$u = a(x) + b(x)v \tag{3.2}$$

which renders an linear input-output map between the new input v to that of the output. From then an outer-loop control strategy can be applied to the resulting linear dynamic system.

To ensure the transformed linear system is of an equivalent representation to the original non-linear dynamic system, the transformation must be a diffeomorphic. If this requirement is held, then Lie derivatives can be the method in which to linearise (3.1) [6].

The goal of Feedback Linearisation in this regard is to produce a transformed system whose states are the outputs y, and its first $(n-1)$ derivatives, such that:

$$\dot{y} = \frac{dh(x)}{dt} = \frac{dh(x)}{dx}\dot{x} \tag{3.3}$$

$$\therefore \frac{dh(x)}{dx}\dot{x} = \frac{dh(x)}{dx}f(x) + \frac{dh(x)}{dx}g(x)u \tag{3.4}$$

For the linearised system, whose outputs are those defined above, it must first be understood how the inputs u is directly involved in this transformed system. This is where the notional of 'relative degree' comes in.

For our system, it is said that the relative degree r at the systems steady-state point x_0 should be considered if:

$$L_g L_f^k h(x) = 0, \quad \forall x \in \Upsilon \subseteq D, \quad k \leq r \tag{3.5}$$

$$L_g L_f^{r-1} h(x_0) \neq 0 \tag{3.6}$$

where Υ is the local neighbourhood of points around the steady-state point x_0, k defines the order of derivative, and the terms L_f and L_g are defined as:

$$L_f h(x) = \frac{dh(x)}{dx} f(x) \tag{3.7}$$

$$L_g h(x) = \frac{dh(x)}{dx} g(x) \tag{3.8}$$

The other notations found in (3.5) and (3.6), and others which will be often referred to in this section are as follows:

$$\begin{aligned} y &= h(x) \\ \frac{dy}{dt} &= L_f h(x) \\ \frac{d^2y}{dt^2} &= L_f^2 h(x) \\ \frac{d^{(r-1)}y}{dt^{(r-1)}} &= L_f^{(n-1)} h(x) \\ \frac{d^r y}{dt^r} &= L_f^r h(x) + L_g L_f^{(r-1)} h(x) u \end{aligned} \tag{3.9}$$

The relative degree r represents the number of times the output function must be differentiated before the input u appears explicitly. For general linear-time-invariant (LTI) systems, the relatively degree is in general the difference between the number of poles and the number of zeros in the system transfer functions.

With the relative degree of the system (3.1) being r, this therefore makes all the Lie derivatives of the form:

$$\sum_{n=1}^{n-1} L_g L_f^i h(x) = 0 \tag{3.10}$$

as first defined in (3.6). What (3.10) therefore directly symbolizes is that the input u has no direct contribution to any of the first $(n-1)$ derivative of y.

The transformation $T(x)$ puts the system into normal form, and is derived from the first $(n-1)$ derivatives, such that:

$$z = T(x) = \begin{bmatrix} z_1(x) \\ z_2(x) \\ \vdots \\ z_{(r-1)}x \end{bmatrix} = \begin{bmatrix} h_1(x) \\ L_f h_1(x) \\ \vdots \\ L_f^{(r_1-1)} h_1(x) \\ \vdots \\ h_m(x) \\ L_f h_m(x) \\ \vdots \\ L_f^{(r_m-1)} h_m(x) \end{bmatrix} \tag{3.11}$$

The transformation matrix $T(x)$ therefore transforms all the trajectories in the original x coordination system, into a new z coordinate system. As long as the functions are subject to the construction of $T(x)$, there will always be a unique solution to z, for which this new dynamic system can be defined as:

$$P_z = \begin{cases} \dot{z_1} = L_f h(x) \\ \dot{z_2} = L_f^2 h(x) \\ \quad \vdots \\ \dot{z_{(r-1)}} = L_f^{(r-1)} h(x) \\ \dot{z_r} = L_f^r h(x) + L_g L_f^{(r-1)} h(x) u \end{cases} \tag{3.12}$$

Simply then, the feedback control law for system in the z coordinate system is:

$$u_z = E^{-1}\Big(- \boldsymbol{\alpha}(x) + v \Big) \tag{3.13}$$

where in the canonical form given m x-coordinate system inputs:

$$E(x) = \begin{bmatrix} L_{g_1} L_f^{(r_1-1)} h_1(x) & \dots & L_{g_m} L_f^{(r_1-1)} h_1(x) \\ \vdots & \ddots & \vdots \\ L_{g_i} L_f^{(r_m-1)} h_m(x) & \dots & L_{g_m} L_f^{(r_m-1)} h_m(x) \end{bmatrix} \tag{3.14}$$

$$\boldsymbol{\alpha}(x) = \begin{bmatrix} L_f^r h_1(x) \\ \vdots \\ L_f^r h_m(x) \end{bmatrix} \tag{3.15}$$

$$v = \begin{bmatrix} y_1^r \\ \vdots \\ y_m^r \end{bmatrix} \tag{3.16}$$

and additionally also renders the following input-output map from v to $z_1 = y$

$$\begin{cases} \dot{z_1} = z_2 \\ \dot{z_2} = z_3 \\ \quad \vdots \\ \dot{z_r} = v \end{cases} \tag{3.17}$$

The linearised system is a cascade of r integrators and the axillary control variables v may be chosen specifically using standard linear control feedback methodology:

$$v = -Kz \tag{3.18}$$

where the transformed state-vector z is the output y and its first $(n-1)$ derivatives, resulting in the new LTI system:

$$\dot{z} = Az + Eu \tag{3.19}$$

with:

$$A = \begin{bmatrix} 0 & 1 & 0 & \dots & 0 \\ 0 & 0 & 1 & \dots & 0 \\ \vdots & \vdots & \vdots & \ddots & \vdots \\ 0 & 0 & 0 & \dots & 1 \\ -k_1 & -k_2 & -k_3 & \dots & -k_r \end{bmatrix} \tag{3.20}$$

and thus with the appropriate selection of the linear control K, we can select the closed loop poles of the closed-loop system.

Feedback Linearisation of the Non-linear AFE Converter

So with the methodology described in (3.1)-(3.20), this can now be applied to the dynamics of the non-linear AFE converter.

The first approach in the attempt in developing a feedback-linearised controller is to apply directly the state equations derived in (2.49) and (2.53), and thus the system in the form required for this approach is as follows:

$$\begin{cases} \begin{bmatrix} \dot{I_{id}} \\ \dot{I_{aq}} \\ \dot{V_{dc_a}} \end{bmatrix} = f(x) + Bu = \begin{bmatrix} -\frac{R_a}{L_a} + \omega I_{aq} + \frac{1}{L_a} V_{cd} \\ -\omega I_{ad} - \frac{R_a}{L_a} I_{aq} + \frac{1}{L_a} V_{cq} \\ -\frac{I_L}{C_a} \end{bmatrix} + \begin{bmatrix} -\frac{1}{2L_a} V_{dc_a} & 0 \\ 0 & -\frac{1}{2L_a} V_{dc_a} \\ \frac{3}{4Ca} I_{ad} & \frac{3}{4Ca} I_{aq} \end{bmatrix} \begin{bmatrix} p_d \\ p_q \end{bmatrix} \\ \begin{bmatrix} y_1 \\ y_2 \end{bmatrix} = \begin{bmatrix} 0 & 1 & 0 \\ 0 & 0 & 1 \end{bmatrix} \begin{bmatrix} I_{ad} \\ I_{aq} \\ V_{dc_a} \end{bmatrix} \end{cases} \tag{3.21}$$

Now, as shown in (3.21), the two system outputs are the states I_{aq} and V_{dc_a} themselves.

Thus the Lie Derivatives derived for the first stage are simply the state equations of the referenced outputs.

$$\dot{y_1} = \dot{I_{aq}} = \left[-\omega I_{ad} - \frac{R_a}{L_a} I_{aq} + \frac{1}{L_a} V_{cd} \right] - \left[\frac{p_q}{2L_a} V_{dc_a} \right] \tag{3.22}$$

$$\dot{y_2} = \dot{V_{dc_a}} = \left[\frac{3p_d}{4C_a} I_{ad} + \frac{3p_q}{4C_a} I_{aq} \right] - \left[\frac{I_L}{C_a} \right] \tag{3.23}$$

As seen in (3.22) and (3.23), the first order Lie Derivatives already have the two input terms $\begin{bmatrix} p_d & p_q \end{bmatrix}^T$ explicitly in their functions. Therefore, in this case the relative degree for both outputs, r_1 and r_2 respectively are 1.

$$r_1 + r_2 = r_T < n \tag{3.24}$$

Because the total relative degree of the system r_T is less than the order of the system, it implicates that I_{ad} is still implicit of the dynamics of the linearised system. Factoring out the terms in (3.22) and (3.23) to those defined in (3.9), the following can be extrapolated:

$$L_{g_1} h_1(x) = 0, \qquad L_{g_2} h_1(x) = -\frac{1}{2L_a} V_{dc_a} \tag{3.25}$$

$$l_{g_1} h_2(x) = \frac{3}{4C_a} I_{ad}, \quad L_{g_2} h_2(x) = \frac{3}{4C_a} I_{aq} \tag{3.26}$$

Therefore, according to (3.13), (3.14) and (3.15), the control law for the system can be defined as:

$$u = \begin{bmatrix} 0 & -\frac{V_{dca}}{2L_a} \\ \frac{3I_{ad}}{4C_a} & \frac{3I_{aq}}{4C_a} \end{bmatrix}^{-1} \left(v - \begin{bmatrix} -\omega I_{ad} - \frac{R_a}{L_a} I_{aq} + \frac{1}{L_a} V_{dc_a} \\ -\frac{I_L}{C_a} \end{bmatrix} \right) \tag{3.27}$$

Thus, according to (3.18), state-feedback control can thus be applied such that:

$$v = \begin{bmatrix} K_1 & 0 \\ 0 & K_2 \end{bmatrix} \begin{bmatrix} e_1 \\ e_2 \end{bmatrix} \tag{3.28}$$

where e is the error between output and reference, as is standard for state-feedback control implementation.

$$e_1 = I_{aq} - I_{aq}^* \qquad e_2 = V_{dc_a} - V_{dc_a}^* \tag{3.29}$$

Substituting (3.28) and (3.29) into (3.27), the following can be received:

$$u = \begin{bmatrix} \frac{2L_a I_{aq}}{V_{dc_a}} & \frac{4C_a}{3I_{ad}} \\ -\frac{2L_a}{V_{dc_a}} & 0 \end{bmatrix} \begin{bmatrix} -K_1 e_1 + \omega I_{ad} + \frac{R_a}{L_a} I_{aq} - \frac{1}{La} V_{cq} \\ -K_2 e_2 + \frac{I_L}{C_a} \end{bmatrix} \tag{3.30}$$

As the output vectors tend to their reference commands, it can be shown that I_{ad} will tend towards:

$$\dot{I_{ad}} = -\frac{R_a}{L_a} I_{ad} - \frac{2I_L V_{dc_a}^*}{3L_a I_{ad}} + \frac{V_{cd}}{L_a} \tag{3.31}$$

which has two equilibrium points equivalent to (2.51) and (2.55), for the resistive and constant power loads respectively. However, the method presented poses a major stability issue which is not seen first hand in this augmentation.

Looking at the phase-diagram of a similar active rectifier system when linearised using feedback linearisation from the study in [6].

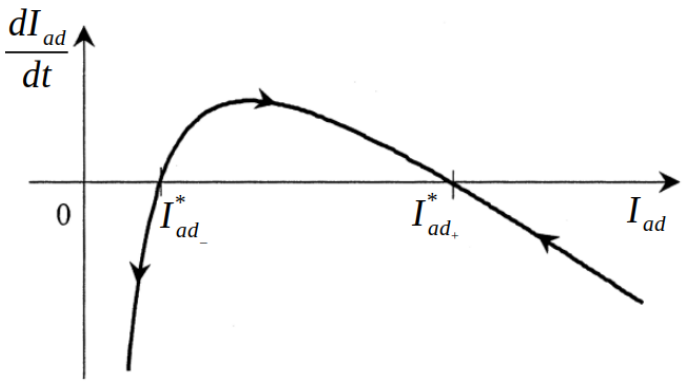

Figure 3.2: Phase Diagram of the Feedback Linearised System at Zero Dynamic [6]

As it can be observed, the minimum current equilibrium point $I_{ad\_}^*$ has vectors tending to infinity, and towards the larger equilibrium point $I_{ad_+}^*$ which can be seen to be a stable. The problem lies in the fact that in the majority of designs, the larger of the two equilibrium points is

often of much higher value than the current rating of most standard converters. Therefore, this attempt of controller design is not feasible in most applications.

Feedback Linearisation of AFE to Overcome the Unstable Equilibrium Point

The effect of this instability is a result of zeros which are found in the right half plane [109]. The study from [6] suggested that to overcome this issue, we could instead of controlling the DC-Link voltage, I_{ad} could be instead controlled to a given reference point. Therefore, in this regard, a reference I_{ad}^* can be set which regulates V_{dc_a} to a desired value.

So, taking (3.21) and reforming it to ensure now currents are the command references to the system we get:

$$\begin{cases} \begin{bmatrix} \dot{I_{id}} \\ \dot{I_{aq}} \\ \dot{V_{dc_a}} \end{bmatrix} = \begin{bmatrix} -\frac{R_a}{L_a} + \omega I_{aq} + \frac{1}{L_a} V_{cd} \\ -\omega I_{ad} - \frac{R_a}{L_a} I_{aq} + \frac{1}{L_a} V_{cq} \\ -\frac{I_L}{C_a} \end{bmatrix} + \begin{bmatrix} -\frac{V_{dc_a}}{2L_a} & 0 \\ 0 & -\frac{V_{dc_a}}{2L_a} \\ \frac{3I_{ad}}{4Ca} & \frac{3I_{aq}}{4Ca} \end{bmatrix} \begin{bmatrix} p_d \\ p_q \end{bmatrix} \\ \begin{bmatrix} y_1 \\ y_2 \end{bmatrix} = \begin{bmatrix} 1 & 0 \\ 0 & 1 \\ 0 & 0 \end{bmatrix} \begin{bmatrix} I_{ad} \\ I_{aq} \\ V_{dc_a} \end{bmatrix} \end{cases} \tag{3.32}$$

Again, performing the Lie derivative on this system results in the follow:

$$\dot{y_1} = \dot{I_{ad}} = \left[-\frac{R_a}{L_a} I_{ad} + \omega I_{aq} + -\frac{1}{L_a} V_{cd} \right] - \left[\frac{p_d}{2L_a} V_{dc_a} \right] \tag{3.33}$$

and $\dot{y_2}$ is the same as (3.23). Both outputs first order Lie derivative hold the input to the system explicitly as before. Therefore, the relative degree is less than the order of the system, as per (3.24), which means that V_{dc_a} is implicit to the dynamics of this linearised system.

As before, the input vector u can thus be found to be:

$$u = \begin{bmatrix} -\frac{1}{2L_a} V_{dc_a} & 0 \\ 0 & -\frac{1}{2L_a} V_{dc_a} \end{bmatrix}^{-1} \left[v + \begin{bmatrix} \frac{R_a}{L_a} I_{ad} + \omega I_{Iaq} + \frac{V_{cd}}{L_a} \\ -\omega I_{ad} - \frac{R_a}{L_a} - \frac{V_{cq}}{L_a} \end{bmatrix} \right] \tag{3.34}$$

Where the closed loop block diagram for the implementation of this control system is given in Figure 3.3.

By closing the loop with state-feedback as performed in (3.28), the internal dynamic equation of the DC-Link voltage can be found to be [6]:

$$\dot{V_{dc_a}} = -\frac{3L_a}{2C_a} \frac{I_{aq}}{V_{dc_a}} \left(\left[K_1 e_1 - \frac{R_a}{L_a} I_{ad} + \omega I_{aq} - \frac{V_{cd}}{L_a} \right] + \left[-K_2 e_2 - \omega I_{ad} - \frac{R_a}{L_a} I_{aq} \right] \right) - \frac{I_L}{C_a} \tag{3.35}$$

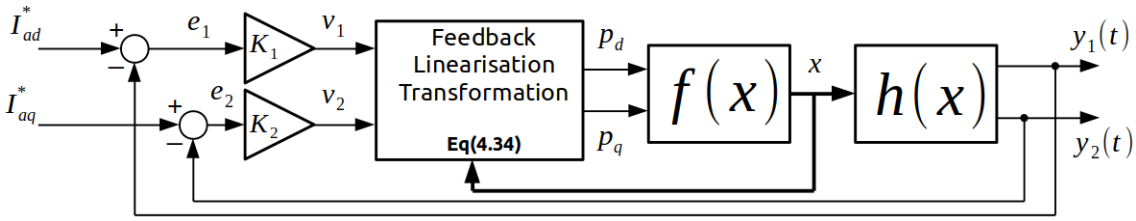

Figure 3.3: Closed Loop Feedback Linearisation Controller with currents as reference inputs [6]

where

$$e_1 = I^*_{ad} - I_{ad} \qquad e_2 = I^*_{aq} - I_{aq} \tag{3.36}$$

At zero dynamic, where I^*_{ad} is fixed and set to the minimum equilibrium point value which results in the required DC-Link voltage V^*_{dc}, and I_{aq} tends to zero for unity PF performance, V_{dc_a} has the zero dynamic form of:

$$\dot{V_{dc_a}} = \frac{1}{R_L C_a V_{dc_a}} \left(V^{*2}_{dc_a} - V^2_{dc_a}\right) \tag{3.37}$$

Analysing the phase diagram of this control system result in the following:

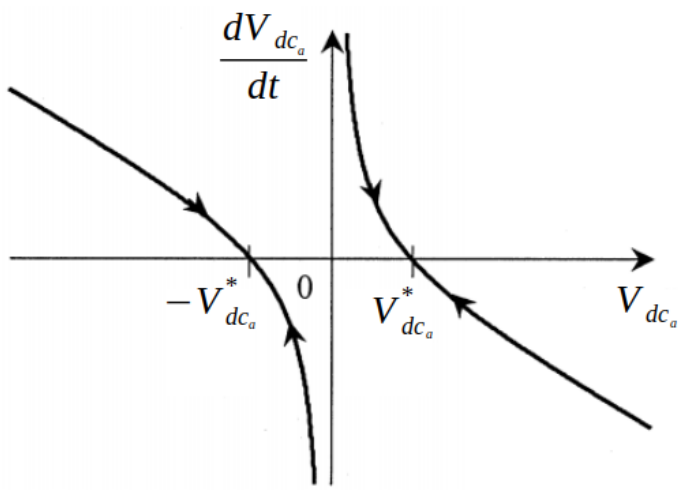

Figure 3.4: Phase Diagram of the Feedback Linearised System at Zero Dynamic for Alternate Input Controller [6]

With this augmentation, is can be clearly seen that both equilibrium points $\pm V^*_{dc_a}$ are stable. In order to ensure we operate at the desired $V^*_{dc_a}$ voltage with zero steady state error, we can control the d-axis current demand by feedback of the required voltage demand using a PI controller. This augmentation is shown in Figure 3.5.

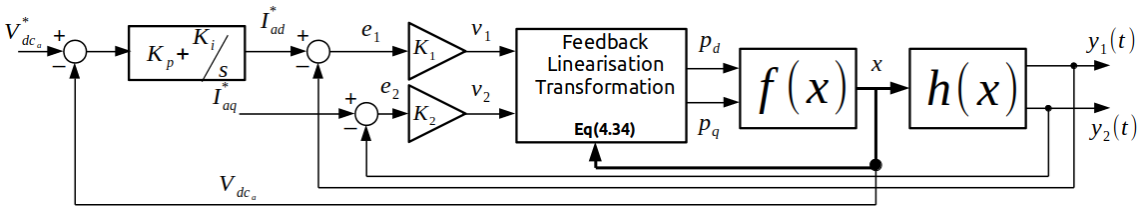

Figure 3.5: Closed Loop Feedback Linearisation Controller with PI controller regulating I_{ad} current reference according to demanded DC-Link Voltage [6]

To analyse how this form of control works in the context of an AFE in an embedded aircraft grid, the system was simulated.

Parameter	Value
Ra	90mΩ
La	400μH
Ca	100μF
ω	800π rads^{-1}
V_{cd}	115V

Table 3.1: AFE Parametric Voltages and Input Voltages

Reference Values	
I_{aq}	0A
V_{dc_a}	400V
P_l	1kW

Table 3.2: Feedback Linearization Control References

Figure 3.6 below shows the average model simulation performed with the parameters in Table 3.1. At 0.05s a 1kW CPL is applied to the AFE to analyse the controllers performance to step loads. All voltage and current references remain constant throughout the test.

The simulative test shows how powerful a method Feedback Linearisation is for a non-linear system. In this test, the highly non-linear characteristic of negative impedance is present during the power transient. Yet, with a deviation from the required reference of only ±4V, and a settling time of only 50ms, it is clear that this form of controller can handle the highly non-linear characteristics very well. In addition, throughout the transient the q-axis current holds strictly to its reference, ensuring that even during the transient, PF is held at unity and efficient power delivery is maintained. The augmentation of the PI controller to regulate the current reference works well in keeping not only a stable current being delivered to the load at steady state, but also ensures zero steady state tracking of the DC-Link voltage to its reference.

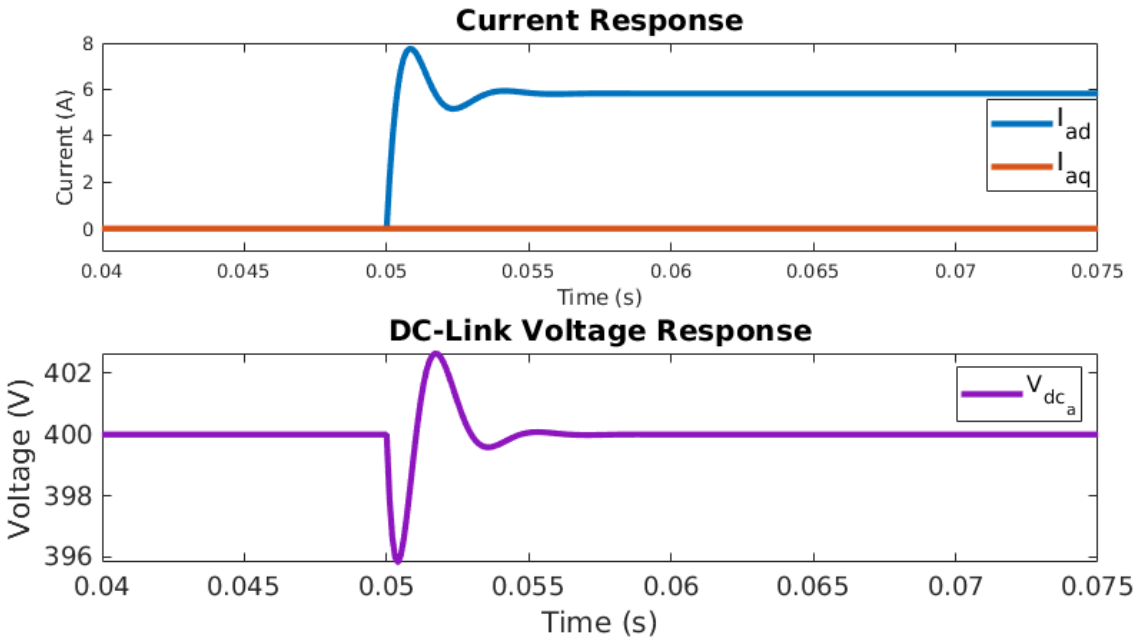

Figure 3.6: 1kW step response of Feedback Linearised Controller with I^*_{ad} PI regulation

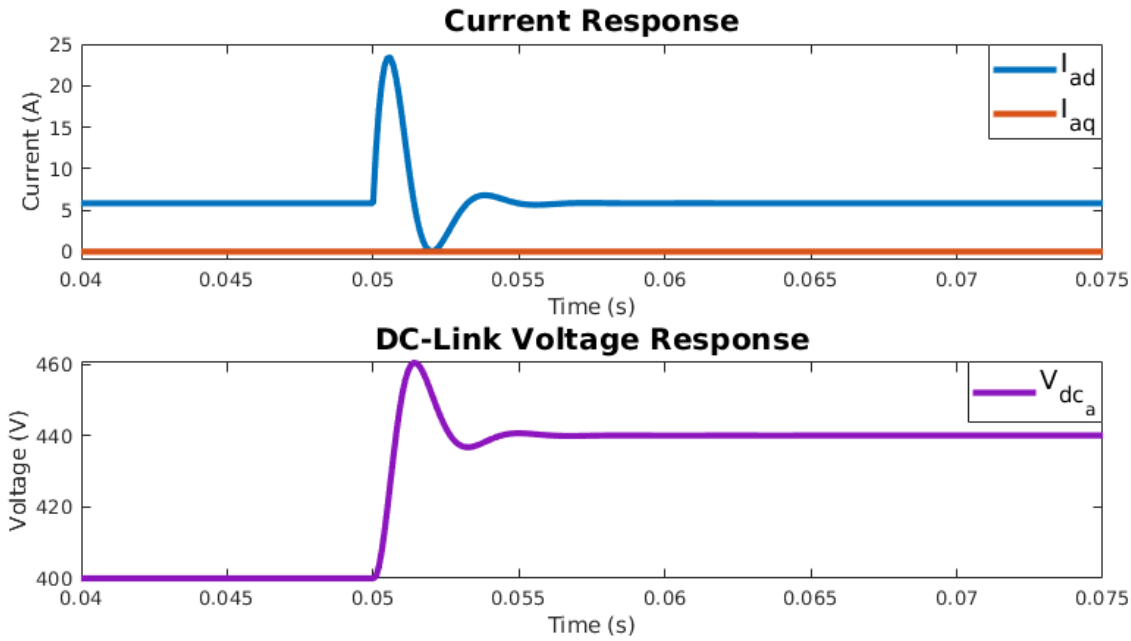

Figure 3.7: Voltage Reference Step Simulation Test of Feedback Linearised Controller

The test shown in Figure 3.7 shows a voltage reference tests. From the notional reference point of 400V, at the time 0.05s the reference voltage is increased by 40V. It is clear, stability is maintained, as it should, as per Figure 3.4 the only region where instability can occur is at 0V.

Good tracking and transient performance of both the current and the voltages can be achieved. With the large voltage change an the 1kW power being delivered to the load, due to the negative resistance characteristic of the load, the current does rise to almost 20A. This is not a fault of the control, but of the non-linearities in the system. However, the system is stabilised around its new operating point as quickly as the power step disturbance.

Augmentation of Feedback Linearised to Global Grid, and its Associated Issues

Clearly, the feedback linearised controller performs extremely well against both the step voltage and power disturbances inflicted to the system, even in the presence of highly non-linear negative resistance phenomena. However, this is the application to only a single converter. As stated previously, though the VSI is intrinsically a linear system, due to the fact we are able to analyse the grid as one global system, where all converters are interfaced to one another, the VSI has a non-linear dynamic; the AFE itself. Thus, if desired to optimize the global system as a whole under one decentralized control scheme whose dynamics are all considered, the VSI must also be augmented in with the AFE for feedback linearisation.

Augmenting the full system, utilising the open-loop zero correction adopted in (3.32), the resultant system to be analysed is:

$$\begin{cases} \begin{bmatrix} \dot{I_{id}} \\ \dot{V_{cd}} \\ \dot{I_{iq}} \\ \dot{V_{cq}} \\ \dot{I_{ad}} \\ \dot{I_{aq}} \\ \dot{V_{dc_a}} \end{bmatrix} = \begin{bmatrix} -\frac{R}{L}I_{id} + \omega I_{iq} - \frac{V_{cd}}{L} \\ \frac{1}{C}I_{id} + \omega V_{cq} - \frac{1}{C}I_{ad} \\ -\omega I_{id} - \frac{R}{L}I_{iq} - \frac{V_{cq}}{L} \\ -\omega V_{cd} + \frac{1}{C}I_{iq} - \frac{1}{C}I_{aq} \\ \frac{R_a}{L_a}I_{ad} + \omega I_{aq} + \frac{1}{L_a}V_{cd} \\ -\omega I_{ad} - \frac{R_a}{L_a}I_{aq} + \frac{1}{L_a}V_{cq} \\ -\frac{I_L}{C_a} \end{bmatrix} + \begin{bmatrix} \frac{V_{dc}}{2L} & 0 & 0 & 0 \\ 0 & 0 & 0 & 0 \\ 0 & \frac{V_{dc}}{2L} & 0 & 0 \\ 0 & 0 & 0 & 0 \\ 0 & 0 & -\frac{V_{dc_a}}{2L_a} & 0 \\ 0 & 0 & 0 & -\frac{V_{dc_a}}{2L_a} \\ 0 & 0 & \frac{3I_{ad}}{4C_a} & \frac{3I_{aq}}{4C_a} \end{bmatrix} \begin{bmatrix} m_d \\ m_q \\ p_d \\ p_q \end{bmatrix} \\ \begin{bmatrix} y_1 \\ y_2 \\ y_3 \\ y_4 \end{bmatrix} = \begin{bmatrix} V_{cd} \\ V_{cq} \\ I_{ad} \\ I_{aq} \end{bmatrix} \end{cases} \tag{3.38}$$

In order to explicitly return the system inputs for the VSI terms, a second order Lie derivative

needs to be performed such that:

$$\ddot{y_1} = \ddot{V_{cd}} = \left[\frac{1}{C}\left(\left(-\frac{R}{L}I_{ad} + \omega I_{iq} - \frac{V_{cd}}{L}\right) - \left(-\frac{R_a}{L_a}I_{ad} + \omega I_{aq} + \frac{V_{cd}}{L_a}\right)\right) + \omega\left(\frac{1}{C}I_{ad} + \omega V_{cq} - \frac{1}{C}I_{ad}\right)\right] + \frac{1}{C}\left[\frac{V_{dc}}{2L}m_d + \frac{V_{dc_a}}{2L_a}p_q\right] \quad (3.39)$$

$$\ddot{y_2} = \ddot{V_{cq}} = \left[\frac{1}{C}\left(\left(-\omega I_{id} - \frac{R}{L}I_{iq} - \frac{V_{cq}}{L}\right) - \left(-\omega I_{ad} - \frac{R_a}{L_a}I_{aq} + \frac{V_{cq}}{L_a}\right)\right) - \omega\left(\frac{1}{C}I_{id} + \omega V_{cq} - \frac{1}{C}I_{ad}\right)\right] + \frac{1}{C}\left[\frac{V_{dc}}{2L}m_q + \frac{V_{dc_a}}{2L_a}p_q\right] \quad (3.40)$$

where the Lie Derivative terms for y_3 and y_4 are exactly those from (3.33) and (3.23) respectively. The total relative degree is 6, which is less than the order of the system and thus fulfils that criteria for feedback-linearisation. However, the major problem when implementing the full system as a feedback linearisation problem comes down to the implementation of the control law (3.13).

When developing the E^{-1} matrix, from the equations (3.39)-(3.40), (3.33) and (3.23), the following is derived:

$$E^{-1} = \left[\begin{array}{cc|cc} \frac{2CL}{V_{dc}} & 0 & \frac{2L}{V_{dc}} & 0 \\ 0 & \frac{2CL}{V_{dc}} & 0 & \frac{2L}{V_{dc}} \\ \hline 0 & 0 & -\frac{2L_a}{V_{dc_a}} & 0 \\ 0 & 0 & 0 & -\frac{2L_a}{V_{dc_a}} \end{array}\right] \quad (3.41)$$

It is absolutely vital, especially in an aircraft system that redundancy, and thus independence between converter sub-systems in implemented into the design of the grid. For one, if systems need to communicate between each other for their controller algorithms, then that would increase the cabling and thus the weight of the system. Additionally if one converter in the whole system were to fail, it would risk shutting down the reset of the electrical system, as controllers of other systems are dependant on that one converters functionality.

This is where the problem with feedback-linearisation occurs for applications such as grid systems. In order to ensure decentralized independent controllers for each subsystem, the E^{-1} matrix, must be diagonal with respect to individual system states. This means the VSI control terms depend only on VSI states and inputs, and likewise for the AFE. As can be observed from (3.41), values are present in the upper right quadrant of the matrix. This means that the VSI in this control implementation is dependant on the dynamics of the AFE. This contradicts the design requirements we look for in the control. Methods were analysed in a way to decouple the system, however all approaches utilised came back inconclusive to the requirements.

So feedback linearisation, as has been shown in numerous literatures is a very effective method of non-linear control for individual non-linear systems. However, when several subsystems are incorporated into the design requiring a decentralized controller approach, feedback linearisation cannot be successfully implemented, in regards to this application. The global system was not simulated or tested using this controller.

So other forms of control system must be utilised for this application.

3.2 Optimal Control Approaches

The previous section portrayed a serious problem which can occur when trying to employ a very popular method of non-linear control, but when decentralization is required problems occur with converters becoming dependant on other converter states. There are other notable methods such as Model Predictive Controls (MPC) or Sliding Mode controls. However, especially with the case of MPC, the control problems becomes far too computationally heavy simply due to the number of states involved in each converter. This makes these kind of control approaches undesirable, even for the simplified notional system, let alone a true power grid, since the time of execution of the algorithm grows exponentially for every new state included into the algorithm. In most cases, system of order 6 and greater may suffer from computational problems.

Whilst a non-linear control would be the preferable option of control of these systems, in order to control across whole regions of operation, such non-linear systems are also very commonly controlled using linear optimal control strategies. This section will analyse the common strategies employed to design and integrate optimal controls to such non-linear systems, beginning first with H_∞ control.

3.2.1 H_∞ Optimization

H_∞ approaches of controller design come from a entirely different perspective than how one would design a control by traditional means. Instead of analysing the problem as a standard control problem, where poles and zeros of the closed loop of the system are chosen specifically for a desired performance, H_∞ analyses the problem in question as a numerical optimization problem, in regards to the minimization of the infinity norm $\|\cdot\|_\infty$ of the dynamic system, which can be defined as follows:

Derivation of a LTI System Infinite Norm $\|\cdot\|_\infty$

Allow $\boldsymbol{M}$ to be of a finite dimensional space. Then when $\forall p \geq 1$, the application of $\|\cdot\|_p$ is a norm, as defined by:

$$\|\boldsymbol{M}\|_p = \left(\sum_i |\boldsymbol{M}_i|^p\right)^{\frac{1}{p}} \tag{3.42}$$

Therefore, the 1-norm of a function $x(t)$ can be given by:

$$\|x(t)\|_1 = \int_0^\infty |x(t)|\, dt \tag{3.43}$$

Thus the 2-norm, which in regards to LTI systems is often referred to as the energy norm, is given by:

$$\|x(t)\|_2 = \sqrt{\int_0^\infty x(t)^T x(t) dt} \tag{3.44}$$

whereby through Parsevals Identity can be found equivalent to [110]:

$$\|x(t)\|_2 = \sqrt{\frac{1}{2\pi}\int_{-\infty}^\infty |x(j\omega)|^2\, d\omega} \tag{3.45}$$

The ∞-norm can then thus be found to be:

$$\|x(t)\|_\infty = \sup_t |x(t)| \tag{3.46}$$

$$= \|x(j\omega)\| = \sup_\omega \|x(j\omega)\| \tag{3.47}$$

Where (3.46) in simple terms can be described as the largest absolute value of $x(t)$ over all time.

The H_∞ is a closed subspace within the L_∞ sub-space of piecewise continuous bounded functions. The L_∞ sub-space is a Banach space of matrix [111] (or scalar value) functions in D which consists of all the complex bounded matrix functions of $x(j\omega), \forall\omega \in \Re$ such that:

$$\sup_{\omega\in\Re} \overline{\sigma}\left[x(j\omega)\right] < \infty \tag{3.48}$$

where $\overline{\sigma}$ denotes the singular value of the system. The H_∞ sub-space is thus all the matrix functions $x(j\omega), \forall\omega \in \Re$, including the open right half plane. The subspace of H_∞, where all the proper and real rational stable transfer matrices being denoted RH_∞.

Typically, in regards to the analysis of the norm to an LTI system in the state-space representation, we analyse the block diagram in Figure 3.8.

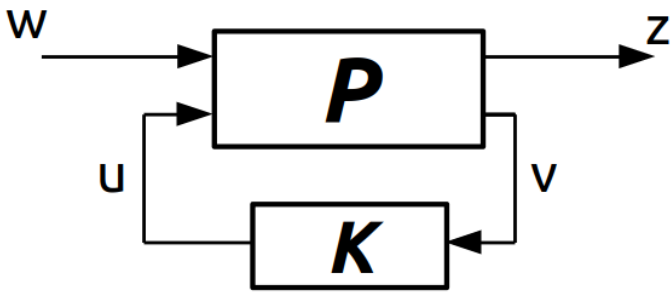

Figure 3.8: Standard Block Configuration for H_∞ analysis

where $\boldsymbol{P}$ is the system plant, which constitutes of the dynamic equations described in (2.62), and $\boldsymbol{K}$ is the closed loop control to be designed. The input w defines the exogenous inputs to the system which include reference, and disturbance signals, and u as usual is the plant inputs. The outputs z are the error signals, or sometimes referred to as the performance signals, and v are all the measurable system states fed back into the control.

The H_∞ norm of this system analyses the transfer function from the disturbance input w, to the performance signal z which belongs to RH_∞. These transfer functions describe the induced energy-to-energy gain, as defined by:

$$\begin{aligned} \|G(j\omega)\|_\infty &= \sup_{\omega\in\Re} \overline{\sigma}\left(G(g\omega)\right) \\ &= \sup_{\omega\in H_\infty} \frac{\|z(s)\|_2}{\|w(s)\|_2} \\ &= \max_{\omega(t)\in L_\infty} \frac{\|z(s)\|_2}{\|w(s)\|_2} \end{aligned} \tag{3.49}$$

Therefore, (3.49) shows that the H_∞ of a proper closed loop LTI system G represents the maximal gain of the frequency response for the transfer function $\frac{z(s)}{w(s)}$. It is also often referred to as the worst case attenuation level in the sense that it represents the maximal amplification the the closed loop system has across the whole frequency set $0 \to \infty$ Hz. In regards to SISO and MIMO systems, it is also a representation of the maximal peak value on the Bode magnitude (singular value) plot of $G(j\omega)$, and thus the largest gain of the system if the system was fed with a harmonic input.

Therefore the closed loop system $G(j\omega)$ will thus be considered BIBO (bounded input, bounded output) stable if and when a bounded input u ($\|u\|_\infty < \infty$) maps to a bounded output y ($\|y\|_\infty < \infty$). A BIBO systems' quantified amplification can thus be evaluated as:

$$y_{peak} = \sup_{0<\|u\|_\infty<\infty} \frac{\|y\|_\infty}{\|u\|_\infty} \tag{3.50}$$

However, in regards to the energy of the system $G(j\omega)$, or in other words, to ensure the system is not too sensitive to the inputs or outputs, it can be quantified using the understanding from (3.44) and (3.49) to result in:

$$y_{energy} = \sup_{0<\|u\|_2<\infty} \frac{\|y\|_2}{\|x\|_2} \tag{3.51}$$

and this is often referred to as the energy gain of the closed loop system, such that:

$$y_{energy} = \sup \omega \, \|G(j\omega)\| = \|G\|_\infty \tag{3.52}$$

and thus overall BIBO stability, and the robustness to sensitivity of a closed loop system can be ensured by minimizing the H_∞ norm of the closed loop system.

Small-Gain Theorem Robustness Analysis

Whilst the above shows how the minimization of the $\|\cdot\|_\infty$ in the controller optimization can aid in the stability and the sensitivity mitigation of the closed loop system, as of yet the value to minimize to, to guarantee the stability across the full frequency set has yet to be discussed. This value will be deduced using what's known as Small Gain Theorem which utilised the block diagram below for its analysis.

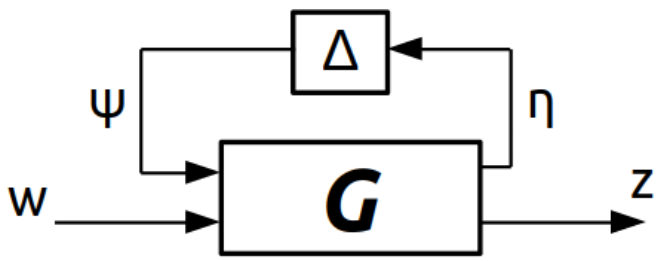

Figure 3.9: Block Diagram to model uncertainty in a system for Small-Gain Theorem

In this case w is an arbitrary input to the system, whilst z are arbitrary outputs. The block Δ characterises the uncertainty dynamics of the system. This can characterise anything from parametric uncertainty to uncertainty in the dynamics of the input and output signals. G characterises the closed loop plant with the controller K inbuilt to stabilize the nominal plant P. Removing Δ thus results in the nominal closed loop system.

In regards to the uncertainty model in Figure 3.9, the stability of such model relies on the assumption that all the transfer functions form the inputs ψ and w to the outputs η and z are all stable. The transfer function representation can be defined as:

$$\begin{pmatrix} \eta \\ z \end{pmatrix} = \begin{pmatrix} M(s) & N(s) \\ J(s) & L(s) \end{pmatrix} \begin{pmatrix} \psi \\ w \end{pmatrix} \tag{3.53}$$

From this, the system transfer function from w to z can be found to be:

$$G_{wz}(s) = L(s) + J(s)\Delta(I - M(s)\Delta)^{-1}N(s) \tag{3.54}$$

It can be shown in [112] that if there is a stable Δ, such that $\|\Delta\|_\infty < 1$, then to guarantee the global stability of G, $\|M(s)\|_\infty < 1$ must be held. From (3.53), M can be defined as the transfer function observed by the perturbation Δ, from the input ψ which imposes the perturbations onto the notional closed loop system G to the outputs η. It is known that all these matrices impart from $\big(I - M(s)\Delta)^{-1}\big)$ are known to be stable, and thus, the system can be considered globally stable when $\big(I - M(s)\Delta)^{-1}\big)$ is guaranteed to be stable $\forall\Delta$. This small gain condition is the condition imposed on the system design on G to ensure global stability of the system.

If the condition $\|M(s)\|_\infty < 1$ is the strict necessity for the global stability of the global controller K, then this allows a designer to select a further constraint in the optimization γ.

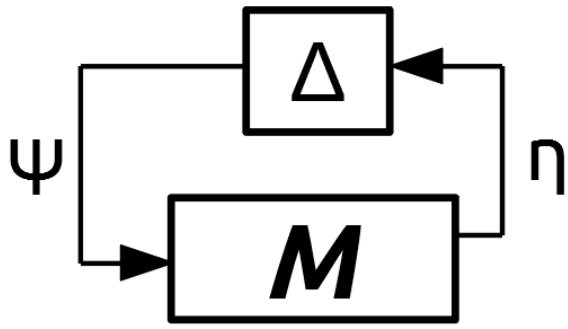

Figure 3.10: Focused Block Diagram on the Small Gain Theorem Stability Constraint

Now suppose that $M(s)$ is RH_∞ stable, and that the constraint γ is a positive scalar. Then this sub-model in Figure 3.10 can be considered a well posed and internally stable system for $\forall\Delta \in RH_\infty$ such that:

$$\|\Delta\|_\infty < \frac{1}{\gamma} \tag{3.55}$$

if and only if

$$\|M(s)\|_\infty < \gamma \tag{3.56}$$

The term γ can therefore be seen as the degree of stability required by the designer. The smaller the value of γ the more globally stable the closed system G is towards uncertainty in the

system. The approach to design a H_∞ optimized controller can thus begin exploring the area of mixed sensitivity controller design.

Mixed Sensitivity H_∞ Controller Design

This is a very well known quote from [113] which discusses the trade-offs of control system design sensitivity and bandwidth performance.

> "The concept of bandwidth is very important in understanding the benefits and trade-offs involved when applying feedback control. It can be easily shown how the peaks in the closed loop transfer functions relate to the quality of the performance. However, for performance we must also consider the speed of response and this leads to the consideration to the bandwidth frequency of the system. In general, a large bandwidth corresponds to a faster rise time, since the high frequency signals are more easily passed onto the outputs. However, a high bandwidth also indicates a system which is sensitive to noise and parameter variations. Conversely, if a bandwidth is small, the time response will be generally slow, and the system usually more robust"

For control designers there is a clear trade-off between designing for a very fast dynamic system, but decreased stability or vice versa. However, optimization techniques such as H_∞ optimization allow for the use of a technique termed mixed sensitivity design to optimize both the closed loop bandwidth and the robust performance of the system.

When designing through by mixed sensitivity approach, the following block diagram is used:

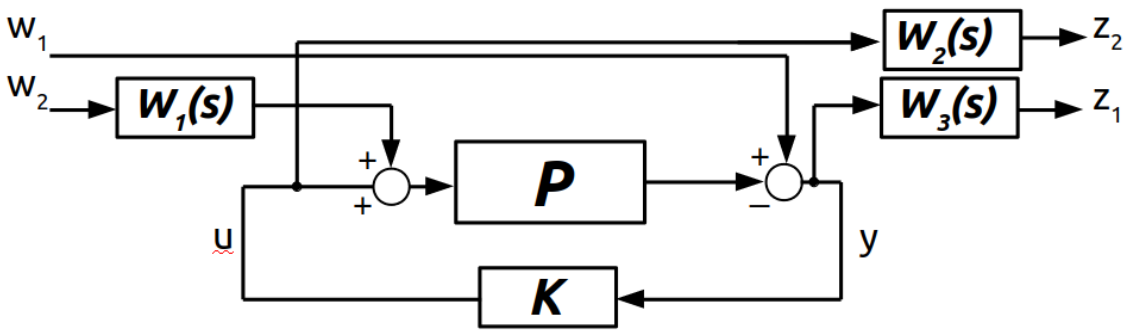

Figure 3.11: Mixed Sensitivity Design Block Diagram

The inputs w_1 and w_2 refer to the system references and input disturbances respectively, whilst z_1 and z_2 refer to the system input and output performance. The shape weighting functions W_1, W_2, W_3 describe the desired transfer function between the inputs w and output z we wish the optimized controller K to follow.

In order to shape the weighting accurately for the application we are designing K for, the concept of **Robust Stability** and **Robust Performance** in regards to these weighting functions must first be understood.

For a closed loop system with a controller K, the system is said to be **Nominally Stable** for a given $P(s)$ when the path of the Nyquist plot does not encircle the point {-1, 0}, as shown in Figure 3.12, where the closed loop is given by:

$$L(j\omega) = K(j\omega)P(j\omega) \tag{3.57}$$

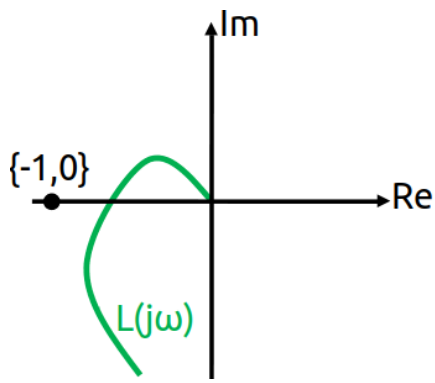

Figure 3.12: Nyquist representing Notional Stability

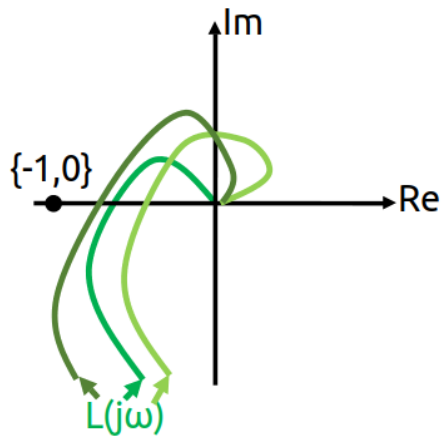

Figure 3.13: Nyquist representing Robust Stability

A system is therefore considered **robustly stable** if for every possible plant $P(s)$ within the given uncertainty set:

$$P(s) \in \Pi \tag{3.58}$$

if, for the closed loop system $G(s)$, none of the probable paths in the Nyquist encircle {-1,0} as shown in Figure 3.13. However, the question in regards to the controller design is; how can this be guaranteed?

If multiplicative uncertainty is considered ([110] - Chapter 4), whereby a perturbation Δ is imposed on the system, and scaled to a given weight w_3, the perturbed system closed loop transfer function becomes:

$$\begin{aligned} L(j\omega) &= P(j\omega)K(j\omega)(1 + w_3\Delta) \\ &= L + Lw_3\Delta \end{aligned} \tag{3.59}$$

This can be represented as a vector equation in the complex plane as shown in Figure 3.14.

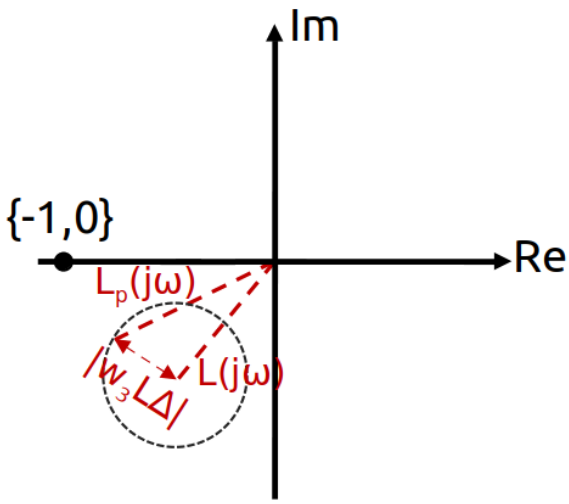

Figure 3.14: Nyquist Derivation for the design of w_3 mixed sensitivity weight

Now since $\Delta(j\omega)$ can have any phase, and that $|\Delta(j\omega)| \leq 1$, the vector term $w_3 L\Delta$ therefore simply defines a disc in the complex plane of a radius $|w_3 L|$. Therefore, the loop transfer function L is a vector from {0,0} to any point within this defined disc. Now since robust stability can be satisfied by these means, it next must be ensured that the disc would never be so large as to touch the instability point {-1,0}.

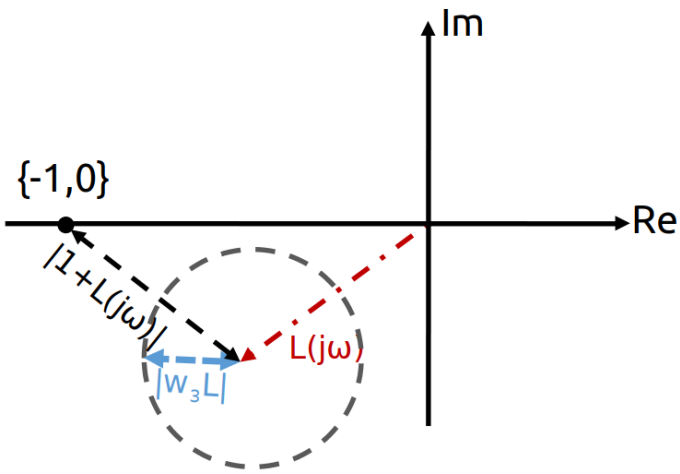

Figure 3.15: Nyquist Derivation for the design of w_3 mixed sensitivity weight

From Figure 3.15, the diagram shows that the disc will never touch the unstable point if:

1. $L(j\omega)$ does not encircle the point {-1,0}
2. $|w_3 L(j\omega)| < |1 + L(j\omega)|, \forall\omega$

The second conditions is equivalent to:

$$\left|\frac{L(j\omega)}{1+L(j\omega)}\right| < \left|\frac{1}{w_3(j\omega)}\right| \tag{3.60}$$

Equation (3.60) defines how to shape what is referred to as the 'complementary sensitivity' in the mixed sensitivity design problem, and is fully defined as:

$$|T(j\omega)| < \left|\frac{1}{w_3(j\omega)}\right| \tag{3.61}$$

Where the left-hand side of (3.61) is stated completely in terms of the nominal closed loop transfer functions, and the right-hand side is stated in terms of magnitude of the uncertainty in the model. Additionally this robust stability condition is <u>not</u> conservative, and it is both sufficient and necessary in order to guarantee the robust stability of the system.

Now, for a closed loop system in a controller $K(s)$, a system can be considered to posses **Robust Performance** if the closed loop conditions meet the performance specifications (however they may be set) for every plausible plant, as described in (3.58).

Consider first the performance specification of:

$$|w_1(j\omega)S(j\omega)| < 1 \tag{3.62}$$

where

$$S = (1+L)^{-1} \tag{3.63}$$

where $S(j\omega)$ is termed the weighted sensitivity and typically the weight w_1 is set as follows:

$|w_1(j\omega)| \gg 1$, for low frequencies of ω
$|w_1(j\omega)| < 1$, for higher frequencies of ω

Now, define an circular region around the instability point such that:

$$\left|\frac{w_1(j\omega)}{1+L(j\omega)}\right| < 1 \Longleftrightarrow |w_1(j\omega)| < |1+L(j\omega)| \tag{3.64}$$

which results diagrammatically in the figure below:

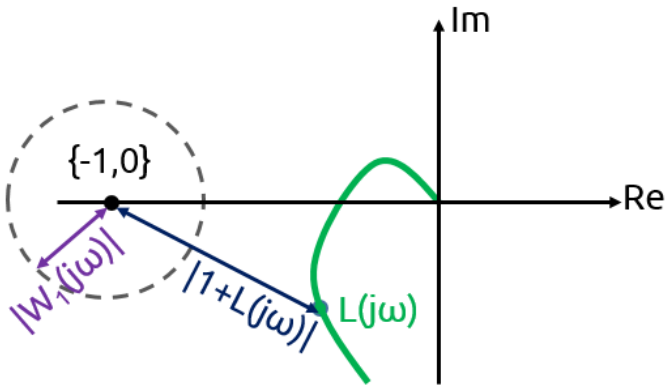

Figure 3.16: Robust Performance Criterion for w_1 weight selection

If the performance specification is then applied to all the possible loops of $L(s)$, where for this instance, the diagram for the robust stability criterion can be re-used, it can be safely assumed from Figure 3.17 that robust performance of the loop controller $L(s)$ is held as long as the two weighted disc do not touch one another.

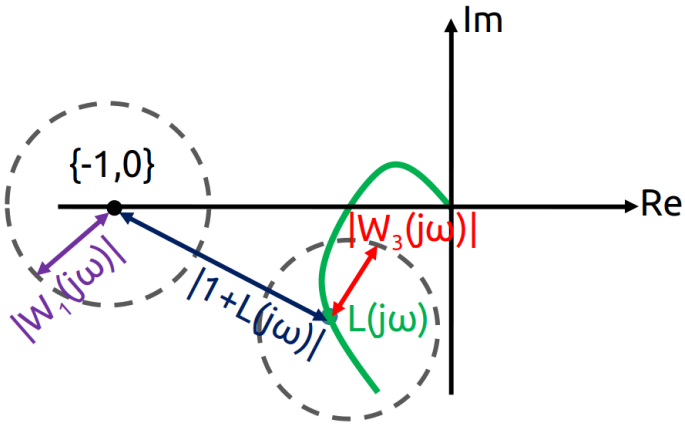

Figure 3.17: The Robust Performance Criterion utilising the performance specification of guaranteed robust stability

The two discs will not touch if:

$$|1 + L(j\omega)| > |w_1(j\omega)| + |w_3(j\omega)L(j\omega))| \tag{3.65}$$

which can be directly written as:

$$|w_1 S(j\omega)| + |w_3(j\omega)T(j\omega)| < 1 \tag{3.66}$$

where $S(j\omega)$ is defined as the sensitivity function.

Equation (3.66) defines the robust performance condition for a specific uncertainty structure.

These diagrams define how each of these weights ensure that the synthesised controller will be robustly stable across all of $L(s)$ for any perturbation defined in Δ. The weight objectives detailed in (3.61) and (3.62) set the criteria for closed loop robust performance, but also attribute to the characteristics of the closed loop controllers in the following manner:

- $\|w_1(j\omega)S(j\omega)\|_\infty \leq 1$ the weighted sensitivity; directly shapes the tracking error response.
- $\|w_2(j\omega)K(k\omega)S(j\omega)\|_\infty \leq 1$ is a weight on the actuation limits. Typically w_2 is set to a constant value.
- $\|w_3(j\omega)T(j\omega)\|_\infty \leq 1$ the complementary sensitivity which directly describes the robustness of the system.

The transfer function from w to z can therefore be defined as:

$$M(s) = \begin{bmatrix} w_1 S \\ w_2 K S \\ w_3 T \end{bmatrix} \tag{3.67}$$

Therefore, through H_∞ optimization, a controller K will be found in order to minimize the H_∞ norm of the transfer function defined in (3.67) such that:

$$\|M(s)\|_\infty = \left\| \begin{bmatrix} w_1 S \\ w_2 K S \\ w_3 T \end{bmatrix} \right\|_\infty \tag{3.68}$$

However, if it is described for the control effort to not be restricted, the weight w_2 can be omitted leaving the H_∞ optimization to search for a K through the minimization of:

$$\|M(s)\|_\infty = \left\| \begin{bmatrix} w_1 S \\ w_3 T \end{bmatrix} \right\|_\infty \tag{3.69}$$

In designing the desired transfer function of the weights, typically w_1 takes the form of a low pass filter:

$$w_1(s) = \frac{s/M + \omega_b}{s + \omega_b \tau} \tag{3.70}$$

where typically $1.5 < M < 2$; ω_b is the expected low pass cut-off frequency in rads^{-1}, and τ is the target lower bound gain of the filter, which is computed as $X_A = 10^{\frac{A}{20}}$ where such a filter thus has the response:

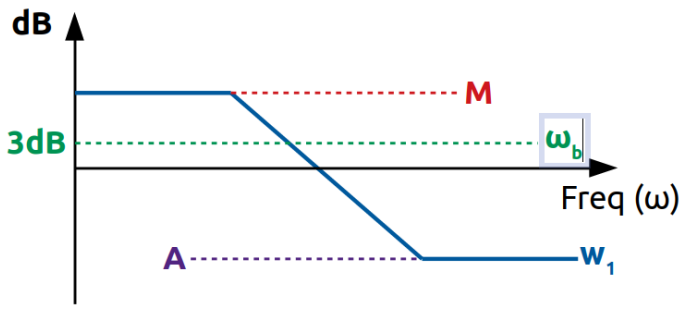

Figure 3.18: Standard bode diagram for the w_1 objective weight

The w_3 weight on the other hand is typically in highpass filter form:

$$w_3 = \frac{s/\omega_{be} + 1/M}{\tau_e/\omega_{be} + 1} \tag{3.71}$$

where the terms ω_{be} and τ_e are the values unique, but equivalent in operation to ω_b and τ for w_1.

H_∞ Control Implementation for the non-linear AFE converter

Because the AFE is the non-linear system of interest in our notional system of interest, the above control strategy will again be applied to this converter. The model which will be used in this design is equivalent to that shown in (3.21), and the references and parametric values equivalent to those in Tables 3.1 and 3.2.

When selecting the cross-over frequencies of each of the weights, it must be ensured that the -3dB crossover frequency of w_1 is below that of $1/w_3$, such that there is a gap between the performance bound w_1 and the robustness bound w_3. Otherwise the expected performance dictated by each of these weights will not be achieved.

The controller which is to be designed combines the matrices P, w_1, w_2, w_3 as the full system which is to be optimised. The augmented plant model including weights thus takes the form:

$$G(s) = \begin{bmatrix} w_1 & -w_1 P \\ 0 & w_2 \\ 0 & w_3 P \\ I & -P \end{bmatrix} \tag{3.72}$$

As the grid frequency input to the AFE is the standard 400Hz, and therefore for the performance bound, the cut-off bandwidth was selected to around 450Hz. Having a very close buffer zone between ω_b and ω_{be} makes the minimization of H_∞ a much harder task. Therefore, to ensure the best possible controller, the position of ω_{be} was set to approximately 1.5kHz. Setting M to be the

maximum of 2, and allowing τ and τ_e to be comfortably small at around 0.1 allows a comfortable region of optimisation of the controller.

Therefore, the following weighting functions for w_1 and w_2 were received:

$$w_1 = \frac{0.5(s+5089)}{s+25.45}, \quad w_3 = \frac{100(s+4712)}{s+9.425e^5} \tag{3.73}$$

which performing the singular value plot, looks as that presented in Figure 3.19.

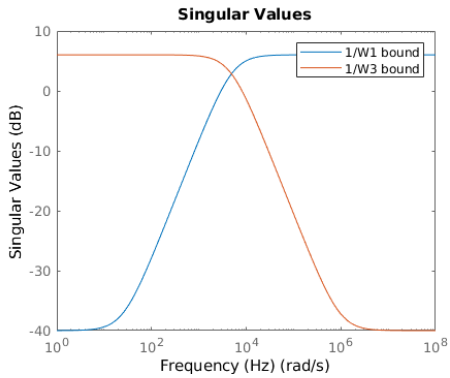

Figure 3.19: Inverted Weight singular plot values for AFE H_∞ controller design

The weight w_2 was kept at a constant of 0.1 as to not impose too great a restraint on the controller optimization.

The controller optimisation is performed using a tool called HIFOO, developed by New York University [114]. Whilst common applications such as MATLAB have their own inbuilt algorithms to deal with H_∞ problems; the MATLAB toolbox is fairly restricted in options to define the output controls, whilst HIFOO has this functionality.

In order to compute the controller K which minimizes $\|M(s)\|_\infty$ HIFOO employs the approach of Quasi-Newton method in order to locate the local minima for varying start points of K. At each located point, a gradient sampling approach by computing the eigenvector or singular vector information is used in order to better approximate the global minima [115]. Now, when a local minima for the $\|H\|_\infty$ is located, it may not necessary be the minima of the whole system, as these kinds of optimization algorithms are non-convex in nature. Therefore in this optimization process, a multiple random starting point approach is adopted. Thus across all these random starting points, the minima of all the located local minima is approximated to be the global minima of the system, however, true global minima cannot be guaranteed.

The open-loop system will be controlled by another linear system:

$$\begin{bmatrix} \dot{\hat{x}} \\ u \end{bmatrix} = \begin{bmatrix} \hat{A} & \hat{B} \\ \hat{C} & \hat{D} \end{bmatrix} \begin{bmatrix} \hat{x} \\ y \end{bmatrix} \tag{3.74}$$

where:

$$K = \begin{bmatrix} \hat{A} & \hat{B} \\ \hat{C} & \hat{D} \end{bmatrix} \tag{3.75}$$

is the controller to be optimised, and where $\hat{x}$ are the internal controller states, and the control system input, is the plant output y, and the controller output is the plant input u [115].

By passing the system described in (2.66)-(2.69) as the plant P, and the defined weights (3.73) into the fully augmented system (3.72) and pass into the HIFOO algorithm, the resultant closed loop sensitivity performance can be found to look as follows:

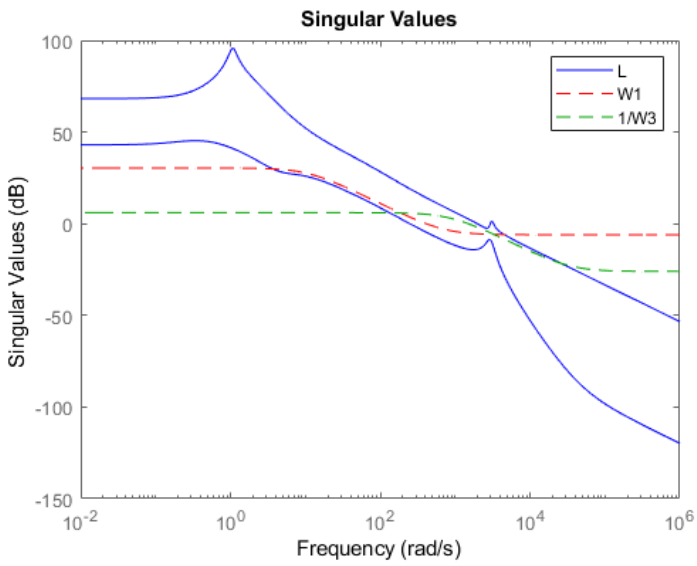

Figure 3.20: Closed loop shape against the defined weights of the system

The system response observed in Figure 3.20 was achieved much by trail and error, conditioning the weights bandwidths as much as possible, in order to have the smallest possible γ from (3.56). Although the closed loop trend observed from Figure 3.20 fits that specified, where S is large within the control bandwidth and becomes very small outside it. However, the smallest γ which could be achieved was anywhere between $1.2 < \gamma < 1.5$ which is well out of the required condition of $\gamma < 1$ to ensure global robust performance required from this control. There is a range of minimums due to the non-convexity of the optimisation algorithm which results in alternative controllers on every run. Whilst the achieved bound is not within the criteria, it actually results in no confidence in

the robustness of the system. This is only the start of the issues associated with this approach. Note that the output controller defined in (3.75) is an linear system. For every iteration step, a series of functions must be solved in order to compute the correct input u to the plant. This is not ideal. For one, this makes the controller more computationally intensive. It wouldn't be as bad as to the computations required if the system were to incorporate controls such as MPC into the design. Ideally however, if we are to use this form of optimal controller approach, a static feedback alternative would be preferred. It not only allows easy constraints to be applied to the system in order to decentralize sub-systems, but also largely reduces the computational effort on the controller. By imposing only static gains in this optimization, the system is going to be even more constrained, and the minimum γ is more likely to rise, than fall like we want it to. The controller still does work totally fine, albeit the slow dynamic responses as a result of the conservative nature the weights applied to the optimisation. But the lack of guarantee to the overall robustness of the controller, and the fact that when further constraints such as decentralization and development of static controls are implemented, the synthesised controller will move even further from the required condition on γ. It is noted in literature [113] that with regards to H_∞ control problems typically only suboptimal solutions can be found. This is general down to the fact that the optimal solution to the H_∞ control is numerically and theoretically very complex, and is often computed by brute force iterative methods until a solution to a control which makes $\gamma < 1$ is found. This was however performed using a large number of random starting points (upto 1000) in the H_∞ minimization algorithm, where no optimal solution for γ could be found. There is however, a controller of a similar family to the H_∞ controller referred to as H_2 optimization, which in itself is an optimal control optimization with fewer conservative rules when compared to H_∞.

It shall be shown in the next sub-section how the less conservative H_2 control method allows an optimal controller to be developed for the non-linear system, whilst meeting all required conditions for optimality, including for the full control notional system.

3.3 The H_2 Controller

As the name suggests, as already discussed with H_∞ control, H_2 also involves the attempt at the minimization of the transfer function in closed loop between the disturbances w and the error outputs z, but a minimization of the $\|\cdot\|_2$ norm in this case.

However, there are many powerful features that are present in H_2, which are not directly drawn through the H_∞ optimization. Here the H_2 optimization algorithm will be discussed in detail highlighting these powerful features. Much of the mathematical derivations highlighted in this section were developed from the theory presented in [116], and have been adapted for our

given system.

3.3.1 H_2 Controller Theory

The H_2 optimal control problem, much like the H_∞ control problem is the optimization of a closed loop controller K in order to minimize the H_2 norm of a given closed loop transfer function.

Let us supposes that we have a given system transfer function $P(s)$ which when described in the state-space representation, is given by:

$$P = \begin{cases} \dot{x}(t) = Ax + Bu \\ z(t) = Cx \end{cases} \tag{3.76}$$

such that in the form of a Laplace transfer function, P can be defined as:

$$P(s) = C(sI - A)^{-1}B \tag{3.77}$$

Where, by integrating $P(s)$ the following can be received:

$$z(t) = Ce^{At}x(0) + \int_0^t H(t-\lambda)u(\lambda)d\lambda \tag{3.78}$$

where the function $H(t-\lambda)$ defines the instant impulse response function which is defined as:

$$H(\tau) = \left\{ \begin{array}{ll} Ce^{At}B, & \text{if } \tau \geq 0 \\ 0, & \text{if } \tau < 0 \end{array} \right\} \tag{3.79}$$

From this, it can be shown that the system Laplace transfer function $P(s)$ is simply a Laplace Transform to the input response function $H(\tau)$, such that:

$$P(s) = \int_0^\infty H(\tau)e^{-s\tau}d\tau \tag{3.80}$$

From the Parseval's theorem shown in (3.45), it can therefore be shown that $\|P\|_2 = \|H\|_2$, such that we can derive the 2-norm of the impulse function as:

$$\|H\|_2 = \left(\int_0^\infty tr\left[H(t)^T H(t)\right]\right)^{1/2} \tag{3.81}$$

It can be observed from this that if the eigenvalues of the state-matrix A are all have strictly negative real components, then the function $H(t)$ will be finite.

Therefore, the $\|\cdot\|_2$ can be directly evaluated as:

$$\|P\|_2 = \|H\|_2 = tr\left[C\left(\int_0^\infty A^{At}BB^T e^{A^T t}dt\right)C^T\right] \tag{3.82}$$

where the matrix Γ will be defined as:

$$\Gamma = \int_0^\infty e^{At} B B^T e^{A^T t} dt \tag{3.83}$$

and thus, (3.82) can be rewritten as:

$$\|H\|_2 = tr\left[C\Gamma C^T\right] \tag{3.84}$$

Now, this directly reflects on one of the most powerful properties of the H_2 optimization. It can actually be found that there is a unique solution to the matrix Γ, in that it is a solution to the standard matrix Lyapunov equation:

$$A\Gamma + \Gamma A^T + BB^T = 0 \tag{3.85}$$

A Lyapunov function is a mathematical expression which, if a unique Γ can be found, defines a given region of the stability of the loop transfer function $P(s)$. This does however mean that if no solution for Γ can be solved, a stable H_2 norm cannot be found, and thus, as explained later means that no stable K can be synthesised.

If there is a unique solution to Γ, the solution to the Lyapunov function can be derived from the differential of:

$$\frac{d}{dt}\left[e^{At} B B^T e^{A^T t}\right] = A e^{At} B B^T e^{A^T t} + e^{At} B B^T e^{A^T t} A^T \tag{3.86}$$

If both sides of the equation (3.86) are integrated in time from $0 \to \infty$, then the left-hand side becomes:

$$\int_0^\infty \left(\frac{d}{dt}\left[e^{At} B B^T e^{A^T t}\right]\right) = e^{At} B B^T e^{A^T t}\Big|_0^\infty \tag{3.87}$$

we are assuming in this case that there is a unique solution Γ, and thus the matrix A must be stable and contain only negative real component eigenvalues. Therefore, the assumption can be made that as t $\to \infty$ the power on the exponential terms will decay down to zero, as to the notion of a stable system. Therefore, the evaluation results in:

$$e^{At} B B^T e^{A^T t}\Big|_0^\infty = -BB^T \tag{3.88}$$

Now performing the same operation on the right-hand side of the equation, and the same assumptions being applied to this problem, the integration results in:

$$\int_0^\infty \left[A e^{At} B B^T e^{A^T t} + e^{At} B B^T e^{A^T t} A^T\right] dt = A\Gamma + \Gamma A^T \tag{3.89}$$

which thus derives the equation in (3.85).

The fact that the solution to the H_2 norm depends on a unique solution to the well known Lyapunov stability criterion is very powerful in the use of locating the most optimal solution to the control problem. However the nature of the optimisation does have some drawbacks, most importantly the problem of being stuck in local minima. This optimisation by nature is non-convex, and optimising to a local minima can result in non-optimal and poorly performing controllers being generated. More on this topic will be discussed in Section 4.1.1. But, if the global minimum of this non-convex optimisation can be located, the resultant unique solution Γ will generate the most optimal controller K which will be robustly stable with in a range defined by the Lyapunov equation. However, for now, in the practical sense of this theory, it is still relatively unclear as to what purpose the minimization of the H_2 norm does to our system P.

Let's now portray the system in terms of its inputs and outputs:

$$z(s) = P(s)u(s) \tag{3.90}$$

and just for the start of this derivation, let (3.90) be SISO (Single-Input, Single-Output), and thus have a 1-dimensional input which for now is set constant to 1. e.g $u(s) = 1$.

Setting the input in its Laplace form to a constant value implies the output contains equal amounts of all frequencies as $u(j\omega) = 1$.

Simply then, the output can be evaluated as:

$$z(s) = P(s) \tag{3.91}$$

Now it has already been defined by (3.45) that the outputs $\|\cdot\|_2$ can be defined as:

$$\|z\|_2 = \left(\frac{1}{2\pi}\int_{-\infty}^{\infty} |P(j\omega)|^2 \, d\omega\right)^{1/2} \tag{3.92}$$

What (3.92) therefore defines is that the H_2 norm of a system is the root-mean-square average gain across all frequencies.

However, with respect to the system we are analysing, our system is a MIMO (Multiple-Input, Multiple-Output) system, and thus not just focusing on a single input.

In order to perform the same analysis on a MIMO system, the input is now defined in vector form, where u_k defines the kth unit of a vector:

$$u_k = \begin{bmatrix} 0 & \cdots & 0 & 1 & 0 & \cdots & 0 \end{bmatrix} \tag{3.93}$$

The system can now take the form:

$$z(s) = P(s)u_k \tag{3.94}$$

and as before, the term derived by (3.45) still holds and thus for a MIMO system

$$\|z\|_2 = \|Pu_k\|_2^2 \tag{3.95}$$

which therefore directly implies that:

$$\|Pu_k\|_2^2 = \frac{1}{2\pi}\int_{-\infty}^{\infty} tr\left[P(-j\omega)u_k u_k^T P(j\omega)^T\right] d\omega \tag{3.96}$$

using the fact that $tr\left[AB\right] = tr\left[A^T B^T\right]$ [116].

Here, we can set each of the inputs to each have a constant set as their Laplace Transform, and thus the $\|\cdot\|_2$ of the inputs can be found to be:

$$\begin{aligned}
\sum_{k=1}^{m}\left[\|z\|_2^2 : u(s) = u_k\right] &= \sum_{k=1}^{m}\|Pu_k\|_2^2 \\
&= \frac{1}{2\pi}\sum_{k=1}^{m}\int_{-\infty}^{\infty}\left[P(-j\omega)u_k u_k^T P(j\omega)^T\right] d\omega \\
&= \frac{1}{2\pi}\sum_{k=1}^{m}\int_{-\infty}^{\infty} tr\left[P(-j\omega)\sum_{k=1}^{m}\left(u_k u_k^T\right)P(j\omega)^T\right] d\omega \\
&= \frac{1}{2\pi}\int_{-\infty}^{\infty} tr\left[P(-j\omega)IP(j\omega)^T\right] d\omega \\
&= \|P\|_2^2
\end{aligned} \tag{3.97}$$

In the time domain, it can be assumed that a function which has a constant value as a Laplace transform is equivalent to that of a Dirac function:

$$\delta(t) = \left\{\begin{array}{ll} \infty, & \text{if } t = 0 \\ 0, & \text{if } t \neq 0 \end{array}\right\} \tag{3.98}$$

Therefore from (3.98), it is clear that:

$$\int_{-\infty}^{\infty}\delta(t) = 1 \tag{3.99}$$

so with the vector input defined as a Dirac impulse on the kth input $u(t) = u_k\delta(t)$, the output can be defined as in (3.78):

$$\begin{aligned}
z(t) &= \int_0^t H(t-\lambda)u_k\delta(\lambda)d\lambda \\
&= H(t)u_k
\end{aligned} \tag{3.100}$$

Therefore, it can be said that:

$$\begin{aligned}\int_0^\infty z(t)^T z(t)dt &= \int_0^\infty u_k^T H(t)^T H(t) u_k dt \\ &= \int_0^\infty tr\left[H(t)u_k u_k^T H(t)^T\right] dt\end{aligned} \tag{3.101}$$

where, when placing back the vectorised input term you can receive:

$$\begin{aligned}&\sum_{k=1}^m \left[\int_0^\infty z(t)^T z(t)dt : u = u_k\delta(t)\right] \\ &= \sum_{k=1}^m \int_0^\infty tr\left[H(t)u_k u_k^T H(t)^T\right] dt\end{aligned} \tag{3.102}$$

which by taking a similar approach to that defined in (3.97), the following result can be achieved:

$$\sum_{k=1}^m \left[\int_0^\infty z(t)^T z(t)dt : u = u_k\delta(t)\right] = \|H\|_2^2 \tag{3.103}$$

Additionally, it can also be observed that in the above solution, if we were to apply a function of white noise to the input vector w such that:

$$w(t)w(t)^T = I\delta(t-\lambda) \tag{3.104}$$

equivalently, the expected power in the error signal can be directly expressed by:

$$\begin{aligned}&\lim_{t\to\infty} \frac{1}{2t}\int_{-t}^t z(t)^T z(t)dt \\ &= tr\left[z(t)^T z(t)\right]\end{aligned} \tag{3.105}$$

which by using the notion from (3.45) can be rightly defined as:

$$\frac{1}{2\pi}\int_{-\infty}^\infty tr\left[M(j\omega)M(j\omega)^T\right] d\omega = \|M\|_2^2 \tag{3.106}$$

where M as described before is the transfer function between the disturbance input w and the error output z [113].

Through all the above derivations of the H_2 norm of our system from [116], with the adaptation for (3.106) provided by [113], in regards to a white noise input, the H_2 norm of a system can be simply defined as the minimisation of the output error power due to these impulses, and simply the H_2 optimisation minimized the average gain of the transfer function from the disturbance, to the error output. As was with the H_∞ control too, a certain bound can be applied to the optimisation to guarantee a given level of stability and robustness. As with (3.56) where γ guarantees a given degree of robustness, so can it be applied to (3.106) such that: [117]

$$\|M\|_2^2 \leq \gamma \tag{3.107}$$

where γ is a value, which for the best robustness to any system uncertainty and disturbances including in H_2 optimisation be set as $\gamma \leq 1$, and this shall be imposed as a strict condition on the controller design. As performed with H_∞, any controller not ensuring this guarantee shall be disregarded as not fit for our system criteria.

So from the theory largely built up on the knowledge provided in [116] and [113], the theory behind the development and synthesis of the H_2 controller is to find a suitable controller K which minimizes the H_2 norm of the transfer function between w and z. This can be described in a more generalised way as to find a controller which minimizes average gain across all frequencies to a given bound γ.

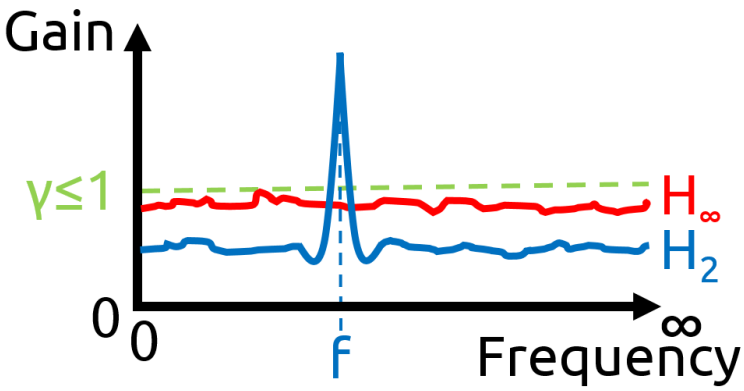

Figure 3.21: Generalised Comparison between the resultant gains across all frequency for each optimization approach

As mentioned when discussing the design of H_∞ controllers in Section 3.2.1, H_∞ attempts to ensure across the whole frequency range, the gain does not go beyond the bound γ, as depicted in Fig. 3.21 . However, the fact that it attempts to identify a controller which imposes a 'maximum' gain seriously complicates, and increases conservativeness in the optimization procedure where there is no guarantee a solution to $\gamma \leq 1$ can be found or even exists. However, H_2 has a far less strict condition imposed. By optimising to ensure the constraint is to the average (root-mean-square) value of the gain across all frequencies it becomes a lot easier to locate a controller with the required imposed bound specified in (3.107). There may be multiple solutions to K which will meet the required criteria, whilst there may only be one solution to H_∞. This means in general for the H_2 controller, firstly, the optimisation time very fast. As an example, comparing the H_2 algorithm to the AFE (will be discussed in a moment) to the H_∞, the following optimization times, to the following minimum γ is achieved, using 20 random starting points for

each optimisation.

	H_2	H_∞
$\min \gamma$	0.4217	1.4574
Optimization Time (s)	5.51	66.12

Table 3.3: Optimization comparison of H_2 and H_∞ with their achieved minimum γ and the optimization time for 20 random points

Secondly, for the majority of controllable systems and those which fit the criteria, which are mentioned in the next subsection, there is almost certainty that a unique controller can be developed with the required condition imposed on γ. Though, it is clear from the derivations of the H_2 optimisation, that the optimisation in general will be less robust than H_∞, the minimisation on the average gain of the transfer function between w and z is a robustification technique for the closed loop system in itself. However, as observed in Figure 3.21, there could be the possibility that at a given frequency f, the gain could tend to ∞. This is the draw back for this controller, however, this is not a certainty. It is important therefore to test any developed H_2 controller that it remains stable to all foreseeable disturbances and all probable kinds of uncertainty.

3.3.2 System Conditions and Requirements for H_2 Controller Optimisation

Before one can consider the H_2 optimal control as their controller of choice for their applications, the system must adhere to some strict criteria direct from the LTI system model itself.

Taking directly from the block diagram in Figure 3.8, the LTI system P can be described as:

$$P = \begin{cases} \dot{x} = Ax + B_1 w + B_2 u \\ z = C_1 x + D_{11} w + D_{12} u \\ y = C_2 x + D_{21} w + D_{22} u \end{cases} \tag{3.108}$$

To proceed on with the design using the system in (3.108), all the following criterion must be met: [113][118]

1. The matrices (A, B_2, C_2) all must be both detectable and stabilizable.
2. Both the matrices D_{12} and D_{21} must be full rank.
3. It must be assumed that the matrices D_{11} and D_{22} are both equal to 0.
4. Both $D_{12}^T C_1$ and $B_1 D_{21}^T$ equal 0.

5. $\begin{bmatrix} A - j\omega I & B_2 \\ C_1 & D_{12} \end{bmatrix}$ must have full row column rank $\forall\omega$

6. $\begin{bmatrix} A - j\omega I & B_1 \\ C_2 & D_{21} \end{bmatrix}$ must have full row rank $\forall\omega$

If a stabilizing controller K is to be found through this optimization, then condition (1) must be ensured; as to ensure that this controller is realisable and proper; then condition (2) must be held. Condition (3) is in-fact an assumption which is always made when performing H_2 problems. The direct feed-through term between v to z needs to be assumed zero in order to attain a finite value for the H_2 norm of the closed system. Whilst for D_{22}, the direct feed-through term between u and y has been assumed zero because physical systems at infinite frequency always have zero gain [116]. Condition (4) again is very common for H_2 controller synthesis. For further understanding as to why $D_{12}^T C_1 = 0$ must be a condition, please refer to [113] as it is a result of a similar control strategy called LQG which is out of scope of this thesis. Whilst the reason $B_1 D_{21}^T = 0$ is due to the fact that in general H_2 optimization problems, there is no correlation between the plant noise, and that on the measurement. Finally, the conditions set in (5) and (6) ensure that no poles or zeros which are located on the imaginary axis are cancelled by the optimal controller K, as that would tend to instability [113].

Now with these conditions, the plant of the system $P(s)$ can be structured into the following state-space matrix, derived from (3.108):

$$P(s) = \left[\begin{array}{c|cc} A & B_1 & B_2 \\ \hline C_1 & \mathbf{0} & D_{12} \\ C_2 & D_{21} & \mathbf{0} \end{array}\right] \tag{3.109}$$

A very well known, often used and remarkably simple form of optimal control is the Linear Quadratic Regulator (LQR). The LQR control is in-fact a very special case of the H_2 optimal control in that to design this controller, the following cost function expression is minimized:

$$J_{LQR} = \sum_{k=1}^{m} \left[\int_0^\infty \left[x(t)^T Q_\gamma x(t) + u(t)^T R_\gamma u(t) \right] dt \quad u : u_k \delta(t) \right] \tag{3.110}$$

where Q_γ is defined as a symmetrical positive semi-definite matrix, and R_γ as a symmetrical positive definite matrix. Both these matrices are designer defined weighting matrices for the system states (x) and the inputs (u) respectively, and will be discussed more fully in later sections. It is clear that the cost function for the LQR optimization is essentially equivalent to that defined by the cost function for minimizing the 2-norm in (3.103). In-fact these terms are equivalent. Due to

the fact that both Q_γ and R_γ are both (semi)-definite matrices, it can be so shown that they can always be factorised as:

$$Q_\gamma = (Q_\gamma^{1/2})^T Q_\gamma^{1/2}, \quad R_\gamma = (R_\gamma^{1/2}) R_\gamma^{1/2} \tag{3.111}$$

this is generally referred to as a Cholesky Factorisation and is what leads to the definition of the C_1 and D_{12} matrices being defined as: [116]

$$C_1 = \begin{bmatrix} Q_\gamma^{1/2} \\ \mathbf{0} \end{bmatrix}, \quad D_{12} = \begin{bmatrix} \mathbf{0} \\ R_\gamma^{1/2} \end{bmatrix} \tag{3.112}$$

and thus, with these definitions, the optimization terms from (3.103) can be revaluated as follows:

$$z(t)^T z(t) = (C_1 x(t) + D_{12} u(t))^T (C_1 x(t) + D_{12} u(t)) = x(t)^T Q_\gamma x + u(t)^T R_\gamma u \tag{3.113}$$

Equations (3.110)-(3.113) thus define the way in which we can tune the resultant optimal controller K in the H_2 optimization. By conditioning the Q_γ matrix, we can influence directly how each of the states can directly impact the performance of the closed loop performance output z; and likewise with conditioning R_γ to influence how the inputs directly influence z.

However, what the conclusion to this particular definition looks like is that the H_2 controller, and the LQR controller are exactly equivalent in terms of the optimization procedure. However, this is not the case. As it shall be shown next.

3.3.3 The Differences between H_2 Optimization and LQR

The LQR is considered a very elegant and classical form of state-feedback control. In order to employ this form of controller into the system, all the states must be available for feedback, however states do not necessarily need to be measured, for use of Kalman filters (observers) to predict values of unmeasurable states can also be utilised. Such a controller would be developed under the Linear-Quadratic-Gaussian (LQG) controls. By this fact, LQR controllers are referred to as a full state-feedback control. This is clear when it is realised that the optimisation searches for a K_l which minimises the cost (3.110) of the form:

$$u = K_l x \tag{3.114}$$

where it can be shown by derivation of the cost function on the open loop state-equation, the closed loop controller K_l is of the form:

$$K_l = -(D_{12}^T D_{12})^{-1} B_2^T \Gamma = R_\gamma^{-1} B_2^T \Gamma \tag{3.115}$$

where as with (3.85) Γ is the unique solution to the Lyapunov based Algebraic Riccati Equation (ARE):

$$\Gamma A + A^T \Gamma - \Gamma B_2 R_\gamma^{-1} B_2^T \Gamma + Q_\gamma = 0 \tag{3.116}$$

for which it is ensured that the closed loop state matrix:

$$A + B_2 K_l \tag{3.117}$$

is completely stable. For more theory behind the LQR control readers should refer to [110, 116, 87] for a more in-depth mathematical understanding of the LQR control, but for this piece of work, the above is all that is required for understanding the difference between this and the H_2 control approach.

As a general brief example of the differences between the two controllers, take for instance the fact that due the LQR relying on an ARE for optimisation, which is always convex [119]. This means that if a solution Γ can be found for the subject test system, an optimal and stable controller can always be found. As has been discussed previously, the H_2 optimisation can lose the guarantee of stability for generated controllers, due to the nature of the optimisation being non-convex and the possibility of getting stuck in local minima. However on the other hand, the LQR is full state-feedback, this means that all state information from the plant P must be provided to the controller in order for the system to function as designed. In some applications states can be inaccessible for measurement providing additional complications in the LQR controller implementation. There are ways around this how however by using Kalman filters to estimate inaccessible states, but this involves designing state-estimators. The H_2 on the other hand can not only, like the LQR, be designed in state-feedback, but can also be designed as output feedback control, meaning only the outputs are required for full functionality of the system. This is because the H_2 optimised controller can be constructed to be of an optimal feedback estimator K_{h_2}, such that:

$$\dot{\hat{x}} = K_{h_2} y \tag{3.118}$$

and thus in closed loop, the state-space representation of this system can be shown to be:

$$\begin{cases} \dot{\hat{x}} = (A - K_{h_2}C_2)\hat{x} + K_{h_2}y \\ \hat{z} = C_1\hat{x} \end{cases} \tag{3.119}$$

This is due to the fact that if only the outputs are available for measurement, the system integrals cannot be made to force the error $r - u = 0$, where r denotes the reference values for the controller. Therefore, to ensure zero-steady state error of the system can be achieved, the estimated states $\hat{x}$ must be evaluated to determine the optimal control signal u such that:

$$u = K_{h_2}\hat{x} \tag{3.120}$$

Equivalently through the analysis presented in [116], the cost function for the H_2 optimal controller K_{h_2} can thus be formulated:

$$J_2\left(K_{h_2}\right) = \sum_{k=1}^{m}\left[\int_0^\infty \left[u(t) - K_{h_2}x(t)\right]^T R_\gamma \left[u(t) - K_{h_2}x(t)\right] dt : u = u_k\delta(t)\right] \tag{3.121}$$

and therefore from (3.120)

$$J_2\left(K_{h_2}\right) = \sum_{k=1}^{m}\left[\int_0^\infty \left[\hat{x}(t) - x(t)\right]^T K_{h_2}^T R\gamma K_{h_2} \left[\hat{x}(t) - x(t)\right] dt : u = u_k\delta(t)\right] \tag{3.122}$$

from which the minimisation of the H_2 norm is given by the minimisation of the cost J due to K_{h_2}. It can be further shown that the equivalent closed loop system can thus take the form:

$$\begin{cases} \dot{\hat{x}}(t) = \left(A + B_2K_{h_2}\right)x(t) + \Phi\left[y(t) - C_2x(t)\right] \\ u(t) = K_{h_2}\hat{x}(t) \end{cases} \tag{3.123}$$

where

$$K_{h_2} = -R_\gamma^{-1}B_2^T\Gamma \tag{3.124}$$

and can be characterised in similar form as with the H_∞ controller as in (3.75). The term Φ is additionally defined as:

$$\Phi = \Gamma C_2^T(D_{21}D_{21}^T)^{-1} \tag{3.125}$$

Again, up to this degree of definition of the H_2 control is all that's required for understanding of this work. For what is the opinion of the author, the best description of the development of the H_2 controller please refer to [116], where many of the derivations in this chapter were derived from.

3.3.4 Decentralised Structure of the H_2 State-Feedback Control

The notional system in this study has all accessible, and thus measurable states. It was mentioned that the LQR and H_2 optimization procedures (3.103) and (3.110) respectively are equivalent, so why discuss the H_2 optimization procedure when the standard output controller results in a Kalman filter for feedback?

In fact, there is another feature which makes the H_2 controller a far more superior form of LQR, due to the fact that a structure can be imposed on the output controller.

Suppose for example the global dynamic system of the notional grid was submitted for LQR optimisation to develop an optimal control for the global system. Described by the matrices (2.94) and (2.95). The resultant controller K_l will be one massive matrix full of gains, for instance:

$$u = K_l x = \left[\begin{array}{ccc|ccc} K_{1,1} & \dots & K_{1,6} & K_{1,7} & \dots & K_{1,11} \\ \vdots & \ddots & \vdots & \vdots & \ddots & \vdots \\ K_{6,1} & \dots & K_{6,6} & K_{6,7} & \dots & K_{6,11} \\ \hline K_{7,1} & \dots & K_{7,6} & K_{7,7} & \dots & K_{7,11} \\ \vdots & \ddots & \vdots & \vdots & \ddots & \vdots \\ K_{11,1} & \dots & K_{11,6} & K_{11,7} & \dots & K_{11,11} \end{array}\right] \left[\begin{array}{c} I_{id} \\ V_{cd} \\ I_{iq} \\ V_{cq} \\ \omega_{V_{cd}} \\ \omega_{V_{cq}} \\ \hline I_{ad} \\ I_{aq} \\ V_{dc_a} \\ \omega_{I_{aq}} \\ \omega_{V_{dc_a}} \end{array}\right] \tag{3.126}$$

where each element of $K_l \in \Re$. It is clear that the sub-matrices in the upper left, and lower right quadrants are controller gains associated to their respected converter states, VSI and AFE respectively. However the remaining quadrants are gains which couple the dynamics of both converters. This in essence means that the resultant LQR controller will require state information across all sub-system converters on the network to operate correctly. Imagine this for a full aircraft embedded grid network. For all the different power electronics units interfaced with the grid, all would need to send their state information to a central controller whereby commands are given with respect to dynamic position of all other states variables submitted by all the other subsystems. This would result in a highly complex communication network, which would result in huge increase in weight and complexity of the system. Not only this, but for the whole electrical system to work, all systems must be working accordingly. But, what if for instance a sub-system encounters a failure or even completely shuts down? This could throw the whole control system into disarray and could even lead to a total shutdown of the electrical system. Both these aspects are totally undesired

behaviours and it's in-fact illegal in aircraft system design. Redundancy is a legal requirement for aircraft, and we wish to reduce the weight of aircraft.

On the other hand, H_2 Optimization can have an imposed structure on the resultant optimal control K_{h_2}, unlike LQR. It has already been said though that K_{h_2} takes the form of a Kalman filter, as in (3.75).

Expanding this Kalman filter controller to the closed loop form, we will get:

$$\begin{cases} \dot{x}(t) = A_K x(t) + B_K u(t) \\ v(t) = C_K x(t) + D_K u(t) \end{cases} \tag{3.127}$$

Now the first constraint which can be imposed onto the H_2 controller is a constraint to receive a static full state-feedback control. From (3.127) and observing the H_2 problem block diagram in Figure 3.8, since all states are measured, $v = x$ and therefore, the static state-feedback controller is thus equivalent to:

$$u(t) = D_K x(t) \tag{3.128}$$

Therefore, imposing a constraint to the optimization that $A_K, B_K, C_K = 0$, ensures a static feedback controller is developed from the H_2 optimization. Now only this constraint will obviously result in a controller of similar form to (3.126). But again, the matrix D_k can be further constrained to give a certain form to the developed static feedback control. If we constrain D_K to be of the form:

$$D_K = \left[\begin{array}{ccc|ccc} K_{1,1} & \dots & K_{1,6} & 0 & \dots & 0 \\ \vdots & \ddots & \vdots & \vdots & \ddots & \vdots \\ K_{6,1} & \dots & K_{6,6} & 0 & \dots & 0 \\ \hline 0 & \dots & 0 & K_{7,7} & \dots & K_{7,11} \\ \vdots & \ddots & \vdots & \vdots & \ddots & \vdots \\ 0 & \dots & 0 & K_{11,7} & \dots & K_{11,11} \end{array}\right] \tag{3.129}$$

Then only the gains which are associated to their respected converters will be synthesised and leaves the other cross-coupled gain terms as zero. This is clear that two independent controllers can be synthesised for their respective converters, without the requirement of knowing the state information of other converters. The system has therefore been 'decentralized'. Systems are no longer dependant on others for their operation, and communication between subsystems minimized; whilst also each independent controller being optimal not only to the closed loop dynamics of their associated converter, but also the closed loop dynamics off all other optimized subsystems. All these highlighted benefits thus made this form of the H_2 controller the ideal candidate for an

optimized controller for an embedded grid for aircraft applications, and forms the crux of the research applied to the following chapters of this thesis.

3.4 Discussion and Summary

In this chapter, different forms of non-linear and linear optimal controls were investigated based on the requirements for the notional embedded grid system. This section highlighted many of the problems that are resultant from applying traditional, as well as modern non-linear optimal controllers, as well as what could be considered as one of the most robust forms of optimal linear control.

Firstly, the traditional non-linear controller termed Feedback Linearisation was investigated and implemented into the design. This control approach is very popular among engineers due to the ability to apply linear based controls onto a non-linear system, and the non-linear model is transformed into an approximate linear system, which the non-linearities are still intrinsically modelled. This mode of control has been widely employed for applications such as the AFE converter with great performance. Optimal global controller design as the problem proposed in this study has yet to be performed, so an analysis into the employment into feedback linearisation for the embedded grid network using this method of control was somewhat novel. However, for grids in aircraft applications, this controller was proved to be not up to the requirements. To ensure decentralised control of the system, the E matrix in the Feedback Linearised control law must have been a diagonal matrix with respect to the respective converter states. However, it was shown that coupling terms between the VSI states, and the states of the AFE were unavoidable in the control law, which meant the controller would always be coupled between the inverters generating the grid, and those converters drawing power from the grid. Aircraft controls must be decentralised for redundancy of the system, and to reduce the required cross-communication between sub-systems. Therefore, it has been shown in this work that feedback linearisation is not a method by which to design controllers for grids in these applications.

Due to many journal reviewers comments on the final proposed controller, it seemed important to briefly note the other forms of non-linear control available, as to highlight why these popular state-of-the-art controllers are not a suitable alternative for optimal embedded grid controls. Model Predictive controls are a very popular form of non-linear control in recent years and have been applied to many applications. They have shown to provide remarkable robustness, as well as performance across the range of systems, however they are relatively computationally heavy. They are very well known for their inability to scale up the control problem. As the system increases, the computations become ever more complex and longer to solve. Eventually for a scaled up full grid

system MPC approaches would be come near impossible, without incredibly fast, and expensive hardware. Although decentralised MPC controllers do exist to help mitigate this problem, they fundamentally still require lots of cross-communication between each distributed controller and thus would not fulfil the requirements set for our electrical system design.

Having investigated popular, and well used methods of intrinsically non-linear controls, the linear H_∞ controller was explored, where tuning is performed by shaping the required bandwidth through a set of weights. This form of optimal control was extensively analysed and the controller synthesis derived. Although a stable response could be received from the controller operating across the embedded grid due to the conservativeness and the well known struggle of finding the optimal solution to the control problem, only a sub-optimal solution could be synthesised. Whilst in normal applications this would probably not to be such a problem, the sub-optimal solution can compromise the robustness of the controller and thus could not be fully considered either.

However, due to the fact that the H_∞ controller was not far from an optimal solution, a less conservative form of controller would be required. Thus, H_2 was selected as the form of decentralized optimal controller for this study. Whilst the H_∞ approach analyses a controller K which achieved a set maximum gain across the disturbance w to error z transfer function across all frequencies, the H_2 performs the less rigid maximum average gain of the same transfer function. Although less robust to the H_∞, it was shown an optimal solution can be obtained, with a very low average gain even when the controller is forced to be a static full-state feedback controller, and with an imposed structure to ensure decentralization. The H_2 controller was shown to meet the required criteria for an optimal decentralized optimal controller without any cross communication between controllers, as well as being non-computationally heavy and being a very easy to implement and design for controller, as shall be shown in the next chapter; where a standard H_2 controller will be designed and implemented onto the notional system.

Chapter 4

The Optimal H_2 Controller Design vs Traditional Design

In the previous chapter, several popular approaches to the control of non-linear systems were presented, and designed around the non-linear AFE converter. It was shown however that whilst certain methods maybe very good with respect to the controller design for the single AFE; when including the dynamics of the VSI converter into the design problems began to occur. Problems arising from the necessity of cross-couple converter dependence, the computational complexity where more specialist hardware maybe required or simply the sub-optimal solution is the only solution viable for the system.

The H_∞ control option fit the latter of these listed problems, and this was drawn out due to the conservativeness of the procedure invoked by the optimization algorithm as only sub-optimal solutions for an individual AFE controller could be found. Whilst in general, and in academic literature where a sub-optimal H_∞ controller has been utilised in the design and shown to deliver considerable performance improvement over other forms of controller, the problem occurs when the complexity of the problem increases. With more converters which will inevitably be installed including our notional test system for grid applications, the constrains imposed will be greater and the challenge of finding an optimal solution will prove an even harder challenge, and may possibly produce even worse max gain criterion γ across the frequency range. Not only that, as observed in Table 3.3, the H_∞ controller also takes considerable time to synthesise a stable control, without the further structural restraint on K as required for static state-feedback. The H_2 control platform, as was shown shares many similarities with that of the H_∞ controller. However, where H_∞ was largely constrained due to the minimal 'maximum' gain requirement across all frequencies for the closed loop transfer function between disturbance (w) and performance, or error output (z). In the

H_2 optimisation on the other hand, the constraint is over the minimal root-mean-square average of the same transfer function. It is clear that minimisation of a global average is far less of a constrained optimisation than ensuring a minimal maximum gain. Therefore, as will be shown throughout this chapter, the H_2 controller is not only faster to come to a solution, but the solution is optimal for the given control problem. In fact, the required γ criterion will be shown to be met, even for not only a constrained static state-feedback control, but also for a controller with an imposed structural constraint on the static state-feedback control in order to decentralise the system.

Often within the industrial sphere of control system design, traditional controllers, typically, Proportional Integral (PI) controllers are very widely used. This is largely down to the technical and mathematical simplicity of these controllers. Methods such as root-locus analysis, Nyquist Criterion and pole placement techniques make it very easy for designers to condition the closed loop response of systems. They are generally very easy to design, and typically lead to very good performance. However, performance optimality is generally not the best these systems could be, and global system stability and global system performance is in general not considered. It will be shown that superior performance can be achieved using optimal control techniques such as H_2. Often, optimal control techniques are considered very hard to implement and design, but this chapter will show the ease of their development, as well as presenting that the implementation of such controls are in-fact very similar to that of the popular PI controllers.

This chapter consists of three parts. The first part covers the methodology of designing a decentralized H_2 controller for grid applications using the theory described in the previous chapter. This will investigate the general design procedure as well as a brief analysis to the general stability of the global system using this controller, as well as an analysis to the parametric robustness of the controller. The second part consists of a brief analysis to the design of traditional controllers, which are typically used in industrial applications today. This model will be continually assessed as a comparison for the rest of the studies presented in this thesis. This analysis also consists of a global and parametric uncertainty analysis for comparison to the proposed approach. The final part in this chapter is a brief comparison of the performance of each of the controllers and highlights of the key features which are brought forwards by the H_2 controller.

4.1 H_2 Controller Implementation and Design

In the previous chapter, the methodology behind the development of a H_2 controller was discussed in aspects of theory. However, it can be daunting to a designer when facing the problem of designing a H_2 controller is, how to go about the design and implementation of such controls. It is very often

perceived within the wider community of electrical engineers that implementing optimal controls such as the H_2 is often a very complex task, and thus often revert to the development of more simple controllers for instance PI which are widely well known and very easy to implement into the system. What this section hopes to detail, is the fairly straight forward nature of the optimal controller design, and actually present that the implementation is somewhat similar to that for traditional PI controllers.

4.1.1 Design Methodology for the H_2 Controller

To start the design procedure, we must first refer back to the optimal control problem block diagram introduced in Figure 3.8. As previously discussed, P represents the dynamic plant of the system which is used to interface the definitions of the external disturbances and performance signals in the model such that:

$$P = \left[\begin{array}{c|cc} A & B_1 & B_2 \\ \hline C_1 & D_{11} & D_{12} \\ C_2 & D_{21} & D_{22} \end{array}\right] \begin{bmatrix} x \\ w \\ u \end{bmatrix} \tag{4.1}$$

In this case, the A matrix as normal defines the state matrix of the system, and describes all the internal dynamics of the global system. The B_1 matrix is the disturbance matrix and describes all the states that can be perturbed. In the case of this study, perturbations are possible across all the states, and therefore the matrix is typically set to an identity matrix of appropriate size. The B_2 is the input matrix, and describes how the inputs to the system are augmented into the state architecture of the system. The matrices C_1 and D_{12} are matrices which define the weights on the states, and inputs respectively as presented in (3.112). It will be discussed later in this section how to correctly tune these terms in order to design a controller of desired performance. As per the assumed rules when performing a H_2 controller design, both matrices D_{11} and D_{22} are assumed to be zero matrices of appropriate size. Finally, C_2 is the state-measurement matrix. As previously defined, due to the fact that all states are measurable, including the integrals, this matrix for this case will be set as an identity matrix.

Many of these matrices have been previously defined in the modelling stage in Chapter 3, and shall be redefined in this chapter for continuity. Additionally, focus shall be given towards the constant power load case in order to exaggerate the non-linearities of the system to show the capabilities of this control. The so far known matrices of the system can thus be defined as:

$$A = \begin{bmatrix} -\frac{R}{L} & -\frac{1}{L} & \omega & 0 & 0 & 0 & 0 & 0 & 0 & 0 & 0 \\ \frac{1}{C} & 0 & 0 & \omega & -\frac{1}{C} & 0 & 0 & 0 & 0 & 0 & 0 \\ -\omega & 0 & -\frac{R}{L} & -\frac{1}{L} & 0 & 0 & 0 & 0 & 0 & 0 & 0 \\ 0 & -\omega & \frac{1}{C} & 0 & 0 & -\frac{1}{C} & 0 & 0 & 0 & 0 & 0 \\ 0 & \frac{1}{L_a} & 0 & 0 & -\frac{R_a}{L_a} & \omega & -\frac{p_d^*}{2L_a} & 0 & 0 & 0 & 0 \\ 0 & 0 & 0 & \frac{1}{L_a} & -\omega & -\frac{R_a}{L_a} & -\frac{p_q^*}{2L_a} & 0 & 0 & 0 & 0 \\ 0 & 0 & 0 & 0 & \frac{3p_d}{4C_a} & \frac{3p_q}{4C_a} & \frac{P_l}{C_a V_{dc_a}^2} & 0 & 0 & 0 & 0 \\ 0 & -1 & 0 & 0 & 0 & 0 & 0 & 0 & 0 & 0 & 0 \\ 0 & 0 & 0 & -1 & 0 & 0 & 0 & 0 & 0 & 0 & 0 \\ 0 & 0 & 0 & 0 & 0 & -1 & 0 & 0 & 0 & 0 & 0 \\ 0 & 0 & 0 & 0 & 0 & 0 & -1 & 0 & 0 & 0 & 0 \end{bmatrix} \tag{4.2}$$

$$B_2 = \begin{bmatrix} \frac{V_{dc}}{2L} & 0 & 0 & v0 \\ 0 & 0 & 0 & 0 \\ 0 & \frac{V_{dc}}{2L} & 0 & 0 \\ 0 & 0 & 0 & 0 \\ 0 & 0 & \frac{V_{dc_a}}{2L_a} & 0 \\ 0 & 0 & 0 & -\frac{V_{dc_a}}{2L_a} \\ 0 & 0 & -\frac{3I_{ad}}{4C_a} & -\frac{3I_{aq}}{4C_a} \\ 0 & 0 & 0 & 0 \\ 0 & 0 & 0 & 0 \\ 0 & 0 & 0 & 0 \\ 0 & 0 & 0 & 0 \end{bmatrix} \tag{4.3}$$

The matrices C_1 and D_{12} are the most essential components to the plant model P as these matrices will shape the desired controller to have the required dynamic response and robustness. This matrices, previously explained in the previous chapter take the form:

$$C_1 = \begin{bmatrix} Q_\gamma^{1/2} \\ \mathbf{0} \end{bmatrix}, \quad D_{12} = \begin{bmatrix} \mathbf{0} \\ R_\gamma^{1/2} \end{bmatrix} \tag{4.4}$$

The feedback matrix K is solved directly for the Algebraic Ricatti equation (ARE) and takes the form:

$$K = R_\gamma^{-1} B_2^T \Gamma \tag{4.5}$$

where Γ is the solution of the Lyapunov equation:

$$\Gamma A + A^T\Gamma + Q_\gamma - \Gamma B_2 R_\gamma^{-1} B^T \Gamma = 0 \tag{4.6}$$

Q_γ and R_γ Weight Matrices

The Q_γ matrix is of a symmetric positive semi-definite form, whilst R_γ is of a symmetric positive definite matrix form, as:

$$Q_\gamma = \begin{bmatrix} q_1 & 0 & 0 & 0 \\ 0 & \ddots & 0 & 0 \\ 0 & 0 & \ddots & 0 \\ 0 & 0 & 0 & q_n \end{bmatrix}, \quad R_\gamma = \begin{bmatrix} r_1 & 0 & 0 & 0 \\ 0 & \ddots & 0 & 0 \\ 0 & 0 & \ddots & 0 \\ 0 & 0 & 0 & r_m \end{bmatrix} \tag{4.7}$$

where n is the number of states contained in A, and m is the number of inputs to the system (the number of columns in B_2).

The matrices Q_γ and R_γ are design parameters which penalise the state variables or control inputs respectively in the closed loop. Their diagonal elements can each dictate how much of either of the states or inputs of the system can vary in order to achieve equilibrium from a disturbance. Each diagonal element of either matrix directly relates to the states or input of the system as they are described in the state-space matrix. In this example, each diagonal element of Q_γ and $R\gamma$ corresponds to the order of the states x and inputs u respectively as shown below:

$$x = \begin{bmatrix} I_{id} & V_{cd} & I_{iq} & V_{cq} & I_{ad} & I_{aq} & V_{dc_a} & \chi_{V_{cd}} & \chi_{V_{cq}} & \chi_{I_{aq}} & \chi_{V_{dc_a}} \end{bmatrix}^T \tag{4.8}$$

$$u = \begin{bmatrix} m_d & m_q & p_d & p_q \end{bmatrix}^T \tag{4.9}$$

The larger the individual diagonal elements in each of the above weighting matrices, the more the signal is penalised in the closed loop. Analysing R_γ first; this statement essentially means that the larger the value specified in r_i, the more the system will attempt to stabilise with less waited energy, as in to not allow the inputs to change vastly in order to stabilise the system, which is often referred to as an expensive control strategy. On the other-hand, if a smaller value is passed to r_i, then greater weighted energy that is allowed on the inputs, allowing the inputs greater movement to achieve system equilibrium; often referred to as cheap control strategy. For the Q_γ matrix, equivalently assigning a large value to q_i results in the closed loop stabilizing the system with the least possible change to the associated state, and likewise, a smaller value, the greater the change allowed. Unlike for traditional PI controllers, whose deigns will be carried out later in this chapter, the allocation of the closed loop poles, and hence the closed loop bandwidth is not possible in this

kind of configuration. The designer when developing a H_2 controller can only control the amount of desired weighted energy across the system inputs and the states; however this does not mean that the designer does not have control over the bandwidth of the system; quite the contrary. Through both these matrices, we can dictate the dynamic speed of the system. As a brief example, as quoted above, the increase in the value of a Q_γ diagonal element, the less change desired on that given state. Therefore, if a step change in the control reference demand was imposed onto the system, the value of this element can dictate the speed of response to the step reference change. The larger the value, the faster the speed and hence bandwidth of that given state, and vice versa. Below is a simple example of a SISO state-space system, where an LQR controller synthesised from different Q_γ and R_γ matrices are formed:

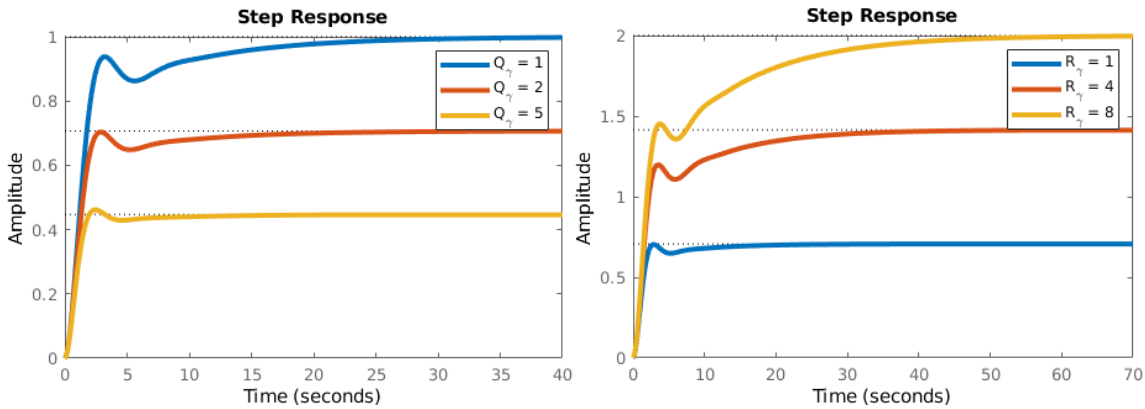

(a) How the closed loop performance changes with the variation of the Q_γ weight, whilst $R\gamma$ weight kept constant.

(b) How the closed loop performance changes with the variation of the R_γ weight, whilst $Q\gamma$ weight kept constant.

Figure 4.1: Comparison of the effect of varying Q_γ and R_γ weights to simple SISO system.

Using a simplified Aircraft Pitch Model found in [120] the above examples were made. As explained, it can be clearly seen that the larger the value imposed on the Q_γ weight, the faster the dynamic response of the closed loop system to an stable equilibrium point. Conversely, the larger the weight in R_γ, the slower the dynamic response becomes. This is easy to understand considering that larger values of the weight in R_γ impose greater restriction on the control energy given to the inputs. This restricts how much the inputs can change. Thus, the resultant response is slower. Therefore, control designers typically weight Q_γ accordingly in order to achieve specified bandwidths for states according to their required dynamics.

However, one can also note that each version of this control sets the system at different settling points. In this example the set-point was set to 1, so why are all the controllers producing different outputs? This is largely down the the fact that in the case of this system, the feedback control is

only based on the proportional error. The controller will only react to an error, if the error is large enough in proportional control based systems.

The methodology of tuning such LQR controllers are based of the Bryson's rule: [121]

$$Q_\gamma = \begin{bmatrix} \frac{\alpha_1^2}{(x_1)^2_{max}} & & & \\ & \frac{\alpha_2^2}{(x_2)^2_{max}} & & \\ & & \ddots & \\ & & & \frac{\alpha_n^2}{(x_n)^2_{max}} \end{bmatrix}, \quad R_\gamma = \begin{bmatrix} \frac{\beta_1^2}{(u_1)^2_{max}} & & & \\ & \frac{\beta_2^2}{(u_2)^2_{max}} & & \\ & & \ddots & \\ & & & \frac{\beta_m^2}{(u_m)^2_{max}} \end{bmatrix} \tag{4.10}$$

Where, $(x_i)_{max}$ and $(u_i)_{max}$ represents the largest admissible error on the state or input signal, and the terms $\sum_i \alpha_i^2 = 1$ and $\sum_i \beta_i^2 = 1$ are relative weightings to give extra control over the dynamics of individual states. Evidently, it is clear that this approach to controller design is based on an allowed error to be allowed across the states.

Integral Control in H_2 Controllers

It has already been discussed in Section 2.2.2 the notion of how integral states can being augmented into the system model. This paves the way for the development of state-feedback control systems with integral control actions that ensures zero steady state error. In equation (4.8) integral states have already been augmented as states χ with their subscripts defining what state the integral state is integrating.

Take the case that this system can be modelled as:

$$\frac{d}{dt}\begin{bmatrix} x \\ \chi_i \end{bmatrix} = \begin{bmatrix} Ax + Bu \\ r - y \end{bmatrix} = \begin{bmatrix} Ax + Bu \\ r - Cx \end{bmatrix} \tag{4.11}$$

where χ_i are states associated to the integral of the error from the desired output r and the actual output y; also termed 'Integral States'. At steady state, these states must be $\dot{\chi} = 0$, and therefore means that $y = r$, which also implies that the states, as defined in Cx must also have reached the required references or equilibrium point values. Therefore, referring back to Figure 4.1a if the integral states were to weighted to have larger values of q_i with respect to the weights in R_γ, then in retrospect the speed of the global system to reach the state-state operating point can be determined by the weighting the integral states solely. Therefore, the weighting matrices can take the form:

$$Q_\gamma = \begin{bmatrix} \mathbf{0}_1 & & & & & & & \\ & \mathbf{0}_2 & & & & & & \\ & & \ddots & & & & & \\ & & & \mathbf{0}_n & & & & \\ & & & & q_{\omega_1} & & & \\ & & & & & q_{\omega_2} & & \\ & & & & & & \ddots & \\ & & & & & & & q_{\omega_m} \end{bmatrix}, \quad R_\gamma = \begin{bmatrix} r_1 & & & \\ & r_2 & & \\ & & \ddots & \\ & & & r_m \end{bmatrix} \tag{4.12}$$

where subscripts on $\mathbf{0}$ defines only the diagonal element number that zero weight is attributed to. Therefore, it can be shown that all the dynamic and disturbance rejection requirements of the system can be dictated totally by the weights to the integrals, whilst also ensuring zero steady-state error to the desired references r [27, 84].

Tuning of the H_2 Controller

Whilst Bryson rule can be typically used as a starting point to the tuning of LQR based controllers, as said before it's a tuning procedure whereby an accepted error value is used in order to tune the controller. When dealing with the weighting of integral states in order to bring the global system quickly to equilibrium the error to a reference integral value has little meaning in this regard. The integral action in itself will ensure that the system states reach zero steady state error with respect to the control references, and therefore the allocated weight in Q_γ results in an equivalent bandwidth for the integral state to reach an equilibrium point. This value changes dependant on the synthesised controller gains, and as it is a non-physical value, this value can be as big or as small as necessary. Therefore the tuning of these controllers often involves elements of trial and error to find the most suitable weights for the closed loop response. However, there are methods which can make the process of finding suitable Q_γ and R_γ weights much simpler.

In general, the easiest starting point is setting the matrices to an identity matrix, such that:

$$Q_\gamma = \begin{bmatrix} \mathbf{0}^{n\times n} & \mathbf{0}^{n\times m} \\ \mathbf{0}^{m\times n} & I^{m\times m} \end{bmatrix}, \quad R_\gamma = \rho I^{m\times m} \tag{4.13}$$

As previously stated, only integral states in Q_γ having identity terms whilst other states are set to zero. Following this the performance of the system can be analysed. Remembering that the H_2 controller guarantees stability about the designed for equilibrium point, the system should output stable performance if the system is at this condition. The second step in the tuning procedure is

then to alter ρ such that satisfactory dynamic performance can be achieved. Note however, this being the standard procedure to controller tuning for standard systems, the adjustment of ρ would generally be adequate in achieving desired system performance. However, in this optimisation two unique sub-system with differing internal dynamics are present. Using ρ in this manner, whilst enabling adequate performance for one sub-system, the other sub-system may not achieve the desired performance in some cases. Therefore, it was found useful to perform tuning using two scaling factors such that:

$$R_\gamma = \begin{bmatrix} \rho_{vsi} & \rho_{afe} \end{bmatrix} \begin{bmatrix} I^{m_v \times m_v} & \mathbf{0}^{m_a \times m_v} \\ \mathbf{0}^{m_a \times m_v} & I^{m_a \times m_a} \end{bmatrix} \tag{4.14}$$

where m_v and m_a defines the number of inputs for the VSI and AFE respectively. Therefore, the performance of each converter can be scaled as required. For instance, if the AFE appears to convey oscillatory behaviour to dynamic change whilst being scaled equally with the weights of the VSI, an increase to ρ_{afe} and restricting the amount of controller energy available specifically to the AFE will keep the desired performance of the VSI, whilst improving the dynamic performance of the AFE also.

Now, having scaled ρ to achieve the desired performance of the controller, any final performance tuning can be performed by adjusting the integral weights in Q_γ. For the VSI, it is sensible to have the weights associated to $\omega_{V_{cd}}$ and $\omega_{V_{cq}}$ equal, due to the fact from Figure 2.9, the d and q axis equivalent circuits are very similar, and thus do not require different bandwidths from each other. There would be no real justifiable reason to do so. However, this is not true for the AFE integral states $\omega_{I_{aq}}$ and $\omega_{V_{dc_a}}$, as one is on the q axis, and the other is a standard DC signal. Therefore, the weights between these two integral states do have justifiable reason to have different values if so required to achieve desired performance. This introduces the methodology behind the tuning of the H_2 controller, and a practical example of its application will be observed later in this chapter.

Decentralization of the Optimal Controller

As has been previously mentioned, the H_2 controller, and the subsequent LQR controller are full-state feedback controllers. This means in order for them to function, all information about the states are required. Typically in the H_2 controller synthesis, the resultant controller as discussed in Section 3.3.3 takes the form of a Kalman filter such that any non-measurable state can be instead estimated, and thus the relevant control action u calculated in order to bring the system to stability. However, in the notional system under investigation, all state variables are accessible for measurement, and thus the Kalman filter part of the controller is unnecessary. As described by use of equation (3.128), a static feedback controller can be formed, by constraining the optimisation

process to search for a control where only the D matrix terms of the Kalman state-space filter are available for optimisation. All other matrices (A, B and C) being forced to null. Interestingly, the solution received from this constraint actually results in the same controller gains as that of the LQR controller, which is always static-state feedback in implementation. However, in this form, one central controller is synthesised, where all the system states of the systems are passed into it to ensure stable global operation. This is undesirable, not only from a redundancy point of view, but also this configuration will require a lot communication between converters and the central controller would be required which would not only increase the overall weight of the aircraft, but also would result in a large increase of complexity in the case of a full size grid. This is where decentralization comes in.

Decentralization, often referred to as distributed control (although there is no defined line between when a system is distributed or decentralized among some studies) is the process of removing the requirement of a central controller, and instead developing individual controllers for each individual sub-system in the global model.

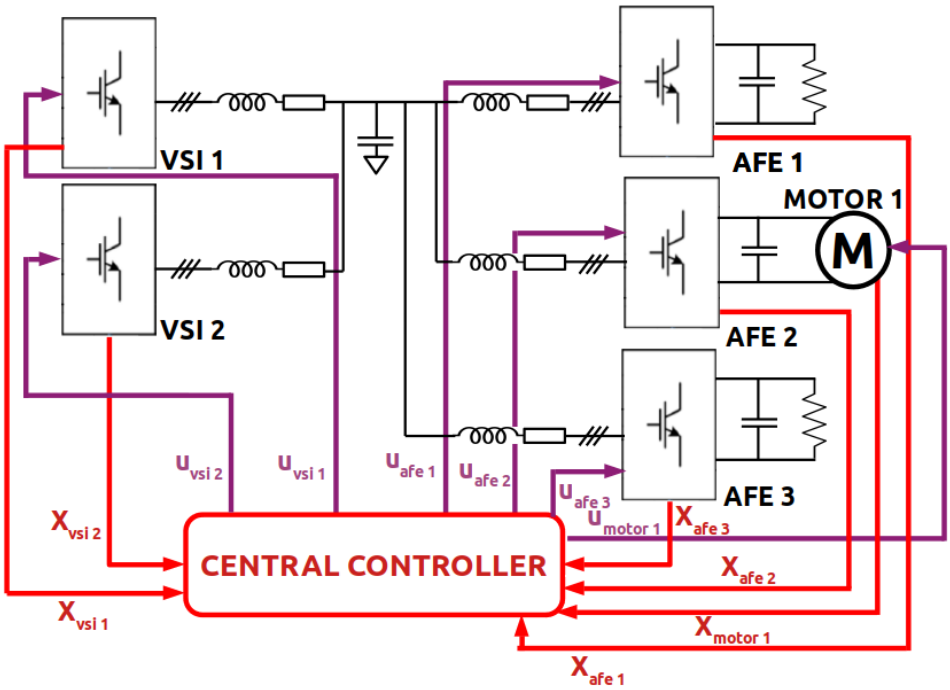

Figure 4.2: Visual Example of a Centralised Control System

Figure 4.2 depicts a more complex notional grid system with multiple converters interlinked on the same grid. Although the goal is to develop a controller for this kind of expanded notional system, this system is used only as a more complex example for visualising the concept of decentralisation and will not be investigated upon in this study. As shown, a centralised control requires a lot of

communication between each of the converters in real time, and fully depends on the correct communication of the state information from all sub-systems to the central controller at any given moment. This is very impractical, when there could possibly be kilometres of cable being utilised just for controller communication alone.

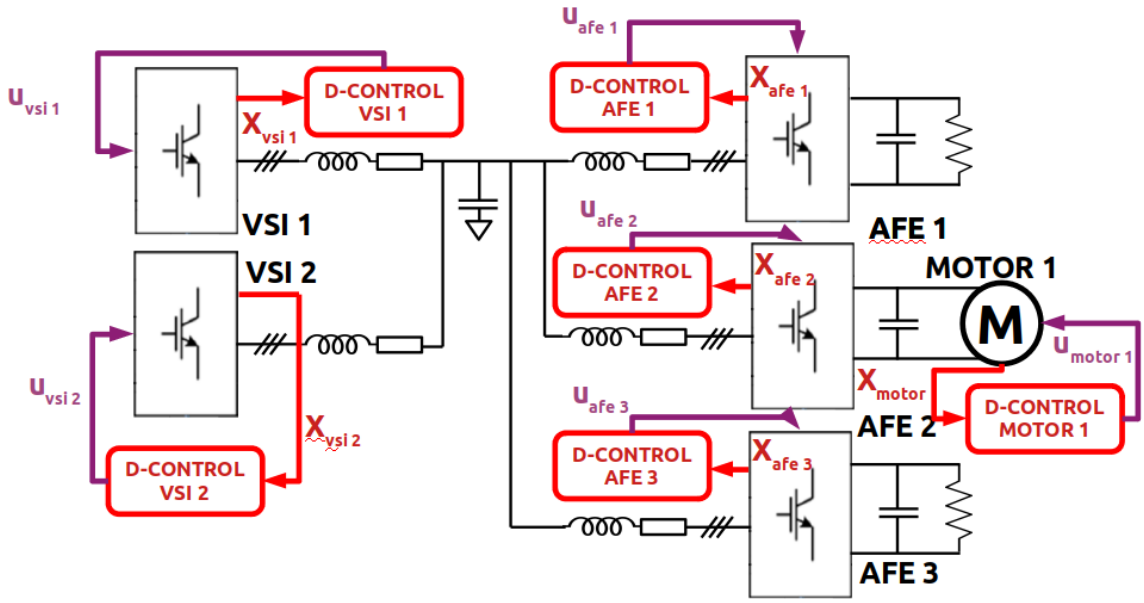

Figure 4.3: Visual Example of a Decentralised Control System

Figure 4.3 presents the alternative decentralised controller scheme, where each sub-system has their own controller. Sub-systems are no longer dependant on the states of others for their correct control actions, and is clearly visible there will be a reduction in the amount of cabling in such schemes. Typically though, these controllers are often optimised and calibrated only to the converter to which it's controlling. Typically commercial converters whereby a manufacturer does not account for the external dynamics to which these converters will be installed into. A large contribution to the novelty of the work proposed in this thesis stems from this issue, as controllers unoptimised for the surrounding grid dynamics can introduce heavy interactions to the system. This will be observed later on in this chapter in Section 4.2 where the design of such a system using PI controllers is carried out.

In this design however, each of these decentralised controllers will be optimised with full consideration to the closed loop dynamics of other sub-system's closed loop controls. Now, it has been previously mentioned that the well known LQR controller is equivalent to the optimal H_2 controller, when H_2 is forced to synthesise a static state-feedback controller. However, LQR is a convex optimisation procedure which doesn't have much in the way of ability to constrain the gain matrix K to a given form. The H_2 synthesis algorithm however does have such ability. The

H_2 controller gains have already been constrained such that a static state-feedback controller is formed. The static gain matrix can be even further constrained such that the resultant K is in a predefined structure. Let's suppose that the control law involving a structured controller K_D is:

$$u = -K_D x \tag{4.15}$$

To ensure K_D develops an optimal decentralised controller, K_D must only allow gains to be synthesised on converter states directly, and make all other sub-system cross-coupled terms null. This results in the imposed structure:

$$K_D = \left[\begin{array}{ccc|ccc|cc|cc} k_{1,1} & \cdots & k_{1,4} & 0 & \cdots & 0 & k_{1,8} & k_{1,9} & 0 & 0 \\ k_{2,1} & \cdots & k_{2,4} & 0 & \cdots & 0 & k_{2,8} & k_{2,9} & 0 & 0 \\ \hline 0 & \cdots & 0 & k_{3,5} & \cdots & k_{3,7} & 0 & 0 & k_{3,10} & k_{3,11} \\ 0 & \cdots & 0 & k_{4,5} & \cdots & k_{4,7} & 0 & 0 & k_{34,10} & k_{4,11} \end{array}\right] \tag{4.16}$$

Multiplying K_D with the states x as defined in (4.8) each of the gains k_{ij} in K_D are attributes only to the converter to which they're applied. Taking $k_{ij}, i = 1, 2, j = 1, \rightarrow 4, 8, 9$ each of these gains are attributed only to VSI states. For $k_{ij}, i = 3, 4, j = 5 \rightarrow 7, 10, 11$ these gains are attributed only to AFE states. The structure imposed on K_D therefore results in two independent controllers with corresponding proportional and integral gains, which can be applied to converters individually. Since both the controllers were synthesised under the same optimisation algorithm, each controller is optimal to the closed loop dynamics of the other sub-system and vice versa; with no additional communication between converters required. Each controller is developed on the knowledge of the rest of the system, which proves powerful when this controller is tested later on in the chapter.

Random Starting Point Selection for Minima Location

Now, a standard LQR controller synthesis is considered a convex optimisation due to the fact that a unique solution exists for the Algebraic Riccati equation as defined in (3.116). This can be observed simply by running the LQR optimisation several times. Because there is a unique solution of Γ, the resultant controller will always be the same, and hence a convex optimisation. However, constraining the gain matrix in the form of K_D increases the complexity of the optimisation greatly. The structure K_D imposes linear constrains directly onto the minimization optimisation problem as defined in (3.122). These imposed linear constraints on the optimisation procedure can be written in the form:

$$K \in \mathcal{S} \tag{4.17}$$

where $\mathcal{S}$ is the subspace of all gains in K_D which stabilize the system. The cost function J becomes a smooth function in K_D which is bounded by every K_D which makes the closed loop global system asymptotically stable.

In order to simplify the understanding as to how the optimization locates as best possible global minimum, a simplified two-dimensional example is discussed below.

When it comes to optimal control, the crux of the synthesis is based on the cost function J. One of the most simple of cost functions for such optimisation is the following:

$$J = h\left(x\left(t_f\right)t_f\right) + \int_{t_0}^{t_f} g\left(x(t), u(t)\right) dt \tag{4.18}$$

Where h and g are scalar functions, t_0 and t_f are the initial and final times of the system evaluation, where commonly t_f is evaluated as infinity. At a given time t, the state will be at a value $x(t)$, with the control signal $u(t)$, the system will follow a given trajectory. Each possible trajectory holds a unique real number value which correspond to the performance. Therefore, the optimisation problem becomes, find the optimal control input $u^*(t)$ such that the trajectories of $x(t)$ minimizes the performance measure J in (4.18) [7].

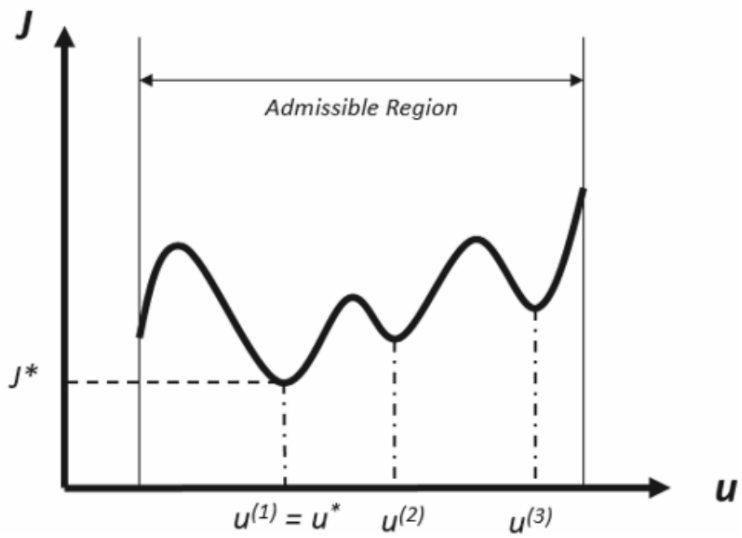

Figure 4.4: Visualisation of the Optimisation of the Cost J [7]

Figure 4.4 aids in the visualisation of locating the minimum and optimal control. Each of the control inputs $u^{(1)}, u^{(2)}$ and $u^{(3)}$ shows each of the points where the performance index J is at a local minimum for some fictional system. It is clear however in this example, that the point associated to $u^{(1)}$ results in the global minimum of the cost J, and thus would be considered the optimal solution to the control problem. Given that the optimal state-feedback H_2 controller being synthesised has the closed loop dynamics generalised by the state-space form $G = A - BK_D$,

where $u = -K_D x$, this cost function can be revaluated such that the optimal controller K_D is synthesised. Thus, K_D ensures for a given input $u(t)$, the associated trajectory of all $x_n(t)$ achieves the global minimum of J. However, as can be observed there are multiple local minima which could be mistakenly evaluated to be the global minimum if the cost is evaluated from a given stating position along $\mathcal{S}$. Algorithms which locate these local minima track the gradient of these multidimensional functions until the zero component of the gradient is located. Quasi-Newtonian methods are the popular method for minima location in these applications, and in the case of this study, the Broyden-Fletcher-Goldfarb-Shanno algorithm (BFGS) was utilised [114]. Therefore, to ensure that the global minimum can be successfully located, a multiple starting point solution must be employed, where many local minimums are evaluated and the one which results in the lowest cost J in (3.122) is the resultant structured optimal controller.

It can be shown that in the time domain, under the influence of constrained gain matrices, the optimisation defined (3.122) can be equivalently evaluated to be: [122]

$$\min_{K_D} J(K_D) = tr\left(B_1' \int_0^\infty e^{(A-B_2K_D)'t}\left(Q + K_D' R K_D\right) e^{(A-B_2K_D)t} dt B_1\right) \tag{4.19}$$

Equivalently, the gradient for a given $K_D \in S$ can be evaluated as: [123]

$$\nabla J\left(K_D\right) = \left(B_2'\Gamma + RK\right)L \tag{4.20}$$

where L is the solution to an additional Lyapunov equation of the form:

$$\left(A - B_2K_D\right)L + L\left(A - B_2K_D\right) = -B_1'B_1 \tag{4.21}$$

Of course with any increase to the size of the system state matrix A, the more complex the optimisation in (4.19). In general, the greater the order of the system, the more random starting points along $\mathcal{S}$ that will be required to evaluate the true minimum. However to help in the guaranteeing the location of the true global minimum a guess of the optimal controller can be given. Considering that the standard LQR is a convex optimisation procedure finding the controller K_D which minimises J globally, the LQR controller can be used as a good initial guess to the location of the global minima in the constrained optimisation, and thus possibly reduce the number of starting points required in the optimisation.

4.1.2 Controller Synthesis and Implementation

Taking all the information from the previous subsection, here a decentralized controller design for the notional VSI + AFE system shall be put to practise including the tuning procedures.

We therefore wish to form the H_2 plant model as shown in (4.1). The matrices A and B_2 have already been predefined in this system in (4.2) and (4.3) respectively. Typically for state-space systems, the C_2 matrix would define how the desired outputs of the system relate to the system states. However, in the case in the model of P, C_2 defines all the states which are accessible for measurement. Since in this case, all states can be measured direct, the C_2 matrix is simply:

$$C_2 = I^{n\times n} \tag{4.22}$$

where for continued simplicity, n now defines the number of system states including integral states. Now, keeping in mind that specific requirements must be met, as stated in Section 3.3.2 the matrices D_{11} and D_{22} must be zero. Therefore, in order to concatenate correctly into the model P, both these matrices must therefore be:

$$D_{11} = \mathbf{0}^{(m+n)\times n}, \quad D_{22} = \mathbf{0}^{n\times m} \tag{4.23}$$

Now for these kinds of controller designs, it is typically assumed that no direct feed-forward terms between the disturbance and inputs are present. So again, the D_{21} matrix can also be assumed zero, such that:

$$D_{21} = \mathbf{0}^{n\times n} \tag{4.24}$$

The B_1 matrix details all the states to which can be affected by external perturbation distances. All the states can be influence by external perturbations, so simply, the B_1 matrix can be set to be an identity matrix:

$$B_1 = I^{n\times n} \tag{4.25}$$

The remaining matrices are those which describe the weight matrices C_1 and D_{12} which are evaluated upon simulation of the model, although as described the the previous sub-section, the default starting position for tuning these matrices should be of the following form:

$$C_1 = \begin{bmatrix} Q_\gamma \\ \mathbf{0}^{m\times n} \end{bmatrix}, \quad D_{12} = \begin{bmatrix} \mathbf{0}^{n\times m} \\ R_\gamma \end{bmatrix} \tag{4.26}$$

Where Q_γ is equivalent to that specified in (4.13) and R_γ has the initial form:

$$R_\gamma = \begin{bmatrix} I_{\rho_{vsi}}^{m_v\times m_v} & I_{\rho_{afe}}^{m_a\times m_a} \end{bmatrix} \begin{bmatrix} I^{m_v\times m_v} & \mathbf{0}^{m_a\times m_v} \\ \mathbf{0}^{m_a\times m_v} & I^{m_a\times m_a} \end{bmatrix} \tag{4.27}$$

Parameters of the Notional System

The notional system under test in this chapter is that depicted in Figure 2.3, where descriptions of the VSI and AFE can be found in Sections 2.1.1 and Section 2.1.2 respectively. The system

is portrayed as accurately as possible as a subsection of the embedded grid of an aircraft. The AC grid then must be generated to a value of $100V_{rms}$, and the DC-Link voltage should be set to 400V. Consideration of the design of the filters, and DC-Link capacitors were based of work performed on a similar system described in [124, 25]. As the emphasis of this work looks at system interactions under low passive filter environments, the passive filters were reduced, whilst ensuring the bandwidth of the filter of approximately 1800Hz, as to not affect the core functionality of the grid. The parametric values presented below shall be those used thought each of the studies conducted in this thesis.

Parameter	Value
R	120mΩ
L	360μH
C	33μF
Ra	0.8Ω
La	565μH
Ca	100μF
ω	400(2π)rads^{-1}
VSI $V_{dc-source}$	290V
Grid V_{ac}	115Vac

Table 4.1: AFE Parametric Voltages and Input Voltages

Control Reference Values	
V_{cd}	141V
V_{cq}	0V
I_{aq}	0A
V_{dc_a}	400V
P_l	1kW
$f_{switching}$	10kHz

Table 4.2: Feedback Linearization Control References

Controller Synthesis

As previously suggested, due to the non-convex nature of the constrained H_2 algorithm with a constrained K_D, to ensure the best guarantee of locating the global minimum of the cost function, it can prove helpful by first generating a full LQR controller which stabilises the system P. In MATLAB, there is an inbuilt function $lqr()$ which can generate an optimal controller K, by supplying A, B_2 and the weights Q_γ and R_γ. P can be populated using parameters in Table 4.1, and by evaluating the equilibrium points of the system p_d, p_q and I_{ad} using equations (2.54)-(2.56) assuming operation at the control references given in Table 4.2.

The resultant unconstrained LQR controller thus becomes:

$$K_{lqr} = 10^{-3}\begin{bmatrix} -3.54 & -0.17 & -1.83 & 0.27 & -2.86 & -4.61 & -4.4 & 850 & -69.6 & -392 & 356 \\ -1.83 & -0.5 & -5.61 & 0.09 & -4.47 & -7.59 & -8 & -37 & 835 & 276 & 476 \\ 1.14 & 0.15 & 1.67 & -0.04 & 6.2 & 4.35 & 5 & 534 & 85.6 & 656 & -527 \\ 2.5 & 0.35 & 4.12 & -0.15 & 6.18 & 13 & 10 & 30 & 539 & -583 & -607 \end{bmatrix} \tag{4.28}$$

Note however that the lqr() MATLAB function assumes this control law will be input as $u = -Kx$, and thus the stable controller will be $-K_{lqr}$. The controller in (4.28) has been adapted into the correct form, and shall be supplied to the H_2 algorithm as the initial guess in the minimization of the H_2 norm in the H_2 controller synthesis.

Next, the constrains on the output controller must be initialised. Noting that the standard form of H_2 controller includes a Kalman filter, and is of the form:

$$\hat{K_{H_2}} = \left[\begin{array}{c|c} \hat{A} & \hat{B} \\ \hline \hat{C} & \hat{D} \end{array}\right] \tag{4.29}$$

and that in order to synthesis a static state feedback controller, the controller must be constrained to only output $\hat{D}$, the controller gain matrices $\hat{A}$, $\hat{B}$ and $\hat{C}$ are all held strict to zero. Additionally in order to develop a decentralised state-feedback control, the output gain matrix $\hat{D}$ must be further constrained such that it takes the form of that described in (4.16):

$$\tilde{\hat{D}}_c = \begin{bmatrix} 1 & 1 & 1 & 1 & 0 & 0 & 0 & 1 & 1 & 0 & 0 \\ 1 & 1 & 1 & 1 & 0 & 0 & 0 & 1 & 1 & 0 & 0 \\ 0 & 0 & 0 & 0 & 1 & 1 & 1 & 0 & 0 & 1 & 1 \\ 0 & 0 & 0 & 0 & 1 & 1 & 1 & 0 & 0 & 1 & 1 \end{bmatrix} \tag{4.30}$$

where entries '1' define this as a gain which can be selected for optimisation, and entries '0' define gains which must be held at zero.

The initial guess which will be supplied to the algorithm, which will be noted at I_G can therefore be simply received by performing the following:

$$I_G = -\tilde{\hat{D}}_c K_{lqr} \tag{4.31}$$

The HIFOO toolbox used for this synthesis assumes the alternate control law $u = K_D x$ in its synthesis, so supplying the inverted form will be correct for HIFOO.

The only requirement left is to define how many random starting points will be required to successfully approximate the global minimum for every run of the controller. This number is largely trivial and depends entirely from system to system. Often, it comes down to trial and error. ON

each run of the algorithm, if each resultant controller is vastly different in gain values and closed loop performance, an increase in the number of random starting points will be required, as this would suggest in the algorithm finding different local minimums and not the true global minimum. Through testing of this system, a value of 10 starting points was enough to synthesise consistent controller gains, and therefore locating the assumed global minimum.

The MATLAB script which was used to synthesise this controller can be seen in Appendix A.1.

The resultant H_2 Optimal Controller using identity weights is the controller detailed in (4.32).

$$K_D = 10^{-5} \begin{bmatrix} 1.35 & -1.79 & -41 & 0.32 & 0 & 0 & 0 & 826 & 46 & 0 & 0 \\ 31 & -7.2 & 7.87 & -6.21 & 0 & 0 & 0 & 57 & 885 & 0 & 0 \\ 0 & 0 & 0 & 0 & 14.7 & -33 & -36 & 0 & 0 & 1.06 \cdot 10^3 & -1.88 \cdot 10^3 \\ 0 & 0 & 0 & 0 & 79 & 109 & 21 & 0 & 0 & -1.57 \cdot 10^3 & -1.26 \cdot 10^3 \end{bmatrix} \tag{4.32}$$

Clearly in this case, the result of the optimisation provided by evaluation of the global minimum of the H_2 norm resulted in a controller far from the initial guess I_G and shows the importance of evaluating with enough random starting points to compute the global minimum..

The Average Simulation and Controller Tuning

In order to validate the control with speed, an average system model can be constructed to analyse mathematically the behaviour of the closed loop system. The average model can be easily constructed in software by formulating the dynamic equations though a ODE45 algorithm, where the controller dynamics are implemented as feedback which controls the control action u to the system. To see how the average model was built up into a ODE45 MATALB script please refer to Appendix A.2.

Running the average simulation, with the state-feedback controller results in the simulation results presented in Figure 4.5.

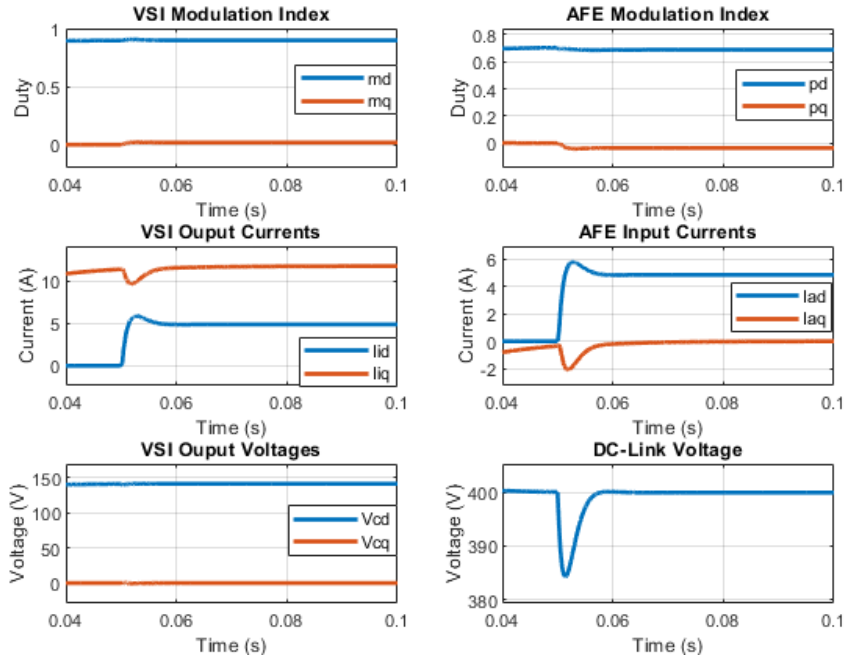

Figure 4.5: Average Simulation of VSI + AFE system with default starting weights Q_γ and R_γ

In this simulation, the CPL is initially set to 0W, and at $t = 0.05s$ a $1kW$ step load is activated on the AFE output, so the simulation analyses the step response to a load change on the AFE. From first observations, it can be observed that with the current weightings, the decentralised controller K_D already provides a very adequate response to a quite serve disturbance on the AFE. Therefore, the weightings on R_γ need not be altered. However, it can be observed that the $q-$axis currents on each converter do present a slow dynamic to steady state, even before the load disturbance takes place. This can be simply solved by increasing the bandwidth, and hence the weight of the associated Q_γ matrix to provide greater bandwidth. Although these states are what is needed to be catered for, increasing the overall weight of Q_γ will provide dynamic improvement across the whole system as a whole. If the Q_γ matrix has its weight increase by $7\times$ such that:

$$Q_\gamma = 7diag\left(\begin{bmatrix}0 & 0 & 0 & 0 & 0 & 0 & 0 & 1 & 1 & 1 & 1\end{bmatrix}\right) \tag{4.33}$$

Then the performance in comparison can be observed in Figure 4.6:

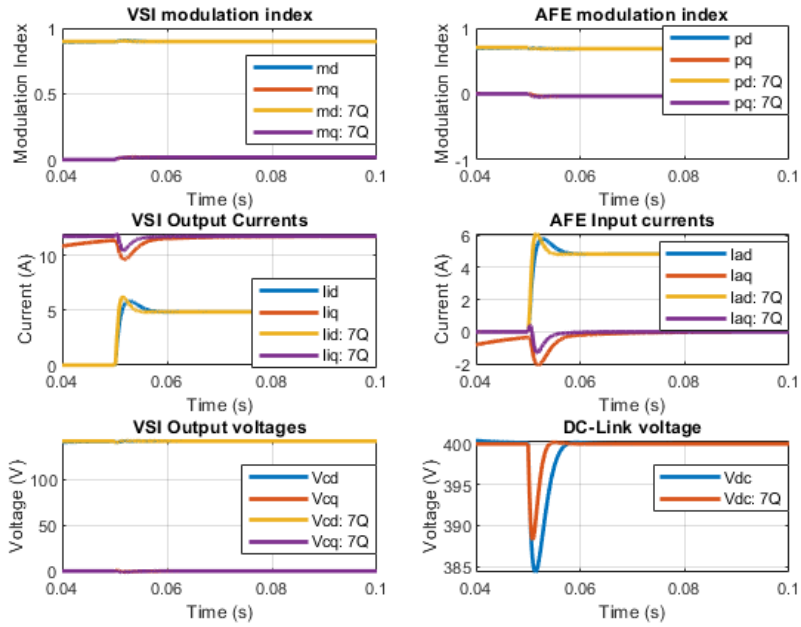

Figure 4.6: Average Simulation of VSI + AFE system with $7Q_\gamma$ and default R_γ

Where signals noted $7Q_\gamma$ are the waveform generated with the increase Q_γ matrix. By adjusting the Q_γ matrix, now all states are sufficiently at the steady-state positions before the CPL is turned on. At the disturbance, it is also evidently clear that the dynamic performance across all of the states has been improved. In fact, the performance can be improved further. Increasing the weight to $14Q_\gamma$, we can get even better performance, although only slight. Going beyond a scaling factor of 14 results in little further improvement to the dynamic performance of the global system and is thus deemed unnecessary to increase further. As the Q_γ matrix increases in size, so do the value of the gains, which could result in the system being dependant on anti wind-up procedures to prevent the system modulation indexes from saturating and may impede performance of the controller. So a weighting which gives sufficient improvement to the dynamics from default settings, and doesn't increase the value of the gains too greatly is satisfactory. Therefore, the final design of the tuning weights for this system is:

$$Q_\gamma = 14diag\left(\begin{bmatrix}0 & 0 & 0 & 0 & 0 & 0 & 0 & 1 & 1 & 1 & 1\end{bmatrix}\right) \tag{4.34}$$

$$R_\gamma = diag\left(\begin{bmatrix}1 & 1 & 1 & 1\end{bmatrix}\right) \tag{4.35}$$

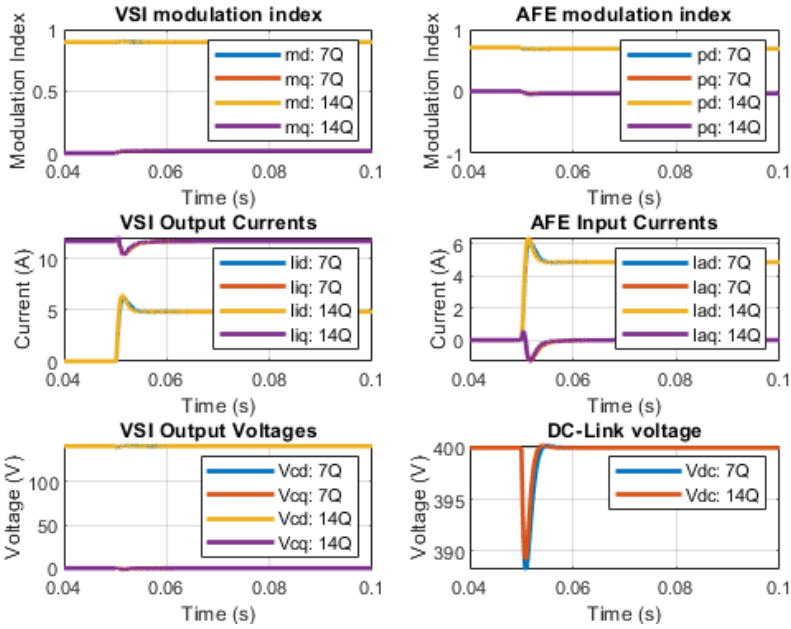

Figure 4.7: Average Simulation of VSI + AFE system with $14Q_\gamma$ and default R_γ

which results in the following decentralised optimal H_2 controller.

$$K_D = 10^{-5}\begin{bmatrix} -4.7 & -12 & -41 & 2.89 & 0 & 0 & 0 & 3.4\cdot 10^3 & -185 & 0 & 0 \\ 20 & -6.4 & 2.67 & -6.17 & 0 & 0 & 0 & 126 & 3.19\cdot 10^3 & 0 & 0 \\ 0 & 0 & 0 & 0 & 13 & 6.62 & 50 & 0 & 0 & 2.63\cdot 10^3 & -5.53\cdot 10^3 \\ 0 & 0 & 0 & 0 & 57 & 105 & 42 & 0 & 0 & -4.79\cdot 10^3 & -3.09\cdot 10^3 \end{bmatrix} \tag{4.36}$$

In Section 4.3 this controller will be analysed in comparison to traditional methods using switching simulation models and in experimental practise to show true performance of this controller.

4.1.3 Overview of the H_2 Centralised Controller Design Process

The full process to the design of the decentralised H_2 controller has been condensed into the following flow chart.

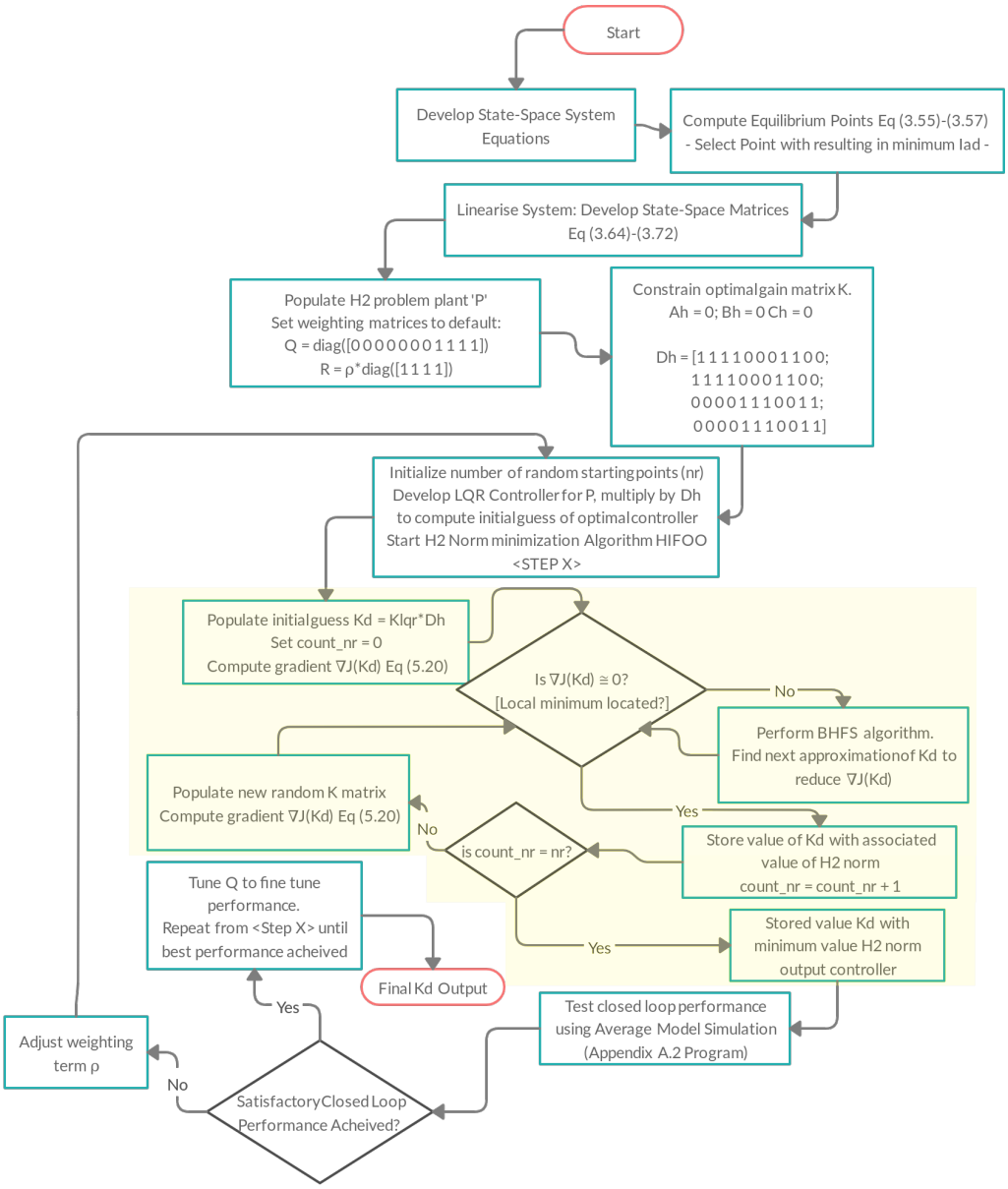

Figure 4.8: Design procedure for designing Optimal H_2 controller

The segmented part of the H_2 is performed using the HIFOO function, whilst all other actions are user determined and decided by the designer. Often when it comes to design of control systems, specific guidelines to the rise time, overshoot etc.. are set. Whilst in traditional forms of design, such as PI where a specific bandwidth can be applied using simple characteristic equations. This however is not possible within the H_2 design and hence a lot of trial and error can occur when tuning Q_γ and R_γ to get satisfactory performance. Along with this, the H_2 controller can be very dependant on an accurate state-space model being determined. A slight error in the dynamic

equations, will result in a controller which will not stabilize the system. In some applications where there maybe underlying dynamic effects which are often disregarded by the designer, can prove fundamental in the proper design of the optimal control. These two points are the main disadvantages associated with this design procedure. However, as will be observed when comparing against the performance of a traditional PI control (which is discussed in the next section), huge benefits can be realised. This shall be observed in Section 4.3.

4.2 Traditional Controller Designs - The PI Control

For many years and still currently today, the PI controller is among one of the most popular forms of control design across both academia and in industry. The reason for this being its pure simplicity in design, easy to understand to the theoretical level and also provides for the majority of design cases very good performance, when designed correctly. For power converters in a micro-grid, the most common form of control by far is the PI controller [125]. In this section, the classical design approach to the development of a standard PI control in these embedded grid application will be designed for and will be compared against the proposed H_2 controller. Due to PI controllers already being very well known, the design procedure will be kept brief as it's expected the reader knows the topology all to well.

4.2.1 Transfer Function and Controller Gain Expressions

In the design of PI controllers for individual power converters, generally design procedures focus on the implementation of cascade control loops, where there is an inner current, and outer voltage control loop. The controller will be setup using this configuration.

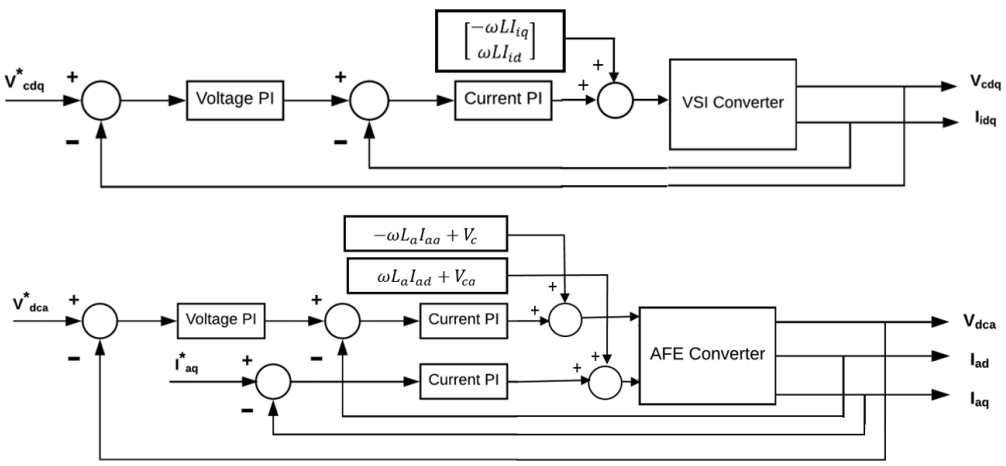

Figure 4.9: Cascade Loop PI Controller for VSI and AFE Converters

The current PI controller controls the current through the inductors, and the voltage PI controller controls the voltage across the capacitors. This arrangement of the controls is typically used in power converters due to firstly that the current is a critical state for the safe operation of power converters. If a disturbance occurs, and the controller is too slow to react, then possibly high currents could follow which could permanently damage the converter. Typically the inner control loop has a bandwidth of 10x that of the outer voltage loop controller [126]. This allows for fast dynamic control of the currents, but also helps in decoupling of the voltage dynamics. The voltage dynamic across a capacitor is also typically slower than that of the current dynamic so naturally also, the voltage is better suited to be the slower controller. It can also be observed from Figure 4.9 that feed-forward terms are also featured in the controller block diagram. This is required in order to decouple the dynamics of the d and q axis coupling terms found in each of the state equations. Additionally voltage terms can also be supplied in the feed forward term. These can be used to ensure the voltages states are at the correct initial value when the control is initiated.

Unlike H_2, the PI control is fundamentally designed direct from the transfer function between input to the system and output.

It is well known, that the transfer functions for the currents across the inductors and voltages across the capacitors have the relationship: [126]

$$I_{TF} = \frac{1}{L_g s + R_g} \tag{4.37}$$

$$V_{TF} = \frac{1}{C_g s} \tag{4.38}$$

where the general inductance and resistance $\langle L_g, R_g \rangle$ can be submitted with either $\langle L, R \rangle$ or $\langle L_a, R_a \rangle$ for either the VSI and AFE respectively. Similarly, C_g can be replaced with C or C_{dc} for either the VSI or AFE converter respectively. By performing pole-placement technique, as described in [22] and extracting the terms K_p and K_i out of the characteristic equation of the closed loop transfer function, the controller gains can be found to be the following [126]:

$$\begin{cases} K_p^v = 4\zeta_v C_g \pi f_v \\ K_i^v = C_g \left(2\pi f_v\right)^2 \\ K_p^i = 4\zeta_i L_g \pi f_i - R_g \\ K_i^i = L_g \left(2\pi f_i\right)^2 \end{cases} \tag{4.39}$$

Where K_p^v and K_i^v correspond the the PI controller gains for the voltages, with a damping ratio of ζ_v, and controller bandwidth f_v. The terms K_p^i and K_i^i correspond to the PI controller gains for the currents, with a damping ratio ζ_i and bandwidth f_i. It is important to note that

according to the current sign convention of the AFE states adopted in these models, the AFE current gains must be negative [126]. Differently again to the H_2 control, each of these converters are in general tuned independently and therefore any interactions which occur between the two systems are observed as disturbances.

4.2.2 Appropriate Selection of Gains

The gains are generated by selection by the designer of the appropriate bandwidths and damping ratios as required by the design. However, there are some limitations which can be determined from the model itself. Most importantly is the controllers intrinsic filtering action on signals. Three-phase converters have intrinsic harmonic components on the outputs due to the non-perfect switching actions of the IGBT modules. The total harmonic content in the output signals of the converter can be computed by the following expression:

$$h = (j \times p) \pm 1 \tag{4.40}$$

where j is an integer: $j = (1, 2, 3, 4, 5, \dots)$, and p is the number of switches on the power electronic device, in this case 6 for each converter.

Therefore, the characteristic harmonics present on in each of the power electronic converters will be:

$$h = (1 \times 6) \pm 1 = \textbf{5th} \text{ and } \textbf{7th} \text{ harmonics}$$

$$h = (2 \times 6) \pm 1 = \textbf{11th} \text{ and } \textbf{13th} \text{ harmonics}$$

$$h = (3 \times 6) \pm 1 = \textbf{17th} \text{ and } \textbf{19th} \text{ harmonics}$$

where the majority of harmonic power is concentrated on the lowest 5th and 7th harmonics which correspond to frequencies at 2000Hz and 2800Hz respectively. Harmonics are totally undesired aspects of power conversion, and thus, to accurately filter these signals from the controller, the gains should be limited to below 2000Hz. This is also an important reason as to why each of the LCR/LR filters must have bandwidths set under this frequency. The design taken place with the H_2 controller was to achieve the fastest possible dynamic response between converters. Therefore, to make the comparisons of the proposed control, and the H_2 control as fair as possible, the PI controllers will be designed to have the fastest dynamic performance possible between the two converters. In general, the best dynamic response for PI controllers is achieved by setting the damping ζ for all controllers to be around 0.707. The bandwidths can thus be selected to be as large as possible, whilst ensuring the global system is still stable. This is because whilst local PI controllers can be stable about their own converter, however, when interfaced with converters

presenting certain dynamics the system, instability can be occur to an otherwise closed-loop stable converter. This phenomena is largely down to the impedance mismatch between converters, and is additional criteria which must be accounted for when designing PI controllers for a grid network. Take for example controllers which have been designed using the bandwidths specified in Table 4.3.

	VSI Voltage BW	VSI Current BW	AFE Voltage BW	AFE Current BW
Test 1	60Hz	600Hz	900Hz	90Hz
Test 2	80Hz	800Hz	900Hz	90Hz

Table 4.3: Bandwidth for each impedance based PI control stability test

Characteristic loci plots, which analyse the Nyquist characteristic of the dq frame impedances and admittance transfer functions of the VSI and AFE respectively can be used to analyse the mismatch phenomenon between these two converters under Test 1. For more information please refer to [126, 127]. It is clear, by understanding of Nyquist criterion that these two independently stable converter feature non-stable behaviour when connected together due to the encirclement of the critical point $(-1, 0)$ on the d-frame.

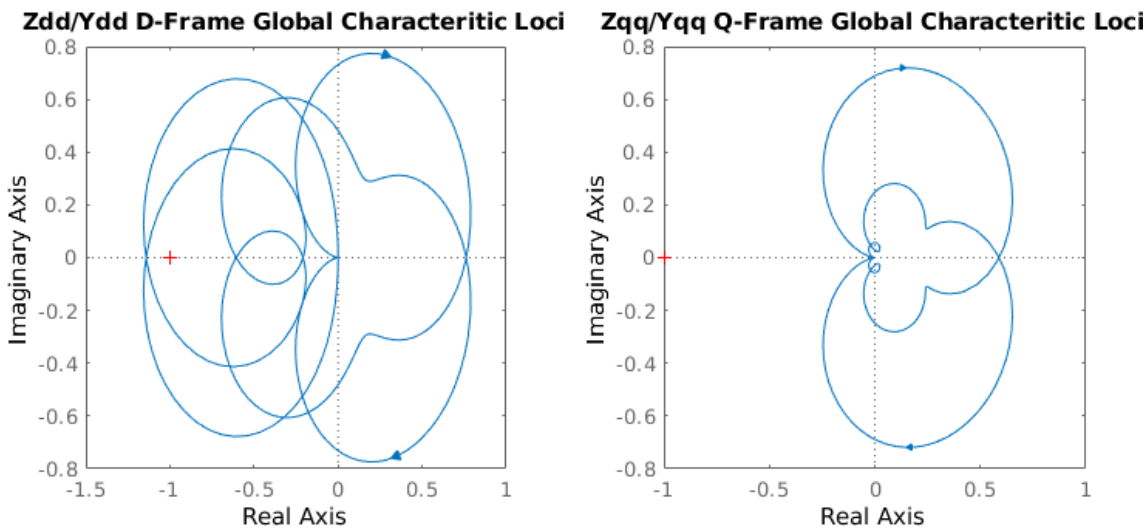

Figure 4.10: **Test 1:** Indicated Instability through Impedance Based Characteristic Loci of Interconnected Converters under PI control as listed in Table 4.3

Where an average model simulation of the interconnected notional system highlighting the unstable characteristic can be observed in Figure 4.11.

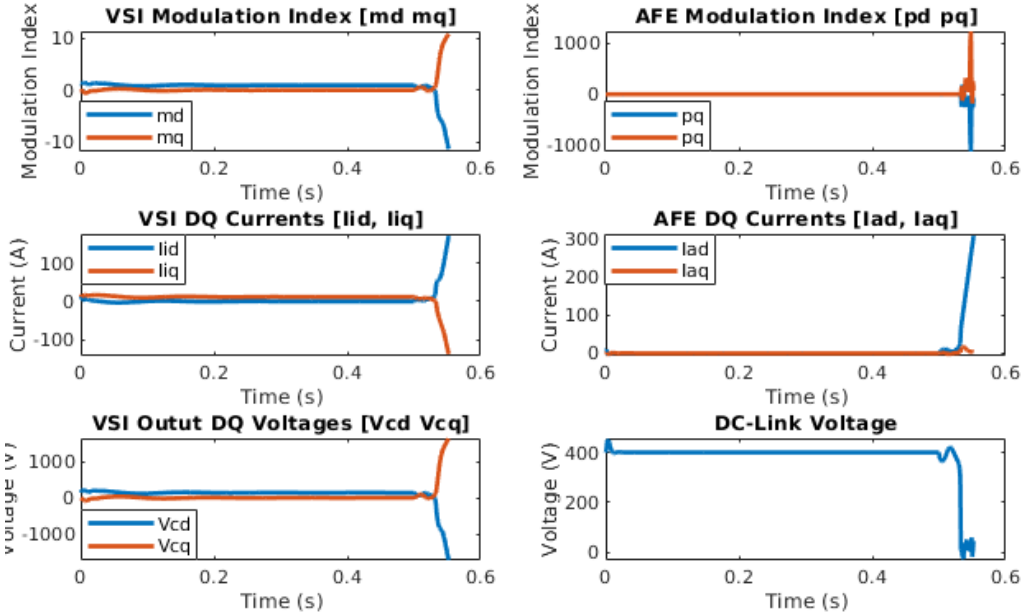

Figure 4.11: **Test 1:** Average Model Simulation of Interconnected PI System highlighting predicted instability from impedance based characteristic loci

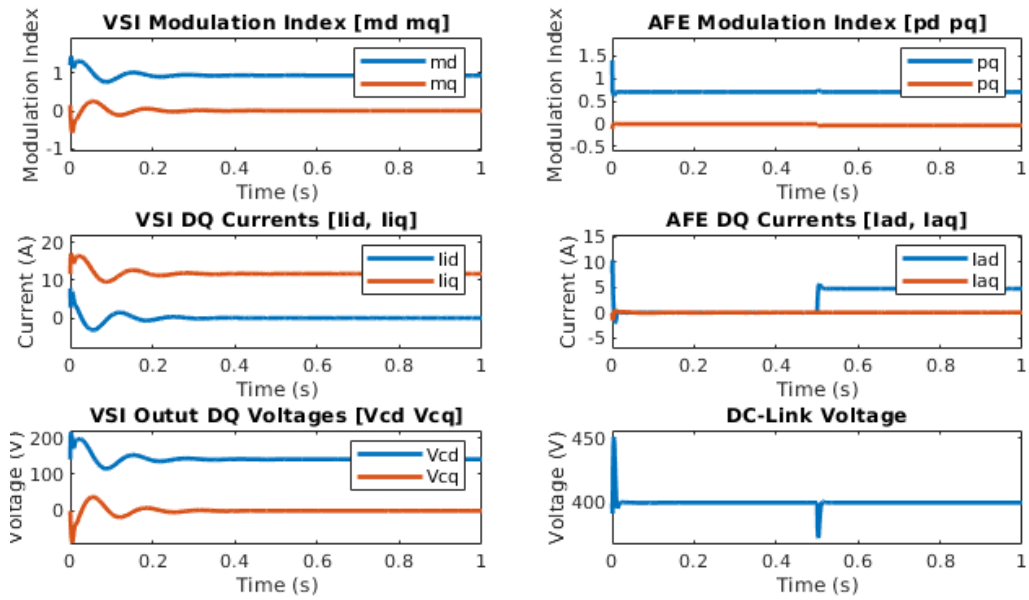

Figure 4.12: **Test 1** controller bandwidths when VSI and AFE converters running independently showing local system stability is present

However, if a simulation is performed where the VSI and AFE are disconnected from each other, non-dependant on the dynamics of the other converter, it is clear that both controllers are inherently stable to their associated converters, as observed in Figure 4.12.

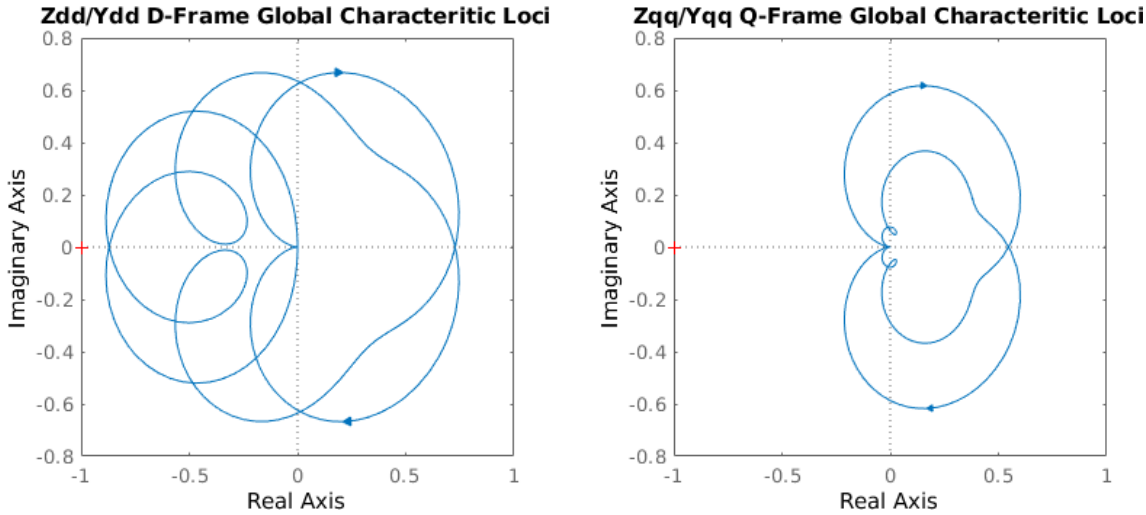

Figure 4.13: **Test 2:** Observed Stability through Impedance Based Characteristic Loci of Interconnected Converters

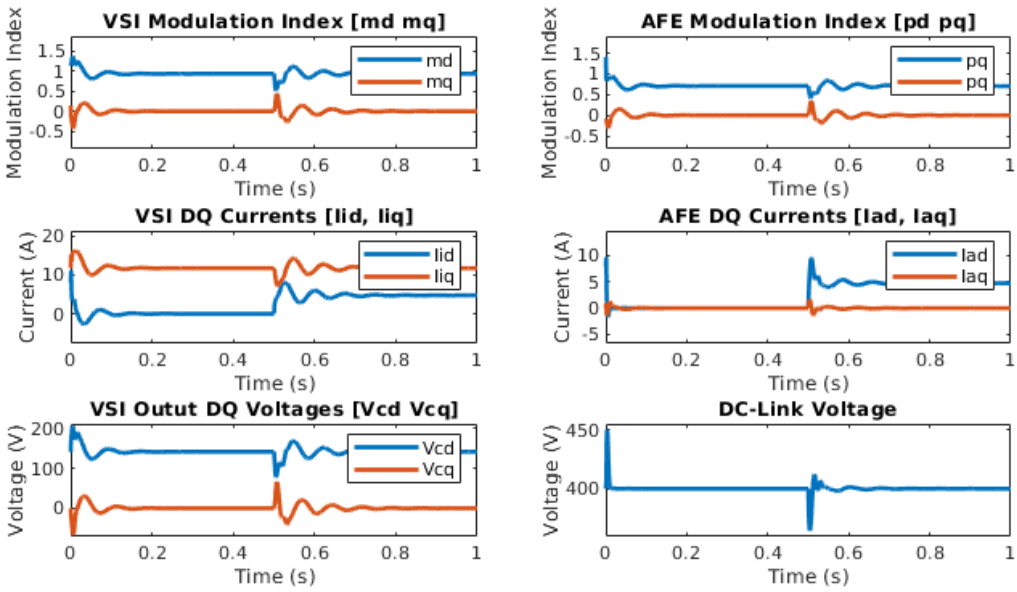

Figure 4.14: **Test 2:** Confirmed Stable Interconnected Performance as predicted by Impedance based Characteristic loci

However, when generating gains to the conditions set in Test 2 of Table 4.3, where the VSI

controller bandwidths are brought to be closer in line with the AFE's controller bandwidth, the instability observed in the impedance based characteristics loci between converters has been eliminated, as shown in Figure 4.13, and the average simulation of this interconnected system shown in Figure 4.14.

This comes to show that although a stable controllers can be synthesised for a local converter, when interconnected into a small closed network, one must also consider influences such as impedance mismatch between converter systems for overall global close loop stability. This occurrence comes from the fact that for a stable global system, the input impedance must be greater than the output impedance of the AFE or else an instability will occur; which for PI based control systems may not be first apparent during their design. As can be seen in the case for this system is that the bandwidths of both controllers must be of a similar range to not compromise system stability.

In order to get the best performance of the PI control in this system under the same system parameters as had been used for the H_2 controller synthesis from Table 4.1 and controller references set in Table 4.2, the bandwidths selected and the following PI gains for each converters generated is shown in Table 4.4

	VSI Voltage	VSI Current	AFE Voltage	AFE Current
Bandwidth (Hz)	120	1200	120	1200
PI Proportional Gain	Kpv = 0.04976	Kpi = 5.3087	Kpv = 0.1508	Kpi = -5.2236
PI Integral Gains	Kiv = 18.7601	Kii = 20465.61	Kiv = 56.849	Kii = -32119.64

Table 4.4: Selected bandwidths for PI controller with corresponding gains

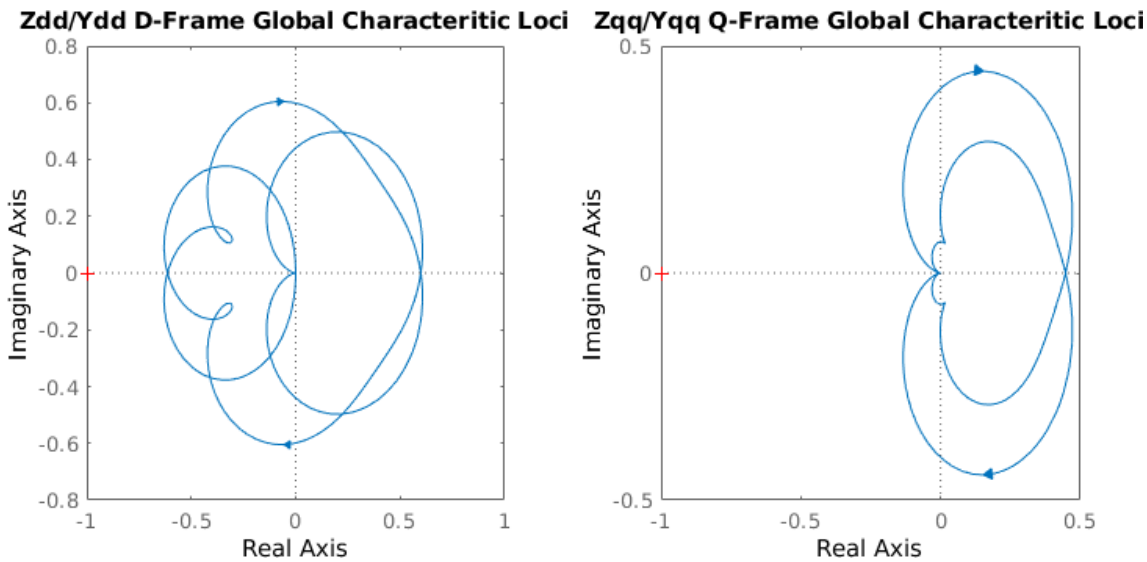

Figure 4.15: Selected controllers from Table 4.4 impedance based characteristic loci

The corresponding system has the following impedance characteristic loci shown in Figure 4.15 showing the global system is comfortable in the stable region when converters are interfaced together, with the following average simulation performance.

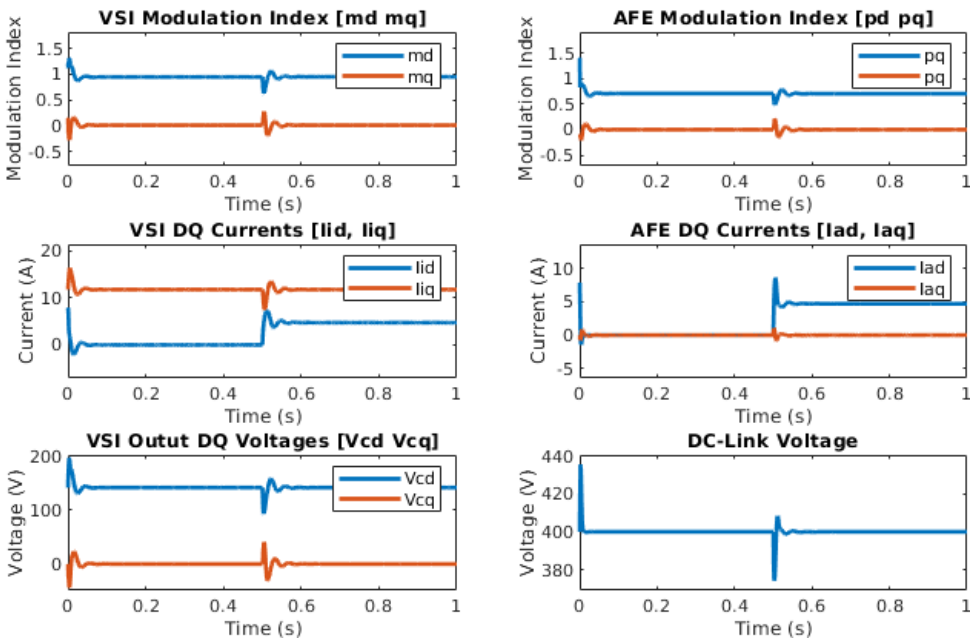

Figure 4.16: Average Model Simulation Performance under 1kW step Load for selected PI gains from Table 4.4

These PI controllers were selected, as they had the overall best performance whilst remaining

stable on the experimental setup and being most comparable in dynamic performance to that of the H_2 control. The performance of this controller, as compared to the proposed H_2 controller shall be analysed in the next section.

4.3 Controller Performance Comparison: H_2 and PI

For the most basic of systems which will be analysed in this study, a traditional PI controller which is considered the industry standard design of today has been designed for to the bandwidths and gains presented in Table 4.4. The theory and implementation of the proposed H_2 controller approach has been extensively covered in Sections 3.3 and 4.1. Both controllers were designed to achieve the best dynamic performance to a 1kW step load (fastest dynamic response to the least over/undershoot). In this section, the proposed H_2 controller approach will be compared against the standard and most commonly employed PI controller approach to analyses the performance of both controls in embedded grid situations. Average model simulations have been conducted on each controller to validate the mathematical stability and dynamic performances, and in this section, a switching model representation along with experimental validation of the system and a customised right setup shall be performed to ensure both controllers work practically across realistic simulations and real life setups.

4.3.1 The Simulative Switching Model

The average model is useful to validate the mathematical dynamic model, to ensure stability and the expected response of the controller. But in average models, everything is assumed perfect. For instance, the average model simulation only analyses the system in the equivalent dq mathematical model. In reality, these converters are operated in the abc domain, and also incur non-linear switching dynamics. We could in theory with the average model have PI controllers working at far higher bandwidths than as proposed thus far, however the effects of real switching inside power electronic converters is neglected, and hence the effects of the already mentioned 5th and 7th harmonics of the power system are left unanalysed. For each controller, the same converter switching models were utilised, where Figure 4.17 shows the VSI switching model used, and in Figure 4.18 that of the AFE.

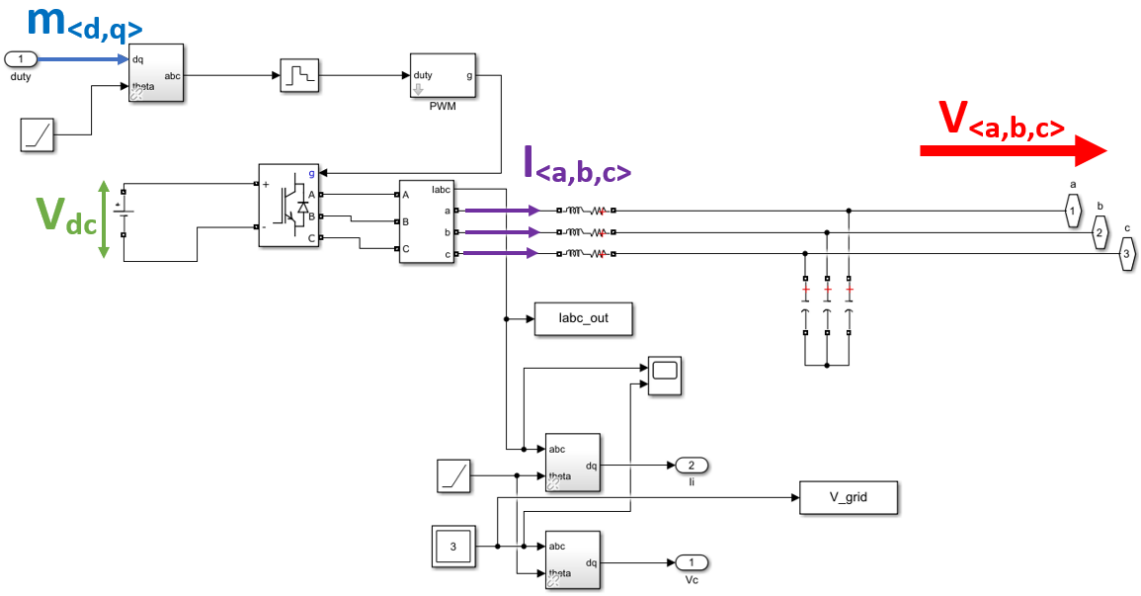

Figure 4.17: MATLAB Simulink Three-Phase VSI Switching Model generating the grid. The interfacing of this sub-model to wider model including controller and AFE shown in Fig. 4.19.

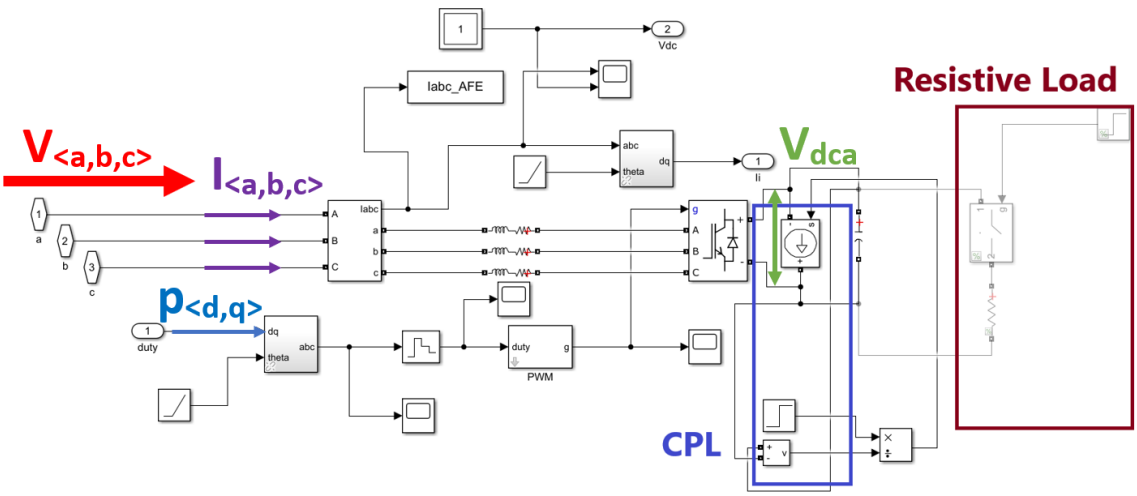

Figure 4.18: MATLAB Simulink Three-Phase AFE Switching Model, CPL and Resistive load configurations are presented, and interfacing of this sub-model to wider model shown in Fig. 4.19.

The AFE has its output configured to have either a resistive load or CPL across the DC Link. The resistive load comprises simply of a power switch across a resistor, and the switch closed at the time when a step load is desired. However, for the majority of test cases in this thesis, a CPL is used to exaggerate further the non-linear dynamics of the converter. Simply a constant power load is constructed in Simulink by use of a controlled current source. The DC link voltage is sensed, and

divided by the required load power P_l, which commands the exact current required by the current source. This in turn then commands a constant power at a given instant in time when the reference $P_l \neq 0$. These are the typical standard converter switching models which are used for the majority of the studies investigated. The PWM assumes a triangular generation signal which has minimum and maximum amplitudes of -1 and 1. The dq frame modulation indexes $m_{\langle d,q \rangle}$ and $p_{\langle d,q \rangle}$ are transformed back into the abc frame, and are fed into the PWM generator, which generates the switching commands to the 6 gates of the IGBT modules inside the 3-phase universal bridge block. The MATLAB code used to generate these switching functions are presented in Appendix A.3. For every case in the test, the capacitor on the DC-Link has an initial voltage set which is equal in value to the DC-Link reference voltage passed to the controller at $t = 0$.

The PI Switching Model

The global switching simulation model for the PI tests is shown in Figure 4.19. The top half of the diagram contains the modelled circuit, the left box containing the model observed in 4.17, and the right containing the model as shown in 4.18. The bottom half of the diagram is where the PI controller was implemented. Decoupling has been implemented, and each PI block is sampling at 10kHz as will be performed on the experimental platform (described in Section 4.3.3). Saturation blocks have also been implemented to hold the modulation indexes to between -1 and 1. The PI controllers are set to sample $2\times$ faster that the converter switching frequency f_s of $20kHz$.

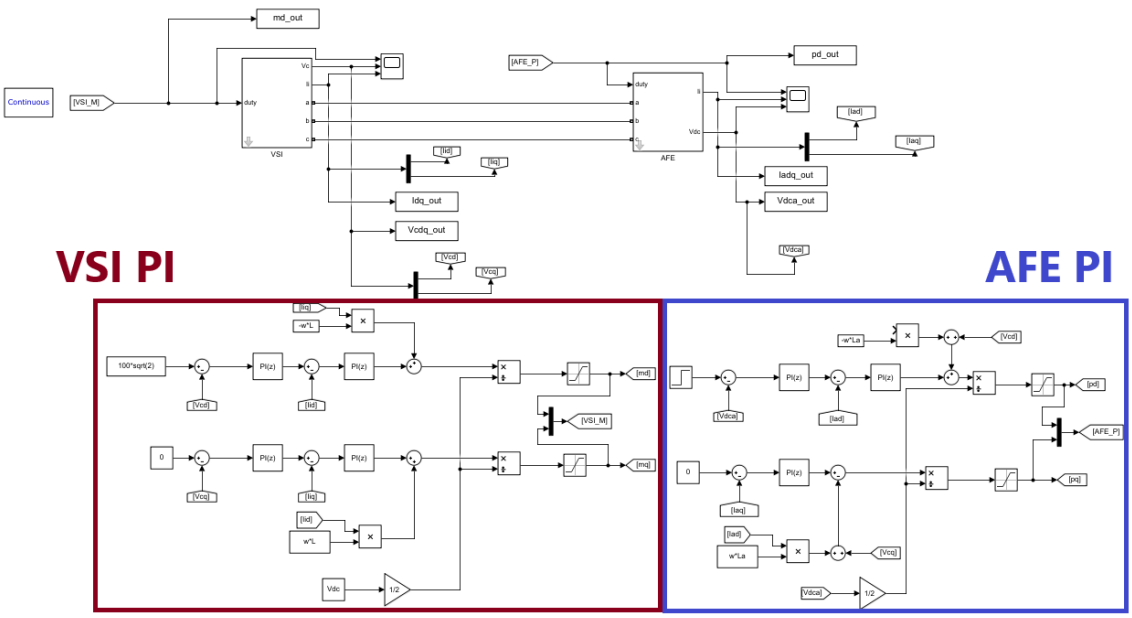

Figure 4.19: Switching Model interfacing the VSI (Fig. 4.17), and the AFE (Fig. 4.18) with the implementation of the global PI controller.

4.3.2 The H_2 Switching Model

Much like the PI controller model, the exact same electrical model is implemented and only the control structure has changed. The Simulink model for the H_2 switching simulation is shown in Figure 4.20

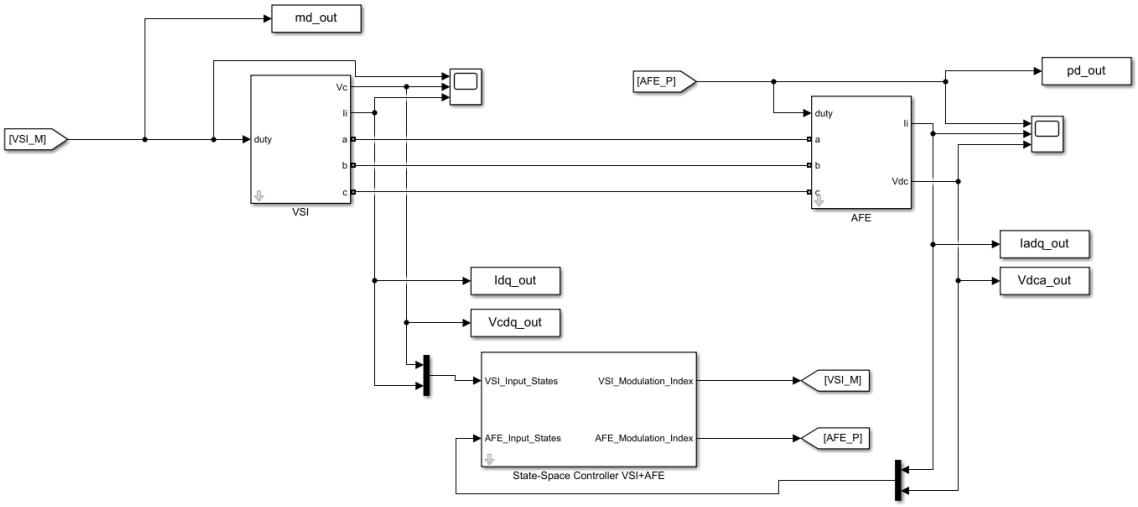

Figure 4.20: Switching Model interfacing the VSI (Fig. 4.17), and the AFE (Fig. 4.18) with the implementation of the proposed H_2 controller.

The H_2 controller block in the figure contains an function block simulating the controller at an equal sampling rate of $20kHz$ as performed with the PI controllers. The internals to this block can be seen in Figure 4.21.

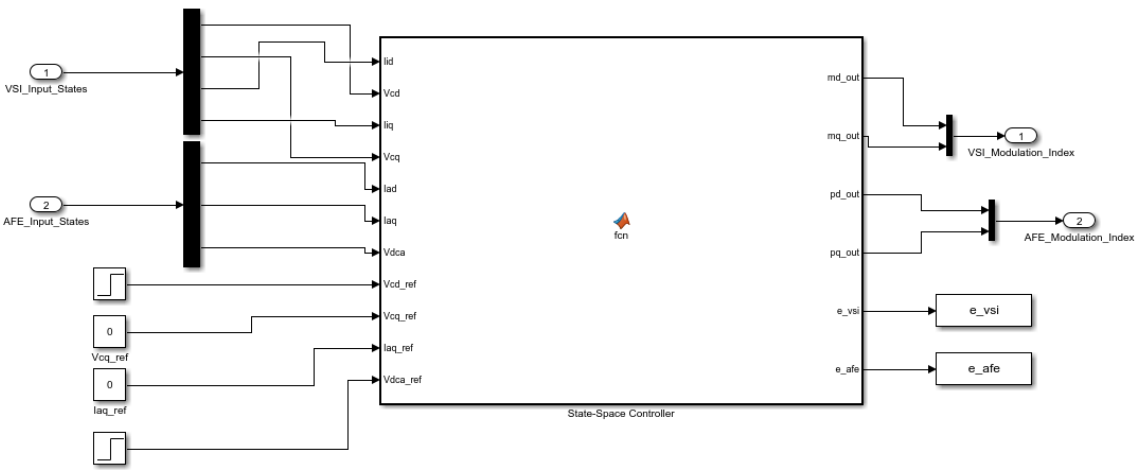

Figure 4.21: H_2 Controller Block used in the Switching Model presented in Fig. 4.20.

As can be seen, all the states of the system are passed into the controller, where the integral states are computed internally, and the modulation indexes outputted are in dq form and are similarly converted for each converter back into the abc frame, and passed into the PWM function described in Appendix A.3. The code used in the function block of Figure 4.21 is shown in Appendix A.4.

4.3.3 The Experimental Rig Setup

In order to validate the theory and the simulation results from the switching model an experimental platform was constructed as shown in Fig 4.22, with the schematic below detailing each segmented part of the rig in

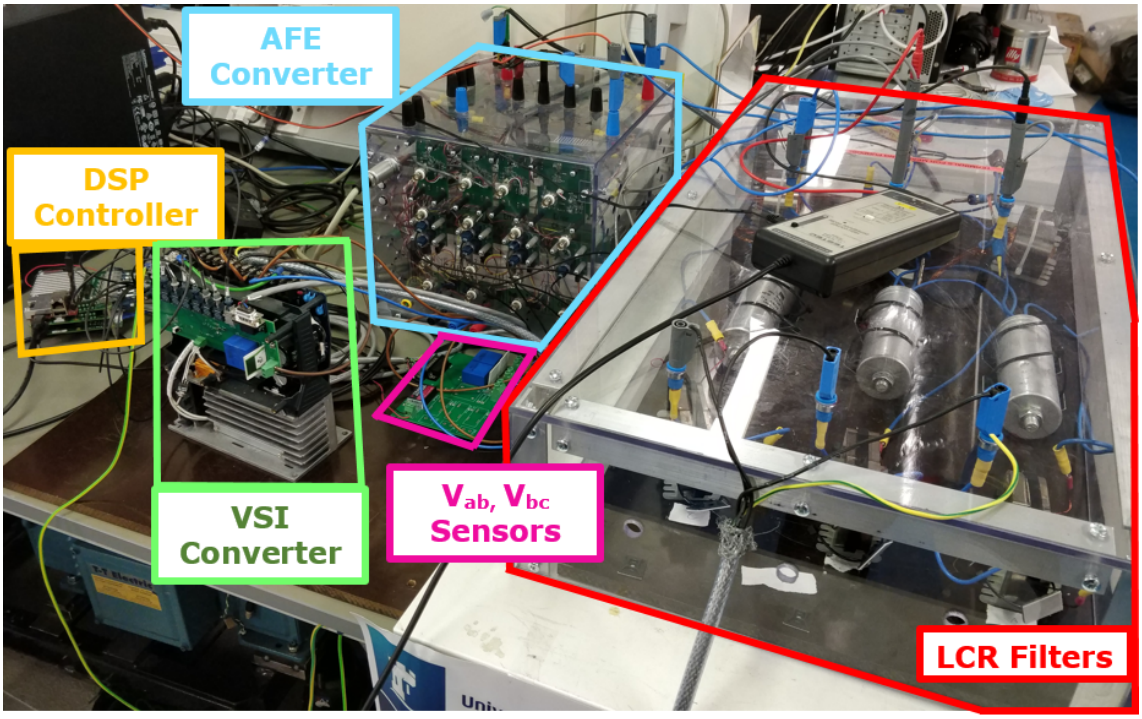

Figure 4.22: The Experimental Rig Platform

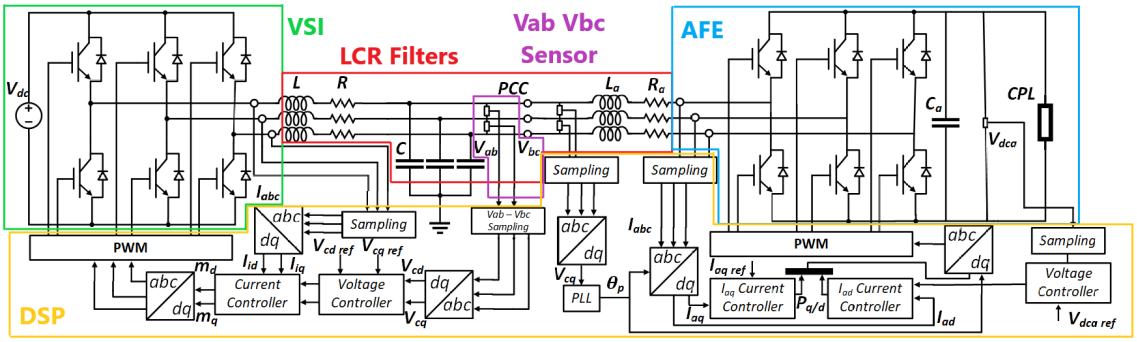

Figure 4.23: Schematic of the Experimental Platform detailing each of the highlighted parts of the prototype

Both converters are commercially available. The VSI converter is a 2kW, 300V 3-phase inverter from BMT (Best Motion Technology). The AFE is a 3kW, 600V converter from Semikron. The AFE converter has inbuilt voltage and current sensors across each of the three-phases. The VSI only has a current sensors across the phases, and a sensor for this input DC-Voltage. Therefore, a PCB board has to be designed where the three-phase voltages can be measured so that V_{cd} and V_{cq} can be computed on the controller setup, which is shown as V_{ab}, V_{bc} sensors in Figure 4.22. Hence the name, this sensor board measures the potential differences between the ab and bc phases. Equation (4.41) can thus be used inside the control platform to retrieve the three-phase voltages to which a DQ transform can be performed on to obtain the grid terms V_{cd} and V_{cq}.

$$V_{abc} = \begin{cases} V_a = \frac{1}{3}\left(2V_{ab} + V_{bc}\right) \\ V_b = \frac{1}{3}\left(V_{bc} - V_{ab}\right) \\ V_c = -\frac{1}{3}\left(V_{ab} + 2V_{bc}\right) \end{cases} \tag{4.41}$$

The inductors were designed in-house using AMC inductor cores and were wound to be as accurate as possible to the values simulated in the average model, detailed in Table 4.1. The DC-Link capacitor which can be seen in the figure is actually inbuilt into the AFE converter. These commercial converters incorporated too large a DC-Link capacitance to showcase the results of this work, so the AFE was part customised with a custom PCB board connected between the positive and negative terminals, with four Panasonic 14-34X 25μF film capacitors connected in parallel to create the 100μF DC-Link capacitor. The VSI is powered by a constant 300V DC source, which has a maximum supply current of 15A.

The control platform used to implement the controllers and command the switching of the IGBT modules for both converters was the uCube, developed by the University of Nottingham. Information on this platform can be found in [128]. The FPGA was pre-programmed for the

purpose of controlling power electronic systems, and thus all that was required was to program using C the control algorithms. The control algorithm is executed every 50μs by CPU interrupt where signals from all the converter sensors are sampled, dq transformations performed and the control algorithms computed. The interrupt routine held in $Ctrl\_Intr\_Handler()$ which is executed every 50μs is presented in Appendix B.1, and the signal conversion and dq transformations, which is called on every interrupt by the function *compute_theta*() is presented in Appendix B.2. The control platform also incorporates some safety features such as current and voltage trips. The VSI converter is rated to 30A and is thus imposed globally across the experimental setup.

In order for the successful turn-on of both converters for experimentation, it is vital to consider the inrush current that can occur when turning on the AFE from the VSI generated grid. These inrush currents occur due to the large initial currents required to charge up capacitive and inductive elements of the circuit. In the case of the AFE, the DC-Link capacitor is the main cause of this phenomenon. To mitigate as much as possible the inrush current without adaption to the hardware, the pre-charging control mechanism was utilised as derived in [129]. It's a very simple procedure where short burst of current are delivered very quickly into the capacitor by having either all the top, or all the bottom switches of each leg in the AFE to be on for a small period of time. As the current is given to the capacitor, its voltage slowly rises, and when the voltage across the capacitor is equal to that of the DC-Link reference voltage, the AFE is allowed to turn on, with minimal inrush current.

Finally, a CPL is implemented onto the AFE to facilitate a more realistic, more non-linear load attached to the system. Typically a DC motor could have been used to facilitate this kind of behaviour on the AFE output however none was available for test. Therefore the CPL was generated using a controlled IGBT module and a resistor connect as shown across the DC-Link terminals in Figure 4.24.

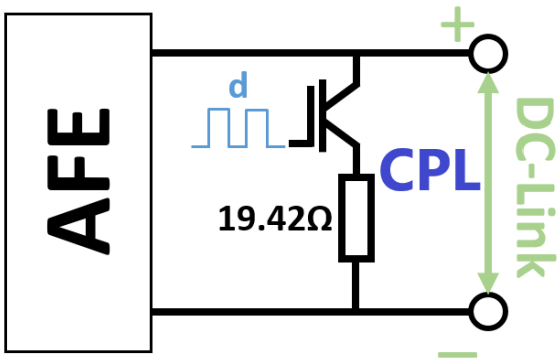

Figure 4.24: Circuit Diagram of Constant Power Load Generator in Experimental Rig

By modulating the IGBT with a duty cycle d and by sensing the DC-Link voltage, the current across through the resistor can be maintained to a value, which ensures the power through the resistor is of a constant value P_l. To ensure this, an open loop controller was implemented, which simply takes the resistor value and the current DC-Link voltage to calculate the required d to maintain the load power at a constant. The evaluation of this duty cycle is shown in (4.42).

$$d = \frac{P_l \times 19.42}{V_{dc_a}^2} \tag{4.42}$$

Where 19.42Ω was the value of the power resistor used in this circuit. The IGBT module used in this circuit was the breaker IGBT inbuilt into the AFE, and a power resistor connected as demonstrated. For this to work, the duty must be $d < 1$ for all probable values of V_{dc_a} at transient for all probable power levels. This can be guaranteed by selecting as small as possible value of power resistor in this setup, and also ensures only minimal current is drawn from the CPL generator.

The next sections, the performance of the dynamic performance, operation away from linearised points and the parametric robustness of the systems shall be presented using both the switching model simulation results and the experimental results. This is to show the accuracy of the Simulink model used to the practical implementation. Experimental results are gathered by reading the buffers from the control platform when a given trigger condition is met, be it when the load turns on, or when the DC-Link voltage drops during the initial load transient. The results in the buffer are then backed up by the result observed on the oscilloscope. The oscilloscope used for these experiments was the Lecroy WaveJet 324.

4.3.4 Dynamic Performance to Load Disturbances

This test is the classical example which has already been performed on both controllers during the average model simulation. Both the VSI and AFE will be brought to a 0W no-load steady state condition initially, and then a 1kW step load load is performed. Both the PI and the proposed H_2 controllers are designed for a linearised system operating at 1kW, however 500W, and the maximum allowed achieved load step across each of the converters to see performance away from the designed point.

1kW Step Disturbance

Presented below are the switching model simulation of the PI Controller in Figure 4.25, and that of the H_2 controller in Figure 4.26.

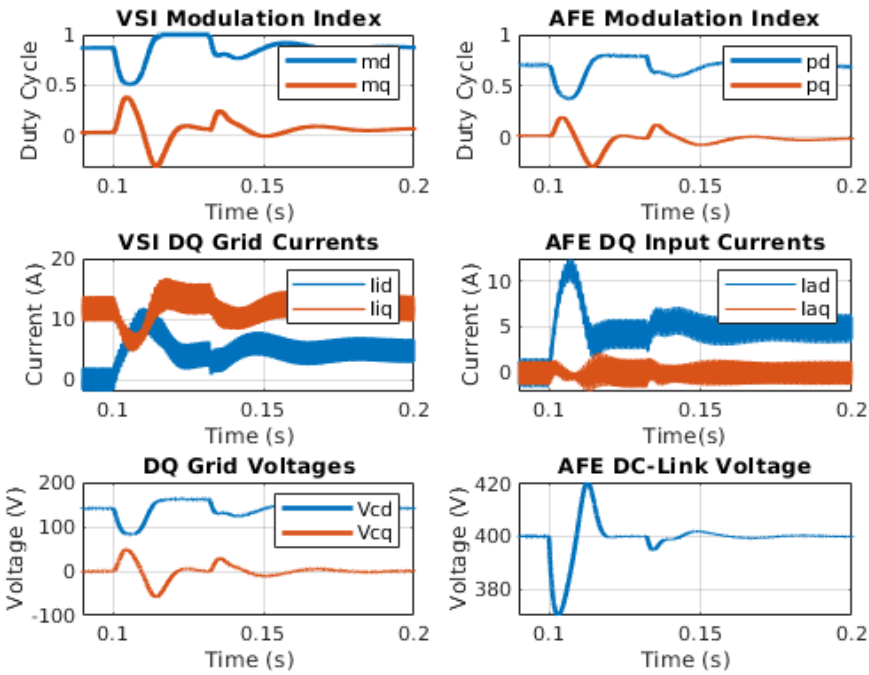

Figure 4.25: Swithing Simulation of the **PI** controller in DQ frame 1kW Step step at 0.1s

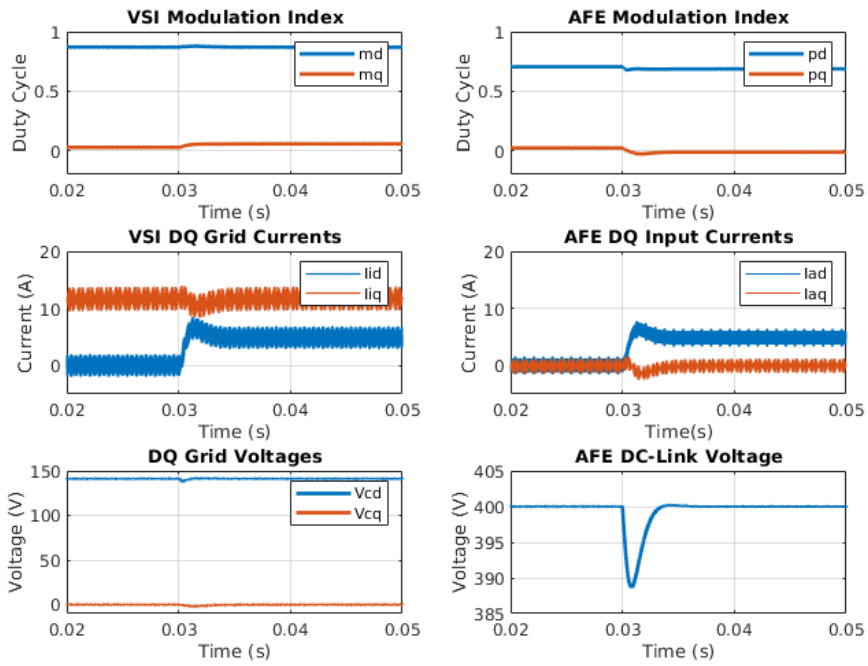

Figure 4.26: Swithing Simulation of the **H2** controller in DQ frame 1kW Step step at 0.03s

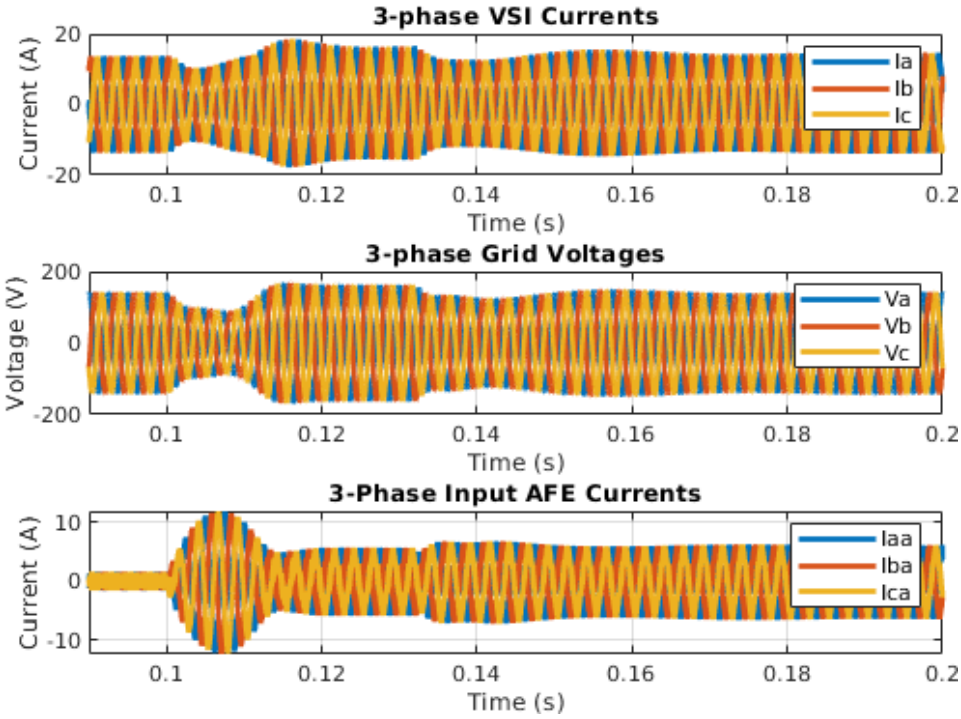

Figure 4.27: Swithing Simulation of the **PI** controller in 3-phase with step 1kW load at 0.1s

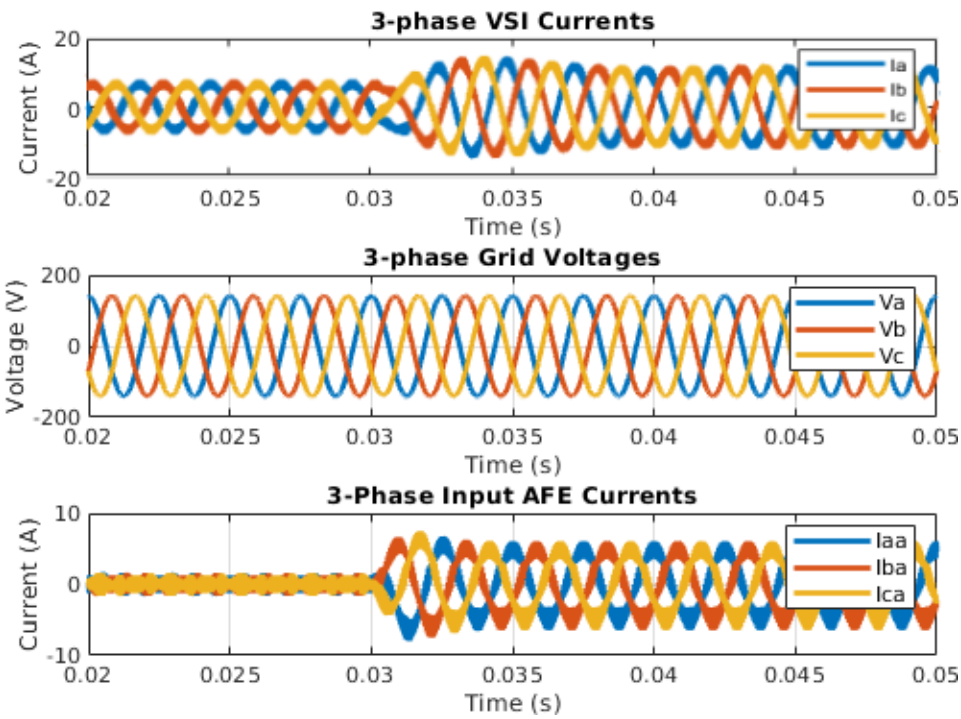

Figure 4.28: Swithing Simulation of the **H2** controller in 3-phase with step 1kW load at 0.03s

In these cases, the step load for the PI test occurs at 0.1s, whilst for the H_2 is at 0.03s. This difference is due to the time from start-up to steady state in each model. The PI controller, due to effects which will be discussed in a moment has a slower dynamic from start-up to steady state than the H_2 control. Also take note the the time scales for each figure is different. This is so that clearer behaviour of each controller can be observed. It must also be reiterated to the reader that the fastest bandwidths for each controller were designed due to the incapability of specific bandwidth definition in the H_2 controllers design. Additionally, each of the datasets in each figure was sampled each 10μs in simulation time.

Firstly, it is evident from the above two figures that the average model simulations from Figures 4.7 and 4.16 for H_2 and PI controls respectively accurately portrays the the behaviour in the switching model. All the system settling times, undershoots and overshoots are all almost equivalent to that of the switching model.

The switching model clearly shows the performance benefits which can be received by developing a H_2 controller. The most significant point being the interactions between converters, for example compare the results of the three-phase voltages between the PI and H_2 controllers from Figures 4.27 and 4.28 respectively. It can be clearly observed that under the H_2 control, the disturbance introduced on the output of the AFE has had little to no interactive effects on the VSI. On the other hand, when looking at the PI system, the same cannot be said. The grid voltages incur a sizeable drop in their values and is clearly interacting with the AFE state disturbance. Additionally this drop in voltage later demands a larger control effort to bring the system back to stability. At no-load steady state, the VSI is almost operating at it maximum output voltage given its 300Vdc supply. The modulation index is thus already high at 0.83 before the interaction. Thus to stabilize the system back to steady state, the controller demands too great an m_d, which causes saturation. This then induces a further slow response across the system whilst the controller states come back to suitable values, which is why in this situation the PI controller is much slower than the H_2, given that both are designed for fastest possible dynamic performance. The performance observed is with anti wind-up being implemented to reduce the effects of modulator saturation.

This highlights one of the major benefits and novelties which can be achieved from this research. This shows that the H_2 controller, in its decentralized for can inherently decouple individual converters on the network. Even when a large disturbance occurs on another converter, the H_2 controller intrinsically decouples these effects between the other converters on the network.

The same effects can be observed on the experimental setup through Figures 4.29 to 4.34. As was said in the introduction to this work, large passive filters are used in attempt to decouple the effects between converter sub-systems. In these systems with reduced passive filters, the PI control clearly suffers from the interaction between VSI and AFE, whilst the H_2 on the other hand

virtually mitigates the interactions observed between the two.

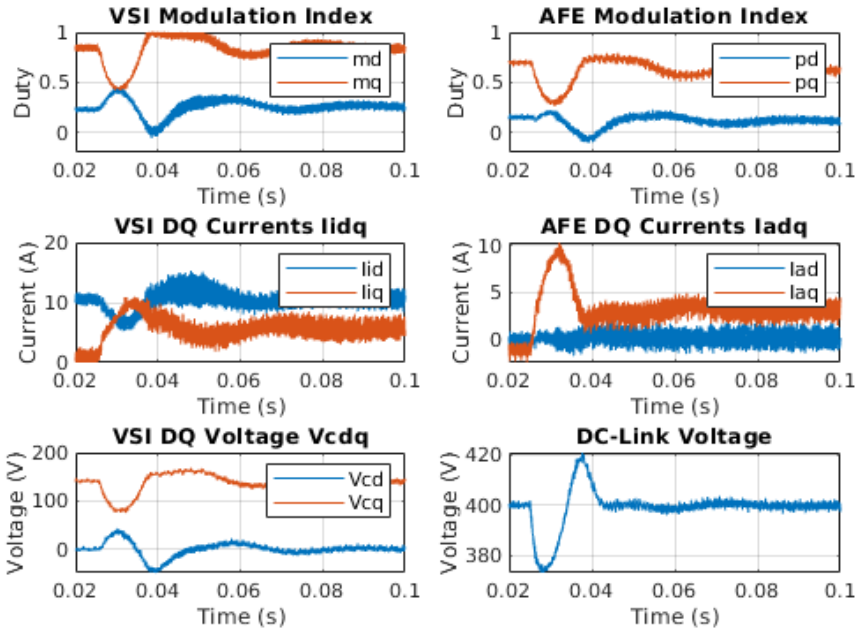

Figure 4.29: Experimental results of the **H2** controller in DQ frame 1kW Step step at 0.025s

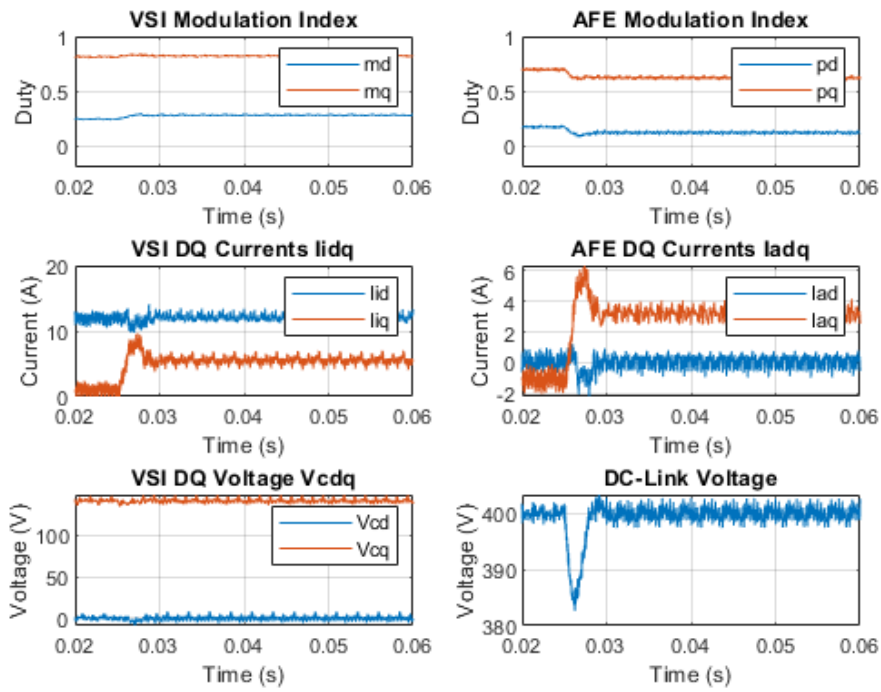

Figure 4.30: Experimental results of the **PI** controller in DQ frame 1kW Step step at 0.025s

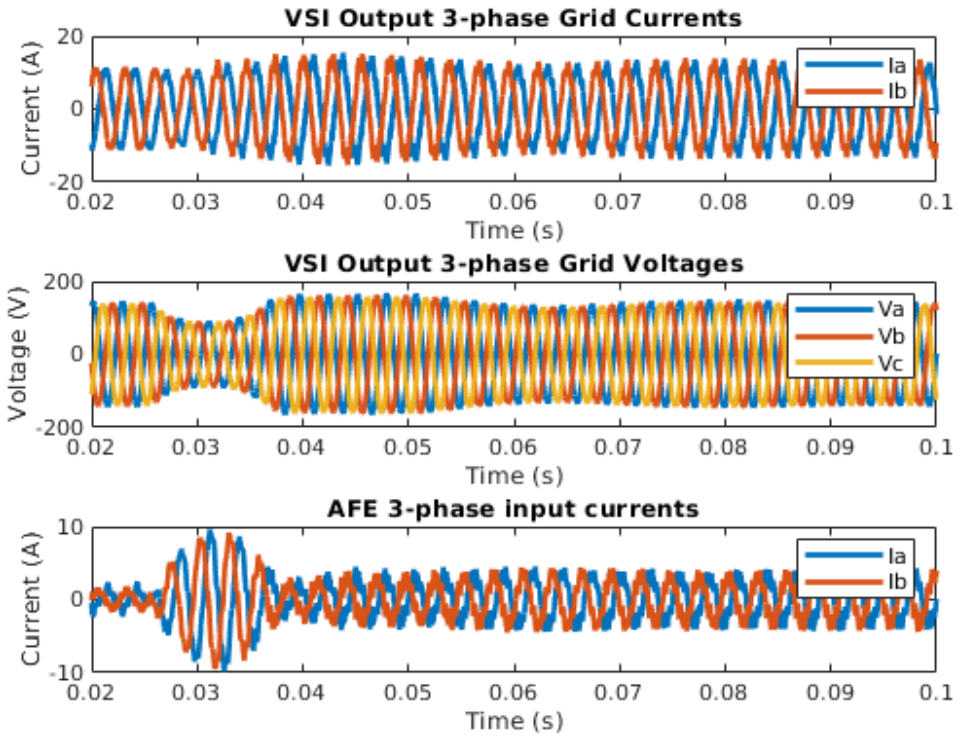

Figure 4.31: Experimental results of the **PI** controller in 3-phase 1kW Step step at 0.025s

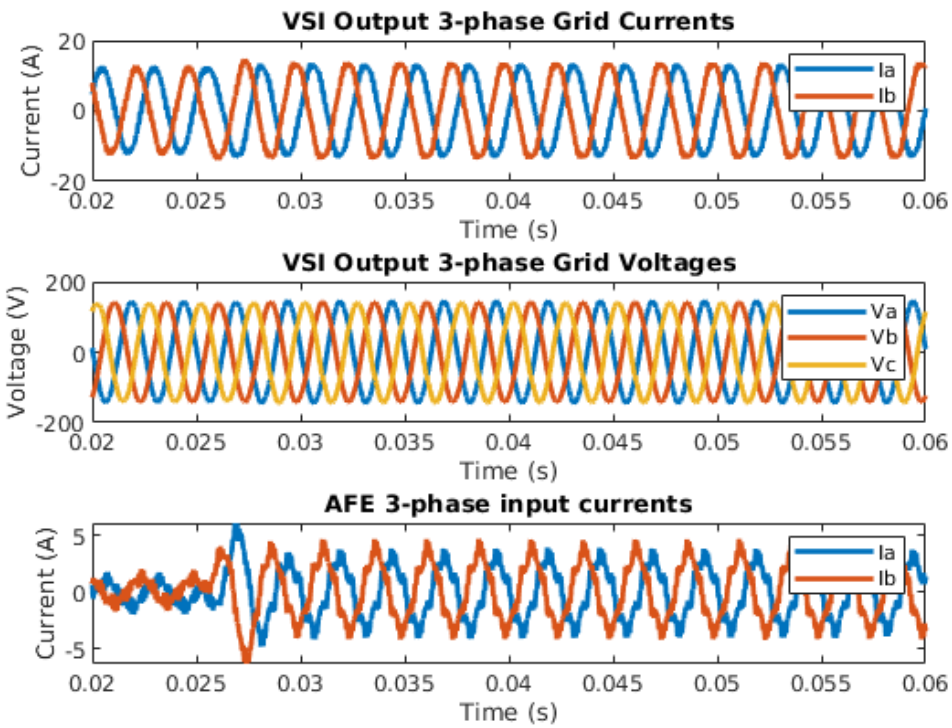

Figure 4.32: Experimental results of the **H2** controller in 3-phase 1kW Step step at 0.025s

This comes down largely down to the fact that each of the two independent H_2 controllers generated from the decentralized H_2 algorithm produces a global controller whose gains are synthesised on the basis of minimizing the average gain of the transfer function between the disturbance and the error. Additionally by computing two independent optimal controllers through constraining a global dynamic optimisation, taking into account all the open-loop dynamics of the system, each independent H_2 controller is not only optimised to the converter dynamics to which it is applied to, but also to the closed loop dynamics of all other sub-systems on the network.

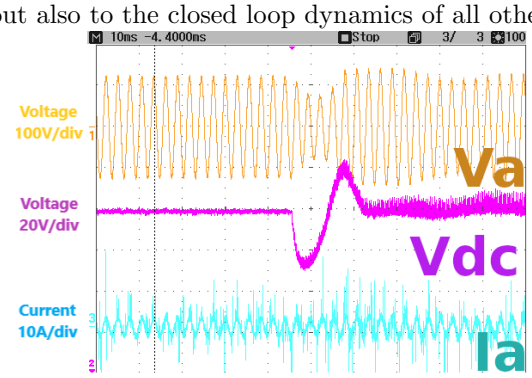

Figure 4.33: **PI** Experimental: Oscilloscope

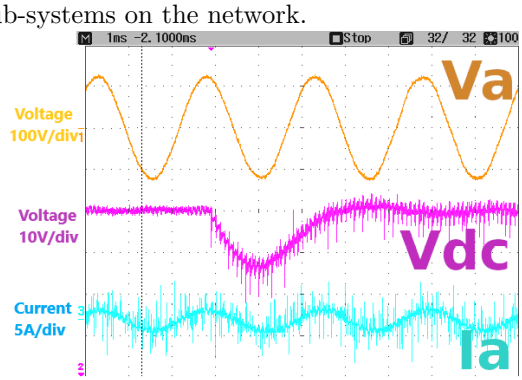

Figure 4.34: **H2** Experimental: Oscilloscope

Therefore, if a single converter in this topology experiences a disturbance, it locally attempts to bring itself back to stability whilst the rest of the system operates with little influence to the disturbance, as these effects have all been accounted for in the controller design.

The PI controller on the other hand is a classical case of a system incorporating locally optimised control systems. The PI controllers can provide good performance locally to the converter, however when interconnected on a localised network with other subsystems, performance between controllers can deteriorate. This was initially observed in Section 4.2.2, where two perfectly stable controllers caused instability when interfaced together. The controllers, not optimal to the outside grid dynamics deteriorates performance further when large unexpected disturbances occur on the system. In this case, the PI whilst incorporating fast dynamics locally, saturated the VSI modulation indexes, and incurred slower than normal responses to the step load on the AFE. So, through validation of the experiment, the direct benefits received of sub-system interaction mitigation by use of the proposed system control structure alone paves ways for the development of light grids for aircraft, as massive passive filters are not required to achieve the same performance as received by optimisation using decentralised H_2 approaches.

On an additional note, it is clear that the dynamic performance which was achieved using H_2 is far faster in dynamic to that achieved for the PI. This again was largely thanks due to the VSI not having interactive effects induced on it during the transient allowing faster dynamic correction of the AFE as the VSI was quickly to back to its steady state operating point. The under/overshoots

incurred across the board was reduced for H_2, especially in the states I_{ad} and V_{dc_a}.

Whilst dynamic performance is an important feature to investigate in controller design, so it the robustness characteristics to uncertainty.

Maximum Power Load Test

As it is closely related to the previous test, it is interesting the to perform a Maximum Power Load Test. In this test, each of the controllers are applied the maximum load step possible before instability occurs. This not only analyses the performance of each controller away from the linearised point, but also analyses the robustness of the control in regards to larger disturbances. Once the CPL is switched on across the DC-Link, all states move to new equilibrium positions, and there is no guarantee that moving from the original state, to the new state positions can be achieved. So this is a test of the region of stability of each controller (more in depth study on this particular area in Chapter 8) It must however be noted that this test is non-perfect due to the limitations on the hardware, such as the maximum current imposed is 30A. If a controller demands a higher current than this the system is immediately switched off for safety.

Firstly let's analyse the H_2 controller. It was found that the maximum power capable using the controller designed in (4.36) on the experimental setup was a 1.65kW step. The experimental results of which are shown in Figures 4.35 to 4.37.

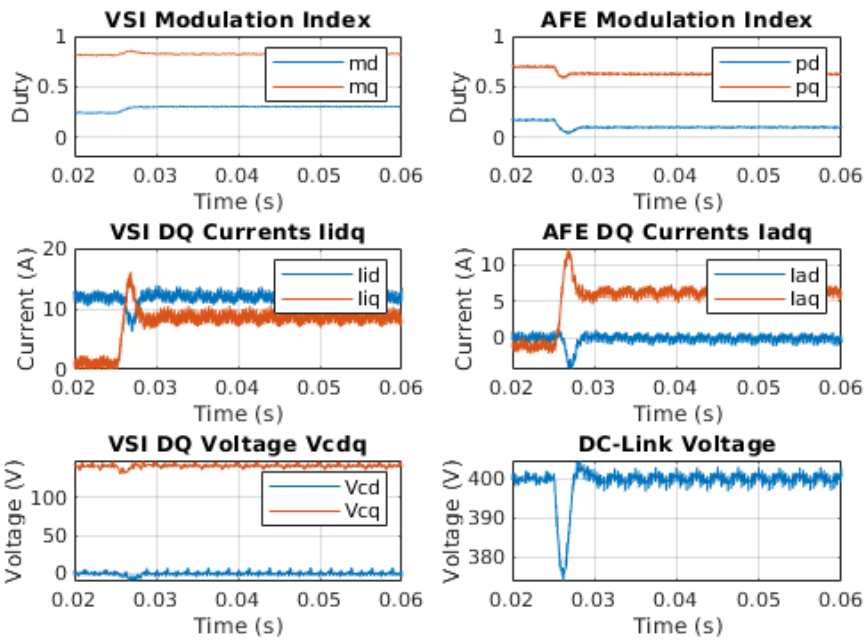

Figure 4.35: H_2 Experimental results in DQ frame with 1.6kW Power Step

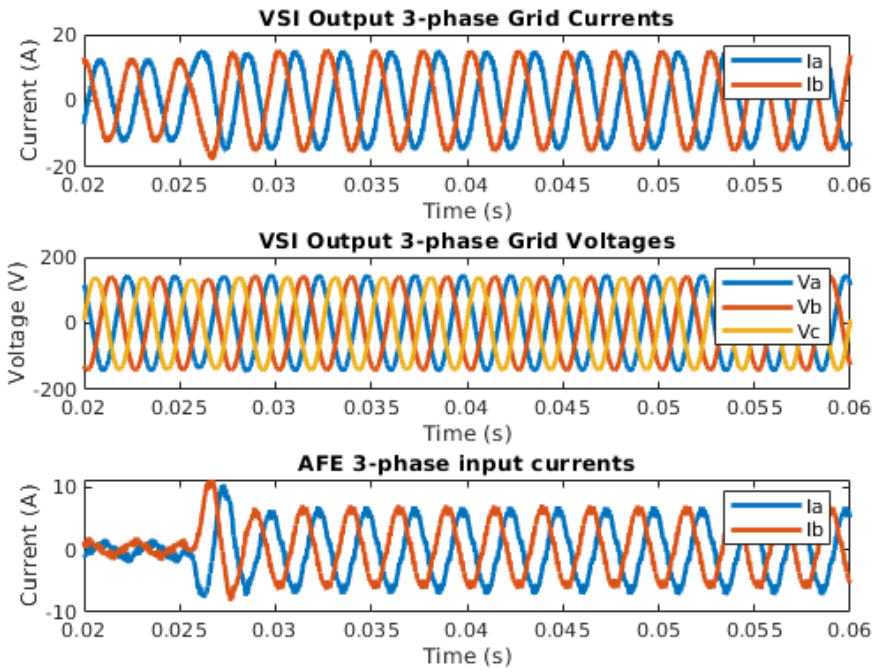

Figure 4.36: H_2 Experimental 3-phase results with 1.6kW Power Step initiated at 0.025s

Even when performing such a high load step away from the linearised point of design, the H_2 controller still portrays its effectiveness against cross interactions during the load disturbance. Be it that V_{cd} and V_{cq} are markedly more perturbed than in the 1kW step test, inspecting the 3-phase voltages it shows that this had little effect on the stiffness of the grid. With this, the modulation indexes are still from saturating allowing the VSI to be fully controllable about the transient. Dynamic performance is maintained, and the settling time of the controller across all states is almost equal to that of the 1kW step test of approximately 10ms. The H_2 is still rigid, and the steady state performance after the disturbance appears almost equivalent to the nominal performance. The reason for the instability beyond this step power is most likely down to the states lying outside the region of stability when more powerful loads are connected to the grid, as voltages were far from saturating the modulation indexes, and currents were far from the limit of 30A.

As observed with the PI in the nominal tests, due to the interactive behaviour between the two converters that occurred during the load transient, this too impeded the performance of the system when attempting to perform ore powerful step loads. The maximum step load which could be applied to the experimental hardware under PI control was only 1.1kW. A mere 10% increase as compared to the 65% increase observed with the H_2. The reason for this was due to the already present interactive behaviour between the two converters.

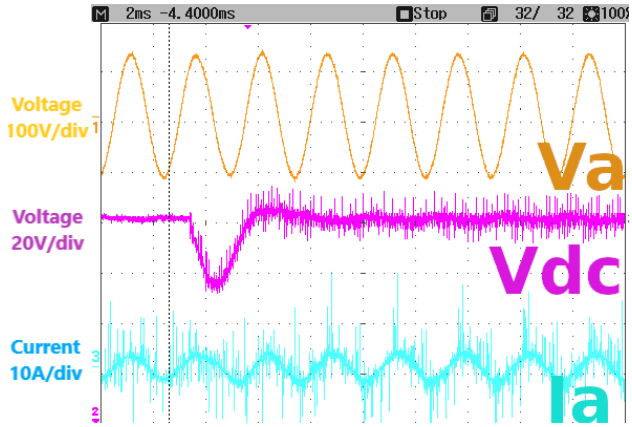

Figure 4.37: **H2** Experimental: Oscilloscope for 1.65kW Step Load

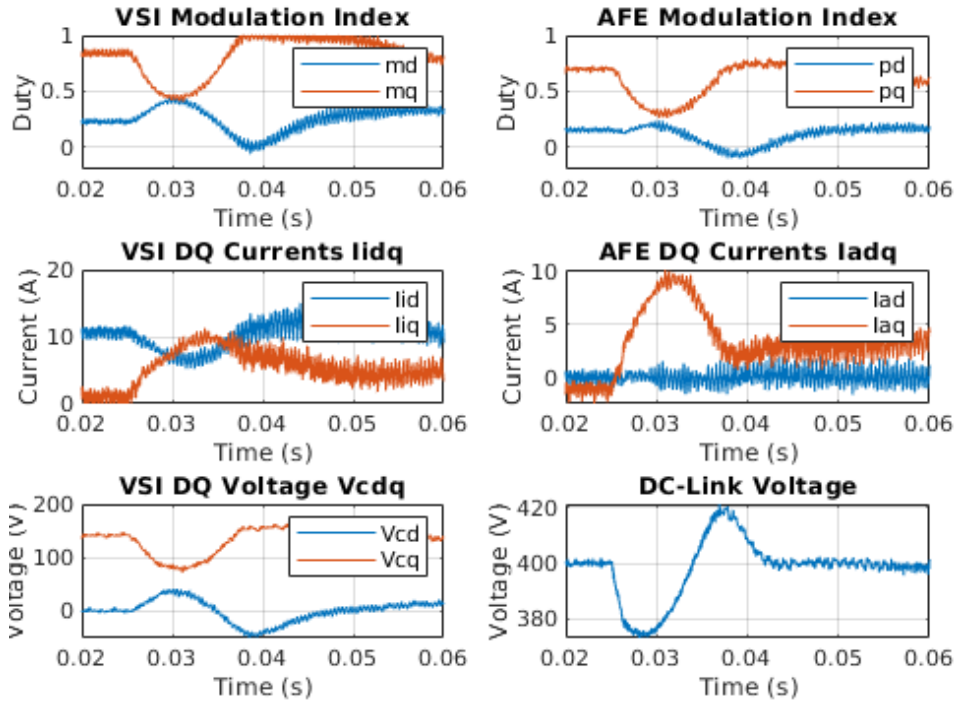

Figure 4.38: **PI** Experimental results in DQ frame with 1.1kW Power Step occuring at 0.025s

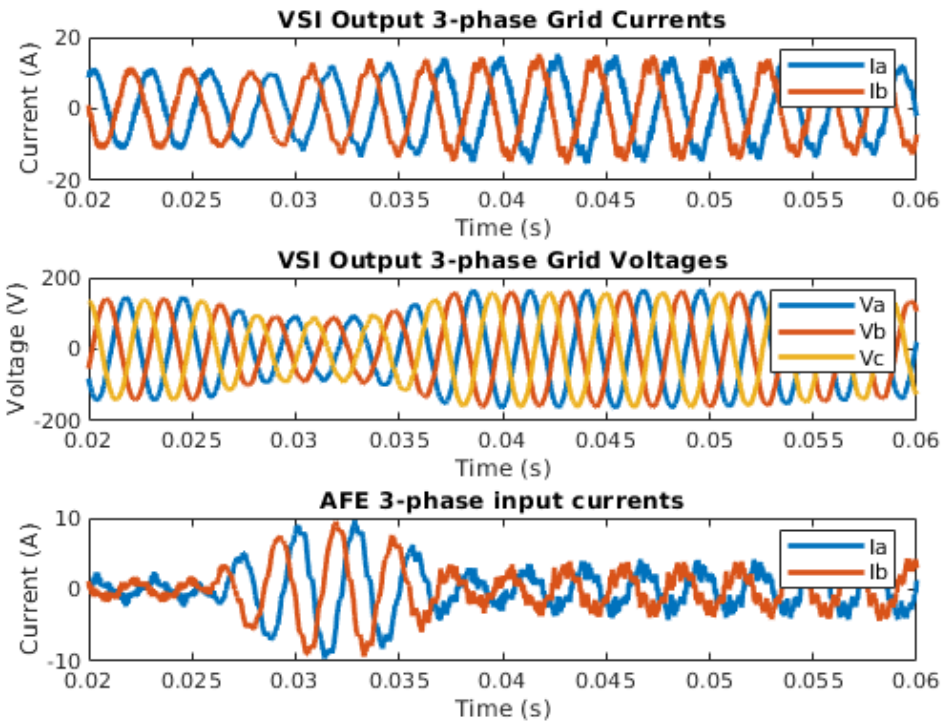

Figure 4.39: **PI** Experimental 3-phase results with 1.6kW Power Step occuring at 0.025s

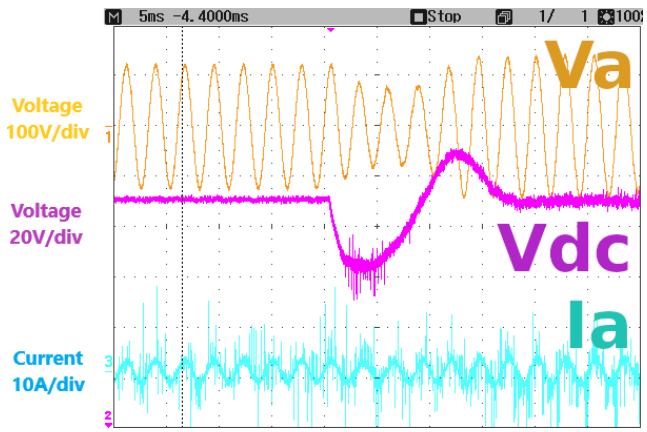

Figure 4.40: **PI** Experimental: occuring at 0.025s for 1.1kW Step Load

When comparing the maximum load PI results shown in Figure 4.38 with that at nominal power in Figure 4.29 it is imminently clear the as expected, the interaction is worse for a larger power steps. m_d is clearly saturated for a longer period of time which in turn results in the dq voltages, and thus the grid voltages to drop further. The likelihood of the instability beyond this power step is likely down to the system dropping out of its linear region of stability for larger load disturbances.

4.3.5 Comparison to Dynamic and Parametric Robustness of Controllers

Whilst analysing the dynamic performance of this system is important for the controller design, analysing the robustness to disturbances and uncertainties is additionally another vital factor to be analysed. The easiest approach in analysing this for a controller is by way of analysing the robustness to parametric uncertainty. This test therefore analyses the performance and robustness of each controller against disturbances which bring the system far from its designed for linearised point of operation.

However, due to the wide variety of components that would be required to be swapped in and out to map the uncertainty characteristic, an alternative approach is used for testing here. In this section, each test takes place on the experimental rig using its default parametric values detailed in Table 4.1. Then, in each test the controller is tuned with an incorrect parametric value for a specific component, and then tested for general stability of the system. The larger the deviation from the true parametric value can be before the system becomes unstable, the better the general robustness of the controller.

Firstly, the PI controls general robustness shall be characterised, and then the H_2 controllers performance compared. The parameters varied in this analysis are the inductors (L, La) and capacitor (C, C_a) for the VSI and AFE respectively.

PI Controller - Parametric Robustness Analysis

The PI controller provides the base results as to which the proposed H_2 controller will be compared against.

Table 4.5 below characterises the maximum values each parameter could be varied until the controller was either unstable, or unsatisfactory grid, load performance was observed. Unsatisfactory meaning either significant harmonic distortion or incapability to cope with nominal step load dynamic, and this performance will be shown through experimental data plots. Each parameter is varied while all other parameters are left at default, for simplicity of the analysis. Values noted N/A meant that the reduction of given value only causes an instability when the value is virtually 0, and hence has little effect on the parametric stability. Values marked ' * ' are terms which have corresponding experimental results to show performance under these conditions.

PI Parametric Uncertainty Stability Limits					
Parameter	Default Value	Minimum Value	Description	Maximum Value	Description
L	360μH	10μH* Fig. 4.41	Degraded Performance (Unloaded)	500μH* Fig. 4.43	Very degraded performance (Unloaded)
C	33μF	$< 0.5\mu$F	Stable for small C	100μF* Fig. 4.45	Degraded Performance (Unloaded)
				125μF	Unstable
La	565μH	$<0.5\mu$H	Stable for small La	750μH	Degraded performance on grid (Unloaded)
				800μH	Unstable
Ca	100μF	50μF	Grid Degradation	750μF* Fig. 4.47	Very degraded performance
		2μF	Unstable		

Table 4.5: The located bounds of parametric stability of the PI Controller

Table 4.5 details the limits of parameter uncertainty observed with the PI controller. Regions where grid performance is stable, but very degraded in terms of qualities of signal are discussed as well as defined points where the system is completely unstable. It is clear that the VSI capacitance and AFE inductance effect the stability little when the value is reduced. Only instability was found when these terms were so small they were practically zero. It can be seen in this system the inductances are the values most sensitive to uncertainty. L can be increased by 39% before instability occurs, whilst for L_a an increase of 50% can occur before the system performance starts becoming poor. Additionally the DC-Link capacitor C_a has a relatively low lower threshold than its upper threshold, where a reduction in value of 50% results in poor performance. Whilst component values do have tolerances, it is unlikely that a specific component will have such large deviations to specified values. However, combinations of components away from their nominal values due to tolerances can reduce the margins of component value deviations quite significantly. Although, this tests do give a general idea to the robustness of the system to parameter uncertainty. Below are results captured from the experimental set-up of the system operating at some of the conditions.

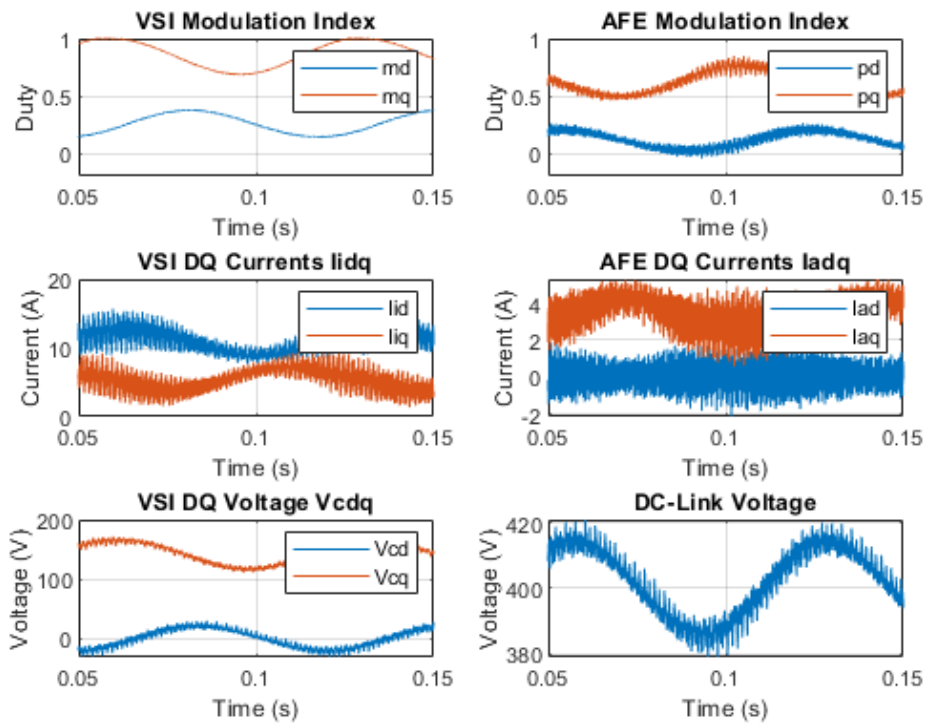

Figure 4.41: **PI** Experimental: Lmin Operation (No Load)

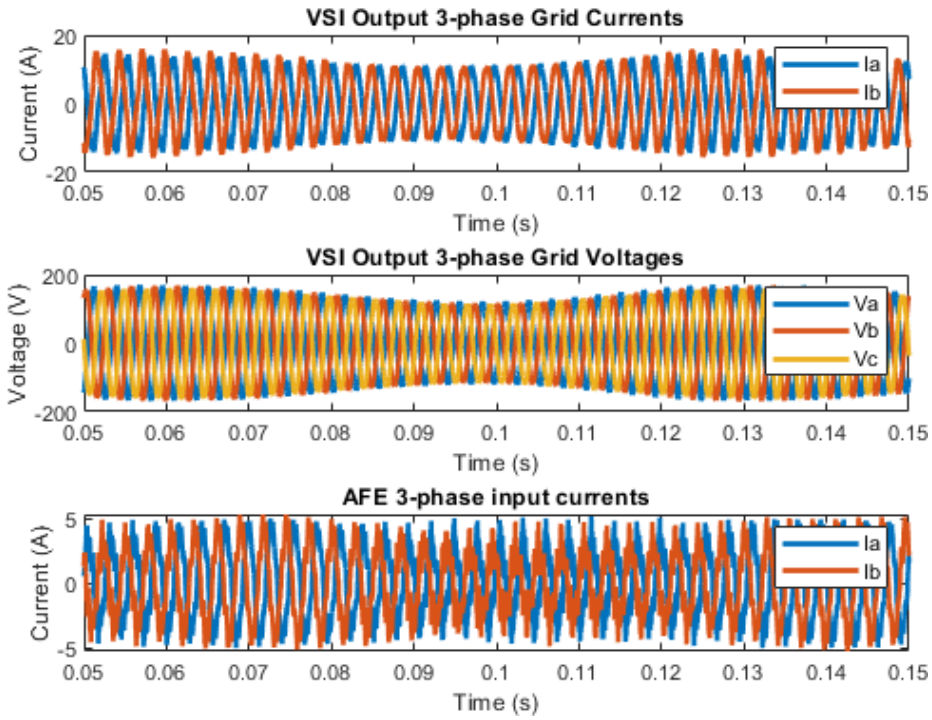

Figure 4.42: **PI** Experimental: Lmin Operation (No Load) 3-phase

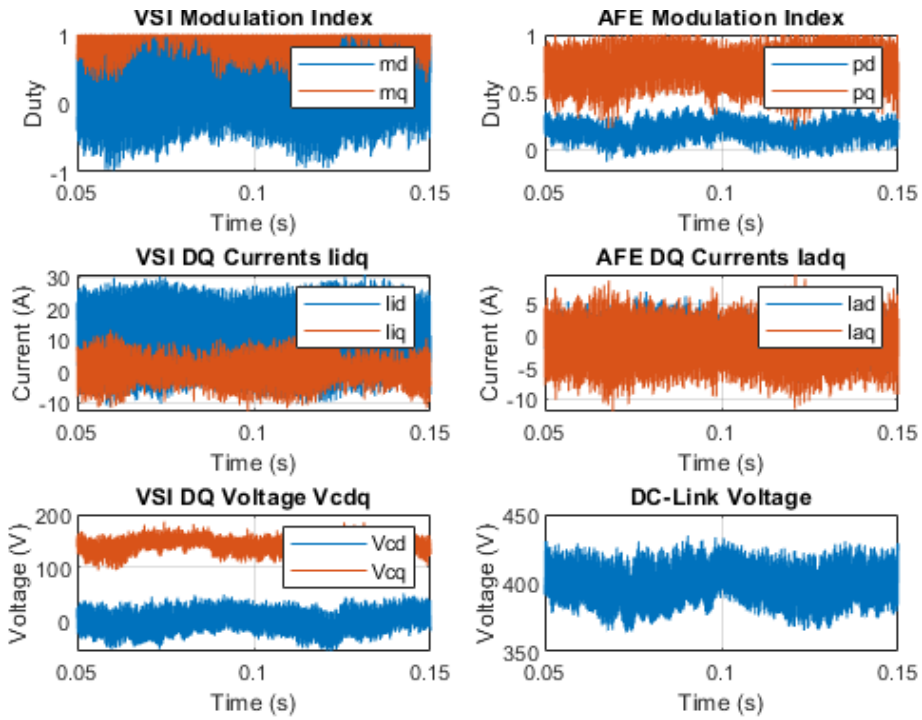

Figure 4.43: **PI** Experimental: Lmax Operation (No Load)

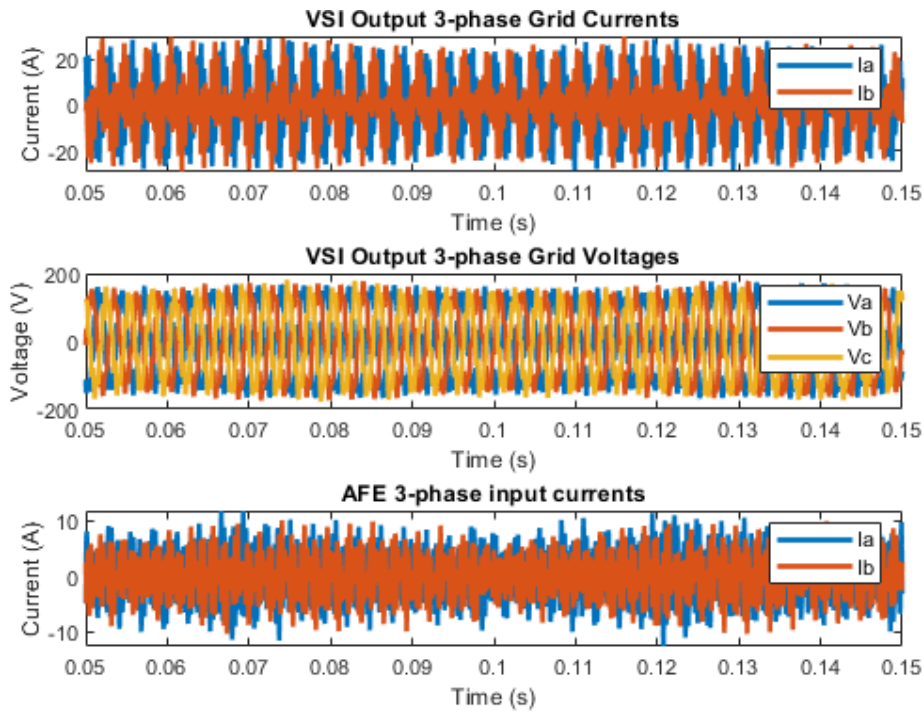

Figure 4.44: **PI** Experimental: Lmax Operation (No Load) 3-phase

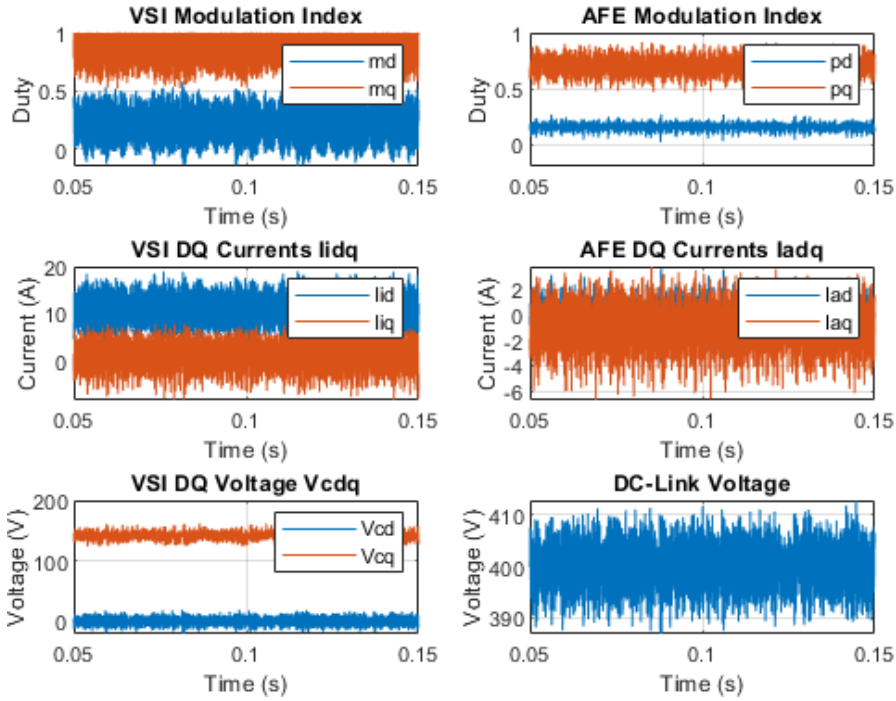

Figure 4.45: **PI** Experimental: Cmax Operation (No Load)

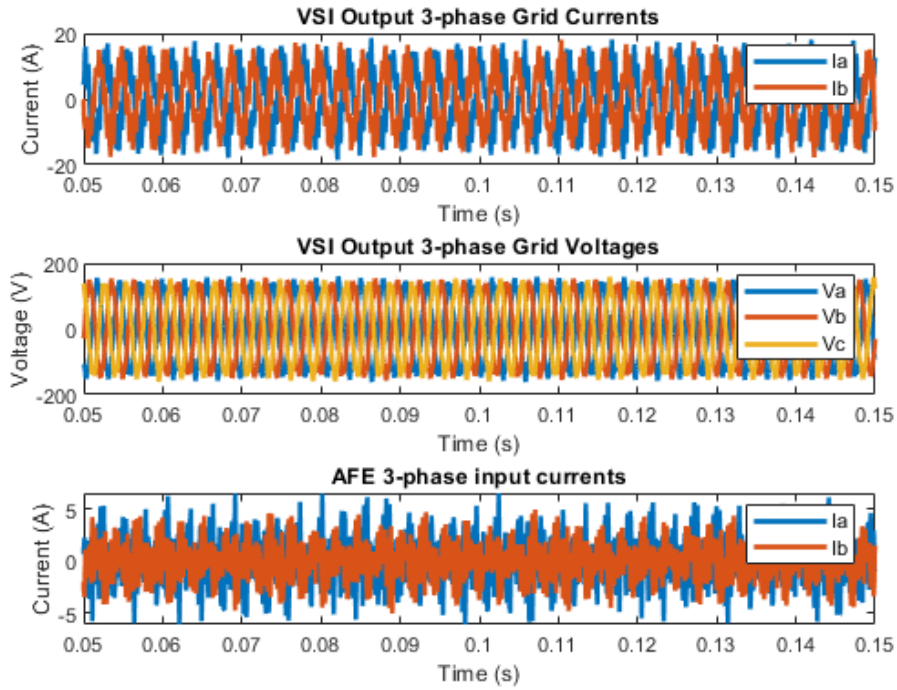

Figure 4.46: **PI** Experimental: Cmax Operation (No Load)

3-phase

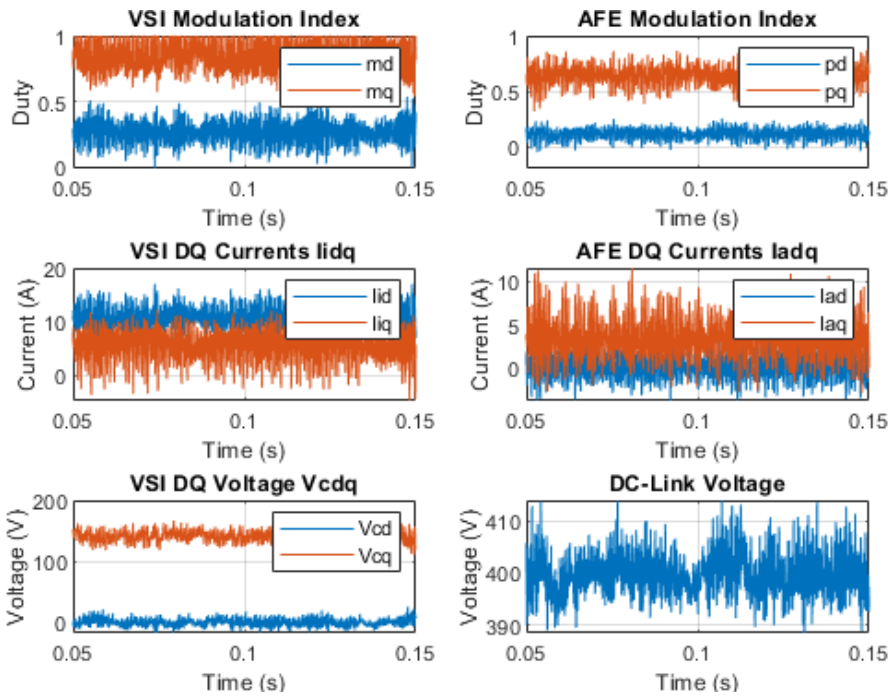

Figure 4.47: **PI** Experimental: C_aMax Operation (No Load)

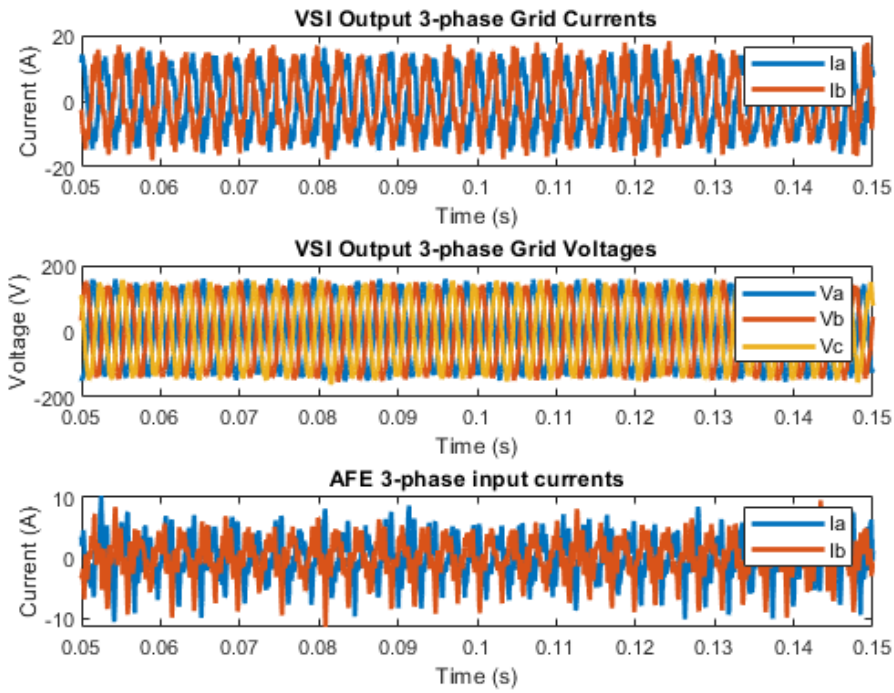

Figure 4.48: **PI** Experimental: $C_a$max Operation (No Load)

3-phase

The majority of the results collected are of parameters very close to their instability region and show variety of oscillatory behaviours which are caused by the inaccuracy of controller design to the model. Next, a comparison to the parametric uncertainty gained here for the PI will be performed for the H_2 controller.

H_2 Controller - Parametric Robustness Analysis

As had been performed for the PI, the exact same procedure was performed in order to locate the bounds of stability to the error in the parametric value in the controller design. The results achieved were as presented in Table 4.6.

H2 Parametric Uncertainty Stability Limits					
Parameter	Default Value	Minimum Value	Description	Maximum Value	Description
L	360μH	$< 0.5\mu$H	Stable for small L	1350μH	Degraded Performance at Load
				1400μH	Unstable at Load
C	33μF	$< 0.5\mu$F	Stable for small C	1150μF	Degraded Performance at Load
La	565μH	$< 0.5\mu$H	Stable for small La	10000μH	Noticeable Performance Degradation
				12000μH	Unstable at Load
				15000μH	Unstable
Ca	100μF	2μF	Unstable at Load	2250μF	Unstable at Load
		1μF	Unstable	5000μF	Unstable

Table 4.6: The located bounds of parametric stability of the H_2 Controller

As can be seen when comparing the results from the PI controller in Table 4.5 with the H_2 controller in 4.6, the robustness has improved on a very large scale. For instance for the AFE inductor L_a, for instability to occur the PI controller could handle a 32.7% increase in value before instability occurred. Whilst in the H_2, an increase of more than 2140% is achieved. This is a huge increase on the intrinsic robustness by employing H_2 control, and it is not unexpected. As discussed when the deriving the H_2 controller, the H_2 controller synthesis is largely based on decreasing uncertainty (or disturbances) characteristics in the closed loop form, so H_2 should have markedly better robustness performance than PI.

Although this method is a good way to ascertain robustness performance for each controller,

the drawback to this kind of analysis is that its not accurately testing the controller we have synthesised. In each test performed, the controller was retuned with the incorrect value and then tested on the rig. For simplicity in the analysis, only one parameter was changed at a time, when in reality it would be a combination of parameter uncertainties. An increase in one value, may result in the tolerance allowed in another component for instance.

H_2 Robustness Analysis - Ideal Testing

So to overcome some of the draw backs o the previous test, a stability analysis was performed numerically to visualize the stability regions of each controller.

In this test, the H_2 and PI controllers which was designed for the nominal system is used throughout, and only the parametric values are changed in order to quantify stability. From all the capacitance and inductance variables, three parameters were changed simultaneously and the stability maps in 3-D coordinates are plotted. Four of these tests are then conducted to accurately map all possible parametric changes.

The results obtained in the more idealistic robustness test shown in Figures 4.49 to 4.52 In these results, each of the colours represent the stability of the system. Red indicates instability, whilst all other colours represent the system as stable, with warmer colours representing systems whose dominant poles are closer to the imaginary axis, and colder symbolising poles further away from imaginary axis (more stable).

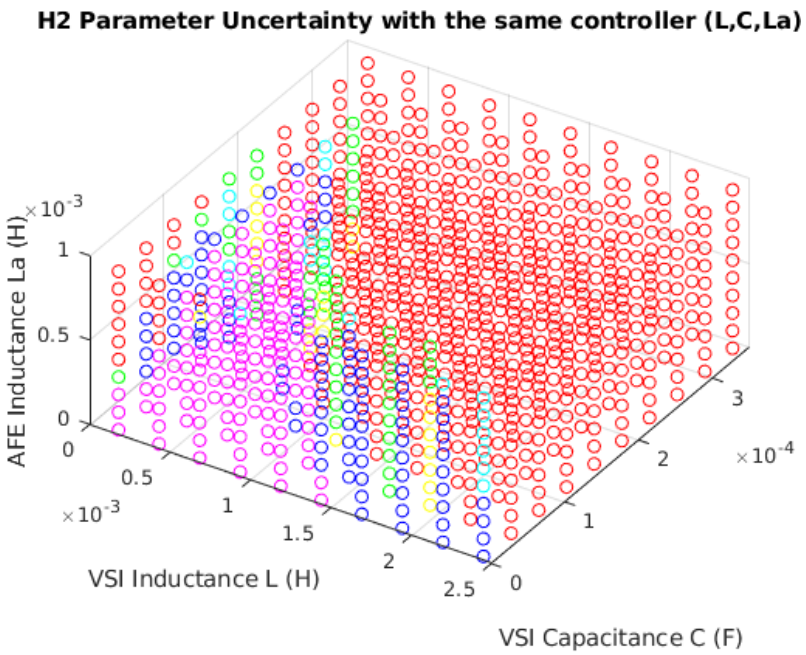

Figure 4.49: Assessment of the H_2 controller stability to parametric changes away from nominal design values, with variations in L, C and L_a. Variations in VSI capacitance showing greatest instability.

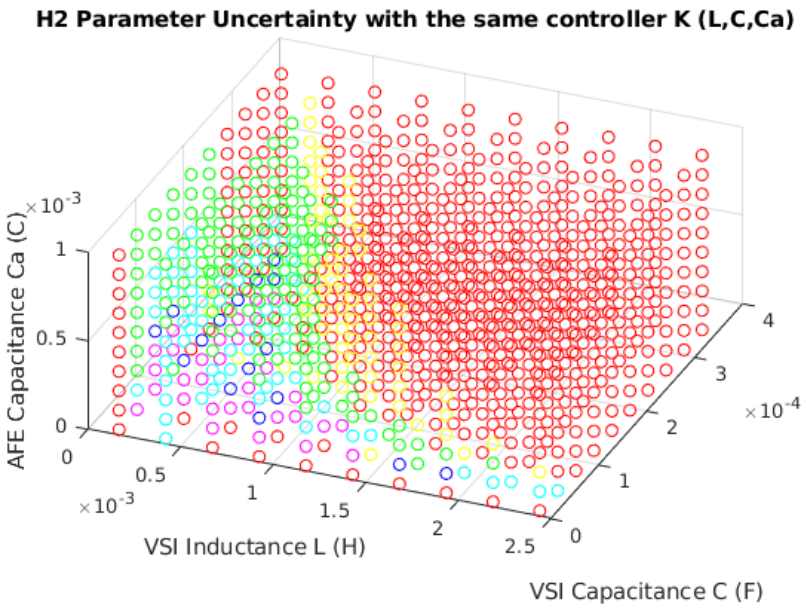

Figure 4.50: Assessment of the H_2 controller stability to parametric changes away from nominal design values, with variations in L, C and C_a. Again, along with Fig. 4.49 showing variation in VSI capacitance causing greatest instability.

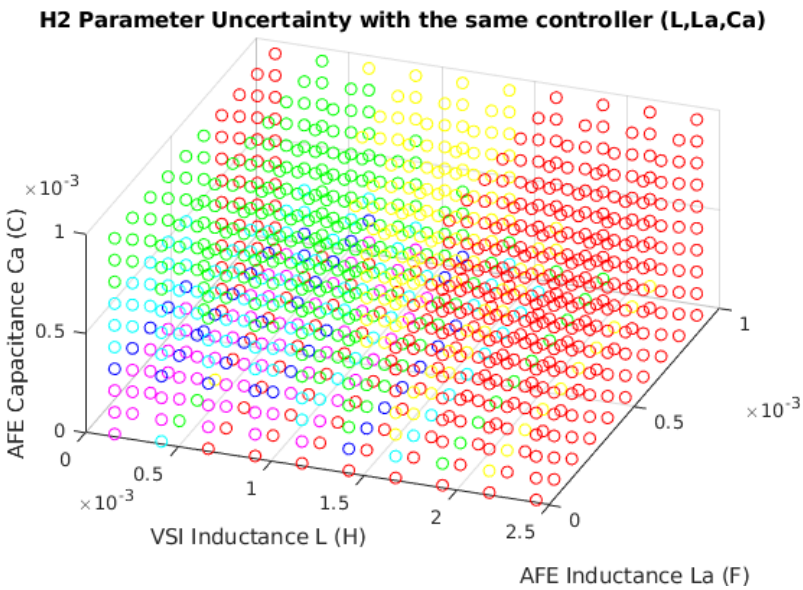

Figure 4.51: Assessment of the H_2 controller stability to parametric changes away from nominal design values, with variations in L, L_a and C_a. Presening how with increase to L_a with respect to the AFE paramters can lead to greater instability.

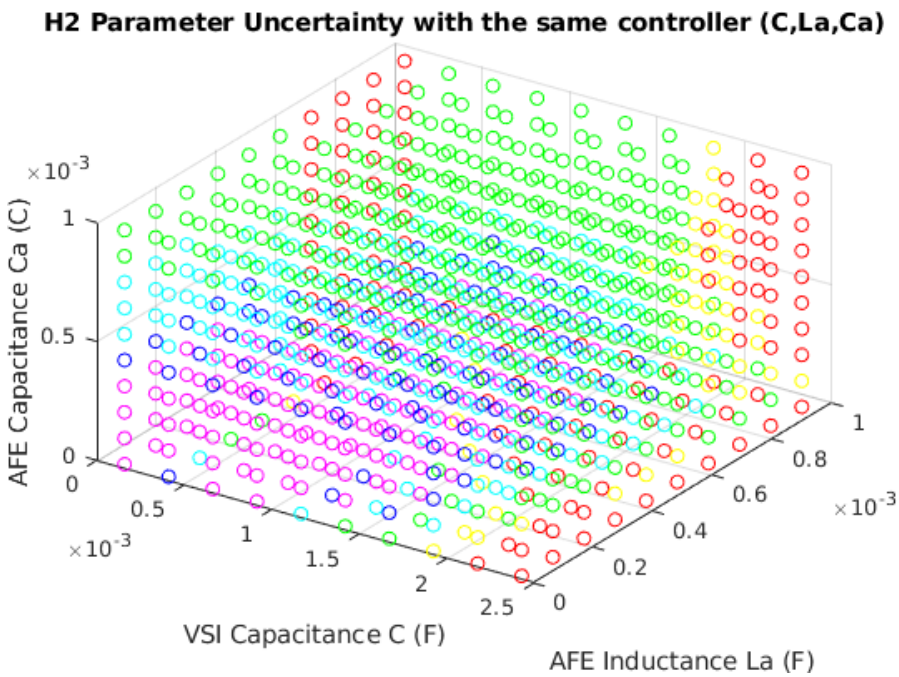

Figure 4.52: Assessment of the H_2 controller stability to parametric changes away from nominal design values, with variations in C, L_a and C_a. This shows variations amoung these values together do not contribute strongly to global system instability.

On this analysis a different picture is portrayed. It is clear that in regards to stability the VSI capacitance is the most sensitive, which also under the error associated with the AFE inductance as seen in Figures 4.49, and 4.50. It is clear that it is an essential limiting factor especially for larger values of capacitances. Overall, what can be observed across all the graphs is that the H_2 controller does indeed have vast areas of parametric robustness. Many values are still tens of times larger than nominal and still present a stable system under the influence of other parametric variances in the system. It also highlights the fact that the capacitances of the system are definitely larger contributors to parametric uncertainty in the system.

4.4 Discussion and Summary

This chapter main focus was to bring the complicated mathematics which make up the synthesis of the H_2 decentralised static full state-feedback controller and present in a simple way how such controllers can be designed and implemented into the system. This chapter also briefly went through the design of standard PI controllers for this system. These system performances were then compared against one another by analysing load transient behaviours as well as to analyse the general robustness of each system by analysing their parameter uncertainty characteristics.

PI controllers are of course, a well trusted form of controller whose mathematical concepts are simple, and thus design of these controls are generally very simple and well understood. The H_2 on the other had is an optimal controller, which although in this chapter it was presented how easy it is to actually design these controllers for grid applications, the general mathematical theory is clearly much more complex. Additionally another drawback in the design of H_2 controllers is the necessity of developing a very accurate state-space model of the system. If all the dynamics are not accounted for in the design, the controller K is unlikely to provide a stable controller in decentralised form and thus a very good understanding of the system is required before controllers can be designed. As opposed to PI controller where only a simple model of the transfer functions to be controlled are required.

However, whilst complex models are not required for the converters in these systems, dynamics such as converter impedance mismatch which may be unforeseen initially by the designer and could cause difficulties in the design of small scale embedded grids.

This however for the H_2 controller is not a matter. With all the system dynamics and interactions all attributed into the optimisation procedure for the decentralized controller, each of the converter controls are independent from one another but at the same time optimal to one another's closed loop performance. Any controller synthesised in H_2 is always guaranteed to be stable, as long as unique solutions to (3.116) can be found. Therefore, such considerations for

the H_2 controller are not required, as the optimisation will guarantee stable performance for each interconnected system.

Additionally the optimisation of each controller to the dynamics of other sub-systems translated into massive dynamic performance increases as opposed to traditional PI controllers. Each controller was tested on the exact same setup, and both designed to have the fastest dynamic performance possible. (Exact bandwidth specification is not possible, as there is not relation between the weights of Q_γ and R_γ and a precise bandwidth of the control) The PI controller suffered numerous problems in performance on the rig, mainly due to the step disturbance causing an interaction on the grid voltage which causes the PI controller to saturate modulators and dynamic performance to decrease drastically. Typically, larger passive filter components would be installed in order to mitigate the effects of interactions from other sub-system disturbances, although this is counter intuitive for the design of MEA embedded grids, as we want these systems to be smaller.

The H_2 controller, however, under the same exact grid conditions showed little to no distortion at all over the grid when under the influence of a load disturbance on the AFE. By having each of the controllers optimised dynamically to one another through the global H_2 optimisation, each controller is designed in mind of the other system dynamics. When one sub-system incurs a disturbance, all the other sub-systems are fast to respond to adjust to the disturbance themselves. In essence the VSI and AFE decentralised H_2 controllers can be seen as a single system wide controller without the need of cross-communication between sub-systems. This has reduced the cross-interaction between converters intrinsically and in turn, resulted in a stable system with good performance, where the PI controller on the same system produced poor, saturated performance. This presents a clear an open path to the design of lighter, and smaller electrical systems with reduced size of passive filters for aircraft embedded grid design.

In addition, the parametric robustness of each controller was evaluated. Firstly by means of analysing much a parameter can shift from the linearised design of the controller before instability was reached. H_2 again, due to the optimisation procedure actively reducing the uncertainty (or disturbance) characteristics of the resultant closed loop controller dynamics offered many times more parametric robustness than the PI counterpart. Another test was also performed checking the robustness of the nominal H_2 controller itself where it was shown that the controller was of course ery robust to parametric uncertainty, but also highlighted the VSI capacitance is the most sensitive factor in the parametric uncertainty of both the H_2 and PI.

So this chapter in brief, the ease of design, the power of intrinsic sub-system cross-coupling interaction mitigation and the robustness of the proposed H_2 control. However, when it comes to grids, this is not how they will be typically designed.

The design presented in this chapter assumes that both the VSI and AFE are operating on

the same dq angle, which is equivalent to the angle of the generated AC grid. This cannot be assumed, and to ensure that synchronisation between the VSI and AFE occur, a Phase-Locked Loop is required for the AFE.

In the next chapter, an investigation into the design and optimisation of a PLL into the H_2 optimisation will take place in order to ensure the AFE is appropriately synchronised to the AFE through the grid. Additionally, a grid in general doesn't constitute of only two converters on a bus. There are multiple converters. The next chapter also briefly investigates the scalability of the proposed control to systems consisting of more than two converters and how we can ensure optimisation of all sub-system performance on more complex grid networks.

Chapter 5

PLL Sub-system Optimisation and System Scalability

This study has so far investigated how a H_2 controller can be developed in a simplified interconnected converter system and how the proposed H_2 optimal control can be integrated into the system. It has been shown that utilising the optimal H_2 controller can provide superior dynamic performance across all the states of the system, can provide intrinsic decoupling between all sub-systems without further modification to the control architecture or hardware, and vastly improve the robustness of the system against parametric uncertainty.

However, the way this system is developed is not sufficient for the application of an embedded power electronic grid. In the design performed previously, the AFE is assumed to be operating at exactly the same dq angle as that of the VSI which is generating the grid. This assumption however is not feasible as in reality the AFE in practicality will not know the angle of operation of the VSI, as no communication is being shared between the two controllers. This is where a Phase-Locked-Loop (PLL) controller is essential. Phase-locked loops compute the angle of the grid, and ensure the synchronous operation of power converters to that of the grid angle. PLLs are notorious in causing instability of systems if improperly designed. Take the case of the impedance mismatch observed when designing the PI control for the interconnected system. It was shown in [124, 25, 37, 130] that without careful consideration to the change in impedance characteristic influenced by the bandwidth of the PLL, instability can occur, much like what was observed in the PI controller design. Therefore the PLL is notably notorious in causing system dynamic degradation if improperly designed [25, 131].

In this chapter a novel approach is presented in which the PLL controller is designed for and optimised by use of the decentralised H_2 control algorithm. In this way, the PLL is guaranteed to

provide stability to the system, optimal in performance against any disturbance on the grid, and have superior dynamic performance to the traditional forms of design. The concept of this design shall be shown through use of simulation and experimental results.

5.1 PLL Sub-system Incorporation into Global Optimization Procedure

Phase Locked Loops (PLL) are an important component in AC electric systems to ensure good power delivery, correct output frequencies and synchronisation of all power electronic sub-systems on an embedded grid [132] As has been previously explained, it is vitally important that the PLL is always correctly designed as it has been shown to influence great effect on the overall stability of the embedded network [37, 133, 49]. In light of these issues, there have been several attempts in literature in order to optimise the PLL [98, 99, 100]. However, the focus among these studies is analysing the intrinsic impedance effect the the PLL has on the converter. As seen previously, if the impedance of the interconnected converters are mismatched due to the control architecture bandwidths, instability can ensue. Current procedures in optimising the PLL to the grid is therefore a process of ensuring the influenced impedance of the PLL doesn't cause a mismatch and thus instability of a given converter on the network. However, as was observed in the previous chapter, the proposed H_2 controller design guarantees the stability of the global system. So in this chapter, a new approach in the area of PLL optimization is explored. Considering the decentralised H_2 optimisation approach guarantees independent controllers which are stable when interfaced together, it should be possible to include the PLL into the optimisation. In this way, it can be then guaranteed that the two converters, as well as any PLL implemented into the system is to be stable, whilst also being tuned for optimal performance. Never before in literature has this kind of procedure been undertaken for the optimisation of PLL sub-systems to the rest of the grid, and this section of the thesis presents the work which contributed to the published journal article in [131].

5.1.1 The SRF-PLL

As was presented in Chapter 2, in order to make the modelling and controller design process less of a trivial task, the use of the synchronous dq frame was used to convert the system from a three-phase time varying system, into a dual coupled DC equivalent form. When dealing with power system modelled in this form, a very common form of PLL is the Synchronous Reference Frame Phase-Locked Loop or SRF-PLL. Although there are many advanced alternatives to the

three-phase and single phase applications of PLLs [134, 135], always the SRF-PLL has been of popular choice. This is largely down to their ease of design, and the simplicity in implementation on low-end digital hardware [136]. The block diagram representation of the PLL is shown in Figure 5.1.

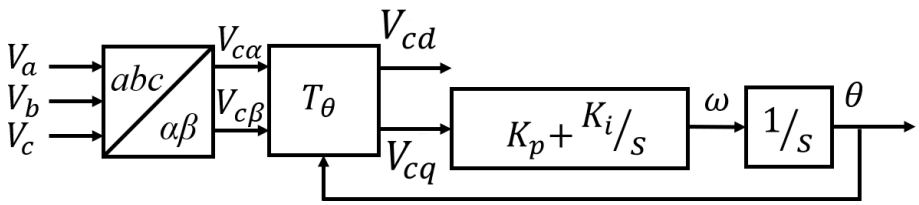

Figure 5.1: Block Digram of the SRF-PLL

The SRF-PLL consists of a Clarke transformation which samples the incoming three-phase grid voltages and converts into the alpha-beta frame. These values are then sampled into a block T_θ. This is essentially a Park dq transform, where the angle generated by the PLL is fed back and used in the transformation:

$$\begin{bmatrix} V_{cd}^P \\ V_{cq}^P \end{bmatrix} = T_\theta \begin{bmatrix} V_{c\alpha} \\ V_{c\beta} \end{bmatrix} = \begin{bmatrix} \cos(\theta_p) & \sin(\theta_p) \\ -\sin(\theta_p) & \cos(\theta_p) \end{bmatrix} \begin{bmatrix} V_{c\alpha} \\ V_{c\beta} \end{bmatrix} \tag{5.1}$$

Therefore, the output of the T_θ block estimates the dq equivalent grid voltages V_{cd}^P and V_{cq}^P using the PLL dq frame. From the previous chapter, it is known that the VSI is to be controlled such that the output AC grid has an equivalent q voltage of 0V in order to ensure unity power factor. Therefore, if the estimated q axis voltage in the PLL dq domain is also equal to zero, then the system is synchronised accurately to the VSI generated grid. So essentially, the signal V_{cq}^P is the error of the angle to the true angle of the grid, and that estimated by the PLL. This error is thus fed into the controller which then actuates an estimate of the speed, which is integrated to estimate the current angle of the grid. This is fed back into T_θ and repeats until the controller actuates the error to zero, resulting in synchronisation.

From the block diagram in Figure 5.1, the dynamic equations for the PLL can be easily received as:

$$\begin{aligned} \dot{\theta}_p &= -K_p \sin(\theta_p) V_{c\alpha} + K_p \cos(\theta_p) V_{c\beta} + x_i \\ \dot{x_i} &= -K_i \sin(\theta_p) V_{c\alpha} + K_i \cos(\theta_p) V_{c\beta} \end{aligned} \tag{5.2}$$

K_p defines the proportional gain of the PLL, whilst K_i is the corresponding integral gain, θ_p is the estimated angle of the grid and x_i is the integral state in the PI controller of the PLL. For later modelling of the PLL, it becomes more convenient to define these equations in terms of the error between the true grid angle θ_0 and that estimated by the PLL.

$$\theta_e := \theta_p - \theta_0 \implies \theta_p = \theta_e + \theta_0 \tag{5.3}$$

The following representation of the angle error can be expressed by the following figure, where subscript '0' terms define the true current position of the grid, 'p' the current estimate of the dq angle position, and 'e' the resultant error between the two.

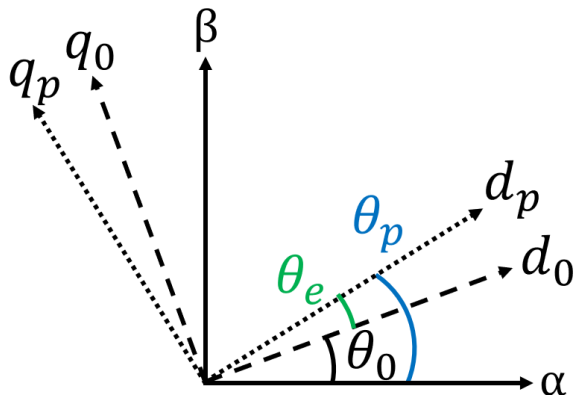

Figure 5.2: DQ Frame Operational Angles between the estimated and true grid angular positions

Since the rotation of $\theta_e + \theta_0$ can be observed as two possible rotations, one in the direction of $\theta_0 \to \theta_e$, and equivalently in the alternate direction of $\theta_p \to \theta_e$, taking this into account, and also noting the fact that the $\alpha\beta$ frame voltages can also be equivalently seen as dq voltages but at zero angle, the transformation T_θ in (5.1) can be manipulated into dq frame only terms, as well as represented fully in terms of θ_e such that:

$$\begin{bmatrix} V_{cq}^p \\ V_{cq}^p \end{bmatrix} = T_\theta \begin{bmatrix} V_{cd} \\ V_{cq} \end{bmatrix} = \begin{bmatrix} \cos(\theta_e) & \sin(\theta_e) \\ -\sin(\theta_e) & \cos(\theta_e) \end{bmatrix} \begin{bmatrix} V_{cd} \\ V_{cq} \end{bmatrix} \tag{5.4}$$

The assumption made in (5.4) is that at steady state, θ_e will be equivalent to zero, and therefore V_{cd}^p and V_{cq}^p will be equivalent to V_{cd} and V_{cq} produced by the VSI. Following this new transformation an equivalent representation of the dynamics equations defined in (5.2) can be evaluated by substitution of (5.3) and (5.4) to get the dynamics in terms of the error angle.

$$\begin{aligned} \dot{\theta}_e &= -K_p \sin(\theta_e) V_{cd} + K_p \cos(\theta_e) V_{cq} + x_i + \omega_0 \\ \dot{x}_i &= -K_i \sin(\theta_e) V_{cd} + K_i \cos(\theta_e) V_{cq} \end{aligned} \tag{5.5}$$

The term ω_0 which has appeared represents the nominal frequency which is expected from the grid. It is vital for the initialization of the PLL upon start-up. This value is constant and is only used in the controller implementation. Therefore it can be dropped during the PLL modelling procedure.

So as had been performed for the VSI and AFE, so that it can be input into the H_2 algorithm, the system needs to be linearised about its operating point. So, if it is assumed that at steady state the error angle is small ($< 0.1rad$), and that $V_{cq}^{p} = V_{cq}^{*}$ where as before ' * ' defines the state equilibrium point which in this case is zero for V_{cq}, then the resultant linearised dynamic equation will be:

$$\begin{aligned} \dot{\theta_e} &= -K_p V_{cd}^{*} \theta_e + x_i \\ \dot{x_i} &= -K_i V_{cd}^{*} \theta_e \end{aligned} \tag{5.6}$$

However, there is something fundamentally inaccurate about this linearised form of the PLL dynamics. Analysing the block diagram of the PLL in Figure 5.1, it is clear that V_{cq} is fundamental to the operation of the PLL and thus for accurate representation of the PLL dynamics, V_{cq} must also be interfaced into the linearised dynamic equation. In order to facilitate the dynamics of V_{cq} into the linearised model, a dummy state y is developed such that:

$$y = V_{cd}\theta_e + V_{cq} \tag{5.7}$$

$$\dot{y} = \dot{V_{cd}}\theta_e - \dot{\theta_e} V_{cd} + \dot{V_{cq}} \tag{5.8}$$

Now, if (5.7) is substituted into the expression of $\dot{\theta_e}$ in (5.5) then the state equation is reformed to become:

$$\dot{\theta_e} = K_p y + x_i \tag{5.9}$$

Now by substituting (5.8) and (5.9) into (5.7) and the x_i term in (5.5), the new accurate closed loop state-equations for the SRF-PLL can be found to be:

$$\begin{aligned} \dot{y} &= -(K_p y + x_i) V_{cd} - \theta_e \dot{V_{cd}} + \dot{V_{cq}} \\ \dot{x_i} &= K_i y \end{aligned} \tag{5.10}$$

The terms represented in (5.10) then defines the PLL controller dynamic equations in terms of error in the estimated angle of the grid, as well as the dynamics of V_{cq} fundamental to the PLL operation. However, the full definition of the PLL dynamics on the system is not yet complete. For instance, unlike the design carried out in Chapter 4, the AFE is not on the same dq frame as that of the VSI. The estimated angle generated by the PLL actually brings the dq frame of the AFE converter to that of the PLL dq frame whilst the VSI in this case is running on its own dq frame. To see clearly the issue that arises from this, first analyse the VSI dq voltage dynamic equations in their standard linearised form.

$$\begin{aligned} \dot{V_{cd}} &= \frac{1}{C} I_{id} + \omega V_{cq} - \frac{1}{C} I_{ad} \\ \dot{V_{cq}} &= -\omega V_{cd} + \frac{1}{C} I_{iq} - \frac{1}{C} I_{aq} \end{aligned} \tag{5.11}$$

As can be seen from the VSI voltage dynamic equations, the cross-coupled AFE terms I_{ad} and I_{aq} are present. Now in the previous design, this was completely correct as both the VSI and AFE were generated off the exact same internally defined angle. But, with the AFE angle generated from the PLL, these terms are no longer on the same dq frame, and thus the effect of the PLL invalidates these state equations.

To make the analysis simpler, all terms as generated in the PLL dq frame will be superscripted with 'p' henceforth.

As observed in Figure 5.2, the angle generated by the PLL can be assumed to be a rotation of θ_e offset to that true (VSI dq frame) angle. To interpolate this interaction between dq frames for AFE terms found in the VSI states, a transformation can be performed on these terms such that:

$$\begin{bmatrix} I_{ad} \\ I_{aq} \end{bmatrix} = T_\theta^{-1} \begin{bmatrix} I_{ad}^p \\ I_{aq}^p \end{bmatrix} \tag{5.12}$$

The transformation matrix T_θ was used to generate the PLL dq frame from the grid which is aligned to the VSI dq frame. Therefore, to observe states generated on the PLL dq from from the VSI perspective, the opposite action, and hence inverse transformation on the PLL dq states needs to occur. Therefore, it is required to perform a T_θ^{-1} transformation. In order to gain an accurate representation of the cross-coupled AFE states I_{ad} and I_{aq} in the VSI equations found in (5.11), the following adaptation must be performed:

$$\begin{aligned} I_{ad} &= I_{ad}^p \cos\left(\frac{V_{cq} - y}{V_{cd}^*}\right) - I_{aq}^p \sin\left(\frac{V_{cq} - y}{V_{cd}^*}\right) \\ I_{aq} &= I_{aq}^p \cos\left(\frac{V_{cq} - y}{V_{cd}^*}\right) - I_{ad}^p \sin\left(\frac{V_{cq} - y}{V_{cd}^*}\right) \end{aligned} \tag{5.13}$$

Similarly, VSI dq terms can be found in the AFE state equations which must also be treated equally. VSI states evaluated into the PLL dq frame need only the standard T_θ transformation conducted.

The AFE terms needing the adaptation are those for I_{ad} and I_{aq}, and with the new notation of different dq axis terms become:

$$\begin{aligned} \dot{I_{ad}^p} &= -\frac{R_a}{L_a} I_{ad}^p + \omega I_{aq} + \frac{1}{L_a} V_{cd}^p - \frac{p_d}{2L_a} V_{dc_a} \\ \dot{I_{aq}^p} &= -\omega I_{ad}^p - \frac{R_a}{L_a} I_{aq}^p + \frac{1}{L_a} V_{cq}^p - \frac{p_q}{2L_a} V_{dc_a} \end{aligned} \tag{5.14}$$

Of course, the terms V_{cd}^p and V_{cq}^p are the VSI terms as observed by the PLL dq frame, and are terms derived directly for the operation of the SRF-PLL.

Therefore, these cross-coupled VSI terms can be found by performing:

$$\begin{bmatrix} V_{cd}^p \\ V_{cq}^p \end{bmatrix} = T_\theta \begin{bmatrix} V_{cd} \\ V_{cq} \end{bmatrix} \tag{5.15}$$

which therefore defines these VSI terms in the AFE equations as:

$$\begin{aligned} V_{cd}^p &= V_{cd} \cos\left(\frac{V_{cq} - y}{V_{cd}^*}\right) + V_{cq} \sin\left(\frac{V_{cq} - y}{V_{cd}^*}\right) \\ V_{cq}^p &= -V_{cd} \sin\left(\frac{V_{cq} - y}{V_{cd}^*}\right) + V_{cq} \cos\left(\frac{V_{cq} - y}{V_{cd}^*}\right) \end{aligned} \tag{5.16}$$

By substituting the terms formulated in (5.13) and (5.16) to their corresponding state-space equations they're redefining, this completes the full definition of the PLL dynamics and interactions caused on the system. Thus, these interactive terms can also be accounted for in the controller design, and largely mitigated when in the presence of a disturbance dynamic.

5.1.2 Augmentation to the H_2 Optimal Control Scheme

So having defined the dynamic state-space equations for the PLL itself, along with the interactive behaviour imposed on the two converters due to the presence of the PLL in the system, the following equations can be used to derive linearised state-space matrices. However, this process is not as straight forward as that presented for the basic VSI/AFE model. In the basic notional model previously designed, all the system equations were defined as open loop for which a full state-feedback controller was to be deigned to stabilize the system. The PLL dynamics thus far presented are in the closed loop form. Therefore the dynamic equations of the PLL must be re-augmented such that the open loop dynamics of the controller can be submitted into the state-matrix, in the correct form for the H_2 optimisation, whilst another part defining how we want the controller gains to be augmented in the optimisation.

The first thing to bear in mind is the state-space representation of dynamic equations:

$$\dot{x} = A_{pll}x + B_{2_{pll}}u \tag{5.17}$$

For full state-feedback systems it is well defined that the control law is $u = Kx$. Therefore, the closed loop plant can be represented as

$$\dot{x} = A_{pll}x + B_{2_{pll}}Kx \tag{5.18}$$

Therefore, we can segment the closed loop form equations which we currently have in the form presented in (5.18) in order to receive equations in the open loop form (5.17) and structure the controller K accordingly.

In this manner we evaluate the state-space matrices from (5.10) to receive:

$$\begin{bmatrix} \dot{y} \\ \dot{x_i} \end{bmatrix} = \begin{bmatrix} 0 & -V_{cd}^* \\ 0 & 0 \end{bmatrix} \begin{bmatrix} y \\ x_i \end{bmatrix} + \begin{bmatrix} -V_{cd}^* & 0 \\ 0 & 1 \end{bmatrix} \begin{bmatrix} \epsilon_1 \\ \epsilon_2 \end{bmatrix} + \begin{bmatrix} \dot{V_{cq}} \\ 0 \end{bmatrix} \tag{5.19}$$

$$\begin{bmatrix} \epsilon_1 \\ \epsilon_2 \end{bmatrix} = K_{pll} \begin{bmatrix} y \\ x_i \end{bmatrix} = \begin{bmatrix} K_p & 0 \\ K_i & 0 \end{bmatrix} \begin{bmatrix} y \\ x_i \end{bmatrix} \tag{5.20}$$

Here, the terms ϵ_1 and ϵ_2 are considered dummy inputs. In standard state-matrix augmentation, the states of the system cannot also be inputs of the system. So the terms ϵ are equivalent to x and only are present for the augmentation of these equations into the H_2 optimisation.

The expression in (5.19) defines the open loop characterised equations which can be augmented directly into the A and B_2 matrices for the global control optimisation for the H_2 optimisation. The expression held in (5.20) defines the structure of the PLL controller with respect to the state-space matrices. As shall be observed a little later on in this section, this becomes vitally important in the decentralisation procedure of the controller in order to obtain independent gains for the PLL which is optimised to the rest of the global system dynamics.

Additionally the interactive elements of the PLL on the converter dynamics needs to be redeveloped into the state-space equations. The state equations which need to be remodelled are as follows (in their new PLL interacted form):

VSI:

$$\dot{V_{cd}} = \frac{1}{C} I_{id} + \omega V_{cq} - \frac{I_{ad}^p \cos\left(\frac{V_{cq}-y}{V_{cd*}}\right) + I_{aq}^p \sin\left(\frac{V_{cq}-y}{V_{cd}^*}\right)}{C} \tag{5.21}$$

$$\dot{V_{cq}} = \frac{1}{C} I_{iq} - \omega V_{cd} - \frac{I_{aq}^p \cos\left(\frac{V_{cq}-y}{V_{cd*}}\right) - I_{ad}^p \sin\left(\frac{V_{cq}-y}{V_{cd}^*}\right)}{C} \tag{5.22}$$

AFE:

$$\dot{I_{ad}^p} = -\frac{R_a}{L_a} I_{ad}^p + \omega I_{aq}^p + \frac{V_{cd} \cos\left(\frac{V_{cq}-y}{V_{cd*}}\right) - V_{cq} \sin\left(\frac{V_{cq}-y}{V_{cd}^*}\right)}{L_a} + \frac{1}{L_a} V_{cd} - \frac{p_d}{2L_a} V_{dc_a} \tag{5.23}$$

$$\dot{I_{aq}^p} = -\frac{R_a}{L_a} I_{aq}^p - \omega I_{ad}^p + \frac{V_{cq} \cos\left(\frac{V_{cq}-y}{V_{cd*}}\right) + V_{cd} \sin\left(\frac{V_{cq}-y}{V_{cd}^*}\right)}{L_a} + \frac{1}{L_a} V_{cq} - \frac{p_q}{2L_a} V_{dc_a} \tag{5.24}$$

Having utilised y as a dummy state to incorporate the dynamics of V_{cq} in the linearised state equation, these equations can now be fully linearised about the equilibrium point of y. Analysis of (5.7) shows that as the error reduces to zero at steady state, y tends to 0. Additionally it is

also known previously that V_{cq}, and I_{aq} are controlled variables with a reference of zero. With this knowledge each of the states described in (5.21)-(5.24) can be linearised to the form:

VSI:

$$\dot{V_{cd}} = \frac{1}{C} I_{id} + \omega V_{cq} - \frac{1}{C} I^p_{ad} \tag{5.25}$$

$$\dot{V_{cq}} = \frac{1}{C} I_{aq} - \omega V_{cd} - \frac{1}{C} I^p_{ad} + \frac{I^p_{ad}}{CV_{cd}} V_{cq} - \frac{I^p_{ad}}{CV_{cd}} y \tag{5.26}$$

AFE:

$$\dot{I^p_{ad}} = -\frac{R_a}{L_a} I^p_{ad} + \omega I^p_{aq} + \frac{1}{L_a} V_{cd} - \frac{p_d}{2L_a} V_{dc_a} \tag{5.27}$$

$$\dot{I^p_{aq}} = -\frac{R_a}{L_a} I^p_{aq} - \omega I^p_{ad} + \frac{2}{L_a} V_{cq} - \frac{p_q}{2L_a} V_{dc_a} - \frac{1}{L_a} y \tag{5.28}$$

Thus we can extend the A matrix from the standard two converter H_2 design presented in (4.2) and extend it with the newly developed PLL states. The order of the states now becomes:

$$x = \begin{bmatrix} I_{id} & V_{cd} & I_{iq} & V_{cq} & I^p_{ad} & I^p_{aq} & V_{dc_a} & y & x_i & \chi_{V_{cd}} & \chi_{V_{cq}} & \chi_{I_{aq}} & \chi_{V_{dc_a}} \end{bmatrix}^T \tag{5.29}$$

and the input matrix u is of the order:

$$u = \begin{bmatrix} m_d & m_q & p_d & p_q & \epsilon_1 & \epsilon_2 \end{bmatrix}^T \tag{5.30}$$

The full complete state-space matrices for the system augmenting a PLL on the AFE can thus be derived as:

$$A_{vsi} = \begin{bmatrix} -\frac{R}{L} & -\frac{1}{L} & \omega & 0 & 0 & 0 \\ \frac{1}{C} & 0 & 0 & \omega & 0 & 0 \\ -\omega & 0 & -\frac{R}{L} & -\frac{1}{L} & 0 & 0 \\ 0 & -\omega & \frac{1}{C} & -\frac{I^*_{ad}}{CV^*_{cd}} & 0 & 0 \\ 0 & -1 & 0 & 0 & 0 & 0 \\ 0 & 0 & 0 & -1 & 0 & 0 \end{bmatrix}, \quad A_{cv} = \begin{bmatrix} 0 & 0 & 0 & 0 & 0 \\ -\frac{1}{C} & 0 & 0 & 0 & 0 \\ 0 & 0 & 0 & 0 & 0 \\ 0 & -\frac{1}{C} & 0 & 0 & 0 \\ 0 & 0 & 0 & 0 & 0 \\ 0 & 0 & 0 & 0 & 0 \end{bmatrix}, \quad A_{pv} = \begin{bmatrix} 0 & 0 \\ 0 & 0 \\ 0 & 0 \\ \frac{I^*_{ad}}{CV^*_{cd}} & 0 \\ 0 & 0 \\ 0 & 0 \end{bmatrix} \tag{5.31}$$

$$A_{ca} = \begin{bmatrix} 0 & \frac{1}{L_a} & 0 & 0 & 0 & 0 \\ 0 & 0 & 0 & 0 & 0 & 0 \\ 0 & 0 & 0 & 0 & 0 & 0 \\ 0 & 0 & 0 & 0 & 0 & 0 \\ 0 & 0 & 0 & 0 & 0 & 0 \end{bmatrix}, \quad A_{afe} = \begin{bmatrix} -\frac{R_a}{L_a} & \omega & -\frac{p_d}{2L_a} & 0 & 0 \\ -\omega & -\frac{R_a}{L_a} & -\frac{p_q}{2L_a} & 0 & 0 \\ \frac{3p_d}{4C_a} & \frac{3p_q}{4C_a} & \frac{P_l}{C_a V^2_{dc_a}} & 0 & 0 \\ 0 & -1 & 0 & 0 & 0 \\ 0 & 0 & -1 & 0 & 0 \end{bmatrix}, \quad A_{pa} = \begin{bmatrix} 0 & 0 \\ -\frac{1}{L_a} & 0 \\ 0 & 0 \\ 0 & 0 \\ 0 & 0 \end{bmatrix} \tag{5.32}$$

$$A_{vp} = \begin{bmatrix} 0 & -\omega & \frac{1}{C} & -\frac{I^*_{ad}}{CV^*_{cd}} & 0 & 0 \\ 0 & 0 & 0 & 0 & 0 & 0 \end{bmatrix}, \quad A_{ap} = \begin{bmatrix} 0 & -\frac{1}{C} & 0 & 0 & 0 \\ 0 & 0 & 0 & 0 & 0 \end{bmatrix}, \quad A_{pll} = \begin{bmatrix} \frac{I^*_{ad}}{CV^*_{cd}} & -V^*_{cd} \\ 0 & 0 \end{bmatrix} \tag{5.33}$$

$$A = \begin{bmatrix} A_{vsi} & A_{cv} & A_{pv} \\ A_{ca} & A_{afe} & A_{pa} \\ A_{vp} & A_{ap} & A_{pll} \end{bmatrix} \tag{5.34}$$

$$B_{vsi} = \begin{bmatrix} \frac{V_{dc}}{2L} & 0 \\ 0 & 0 \\ 0 & \frac{V_{dc}}{2L} \\ 0 & 0 \\ 0 & 0 \\ 0 & 0 \end{bmatrix}, \quad B_{afe} = \begin{bmatrix} -\frac{V_{dc_a}}{2L_a} & 0 \\ 0 & -\frac{V_{dc_a}}{2L_a} \\ \frac{3I^*_{ad}}{4C_a} & \frac{3I^*_{aq}}{4C_a} \\ 0 & 0 \\ 0 & 0 \end{bmatrix}, \quad B_{pll} = \begin{bmatrix} -V^*_{cd} & 0 \\ 0 & 1 \end{bmatrix} \tag{5.35}$$

$$B_2 = \begin{bmatrix} B_{vsi} & \mathbf{0} & \mathbf{0} \\ \mathbf{0} & B_{afe} & \mathbf{0} \\ \mathbf{0} & \mathbf{0} & B_{pll} \end{bmatrix} \tag{5.36}$$

PLL Controller Design and Tuning

The procedure in order to tune and receive the controller gains is the same had been performed before in order to decentralise the VSI and AFE controller gains from the synthesised global controller.

When deriving the state-space equations for the PLL, the control law matrices were also defined in (5.20). The matrix containing the PI gains for the PLL are already in the correct structure which needs to be constrained onto the output matrix. Therefore, when submitting the matrices in (5.34) and (5.36), the constrained control law will be:

$$u = K_{constr}x = \left[\begin{array}{cccccc|ccccc|cc} 1 & 1 & 1 & 1 & 1 & 1 & 0 & 0 & 0 & 0 & 0 & 0 & 0 \\ 1 & 1 & 1 & 1 & 1 & 1 & 0 & 0 & 0 & 0 & 0 & 0 & 0 \\ \hline 0 & 0 & 0 & 0 & 0 & 0 & 1 & 1 & 1 & 1 & 1 & 0 & 0 \\ 0 & 0 & 0 & 0 & 0 & 0 & 1 & 1 & 1 & 1 & 1 & 0 & 0 \\ \hline 0 & 0 & 0 & 0 & 0 & 0 & 0 & 0 & 0 & 0 & 0 & 1_a & 0 \\ 0 & 0 & 0 & 0 & 0 & 0 & 0 & 0 & 0 & 0 & 0 & 1_b & 0 \end{array}\right] x \tag{5.37}$$

The first four rows and columns of the constraint matrix in (5.37) is exactly the same as that derived in (4.30) to develop the decentralised controllers for the VSI and AFE. For the bottom two rows of the constraint matrix, this relates to the structure derived in (5.20), where the a and b terms will result in the proportional and integral gains K_p and K_i to be optimised respectively.

With the augmentation of the PLL states and gains into the optimisation algorithm, it does change slightly how the system is to be tuned by not in a major way.

As more states are now present in this system, so too must the tuning matrices Q_γ and R_γ be extended to incorporate the new states and inputs from the PLL.

So the default weights to begin tuning are therefore:

$$Q_\gamma = \begin{bmatrix} \mathbf{0} & & & & & \\ & I^{j_{vsi}\times j_{vsi}} & & & & \\ & & \mathbf{0} & & & \\ & & & I^{j_{afe}\times j_{afe}} & & \\ & & & & \mathbf{0} & \\ & & & & & I^{j_{pll}\times j_{pll}} \end{bmatrix}, \quad R_\gamma = I^{m\times m} \tag{5.38}$$

Where j is the number of integral states for the subscripted system, and m are the number of inputs which is now equal to six. Again in Q_γ only the integral states are weighted to define the required performance of the global control, which for the case of the PLL the weight is on the state x_i.

As before, the R_γ matrix is first tuned by adjusting a constant ρ until the system is of near to desired performance. In Chapter 4, the constant ρ was split into two different constants with each scaling the weight to the corresponding sub-system inputs, as previously seen in (4.14). With the PLL being a 3rd sub-system being optimised, this coefficient ρ will be now split in three to scale the R_γ matrix tuning for the VSI, AFE and PLL independently.

$$R_\gamma = \begin{bmatrix} \rho_{vsi}^{1\times m_{vsi}} & \rho_{afe}^{1\times m_{afe}} & \rho_{pll}^{1\times m_{pll}} \end{bmatrix} \begin{bmatrix} I^{m_{vsi}\times m_{vsi}} & & \\ & I^{m_{afe}\times m_{afe}} & \\ & & I^{m_{pll}\times m_{pll}} \end{bmatrix} \tag{5.39}$$

So as performed previously, the inputs of each converter can be individually penalised by adjusting the corresponding ρ to bring the system close to the required operating performance.

Now, it isn't as simple as taking the original R_γ for the previous system of two converters and tuning the ρ_{pll} from there. The system equations have fundamentally changed with the presence of the PLL, and also have the interactive dynamics which have to be optimised over again. So unfortunately the system will need to be retuned.

The system being designed for is exactly the same as the parameters presented in Tables 4.1 and 4.2, and with the PLL dynamic present, the R_γ matrix selected which brought system stability and the best overall dynamic performance was:

$$R_\gamma = \begin{bmatrix} 10 & 2 & 10^{-9} \end{bmatrix} \begin{bmatrix} I^{m_{vsi} \times m_{vsi}} & & \\ & I^{m_{afe} \times m_{afe}} & \\ & & I^{m_{pll} \times m_{pll}} \end{bmatrix} \tag{5.40}$$

Following this, the Q_γ matrix is tuned such that the best dynamic performance is achieved, whilst ensuring the that gains themselves don't become to big compromising the robustness of the system. The Q_γ matrix which was found to offer the best compromise was found to be:

$$Q_\gamma = diag\left(\begin{bmatrix} 0 & 0 & 0 & 0 & 1 & 1 & 0 & 0 & 0 & 2 & 4 & 0 & 10^{-4} \end{bmatrix}\right) \tag{5.41}$$

where the weight 10^{-4} is applied to the PLL integral state x_i. In general when designing for various parameters of the same system setup, it was found the the PLL integral weight on x_i had to be magnitudes lower than that of the rest of the states in Q_γ. If this weight was of similar order then the gains of K would become too large and compromise the robustness and stability of the system to uncertainty and noise. In general the x_i weight being of 3 magnitudes of order less than the other weights prevented this situation, whilst still resulting in overall speedy dynamic performances as shall be shown next.

Since the order to the system, and the respective controller has increased to a 13th order system, as opposed to an 11th order of simpler system, more random starting points are needed in order to find the true minimum of the $\|\cdot\|_2$. In this case, it was found that using 40 random starting points in the H_2 algorithm resulted in consistency across the controller gains, signifying the location of the global minimum. The resultant controller gains for the converter using the weights in (5.40) and (5.41) was the following:

$$K = 10^{-3} \begin{bmatrix} K_{vsi} & \mathbf{0} & \mathbf{0} \\ \mathbf{0} & K_{afe} & \mathbf{0} \\ \mathbf{0} & \mathbf{0} & K_{pll} \end{bmatrix} \tag{5.42}$$

$$K_{vsi} = \begin{bmatrix} 4.2 & 0.7 & 0.23 & 0.35 & 15.5 \cdot 10^3 & 36.2e \cdot 10^3 \\ 5 \cdot 10^{-2} & 0.52 & 4.82 & 6.4 \cdot 10^{-2} & 6350 & 15.5 \cdot 10^3 \end{bmatrix} \tag{5.43}$$

$$K_{afe} = \begin{bmatrix} 8.4e \cdot 10^{-2} & 0.28 & 6 \cdot 10^{-3} & 2170 & 42.5 \\ 1.25 & 25.2 & 0.78 & 1400 & 73 \end{bmatrix} \tag{5.44}$$

$$K_{pll} = 10^3 \begin{bmatrix} 1.4234 & 0 \\ 1.4239 & 0 \end{bmatrix} \tag{5.45}$$

5.1.3 Transfer Function Derivation and Closed Loop Design

As had been performed before for the standard H_2 controller, in order to analyse and compare the performance of the PLL augmented and optimised in the H_2 optimisation, the PI alternative shall be developed.

The SRF-PLL has been extensively researched as a stand-alone control system, so an in-depth analysis of the standard form of SRF-PLL will not be conducted in this section.

To design the PI controller gains for the PLL, the transfer function between the error, and the estimated angular frequency of the grid must first be formulated. Again it is easier to analyse the the SRF-PLL in terms of θ_e than in the estimated angle θ_p point of view. From 5.4 we can also attain the dynamic equations for which the transfer function can be yielded. Unlike when implementing into H_2, the standard linearised form of the SRF-PLL dynamics is all that's required to design the PI gains, and the modelling of V_{cq} is not essential, as it was for H_2.

By directly linearising the equations developed in (5.4), the following is received:

$$\tilde{V_{cq}^P} = -V_{cd}^P \sin(\theta_e) + V_{cq}^{P*} \cos(\theta_e) \tag{5.46}$$

$$\tilde{V_{cq}^P} \approx -V_{cd}^P \theta_e \tag{5.47}$$

If we assume at steady state $V_{cq}^{P*} = 0$ and that only small variations in θ_e will occur. As V_{cd}^P is not fed directly into the controller, the linearisation of this dynamic equation is not required to develop the transfer function. By analysis once more of Figure 5.1, the following block diagram for the system can be assumed:

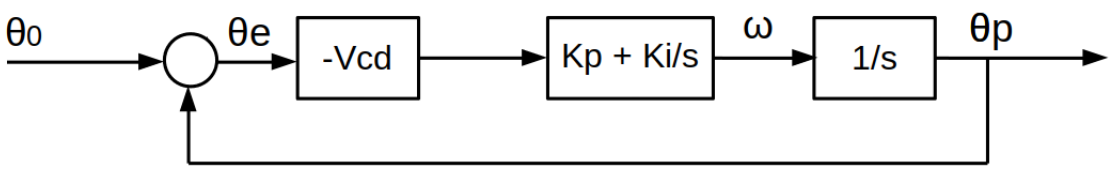

Figure 5.3: The Transfer Function Block Diagram of the SRF-PLL

The method of then formulating the expressions for designing the gains is not trivial. By method of pole-placement the controller gains for the PLL can be designed by [137]:

$$K_p = \frac{2\zeta\omega_n}{V_{cd}}, \quad K_i = \frac{\omega_n^2}{V_{cd}} \tag{5.48}$$

where ζ is the damping factor and ω_n are the desired bandwidth and damping radio of the controller. As usual in controller design ζ is selected to be around 0.707. In terms of the selection

of the bandwidth, this can be a far more trivial process than that of H_2. As we had seen with the PI controller design of the notional system, the aspect of cross-converter impedance must be taken into consideration and the PLL has a very influencing role. The details of the contribution the PLL has to the impedance characteristic of the system will not be detailed here as it has already been extensively covered in literature [37, 133, 49]. For the fairness of the comparison the PI controllers for the two converters were kept to the same bandwidth as previously performed in the experiments in Chapter 4, presented in Table 4.4. For the PLL design, a bandwidth was selected that was close to the dynamic speed achieved by the H_2 optimisation. The bandwidth ω_n of the controller was thus set to 300Hz, with a ζ equal to 0.707. This resulted in the controller gains:

$$K_p = 4.242, \quad K_i = 900 \tag{5.49}$$

5.1.4 H_2 Optimised and Local PI Controller Performance Comparison

In order to assess the benefits of this approach to controller design, as had been performed previously, the H_2 controller will be compared against a PI controller. Both the H_2 and PI controller dynamics have been designed in order to achieve the best performance possible across all states, and the experimental setups are the same for each test and is detailed in Table 4.1, with the same reference values for the control set in Table 4.2. We have seen in the previous chapter the enhanced parametric robustness that can be achieved when utilising the proposed H_2 controller and therefore it was deemed unnecessary to repeat the testing for this adaptation to the system. This test as before involves the analysis of a 1kW step load being applied to the system and the performance of all states observed.

Notional H_2 System with PLL: Step Load Performances

In this test, the same exact conditions are performed as with the 1KW step experiment for the basic H_2. In this case however, the AFE being augmented with a PLL. The system was first tested using an average model simulation to prove the concept of the controller design, the result of which is shown in Figure 5.4.

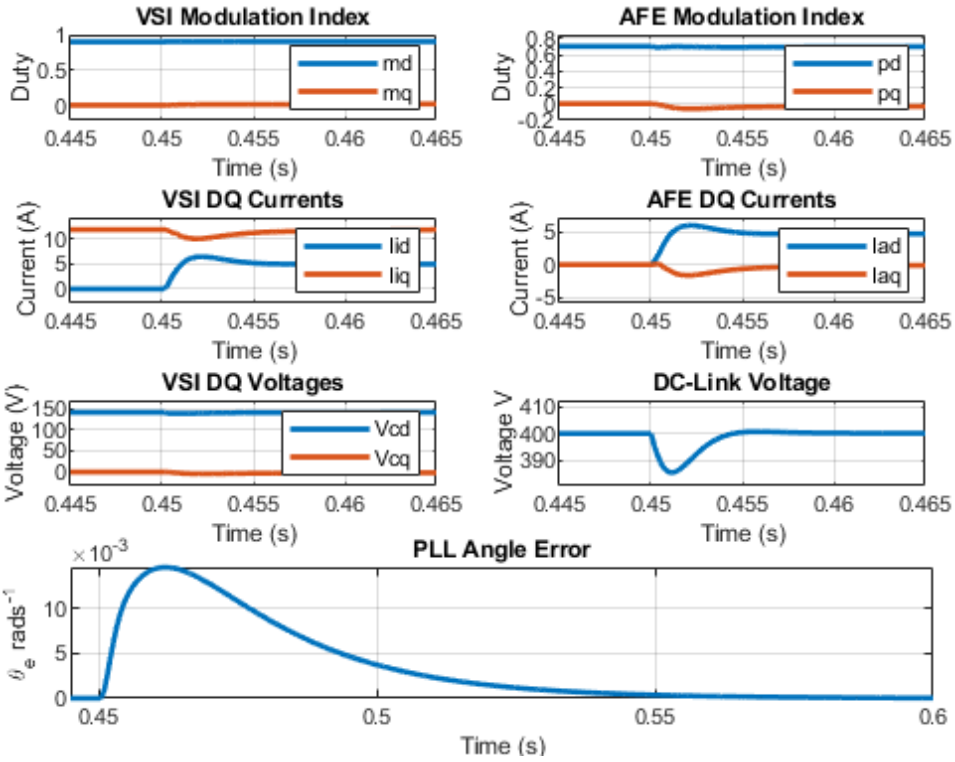

Figure 5.4: H_2 Average Model: 1kW Step Load under influence of optimised PLL

Again, from the average model, it is shown that the inclusion of the PLL dynamics on the AFE has little effect to the interaction mitigation effects that was achieved in the notional model. Although the gains had to be retuned, similar performance could be achieved across all the converter dynamics and thus PLL is shown to be non-detrimental to the performance. Analysing the dynamic performance of the PLL dynamic itself, the error θ_e is kept very small, with only an overshoot of approximately 15×10^{-3} radians, which translates to a maximum error in degrees of approximately 0.086°. Though the PLL dynamic looks rather slow when compared to the rest of the system, do note that the maximum overshoot is very small indeed, showing only a very small deviation in θ_e occurring at transient. The figures below show the experimental results, and oscilloscope capture of the experimental validation of the average model test.

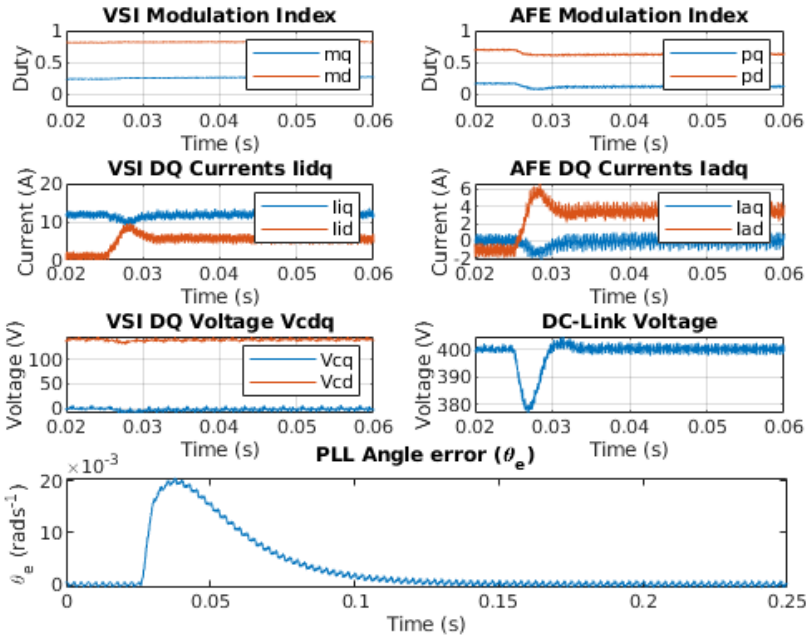

Figure 5.5: H_2 Experimental: 1kW Step with PLL

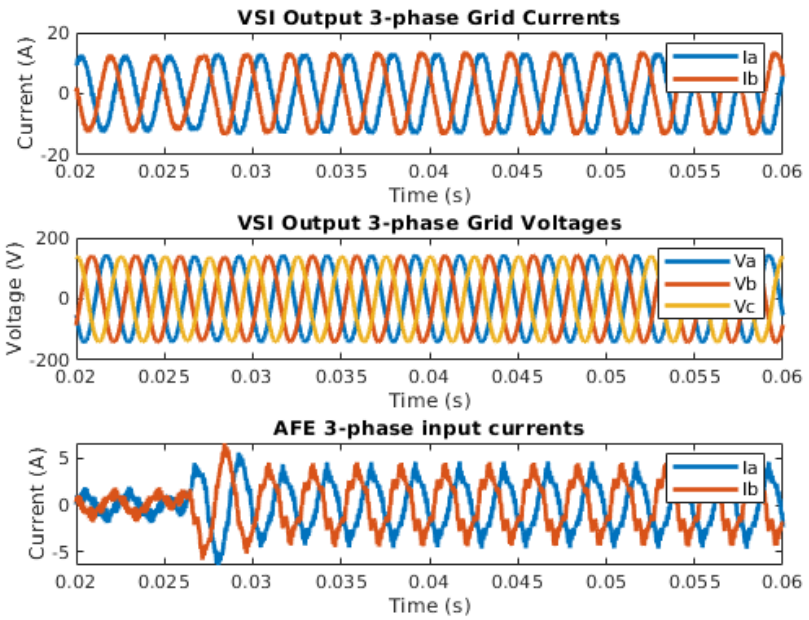

Figure 5.6: **PI** Experimental: 1kW Step with PLL

Power Step 3-Phase

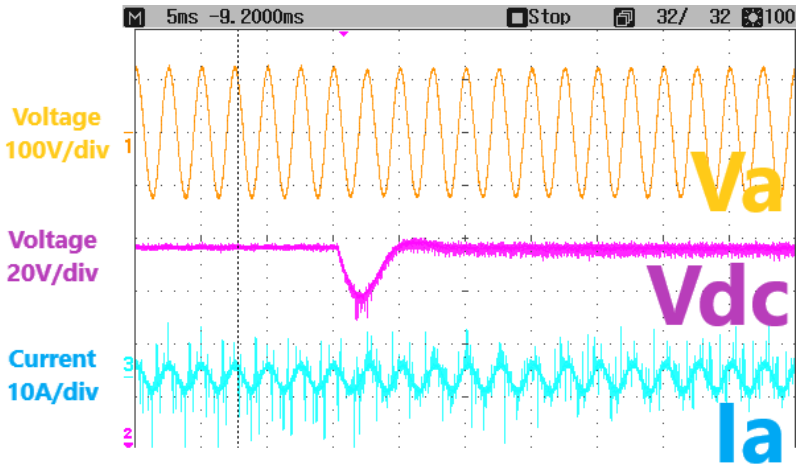

Figure 5.7: H_2 Experimental: Osciloscope Capture of 1kW Step Load with optimal PLL

From the experimental results, it confirms clearly the dynamics as observed from the average model. The results clearly clearly confirm that the PLL has little to no effect to the interaction mitigation effects on the grid as had been observed in the average model. During the step load disturbance, it is clear that the VSI states again do not have an negative interactive effects direct from the AFE except for new demand in current into the grid to power the load. The grid voltage remain steady and fixed to the set reference, with no noticeable change in the to amplitude or phase. Further considering the phase, the PLL dynamics hold true as predicted in the average model. The error magnitude is slightly larger by 5×10^{-3} radians, but that is not a large enough difference to render the model inaccurate.

Traditional PI Control Comparison: The Step Load Test with individually optimised PI sub-system controls

We have seen how the H_2 controller can develop fully optimised sub-system controllers for the whole system, and guarantees stability and overall desired performance across all states. Here the classical method of controller design with have its performance compared to that of the H_2 controller.

The converter controllers have been designed to operate at the fastest dynamic speed possible, the PLL has been designed to have similar dynamic speed to that of the H_2 performance. This was done utilising the phase-shift test on each controller, and tuning ω_n in (5.48) until similar dynamic performance was achieved between the two systems.

Starting with the 1kW Step load test, the performance achieved is shown below:

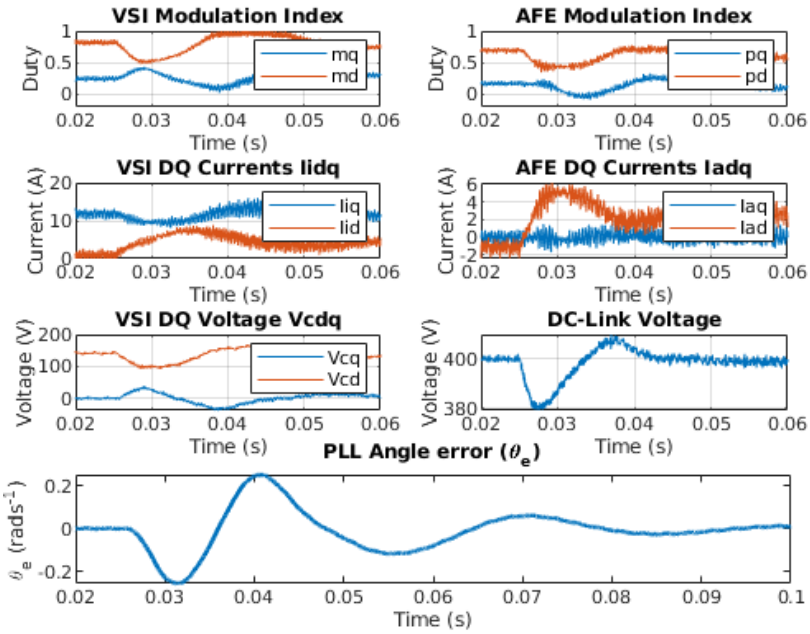

Figure 5.8: **PI** Experimental: Step Load with local PLL

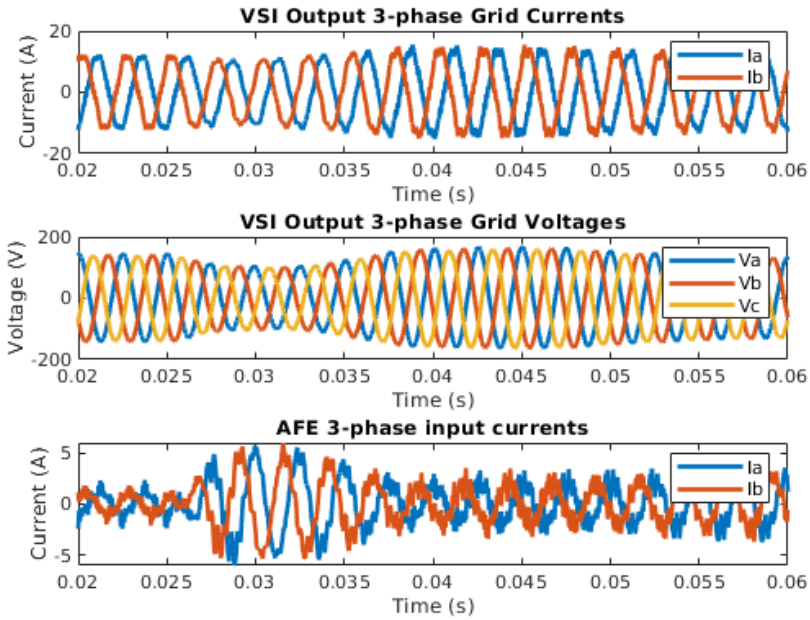

Figure 5.9: **PI** Experimental: Step Load with local PLL

Power Step 3-Phase

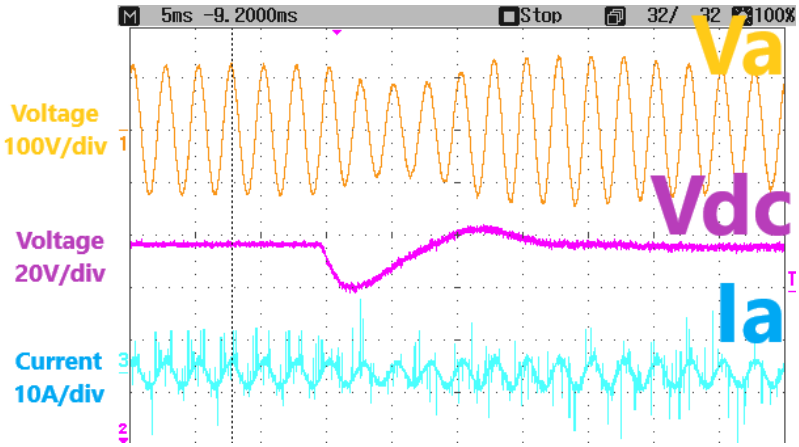

Figure 5.10: H_2 Experimental: Osciloscope Capture Step Load using Local PI Controllers for each sub-system

The PI controllers used on the converters in these tests are exactly the same as the ones used in the experiments in Chapter 4 and therefore the base performance of the system is exactly the same as previous, with only a PLL augmented to the system.

If one compares the PI system with no PLL system from Figure 4.29, you can see that incorporation of the PLL does provide a small performance improvement to the PI control, with the AFE current overshoot reducing to 6A, as well as reductions in the grid voltage undershoots. However, as occurred previously, the PI controlled system still experiences saturation of the modulation indexes during the disturbance due to the interaction experienced from AFE dynamics to the VSI. This too shows to influence a lot the PLL of the system. Note that the PLL is designed to the same dynamic speed of that derived from the H_2 control synthesis, and the radial errors occurred are far larger. In fact, the error incurred was 10x larger at approximately 0.2 radians of error on disturbance infliction. Though the larger PLL dynamic disturbance observed, the rate at which the PLL returns to the correct approximation of the grid angle within similar time to that of the H_2 controller, albeit a lot more oscillatory in response, largely down the interactive dynamics exhibited onto the grid. However the PLL has, already mentioned does decrease the effect of the interactive behaviour somewhat. But on comparison between H_2 and PI controls, it truly shows the optimal nature of incorporating the PLL design into the global optimisation. The H_2 in this case shows to mitigate much of the interaction observed across the converter states, and also the PLL states too, with only minimal deflection occurring in the predicted grid angle.

5.1.5 PLL Phase Shift Tests

The PLL has been compared in performance between PI and H_2 controllers for load disturbances, where is is clear the the H_2 optimised system not only tracks as well as the standard PLL, but also delivers the benefits of interaction mitigation to the system, and overall improvement across all the states. However, this kind of test does not directly test the PLL controller on its ability to correct disturbances on its core state; the angle error.

Therefore in this section, a test on the PLL itself and the infliction caused on the rest of the system shall be analysed through a phase shift test. In this test, the system will be running at steady-state loaded condition when through software, the angle of the grid generated will be manually shifted ahead by $\frac{\pi}{3}$ radians. The system will be then analysed across all system states.

In Figures 5.11, and 5.12, the DQ representation of the experimental results is shown for the PI and H_2 controller respectively, with the three-phase results followed for each respectively after in Figures 5.13 and 5.14.

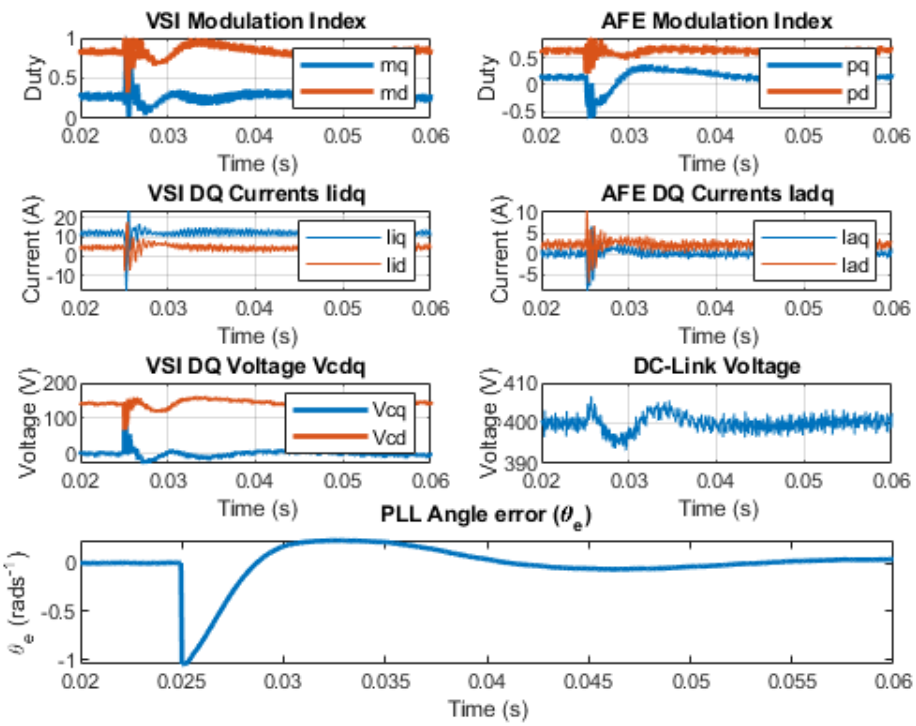

Figure 5.11: **PI** Experimental: Phase Shift Test in DQ Frame

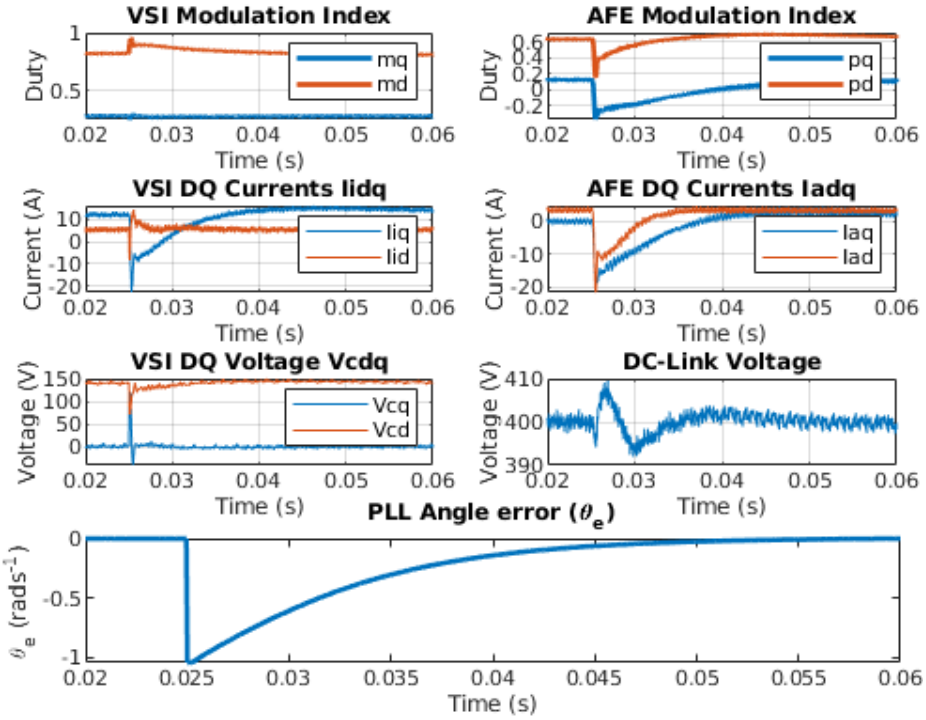

Figure 5.12: H_2 Experimental: Phase Shift Test in DQ Frame

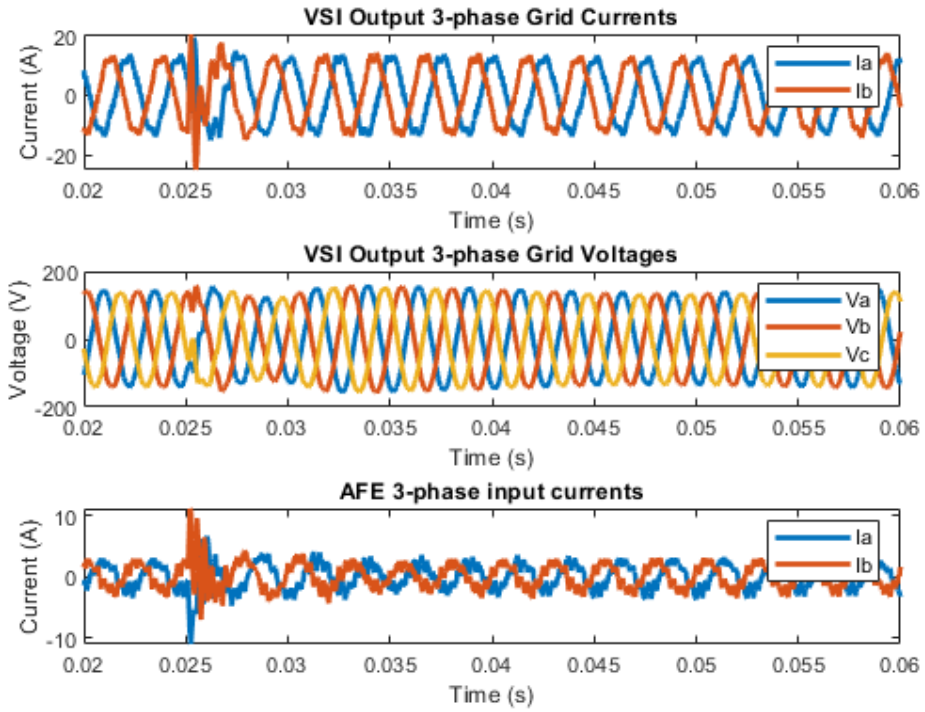

Figure 5.13: **PI** Experimental: Phase Shift Test in 3-phase representation

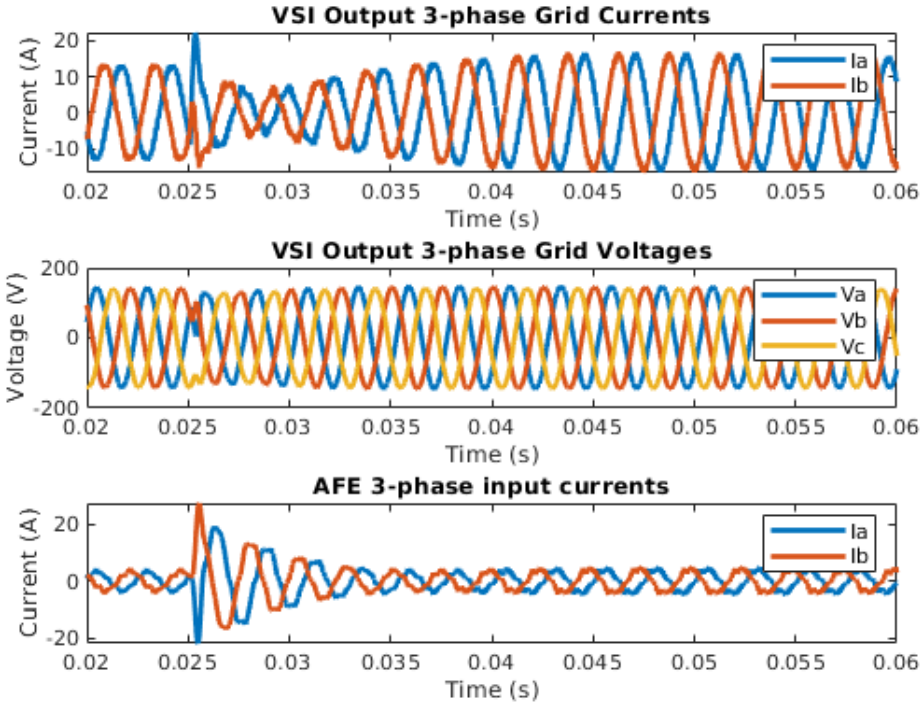

Figure 5.14: H_2 Experimental: Phase Shift Test in DQ Frame

What is clear between the H_2 and PI controllers is that for one the relative bandwidth of each PLL is the same, with each achieving zero steady-state error within approximately the same amount of time. However, in the case of the performance there are clear differences. For one, the currents of the PI controller for once actually seem to outmatch that of the H_2 control, whilst on the contrary, the grid voltages of the H_2 seem to out perform that of the PI system. The reason as to why the currents in the H_2 system are quite poor in this case is likely down to the fact that a more damped response to the θ_e dynamic, prolonging the size of the error for longer. Whereas the PI based systems PLL more rapidly reduces the error, although exhibits more oscillatory behaviour about the steady state point. The voltages on the other hand for the H_2 controller does experience a slight interaction, with the grid voltages momentarily dropping 20V, but quickly recovers. The PI control system grid voltages remarkably also exhibits good performance through quick recovery of the offset, however the grid as observed in previous tests exhibited larger interaction, for more prolonged time. The V_{dc} dynamic of each control system is very similar, however this is to be expected. In previous test the PI based system incurred large interactions due to the sudden change in current demands due to the load step, and the unmoddeled interaction between converters not being automatically compensated in the controller design. But in this case, the phase shift does not incur any new demands on the currents or voltages, but only a phase error between converts.

Therefore, as long as the PLL is well designed on the PLL system the system can be well maintained in the case of phase shift. Evidently there are positives and negatives to the utilisation of either controller in regards to a phase shift disturbance. Whilst the H_2 current dynamics are worse, it is important to note the aviation standards in MIL-STD-704 detail no requirements on the extent of current dynamics to disturbance; whilst grid voltage is a core requirement. Therefore, even with worse H_2 performance in the current dynamics, it still holds better performance overall to the set aviation requirements due to maintaining the grid voltage. Also, such extreme phase shift changes are incredibly unlikely in practise, as a $\frac{\pi}{3}$ phase shift should not occur on aircraft. This test is showing the extremes of the performance of each systems PLL.

What has been shown is that the optimised H_2 control is still able to maintain system stability under large phase shift phenomena. Whilst in contrast to the PI controller the current dynamic appeared to be worse off, the grid voltages were still maintained to acceptable levels which, to aircraft specification is more desired over current dynamics, and therefore deemed acceptable for application. However, please do note that for these tests, the H_2 controller was tuned to achieve similar performance to the best PI controller which could be designed for this system. Therefore the presented system is slower than the best H_2 system that can be designed. With some tweaking of the Q_γ and R_γ matrices to improve the bandwidth, much more superior performance can be achieved for the H_2 system.

5.2 Discussion and Summary

This chapter has presented and explored the methodologies of incorporating additional subsystems into the optimisation procedure. Firstly, a PLL which was to be augmented into the AFE control architecture was presented. It was shown how in order to ensure the accurate modelling of the PLL, a new state y had to be defined in order to incorporate the PLLs dependence of the $q-$axis grid voltage V_{cq}. It was shown to be a non-trivial process, and through reverse engineering of the SRF-PLL block diagram, the state-space matrices and control structure to be imposed for the control of the PLL states was derived. Due to the fact the PLL aligns the dq axis of the AFE to its estimated angle, and not that of the grid, it was shown how to augment the two alternate dq frame models under the same state-space model to improve accuracy in the optimisation. With all the proper considerations taken place in the model development, the synthesised H_2 controller was shown again to retain interaction mitigation characteristic which was observed earlier in Chapter 4. PLLs have been shown in literature to be notorious in effecting the overall dynamic stability of if improperly designed, but this chapter has effectively shown a procedure in which the PLL

can be automatically tuned considering the dynamics of the target converter it will be augmented into as well as the wider system. Through the proposed procedure, all sub-system controllers are guaranteed to deliver stable robust performance, and thus ensuring the dynamics of the PLL never lead the global system to instability. Additionally, as was shown previously, improved dynamic performance across all sub-system states including those of the PLL could be achieved over traditional methods of control.

The success in the augmentation of additional non-physical sub-systems, leads the the possibility of augmenting further power electronic sub-systems into the optimisation, and the capability of optimising large scale power systems grid into the control optimisation procedure.

In the next chapter, the scalability of the controller shall be presented by which the same methodologies as employed when augmenting the PLL shall be performed for optimising an additional AFE converter onto the AC network, along with its own PLL. Proving the concept, and the ease by which of augmenting more complex grid like structures into the proposed decentralised controller optimisation.

Chapter 6

Optimisation Scalability and System Expansion

At this point, the reader may be wondering that this work is all about the control optimisation of grids but the example which is presented is only a network of two interconnected converters. Such an example could be observed as an oversimplification of an actual grid. Whilst this is a valid point, the section will address this.

As was mentioned in Chapter 2, this chapter investigates the application of the proposed controller design thus far in more 'grid-like' environments to show how the controller can be scaled up to incorporate a larger electrical systems. Here, a scaled up system shall be investigated which includes a single VSI generating the AC bus, and two AFE's interconnected onto the grid. It is hoped from this chapter that the reader recognises the ease in the scalability of the controller design for global system including a greater number of sub-systems, and how the the benefits observed on the simplified system can be carried over to more grid like systems.

6.1 Multiple Converter, Multiple Load Micro-grid Modelling

The system under investigation in this section is only an extension on the notional model presented in Figure 2.3, where both AFE's have SRF-PLLs as described from the previous chapter. Thus, the notional system under test is of the form:

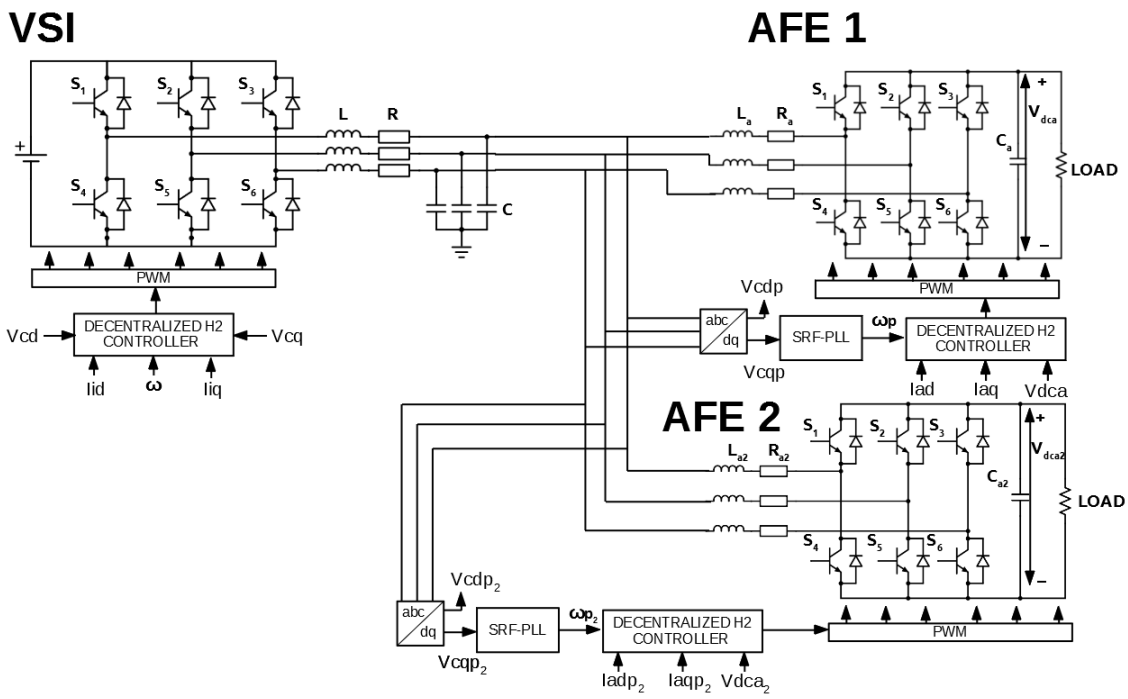

Figure 6.1: The Expanded Notional System Under Test

In Section 5.1.2 it was seen how the PLL dynamics influences both the nominal models of the VSI and AFE, due to the fact that the PLL brings the AFE to an alternative dq frame to that of the VSI. However now two such AFE's are now interfaced onto the grid. To get a general understanding of how the two PLL's influence the behaviour of the whole system, it helps to first build the system model neglecting the PLLs, performing a similar modelling method to that presented in Chapter 2. This would simply result in the following dynamic equations:

$$\textbf{VSI:} \quad \begin{cases} \dot{I_{id}} = -\frac{R}{L}I_{id} - \frac{1}{L}V_{cd} + \omega L I_{iq} + \frac{m_d}{2L}V_{dc} \\ \dot{V_{cd}} = \frac{1}{C}I_{id} + \omega V_{cq} - \frac{1}{C}I_{ad} \\ \dot{I_{iq}} = -\omega I_{id} - \frac{R}{L}I_{iq} - \frac{1}{L}V_{cq} + \frac{m_q}{2L}V_{dc} \\ \dot{V_{cq}} = -\omega V_{cd} + \frac{1}{C}I_{iq} - \frac{1}{C}I_{aq} \end{cases} \tag{6.1}$$

$$\textbf{AFE 1:} \quad \begin{cases} \dot{I_{ad1}} = \frac{1}{L_{a1}}V_{cd} - \frac{R_{a1}}{L_{a1}}I_{ad1} + \omega I_{aq1} - \frac{p_{q1}}{2L_{a1}}V_{dc_a1} \\ \dot{I_{aq1}} = \frac{1}{L_{a1}}V_{cq} - \omega I_{ad1} - \frac{R_{a1}}{L_{a1}}I_{aq1} - \frac{p_{q1}}{2L_{a1}}V_{dc_a1} \\ \dot{V_{dc_a1}} = \frac{3}{4C_{a1}}(I_{ad1}p_{d1} + I_{aq1}p_{q1}) - \frac{I_{L1}}{C_{a1}} \end{cases} \tag{6.2}$$

$$\textbf{AFE 2:} \quad \begin{cases} \dot{I_{ad2}} = \frac{1}{L_{a2}} V_{cd} - \frac{R_{a2}}{L_{a2}} I_{ad2} + \omega I_{aq2} - \frac{p_{q2}}{2L_{a2}} V_{dc_a 2} \\ \dot{I_{aq2}} = \frac{1}{L_{a2}} V_{cq} - \omega I_{ad2} - \frac{R_{a2}}{L_{a2}} I_{aq2} - \frac{p_{q2}}{2L_{a2}} V_{dc_a 2} \\ \dot{V_{dc_a 2}} = \frac{3}{4C_{a2}} (I_{ad2} p_{d2} + I_{aq2} p_{q2}) - \frac{I_{L2}}{C_{a2}} \end{cases} \tag{6.3}$$

Where the terms subscripted with '1' and '2' are AFE states associated with AFE1 and AFE2 respectively. What is very apparent at first is that there is no cross-interaction between the two AFE state dynamics; that is no states of one AFE end up in the dynamics equations of the opposing AFE. This would coincidently make the modelling of the full system depicted in Figure 6.1 relatively easy as no interactive terms between the two AFE's on two alternate dq frames need to be taken into account. However, both the AFE's do have interactive behaviour with the VSI and vice versa. Therefore, the two different dq frames for each AFE must be attributed into the VSI dynamic equations. This however is also a non-trivial process.

The interactive terms of the VSI are the states I_{ad} and I_{aq} found in the state equations for V_{cd} and V_{cq} respectively. These currents are the input currents for each of the two AFEs whose values are determined by the demand current demand of the load, from the grid. Therefore, these currents on the VSI state equations can be simply evaluated to be:

$$\begin{aligned} I_{ad} &= I_{ad1} + I_{ad2} \\ I_{aq} &= I_{aq1} + I_{aq2} \end{aligned} \tag{6.4}$$

Therefore, to model the I_{ad} term accurately across the two AFEs PLL dq frames, the translations as performed in (5.21) and (5.22) can be used to evaluate the following expressions:

$$\dot{V_{cd}} = \frac{1}{C} I_{id} + \omega V_{cq} - \frac{1}{C} \Bigg[\left[I^p_{ad1} \cos\left(\frac{V_{cq} - y_1}{V_{cd^*}}\right) + I^p_{aq1} \sin\left(\frac{V_{cq} - y_1}{V_{cd^*}}\right) \right] + \left[I^p_{ad2} \cos\left(\frac{V_{cq} - y_2}{V_{cd^*}}\right) + I^p_{aq} \sin\left(\frac{V_{cq} - y_1}{V_{cd^*}}\right) \right] \Bigg] \tag{6.5}$$

$$\dot{V_{cq}} = \frac{1}{C} I_{iq} - \omega V_{cd} - \frac{1}{C} \Bigg[\left[I^p_{aq1} \cos\left(\frac{V_{cq} - y_1}{V_{cd^*}}\right) - I^p_{ad1} \sin\left(\frac{V_{cq} - y_1}{V_{cd^*}}\right) \right] + \left[I^p_{aq2} \cos\left(\frac{V_{cq} - y_2}{V_{cd^*}}\right) - I^p_{ad2} \sin\left(\frac{V_{cq} - y_2}{V_{cd^*}}\right) \right] \Bigg] \tag{6.6}$$

Therefore, for every additional AFE which is attached to the grid, one needs only to add additional inverse transformed (T_{θ_e}) input current terms, as shown above.

The cross coupled terms V_{cd} and V_{cq} for each of the two AFEs are identical, and thus the state-equations from AFE1 can be simply copied, and have the corresponding states attributed to AFE2 replaced for the terms in the equation.

There is however something, which if designing by PI transfer function method which may not be inherently obvious at first, but in the state-space approach becomes very clear in regards to cross-converter interactions due to the presence of PLLs.

Firstly, linearise (6.5) and (6.6) to get the equations into state-space form, and one receives:

$$\dot{V_{cd}} = \frac{1}{C} I_{id} + \omega V_{cq} - \frac{1}{C}\left[I^P_{ad1} + I^P_{ad2}\right] \tag{6.7}$$

$$\dot{V_{cq}} = -\omega V_{cd} + \frac{1}{C} I_{iq} - \frac{1}{C}\left[I_{aq1} + I_{aq2} + \frac{I_{ad1}}{V^*_{cd}} y_1 + \frac{I_{ad2}}{V^*_{cd}} y_2 + V_{cq}\left[\frac{I_{ad1}}{V_{cd}} + \frac{I_{ad2}}{V_{cd}}\right]\right] \tag{6.8}$$

From (5.20) it was presented that for our augmentation of the state $y_{\langle 1,2\rangle}$ (where again, subscripts 1 and 2 defines the 'y' PLL states for AFE1 and AFE2 respectively) is dependant on the dynamic $\dot{V_{cq}}$. As can be seen from (6.8), $\dot{V_{cq}}$ includes both the current states from both AFE converters. Whilst it has been shown that when each of the AFEs are augmented without a PLL the two AFEs are isolated dynamically from one another. But with the augmentation of a PLL, and the state y being dependant on V_{cq}, both AFEs are no longer independent of one another. Taking this fact into account, it can be shown that the process to scale up the controller implementation for the additional converter and PLL is very easy, and is largely a copy a paste exercise, and inclusion of these I_{aq} interactions are expanded onto the V_{cq} state equations.

6.2 Scalability of the Optimization Procedure to Expanded Networks

Referring back to the definitions of A and B_2 matrices described in (5.34) and (5.36) for the two converter system, only four adapted matrices need to be derived to augment the new converter into the new grid based global model. The first three being:

$$A_{ca_2} = \begin{bmatrix} 0 & \frac{1}{L_{a2}} & 0 & 0 & 0 & 0 \\ 0 & 0 & 0 & 0 & 0 & 0 \\ 0 & 0 & 0 & 0 & 0 & 0 \\ 0 & 0 & 0 & 0 & 0 & 0 \\ 0 & 0 & 0 & 0 & 0 & \end{bmatrix}, \quad A_{afe_2} = \begin{bmatrix} -\frac{R_{a2}}{L_{a2}} & \omega & -\frac{p_{d2}}{2L_{a2}} & 0 & 0 \\ -\omega & -\frac{R_{a2}}{L_{a2}} & -\frac{p_{q2}}{2L_{a2}} & 0 & 0 \\ \frac{3p_{d2}}{4C_{a2}} & \frac{3p_{q2}}{4C_{a2}} & \frac{Pl_2}{Ca_2 V^2_{dc_{a2}}} & 0 & 0 \\ 0 & -1 & 0 & 0 & 0 \\ 0 & 0 & -1 & 0 & 0 \end{bmatrix}, \quad A_{pa2} = \begin{bmatrix} 0 & 0 \\ \frac{1}{L_{a2}} & 0 \\ 0 & 0 \\ 0 & 0 \\ 0 & 0 \end{bmatrix} \tag{6.9}$$

Where these matrices are in fact just exact copies of the dynamics detailed in A_{ca}, A_{afe} and A_{pa} from (5.33) for AFE$_1$ but containing the parametric values for the 2nd AFE. Consequently, the interactive behaviour of the new AFE on the VSI dynamics must also be augmented, resulting

in the final required matrix A_{pv2} in addition to an adaptation to A_{vsi} element $\{4,4\}$ which needs the additional current I_{ad_2} augmented, resulting in:

$$A_{pv2} = \begin{bmatrix} 0 & 0 \\ 0 & 0 \\ 0 & 0 \\ \frac{I^*_{ad_2}}{CV_{cd}} & 0 \\ 0 & 0 \\ 0 & 0 \end{bmatrix}, \quad A_{vsi_n} = \begin{bmatrix} -\frac{R}{L} & -\frac{1}{L} & \omega & 0 & 0 & 0 \\ \frac{1}{C} & 0 & 0 & \omega & 0 & 0 \\ -\omega & 0 & -\frac{R}{L} & -\frac{1}{L} & 0 & 0 \\ 0 & -\omega & \frac{1}{C} & -\frac{I^*_{ad}+I^*_{ad_2}}{CV^*_{cd}} & 0 & 0 \\ 0 & -1 & 0 & 0 & 0 & 0 \\ 0 & 0 & 0 & -1 & 0 & 0 \end{bmatrix} \tag{6.10}$$

The final state matrix A_{ext} describing the whole expanded system can thus be derived to be:

$$A_{ext}x = \begin{bmatrix} A_{vsi_n} & A_{cv} & A_{cv} & A_{pv} & A_{pv2} \\ A_{ca} & A_{afe} & \mathbf{0} & A_{pa} & \mathbf{0} \\ A_{ca2} & \mathbf{0} & A_{afe2} & \mathbf{0} & A_{pa2} \\ A_{vp} & A_{ap} & A_{ap} & A_{pll} & \mathbf{0} \\ A_{vp} & A_{ap} & A_{ap} & \mathbf{0} & A_{pll} \end{bmatrix} x \tag{6.11}$$

Where the states are in the order of:

$$x = \begin{bmatrix} x_{VSI} & x_{AFE_1} & x_{AFE_2} & x_{pll_1} & x_{pll_2} \end{bmatrix}^T \tag{6.12}$$

where

$$x_{VSI} = \begin{bmatrix} I_{id} & V_{cd} & I_{iq} & V_{cq} & \chi_{V_{cd}} & \chi_{V_{cq}} \end{bmatrix}, \quad x_{pll_1} = \begin{bmatrix} y_1 & x_{i_1} \end{bmatrix}, \quad x_{pll_2} \begin{bmatrix} y_2 & x_{i_2} \end{bmatrix} \tag{6.13}$$

$$x_{AFE_1} = \begin{bmatrix} I_{ad} & I_{aq} & V_{dca} & \chi_{I_{aq}} & \chi_{V_{dc_a}} \end{bmatrix}, \quad x_{AFE_2} = \begin{bmatrix} I_{ad_2} & I_{aq_2} & V_{dca_2} & \chi_{I_{aq2}} & \chi_{V_{dc_a2}} \end{bmatrix} \tag{6.14}$$

For the input matrix, only a copy of B_{afe} from (5.35) needs to be adapted for the parameters of AFE$_2$, such that:

$$B_{afe2} = \begin{bmatrix} -\frac{V_{dc_{a2}}}{2L_{a2}} & 0 \\ 0 & -\frac{V_{dc_{a2}}}{2L_{a2}} \\ \frac{3I^*_{ad2}}{4C_{a2}} & \frac{3I^*_{aq2}}{4C_{a2}} \\ 0 & 0 \\ 0 & 0 \end{bmatrix} \tag{6.15}$$

Resulting in the final input matrix of:

$$B_{2_{ext}} = \begin{bmatrix} B_{vsi} & \mathbf{0} & \mathbf{0} & \mathbf{0} & \mathbf{0} \\ \mathbf{0} & B_{afe} & \mathbf{0} & \mathbf{0} & \mathbf{0} \\ \mathbf{0} & \mathbf{0} & B_{afe2} & \mathbf{0} & \mathbf{0} \\ \mathbf{0} & \mathbf{0} & \mathbf{0} & B_{pll} & \mathbf{0} \\ \mathbf{0} & \mathbf{0} & \mathbf{0} & \mathbf{0} & B_{pll} \end{bmatrix} \tag{6.16}$$

As it can be seen, to scale the system, incorporating a new converter, including its additional PLL, it is really a matter of copying and placing the new converter matrix equations, an adaptation of already pre-defined interaction matrices for the new AFEs parameters, and extension specifically of the V_{cq} state in the VSI to capture the I_{ad} and I_{aq} output current from the VSI being shared across the two AFEs, as defined in (6.4), as well as the interactive effects of PLL_2 on the VSI through V_{cq} as derived in (6.8), all of which are simple tasks. In this studies case, I_{aq} is assumed to be zero at steady state since I_{aq} of both AFEs is controlled to zero. Therefore, $\dot{V_{cd}}$ did not need expansion of its states, however if this is different, then $\dot{V_{cd}}$ will need to be properly expanded as has been performed for $\dot{V_{cq}}$, except for I_{ad} terms.

Again, when constraining the optimal controller gain matrix, only a replication of the AFE and PLL sectors need to be augmented:

$$K_{D_{ext}} = \left[\begin{array}{cccccc|ccccc|ccccc|cc|cc} 1 & 1 & 1 & 1 & 1 & 1 & 0 & 0 & 0 & 0 & 0 & 0 & 0 & 0 & 0 & 0 & 0 & 0 & 0 \\ 1 & 1 & 1 & 1 & 1 & 1 & 0 & 0 & 0 & 0 & 0 & 0 & 0 & 0 & 0 & 0 & 0 & 0 & 0 \\ \hline 0 & 0 & 0 & 0 & 0 & 0 & 1 & 1 & 1 & 1 & 1 & 0 & 0 & 0 & 0 & 0 & 0 & 0 & 0 \\ 0 & 0 & 0 & 0 & 0 & 0 & 1 & 1 & 1 & 1 & 1 & 0 & 0 & 0 & 0 & 0 & 0 & 0 & 0 \\ \hline 0 & 0 & 0 & 0 & 0 & 0 & 0 & 0 & 0 & 0 & 0 & 1 & 1 & 1 & 1 & 1 & 0 & 0 & 0 \\ 0 & 0 & 0 & 0 & 0 & 0 & 0 & 0 & 0 & 0 & 0 & 1 & 1 & 1 & 1 & 1 & 0 & 0 & 0 \\ \hline 0 & 0 & 0 & 0 & 0 & 0 & 0 & 0 & 0 & 0 & 0 & 0 & 0 & 0 & 0 & 0 & 1 & 0 & 0 \\ 0 & 0 & 0 & 0 & 0 & 0 & 0 & 0 & 0 & 0 & 0 & 0 & 0 & 0 & 0 & 0 & 1 & 0 & 0 \\ \hline 0 & 0 & 0 & 0 & 0 & 0 & 0 & 0 & 0 & 0 & 0 & 0 & 0 & 0 & 0 & 0 & 0 & 0 & 1 \\ 0 & 0 & 0 & 0 & 0 & 0 & 0 & 0 & 0 & 0 & 0 & 0 & 0 & 0 & 0 & 0 & 0 & 0 & 1 \end{array}\right] \tag{6.17}$$

To showcase the performance of the grid accurately, both the AFEs will have different filter dynamics and different operating points to one another. Below is the table of all the system parameters for the expanded network as well as the controller references.

Parameter	Value
R	120mΩ
L	464μH
C	33μF
Ra	0.8Ω
La	579μH
Ca	100μF
Ra_2	90mΩ
La_2	529μH
Ca_2	1880μF
ω	$400(2\pi)\text{rads}^{-1}$
VSI $V_{dc-source}$	290V
Grid V_{ac}	115Vac

Table 6.1: Parametric Values for the expanded grid

Control Reference Values	
V_{cd}	100V
V_{cq}	0V
I_{aq}	0A
V_{dc_a}	400V
I_{aq2}	0A
$V_{dc_{a2}}$	270V
P_l	800W
P_{l2}	400W
$f_{switching}$	10kHz

Table 6.2: Control References for the expanded network

Both the VSI and AFE_2 are the exact same commercial converter and therefore share the same voltage and current ratings, 300V and 30A respectively. To ensure the current doesn't go beyond the VSI rating when powering the grid at full load, the demanded power for AFE_2 has thus been set lower than 1kW.

6.3 Simulative Results for the expanded system

Here, the proposed H_2 controller will be tested in a simulative environment in order to analyse its performance.

Using the procedures detailed in Section 5.1.2, a H_2 controller of similar performances when compared to that of the two converter tests in Chapter 5 have been designed, and AFE_2 is designed to attempt to achieve the best possible dynamic performance to a step load disturbance, as with the designs for previous chapters, where the Q_γ and R_γ matrices below were developed which delivers the required performance.

$$Q_\gamma = diag\left(\begin{bmatrix}0 & 0 & 0 & 0 & 1 & 1 & 0 & 0 & 0 & 1 & 1 & 0 & 0 & 0 & 1 & 20 & 0 & 10^{-3} & 0 & 10^{-3}\end{bmatrix}\right) \quad (6.18)$$

$$R_\gamma = diag\left(\begin{bmatrix}4 & 4 & 1 & 1 & 1 & 1 & 10^{-9} & 10^{-9} & 10^{-9} & 10^{-9}\end{bmatrix}\right) \quad (6.19)$$

The switching model simulation used in Simulink is presented below

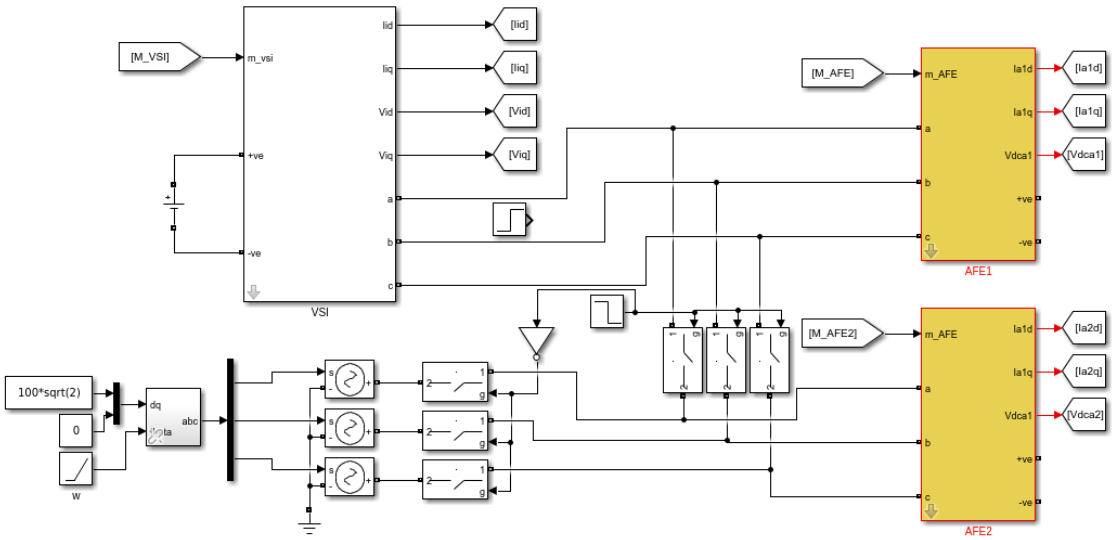

Figure 6.2: The Expanded Notional System Under Test

For a grid network, it becomes an important question about the fault tolerance of the controller, if for example one of the AFE converters fails. In order to test the fault tolerance of both converters AFE_2 has been implemented with switches, one from the notional grid, and one to an ideal grid. Simulink throws a simulation error when there is 0V across the switch module of any converter. In order to avoid this, when the switch is set open, disconnecting AFE_2 from the notional grid replicating a major converter fault, the switch for the ideal grid is simultaneously closed, such that AFE_2 is then powered from an ideal grid in order to avoid error in the simulation, and all states from AFE2 to its controller forced to zero . The ideal grid is never connected directly to the notional grid.

As was observed in Chapter 5, the PI controller operates noticeably poorer to the H_2 controller, which was expected. Therefore, it is of more interest to compare the proposed controller against another optimal controller to compare relative performance. Therefore the tests in this section will be performed against several LQR controllers, optimised for each individual converter. A full-state feedback approach to the LQR controller is not selected, as that type of controller would not be permitted on aircraft due to redundancy issues, and therefore for this expanded grid, the decentralised H_2 control will be pitted against the closest form of decentralised LQR control, and performances observed between the two. Tests shall start with the observations in simulative performance of the H_2 controller.

6.3.1 Step Load Simulative Tests - Optimal H_2 Control

Simulating the experimental rig as closely as possible, providing the parameters from Table 6.1 and Table 6.2 step load transient tests have been performed on the system operating under optimal H_2 control using the process of design defined in section 6.2.

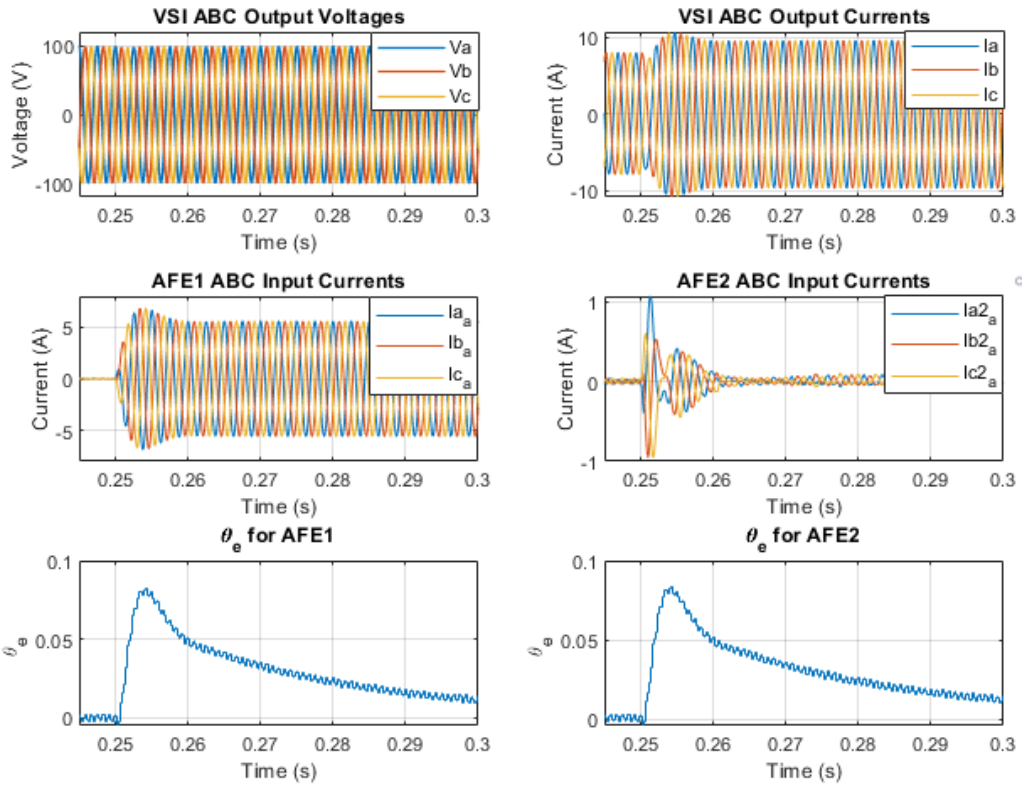

Figure 6.3: The Expanded Notional System Under 800W Step Load Test on AFE_1 in abc domain using proposed H_2 Control

Figures 6.3 and 6.4 present the results where AFE1 was step loaded to 800W, and AFE2 left unloaded. From these simulative results it is clear that the controller continues to deliver performance with minimal interactive effects between each of the converters. On the VSI, the only noticeable effect from AFE1 loading is the current output increasing to provide the additional required current to AFE1. I_{iq} does experience a small dip as a result of the rapid rise of I_{id}, but more importantly, especially in terms of aircraft grids is that the 3-phase voltages remain largely constant throughout the transient, providing the required voltages to AFE2. There is a slight deviation in V_{cq} however, which did mean the PLLs experienced an error dynamic, and thus AFE2 did experience non-alignment to the grid for a time, which briefly caused the currents to raise 1A momentarily. However, due to the PLL being optimised to the closed loop grid performance,

the error was kept minimal, and therefore the current deviation experienced on AFE2 was quickly alleviated. The DC-Link voltage on AFE1 dropped only 15V, which is of similar performance as observed in the 2 converter setup, and AFE2, largely down to the large DC-Link capacitor (which couldn't be removed due to it being integrated onto the physical converter) experience negligible voltage change. From these initial test results, it can be seen that the new expanded controller can provide the same or similar performance than that of the two converter decentralised controller in developed in Chapter 5, and largely mitigates the interactions globally across the grid.

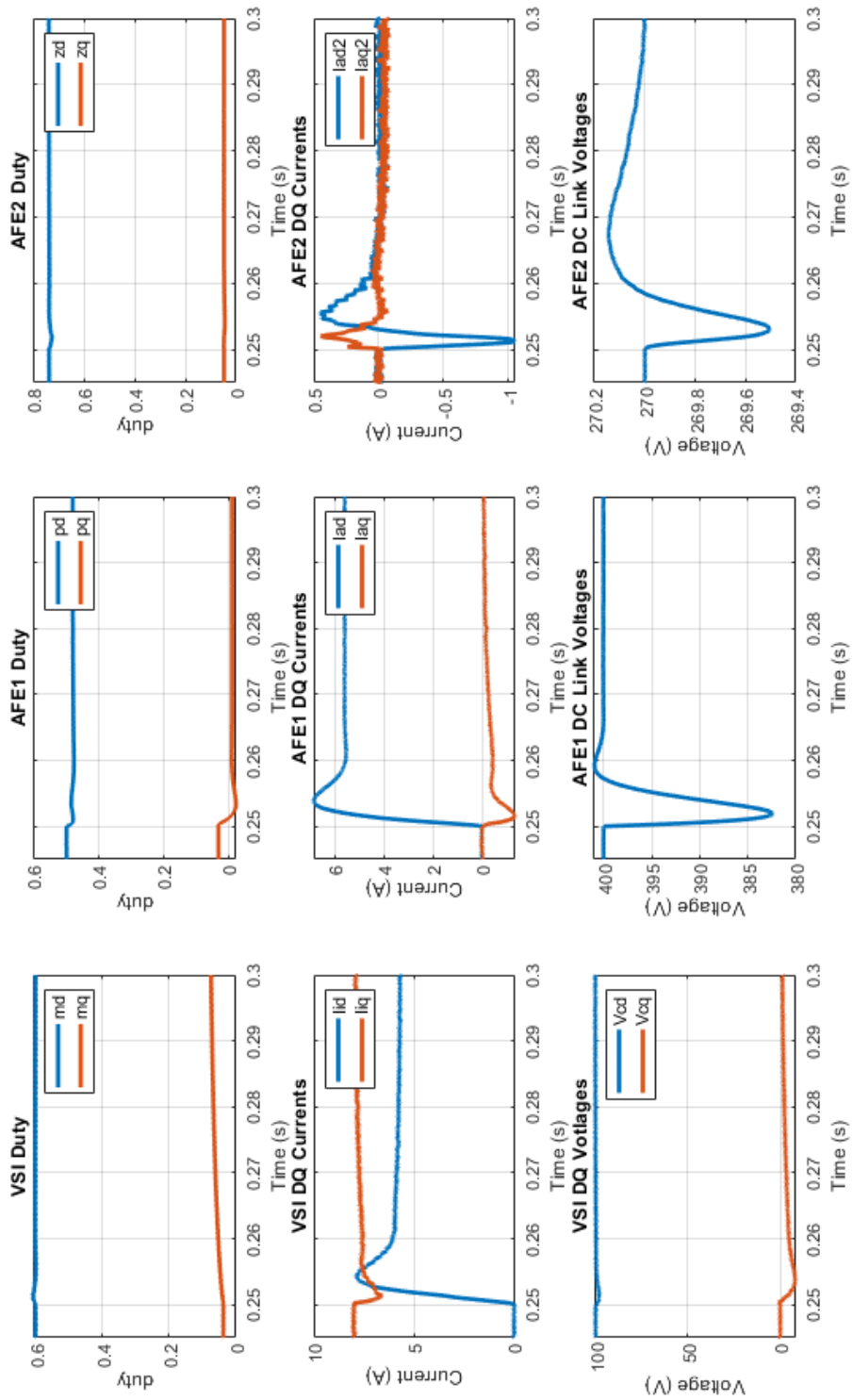

Figure 6.4: The Expanded Notional System Under Step Load Test on AFE_1 in DQ domain using proposed H_2 control

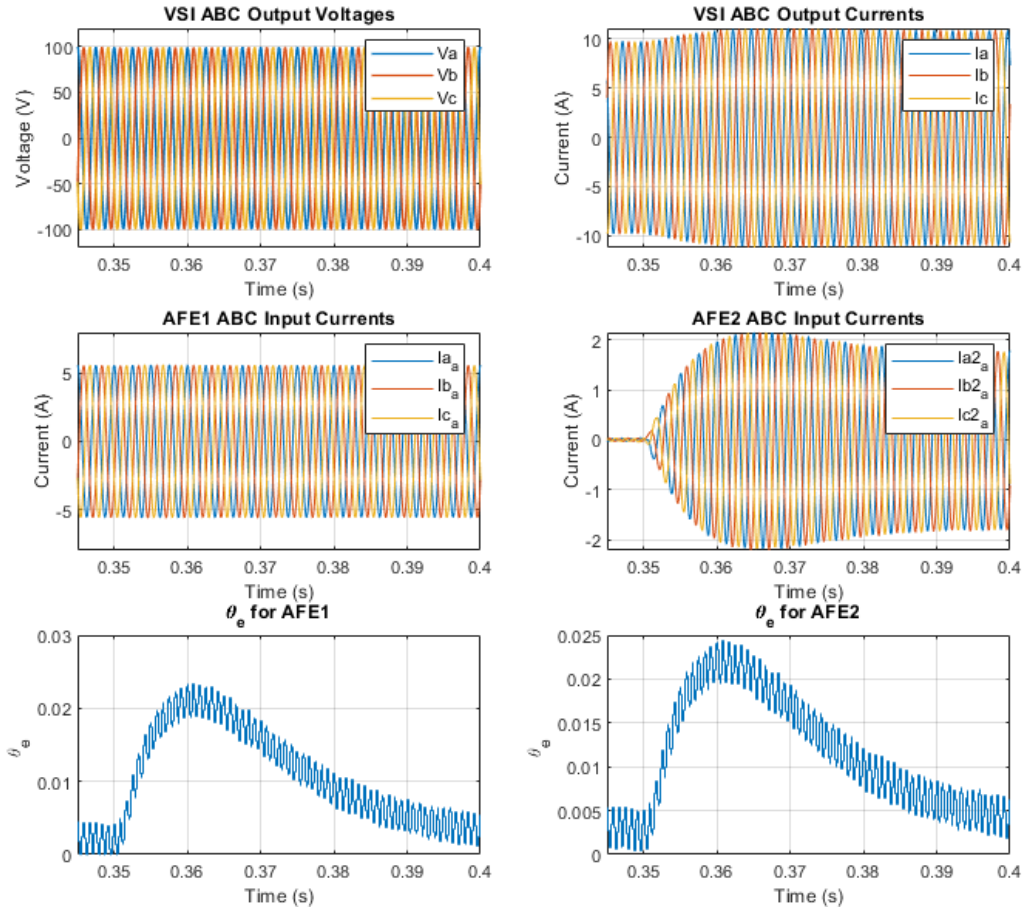

Figure 6.5: The Expanded Notional System Under Step Load Test on AFE_2 in abc domain using proposed H_2 Control

Here, Figures 6.5 and 6.6 present the results when AFE2 is loaded with a 400W while AFE1 is still loaded. Again, very similar performances can be observed as was observed when loading AFE1 only. VSI output voltages are left relatively unchanged, with only a slight decrease in V_{cq} in transient which again causes the PLLs on each AFE to become unaligned with the grid. However, this can be largely credited to the reduced load used on AFE2. Impressively, it is clear how AFE1 has not incurred at detrimental effect whatsoever. AFE1 currents, and voltages remained practically constant throughout the transient. There was slight deviations in the Q-axis due to the PLL but performance was maintained throughout the transient, showing the controllers have been decoupled.

So as can be seen, the H_2 controller is relatively easy to scale up to include more converters on the AC bus. In turn, with these more grid like conditions many of the features of the two converter system are retained. The grid voltages remain largely stiff and stable, the PLLs always optimised

for stable performance and offers greater flexibility in the design of given states through the q_γ and R_γ matrices to give far superior performance.

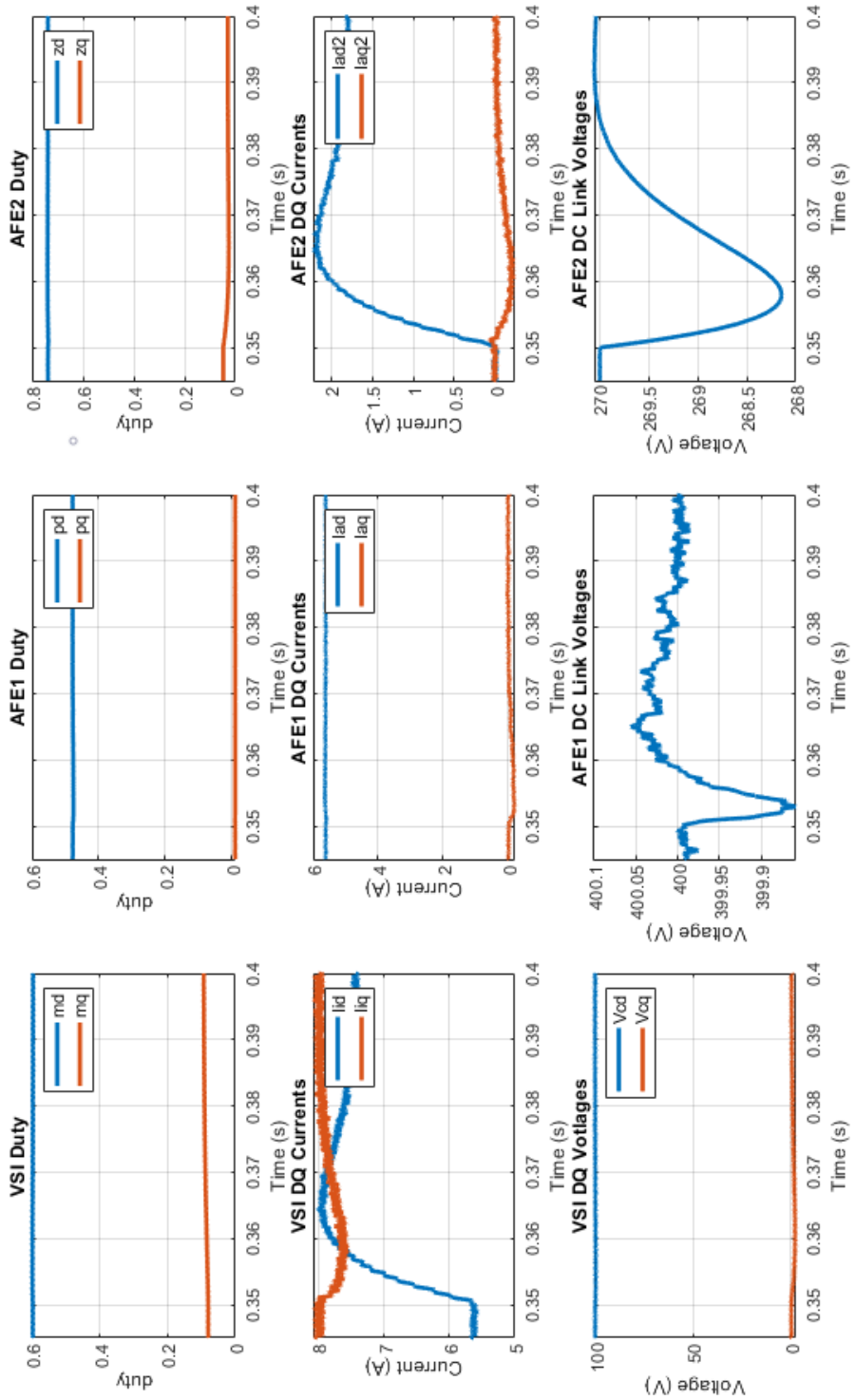

Figure 6.6: The Expanded Notional System Under Step Load Test on AFE_2 in DQ domain using proposed H_2 control

An additional question that may be brought up when analysing the system is what if a fault were to occur on the system, for instance one of the AFE units is lost or damaged. In centralised control schemes this can be devastating for performance since the controller is dependent on the state information of the other converters for its correct operation. Typically in this case, the moment a sub-system goes offline, the validity of the model to which the controller is designed for is no longer true. This is very likely to cause a global instability in the system. For independent LQR controllers, the sister controller to the proposed H_2 controller, each controller is optimised about the local state dynamics of the subject converter, and shouldn't be affected by change in the larger global model. So it would therefore be expected to function as normal. The H_2 controller on the other hand is synthesised on the basis of a fully functioning grid. A global model is input into the optimisation, and controller gains optimised based on the closed loop performance of all other sub-systems on the network. Therefore, if loss of a converter were to happen, hypothetically, this may cause instability in the network, risking system redundancy. However, for the decentralised H_2 controller, this actually isn't the case. Whilst each of the gains for each controller is synthesised with the knowledge of the dynamics for every other closed loop sub-system, each independent sub-system controller is dependant only on its own system states, and not the global states. Therefore, if a sub-system were to go offline, all the other subsystems will be able to carry on as normal. The gains are synthesised with the knowledge of the lost converters' internal dynamics, but are not dependant on them for stable operation.

Figures 6.7 and 6.8 show the simulative results from when AFE2 is completely disconnected from the grid at a time t = 0.45s.

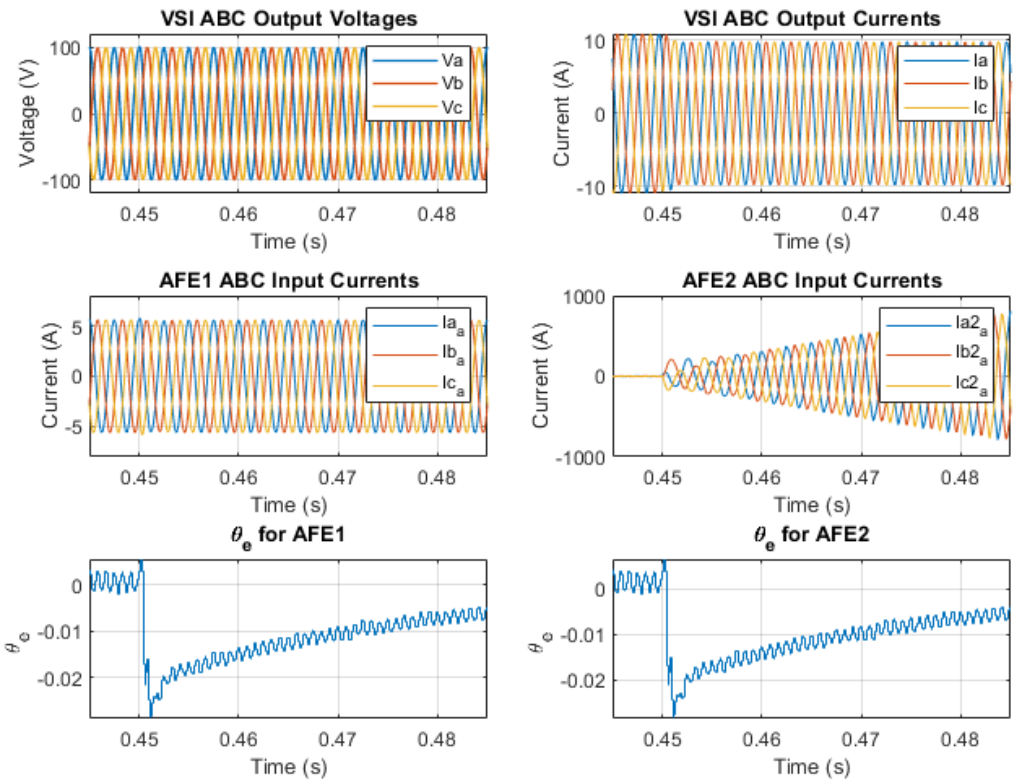

Figure 6.7: Expanded Notional System with AFE2 disconnection (AFE 2 Failure) under H_2 optimal control in abc domain

As expected, the system handles the disconnection, and continues to operate under stable operation. The disconnection is largely unnoticed and the system quickly returns to their references values. The currents however, across the VSI and AFE1 are the states which are affected most, since suddenly the VSI no longer needs to provide current to AFE2. However, the currents do quickly return to normal, and the grid voltages, and DC-Link voltage of the VSI and AFE1 respectively had negligible effects due to the fault. This simulation proves the theory of that the sub-systems are largely independent of external factors of the rest of the global system, and is to some regard fault tolerant to large failures.

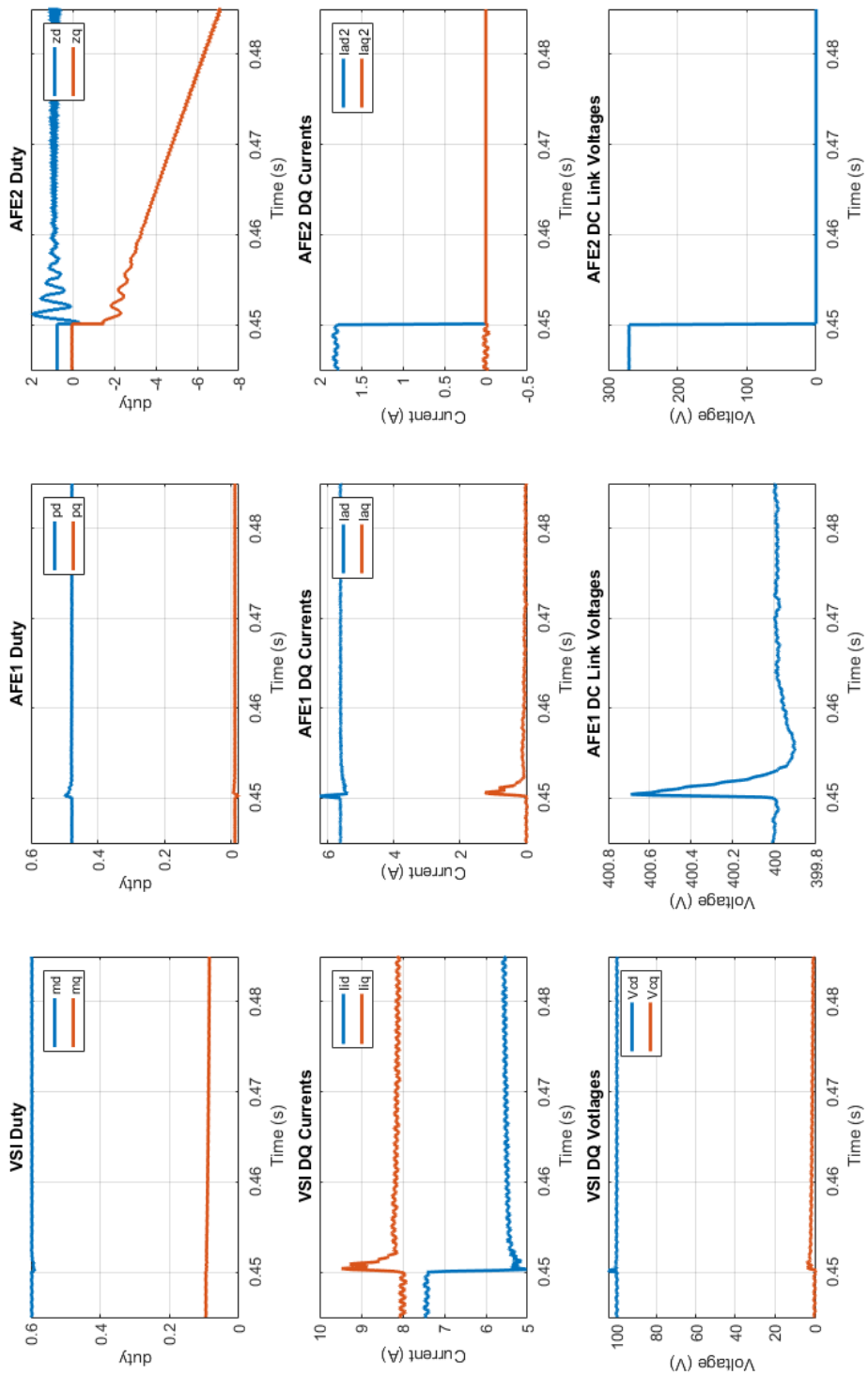

Figure 6.8: Expanded Notional System with AFE2 disconnection (AFE 2 Failure) under H_2 optimal control in dq domain

6.3.2 Step Load Simulative Tests - Optimal LQR Control

It was already shown in previous chapters that the PI controller will always provide poorer performance due to it not being optimal to the grid dynamics. However, performance on the expanded grid still needs to be evaluated and compared against. Therefore, it is seen as more interesting to compare the performance of a decentralised LQR controller, with the decentralised H_2 controller. The decentralised LQR controller is made up of three LQR controllers, each locally optimised to their respective converters, as it would normally be implemented in similar applications. Therefore, the LQR controllers should provide comparable performance to that of the H_2 on a converter to converter basis, but cross-coupled dynamics have not been attributed, and the effects of these unmodelled effects should be observed when analysing the performance of the LQR controller.

Tuning of the controller again follows the same tuning process as for the H_2 controller, with again the only difference being tuning is done for each of the controller independently since the LQR controller cannot be fully decentralised, unlike the H_2 control.

The following matrices and weights were used in developing each of the converter controllers, where each controller has been tuned in order to match the performance of the H_2 controller in order to provide a fair comparison on global performance.

VSI: LQR Tuning Matrices

$$A_{VSI_{lqr}} = \begin{bmatrix} -\frac{R}{L} & -\frac{1}{L} & \omega & 0 & 0 & 0 \\ \frac{1}{C} & 0 & 0 & \omega & 0 & 0 \\ -\omega & 0 & -\frac{R}{L} & -\frac{1}{L} & 0 & 0 \\ 0 & -\omega & \frac{1}{C} & 0 & 0 & 0 \\ 0 & -1 & 0 & 0 & 0 & 0 \\ 0 & 0 & 0 & -1 & 0 & 0 \end{bmatrix} \quad B_{VSI_{lqr}} = \begin{bmatrix} \frac{V_{dc}}{2L} & 0 \\ 0 & 0 \\ 0 & \frac{V_{dc}}{2L} \\ 0 & 0 \\ 0 & 0 \\ 0 & 0 \end{bmatrix} \tag{6.20}$$

$$x = \begin{bmatrix} I_{id} & V_{cd} & I_{iq} & V_{cq} & \omega_{V_{cd}} & \omega_{V_{cq}} \end{bmatrix}^T \quad u = \begin{bmatrix} m_d & m_q \end{bmatrix}^T \tag{6.21}$$

$$Q_{\gamma_{vsi}} = diag\left(\begin{bmatrix} 0 & 0 & 0 & 0 & 2 & 4 \end{bmatrix}\right) \quad R_{\gamma_{vsi}} = diag\left(\begin{bmatrix} 1 & 1 \end{bmatrix}\right) \tag{6.22}$$

AFE1: LQR Tuning Matrices

$$A_{AFE1_{lqr}} = \begin{bmatrix} -\frac{R_a}{L_a} & w & -\frac{p_d}{2L_a} & 0 & 0 \\ -w & -\frac{R_a}{L_a} & -\frac{p_q}{2L_a} & 0 & 0 \\ \frac{p_d}{4C_a} & \frac{p_q}{4C_a} & \frac{P_l}{C_a V_{dca}^2} & 0 & 0 \\ 0 & -1 & 0 & 0 & 0 \\ 0 & 0 & -1 & 0 & 0 \end{bmatrix} \quad B_{AFE1_{lqr}} = \begin{bmatrix} -\frac{V_{dca}}{2L_a} & 0 \\ 0 & -\frac{V_{dca}}{2L_a} \\ \frac{3I_{ad}}{4C_a} & \frac{3I_{aq}}{4C_a} \\ 0 & 0 \\ 0 & 0 \end{bmatrix} \tag{6.23}$$

$$x = \begin{bmatrix} I_{ad} & I_{aq} & V_{dca} & \omega_{I_{aq}} & \omega_{V_{dca}} \end{bmatrix}^T \quad u = \begin{bmatrix} p_d & p_q \end{bmatrix}^T \tag{6.24}$$

$$Q_{\gamma_{afe1}} = diag\left(\begin{bmatrix} 0 & 0 & 0 & 1 & 1 \end{bmatrix}\right) \quad R_{\gamma_{afe1}} = diag\left(\begin{bmatrix} 1 & 1 \end{bmatrix}\right) \tag{6.25}$$

AFE2: LQR Tuning Matrices

$$A_{AFE2_{lqr}} = \begin{bmatrix} -\frac{R_{a2}}{L_{a2}} & w & -\frac{z_d}{2L_{a2}} & 0 & 0 \\ -w & -\frac{R_{a2}}{L_{a2}} & -\frac{z_q}{2L_{a2}} & 0 & 0 \\ \frac{z_d}{4C_{a2}} & \frac{z_q}{4C_{a2}} & \frac{P_{l2}}{C_{a2}V_{dca2}^2} & 0 & 0 \\ 0 & -1 & 0 & 0 & 0 \\ 0 & 0 & -1 & 0 & 0 \end{bmatrix} \quad B_{AFE1_{lqr}} = \begin{bmatrix} -\frac{V_{dca2}}{2L_{a2}} & 0 \\ 0 & -\frac{V_{dca2}}{2L_{a2}} \\ \frac{3I_{ad2}}{4C_{a2}} & \frac{3I_{aq2}}{4C_{a2}} \\ 0 & 0 \\ 0 & 0 \end{bmatrix} \tag{6.26}$$

$$x = \begin{bmatrix} I_{ad2} & I_{aq2} & V_{dca2} & \omega_{I_{aq2}} & \omega_{V_{dca2}} \end{bmatrix}^T \quad u = \begin{bmatrix} z_d & z_q \end{bmatrix}^T \tag{6.27}$$

$$Q_{\gamma_{afe2}} = diag\left(\begin{bmatrix} 0 & 0 & 0 & 1 & 1 \end{bmatrix}\right) \quad R_{\gamma_{afe2}} = diag\left(\begin{bmatrix} 1 & 1 \end{bmatrix}\right) \tag{6.28}$$

PLL Controller for both AFEs

$$\omega_{PLL} = 10Hz \quad \zeta = 0.707 \tag{6.29}$$

$$K_{P_{PLL}} = \frac{2\zeta\omega_{PLL}}{V_{cd}} \quad K_{I_{PLL}} = \frac{\omega_{PLL}^2}{V_{cd}} \tag{6.30}$$

Simulation Results of LQR Controller

As had just been done with the H_2 controller, firstly, what shall be investigated is the performance when AFE1 is loaded with a 800W load, where the three-phase and dq results are presented in Fig. 6.9 and 6.10.

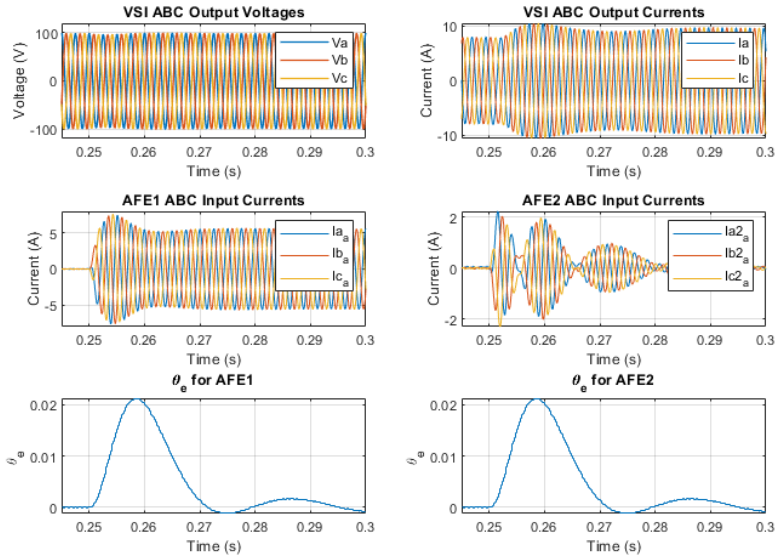

Figure 6.9: Three-Phase Results when loading AFE1 with 800W using LQR controller.

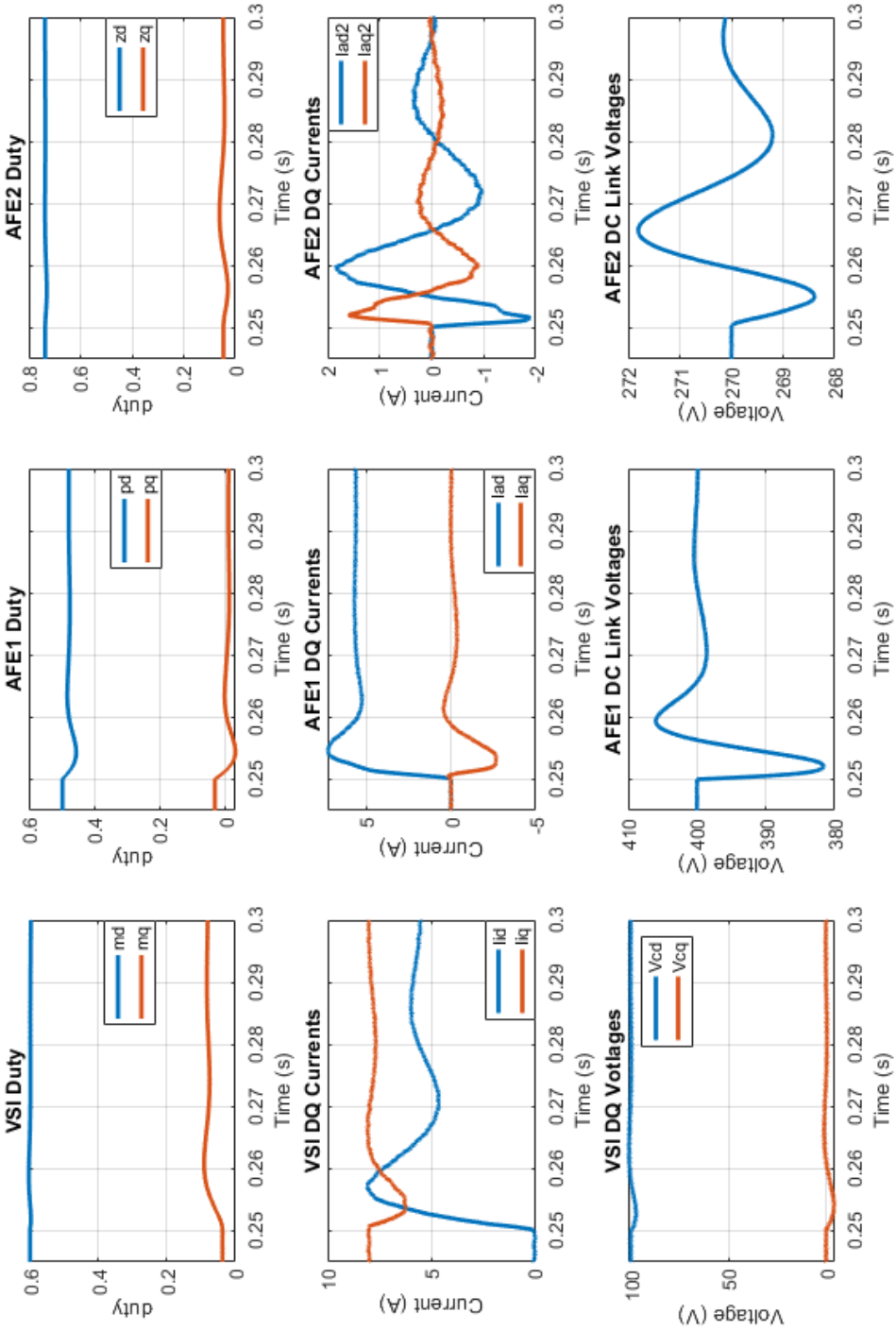

Figure 6.10: dq frame results when loading AFE1 with 800W using LQR controller.

When comparing these results with those performed with the H_2 controller in Fig. 6.3 and 6.4 it can be seen for the most part that across the majority of states, the speed at which equilibrium is reached is relatively similar, as well as the same negligible distortions which occur on the grid voltages. However, most noticeably AFE2 shows a little more interaction than previously observed. When using the H_2 controller, the currents peaked briefly to approximately -1A for I_{ad} and 0.5A for I_{aq}. For the LQR controller currents on both axes approach 2A, and incur a prolonged oscillation back to equilibrium. Similar effects are observed on V_{dca2}, where previously using H_2 the oscillation due to AFE1 disturbance was only to a maximum magnitude of 0.5V oscillation where voltages returns to equilibrium within 40ms. The LQR on the other hand, as with the currents, incurred more pronounced oscillation, of magnitudes 4x that of the H_2 controller, again contributed to interactive effects between subsystems. This is somewhat expected, and backed by the controller theory.

Since LQR itself is a form of optimal control, and shares roots with the H_2 controller, it is to be expected that similar dynamic performance can be achieved, for each of the states in localised disturbances, as is evident when analysing performance in this AFE1 step load test between the H_2 and LQR controllers. However, the LQR doesn't account for the closed loop dynamic effects of the other converters in the system, and therefore, as observed in this simulation, some interactive oscillations do occur. Greater than that of H_2 where dynamics (and system uncertainties as shall be observed later) are fully accounted for in the controller synthesis.

Additionally, due to the converter power ratings on the experimental rig, the step-load disturbances are smaller than that with the two converter setup from Chapter 5. Therefore, the interactive behaviour between converters will be less pronounced than observed previously. However, from simulative and experimental results received from Chapter 5 and comparing the performance to here, it is expected if larger step load disturbances incur of this system, interactive behaviour will be more pronounced.

Of course, experts of LQR could simply suggest "why not increase the weightings of these states in the Q_γ matrix of each controller in order to speed up the response, and as such keep each of the states 'in theory' closer to there references values?". Whilst this can be a easy argument to make initially, Figure 6.11 shows the effects the dynamic performance of the same simulative test when both the Q_γ matrix of both AFE1 and AFE2 are set to $Q_\gamma = diag\left(\begin{bmatrix}0 & 0 & 0 & 4 & 8\end{bmatrix}\right)$.

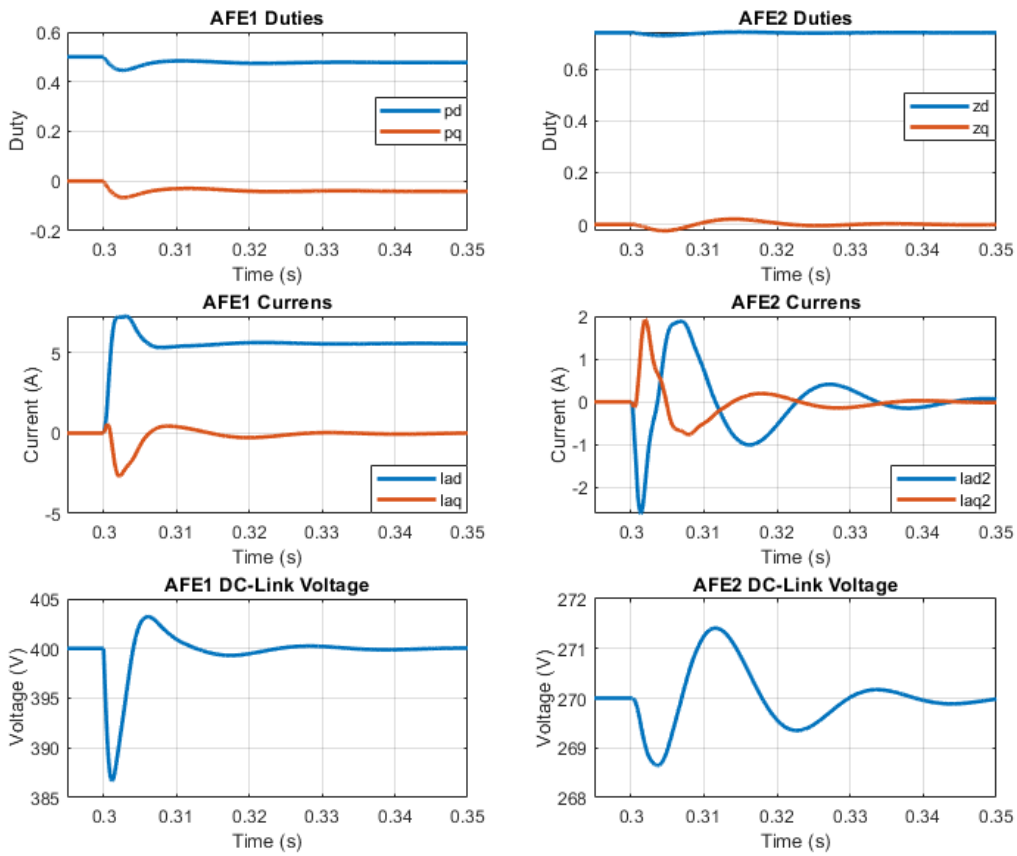

Figure 6.11: AFE1 Load Test comparing the performance with larger weights applied to Q_γ of each AFE to see how interactive effects behave. This figure shows how increase weights does little in reducing the interactive dynamics between converters.

Now, whilst states in AFE1 does have a bit of a performance increase which is to be expected, increasing the weights on AFE2 has done little in mitigating the interactive effects observed. In fact, the currents have come out worse, nearing an oscillation 3A in magnitude. Hence, the selection of the weighting matrices in (6.22), (6.25) and (6.28) were selected balancing performance close to that of the H_2 controller, and mitigation of interactive effects as much as possible. Also, this quick simulative test confirms that tuning the each individual controller does not counteract the interactive effects from other converters, and these dynamics are as a result from unmoddeled dynamics in the controller design.

Moving onto analysing the effects when AFE2 is then loaded onto the system, as was performed with the H_2 controller previously, the Figures 6.12 and 6.13 show the 3-phase and dq simulative responses respectively when a 400W load is applied under the LQR controller using the default weights at the start of this section.

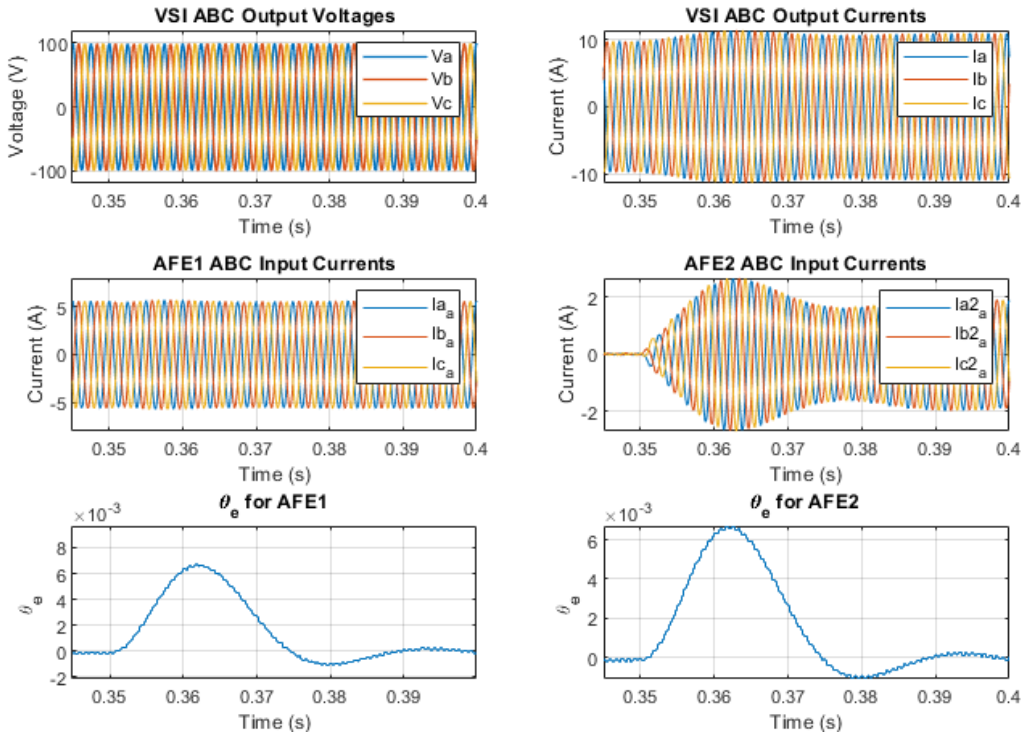

Figure 6.12: Three-Phase Results when loading AFE2 with 400W using LQR controller with AFE1 already loaded with 800W.

Again, since the capacitor is relatively large in comparison to AFE1, the voltage deviations are quite minimal which therefore means the interactive effects between converters are innately reduced. Nevertheless, performance difference between the the H_2 and LQR controllers can still be made. Notably through observation, the interaction of the DC-Link voltage is 10x more than that observed with the H_2 controller. Whilst, in the greater schemes of things, this interactive behaviour for the majority of similar cases would be considered negligible, it must be noted that if a smaller capacitor was installed on AFE2, these deviations could be far more noticeable, and far more pronounced.

For instance, observe Fig 6.14 and 6.15 below where the capacitor C_{a2} is reduced to $188\mu F$ for the H_2 and LQR controllers respectively. Each controller is retuned using their default weights and account for the new capacitor in each of their system models.

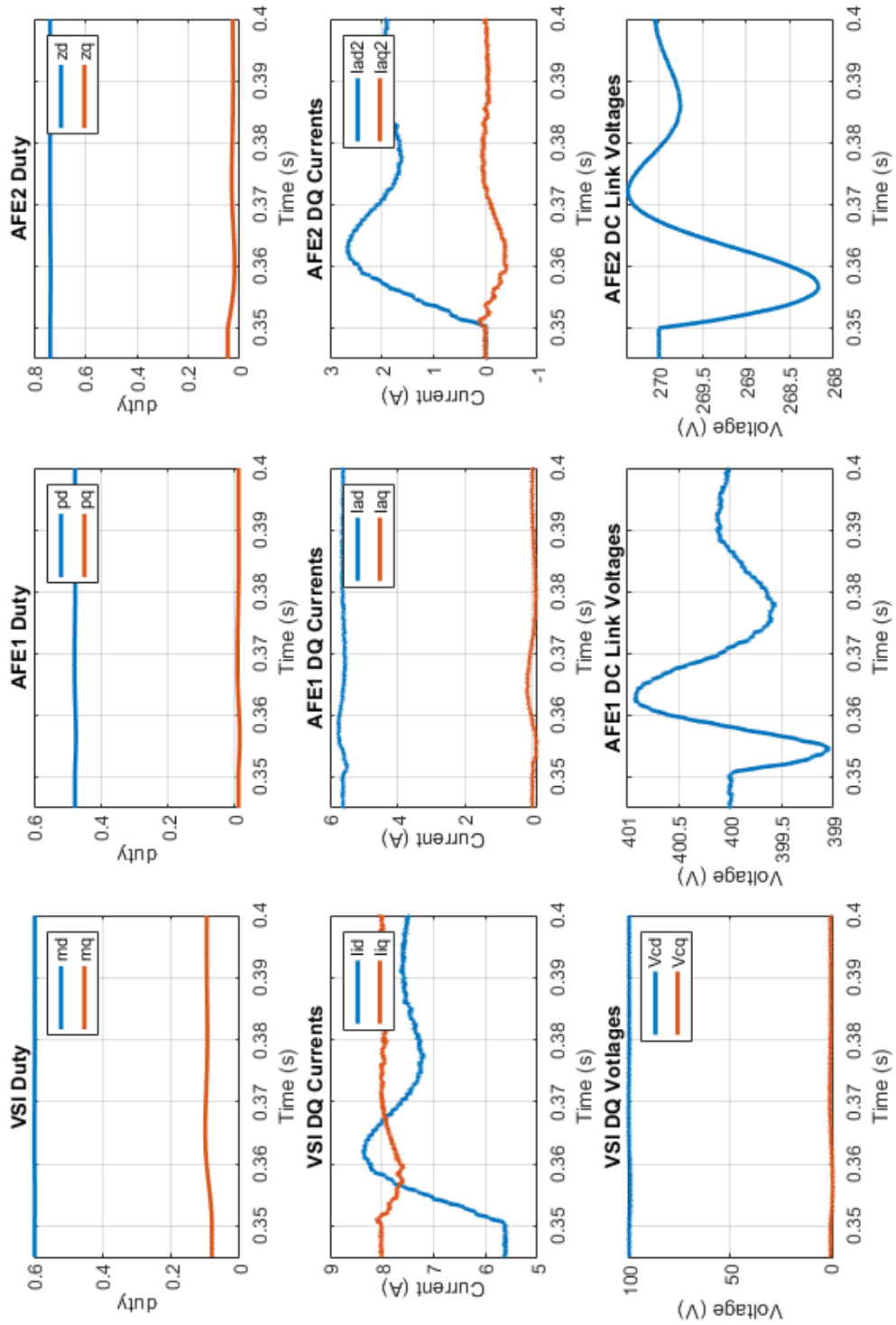

Figure 6.13: Results in the dq frame when loading AFE2 with 400W using LQR controller with AFE1 already loaded with 800W.

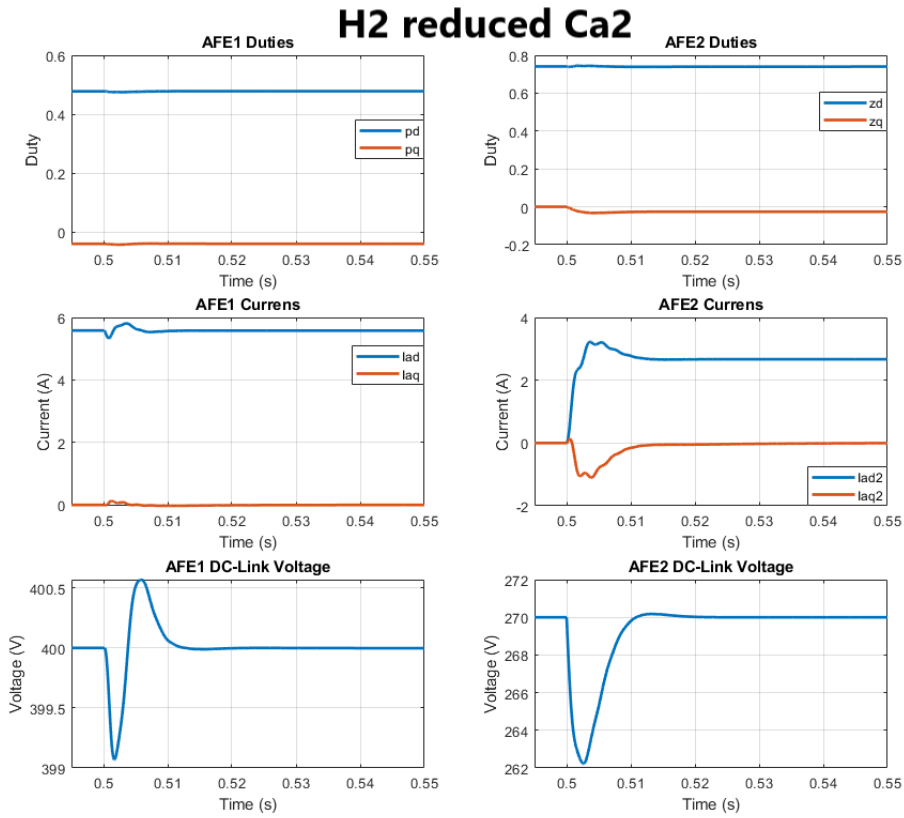

Figure 6.14: The effect of the AFE2 400W loading test under the influence of a H_2 controller

As expected, when C_{a2} is reduced, the interaction across both the H_2 and LQR systems become far more pronounced. However, the LQR produces a far more oscillatory response and far more severe interactive effects than that of the H_2 controller. Arguments however again could be made that the LQR simply needs some retuning and the performance can be improved. Again yes, this is bound to be the case, however as we observed in the results between Fig 6.10 and 6.11, tuning of the gains themselves will improve performance somewhat, interactions are not counteracted. Interestingly for the H_2 controller, whilst interactions are more noticeable, the dynamic performance of the controller itself has little change. This leads to some interesting and powerful properties of the H_2 control, over the LQR controller which will be discussed in Section 6.5, where each of these controllers susceptibility are compared when subjugated to parametric uncertainty. As is it seems to be clear from Fig. 6.15, the LQR seems to suffer somewhat in comparison to H_2 for varying parametric values.

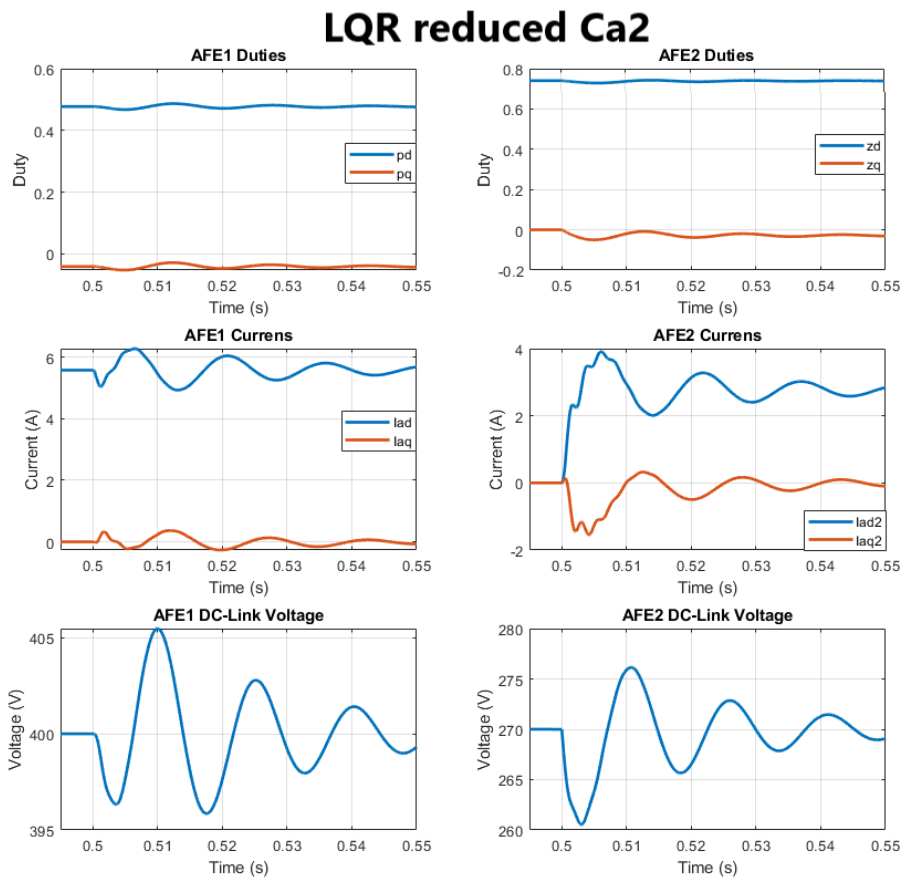

Figure 6.15: The effect of the AFE2 400W loading test under the influence of a H_2 controller

Therefore from the simulation results, what has been concluded is that when the system is operating at nominal conditions, both the H_2 and LQR controllers can deliver similar dynamic performance to the converter which is being perturbed with a load disturbance. This is expected, since both the controllers are of the same family when it comes to the synthesis of controls on individual converter basis, similar performances should be achieved, since closed loop controllers depend on the same state-space model of that converter. However, where the controller topologies differ is when it comes to the interactive proprieties between converters.

For the LQR controller, only the local dynamics of each converter is optimised, without accounting for the dynamics of the other converters. Without knowledge for the dynamic effects between converters, interactive effects between converters are thus, not accounted for, and therefore, when one converter encounters a large disturbance, the other converters suffer more noticeably from state interactions.

The H_2 controller on the other hands is able to develop optimal decentralised independent controls for each of the sub-systems on the network. Each of these controllers have been optimised

with the knowledge of the closed loop dynamics of the other converters, and the interactive effects between them. When performing the same simulative tests on the H_2 controller, it was clear first hand how the interactive effects between sub-systems have been largely mitigated when it was compared against the results from the LQR controller. This ability to intrinsically reduce the interactive effects was also observed in the two converter setup in Section 5, and therefore these simulations conclude that the proposed H_2 controller is not only easily expandable for growing networks, but also the performance as observed on the small scale can also be delivered to larger scale networks.

In the next section, experimental results shall be conducted in order to verify the simulation models reflect well that in practical application.

6.4 Experimental Analysis of H_2 and LQR Controllers

So far in this chapter, it has been shown how the proposed optimal controller design is easily expandable when dealing with multi-converter systems, where it is largely a copy of the system states between AFEs, and expanding the VSI states to attribute for the the additional d and q axis currents the VSI must provide for the additional converter. Again, with the new states of AFE2, the controller constraints had to be redefined, as per (6.17), such that decentralised controls can now also be obtained for AFE2 in conjunction with all the other decentralised controllers for the other converters, which again was shown to be very non-trivial.

Through the simulative tests in Section 6.3.1, it has been shown that when comparing with the performance of the original two converter system from Chapter 5, there is no evident detriment to the closed loop performance when utilising the expanded decentralised controller.

In this section, experimental validation of that observed in simulation will be provided, for both the H_2 and LQR controllers.

H_2 Experimental Results

Experimental testing was conducted on the hardware in Fig. 6.16, with the corresponding colour coordinated schematic in Fig. 6.17.

The VSI, and AFE1 converters are exactly the same as those performed in the hardware tests in Chapter 5. For AFE2, this converter is the same model BMT converter as is used for the VSI with the same power ratings. The input inductors used for AFE2 is the exact same type of inductors utilised for AFE1, albeit smaller in value. The controllers for each of the converters have been implemented on the uCube controller as described previously in Section 4.3.3, and have been implemented in a decentralised manner.

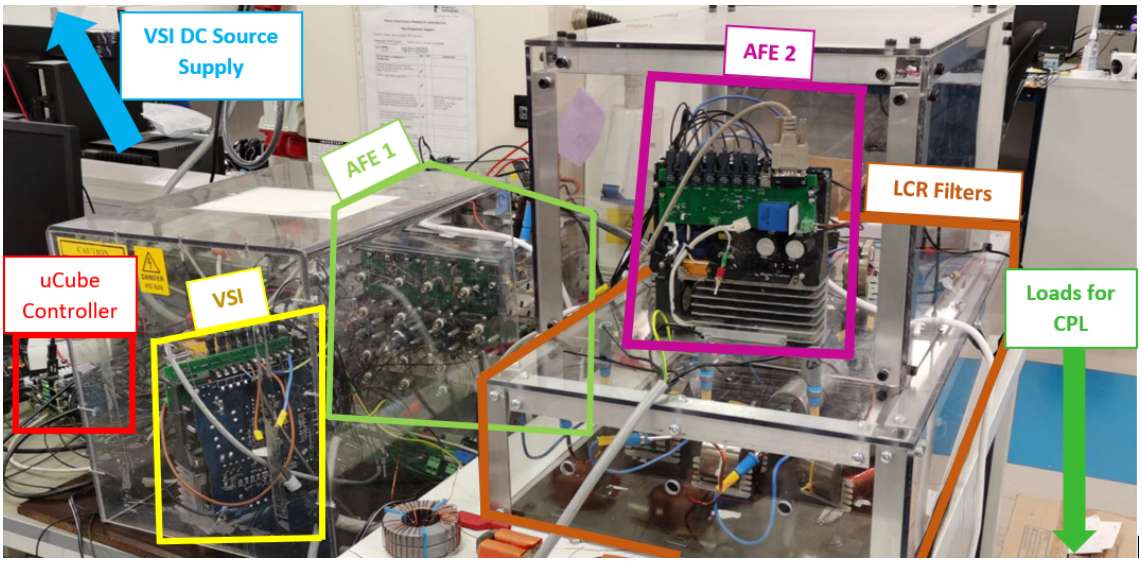

Figure 6.16: The experimental rig used to conduct expanded network tests

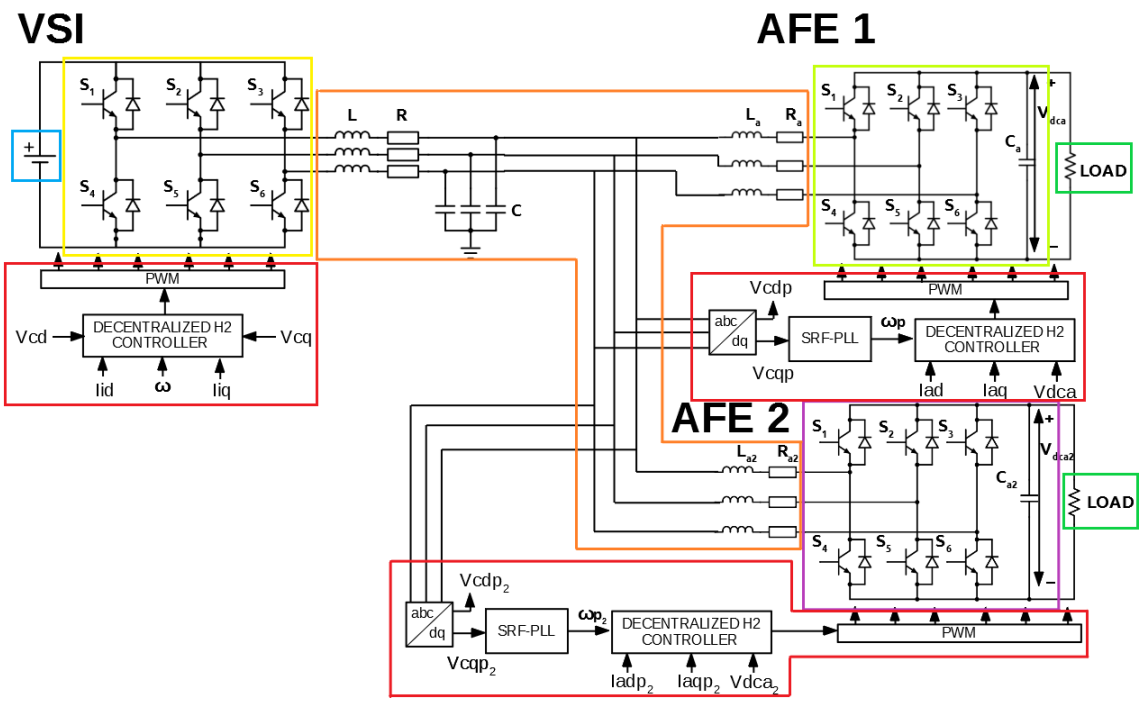

Figure 6.17: The Three-Phase Expanded System Schematic Segmenting each part as per coloured regions in 6.16

In order to fully tests all the different kinds of operations which could be subjugated to the converter, the following experimental tests shall be conducted on the H_2 based system:

A No Load - Steady State Performance

B Step load on AFE1, AFE2 Unloaded Dynamic Test

C Step load on AFE2, AFE1 Unloaded Dynamic Test

Each of these tests are performed in order to highlight how each of the converters operate, when the other converter is not yet operating at the designed for operating point, how the system operates at different steady-state conditions and also to test the performance of the optimised PLLs.

Staring with test (A) observing the performance of the expanded grid under H_2 control when no converters are loaded, Figures 6.18, 6.19 6.20 present the performances of the the VSI, AFE and AFE2 respectively:

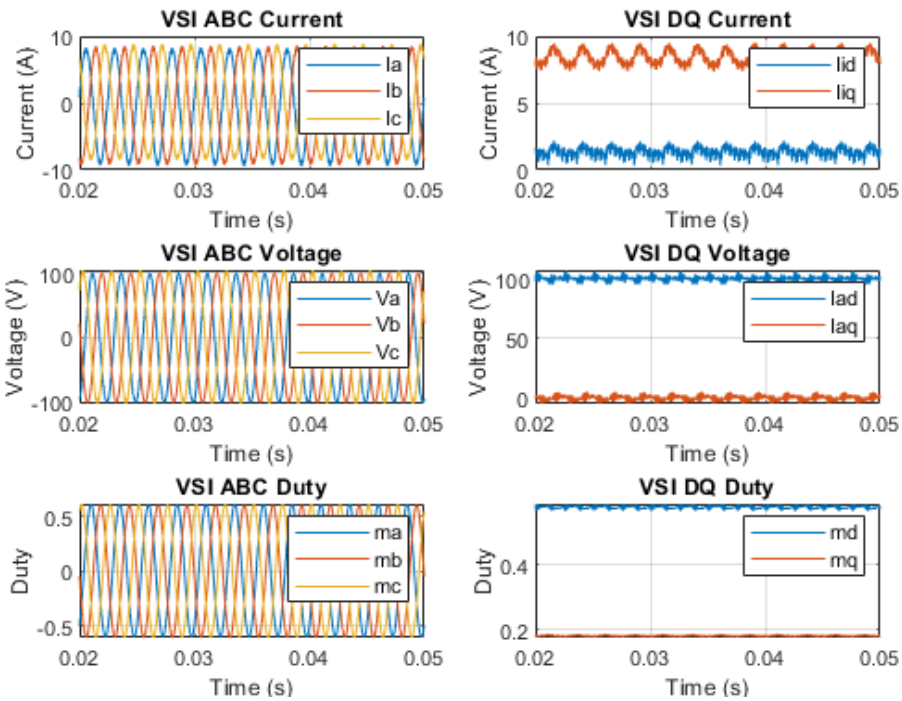

Figure 6.18: Expanded grid VSI steady state performance under zero load

In these no load steady state tests, it is shown that each of the states is controlled to each of their reference values as per Table 6.2. The grid dq voltages have minimal variation at steady state resulting in clean abc grid voltages being provided to the grid. The DC-Link voltages for each of the AFEs have a variation of about 2V about the reference. This variance in each of the DC-Links attributes to less than a 1% variation and therefore is deemed acceptable. As for the currents, since the inductor on AFE1 is slightly bigger, more sinusoidal currents at the fundamental

frequency of 400Hz. AFE2 evidently has a some more ripple associated to the currents, which is largely down to the reduced filtering effects of its input filter, due to reduced inductance, as well as the controller operating further away from its operating point, since the controller is designed to operate at 800W. Additionally, this ripple could possibly be accredited to imbalance in the dq calculations, which would explain the 400Hz oscillation. However, with all these considerations, at no load, the system is behaving as is expected.

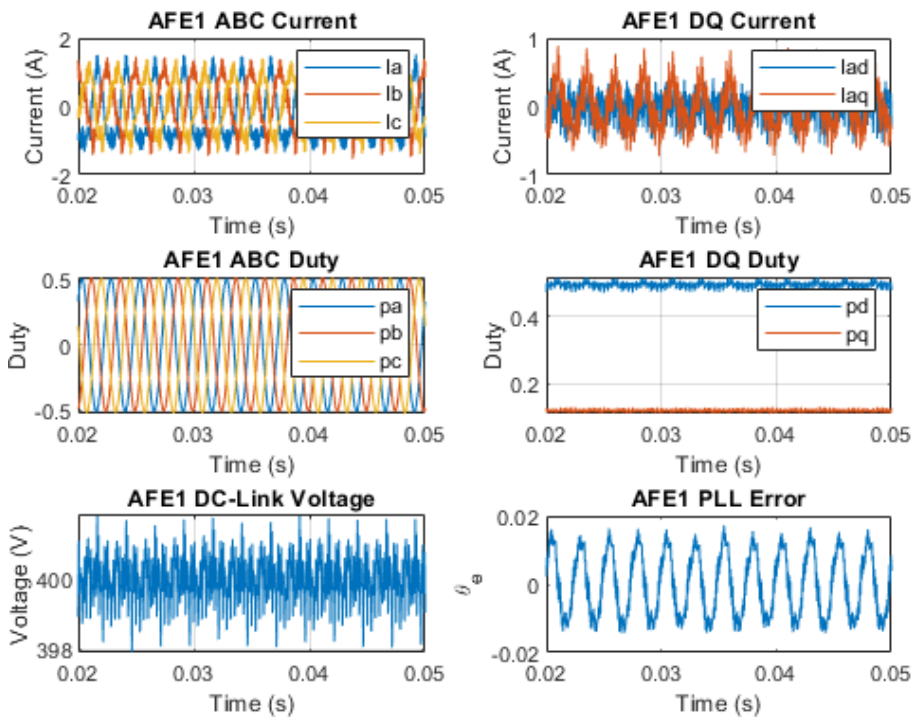

Figure 6.19: Expanded grid AFE1 steady state performance under zero load

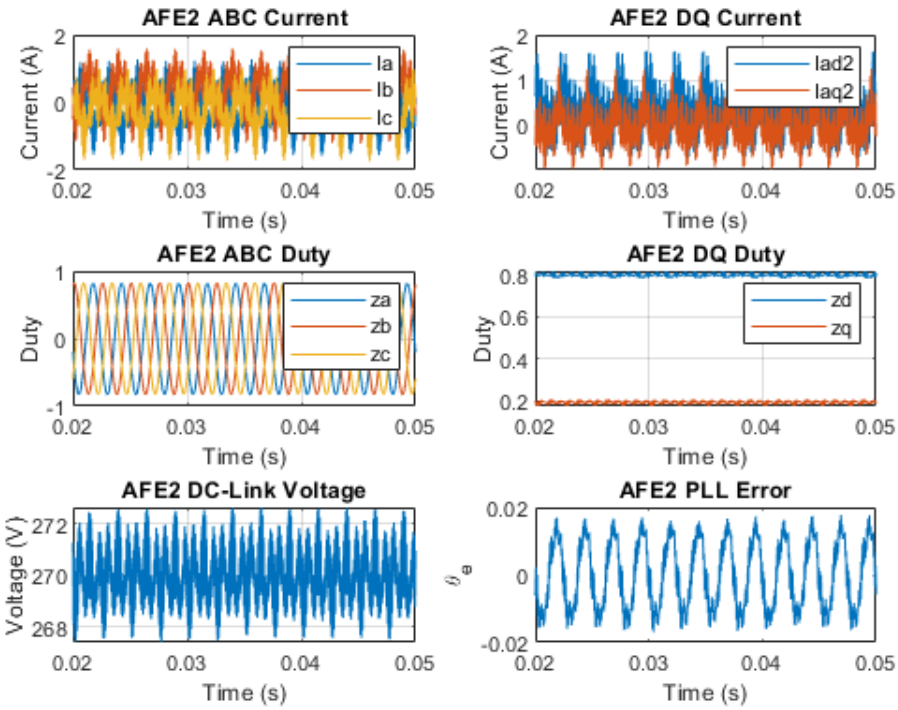

Figure 6.20: Expanded grid AFE2 steady state performance under zero load

As for test (B) where now AFE1 is step loaded with 800W, and the performances of the VSI, AFE1 and AFE2 states are observed in Figures 6.21, 6.22 and 6.23 below:

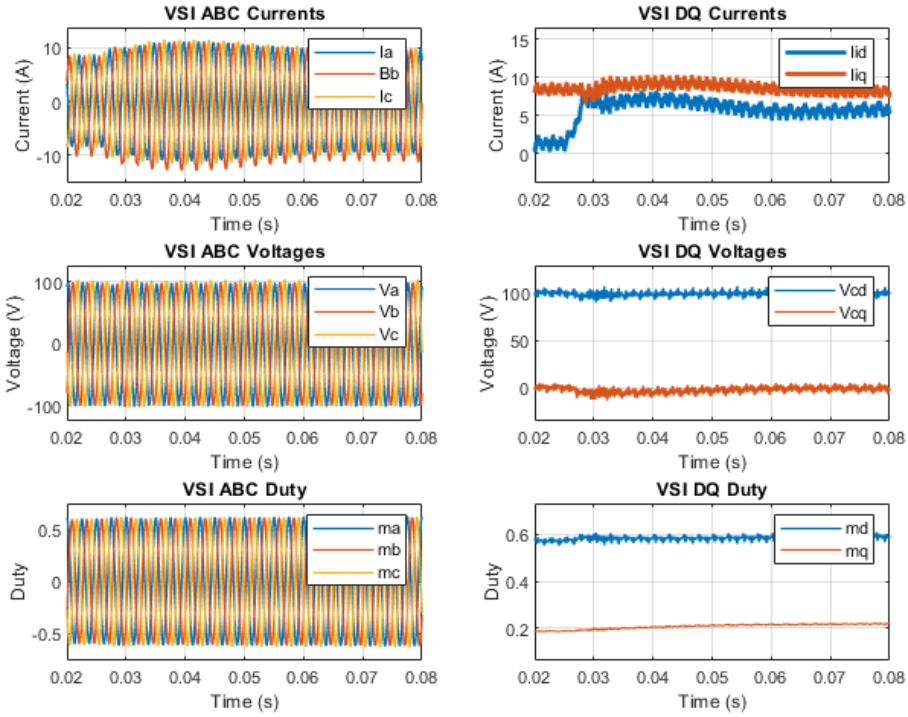

Figure 6.21: Expanded grid VSI when AFE1 undergoes 800W Step Load with decentralised H_2 control

In these figures, a 800W CPL is applied to AFE1 at 0.025s. Upon first observations of the VSI states, it is clear, much like as was shown in the two converter setup that the grid voltages, albeit a small decrease of roughly 3V in both d and q means that the grid voltages experienced only a 3% deviation from reference for about 1.7ms. This is a bigger percentage drop is accredited to that in these tests, in order to keep within the voltage limits of AFE2, the V_{cd} reference is lower in these tests. Therefore, at aircraft specifications of 115Vrms, this percentage decrease for this load will be noticeably lower. So in this aspect, this more pronounced drop is as expected and deemed acceptable. As for the currents of the VSI, the d and q axis currents largely reflect that of the demand of the AFE1 CPL once it's turned on, and is thus expected. But it is clear from the VSI, that the VSI voltage and current states have retained decoupling, with grid voltages being maintained even under large step loads on AFE1.

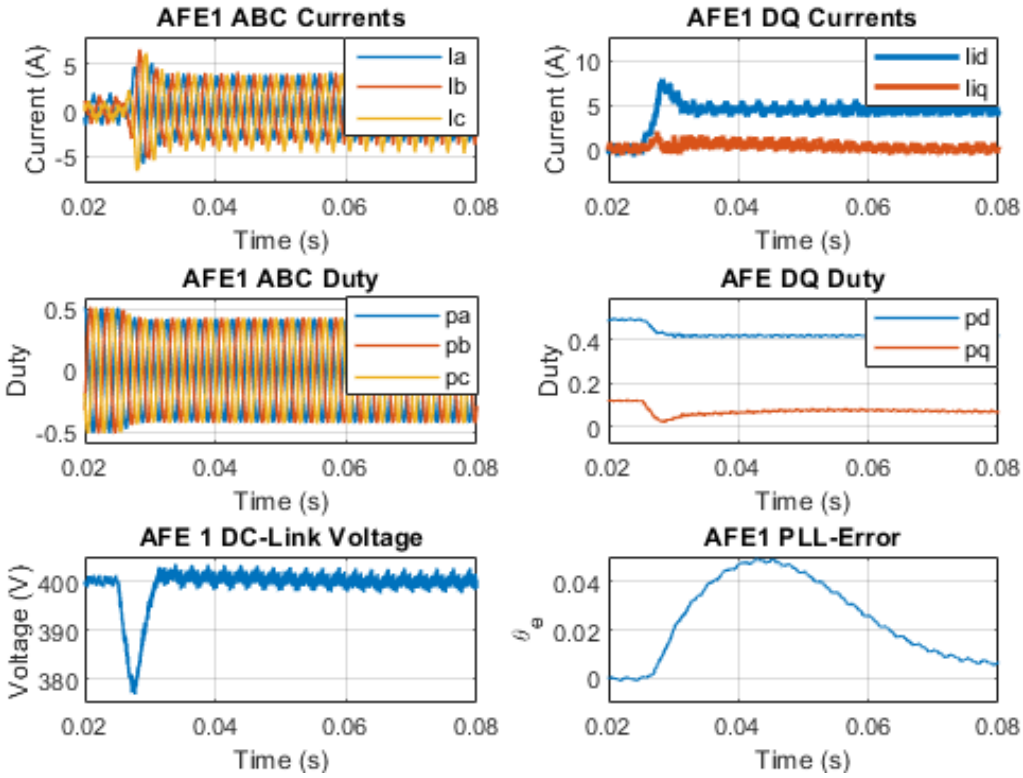

Figure 6.22: Expanded grid AFE1 when it undergoes 800W Step Load with decentralised H_2 control

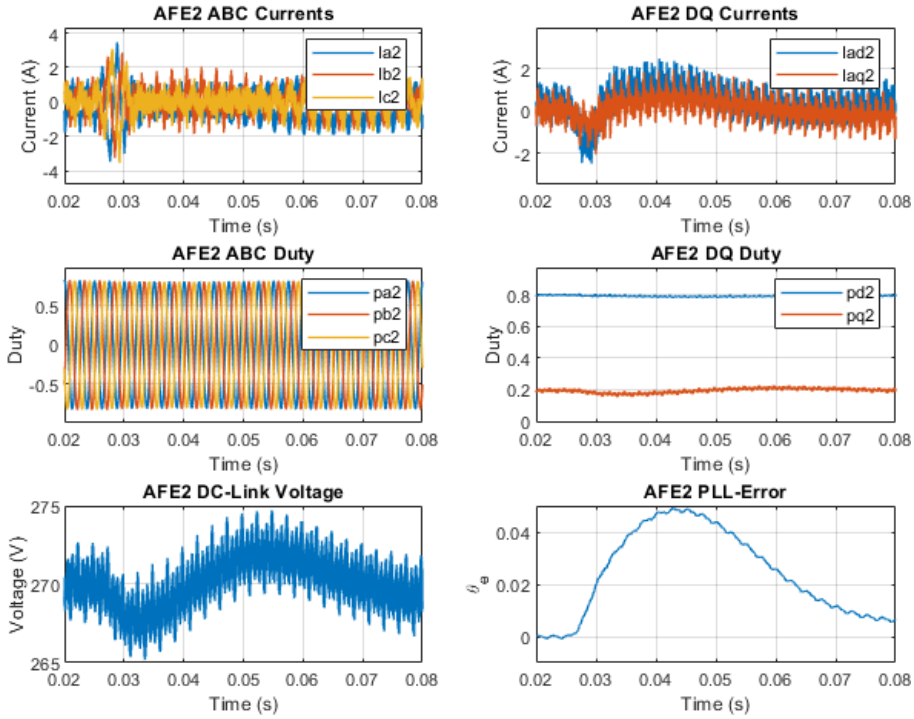

Figure 6.23: Expanded grid AFE2 when AFE1 undergoes 800W Step Load with decentralised H_2 control

Looking at AFE1 states, as was explained previously, the currents I_{ad} and I_{aq} are largely mirrored to that of the VSI currents I_{id} and I_{iq} since these currents are what AFE1 is demanding from the VSI. The DC-Link voltage, due to the nature of the CPL will generally face a large offset upon step load as the current rises to the its new equilibrium point, which is observed. The DC-Link drops just over 20V before quickly recovering back to its reference 400V, in line when I_{ad} returns to reference, in a time of around 15ms. Finally for AFE1 is the PLL, which when compared to the performance in the two converter setup can be observed to be somewhat similar in terms of the closed loop response, but the error is slightly larger. This is again, largely down to the larger respective drop in voltage from reference in V_{cq} from reference, from using lower grid voltages. This in turn results in a slightly larger error in the PLL which is therefore expected. Therefore considering this, and that different weights and system parameters were used in each of the tests, it can be said that the PLL performance is maintained even when incorporating additional converters into the global system. So from the analysis from both the VSI and AFE1, it is safe to say that the performance which was observed in the two converter setup in Chapter 5 has bee retained even when expanding the controller to incorporate additional converters into the global model.

Now most interestingly to observe is how AFE2 behaves during this disturbance. From the

theory discussed in Section 6.2, from the state-space model it was shown that the two AFE do not share any interactive terms, and therefore it should be observed that AFE2 has minimal interaction when a disturbance occurs on AFE1. Since this is on the basis of the open loop model, no matter the control topology this should be the case. From the results presented in Figure 6.23 this is largely observed since minimal interaction occurs. Since both AFE1 and AFE2 share the states V_{cd} and V_{cq} in their state equations, if one disturbs either of these voltages, interactions between the two AFEs will occur. Thankfully since the H_2 controller results in interactions between VSI and the AFEs are largely minimized, the distortion on V_{cq} is largely minimized resulting in little in the way of interaction on AFE2 during a disturbance of AFE1. This explains to why near identical performance between PLL1 and PLL2 is observed. Overall, very minimal distortion is observed across all the states. Currents do suddenly increase to about 2A for a time, but quickly returns to zero, and the DC-Link suffers a distortion of about 2V which can be considered largely negligible. Overall, as expected from theory, minimal distortion has occurred.

Now moving onto test C, where AFE2 is loaded while AFE1 is at full load, one can observed how the controller performs stepping to a full load condition. The results are presented in Figures 6.24 to 6.26 below.

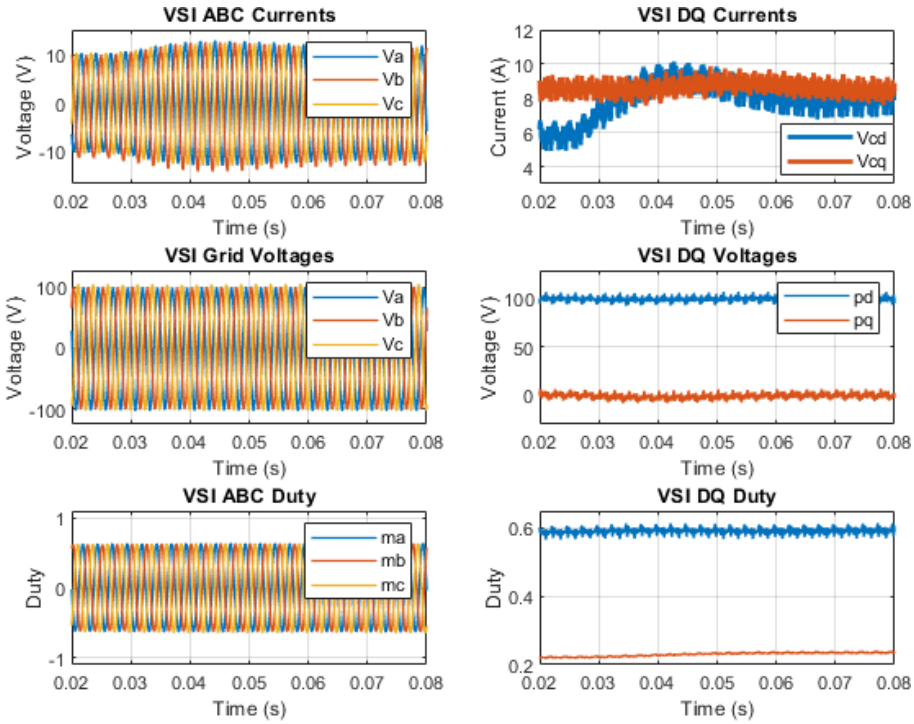

Figure 6.24: Expanded grid VSI when AFE2 undergoes 400W Step Load with decentralised H_2 control whilst AFE1 at full load

Here, a 400W load is applied to AFE2. This had to be lower due to current demands of the BMT converters, and here we too can analyse similar affects as was observed in the test loading AFE1. Due to the lower load, and the fact a larger capacitor used, the voltage deviation of the DC-Link is markedly minimal, 5V in total, which therefore reduces the overall interactive behaviour between the VSI and AFE converters. This therefore results in less distortion of the grid voltages, and in turn means that the incurred PLL errors are reduced, resulting into almost unseen distortion in any of the states in AFE1, apart from the PLL, which is down to the small drop in grid voltage. In regards to the VSI, again, I_{iq} has negligible distortion due to the increased weighting on the q axis current states on each of the AFEs , whilst I_{id} follows the extra current demanded by AFE2 during the interaction. The grid voltage again remains completely at reference value, largely due to the big capacitor on AFE2 restricting overall voltage change.

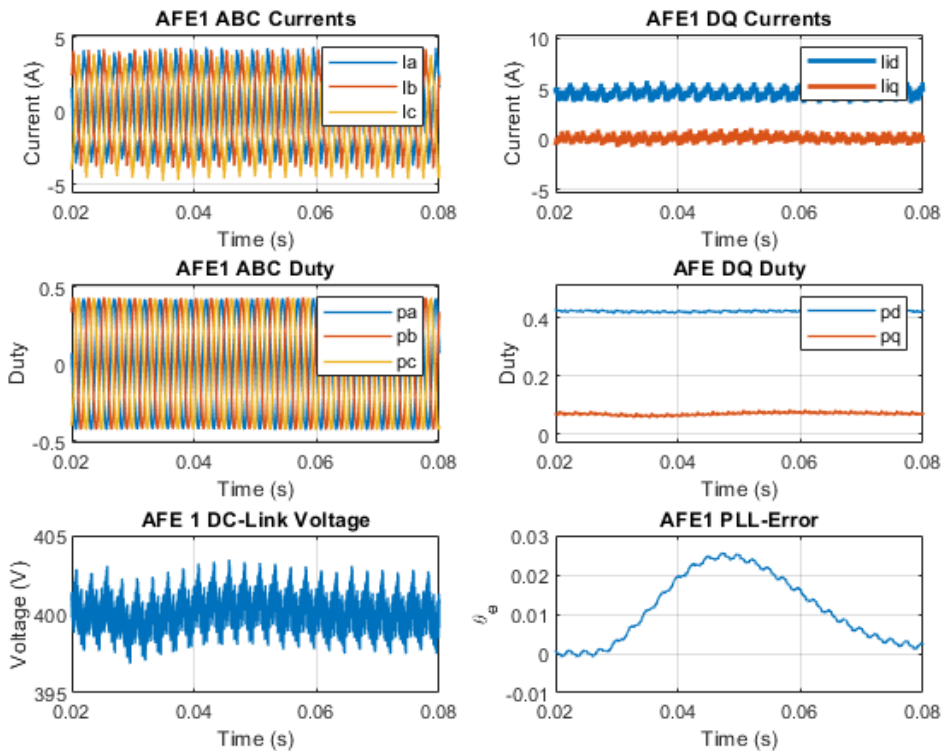

Figure 6.25: Expanded grid AFE1 when AFE2 undergoes 400W Step Load with decentralised H_2 control whilst AFE1 at full load

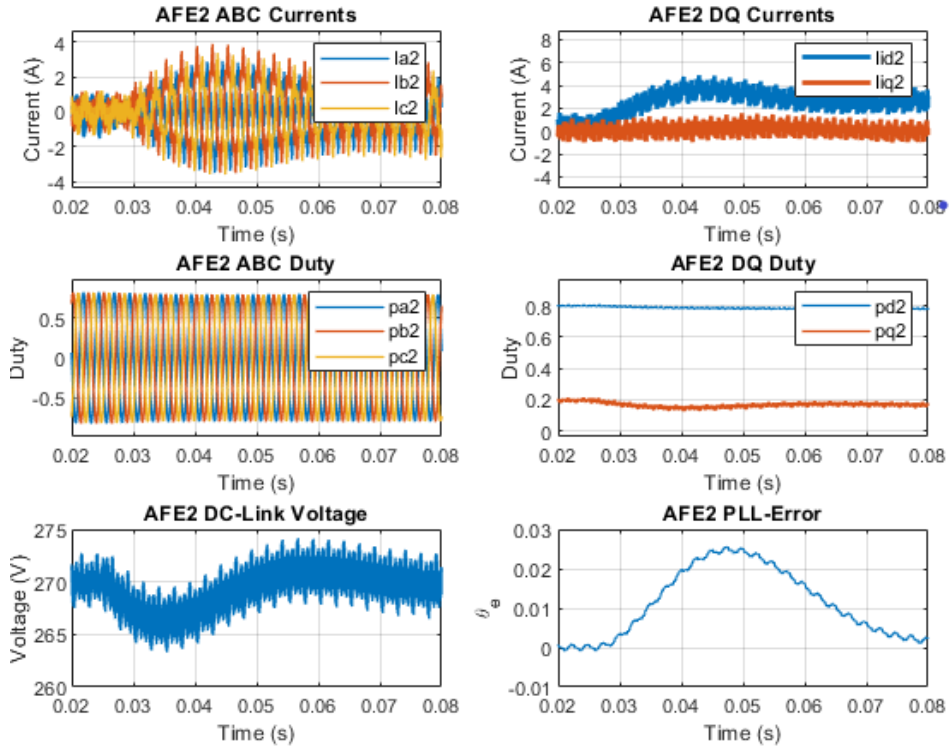

Figure 6.26: Expanded grid AFE2 when it undergoes 400W Step Load with decentralised H_2 control whilst AFE1 at full load

LQR Experimental Results

As performed with the H_2 controller, to confirm that the simulative analysis of the LQR controller reflects that in practise, the LQR controller performance shall be analysed using the same experimental rig setup as the H_2 controller, against the two key tests that were performed in the simulative analysis; loading each of the AFEs in turn. The weights used for each of the converters LQR controllers are those defined in equations (6.22), (6.25) and (6.28).

To start, lets first analyse the performance when AFE1 is step loaded with 800W and AFE2 left unloaded. The results can be observed in Fig. 6.27 - 6.29.

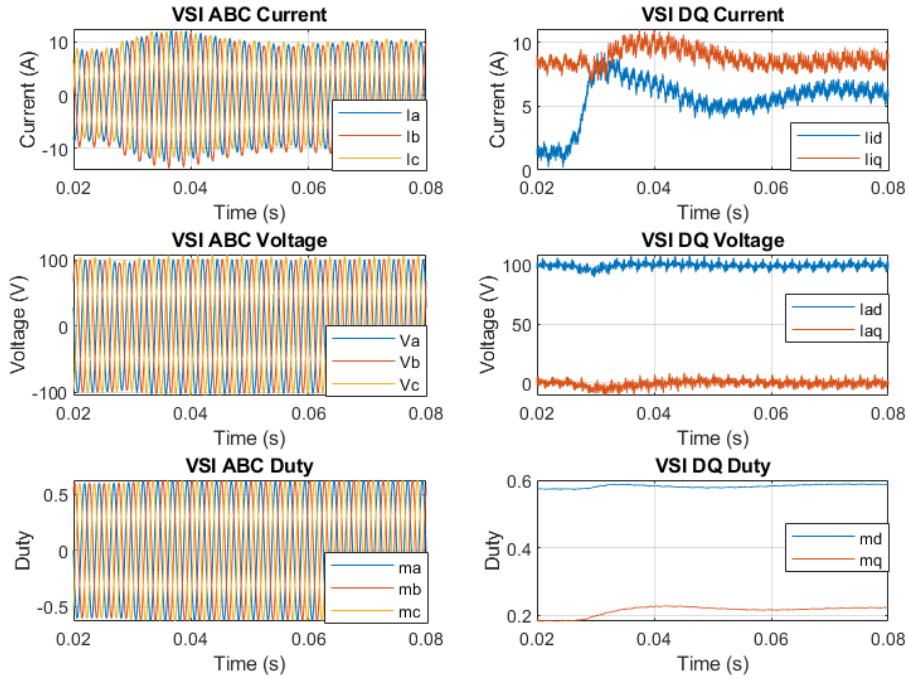

Figure 6.27: Expanded grid analysing VSI states when AFE1 undergoes 800W Step Load under independently optimised LQR controllers

Comparing the VSI result here with that of the exact same test under the H_2 controller in Fig. 6.21 there are some noticeable differences in terms of the controller performances. First, the grid voltages drop further than that observed for H_2 control, which largely lies down the the fact that the DC-Link voltage on AFE1 drops almost 8V lower when compared to H_2 performance, as observed in Fig. 6.28 . As such, the grid voltages also drop a little further by around 3-4V. Again, it could be argued that increasing weight in $Q_{\gamma_{afe1}}$ such that the DC-Link voltage bandwidth increases and thus stays closer to reference would reduce this. In theory this is correct, and grid voltages wouldn't be as distorted, however, again, as observed in simulation results (Fig. 6.11), whilst improvement can be gained in one state, other states tend to suffer degradation and is not an immediate fix.

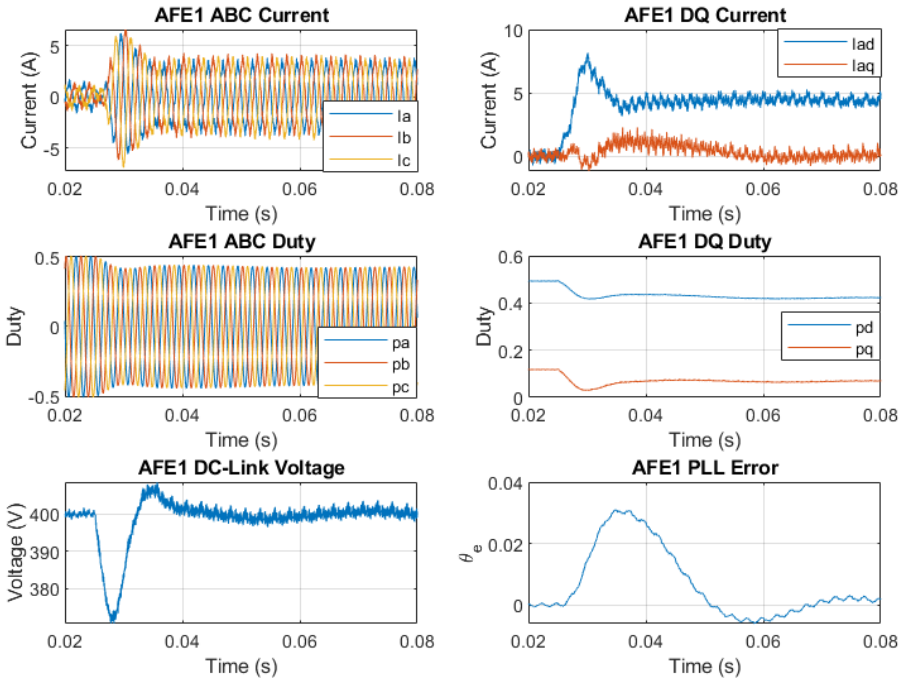

Figure 6.28: Expanded grid analysing AFE1 states when it undergoes 800W Step Load under independently optimised LQR controllers

The VSI currents I_{id} and I_{iq} of both the H_2 and LQR controllers share similar dynamic performances to the load, as was observed in the simulation results of Fig 6.4 and 6.10 respectively. Simulations observed similar overshoots to the load disturbance and also showed how the LQR control while quick returns to equilibrium, the response remains somewhat oscillatory for a time, whilst not overly detrimental to overall performance of the grid. This is also observed in the experimental results. Typically when the VSI current dynamics I_{id} and I_{iq} were observed under H_2 control, the dynamic followed the changing current demands of the perturbed converter quite strictly. However, observing the current demand of I_{ad} and I_{aq} the of AFE1 in Fig. 6.28, these currents do not match. This is due to the interactive effects observed on AFE2. Comparing H_2 and LQR results in Fig. 6.23 and 6.29 respectively the H_2 controller also suffers slightly from this effect, but the interaction through LQR is far more pronounced and severe. I_{ad2} for the H_2 controller did incur a sudden drop of 2A before very quickly recovering back to its equilibrium position of 0A under no load. This did influence the VSI currents for a period of time, but for the LQR controller, I_{ad2} drops drops 2A and then peaks to 3A and recovers slowly back to equilibrium position, which in turn caused greater oscillatory performance on the VSI currents when compared with H_2. The same performance was observed in simulation in Fig. 6.10, which does confirm the simulation model of the LQR is accurate to that in practise. As such, attempts to increase the

bandwidth of the currents in the LQR controller for AFE2 did not result in noticeable reduction in the interactive effects, and is an effect of the LQR controller design not considering the dynamics of the closed loop system as a whole in its controller synthesis.

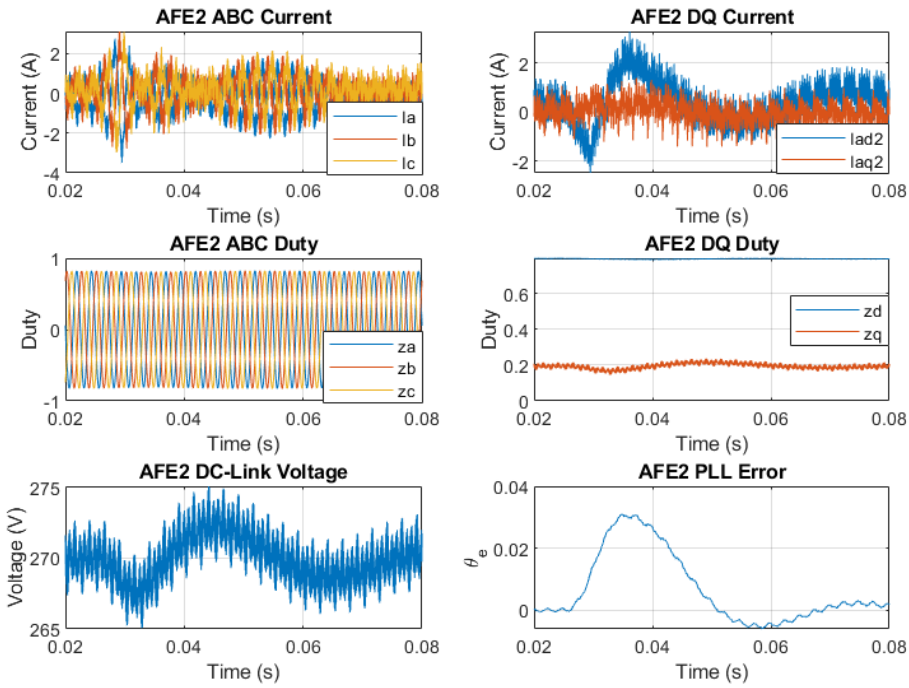

Figure 6.29: Expanded grid analysing AFE2 states when AFE1 undergoes 800W Step Load under independently optimised LQR controllers

Finally, the dynamic performance of the LQR controller is tested when subjected to a 400W step load, whilst AFE1 at full load, as was performed with the H_2 controller. The results of the VSI, AFE1 and AFE2 states are presented in Figures 6.30 - 6.32 below.

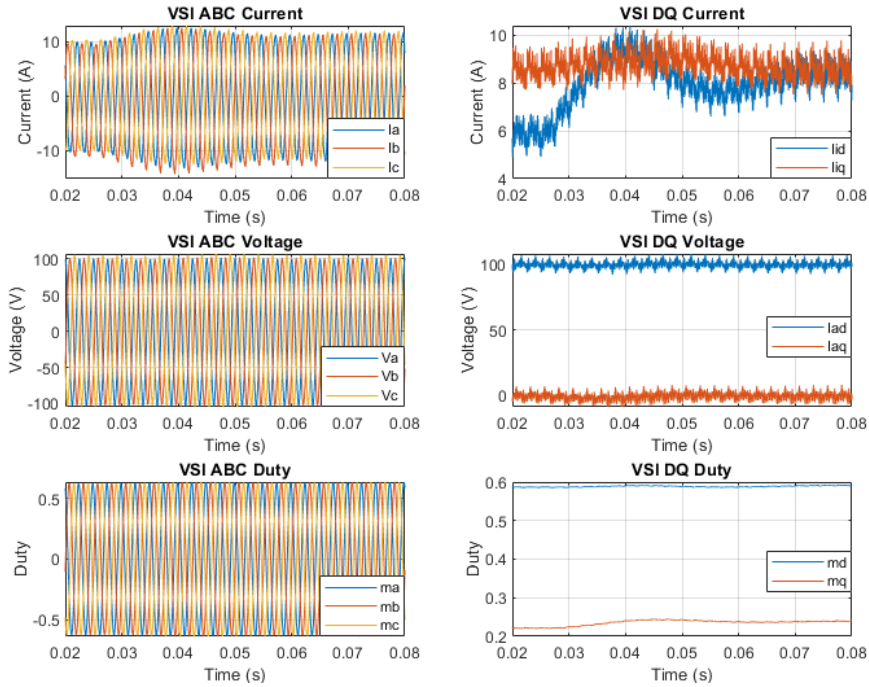

Figure 6.30: Expanded grid analysing VSI states when AFE2 undergoes 400W Step Load under independently optimised LQR controllers, whilst AFE1 fully loaded at 800W

Now, as had previously described when analysing the simulative results, the problematically large capacitor on the DC-Link of AFE2 does somewhat make it difficult to analyse the interactive effects in this test, even when taking into considering the switching noise of the converter.

Firstly, analysing the VSI performance of the LQR controller with that of the H2 controller in Fig. 6.30 and 6.24 respectively. On first observation again are the VSI currents I_{id} and I_{iq} this time largely follow AFE2s demanded current, albeit it is more oscillatory in response than that of the H_2 controller. Since the DC-Link voltage on AFE2 drops so little in the disturbance, due to the reduced step power, and the size of the DC-Link capacitor the VSI voltages vary very little. Therefore the states V_{cd} and V_{cq} which are the only terms which cross-couples between both AFEs distorts little during the transition, which results in AFE1 having little interactive effects in this test. As had been explained in Chapter 1, large passives are often used to dampen the interactive effects between converters, and this test shows this well. The only discernable interaction which can be observed on AFE1 is that of the DC-Link voltage. Whilst minimal, comparing the H_2 and LQR results does show that an oscillatory response incurs on V_{dca} and AFE2 incurs the disturbance. So some interaction is evident between the two AFE converters, but the large capacitor does reduce it somewhat. However, as mentioned in the introduction to this work, the idea is to develop controls for systems in lower passive filter environments in order to reduce the size and weight of these

electrical system, and therefore having such a large capacitor is non-ideal.

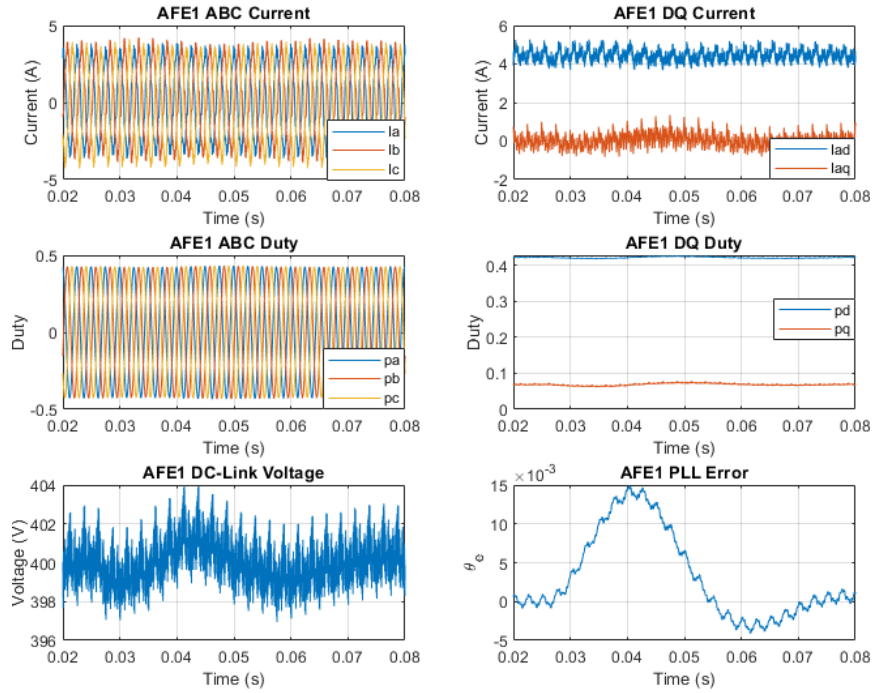

Figure 6.31: Expanded grid analysing AFE1 states when AFE2 undergoes 400W Step Load under independently optimised LQR controllers, whilst AFE1 fully loaded at 800W

Unfortunately the capacitors were inbuilt to the converter and therefore was not easily adaptable for testing in lower capacitor environments. But comparing the figures that have been collected from experimental testing with those from simulation testing, it is very clear that the simulation complements very accurately the true performance of the practical setup. Therefore, the simulative test of the reduced capacitor environment should reflect that in practice. As was observed in Fig. 6.15, in reduced capacitor environments, there will of course be more evident interactions between sub-systems, where in LQR control this could lead to very oscillatory behaviour, if the controller weights are not retuned to accommodate for the changing state dynamics. On the other hand, in similar environment, and in fact through all the simulative and experimental tests which have been conducted, the H_2 controller has shown to mitigate much of the interactive effects between all sub-systems, even in the presence of systems with low passives. Impressively also, when comparing the performance between Fig. 6.14 and 6.15 is that even without needing to retune the weights Q_γ and R_γ for the H_2 controller, even when the capacitor C_{dca2} is reduced by factor of 10, performance is maintained, whilst the LQR deteriorates due to interactions severely. This leads to another interesting and powerful property of the H_2 controller over the LQR, as will be shown in the next section. The H_2 controller is incredibly robust in the face of parameter uncertainty and

variation over LQR.

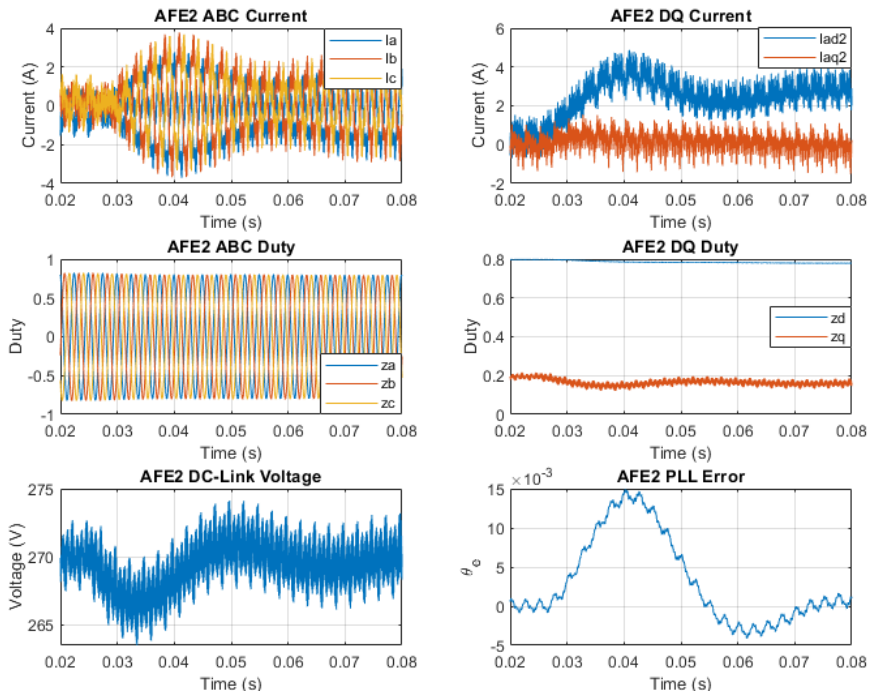

Figure 6.32: Expanded grid analysing AFE2 states when it undergoes 400W Step Load under independently optimised LQR controllers, whilst AFE1 fully loaded at 800W

6.5 Parametric Uncertainty Analysis between H_2 and LQR

In the previous section, it was observed that when the capacitor C_{a2} was reduced in order to analyse the further interacting effects between the converters, what was impressively shown was how each, the LQR and H_2 controllers react when the model was changed. In each case the controller was retuned to the new capacitance but what was observed was that whilst the H_2 (with all the Q_γ and R_γ weights unchanged) was able to keep somewhat similar dynamic performance across the grid, the LQR suffered more greatly from the interactive effects between converters, and even outputted a more oscillatory response, vastly different to how the LQR was originally designed for increased capacitance. What this begs to show is that not only is the proposed H_2 versatile to component value changes without real need to go through the whole tuning procedure again, unlike the case for LQR, but also begs the question how either controller performs when uncertainties in the state model are introduced.

Each, the H_2 and LQR controllers are very dependant on the accuracy of their state-space models in order to attain the desired performance on physical hardware. However, since components

have tolerances due to imperfect manufacture; or in the case with aircraft applications where aircraft could operate in the heat of deserts of temperatures up to 50°C, to upper atmosphere or arctic temperatures of down to -60°C, this can give rise to large variance in component parametric values due to large sways in temperature or component stresses. This gives rise to great uncertainty across the state-space model, moving away from the designed for values for which each of the controllers were optimised to.

In the following simulative tests, each of the H_2 and LQR controllers which have been extensively tested throughout Sections 6.3 and 6.4 shall be further tested to see how they behave given large parameter uncertainty. Unlike in Section 6.3.2 where the controllers were retuned to the new parameters, all tests in this section are performed on the exact same controller, optimised around the nominal model, and are not re-optimised around differing component values, simulating probable parameter changes which can occur.

6.5.1 H_2 Parametric Variation Tests

Now, we shall analyse the proposed H_2 controller, and analyse how its performance changes with parameter variation. The controller weights for the test are the exact same as those detailed in (6.18) and (6.19). In the test, all passive parameters have their value changed collectively by the same percentage, within the range of ±55%, and the AFE1 and AFE2 load tests from the previous sections are performed.

The results are presented across Fig. 6.33 to 6.36, and show very interesting results.

As can be seen from these figures, whilst the performance does significantly change across the variation range, for the most part, the H_2 controller remains very stable, and still shows very damped responses back to the equilibrium point. As would make sense from theory, as the DC-Link capacitors increase, voltage dynamics would be expected to slow down, and this is what is observed. Likewise with the currents, with increases in the inductor values, the dynamic of the currents slows to each of the disturbances, and hasten with reduced values. However, its impressive to observe such responses from the H_2 controller since the controller relies heavily on the accuracy of the whole global model of the system. At the extremities of the variation, the controller is operating very far from its design point and yet, the H_2 controller is still able to maintain performance of the grid entirely at roughly the performance which is was designed to. Therefore in regards to the parameter variation which is a regular occurrence through the general operation of aircraft, these tests would suggest that a single decentralised H_2 controller could be synthesised which would cater to all possible parametric variations which could occur on aircraft.

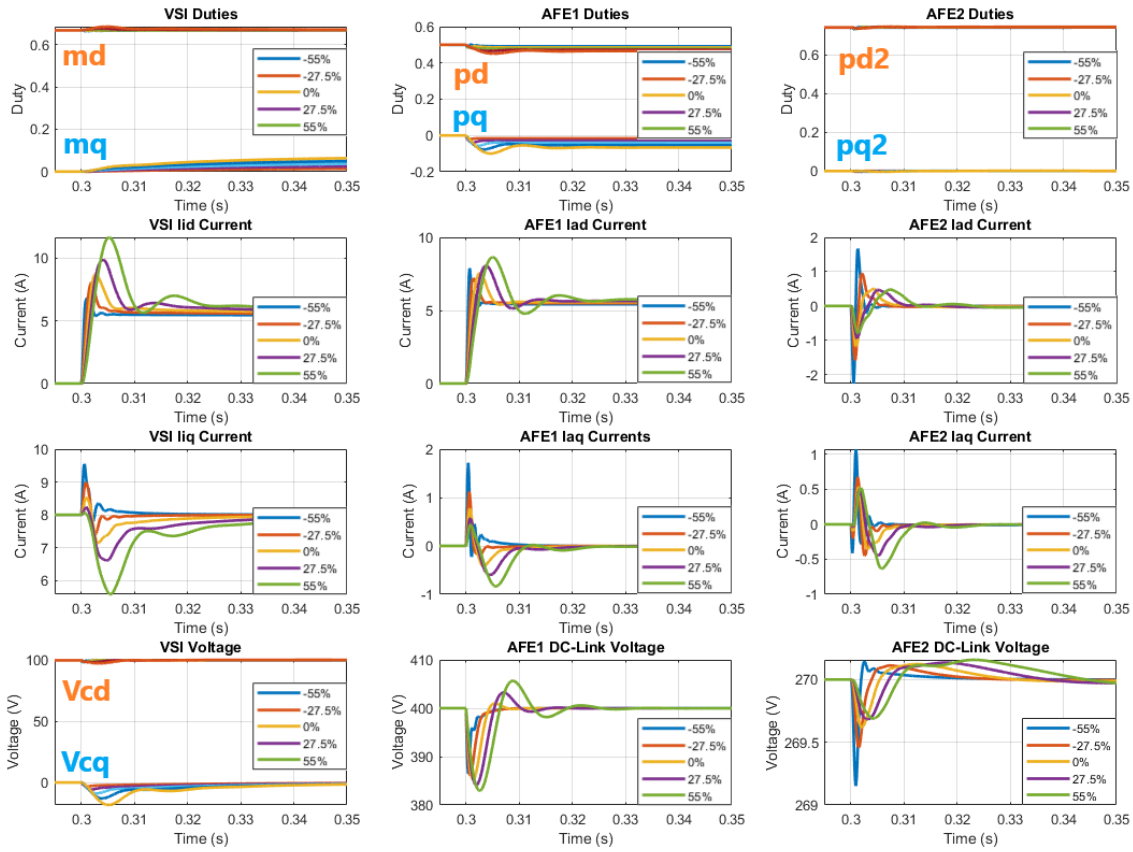

Figure 6.33: Parameter variation of ±55% of the system using the proposed decentralised H_2 controller undergoing the 800W Step load Test on AFE1

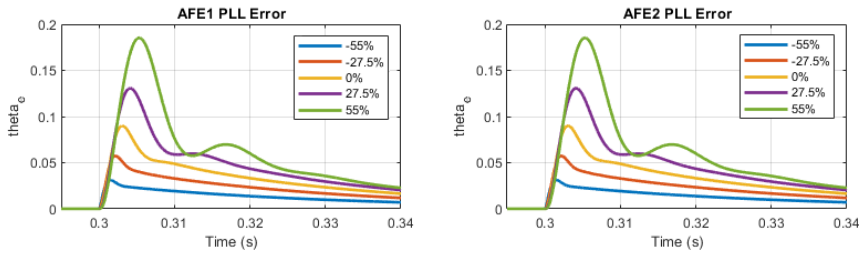

Figure 6.34: The H_2 optimised PLL performance as system parameters are varied ±55% when also undergoing the 800W Step Load Test on AFE1

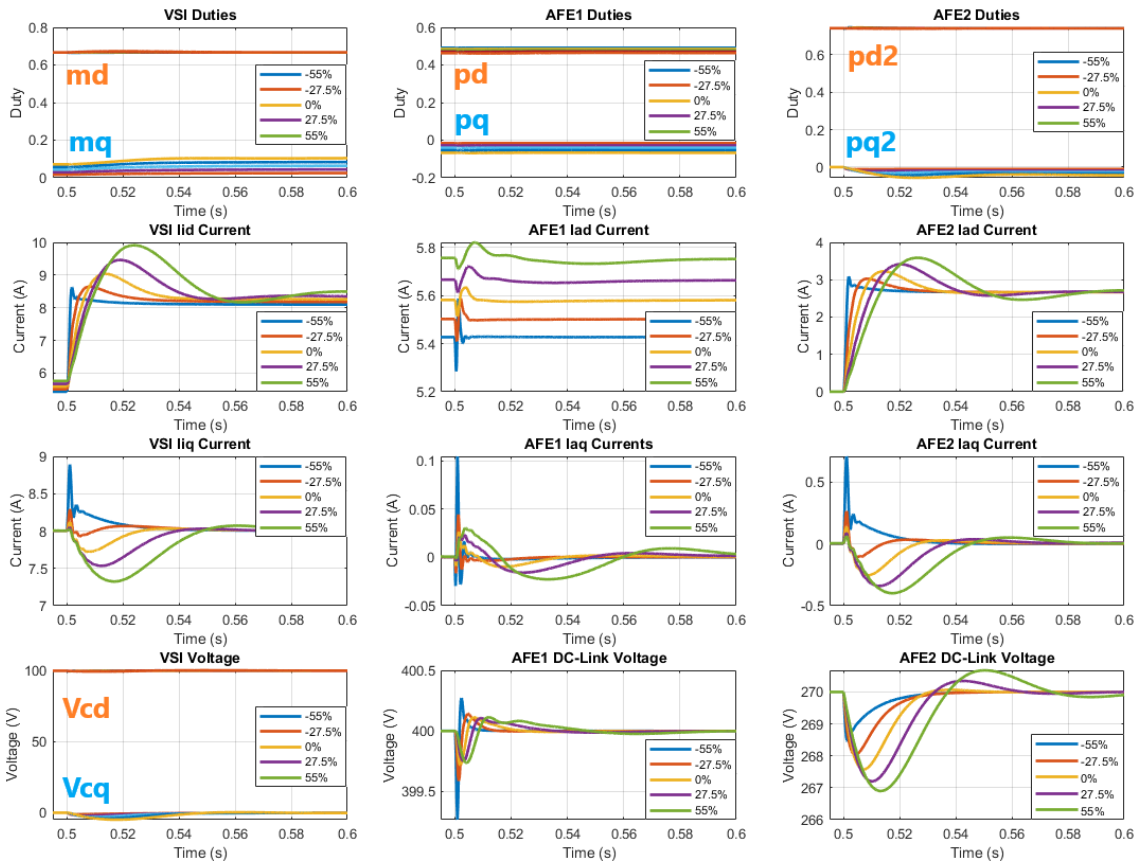

Figure 6.35: Parameter variation of ±55% of the system using the proposed decentralised H_2 controller undergoing the 400W Step load Test on AFE2 whilst AFE1 is already loaded at 800W

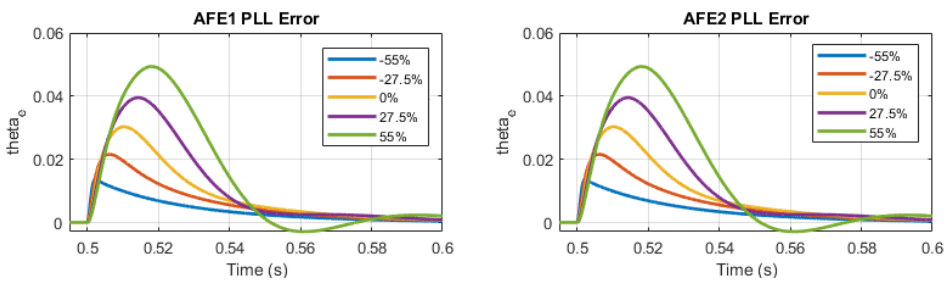

Figure 6.36: The H_2 optimised PLL performance as system parameters are varied ±55% when also undergoing the 400W Step Load Test on AFE2 whilst AFE1 is already loaded at 800W

6.5.2 LQR Parametric Variation Tests

As was performed with the H_2 controller, the exact same tests were performed for the LQR controller, using the weights and state equations defined in (6.20)-(6.30). The exact same LQR

controller, synthesised using nominal operating conditions has bee used throughout all the tests. The LQR parametric variance performance tests are presented below in Fig.

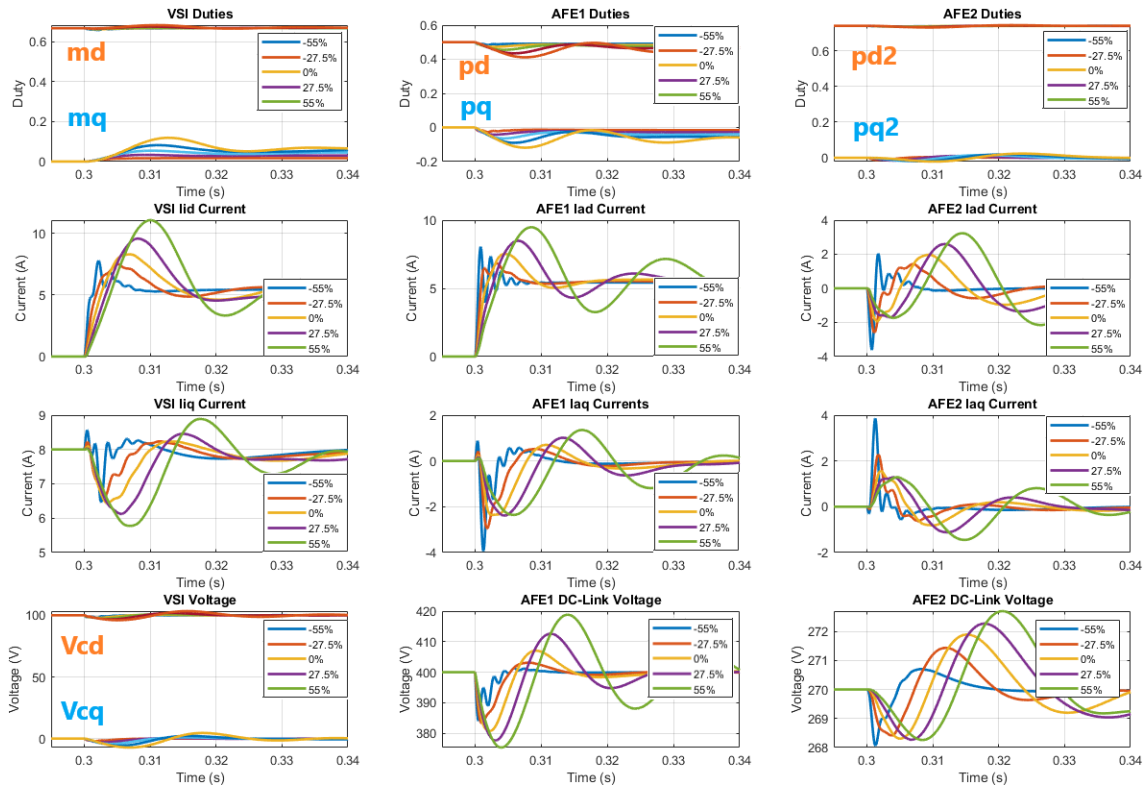

Figure 6.37: Parameter variation of ±55% of the system using the proposed decentralised LQR controller undergoing the 800W Step load Test on AFE1

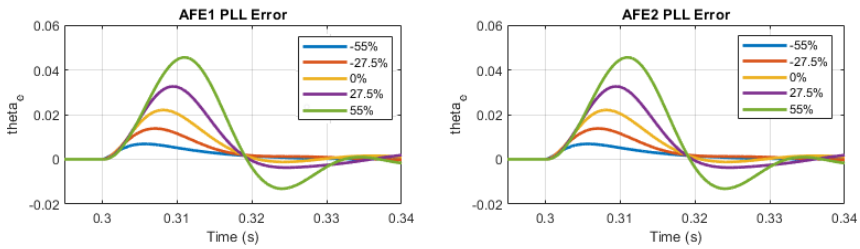

Figure 6.38: The LQR optimised PLL performance as system parameters are varied ±55% when also undergoing the 800W Step Load Test on AFE1

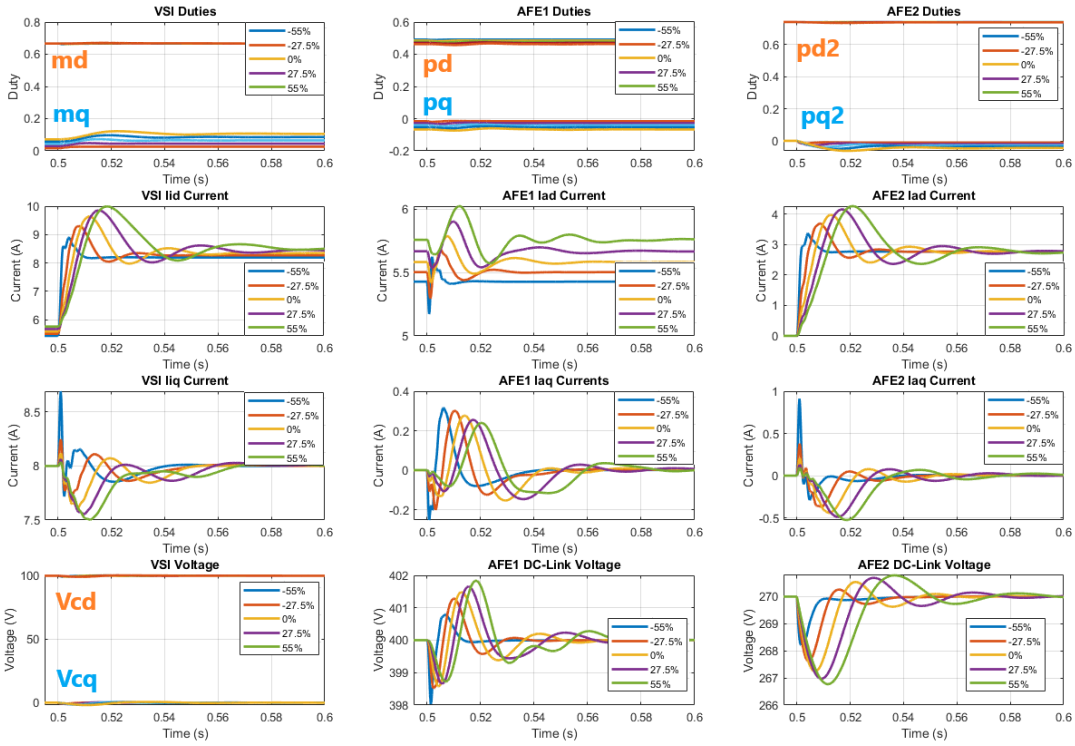

Figure 6.39: Parameter variation of ±55% of the system using the proposed decentralised LQR controller undergoing the 400W Step load Test on AFE2 whilst AFE1 is already loaded at 800W

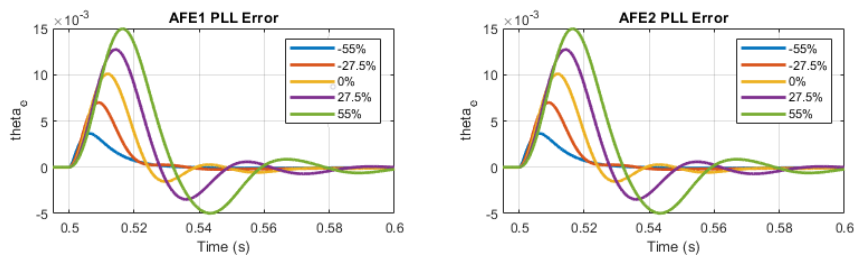

Figure 6.40: The LQR optimised PLL performance as system parameters are varied ±55% when also undergoing the 400W Step Load Test on AFE2 whilst AFE1 is already loaded at 800W

Here, there is a plenty to analyse for the LQR controller performance. Most evident from the LQR performance when the parameters are varied and compared to the H_2 results is that the responses gets very oscillatory the more the parameter values increase. With the H_2 controller, whilst responses did of course get longer, the H_2 performance did not become what one would call oscillatory. Performance was maintained and quickly brought back to equilibrium, and the increase to the response time is small in comparison to that of the LQR. For the LQR controller, the oscillatory responses also result in significantly larger peak currents and voltages to be exhibited

onto the components. For instance, during the AFE1 load test, whilst V_{dca} for the H_2 controller did show a more significant overshoot than at nominal conditions, this only amounted to +5V above reference, for a period of 50ms. LQR on the other hand exhibited 19V increase for almost twice the length of time, and continued oscillating ±10V for more than 200ms. This voltage is what exhibited one of the larger changes in comparison with LQR, but similar cases were also observed across each of the currents across all converters. I_{ad} for instance had almost twice the current overshoot than H_2. From basic observation between the performance of the two controllers, it is quite clear than even with the most severe parametric changes subjugated to the each of the controllers, the H_2 controller significantly outperforms the LQR control. All responses of the H_2 controller return to reference faster, overshoots and undershoots remain minimal in comparison to LQR and overall, the performance is maintained.

Typically, in order to avoid the degradation in performance that the LQR suffers, one would gain schedule the controller. This involves developing a controller for every eventuality the system can be brought to, and have the control platform switch to an appropriate controller given current system conditions. This in general complicates design and implementation and increases hardware costs. However, what is shown with the proposed H_2 controller is that this controller handles well system uncertainty, and even with a single H_2 controller, performance is guaranteed over large variations. In theory, if this system was onboard an aircraft, a single controller could possibly be used for a large case of eventualities, resulting in ease of implementation, as well noticeable performance other improvements such mitigations against sub-system interactions in small filter parameter environments.

Therefore, throughout all the simulative and experimental tests, it has been shown that the proposed H_2 controller not only can be decentralised yet still provide optimal performance against another form of decentralised controller, but also intrinsically mitigates against cross-converter interactions which not only improves performance across the whole system, but also allows the proposed controller to be more robust to parametric uncertainty and improves the overall robustness of the system.

6.6 Discussion and Summary

As an extension to Chapter 5, this chapter investigated the expansion and inclusion of additional power electronic systems onto the AC network. Here an additional AFE was augmented into the global state-space model, along with its own PLL. It has been shown that when using the proposed controller optimisation procedure, incorporating additional converter states is highly non-trivial and for the most part is largely a copy and paste exercise, transferring the already described AFE

dynamics as the second converter states, whilst also taking into account the additional dq frame exhibited on the system caused by the second PLL. When the controller is augmented, the same interaction mitigation as was presented for the two converter system can be also observed in the extended system. Stability was maintained, and the performance of each of the PLLs was shown to be optimal to their augmented converters, as well as guaranteeing the global stability of the system. It was also shown, that even though the H_2 controller depends on the full global state-model and thus assumes in its design assumes full operation of all sub-systems, redundancy is still maintained across the two AFE converters. It was shown that even if one of the converters was switched offline, normal operation between all the working systems can still resume unaffected, which is an extremely strict requirement when designing aircraft power systems, without loss in performance in all other operating sub-systems. The loss of a converter was shown not to effect the transient or steady state performance, showing the proposed optimisation procedure allows full decentralisation between converters, and continued optimal performance.

Experimental verification was in addition performed to verify the simulative analysis, where the experimental results showed that the simulations were largely accurate and represented well how the system would behave in practise, providing confidence to the observations found.

In addition to the performance at nominal conditions, LQR and the proposed controller were compared against when subjugated to parametric changes to see how the H_2 and an commonly employed LQR controller compare when it comes to parametric uncertainty. What was observed was that not only under severe parametric change the H_2 controller can retain largely the properties of sub-system interaction mitigation, but can also largely retain performance close to that of the nominal conditions which was very impressive. The traditional LQR optimal controller, where each of the controllers are independently optimised showed very noticeable performance degradation to parameter change. Parameter changes are a common occurrence during a typical aircraft operation and therefore in order to retain performance for the system utilising an LQR controller, it would likely be sensible to employ gain scheduling techniques to retain optimality of the micro-grid. However, in the scenario if this grid was employed onto an aircraft, utilising a single H_2 controller could be considered enough to ensure optimal and robust performance against parameter uncertainty and variation which could significantly ease the controller design process for aircraft based micro-grids.

In conclusion, the proposed approach has been shown to be very easy to scale up to larger systems. Performance can be maintained globally across all sub-system for any size of system, whilst still maintaining redundancy across the sub-systems as required legally for aircraft power systems. Of course, in future work an additional VSI should be included into the optimisation. In general this should also be a simple procedure however there is more to adding grid generators and

grid loaders. Typically multiple VSIs on a grid are synchronised using droop control. Therefore, the droop characteristics need to be characterised into each of the VSI models and optimised together with all the AFEs on this grid. There was not enough time as part of this PhD to conduct these tests and as a result this will be needed to be done in the future.

Chapter 7

H_2 Optimisation of Variable Frequency Systems

With the ongoing shift of aircraft systems moving towards electrical alternatives, this to has also influenced a change in the electrical characteristics of the grid. The electrical grid on aircraft is largely generated directly from the turbofan jet engines. Typically for the ease of design of the electrical system, traditional commercial aircraft electrical grids were typically held fixed at a constant frequency of 400Hz. However, the jet engines are not constantly operating at a constant rotational speed. Therefore, to produce this fixed grid frequency a variable speed shaft direct from the engine was fed into a mechanical gearbox, which in turn ensured a fixed rotational frequency of the electrical generator [138, 139, 101]. However, on modern day MEA, the main AC bus of the aircraft grid is now typically variable frequency in the range of 360-800Hz. Allowing the grid to now operate at variable frequency (also referred to as frequency wild) allows for the elimination of the heavy mechanical couplings in the gear box, in place with lighter and smaller power electronic systems. Increased adoption of this new approach of grid generation has already been employed in aircraft such as the Boeing 787, Airbus A380 and the Airbus A350 today, and therefore over recent years there have been a renewed research effort towards the design, control and optimisation of power electronic converters in such electrical networks [140, 141]. However problems do arise when modelling such systems by the state-space approach in that these systems are linearised about a given known operating point. In frequency wild systems, with large enough deviations from the notional operating point, these state-space systems for which these controller optimisation techniques are based upon start becoming time variant problems [142, 143]. The standard approach conducted when tackling time variant optimal problems is to what is called 'gain schedule' the control whereby a pre-stored controller is selected from the control architecture

dependant on the current systems operational state [144, 145]. Gain scheduling it sometimes not ideal since in general would require more advanced hardware which can store man different controllers for all eventual situations in the system. Therefore when it comes to systems with frequency variation, PI controllers are often adopted as the transfer functions of the voltages and currents in these converters, for which the PI controller design is based upon are not frequency dependant, and therefore does simplify the controller design for these time variant systems, as shown in [84]. Although, as we have seen in previous chapters, whilst PI controllers are easy to design and in general work very well for their application, they do succumb to the effects of other sub-system dynamics through interactive effects which generally leads to reduced performance; all which has been shown to be mitigated against using the proposed optimal control approach.

In this chapter, it shall be presented how using the proposed H_2 optimal controller, can be adapted to use gain scheduling techniques in order a simple and elegant way which not only ensures the same optimal performance characteristics observed on simple fixed frequency systems, but ensures this across all designed for frequencies. All this is achieved by simple interpolative techniques to make the H_2 controller have polynomial gains with respect the the electrical grid frequency.The work in this chapter forms the basis of this [146] published paper.

7.1 Variable Frequency Electrical Systems in Aircraft

Figure 7.1 shows an example of the aircraft electrical system whose architecture is the focus of this study. As mentioned before, previously, a gearbox was used to ensure the grid frequency output from the synchronous generators was constant. Today however aircraft have variable frequency electrical systems, and the power electronics built in must be able to condition and control to the correct demanded voltage and power outputs no matter the current operating frequency.

7.1.1 The Methods of Variable Frequency Controllers of Today

Typically, a PI controller would be selected for the purpose of power electronic control. It has already been discussed in Chapter 4 the reasons as to why PI controllers are selected over more advanced optimal control strategies but there is an added benefit that occurs when analysing systems in frequency wild conditions.

PI controller design is fundamentally based upon the transfer function of the system open loop, and conditioning the performance with negative feedback gains. With regards to the notional system which was analysed, the transfer functions for the currents and voltages are those presented in equation (7.1)

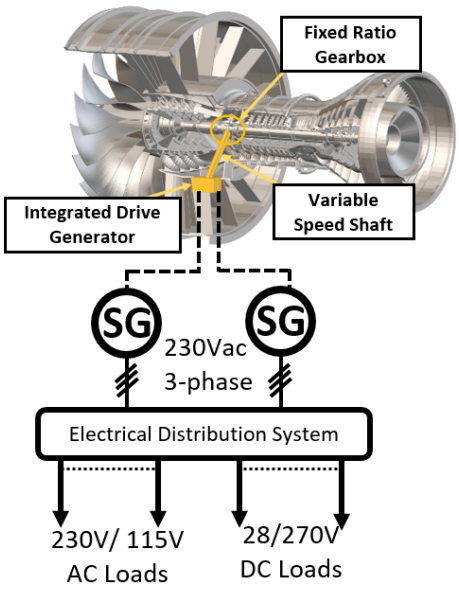

Figure 7.1: MEA Electrical System generation direct from jet turbine engine

$$I_{TF} = \frac{1}{L_g s + R_g}, \quad V_{TF} = \frac{1}{C_g s} \tag{7.1}$$

As can be seen, the transfer functions are completely independent from grid frequency. Therefore, the gains developed from the pole placement on these transfer functions will provide the designed for dynamic performance for each converter exclusive of the grid frequency.

On the contrary, for the proposed optimal control approach, such is not the case. The controller K is dependent on all of the state dynamics of the system, whereby almost all the states (except for DC-Link) voltages are totally dependent on the grid frequency ω. This is a potential downside to the use of the proposed optimal controllers. The proposed control is only valid for a given linear region, and if ω moves far away from the region of linear stability, instability can in-sue. Therefore, to overcome this problem gain-scheduling techniques are very commonly employed [147]. Gain scheduling techniques are usually split into two types. One is where a lookup table is employed, and given certain state conditions, the appropriate linear controller is selected and uploaded onto the control platform. The gains are interchanged once over a given threshold and so forth [148]. The other, which will be investigated further in this chapter is by the interpolation approach. This is where the gains can become a function dependant on a given state variable, and are adjusted directly and automatically given the state condition [149] .

Whatever the strategy selected, there are some inherent problems with gain scheduling which are reported in [147].

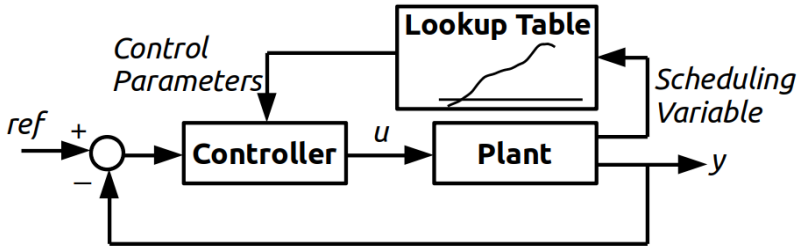

Figure 7.2: Lookup Table Gain Scheduling Block Diagram

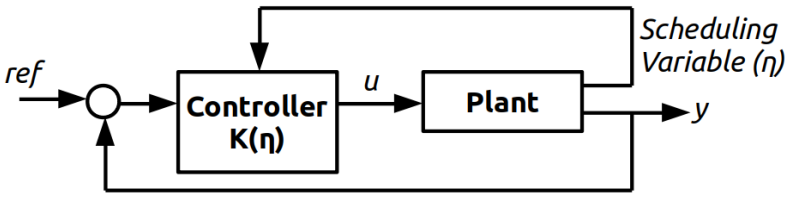

Figure 7.3: Interpolation based Gain Scheduling Block Diagram

For a quick example let's take the interpolation approach. Given the a specific plant parameter is chosen to interpolate the closed loop gains of the system; states which had previously been independent to that given parameter change are now no longer independent in closed loop, as the linear plant, and the linearised controller no longer match the initialized closed loop plant. With this not being modelled, the difference between the designed for closed loop models could lead to detriment performance and limit potential performance of the system. Therefore, designers of these systems must take note of the speed the subject plant variable can change.

On the other hand, when it comes to the lookup table approach, the controller gains set for a given state condition, and the gains for a upcoming state condition could be vastly different. Switching of the controllers in fast succession can cause switching instants, causing additional unmodelled plant dynamics which can also lead to detrimental performance.

So clearly, from the start, PI control has advantages in terms of its implementation and design. However, as we have seen over the course of these thesis, the unmodelled interactive dynamics of the system itself leads to the detrimental performance of the grid as a whole, where H_2 control has shown to largely mitigate such interactive behaviours, as these interactive behaviours are taken into account in the controller design. So even though augmenting the optimal control into a gain scheduled approach can be far more complex to design for, the benefits achieved through H_2 optimal control across all operating frequencies would be deemed a good investment.

7.1.2 Interpolated Gain Scheduling of the Optimal Controller

Now, for the reader of this work, it probably isn't particularly interesting seeing the research presented so far in this thesis in just another form. In this chapter, this variable frequency H_2 controller will be applied to a more industrial scenario using the theory from previous chapters.

Under realistic circumstances of controller design for micro-grid interfaced converters, typically the engineer may not have global access to all interconnected sub-systems. Many of these additional interfaced converters may be commercial systems which already have embedded control software, and possibly could be in hard to reach places, proving difficult to perform any physical modifications.

Therefore, in this analysis an investigation will be undertaken which looks into the design and optimisation of a single AFE converter, to the rest of a pre-designed network. For ease of the presented analysis the rest of the network will be a pre-designed VSI converter which has been designed using a PI controller which is assumed to be inaccessible. The goal of this chapter is therefore to optimize the controller for the single AFE, and then ensure the resultant optimal controller is adapted for frequency wild applications.

System Modelling of Closed Loop VSI and to-be-designed AFE

The VSI state-space equations should already be very familiar by now. However, as we have observed in section 4.2 two cascaded PI controllers are required in order to successfully control the VSI to the desired references. In state-space form we have seen that the integral states of the controller are essential to modelling in full all the dynamics of the system. This is also true when analysing the system under PI control. Along with the states of the VSI, the integrals of each PI controller need to also be modelled to characterise in full the closed loop dynamics of the pre-designed VSI converter. It is well known if the PI controller is broken into its fundamental blocks, it takes the following form:

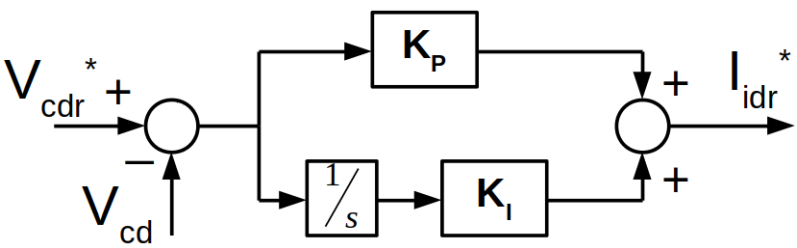

Figure 7.4: Fundamental Block Diagram of the PI controller for d-axis voltage on the VSI

In this case Figure 7.4 represents the outer control for the d-axis voltage. Referring again back to section 4.2 we know that the output of this controller is the current reference for the inner d-axis

current controller. The expression for this reference term can therefore be evaluated as:

$$I_{idr} = K_P \left(V_{cdr} - V_{cd}\right) + K_I \left(\int \left(V_{cdr} - V_{cd}\right) dt\right) \tag{7.2}$$

Where V_{cdr} is the reference demand for V_{cd}. State space equations are the differential terms of given states in the systems, simply then, the state-space expression for the current reference of the inner d-axis current controller can thus be defined as:

$$\dot{I_{idr}} = K_P \left(\dot{V_{cdr}} - \dot{V_{cd}}\right) + K_I \left(V_{cdr} - V_{cd}\right) \tag{7.3}$$

Where the differential $\dot{V_{cd}}$ is the state-space equation of the V_{cd} dynamic. As shown, it is relatively non-trivial to attain the PI dynamic in state-space form. This is then repeated for all the PI controllers interfaced to the system. Using the following procedure, the VSI PI controller states x_{PI} in their full form can be found to be:

$$x_{PI} = \begin{bmatrix} I_{idr} & V_d & I_{iqr} & V_q \end{bmatrix} \tag{7.4}$$

$$\dot{I_{idr}} = K_{pv}\Lambda_1 - K_{iv}\left(V_{cd} - V_{cdr}\right) \tag{7.5}$$

$$\dot{V_d} = K_{pi}\left(K_{pv}\Lambda_1 - K_{iv}\left(V_{cd} - V_{cdr}\right) + \frac{V_{cd} - V_d + I_{id}R}{L}\right) - K_{ii}\left(I_{id} - I_{idr}\right) \tag{7.6}$$

$$\dot{I_{iqr}} = K_{pv}\Lambda_2 - K_{iv}\left(V_{cq} - V_{cqr}\right) \tag{7.7}$$

$$\dot{V_q} = K_{pi}\left(K_{pv}\Lambda_2 - K_{iv}\left(V_{cq} - V_{cqr}\right) + \frac{V_{cq} - V_q + I_{iq}R}{L}\right) - K_{ii}\left(I_{iq} - I_{iqr}\right) \tag{7.8}$$

where Λ_1 and Λ_2 are as follows:

$$\Lambda_1 = \dot{V_{cdr}} - V_{cq}\omega - \frac{I_{id}}{C} + \frac{I_{ad}^P \cos(\theta_e) - I_{aq}^P \sin(\theta_e)}{C} \tag{7.9}$$

$$\Lambda_2 = \dot{V_{cqr}} - V_{cd}\omega - \frac{I_{iq}}{C} + \frac{I_{aq}^P \cos(\theta_e) - I_{ad}^P \sin(\theta_e)}{C} \tag{7.10}$$

and the terms V_d and V_q are the unconditioned actuation demands for the switching, such that:

$$m_d = 2\left(\frac{V_d - I_{iq}\omega L}{C}\right), \quad m_q = 2\left(\frac{V_q + I_{id}\omega L}{C}\right) \tag{7.11}$$

The above equation already assume the AFE is augmented with a PLL, and the term with ω being the decoupling terms for each axes controller. With these equations, the assumed pre-designed closed loop VSI system can be modelled in state-space.

In addition, as the PLL is not being optimised in this particular optimisation, the closed loop state-space form must also be incorporated into the state-space model. The closed loop form of the PLL was previously shown in (5.5). The need for the state y presented before is no longer needed, as this was only necessary to ensure accurate representation of the fundamental V_{cq} dynamic for the

optimization of PLL gains. Equation (5.5) represents the dynamics required for the optimisation of the AFE and therefore can be submitted directly into the state-space model, having θ_e now as a state to the system. The AFE retains the same open loop matrix equations as has been used throughout this thesis, with the exception of utilizing the state θ_e for the PLL interactive dynamics. With this, the full state-space matrix for the subject system becomes:

$$x = \begin{bmatrix} x_{VSI} & x_{PI} & x_{AFE} & \omega_{I_{aq}} & \omega_{V_{dc_a}} & \theta_e & x_i \end{bmatrix} \tag{7.12}$$

$$A = \begin{bmatrix}
-\frac{R}{L} & -\frac{1}{L} & 0 & 0 & 0 & \frac{1}{L} & 0 & 0 & 0 & 0 & 0 & 0 & 0 & 0 & 0 \\
\frac{1}{C} & 0 & 0 & \omega & 0 & 0 & 0 & 0 & -\frac{1}{C} & 0 & 0 & 0 & 0 & \frac{I_{aq}^P}{C} & 0 \\
0 & 0 & -\frac{R}{L} & -\frac{1}{L} & 0 & 0 & 0 & \frac{1}{L} & 0 & 0 & 0 & 0 & 0 & 0 & 0 \\
0 & -\omega & \frac{1}{C} & 0 & 0 & 0 & 0 & 0 & 0 & -\frac{1}{C} & 0 & 0 & 0 & -\frac{I_{ad}^P}{C} & 0 \\
-\frac{K_{pv}}{C} & -K_{iv} & 0 & -K_{pv}\omega & 0 & 0 & 0 & 0 & \frac{K_{pv}}{C} & 0 & 0 & 0 & 0 & -\frac{I_{aq}^P K_{pv}}{C} & 0 \\
\sigma_1 & \sigma_2 & 0 & -\sigma_3 & K_{ii} & -\frac{K_{pi}}{L} & 0 & 0 & \frac{K_{pi}K_{pv}}{C} & 0 & 0 & 0 & 0 & -\frac{I_{aq}^P K_{pi} K_{pv}}{C} & 0 \\
0 & K_{pv}\omega & -\frac{K_{pv}}{C} & -K_{iv} & 0 & 0 & 0 & 0 & 0 & \frac{K_{pv}}{C} & 0 & 0 & 0 & \frac{I_{ad}^P K_{pv}}{C} & 0 \\
0 & \sigma_3 & \sigma_1 & \sigma_2 & 0 & 0 & K_{ii} & -\frac{K_{pi}}{L} & 0 & \frac{K_{pi}K_{pv}}{C} & 0 & 0 & 0 & \frac{I_{ad}^P K_{pi} K_{pv}}{C} & 0 \\
0 & \frac{1}{L_a} & 0 & 0 & 0 & 0 & 0 & 0 & -\frac{R_a}{L_a} & \omega & -\frac{p_d}{2L_a} & 0 & 0 & \frac{V_{cq}}{L_a} & 0 \\
0 & 0 & 0 & \frac{1}{L_a} & 0 & 0 & 0 & 0 & -\omega & \frac{R_a}{L_a} & -\frac{p_q}{2L_a} & 0 & 0 & -\frac{V_{cd}}{L_a} & 0 \\
0 & 0 & 0 & 0 & 0 & 0 & 0 & 0 & \frac{3p_d}{4C_a} & \frac{3p_q}{4C_a} & \frac{P_l}{C_a V_{dca}^2} & 0 & 0 & 0 & 0 \\
0 & 0 & 0 & 0 & 0 & 0 & 0 & 0 & 0 & -1 & 0 & 0 & 0 & 0 & 0 \\
0 & 0 & 0 & 0 & 0 & 0 & 0 & 0 & 0 & 0 & -1 & 0 & 0 & 0 & 0 \\
0 & 0 & 0 & K_{p_{pll}} & 0 & 0 & 0 & 0 & 0 & 0 & 0 & 0 & 0 & -K_{p_{pll}} V_{cd} & 1 \\
0 & 0 & 0 & K_{i_{pll}} & 0 & 0 & 0 & 0 & 0 & 0 & 0 & 0 & 0 & -K_{i_{pll}} V_{cd} & 0
\end{bmatrix} \tag{7.13}$$

where,

$$\sigma_1 = -K_{ii} - K_{pi}\left(\frac{K_{pv}}{c} - \frac{R}{L}\right), \quad \sigma_2 = -K_{pi}\left(K_{iv} - \frac{1}{L}\right), \quad \sigma_3 = K_{pi}K_{pv}\omega \tag{7.14}$$

The input matrix is far easier to determine. Considering only an AFE controller is being designed and optimised to the rest of the pre-designed system, the only inputs to the system are the AFE inputs, and these remain unchanged from the previous examples. Thus, the input matrix for the AFE controller optimisation is simply:

$$B_2 = \begin{bmatrix} 0 & 0 & 0 & 0 & 0 & 0 & 0 & 0 & -\frac{V_{dc_a}}{2L_a} & 0 & \frac{3I_{ad}^P}{4C_a} & 0 & 0 & 0 & 0 \\ 0 & 0 & 0 & 0 & 0 & 0 & 0 & 0 & 0 & -\frac{V_{dc_a}}{2L_a} & \frac{3I_{aq}^P}{4C_a} & 0 & 0 & 0 & 0 \end{bmatrix}^T \tag{7.15}$$

Variable Frequency H_2 Controller Design

To design a interpolated gain scheduled controller in order to enable the H_2 controller to operate across a large frequency range optimally, two alternative approaches can be utilised.

1. Tune the Q_γ and R_γ matrix for numerous frequencies and interpolate resultant gains.
2. Tune only a single Q_γ and R_γ matrix, which provides satisfactory performance at the operable frequency extremes, and interpolate numerous controllers using these weights.

Advantages which can be gained from approach 1 in that at each and every frequency, the performance of the system is known and ensured to be completely optimal for every single frequency. However, major disadvantages with this approach come as it is a time consuming process to design each and every Q_γ and R_γ matrix for all frequencies, and that the non-convexity of the H_2 optimization may not necessarily produce smooth functions in K whilst also changing the weights.

Although the later reason also applies to approach 2, the likelihood of receiving a smooth function is increased, as the weights are the same throughout the full optimisation. Additionally, approach two is not as time consuming since only one weight needs to be found for the full optimisation. If one finds weights which provide adequate performance at both 360Hz and 800Hz, then it is certain that frequencies in-between will also be stable, and provide roughly the same desired performance. Each resultant controller in $K(\eta)$ won't be as optimal to the desired performance as one would receive from approach 1, but with the cost of time being saved by this approach for satisfactory performance across all frequencies, approach 2 will be used for this study.

To start, weighting matrices were first designed and selected for operation at 360Hz using the tuning method described in section 4.1.3.

Because only the AFE in this regard is being tuned, the only states which need to be weighted in Q_γ are $\omega_{I_{aq}}$ and $\omega_{V_{dc_a}}$.

Following the procedure, the weights which delivered satisfactory dynamic and robust system performance was as follows:

$$Q_\gamma = diag\left(\begin{bmatrix} \mathbf{0}^{1\times 11} & 0.2 & 10 & \mathbf{0}^{1\times 2} \end{bmatrix}\right) \tag{7.16}$$

$$R_\gamma = I^{2\times 2} \tag{7.17}$$

These weights were testing using a mathematical average simulation at $\omega_n = 360Hz$ and $\omega_n = 800Hz$ and the performance to a 800W step load at each frequency is shown below:

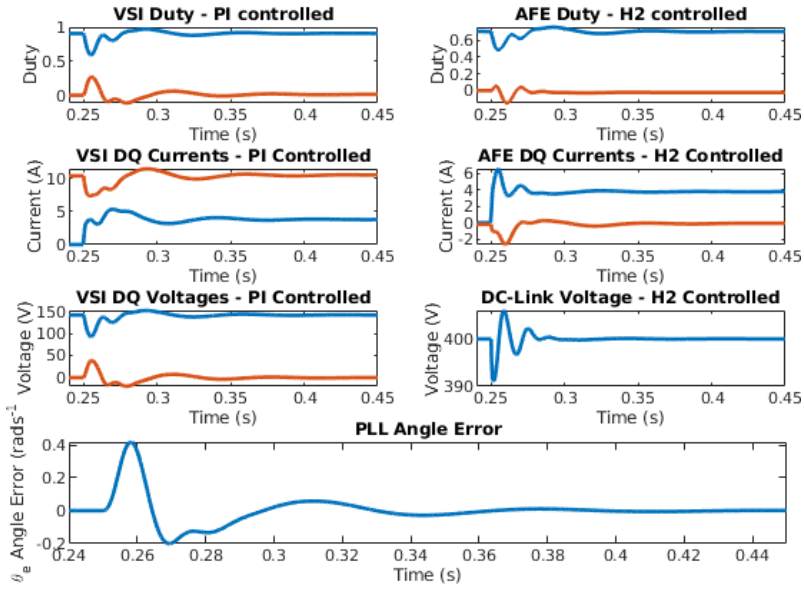

Figure 7.5: Performance of a pre-designed VSI converter using PI control integrated with H2 optimised AFE with weights specified in (7.16) and (7.17) operating at 360Hz grid frequency

As can be seen between the two simulations, the VSI largely remains the same in dynamic performance; expected since the bandwidths of the control are fixed and the controller is independent to grid frequency. For the H_2 optimised AFE converter you can see that when the system is operating at 800Hz, the dynamics appear to be largely faster than that of 360Hz.

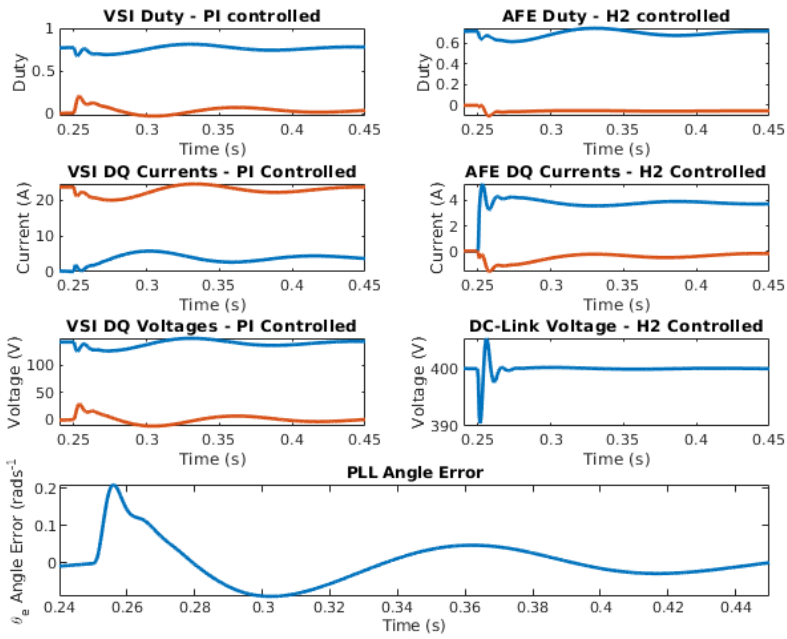

Figure 7.6: Performance of a pre-designed VSI converter using PI control integrated with H2 optimised AFE with weights specified in (7.16) operating at 800Hz grid frequency

This is however very easily explained when analysing the pole-zero map of the closed loop AFE system when developing the controller at equal intervals frequency in the operable range as is shown in Figure 7.7.

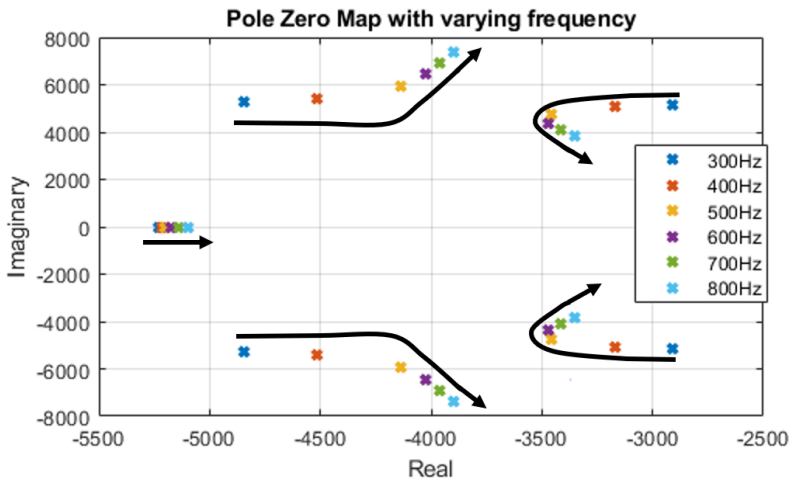

Figure 7.7: Pole-zero map of the closed loop AFE system using H_2 weights defined in (7.16) and (7.17) for varying operating grid frequencies

From the initial setting at 360Hz, it can be seen that as the frequency increases on the grid the

most dominant poles of the system move more to the left signifying an increase in bandwidth in the control. In this case, at a grid frequency 300Hz with a dominant bandwidth of approximately 4.1kHz when assuming a damping ratio close to 0.707, and a maximum bandwidth of approximately 4.95kHz at a grid frequency of around 600Hz. At grid frequency of around 800Hz, the bandwidth is approximately 4.7kHz, which backup the increase in dynamic performance at 800Hz in the simulative results of the H_2 controller. Therefore, this shows that using the optimisation weights (7.16) and (7.17) will maintain or improve on the performance observed at 360Hz. This is not guaranteed for all systems, and to ensure this the equivalent pole-zero map will need to be generated to ensure performance of the converter, and that through the frequency range, poles do not move too close the right side of the complex plane.

7.1.3 Interpolated Gain Scheduling of the H_2 and LQR Controllers

To asses the performance of the proposed controller design in the scenario of optimising the controller to a pre-deigned commercial system, again it must be pitted against other controllers which are widely used in these applications. The PI controller by now is very well understood, and the controllers used in this comparison is the same used as those presented in the previous studies. Refer to Table 4.4 for the gains and bandwidths used.

However, throughout this study the LQR controller has been largely neglected for comparison. This was largely down to the impracticality of using LQR control for multiple converter applications due to the necessity of LQR controllers having full state-feedback and thus requiring every state of the system in order to operate properly.

However, in this regard, only the AFE converter is being controlled. Therefore, the LQR controller can be used to optimise the performance of the AFE, to possibly deliver superior performance over the PI-PI system. In the design of the controller, we cannot include the dynamics of the PLL and the VSI, because this would mean extra communication between converters which is unfeasible for aircraft micro-grid design. Therefore, the LQR controller will be based only on the dynamics of the AFE.

Simply to design the LQR controller, the following matrices are used:

$$A_{lqr} = \begin{bmatrix} -\frac{R_a}{L_a} & \omega & \frac{p_d}{2L_a} & 0 & 0 \\ -\omega & -\frac{R_a}{L_a} & \frac{p_q}{2L_a} & 0 & 0 \\ \frac{3p_d}{4C_a} & \frac{3p_q}{4C_a} & \frac{P_l}{CaV_{dca}^2} & 0 & 0 \\ 0 & -1 & 0 & 0 & 0 \\ 0 & 0 & -1 & 0 & 0 \end{bmatrix}, \quad B_{lqr} = \begin{bmatrix} -\frac{V_{dc_a}}{2L_a} & 0 \\ 0 & -\frac{V_{dc_a}}{2L_a} \\ \frac{3I_{ad}}{4C_a} & \frac{3I_{aq}}{4C_a} \\ 0 & 0 \\ 0 & 0 \end{bmatrix} \tag{7.18}$$

Where of course ω is the varying grid frequency. As shall be shown later, optimising without

consideration of the grid dynamics (especially so for a small scale 2 converter setup) can cause instability if the input impedance of the converter including the controller is greater than that of the commercially designed VSI. When selecting the weights for the LQR controller the same procedure is used with that of the H_2 control. In this regard, the LQR controller was designed such that it offered similar performance to the H_2 controller presented above, in regards to the control of the AFE alone, in order to provide as close to a fair comparison as can be attained.

Following the standard procedure, the LQR controller was designed with the weights:

$$Q_{\gamma_{lqr}} = 60diag\left(\begin{bmatrix}0 & 0 & 0 & 1 & 4\end{bmatrix}\right), \quad R_{\gamma_{lqr}} = I^{2\times 2} \tag{7.19}$$

Interpolation Gain Scheduling

Due to the state-space equations for which both the H_2 and LQR controls are reliant on for the controller synthesis, this also makes both controllers dependant on the grid frequency for their stability and performance.

For both controllers, each has the following controller structure for the AFE, for a specific frequency of operation.

$$K_{\langle H_2,lqr\rangle} = \begin{bmatrix} K_{11} & K_{12} & K_{13} & K_{14} & K_{15} \\ K_{21} & K_{22} & K_{23} & K_{24} & K_{25} \end{bmatrix} \tag{7.20}$$

Placing ω as the scheduling variable, the form of both controllers becomes that presented in (7.21) based on Figure 7.3

$$K_{\langle H_2,lqr\rangle}(\omega) = \begin{bmatrix} K_{11}(\omega) & K_{12}(\omega) & K_{13}(\omega) & K_{14}(\omega) & K_{15}(\omega) \\ K_{21}(\omega) & K_{22}(\omega) & K_{23}(\omega) & K_{24}(\omega) & K_{25}(\omega) \end{bmatrix} \tag{7.21}$$

The first procedure in developing interpolated gains as a function of ω is to cycle through all the possibilities of operable frequency. For the H_2 controller synthesis, two things need to be considered. Firstly the resolution of the interpolation, in other words, how many points in ω shall be used in order to interpolate $K(\omega)$, and the second point being the number of random starting points required to optimise the controller for each ω. With the LQR controller being a convex optimisation procedure, the latter is not required. For the case of H_2 control, a sampling resolution of 22.5Hz was selected, and in Figure 7.8, selections of 10, 80 and 250 random starting points for the optimisation were taken, and the associated minimal gains calculated presented. It is clear that with each of the number of points used, a smooth function of points can be obtained. Especially so for the gains computed using using 250 random starting points. For some of these

gains, it can be seen that whilst using lower number of points, a function seems to be clearly defined, but very different to that when using 250 random points.

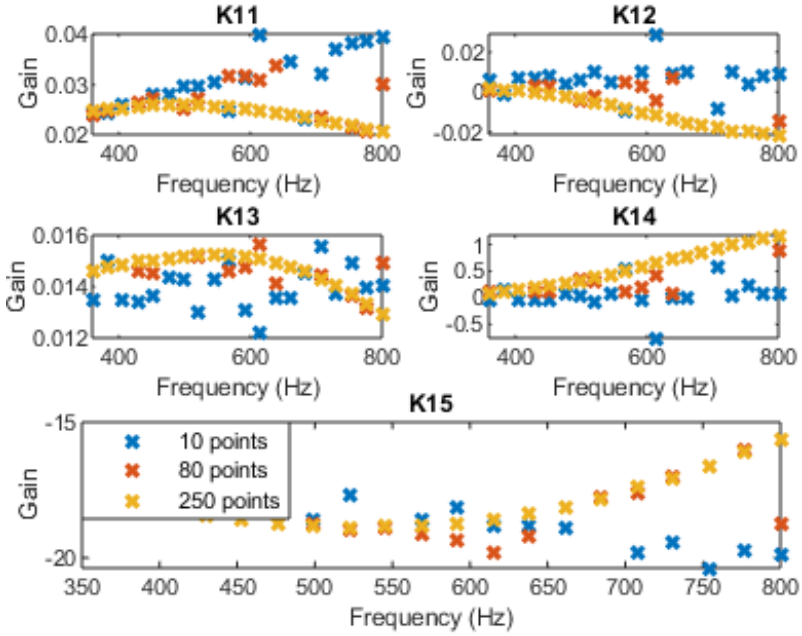

Figure 7.8: Interpolation of the gains in $K(\omega)_{(1,x)}$ for varying number of random points in the H_2 optimisation

This may suggest that there maybe lots of local minima in very close proximity during the optimisation, and that a large number of points is required to evaluate the true minimum. Evidently a number of random points required to evaluate the true minimum of the H_2 norm for each ω is around the 100-200 mark for guaranteed acquisition of the minimization function.

There are many methods which can be utilised to interpolate the gain functions. A common method which is employed when there is a certainty of error in the computed points is using the Least Square Optimisation. In this approach, a line of best fit is computed between the points in which minimizes the sum of the squared distances from each of the constituent points to that of the line. This is very simple procedure to apply to our set of data.

Assume first of all, that each of the gains in (7.21) is to take the form:

$$K_{ij}(\omega) = \begin{bmatrix} 1 & \omega & \omega^2 \end{bmatrix} \begin{bmatrix} a_0^{ij} \\ a_1^{ij} \\ a_2^{ij} \end{bmatrix} \tag{7.22}$$

Where a defines each of the quadratic coefficients in $K_{ij}(\omega)$ which we want to find. Equation (7.22) can thus be transformed to make the terms a_x^{ij} the subject to be solved, as shown below:

$$\begin{bmatrix} a_0^{ij} \\ a_1^{ij} \\ a_2^{ij} \end{bmatrix} = \left[\begin{bmatrix} 1 & \omega_1 & \omega_1^2 \\ 1 & \omega_2 & \omega_2^2 \\ \vdots & \vdots & \vdots \\ 1 & \omega_{n_{res}} & \omega_{n_{res}}^2 \end{bmatrix}^T \begin{bmatrix} 1 & \omega_1 & \omega_1^2 \\ 1 & \omega_2 & \omega_2^2 \\ \vdots & \vdots & \vdots \\ 1 & \omega_{n_{res}} & \omega_{n_{res}}^2 \end{bmatrix} \right] \times \left[\begin{bmatrix} 1 & \omega_1 & \omega_1^2 \\ 1 & \omega_2 & \omega_2^2 \\ \vdots & \vdots & \vdots \\ 1 & \omega_{n_{res}} & \omega_{n_{res}}^2 \end{bmatrix}^T \begin{bmatrix} K_{ij}(\omega_1) \\ K_{ij}(\omega_2) \\ \vdots \\ K_{ij}(\omega_{n_{res}}) \end{bmatrix} \right] \tag{7.23}$$

Where n_{res} is number gain points to be interpolated, which in the above example is 20. When optimising a fairly high order system such as this one with many random starting points required for evaluation of the true minimum H_2 norm, it is preferential to use parallel computing functionality such as the Matlab function *parfor* due to the length of time it can take single core machines to compute the interpolation function.

The resultant interpolated functions using this procedure can be seen below in Figure 7.9. This figure also highlights the need for the use of some many random starting points in order to compute the correct optimal functions for the controller; especially so for the integral gains K_{14} and K_{15}. Figure 7.10 shows the interpolated gain functions for the second row of $K(\omega)$ in (7.21). The LQR follows the same procedure for the interpolation of its gain scheduled controllers which too presents smooth functions of $K(\omega)$.

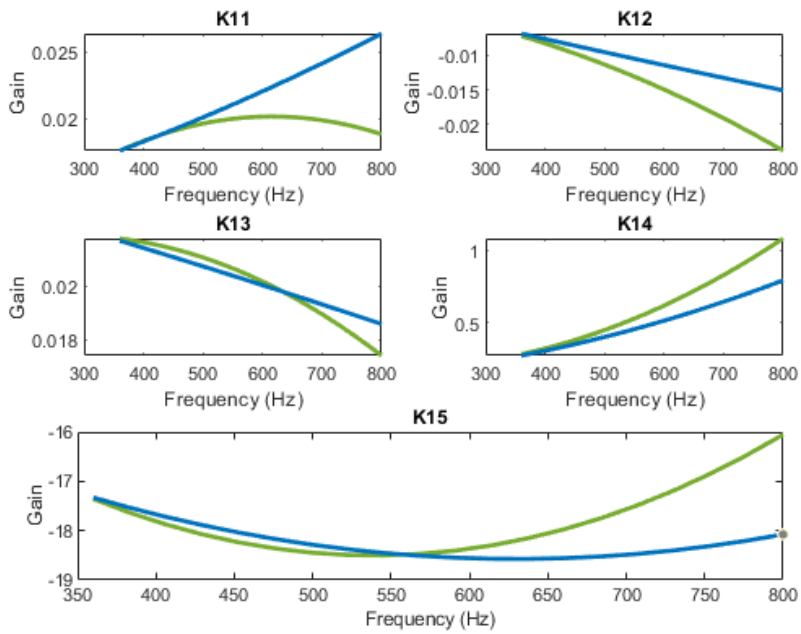

Figure 7.9: The interpolated functions of $K(\omega)_{i,x}$ using Least Square Optimisation procedure defined in (7.23)

Green: 250 point optimisation, **Blue**: 10 point optimisation

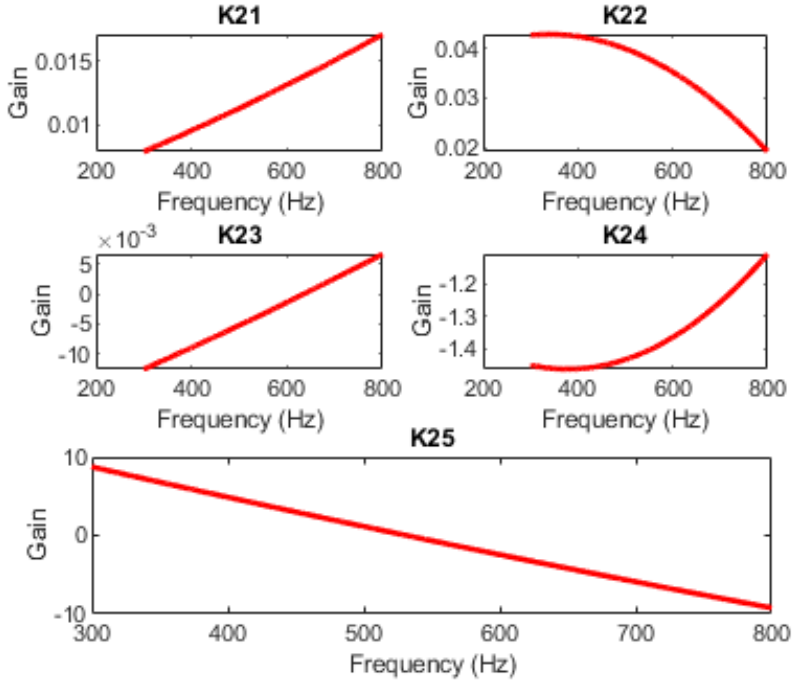

Figure 7.10: Interpolated functions for $K_{2,x}$ using 250 random points and $n_{res} = 20$

Robustness of Interpolated Controller to Parameter Uncertainty

From section 6.3, we have seen that in the expanded form of the H_2 controller, it is not susceptible to failures of other subsystems, and from section 4.3.5 it was shown how the H_2 controller is vastly robust to parametric uncertainties of the system. Now in this regard, the robustness to parametric uncertainties should not change, but interpolating the gain functions offer a new insightful way to observe the overall robustness of the control.

For example, observe Figure 7.11 and 7.12 where each of the parameters of the AFE are changed by $\pm 30\%$ independently, as well as changing all parameters by the same degree for the most extreme case.

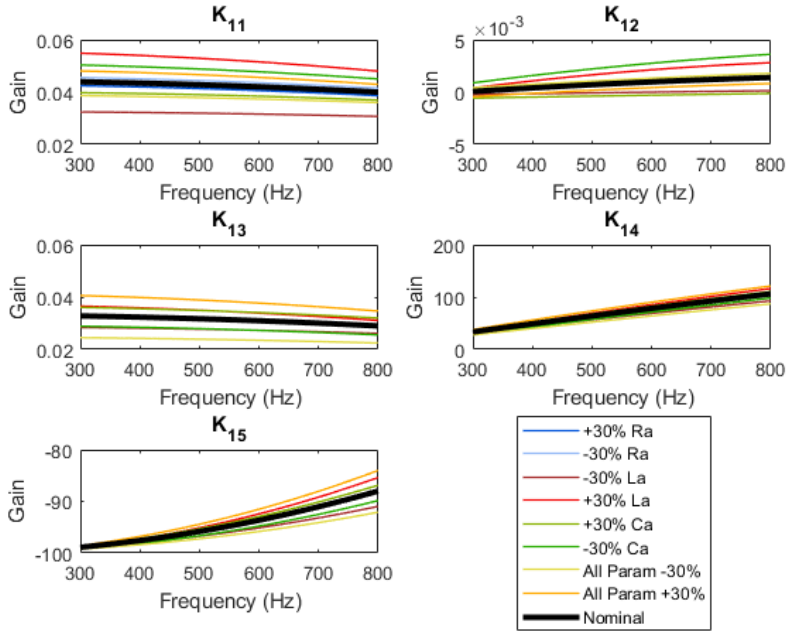

Figure 7.11: The interpolated gain functions for $K(\omega)_{1,x}$ for parameter variations of $\pm 30\%$

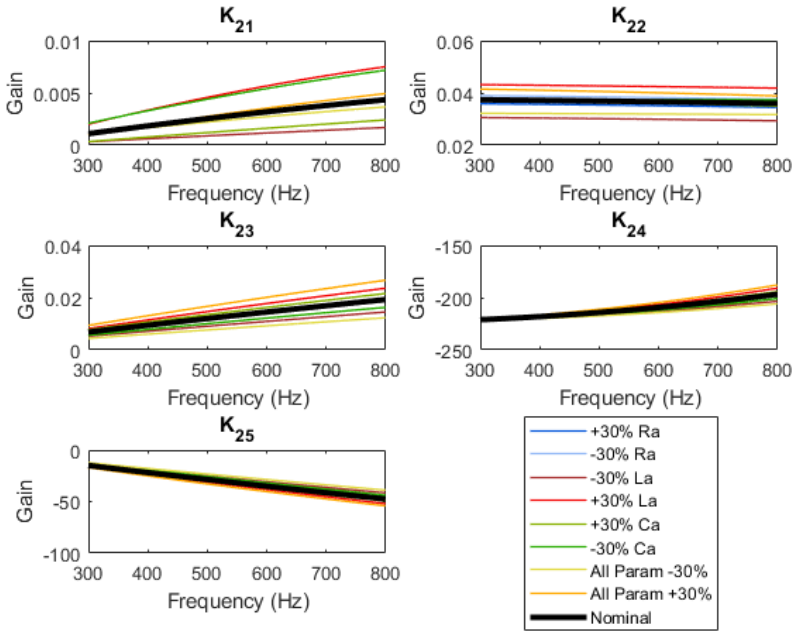

Figure 7.12: The interpolated gain functions for $K(\omega)_{2,x}$ for parameter variations of $\pm 30\%$

What is trying to be shown here is that even under large variations of parametric value, the controller gains remain largely static. The higher the frequency the greater the variation in the controller gains, especially with the larger integral gains. However the relative magnitude of all the

gains does not change vastly with parameter error, where the maximum change from the nominal gain functions being approximately 7% at 800Hz. Even though the electrical systems on aircraft are variable frequency in nature, the aircraft nominally operates at 400Hz, which as can be seen in the above figures shows little variation across all the gains for all parameter variations. This means even with a parameter variation of ±30% the system will remain largely optimal at nominal operation, and close to optimal at higher frequency operation.

7.2 Performance Analysis of AFE converter interfaced to commercial converter using PI, LQR and H_2 Controls

With each of the controllers designed and the H_2 and LQR controllers adapted for variable frequency operation, this section analyses the performance of each controller when operating on the same electrical system.

Firstly, we can compare each of the controls using average modelling to characterise the behaviour expected in the experimental setup. As a reminder, the H_2 and LQR controllers have been designed to have as close a performance to the PI as possible for fairness of the test. Both the LQR and H_2 controllers can run noticeable faster by increasing the weights of the Q_γ matrix.

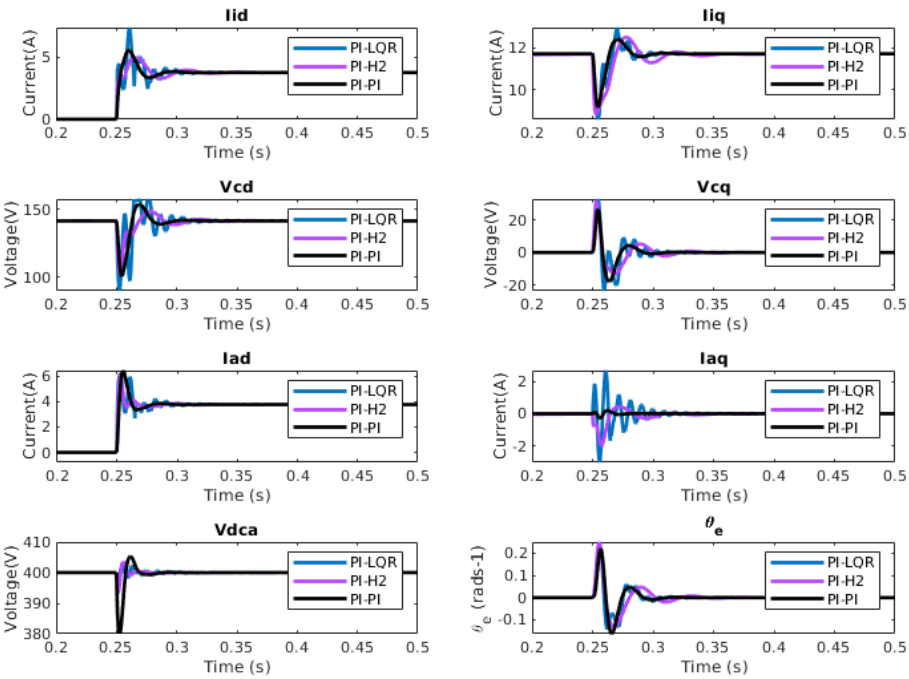

Figure 7.13: **(400Hz)**Average Simulation of the three controllers on a system with a pre-made VSI and the subject AFE being controlled. Subjected to a 800W power step on the DC-Link

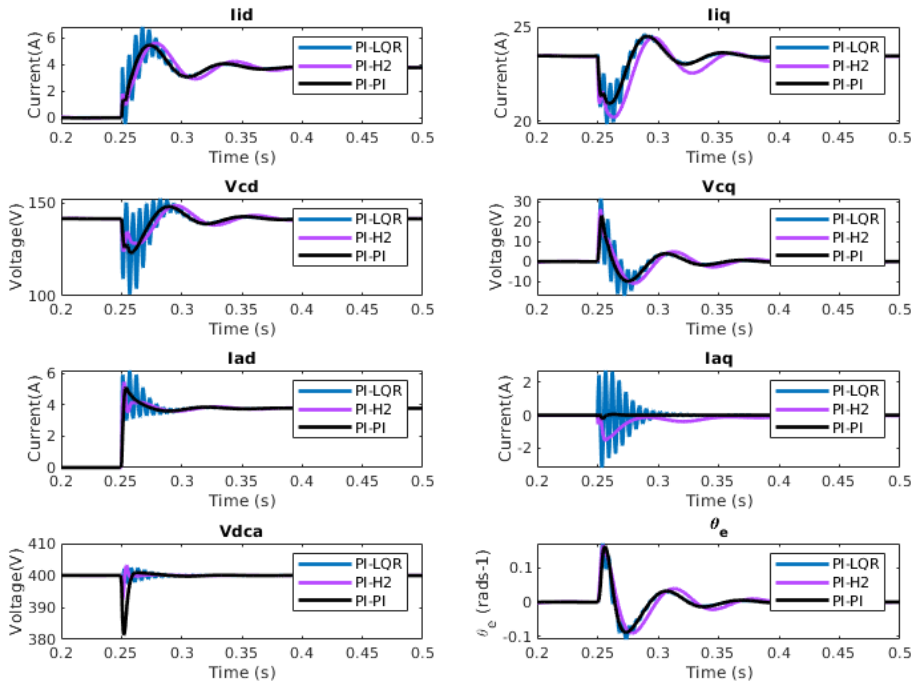

Figure 7.14: **(800Hz)**Average Simulation of the three controllers on a system with a pre-made VSI and the subject AFE being controlled. Subjected to a 800W power step on the DC-Link

From the average results comparison of the controllers it is clear that the H_2 control is able to deliver non oscillatory performance across both the converters, and as expected can largely improve the performance of the AFE states, especially for I_{ad} and V_{dca}. It is fairly clear that optimising the AFE to the closed loop VSI dynamics has allowed for the VSI to operate largely unaffected. As can be seen for the VSI states, I_{id}, I_{iq}, V_{cd} and V_{cq}, they have almost exactly the same dynamic performance between the PI and H_2 results. Therefore the H_2 controller allows the VSI to operate as designed with little interaction, due to the optimization including the closed loop VSI dynamics. The system incorporating LQR control on the other hand shows severe oscillations occurring across all the states. The LQR controller is only locally optimised to the AFE dynamics. Therefore there is no guarantee on the performance of the system and its stability which in this case leads to interactive effects across the whole grid. As we had seen before when designing the PI control, not designing without full dynamics of the global system can lead to poor dynamic behaviour and even instability, even though all systems are locally stable. Increasing or decreasing the bandwidth of the controller can minimise the presence of the oscillations, but will always be present in some form. Refer to the Appendix C for comparative performance of the average model simulations for the LQR controller.

Experimental Results

Confirming the performance of the controllers, each of the controls have been implemented onto the experimental test rig as described in section 4.3.3 with the exact same parametric components. In the simulative results, performance of each controller at each of the two ends of the operable frequency range was tested, and observed that implementation of the LQR control does cause some cross-interaction issues. In this test, the full capability of the gain scheduled control will be tested. The experiment will involve applying the step-load of 800W as the grid is ramping up in frequency between 360-800Hz by changing the DQ rotation frequency in the control platform. This not only enhances the non-linear characteristics of the AFE as much as possible but additionally shows the performance of the PLL to correct the angle back the estimated grid frequency during the ramp, and also performs a good analysis of the converter during dynamic behaviour across large region of operable frequency.

Each test begins with the system being at a no-load steady state condition before the frequency starts to ramp. Once the grid frequency reaches around 570Hz, a 800W CPL load is applied to the DC-Link and the performance of the system is then observed.

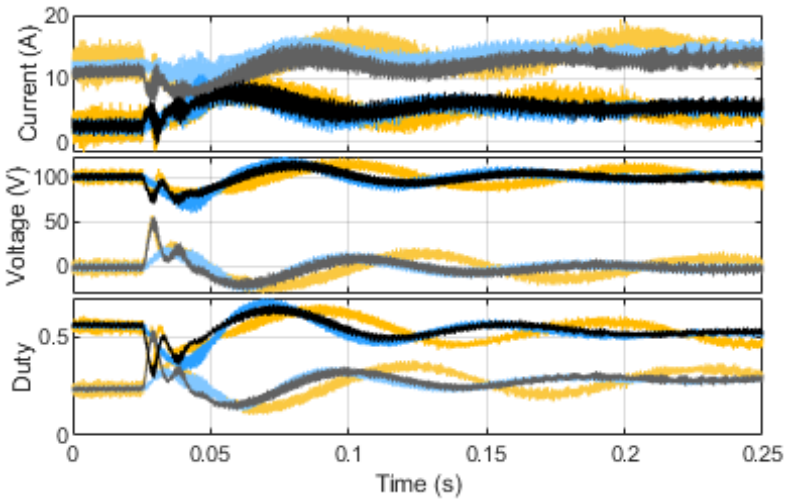

Figure 7.15: VSI Performance of the Variable Frequency Step Load Test
Blue: PI-PI, Black: PI-H_2, Orange: PI-LQR
$I_{a\langle d,q\rangle}$ (Top graph, [d-axis bottom, q-axis top]), $V_{c\langle d,q\rangle}$ Middle Graph (Top and Bottom respectively), $m_{\langle d,q\rangle}$ Bottom Graph (Top and Bottom respectively)

As previously shown through the average model simulations in Figure 7.15, it again portrays that the H_2 largely allows the VSI to operate closely to how it was initially designed for. The H_2 and PI dynamics on the VSI track very close together. Just as we had seen in the H_2 global

optimisation in the previous experiments, the global optimisation of the AFE using H_2 control shows to mitigate interactions on the VSI. In-fact, it could be considered that the performance of the VSI has slightly improved in that the amplitude oscillations are marginally reduced. The LQR also shows good performance when compared to the other two controllers, but is noticeably more oscillatory and once PI and H_2 have settled at their equilibrium values, the LQR continues to noticeably oscillate. This is coherent with the average simulation results where greater oscillation was observed upon load transient.

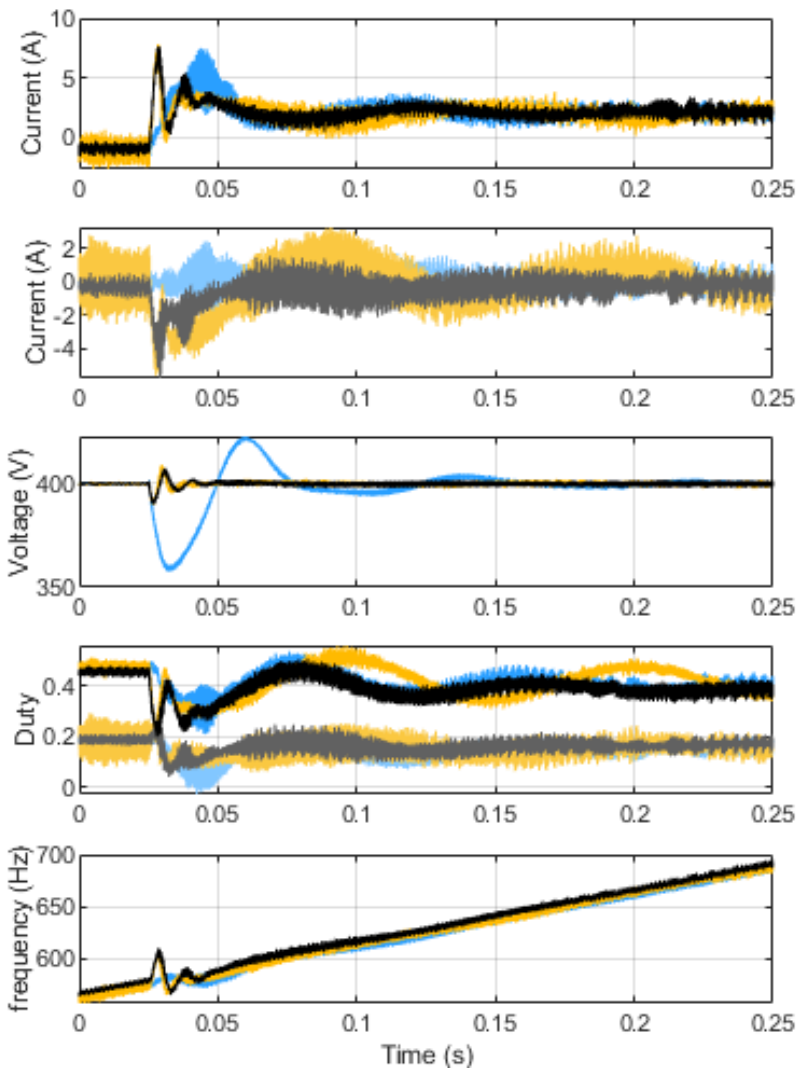

Figure 7.16: Variable Frequency Control Experimental Performance of the AFE

Blue: PI-PI, Black: PI-H_2, Orange: PI-LQR

$I_{a\langle d,q\rangle}$ (Top two receptively), V_{dc_a} (3rd), $p_{\langle d,q}$ (4th, top and bottom respectively), PLL estimated grid frequency

Analysing the states of the AFE performance shown in Figure 7.16, it is clear that the closed loop performance of the H_2 and LQR controllers have almost identical dynamic performance to the disturbance. Both these controllers, as expected deliver far superior performance to that of the PI as has been repeatedly seen throughout this work. Similar dynamic performance for both the optimal controls can in fact been seen across all the states. Although only for I_{aq} is the performance worse in comparison to the optimal controllers.

During the load instant, the PI control on the AFE can maintain I_{aq} relatively steady, when both the H_2 and LQR controls introduce a instantaneous 4A drop. This is likely down to the compensation each of the controllers gives to power the CPL instantaneously. The PI sacrifices the voltage dynamic performance for the current, whilst the opposite occurs for the optimal controllers. According to MIL-STD-704F [150] for which characterises the onboard electrical requirements of aircraft grid, there is more strict conditions on maintaining the voltage within a given envelope, and no requirements on the current. Therefore, even though a large drop in I_{aq} is induced, this dynamic is preferred over drops in voltage in order to meet official regulations on the DC power performance. Overall, the LQR controller does deliver good performance, but due to more oscillatory behaviour induced on the VSI, the AFE states for the LQR controller are noticeably more oscillatory than the proposed H_2 control. Again, this test has shown that the benefits from using the H_2 optimisation improves overall dynamic performance and mitigates cross-interaction across all converters whose dynamics are supplied into the optimisation procedure. It is additionally clear that the interpolated controllers also work incredibly well in ensuring optimal performance across all operable frequencies, where there seems to be no performance impact across many of the states due to the frequency transient, as if its not even occurring.

Now, it is additionally important to gauge how the performance of the controller is at static frequency conditions. Oscillations are smaller at 400Hz as was observed in the average simulation, and greater at higher frequencies. Additionally as was seen in the parametric analysis of the gains, uncertainty is greater at high frequencies. So an additional test undertaken was analysing the performance with the system running at 800Hz.

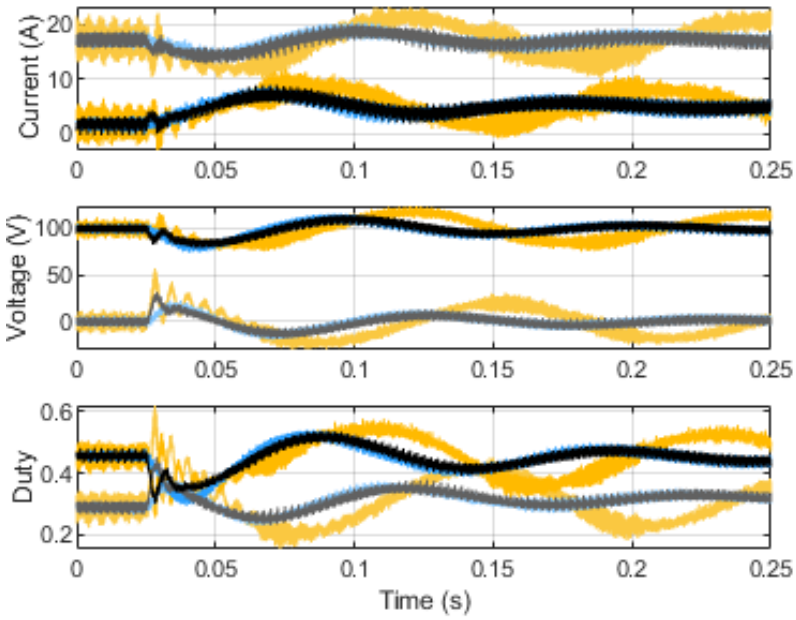

Figure 7.17: VSI Performance of the Variable Frequency Controller at 800W step load at a static 800Hz grid frequency

Blue: PI-PI, Black: PI-H_2, Orange: PI-LQR

$I_{a\langle d,q\rangle}$ (Top graph, [d-axis bottom, q-axis top]), $V_{c\langle d,q\rangle}$ Middle Graph (Top and Bottom respectively), $m_{\langle d,q\rangle}$ Bottom Graph (Top and Bottom respectively)

Again, as was observed in the average simulations and to be expected, the VSI states where the LQR is augmented on the AFE displays sizeable oscillations on the transient event. In-fact, the oscillations appear larger on the experimental setup. The average simulation suggested the majority of the oscillation should occur as the states verge back to equilibrium, although it is clear that the oscillation last a long time afterwards. The H_2 controller again, shows to match the performance of the full PI based control system, confirming that the global H_2 control mitigates much of the interactive effects once more and allows the VSI to operate as was designed.

Analysing the AFE performance in Figure 7.18, due to the interactive oscillations, which the LQR interfaced control system suffers more greatly, the states clearly oscillate about the equilibrium point for extended periods of time. Whilst the H_2 control shows stable, and faster dynamic speeds as predicted for the pole zero map as that observed when compared with the previous experiential test.

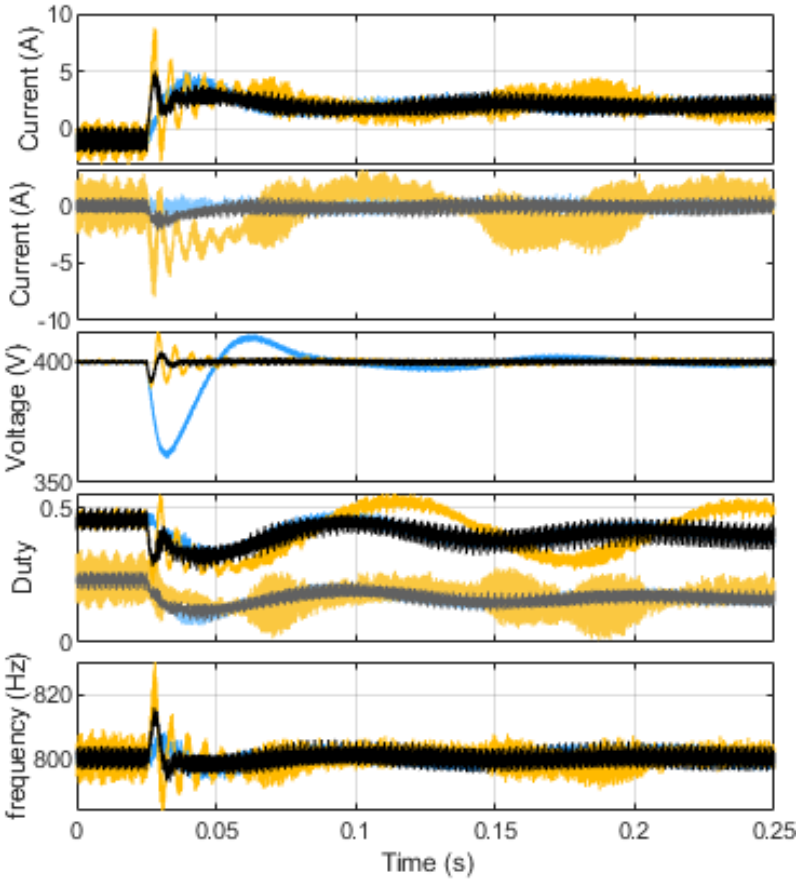

Figure 7.18: Variable Frequency Control Experimental Performance of the AFE for a 800W step load at 800Hz constant grid frequency

Blue: PI-PI, Black: PI-H_2, Orange: PI-LQR

$I_{a\langle d,q\rangle}$ (Top two receptively), V_{dc_a} (3rd), $p_{\langle d,q}$ (4th, top and bottom respectively), PLL estimated grid frequency

It is clear with these experimental results that whilst the design of an LQR controller for this simple grid application, using the H_2 and optimising single converter controls to the rest of the grid system provides improvements in performance on the target converter, as well ensures pre-designed sub-systems can run as has been designed with little interaction. Additionally, even though the optimisation procedure for the H_2 is non-convex, providing a large number of random starting points in order to accurately locate each of the local minimum at each frequency of the systems enables easy interpolation of the controller. The interpolated controller worked as intended providing optimal performance across the full range of frequencies which would be found on current day more electric aircraft. During frequency transients both the H_2 and LQR controls operated as if a frequency transient wasn't occurring at all and especially in the case of the H_2 control provide

optimal and robust performance, whilst still providing interaction mitigation across all subsystems at all operable frequencies.

As per the requirements for variable frequency electrical systems on aircraft, set by the MIL-STD-704, electrical system must be able to cope with frequency variations of up-to 250Hz/s. This was easily achieved with our control where for these tests the frequency ramp was set to 1kHz/s, operating extremely well at more than 4x the required speed.

7.3 Discussion and Summary

This chapter has presented two fundamental additional features which can be attained by implementing the proposed H_2 controller design in MEA micro grid setting.

In this chapter, a hypothesis was taken that in general designers will not have full authority over the full design of the micro-grid on aircraft. More often than not, the converter whose controllers are to be designed are likely to be installed into a system made up of numerous pre-designed commercial converters, who may already have pre-programmed control architectures and pre-design parametric components. An intuitive method has been presented in which an engineer can model all the dynamics of the system and decentralize the resultant controller gains to the states of the target converter in order to synthesise a controller for said converter; which is optimal in operation to the rest of the global system to which it is being installed into. The method is simple to apply as long as the designer has all the relevant information about all the subsystems available. The resultant controller has been shown to mitigate interaction between sub-systems. This was a fundamental feature of the controller that was achieved when developing global control schemes, and this chapter has shown the same characteristics can be attained when optimising single converters to a larger system. A major drawback to this design is the need to know all of the sub-system parameters and controller information in order to develop the control. However, this issue is addressed in the next chapter, where state-space identification techniques can be used to characterise an estimated state-space model of the system to which H_2 control optimisation can then be applied in fairly similar manner to optimise target converter controls in unknown electrical systems.

The second, and most significant contribution of the work presented in this chapter is the adaptation performed to ensure the proposed H_2 controller meets the electrical requirements of modern day MEA variable frequency grids. Previous chapters detailed the method of design for a notional frequency of 400Hz, which although today is still the typical and nominal operating grid frequency of all aircraft, with the advancement of lighter power electronics, today's MEA have incorporated a variable frequency grid topology. In order to keep the optimal and stable

performance across the operational range of modern aircraft electrical systems, an interpolated gain scheduling approach was devised. Considering the H_2 optimization is a non-convex optimisation, it was found that generating enough random starting points to run in the optimisation for sampled frequencies, smooth function of K can be obtained with frequency. Using a Least Square Optimisation in order to approximate the best regression line between of the located gains for each frequency, the H_2 controller can be transformed into a polynomial gain functions with grid frequency as the scheduling term. Although parallel computing may be required for gain computation of more complex systems, the design is fairly simple, with the resultant controller working perfectly as required. The variable frequency adapted H_2 controller was shown to handle a grid frequency ramp transient, and control the states of the AFE as if there was not transient going on at all, and able to achieve well beyond the legal requirements set for variable frequency aircraft grids. Although the analysis was only analysed on a simple grid setup for simplicity in the analysis, following the procedures introduced in Chapter 6 it can be easily applied to larger more complex systems with ease.

Chapter 8

Region of Attraction of Three-Phase Power Systems

Throughout this work, in many different ways, it has been shown how the proposed approach can deliver many benefits to the system in question. For instance, the ability to attain better global performance; attaining cross sub-system interaction mitigation and increased robustness against parametric uncertainty and disturbances. However, with these multi-dimensional non-linear systems it is often a very complicated task to quantify the robustness of a system.

Now robustness is rarely put singularly as a number. Instances where this is the case is for instance the bound γ used to ascertain how robust a certain controller is with regards to the transfer function of signal disturbance to system performance (as shown in Chapter 4). But still, γ does not quantify how robust a system it. It's more a value for which engineers can use to ascertain the controller will be robust from one specific aspect, the aforementioned transfer function.

In order to accurately record the robustness of a system, the notion of a Region of Attraction (ROA) or Domain of Attraction (DOA) are widely used. In this thesis, the term ROA is used. The Region of Attraction is a vector map focussing on an equilibrium point of a system. The map analyses a large set of initial condition points and draws out the vector space from all these points to map whether the trajectories converge to the equilibrium point asymptotically [151]. It is vitally important in the analysis of closed loop non-linear systems to find and analyse these regions to ascertain how far systems can be pushed before stability can no longer be guaranteed. However, the computations for finding these regions can be very costly, and there are also numerous problems with accuracy of these regions as will be shown later in this chapter. There are numerous approaches which can be conducted to attain the ROA of non-linear systems, where each of these approaches can be categorised as one of two classifications, Lyapunov, or non-Lyapunov based

[152].

Typically for Lyapunov based ROA approximations a candidate Lyapunov function is first generated based on the system states, which is used initially to define a small region of points within the n-dimensional space (where n is the number of states in the global system) where asymptotic stability of the chosen equilibrium point is held. Next, approximation methods are used to find the largest sublevel set for this Lyapunov function which is then extrapolated as the ROA of the non-linear system [153].

Non-Lyapunov methods on the other hand could be observed as more a brute force method of locating ROA. Such methods include reverse trajectory methods, where the differential state equations are reversed until the limit cycle of the ROA establishes itself, or a vector analysis, the test if each given point in space naturally wants to decay back into the equilibrium.

A helpful diagram which depicts these current day common approaches to ROA estimation can be found in [8], and is shown in Figure 8.1.

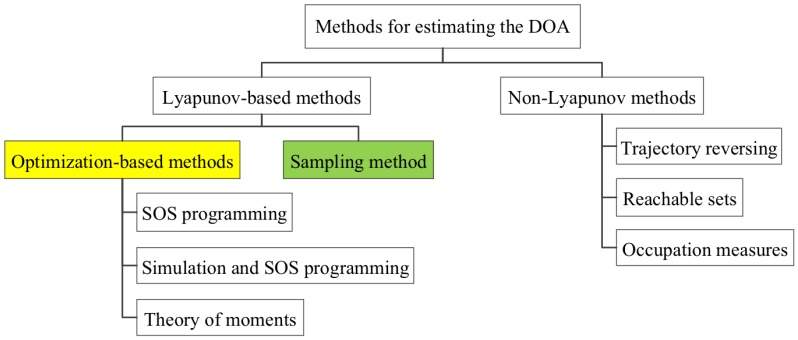

Figure 8.1: Diagram from [8] depicting all the common methods for modern day ROA approximations

Whilst approximating the region of attraction is by no means new in the way of research novelties, the problems investigated in literature in regards to power electronic converter ROA analysis is that often oversimplifications are made to make the analysis easier. But in doing so, the ROA generated is not truly representative of all states of the converter [154, 155, 156, 157]. Much of these works have simplified the system down to a 2D, or a 3D approximation of the ROA, whilst it is well known from the work already presented in this thesis that the AFE converter with controller augmented in closed loop constitutes a 5-dimensional system, and thus a lot of information is lost from the ROA approximations in these works. Though it is understandable, it is hard to present a 5D ROA for these converters as 3D is all that can be possibly perceived in a static frame of reference.

This chapter investigates the method of developing a full 5D representation of the ROA for

the non-linear AFE converter with no simplifications. This work constituted the final part of the research conducted during the time of PhD and unfortunately there was not enough time to fully explore the potentials of these methods. Therefore this chapter is here to present the current development of this research as of today which includes comparison of popular methods of ROA approximation, and how these methods compare to when applied to high order systems.

This research had the aim of trying to envelop ROA approximation techniques into the H_2 controller synthesis in order to develop optimal decentralised controls with maximised stability regions. This is still work that is wished to be investigated in the future but as of now this research is still much in its infancy, and here is presented some of the results received from the short time spend researching in this area.

8.1 Popular Approaches to the ROA Estimation Problem

As it can be imagined, non-linear systems can be very complex to estimate their regions of stability due to the complex shapes of their vector fields, and the problem only increases the more system states there are. In this section, a brief summary of the popular methods of ROA approximation will be shown here. This section will not go into to much mathematical depth as this can be read in currently published articles, but examples will be presented, and the general theory behind each approach will be discussed.

Throughout research of ROA approximation, the Van der Pol (VDP) generator is typically used. Reason being that it is a very simple 2nd order system which has a small enclosed stability region about an equilibrium point $(0, 0)$. Each method shall be presented first using the Van der Pol generator before upscaling to a simple DC electrical system for further comparison before applying it to the closed loop AFE system.

In this section, firstly the popular approaches to ROA approximation shall be presented using VDP oscillator. The approaches considered here are the Lyapunov approaches of Sum of Square Optimisation (SOS), Random Sample Approximation, TS-Fuzzy and the non-Lyapunov approach; the Reverse Trajectory approximation.

All these methods will then be compared against a more practical simplified electrical system of known ROA before being applied to 5D AFE system.

8.1.1 Sum of Square Approximation

The Sum of Square Approximation in literature is one of the most popular methods used in ROA approximation and uses Lyapunov based methods in order to estimate the ROA.

As we had extensively shown in Chapter 3 and 4 the generation of Lyapunov functions are fundamental to the H_2 controller synthesis as if there is a unique solution to Γ which can be computed, it guarantees the given operation point is stable for the given synthesised controller. This is because the Lyapunov function, if stable should hold to the following conditions at this point:

$$\begin{aligned} V(x) &\geq 0 \\ \dot{V}(x) &< 0 \end{aligned} \tag{8.1}$$

What this means is that for a positive semi-definite function Lyapunov function $V(x)$ the selected point must have a negative differential which indicates it is forever decaying back to an equilibrium, and is thus stable. Therefore, about this equilibrium point, which shall be referred to as x_0, the region of attraction can be defined as the region of points in x whereby condition (8.1) is held, as for any positive $V(\dot{x})$ would indicate a trajectory of the state going to infinity and is thus unstable. Also important to note, the Lyapunov conditions in (8.1) can only validate the system stability for equilibriums located at the origin. As for the majority of systems, if the equilibrium is not at the origin, system equations will have to be translated such that the equilibrium is forced to zero for these following analyses. The process in order to do this is shown later on in the chapter.

To clarify understanding of these conditions, a single dimensional example can be presented:

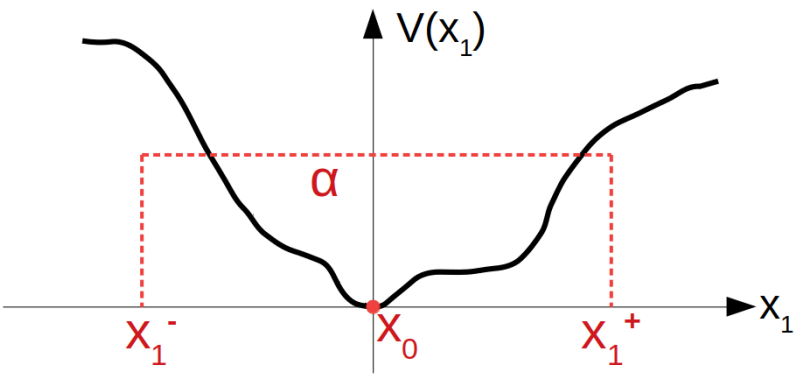

Figure 8.2: 1D state representation of the Lyapunov Function

Suppose a bound α is appied across this function as shown in Figure 8.2, and the conditions which are defined in (8.1) are checked against. If (8.1) is held within the bound then the state can be deemed globally stable, and the points x_1^- and x_1^+ are variations from the equilibrium point x_0 which are ensured to decay back to x_0. If α is increased to an extent that the points x_1^- and x_1^+ no longer hold the conditions in (8.1), this is a region as to where the points will not decay back to x_0 and instead tend towards infinity. These points therefore define the region of stability of the

system, or the region for which points will be attracted back to the equilibrium, hence the name Region of Attraction, and these points will define the ROA of this 1D system.

Increasing the complexity slightly to a 2D system is therefore non-trivial and the same concepts can be applied.

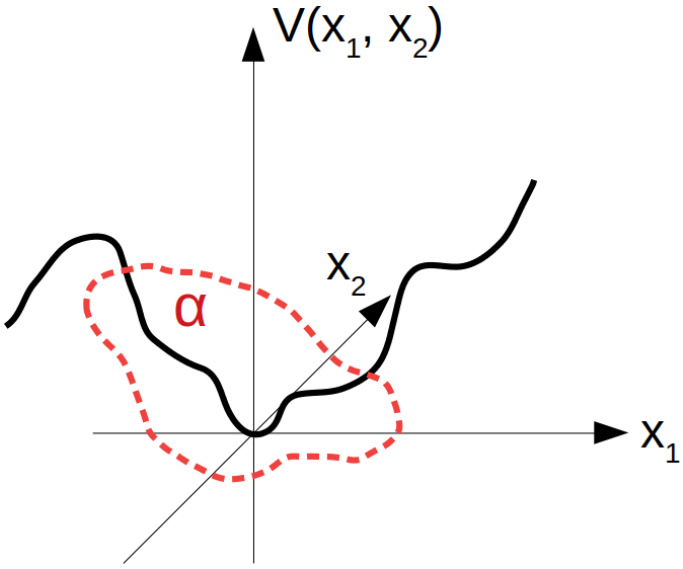

Figure 8.3: 2D representation of the Lyapunov function and ROA bounds

Here, the bound α takes an area in the 2D plane, where the condition set in (8.1) can be checked as was done in the 1D case. This region can then be expanded as before across the two dimensions until the condition becomes invalid which then defines the ROA of this 2D system.

In essence, the methodology consists to check what is the maximum bound α which can be obtained or a given $V(x)$ which holds the condition (8.1) true. Therefore the maximum domain α is the approximation to the system ROA.

But generating a Lyapunov function is not an easy task, and to find one that will provide the most accurate approximation of the ROA is very tough. There are simple formulae which can help construct simplistic Lyapunov functions but typically these functions provide poor approximations for the ROA. These problems can be analysed taking the VDP.

The VDP is a simple 2nd order system which has the following state equations.

$$P_{vdp} = \begin{cases} \dot{x_1} = -x_2 \\ \dot{x_2} = x_1 + (x_1^2 - 1)x_2 \end{cases} \tag{8.2}$$

The limit cycle of this system can be clearly seen in Figure 8.4 represented by the black line.

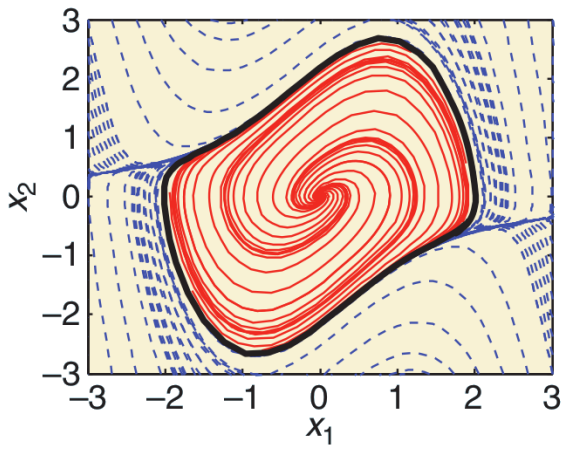

Figure 8.4: The limit cycle of the Van der Pol system. The black line defining the true ROA of this second order system. This image comes from [9]

The easiest procedure in generating the Lyapunov function for any order non-linear system is by evaluating:

$$V := x^T Q x \tag{8.3}$$

where Q is a diagonal positive semi-definite matrix which is a decision variable. Typically though $Q = I$ is selected for the majority of cases. However, with the selection of Q the Lyapunov function changes shape, and as a result can lead to better or worse approximations of the ROA. For instance look at Figure 8.5 where the associated bounds of the approximated ROA for the conditions in (8.1) are given as follows (from [9]):

$$Q = \begin{bmatrix} 1 & 0 \\ 0 & 1 \end{bmatrix} \quad \text{(red)}, \quad Q = \begin{bmatrix} 1 & 0 \\ 0 & 2 \end{bmatrix} \quad \text{(black)}, \quad Q = \begin{bmatrix} 5 & 0 \\ 0 & 2 \end{bmatrix} \quad \text{(green)}$$

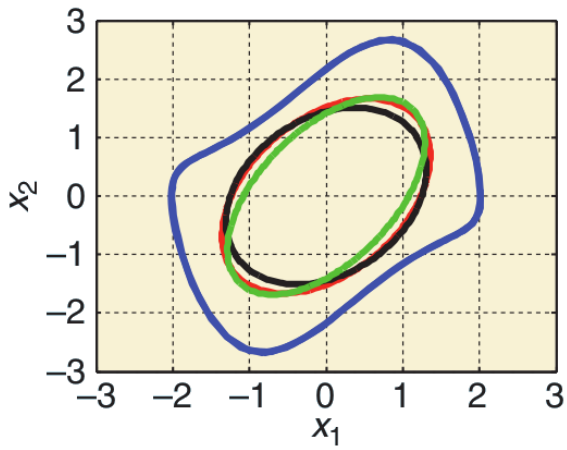

Figure 8.5: Varing limit cycle approximation for varying Q in the Lyapunov function generator [9]

Two problems immediately arise from this. Firstly the question of what Q shapes the Lyapunov best to give the best approximation, and secondly a matter of the Lyapunov function generation. The construct in (8.3) in its current form is elliptical whilst the true ROA is not. Therefore an optimisation needs to take place where the Lyapunov is expanded and increased in order, such that a less elliptical bound of the ROA approximation more closely fits with that of the true ROA. This is where the SOS optimisation comes in.

The core mathematical principles will not be discussed here as they are well documented though many sources in literature [9, 158] .

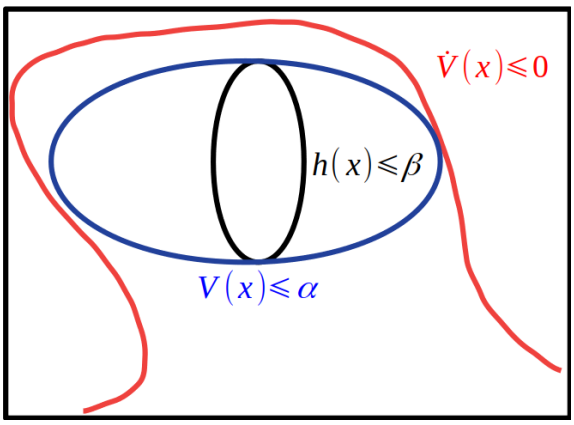

Figure 8.6: Simplified diagram showing how the ROA bound α , and the corresponding shaping functions $h(x)$ and the maximum inner bound of this function as subset of the ROA β are related

The core principles behind the SOS optimisation is to expand and adapt the Lyapunov function from expanding an internal region h from within. Through an iterative process, the Lyapunov can

gradually be reshaped until it is largely at the bounds of the true ROA.

By following the procedure detailed in [159] the following algorithm can be derived for the expansion of Lyapunov approximation of the ROA by SOS.

Step 1 - To start the VS iteration algorithm, first the generation of the initial Lyapunov function needs to be generated through the linearisation of $\dot{x} = f(x) = Ax$, around a known operable equilibrium point, where 'A' is the Jacobian of the state equations $f(x)$. If all the eigenvalues of A all have negative real parts, then a positive definite Γ can be found given a positive definite Q such that:

$$A^T\Gamma + \Gamma A + Q = 0 \tag{8.4}$$

where Γ can then be submitted into the default construct of the Lyapunov function (below) to provide the initial $V(x)$ for the ROA approximation.

$$V(x) = x^T\Gamma x \tag{8.5}$$

Step 2 - Here the first SOS optimisation occurs. Here, $V(x)$ from Step 1 is held fixed, and the maximum α and the associated s_2 are determined via the optimisation:

$$\begin{aligned} &\max_{\alpha,s_2} \quad \alpha \\ \text{s.t} \quad & \\ &-(l_2 + \nabla V(x)f(x)) + s_2(V-\alpha) \in \sum[x] \end{aligned} \tag{8.6}$$

where

$$l_2(x) = \epsilon x^T x \tag{8.7}$$

where ϵ is a very small value, $f(x)$ are the state equations, s_2 is a positive semi-definite polynomial to be found, and α the maximum bound of $V(x)$ which approximates the ROA. The term $\sum[x]$ is the general representation of an SOS function.

In this step, the largest bound α for which the conditions (8.2) are held is computed. The associated s_2 term is synthesised for each test α to ensure the resultant function SOS. Here α is selected through bisection method which is necessary due to the optimisation being bilinear between α and s_2.

Step 3 - Now the aim in this step is to perform the expansion of the internal region, and thus maximize the bound β for the shaping function $h(x)$, as shown in Figure 8.6.

First, keep $V(x)$ and α found form step 2 fixed, perform the following optimisation:

$$\begin{aligned} &\max_{\beta, s_1} \quad \beta \\ \text{s.t} \quad & \\ & -\left[(\beta - h)s_1 + (V - \alpha)\right] \in \sum [x] \end{aligned} \tag{8.8}$$

Here s_1 like s_2 is a positive semi-definite polynomial to be found, and β is the maximum bound of $h(x)$ for the inner estimate of the ROA produced by $V(x)$.

Again a bilinear optimisation problem occurs but is easily solved by fixing a value of β which is selected by bisection method (as previously performed for α) and optimising for s_1, and this find the maximum β for which the constraint in (8.8) and output the associated generated s_1.

Step 4 - Now, from the original $V(x)$ we have found the maximum bound α for which the Lyapunov conditions are held true, and the associated s_2 polynomial. From the previous step, from a user defined shaping function $h(x)$ a maximum bound β is found for which the condition held in (8.8) is SOS, as well as the corresponding value s_1 for this value. In this step, a full optimisation, invoking all the constraints presented in [159] is performed in order to approximate better, more fitting Lyapunov function, which can be of higher order if so requested by the user.

$$\begin{aligned} &\text{find} \quad V \\ \text{s.t} \quad & \\ & V(0) = 0, s_i \in \sum [x], \beta > 0 && (1) \\ & V - l_1 \in \sum [x] && (2) \\ & -\left[(\beta - h)s_1 + (V - \alpha)\right] \in \sum [x] && (3) \\ & -(l_2 + \nabla V(x) f(x)) + s_2(V - \alpha) \in \sum [x] && (4) \end{aligned} \tag{8.9}$$

Here V is the only decision variable in this step, and if a better approximation can be evaluated, V is output, and the iterative process can commence starting from **Step 2**. This can be repeated until either a better approximation can not longer be found, or the computed $V(x)$ is accurate enough.

Using the VDP we can get the following results, where Figure 8.7 shows the result from just running **Step 2** a single time, which shows when compared with the limit cycle shown in Figure 8.4 how inaccurate it is.

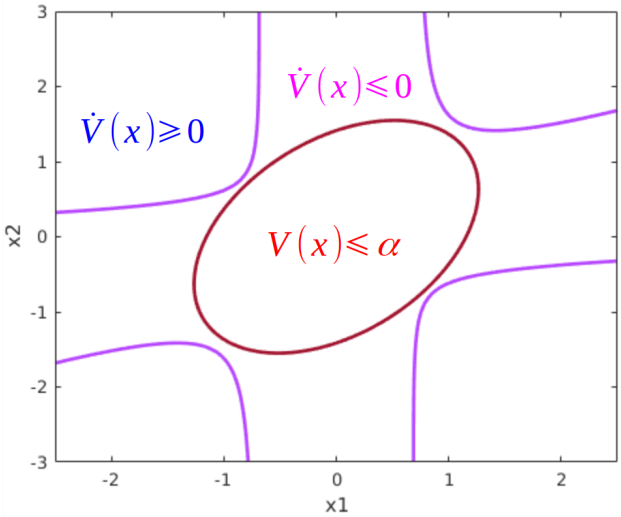

Figure 8.7: Initial computed SOS region of VDP with a $Q = I$ computed using only Step 2 of SOS optimisation region

Employing the VS optimisation method described above and the expansion can be observed from the figure below:

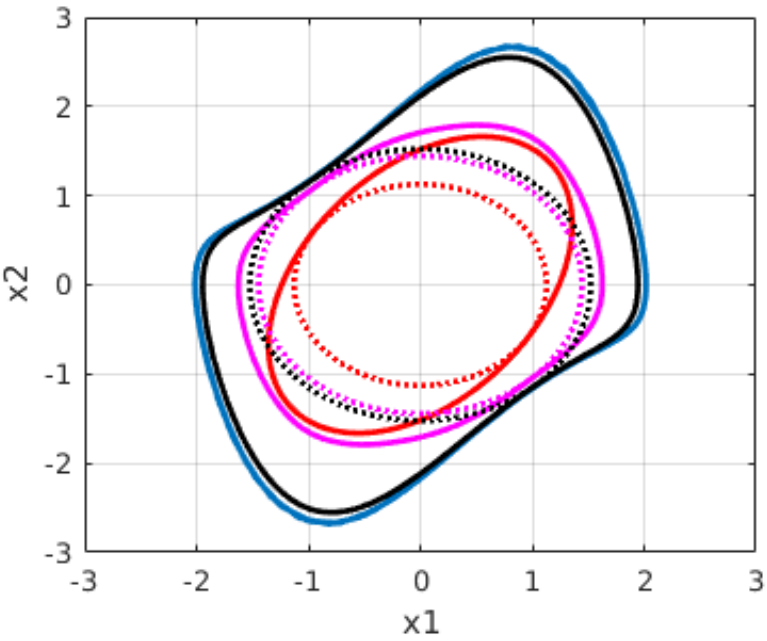

Figure 8.8: VS Iteration expansion of the Lyapunov approximation of the VSP ROA

The solid line of each colour represents the approximated ROA (the region of $V(x)$ bounded by α which guarantees stability), and the dashed line represents the inner expansion of the shaping

function $h(x)$ bounded by β. For simplicity, the shaping function was set to be:

$$h(x) = x_1^2 + x_2^2 \tag{8.10}$$

Although for more complicated system, $h(x)$ may have to be a function which orientates the bounded ellipse to the predicted extremities of the ROA of the system, to align the Lyapunov more accurately.

The different colours represented are described below:

Blue - This is the true ROA of the VDP Oscillator. The region to be approximated.

Red - This region is the first initial approximation given by the first iteration of step two. These regions are exact to that presented in Figure 8.7.

Purple - This represents the 10th iteration of the VS algorithm, where $V(x)$ is now forced to be 4th order to move ROA approximation away from an ellipsoid. Previous estimation was a 2nd order Lyapunov function.

Black - This represents the 30th iteration of the VS algorithm using a 4th order Lyapunov.

The SOSOPT toolbox [160] using SeDuMi Optimizer [161] was used to produce the results presented, with the software script used presented in Appendix D.1.

As it can be seen, it does take many iterations of the algorithm to obtain a relatively accurate approximation of the ROA, with each of the steps optimisations being quite a mathematical challenge. For this reason, this optimisation procedure can result in relatively accurate approximations of the ROA, given a good shaping function is provided, at a cost a long computing time. This optimisation took a total of 302.42s on a Intel i7-7700HQ processor, which is quite long considering this is only a simple second order system.

8.1.2 Random Sample Approximation

Another popular method which utilises Lyapunov functions is the Random Sample approach. This method is a lot faster, and in essence a far simpler approach to the ROA approximation than performing SOS optimisation. This method originated from the paper [8] and the methodology of this paper will be briefly described here taking the example again of the Van der Pol oscillator.

Much of the fundamental theories behind this algorithm is shared with that of the SOS, where

a Lyapunov function which is based on the states of the system is generated, and the aim is to contain a region in the space $\Re^n$ where the conditions described in (8.2) is held. However it directly addresses two problems that are associated with the SOS procedure.

The first problem which occurs with the SOS optimisation is that due to the condition imposed in Steps 2-4 require the constraints to be a Sum of Squares polynomial, which limits the function that can be submitted into the algorithm to be non-rational functions. For the VDP this is not an issue at these system equations are represented in polynomial form. For the AFE equations, rational terms are present which poses some issues, although a work around will be presented in a later section. The second, and most problematic is the length of time the SOS optimisation takes. An optimisation which takes 5 minutes for such a simple system as the VDP will take huge amounts of time for larger order systems for ROA approximation. This approach focuses on speed of the optimisation over ROA accuracy.

In summary, let suppose for simplicity that the initial Lyapunov function as was used for the SOS optimisation, (8.5), is selected for this example. Therefore, the ROA to be approximated by this method is that presented in Figure 8.7.

This approximation method is incredibly simple to perform as it deals with selecting random samples of $x \in \Re^n$ and testing whether it meets the following conditions:

$$\begin{aligned} \dot{V}(x_i) &\leq 0 \quad (i) \\ V(x_i) &< \hat{c} \quad (ii) \end{aligned} \tag{8.11}$$

$\hat{c}$ defines the maximum bound on $V(x)$ for which (i) was found to hold true. In this case, $\hat{c}$ can be seen as α from the SOS.

To start the derivation of the random sample algorithm, we have the variables which represent the upper bound approximation $\bar{c}$ set to ∞; and the lower bound approximation $\underline{c}$ set to 0.

Assume now a random point in space x_i is selected, and will be tested according to the bounds:

$$\begin{aligned} \dot{V}(x_i) &< 0 \\ \underline{c} < V(x_i) &< \bar{c} \end{aligned} \tag{8.12}$$

If it meets these bounds which suggests the point is a decaying point in the Lyapunov function, then the lower bound of c can be set to:

$$\underline{c} = V(x_i) \tag{8.13}$$

Otherwise, if it was found that $\dot{V}(x_i)) > 0$, this indicates an un-guaranteed stable point and the upper bound can be brought to $\bar{c} = V(x_i)$.

A new random point x_i is then selected, and tested again against the bounds in (8.12), and dependant if it meets the conditions or not, gradually brings the bounds of $\bar{c}$ and $\underline{c}$ closer together until this bound converges with the best estimate of the bound which forms the ROA.

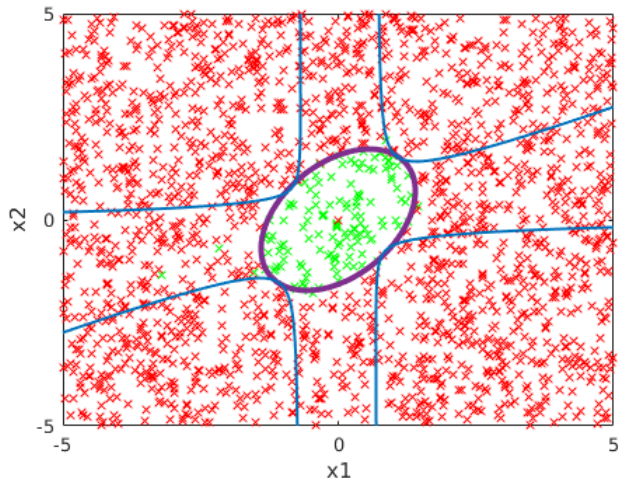

Figure 8.9: Result of the Fast Sample ROA Approximation. Red points mark points that did not meet the bound in (8.12) and green, those that did

The result is very clear and forms an estimate of the ROA as was obtained from SOS in Figure 8.7.

In comparison of the computation times, the Random Sample approach takes 0.22s whilst SOS using SOSOPT takes 0.55s so is more than twice as fast for the same approximation, which becomes more greatly noticed for higher order systems such as the AFE under investigation.

As previously mentioned however, using the basic Lyapunov construct used in this example will only give elliptical approximations and thus always a poor approximation of the true ROA of non-linear systems. This can however be solved using Maximal Rational Lyapunov functions which take the form of:

$$V(x) = \frac{N(x)}{D(x)} = \frac{\sum_{i=2}^{\infty} R_i(x)}{1 + \sum_{i=1}^{n-2} Q_i(x)} \tag{8.14}$$

These functions can be constructed following the optimisation presented in [162], and with this better approximations of the ROA can be yielded within the exact same optimisation time. For instance, the below figure shows the result from the study [8] of using rational Lyapunov functions for better estimations of the VDP ROA.

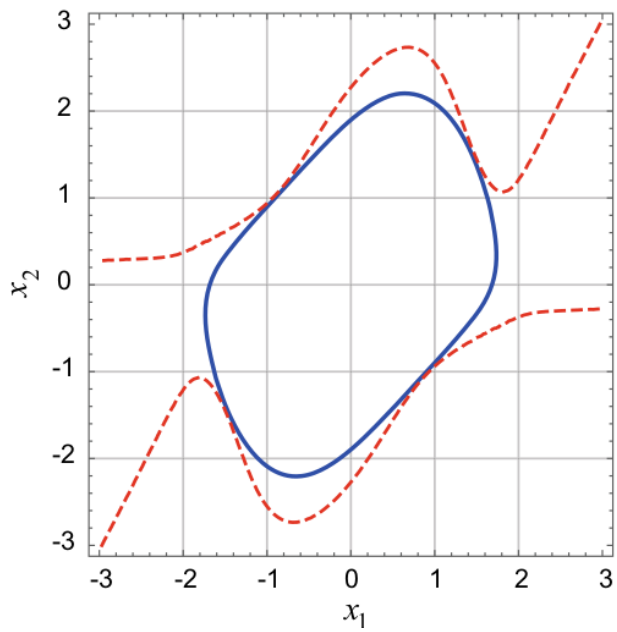

Figure 8.10: Result of Fast Sample Approximation using Maximal Rational Lyapunov Functions from study [8] presented better approximations can be made through previously documented Lyapunov construction techniques

8.1.3 Takagi-Sugeno Fuzzy Logic Region of Attraction Approximation

So far two of the most common methods of ROA approximation using Lyapunov based theories has been presented. Now, as has been observed in these approaches, they are completely reliant on the construction of a Lyapunov function which is accurately modelled around the true limit cycle of the system. As shown through the SOS method which delivers the best approximation, this is a long and computationally heavy approximation to perform. On the other hand, Fast Sample method approximates the ROA for a given $V(x)$ much faster, but can be quite inaccurate with respect to the true ROA. The problem in general stems from the Lyapunov itself, and thus a few numerical methods have been devised which moves away from the Lyapunov or use it in an alternative way.

One such method, which is by far the most popular method of these alternative approaches is what is known as the Takagi-Sugeno method, or more widely referred to as; the TS-Fuzzy Approximation. The notion of fuzzy logic should be familiar to control engineers, and if is understood, the approach to the approximation is very similar in process to that of the fuzzy-logic controller operation itself, where strict rules are set on the controller, and based on a given condition of the system, certain actuations are performed. However in this case, the rules are set strictly to

check the stability of the system at a given condition, and stability is checked globally. When an unstable system condition is detected, this shows the limit of the system. As was discussed before as part of the H_2 controller theory, it is known when a system is stable, when a unique solution to W can be found for the Lyapunov constraint:

$$A_i^T W + A_i W < 0 \tag{8.15}$$

where

$$W < 0 \tag{8.16}$$

and is symmetrical.

Now whilst a Lyapunov is still being used here, it's being used in a different way to verify the region of attraction. Instead of using the multidimensional shape of the Lyapunov function to size an estimate, the Lyapunov here is instead used to determine if a given test operating point is inherently stable. Much like how a Lyapunov is used in the H_2 synthesis; to test if the desired operating point is inherently stable before controller synthesis.

To put simply how the ROA is estimated using the TS-Fuzzy approximation firstly lets start with the Jacobi matrix of the VDP (equivalent to the A matrix in state-space).

$$A_{VDP} = \begin{bmatrix} 0 & -1 \\ 2x_1x_2 + 1 & x_1^2 - 1 \end{bmatrix} \tag{8.17}$$

It is known for a fact that the VDP has an equilibrium point at $(0, 0)$ and therefore, submitting this point into A_{VDP} and solving for the Linear Matrix Inequality (LMI) with the constraints defined in (8.15) and (8.16), then due to the system being stable at this point, a W should be evaluated.

Now, to evaluate the stability using the above constraints, the values of both x_1 and x_2 can be increased by a small amount δ, and the system again re-evaluated using all the combinations of $\pm x_1$ and $\pm x_2$ to see if a W can be uniquely solved. All these possible combinations of x_1 and x_2 are held in matrices A_i where $i = 1 \rightarrow 4$. When the LMI becomes unfeasible the resultant Lyapunov using W_{N-1} is the candidate Lyapunov to approximate the ROA, where the bound is drawn up by the region as to where the extremity in either x_1 or x_2 is held at point of infeasibility.

The algorithm therefore the the TS-Fuzzy approximation is as follows:

Algorithm 1: TS-Fuzzy ROA Approximation

Result: Unqiue W at maximum stabilty bound

Translate equilibrium point $x_n \leftarrow 0$;

Set $x_{1P}, x_{2P} = 0$;

Set $x_{1N}, x_{2N} = \delta_1, \delta_2$;

Compute A_i for $i = 1 \rightarrow 4$;

Check feasibility of (8.15) and (8.16);

while (8.15) *and* (8.16) *are feasible* **do**

  Set $[x_{1P}, x_{2P}] = [x_{1N}, x_{2N}]$;

  Enlarge ROA test region by $[x_{1N}, x_{2N}] = [x_{1N}, x_{2N}] + [\delta_1, \delta_2]$ Recomute new A_i for $i = 1 \rightarrow 4$;

  Check (8.15) and (8.16);

end

Estimate ROA using $[x_{1P}, x_{2P}]$

.

From [156] it can be shown that by following similar procedure, the ROA bound $\mathcal{J}$ is contained as follows:

$$\mathcal{J} = \{x \in \Re^n || b^T x| < r = max(x_{iP})\} \tag{8.18}$$

where $b = \begin{bmatrix} 0 & 1 \end{bmatrix}^T$, and $max(x_{iP})$ defines the maximum value between x_{1P} or x_{2P} at point of infeasibility. The largest $\mathcal{J}$ set in the Lyapunov function $V(x) = x^T W x$ can therefore be found as [156]:

$$\min x^T W x = \frac{r^2}{b^T W^{-1} b} \triangleq \tau \tag{8.19}$$

where the ROA is now defined as $\Omega_\tau = \{x \in \Re^n | x^T W x < \tau\}$

As a result, for the VDP the following ROA can be evaluated using the above algorithm, where a maximum stable point evaluated was $x_{1P} = 0.25, x_{2P} = 1.58$.

Unlike the approach presented in [156], when dealing with two or more states in the Fuzzy rules, the selection of δ becomes the critical point in enlargement of the Lyapunov. States which are known to be more inherently stable than another should have larger δ attributed. In this way, the ROA bound τ becomes more representative of the true bound of the system, instead of being restricted by the more attributing state.

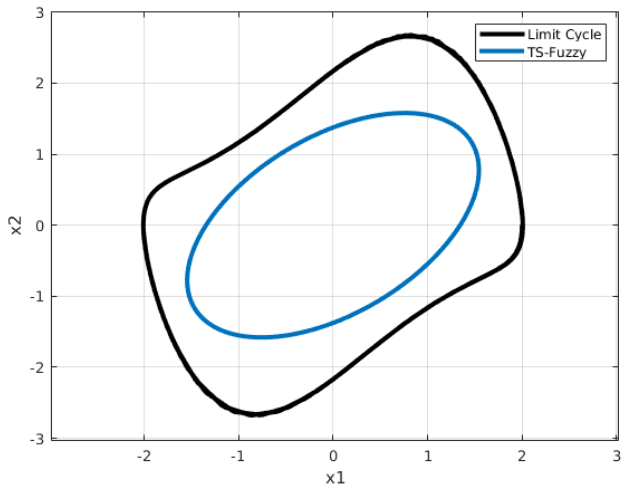

Figure 8.11: Approximated ROA using TS-Fuzzy Approach on VDP Oscillator

Again, the major problem which occurs in this type of optimisation is due to the fact that the Lyapunov candidate is stuck as a second order function which can only give elliptical approximations. As is already clear with the other approaches to the approximation, this is not entirely accurate. Although compared with the previous Random Sample approximation, TS-Fuzzy can deliver larger ROA approximations even when using more fundamental Lyapunov equations. The MATLAB script for this approximation is given in Appendix D.2.

8.1.4 Reverse Trajectory Limit Cycle

Now, we have seen three popular approaches to ROA approximation which all rely on the Lyapunov properties. They all have their pro's and con's but ultimately the major con among all of them is that they are highly inaccurate. All have noticeable dispensaries and therefore if very accurate results are required then these approaches may not be sufficient, but are still very effective at quantifying the robustness of the system.

However, there is a simple, and fast way, known as the reverse trajectory method, which can be performed which can deliver very accurate limit cycles, at the cost of not being able to quantify a robustness to a given closed loop system. This is more for visual analysis.

The name of the method is self exoplanetary to its operation. Typically, when analysing a given points stability, we want to ensure that the trajectory it follows as time goes to infinity is towards the equilibrium point. If it's anything otherwise it would in general be considered unstable.

Taking the VDP as an example, and three starting points within the known ROA, we can see that each of these points through time decays down back to the equilibrium at $(0, 0)$ in Figure 8.12. An additional point is shown going to infinity when outside this region.

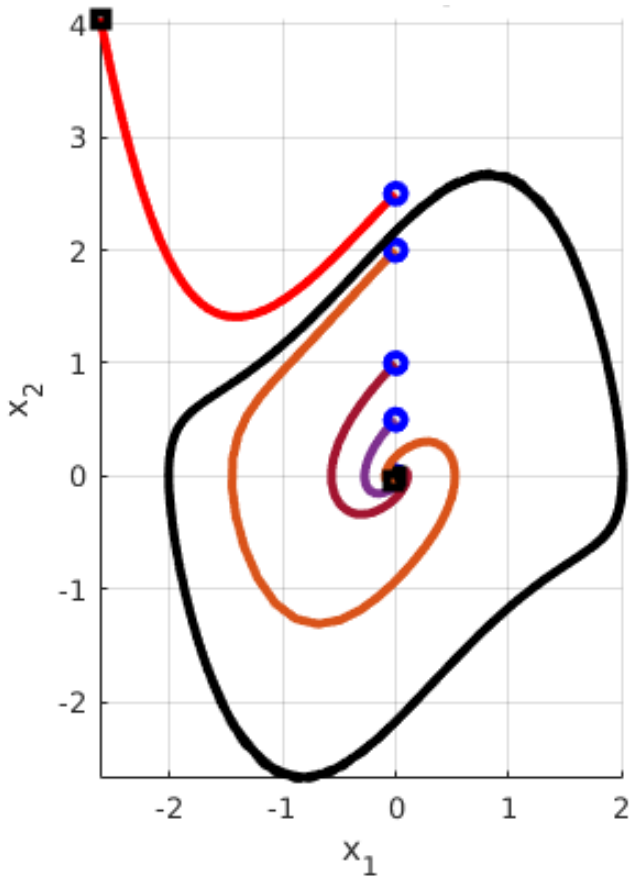

Figure 8.12: The trajectories of four points about the VDP limit cycle

Now, we can in turn analyse the reverse of this trajectory, from $(0, 0)$ backwards. Following this reverse trajectory, it is not possible for this trajectory to go into a region of instability, as this would signify unstable points can eventually decay to equilibrium; this is mathematically impossible. What this trajectory instead does in this case is track the absolute bounds of the stability region of the system, and thus the real and true ROA of the system. In fact, for each of these figures where the limit cycle is shown (Figures 8.8, 8.11, 8.12) had been evaluated by using a reverse trajectory simulation. These are incredibly easy to perform as all it requires is the system equations, invert their differentials and to plot the points the trajectory traces after a significant amount of time. The MATLAB script in order to perform this for the VDP is only 5 lines long at most, is very fast and extremely accurate, as shown below.

```
[t, y] = ode23(@VDP, [0 100], [2; 0]);
plot(y(:,1),y(:,2), '-k', 'Linewidth',3)
function dydt = VDP(t,y)
        dydt = -[-y(2); y(1) + (y(1)^2 - 1)*y(2)];
end
```

So why discuss all the different approaches for approximating the ROA design when simply a Reverse Trajectory can do get a completely accurate ROA very efficiently?

Well, if it is desired to augment an ROA expanding algorithm within the H_2 controller synthesis, a quantifiable measure of the ROA is required, which the three other algorithms provide. Additionally, accuracy is not everything in this regard. For if many closed loop controllers are analysed with the same Lyapunov structure, the larger the approximated ROA, the more robust that system is going to be, and as such precise approximation is not necessary for the quantification of robustness.

However, analysing literature in this field in the aspect of power electronics, there has not been much research in regards to a full comprehensive study into the full stability of high order systems. Typically, any power electronic system which in closed loop is higher than 3rd order is typically simplified down in some way to make the analysis easier [155, 156, 157, 163, 164, 165].

So it was proposed to attempt to investigate two problems using this prior understanding to ROA approximation. Firstly, what is the best quantitative approach for high dimensional systems for integration to the optimal control synthesis in single converter applications; and a study in the visual analysis of stability of optimally controlled power electronic converters.

To reiterate, the research presented in the rest of this chapter is incomplete due to PhD project time, and serves the purpose of presenting prior work made in this area such that if desired someone can follow up on the current work made.

8.2 ROA Approximation to Electrical System Applications

Before we apply to the closed loop controlled AFE converter, it is thought best to perform a comparison of all the test performed on a simplified DC electrical system which in itself is inherently stable. The example presented her will show methods of adaption of the system equations such that SOS can be applied, and additionally observe how each of the methods behaves when applied away from the classical VDP model.

8.2.1 Application of ROA methods on simple DC electrical system

Typically for the majority of systems, the equilibrium point of the system is not generally at (0,0) and therefore translation of the system states needs to be performed, to move the equilibrium point to this location,so that the aforementioned methods work correctly.

The electrical system is a standard DC source, with a inductor and resistor in series, and capacitor across the terminals.

The state space equation of the system is:

$$\begin{cases} \dot{x_1} = -\frac{x_2 - V_g + x_1 R}{L} \\ \dot{x_2} = \frac{x1}{C} - \frac{P_0}{C x_2} \end{cases} \tag{8.20}$$

The equilibrium points for this system can this be found to be:

$$\begin{aligned} \bar{x_1} &= \frac{\frac{V_g}{2} - \frac{\sqrt{V_g^2 - 4P_0 R}}{2}}{R} \\ \bar{x_2} &= \frac{V_g}{2} + \frac{\sqrt{V_g^2 - 4P_0 R}}{2} \end{aligned} \tag{8.21}$$

Where the values used in the examples which will be discussed here are as follows:

Parameter	Value
R	90mΩ
L	230μH
C	100μF
V_g	290V
P_0	1kW

Table 8.1: Parameters of the simplified DC system defined in (8.20)

As was previously mentioned, in order to evaluate the ROA for a given equilibrium point using Lyapunov theory, the equilibrium point of the test system must be set to the origin. Therefore, to translate (8.20) to have an equilibrium at this point, a simple change of the states is all that is required such that the state equations now become:

$$\begin{cases} \dot{x_{1s}} = -\frac{(x_2+\bar{x_2})-V_g+(x_1+\bar{x_1})R}{L} \\ \dot{x_{2s}} = \frac{(x_1+\bar{x_1}}{C} - \frac{P_0}{C\bar{x_2}}\frac{x_2}{x_2+\bar{x_2}} \end{cases} \tag{8.22}$$

Where x_{1s} and x_{2s} are the new states used for the translation.In f_3 the fractional non-linearity is translated as in example (8.23) to properly account for the shift in equilibrium point [155, 156]. An additional point to note is that when transitioning the system to anew equilibrium state when the non-linearity result from the division of a state, as is the example in (8.20) where $\frac{P_0}{Cx_2}$ can be seen. In order to properly account for the shift to a new equilibrium point within the state-equation for such terms requires the following manipulation:

$$\frac{P_0}{C\bar{x_2}}\frac{x_2}{x_2+\bar{x_2}} \tag{8.23}$$

as is shown in (8.22) [154, 156]. With the new equilibrium point now at $(0, 0)$, this means that for any approximated ROA shown graphically, it represents the bounds for which a given state can vary or shift from its equilibrium value before stability can not longer be guaranteed. For example, if the point $(10, 0)$ is shown to be within the stability region, then it is guaranteed if x_1 during operation suddenly shift in value by 10, the system will fall back to equilibrium. However, if $(20, 0)$ is not in the ROA, this point is not guaranteed to be stable, and the user should refrain from the system operating so high, or to redesign the system if that is not possible scenario for the application.

Now, as it may be recalled, there is a problem with the form in the model (8.22) with the fact that $\dot{x_{2s}}$ is not in polynomial form, due to the $((x_2+\bar{x_2}))^{-1}$ term. Therefore, this form cannot be applied successfully to the SOS optimisation.

When problems such as these are faced, in particular trigonometric terms, a Taylor series approximation can be utilised to develop a polynomial approximation of the rational terms [166]. However, this is more suitable for states where small predicted actuations may occur. Therefore, signals such as the voltages or currents, where significant transients could occur, the accuracy of the Taylor Series is limited. High order Taylor series functions can be used for better approximations, however, this can seriously complicate the ROA approximation computation time, especially in the case of SOS, where optimisation has to process multiples of several 20-order polynomials.

A much simpler solution is available for non-trigonometric rational functions. The problem term in the SOS optimisation is $\nabla V f(x)$ and was found in [167] that simply multiplying the problem

term across all of $\nabla V f(x)$ will remove the rational polynomial problem, whilst still approximating the ROA to the same accuracy.

Simply then, to allow for SOS approximation of this system only only needs to perform the following multiplication, each time the differential of the approximated Lyapunov term is evaluated:

$$\nabla V \hat{f}(x) = \nabla V f(x) \times ((x_2 + \bar{x_2}))^2 \tag{8.24}$$

Squared is required because we do not wish to fully eliminate the term from the state $\dot{x_{2s}}$. This was first tested using the VDP by multiplying x_1^2 and x_2^2 on its equivalent $\nabla V f(x)$ term, and was shown to approximate precisely with no change in the ROA approximated area using SOS.

Important note when applying this into software

In MATLAB 2019b which is current release as of writing, a small workaround needs to be performed when utilising the Symbolic toolbox and performing the action in (8.24). If the transformation factor which is being multiplied ($\bar{x_2}$) is not an integer the toolbox tends to express this term as a fraction symbolically. Directly multiplying (8.24) tends to therefore leave polynomial factors in the solution and not expand the equation multiplication correctly. To fix this in MATLAB, one first needs to perform $expand()$ on the computed expression of $\dot{V}$, perform the multiplication, and then $simplify()$ the expression to get the correct output. It is not known if this is a software glitch within MATLAB itself.

```
for i = 1:length(vars)
        v_dot = v_dot + diff(v,vars(i))*f(i);
end

v_dot = expand(v_dot);
v_doty = v_dot;
v_dot = v_dot*(x2+x2s)^2;
v_dotx = v_dot;
v_dot = simplify(v_dot);
```

This code is the process required to do this. Where v is the current Lyapunov expression in software, either defined or solved by step 4 of the VS algorithm. $vars()$ is an array of all the states of the system and $f()$ contains all the state-space expressions.

With this adaptation allowing for the SOS optimisation to be performed on a intrinsically non-polynomial system, each of these approximations can be applied to this basic electrical system,

where the following approximations can be made:

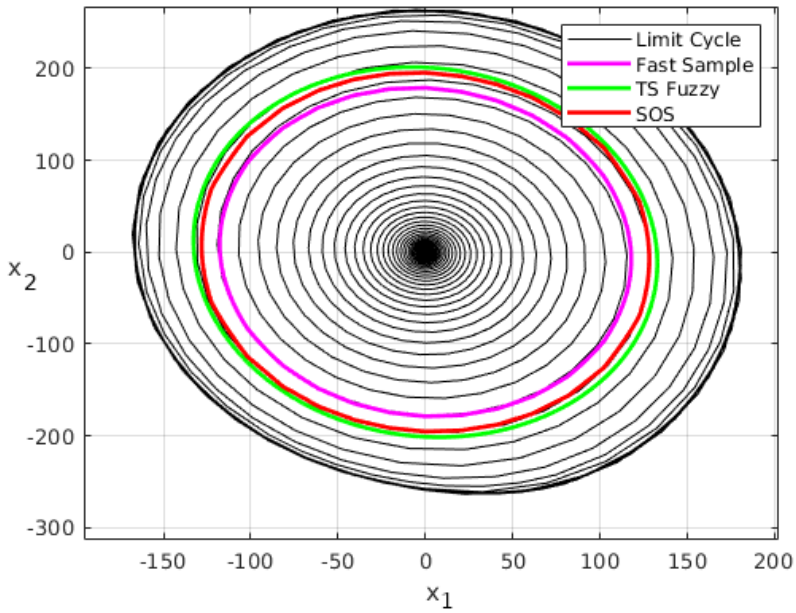

Figure 8.13: Comparison of the best approximations made with the three main approximation methods, and reverse trajectory limit cycles on the system (8.22)

As can be observed in Figure 8.13, in this case the TS-Fuzzy was able to realise the best approximation of the ROA, better so surprisingly than the SOS approach. The fast sample method, being by far the fastest approximation having a very accurate result in comparison.

It may be surprising considering the result obtained in the VDP example that the SOS was not on top. This happened primarily due to the fact the further approximations of the Lyapunov could not be generated, given the terms generated in Steps 2 and 3. It is still an area of question as to why a Lyapunov function cannot be repeatedly generated, and was considered mathematically complex and out of scope of the project criteria to solve, and would be an investigation in future work. However, it has been shown to work for similar systems with similar reaches of approximation, utilising an alternate approach to address the rational term [168].

In addition, to approximate this SOS function alone (using a 4th order Lyapunov approximation) takes a tremendously long period of time in regards to evaluate the area shown.

The time it takes each optimisation to complete is shown in the table below:

Procedure	Computation Time
SOS	441.22s
TS-Fuzzy	1.45s
Fast Sample $N_s = 1e^6$	0.63s
Reverse Trajectory (Simulation Time 1s)	0.2s

Table 8.2: Optimisation times for each ROA approximation algorithm

Even if more accurate approximation of the ROA could be attained using SOS, due to the length of time it takes to perform, for even comparable ROA's to the faster methods, it doesn't seem worth it to perform this optimisation. The end goal would be to augment one of these approaches into an controller synthesis algorithm, and having to perform an SOS optimisation algorithm, within a controller synthesis algorithm seems extremely convoluted.

In addition, the SOS approach was attempted on the AFE system which shall be presented in the next sub-section, and due to the large order and size of the system, the time it takes for expansion using the simplest Lyapunov's can take in excess of half an hour. Therefore, the SOS shall not be investigated further. The methodology however, if it is of interest in the future for fully accurate high order ROA approximations using SOS for rational systems has been presented here.

8.2.2 Application of Revised ROA Methods on a H_2 Optimised AFE Converter

Having further investigated a different system with a much larger ROA to approximate, the TS-Fuzzy, the Random Sample and the Reverse Trajectory methods shall be used in order to approximate the ROA for a H_2 controlled AFE converter. Again, there are two novel methods which are hoped to be analysed in this branch of work.

1. A quantifiable measure of robustness, such that it can be implemented into a controller optimisation.

2. An approach to visual ROA representation of high order closed loop systems

Item 1 shall be considered first. When we refer to a quantifiable measure of robustness, this means that we want an associated number which directly links how robust one version of the

system is when compared to an alternative. For the SOS approach, this value would have been α as this expresses the largest bounded region which defines the ROA approximation. Therefore, this would eliminate the Reverse Trajectory as this only outputs a visual representation.

For the Random Sample approach, the quantifiable region will be that defined in (8.19) where τ is the largest bound of the approximated ROA, and can be seen as equivalent in function as α was for the SOS. The TS-Fuzzy however is more direct in quantifying in that the bounds are determined directly by how far the state will go in all n dimensional directions until predicted instability occurs.

The TS-Fuzzy is more preferential and direct, as τ for Random Sample is not only dependant on the subject system, but also the Lyapunov function which is used. Generally in Random Sample the same Lyapunov function would be used for every robustness test, but this does increase the conservativeness of the overall optimisation. In addition, TS-Fuzzy approximations, whilst it takes longer to compute, but was shown to be more accurate that Random Sample, as was shown in Figure 8.13. For these reasons, a TS-Fuzzy approach was tested as a first choice for augmenting an quantifiable robustness algorithm.

TS-Fuzzy Stability Approximation for an Controlled AFE

For this study, the case AFE has been independently considered such that the controller is synthesised utilising only the local dynamics of the AFE. Additionally for simplification of the study the PLL is not considered as a dynamic interfaced to the AFE. As such this study can also be considered a stability study of a locally LQR optimised AFE. This doesn't mean the approaches shown here cannot be used for the systems that have been analysed throughout this thesis, as globally optimised AFE controllers will contain the same general control architecture.

To start with, as was explored in Section 8.2.1, for any ROA analysis the point of equilibrium must be shifted to the origin.

Here, the AFE under investigation has the same parameters as with all the previous tests, as shown in Table 8.3.

Parameter	**Value**
R_a	0.8Ω
L_a	565μH
C_a	100μF
P_l	1kW
V_{cd} (grid input)	$100\sqrt{2}$V
V_{cq} (grid input)	0V
I_{aq}	0A
V_{dc_a}	400V
Grid Frequency (ω)	800π rads^{-1}
H_2 Weights	$Q_\gamma = \begin{bmatrix} 0 & 0 & 0 & 2\cdot 10^3 & 2\cdot 10^3 \end{bmatrix}$ $R_\gamma = 10^3 \begin{bmatrix} 1 & 1 \end{bmatrix}$

Table 8.3: AFE Parameters for ROA analysis

As it should be already known from reading the earlier parts of this thesis, the state I_{ad} is floating, dependant on how the controlled voltages are actuated. It was shown in Section 2.1.2 with equation (2.54) how this equilibrium points for a Constant Power Load case (which is the load considered) can be calculated:

$$I_{ad}^* = \frac{V_{cd}^* - \sigma}{2R_a} \tag{8.25}$$

$$\sigma = \pm\sqrt{R_L V_{cd}^{*2} - \frac{8R_a V_{dc_a}^*}{3}} \tag{8.26}$$

All the other required state equilibriums are known as they are reference inputs to the controller. Each of these equilibrium points in this example will be noted with an asterisk, as shown in (8.25) The matter of the modulation index operating points will be considered shortly.

The system state-equations originally defined from (2.70) can therefore be translated to have its equilibrium point at the origin by having the state-equations now evaluated as:

$$f_{CL}(I_{ad_s}, I_{aq_s}, V_{dc_{a_s}}, \omega I_{aq_s}, \omega V_{dc_{a_s}}) = \begin{cases} f_1 = \frac{1}{L_a} V_{cd} - \frac{R_a}{L_a}\left[I_{ad} + I_{ad}^*\right] + \omega\left[I_{aq} + I_{aq}^*\right] - \frac{p_d}{2L_a}\left[V_{dc_a} + V_{dc_a}^*\right] \\ f_2 = \frac{1}{L_a} V_{cq} - \omega\left[I_{ad} + I_{ad}^*\right] - \frac{R_a}{L_a}\left[I_{aq} + I_{aq}^*\right] - \frac{p_q}{2L_a}\left[V_{dc_a} + V_{dc_a}^*\right] \\ f_3 = \frac{3p_d}{4C_a}\left(\left[I_{ad} + I_{ad}^*\right] + \left[I_{aq} + I_{aq}^*\right]\right) - \frac{P_l}{C_a V_{dc_a}^*}\frac{V_{dc_a}}{\left[V_{dc_a} + V_{dc_a}^*\right]} \\ f_4 = -\left[I_{aq} + I_{aq}^*\right] \\ f_5 = -\left[V_{dc_a} + V_{dc_a}\right] \end{cases} \tag{8.27}$$

Where f_4 and f_5 are the translated integral states. Now, the modulation indexes, though not states, do have equilibrium points based on the states themselves. Therefore the proper way to translate the equilibrium points of p_d and p_q is by internal translation, such that:

$$p_d = \frac{V_{cd} + \sqrt{V_{cd}^2 - \frac{8P_l R_a}{3}}}{2R_a}, \quad p_q = -\frac{L_a\omega(V_{cd} - \sqrt{V_{cd}^2 - \frac{8P_l R_a}{3}})}{R_a V_{dc_a}^*}\frac{V_{dc_a}}{\left[V_{dc_a} + V_{dc_a}^*\right]} \tag{8.28}$$

As you can see, p_d is unaffected, but p_q has a translation term in its denominator.

As normal, the H_2 controller synthesis can be applied to the standard state equations following procedures highlighted in Chapter 4. Then by evaluation of the Jacobian of $f(x)$ in relation to the states to get A_f, and to inputs B_f, the closed loop state-equations can be found by evaluating:

$$f_{CL} = A_f + B_f K_f \tag{8.29}$$

where K_f is the synthesised H_2 controller. Applying a further Jacobian on the state-equations defined in f_{CL} the closed loop state matrix A_{CL} can be defined which is the key term required for the TS-Fuzzy Optimisation.

The resultant A_{CL} thus has to form:

$$A_{CL} = \begin{bmatrix} -\frac{R_a}{L_a} - K_{11}\sigma_1 & \omega - K_{12}\sigma_1 & -\frac{p_d}{L_a} - K_{13}\sigma_1 & -K_{14}\sigma_1 & -K_{15}\sigma_1 \\ -\omega - K_{21}\sigma_1 & -\frac{R_a}{L_a} - K_{22}\sigma_1 & -\frac{p_q}{2L_a} - K_{23}\sigma_1 & -K_{24}\sigma_1 & -K_{25}\sigma_1 \\ \frac{3p_d}{4C_a} + K_{11}\sigma_2 + K_{21}\sigma_3 & \frac{3p_q}{4C_a} + K_{12}\sigma_2 + K_{22}\sigma_3 & K_{13}\sigma_2 + K_{23}\sigma_3 + \frac{P_l}{C_a V_{dc_a}}\sigma_4 & K_{14}\sigma_2 + K_{24}\sigma_3 & K_{15}\sigma_2 + K_{25}\sigma_3 \\ 0 & -1 & 0 & 0 & 0 \\ 0 & 0 & -1 & 0 & 0 \end{bmatrix} \tag{8.30}$$

where

$$\sigma_1 = \frac{V_{dc_a} + V_{dc_a}^*}{2L_a} \quad \sigma_2 = \frac{3(I_{ad} + I_{ad}^*)}{4C_a} \quad \sigma_3 = \frac{3(I_{aq} + I_{aq}^*)}{4C_a} \quad \sigma_4 = \frac{1}{\left[V_{dc_a} + V_{dc_a}^*\right]} \tag{8.31}$$

The integral states $\omega_{I_{aq}}$ and $\omega_{V_{dc_a}}$ do not appear explicitly as variable states in A_{CL} which simplifies the optimisation somewhat. Normally a five variable fuzzy optimisation will have had to have taken place. If this was the case, the use of 2^5 LMI constraints would have been required for the optimisation. However, only three-states are variables which have to be tested, requiring only 2^3 LMI to optimise around.

Now the TS-Fuzzy ROA optimisation can begin on this system. Again, we have 2^3 LMIs such that all the plus minus variations of the states are tested for their stability. Such that in this case, the LMI optimisation is conducted using the following algorithm:

Algorithm 2: TS-Fuzzy ROA Approximation on 5-dimension closed loop AFE converter

Result: Unqiue W at maximum stabilty bound

Translate equilibrium point $(I_{ad}, I_{aq}, V_{dc_a}, \omega_{I_{aq}}, \omega_{V_{dc_a}}) \leftarrow \{0, 0, 0, 0, 0\}$;

Set $I_{ad_P}, I_{aq_P}, V_{dc_P} = 0$;

Set $I_{ad_N}, I_{aq_N}, V_{dc_N}, = \delta_{I_{ad}}, \delta_{I_{aq}}, \delta_{V_{dc_a}}$;

Compute A_i for $i = 1 \rightarrow 8$;

Check feasibility of (8.15) and (8.16);

while (8.15) *and* (8.16) *are feasible* **do**

  Set $[I_{ad_P}, I_{aq_P}, V_{dc_P}] = [I_{ad_N}, I_{aq_N}, V_{dc_N}] + [\delta_{I_{ad}}, \delta_{I_{aq}}, \delta_{V_{dc_a}}]$;

  Recomute new A_i for $i = 1 \rightarrow 8$;

  Check (8.15) and (8.16);

end

Estimate ROA using $[I_{ad_P}, I_{aq_P}, V_{dc_P}]$

.

Where A_i here are all the possible combination of A_{CL} when substituting in the values $\pm I_{ad_N}, \pm I_{aq_N}$ and $\pm V_{dc_N}$.

It is important to note again that it becomes very important that the values of $\delta_{I_{ad}}, \delta_{I_{aq}}, \delta_{V_{dc_a}}$ are selected appropriately. Reason for this is suppose each of δ was set to one. A point of infeasibility could occur at 20A for I_{aq} for instance. This would produce a ROA about a region of 20A in I_{aq} and 20V in V_{dc_a}. Now, this is very small in comparison to the potential the ROA could be. In the case of this optimisation, each of the δ have been set as follows, to allow as big an expansion as possible.

$$\delta_{I_{ad}} = 0.1, \quad \delta_{I_{aq}} = 0.1, \quad \delta_{V_{dc_a}} = 1 \tag{8.32}$$

Therefore, as with SOS there are methods of increasing the predicted ROA by internal expansion; for TS-Fuzzy systems of more than 1-dimension of freedom, adjustments in the values of δ can attribute to the expansion of the ROA. There is still question about how to best evaluate the best

approximations of the ROA in this area. Another possible approach to δ optimisation was to find the maximum bound of each state, while every other state is set to equilibrium. This will find the maximum stability given when only one state changes and then evaluating all the maximums, and attributing the δ according to the resultant ratio of maximums. However the problem with this method is it doesn't attribute the bounds of stability across all directions and may make certain states move very quickly when they have narrow bounds of stability with respect to the changes of other states. The optimisation of δ for maximizing the ROA through a TS-Fuzzy approximation is still an open question for research.

Using the δ in (8.32), the following ROA was achieved:

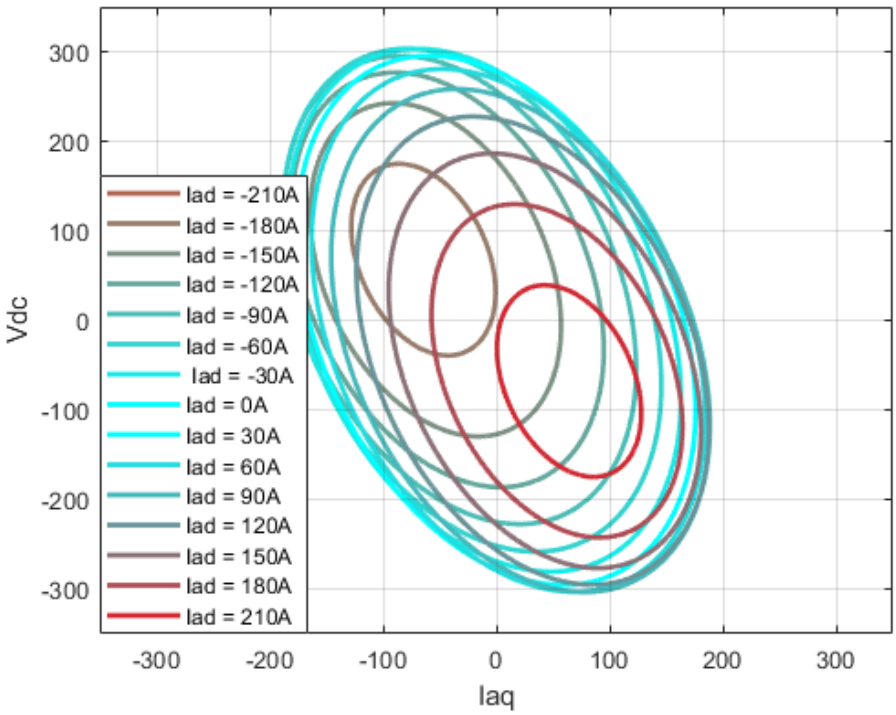

Figure 8.14: The approximated ROA of the closed loop AFE using TS-Fuzzy, with ROA dimensional slicing performed on I_{ad}, with respect to state deviations in I_{aq} and V_{dc_a}

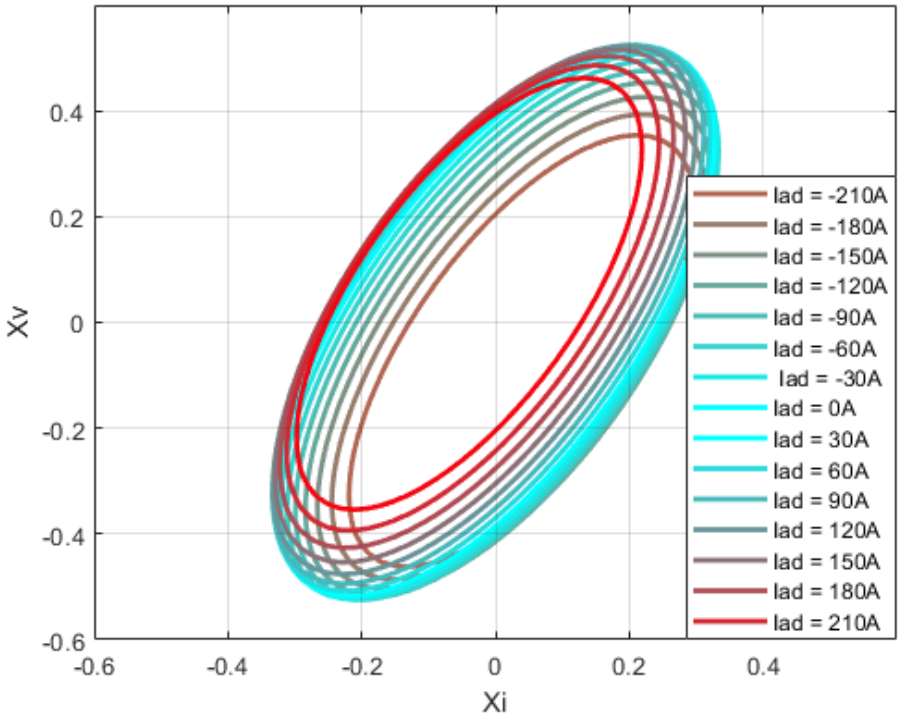

Figure 8.15: The approximated ROA of the closed loop AFE using TS-Fuzzy, with ROA dimensional slicing performed on I_{ad}, with respect to state deviations of the current integral state X_I and voltage integral state X_V

The approximated bound χ can be evaluated by adaptation of (8.19) such that we can evaluate the largest set in the Lyapunov $V(x) = x^T W x$ as follows [156]:

$$\min x^T W x = \frac{I_{ad_P}^2 + I_{aq_P}^2 + V_{dc_P}^2}{b^T W^{-1} b} \triangleq \chi \tag{8.33}$$

where $b = (1, 1, 1, 0, 0)^T$.

Figures 8.14 and 8.15 shows again that the approximation of the ROA is a 3-dimensional ellipsoid

As this optimisation attempts to analyse the stability region based on the maximum possible distance away from the origin in all evaluated dimensions, an other measure of robustness can be seen to be the magnitude point furtherest away from the origin:

$$r = \sqrt{I_{ad_P}^2 + I_{aq_P}^2 + V_{dc_P}^2} \tag{8.34}$$

Analysing this region for the true stability of the system shows that the predicted region in Figures 8.14 and 8.15 shows that these regions accurately portray the areas of guaranteed stability,

as it should. To show this, five random points at the extremities of the approximated ROA shall be selected, and steady state simulations performed as presented below. Since the ROA is only perceivable in three dimensions, it means that for each test two states will be set initially to zero, but the ROA will be shown to still hold accurate considering this.

The points selected are shown in Figure 8.16:

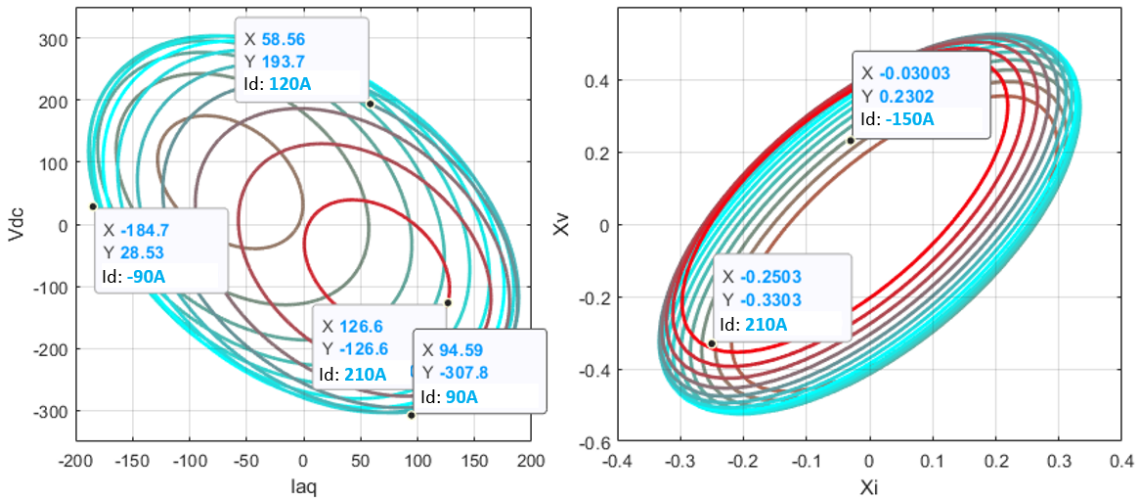

Figure 8.16: Randomly selected points on the extremities of the TS-Fuzzy formulated ROAs for Steady-State Simulation Testing

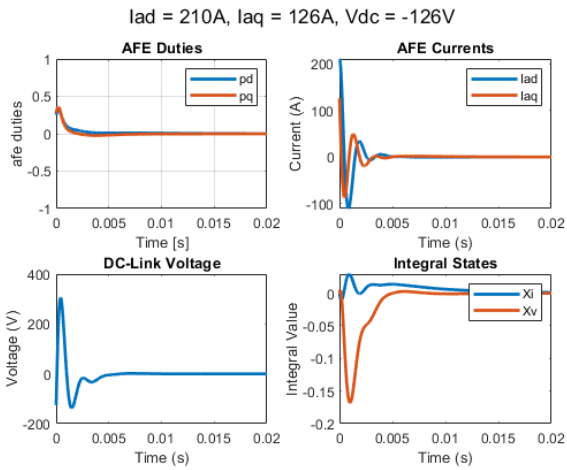

Figure 8.17: TS-FUZZY ROA Stability Test 1: $I_{ad} = -210A, I_{aq} = 126A, V_{dc_a} = -126V$

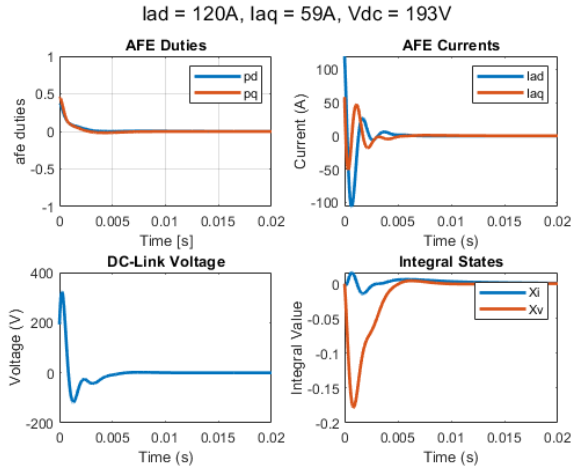

Figure 8.18: TS-FUZZY ROA Stability Test 2: $I_{ad} = 120A, I_{aq} = 59A, V_{dc_a} = 193V$

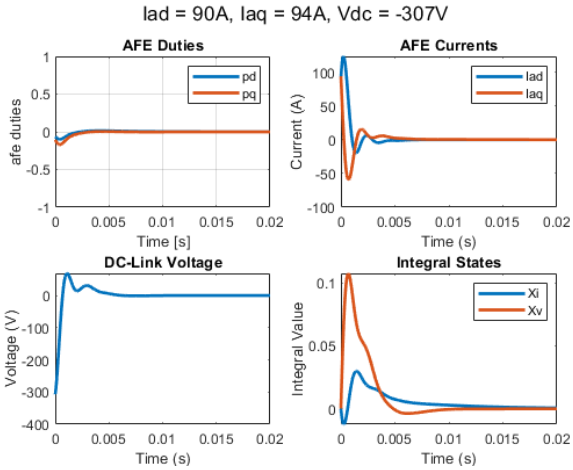

Figure 8.19: TS-FUZZY ROA Stability Test 3: $I_{ad} = 90A, I_{aq} = 94A, V_{dc_a} = -307V$

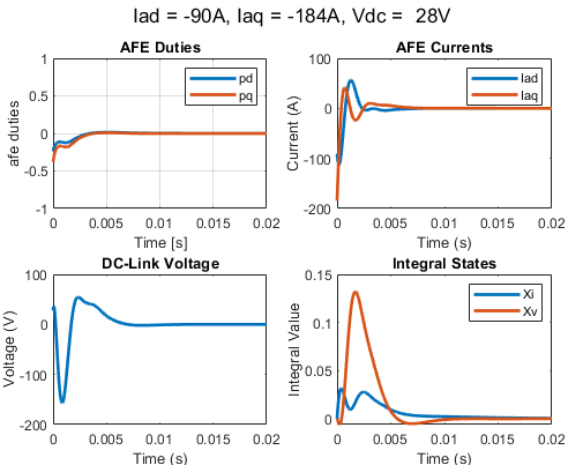

Figure 8.20: TS-FUZZY ROA Stability Test 4: $I_{ad} = -90A, I_{aq} = -184A, V_{dc_a} = 28V$

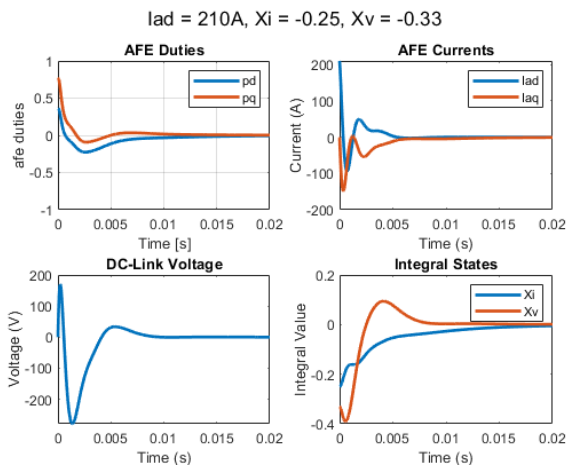

Figure 8.21: TS-FUZZY ROA Stability Test 5: $I_{ad} = 210A, X_I = -0.25, X_V = -0.33$

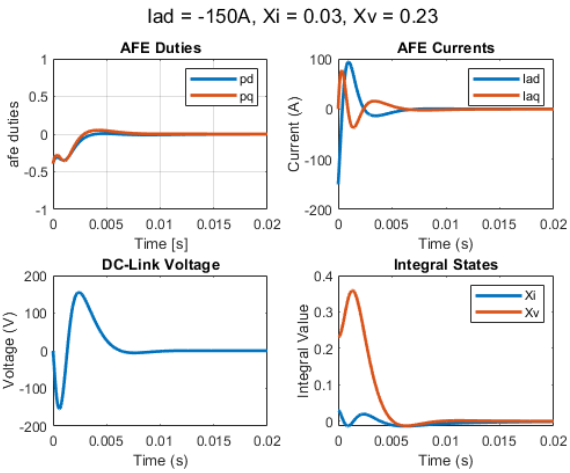

Figure 8.22: TS-FUZZY ROA Stability Test 6: $I_{ad} = -150A, X_I = -0.03, X_V = -0.23$

As can be observed, all the points selected all converge back into the stable equilibrium point, signifying that all points contained within the ROA approximation above contain all the stable points of deviation into the system, which will decay back into stable equilibrium.

As we had seen in the Van der Pol introductory examples, the TS-Fuzzy is not an 100% accurate depiction of the ROA, but this approximation is close to the true instability regions. For example, take the test in Fig. 8.19. Here, if the voltage deviation is pushed 27V further to -330V, the system becomes unstable. Likewise with the integral states. Taking the test in Fig. 8.21 and decreasing each X_I and X_V by a further -0.3, then instability also occurs. Additionally, from the test conducted in Fig. 8.22, decrease the current down slightly to -170A and instability also

ensues. Therefore, the ROA is actually not far from the true region of instability, and the TS-Fuzzy approximation provides a relatively accurate depiction of the true region of attraction. However, it is important to note that through testing, deviations in I_{aq} didn't detriment the stability as much as the other states of the system. In fact, taking the tests conducted in Fig. 8.22 and Fig. 8.20 and applying an I_{aq} of +1000A and -500A respectively, the system can still be shown to be stable, as shown in Fig. 8.23 and 8.24.

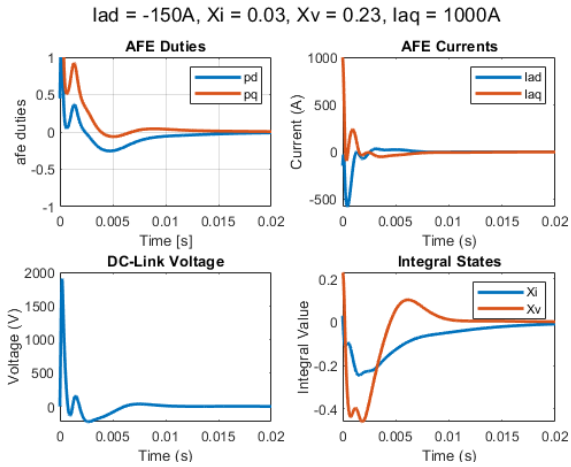

Figure 8.23: TS-FUZZY ROA Stability Test 7: $I_{ad} = -150A, X_I = -0.03, X_V = -0.23,$ $I_{aq} = 1000A$

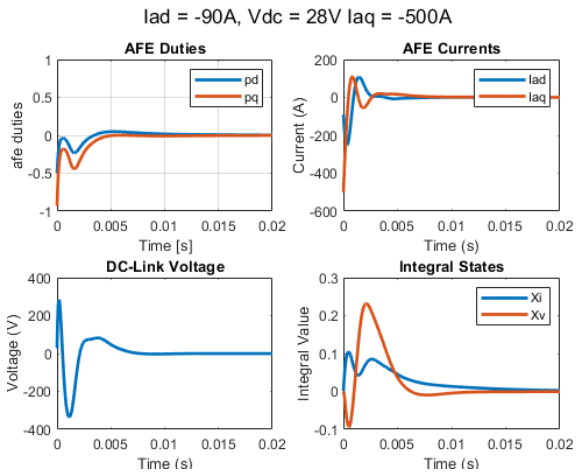

Figure 8.24: TS-FUZZY ROA Stability Test 8: $I_{ad} = -90A, I_{aq} = -500A, V_{dc_a} = 28V$

Therefore, the resultant ROA acquired from the TS-Fuzzy method is relatively accurate across all but the I_{aq} state, and can be used as a decent estimation for the ROA approximation of closed loop three-phase power systems.

Random Sample Approximation for an Controlled AFE

As we had seen previously in Section 8.1.2, the Random Sample approximation was able to resolve a similar sized ROA to that of the TS-Fuzzy method, but it can be computed somewhat faster, more efficiently and also doesn't require tuning of variables such as δ for the TS-Fuzzy to acquire the best possible ROA for the system.

In this approximation, the already defined transformed system equations in (8.27) can be used to form the constraint:

$$\begin{aligned} \nabla V f_{CL}(I_{ad_s}, I_{aq_s}, V_{dc_{a_s}}, \omega I_{aq_s}, \omega V_{dc_{a_s}}) < 0 \\ V(I_{ad_s}, I_{aq_s}, V_{dc_{a_s}}, \omega I_{aq_s}, \omega V_{dc_{a_s}}) > 0 \end{aligned} \tag{8.35}$$

where V is a basic Lyapunov function constructed by $V(x) = x^T Q x$ where Q is a symmetric positive define matrix defined by the user.

For the Random Sample Approximation, the range of values which will be tested for each state becomes very important for the ROA approximation. More down to the fact that if too large a range is selected, not enough points maybe evaluated within the region of stability such that too small an approximation is made. In the case for the approximation used here, the following ranges were applied to each state for testing:

$$\begin{aligned} -100A \leq I_{ad_s} &\leq 100A \\ -300A \leq I_{aq_s} &\leq 300A \\ -400V \leq V_{dc_{a_s}} &\leq 400V \\ -2 \leq \omega_{I_{aq_s}} &\leq 2 \\ -2 \leq \omega_{V_{dc_{a_s}}} &\leq 2 \end{aligned} \tag{8.36}$$

These were largely chosen based on the stability limits found when keeping all states at zero during a TS-Fuzzy approximation and evaluating how stable an individual state is when no other states are varying. As it can be see, the state I_{aq} can be brought very far away from the system equilibrium point and still decay back to equilibrium. Something, additionally that the TS-Fuzzy was not able to determine for the full system, as shown in Figures 8.14 and 8.15.

Conduction the Random Sample algorithm described in Section 8.1.2, and using $N_s = 10e^6$ random samples of x in the range (8.36) the following ROA can be approximated:

In Figure 8.25 it may be noticeable that multiple contours can be observed. This figure is actually slicing through I_{aq} up to 150A to show how little it effects the stability characteristics of the system. Each of the data points shows an operating point predicted by the ROA to be a guaranteed stable point. Below are steady state simulations which have been performed at each of these points which confirms the ROA approximation to be valid. Additionally each of these simulations place I_{aq} to 150A, to show that the ROA is accurate for each of the I_{aq} slices.

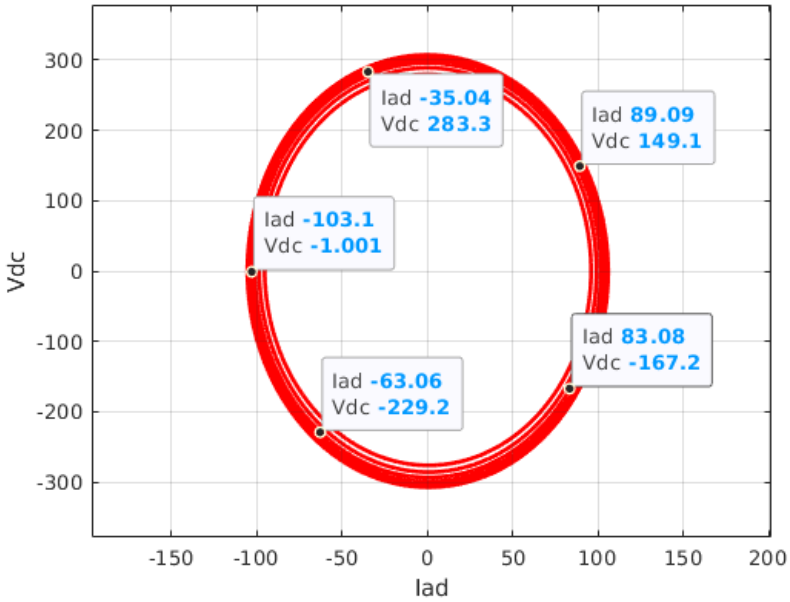

Figure 8.25: Approximated ROA using Random Sample Approximation on Closed Loop H_2 AFE System with I_{aq} dimensional slices

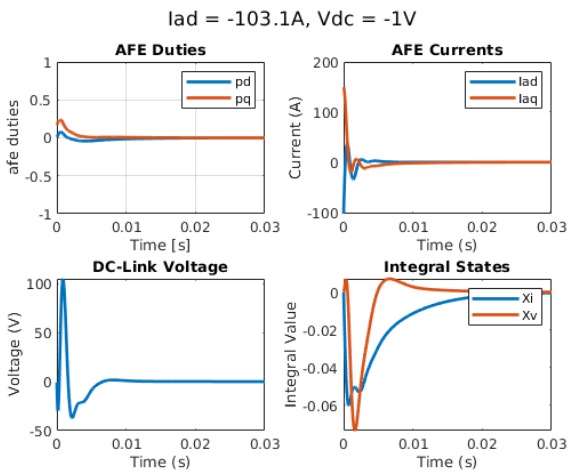

Figure 8.26: Random Sample ROA Approximation $I_{ad} = -103A, V_{dc_a} = -1V$

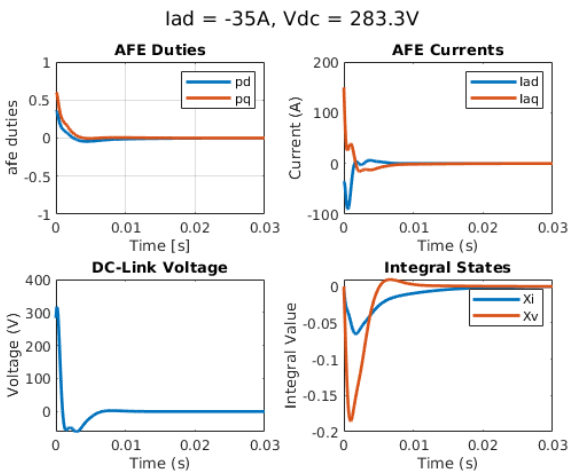

Figure 8.27: Random Sample ROA Approximation $I_{ad} = -35A, V_{dc_a} = -283.3V$

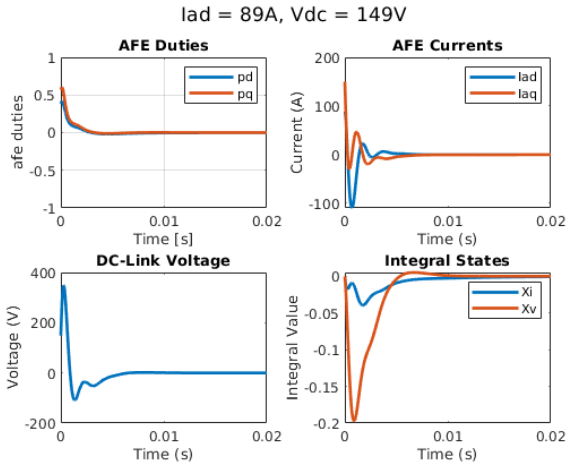

Figure 8.28: Random Sample ROA Approximation $I_{ad} = 89A, V_{dc_a} = -149V$

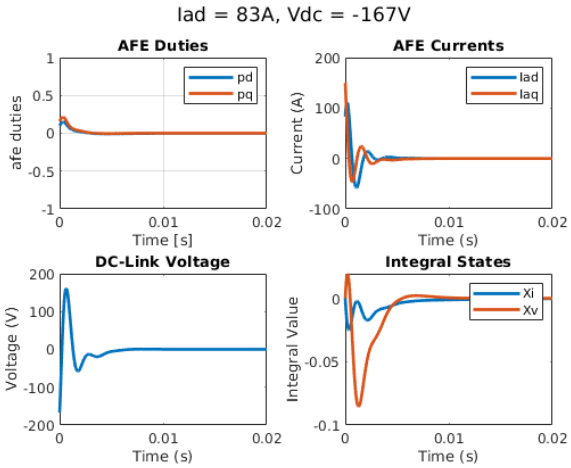

Figure 8.29: Random Sample ROA Approximation $I_{ad} = 83A, V_{dc_a} = -167V$

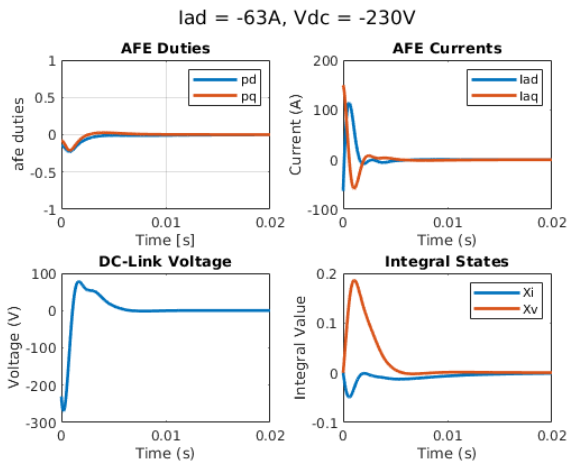

Figure 8.30: Random Sample ROA Approximation $I_{ad} = 83A, V_{dc_a} = -167V$

In addition, the ROA approximation of the integral states sliced each of the electrical states can be observed in Figures 8.31 through 8.33. From these figures, it is clear all the points selected on close to the approximated limit cycle are all definitely stable, and each of the dynamics presented in Figures 8.26 through 8.30 remain well within the approximate regions of stability. In addition, this would confirm that from the popular methods of ROA approximation discussed throughout this chapter, for the fastest, and most accurate approximation for this particular closed loop non-linear system, Random Sampling is a good choice to follow.

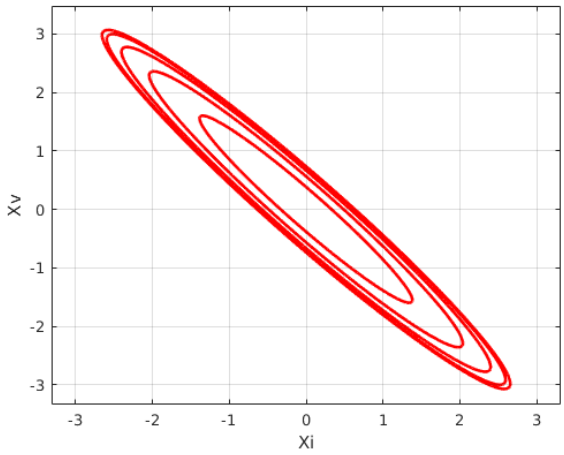

Figure 8.31: Integral State ROA with I_{ad} slices upto 125A

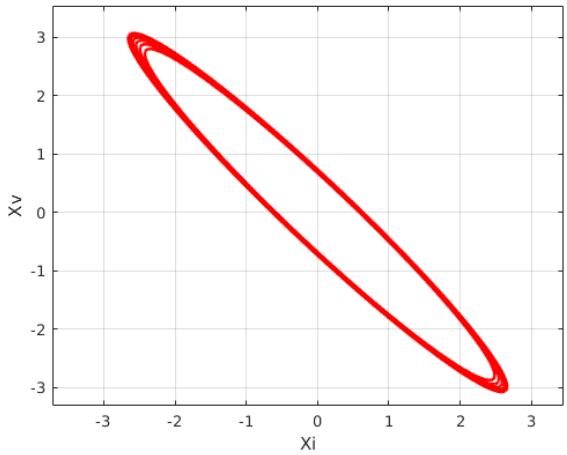

Figure 8.32: Integral State ROA with I_{aq} slices upto 150A

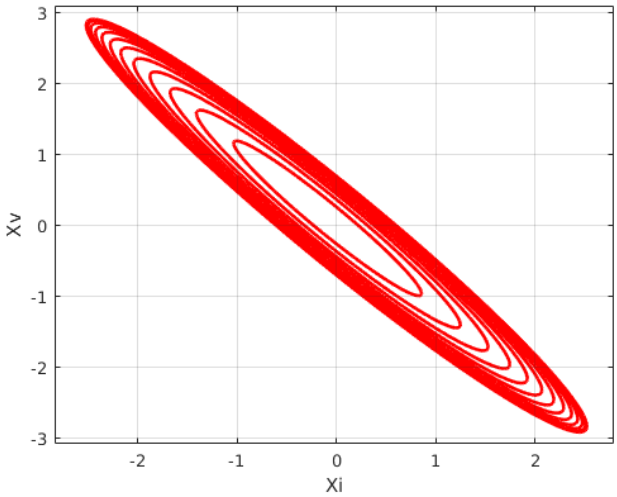

Figure 8.33: Integral State ROA with V_{dc_a} slices upto 400V

With this, the two aims have been addressed. If an accurate and quantifiable term is desired, especially in the case of incorporating into the H_2 controller synthesis, then using TS-Fuzzy and evaluating τ is from the selection analysed in this chapter, the preferred method. But, visually analysing the resultant ROA, this approach is not recommended.

As a conclusion, it can be safely said that what if dealing with closed loop systems where the inclusion of integral states are common, of the methods analysed, the Random Sample Method will quickly and accurately provide a Region of Attraction which for these systems with guaranteed points of stability. On the other hand, if analysing open-loop systems for which all the states in the state-space linearised form can be tested for stability, then the TS-Fuzzy can be applied and

can record more accurate and enlarged ROA, when compared with Random Sample Method.

Additionally, if it is desired to visually analyse the true ROA of the system then Reverse Trajectory methods can be used, however when analysing systems greater than 3D any visual representation will be inaccurate to a degree. The reverse trajectory will not be investigated here as that approach doesn't fit the scope of this research. However if of interest to the reader, the procedure is exactly that explained in Section 8.1.4, however to observe the full ROA, 2^n figures must be presented slice the 5-D shape across all dimensions for accurate 3-D model. This therefore becomes exponentially more complex to analyse for greater systems.

8.3 Discussions and Summary

This chapter presented some preliminary research undertaken with the larger focus of incorporating Region of Attraction Stability analysis, and augmenting this into the optimisation of H_2 controllers to enable optimal performance and robustness into one. Whilst the work presented in this chapter did not end with the final goals achieved, it is hoped what has been presented will help further the work in this area.

This chapter began with a summarisation of all the popular methods in literature today, and using the commonly used Van der Pol oscillator, were explained in how their ROAs are evaluated. By far the most common approach in research is the Sum of Squares optimisation, and it was presented how non-polynomial systems can be successfully applied in this optimisation. Whilst for the Van der Pol system, the SOS approach was able to deliver the most accurate approximation of the true limit cycle, problems incurred when applying to the simplest of DC electrical systems. The SOS was shown for this DC system to not only be slow, but additionally prove to not be able to find better solutions of the Lyapunov after a certain amount of iterations.

The SOS compared with the other presented approximation methods was shown therefore to be not good for purpose. Largely down to the fact that due to it being much more computationally intensive to the other presented methods, it takes far too long when the faster approaches can yield similar approximations. Therefore, among the common methods, the Takagi-Sugeno Fuzzy Logic Approximation and the Fast Sample Approximations were presented and carried forward.

The TS-Fuzzy was the first to be investigated, and was shown to not only be relatively simple in terms of the theoretical understanding as to how the ROA is approximated, unlike SOS, but was also shown to be very accurate in approximating an ROA, which was close to that of the true ROA, as shown by simulative analysis. Additionally this method provides two possible measures of determining the stability which could be incorporated into optimisation. Since SOS and Random sample have their ROA determined by a relative bound, α and τ respectively, where it can be

determined a bigger value of either of these bounds suggests a more robust system. Not only does the TS-Fuzzy provide it's equivalent bound χ through (8.33), the robustness can be determined directly from the states themselves, by analysing the maximum deviations achieved, and thus using Pythagoras to determine quantify the furthest capable deviation of the closed loop system. This could potentially allow the ability to prioritize stability for a given state if required, rather than all system states as a whole, which occurs with the other two methods. The TS-Fuzzy method has shown to be a fast, and accurate method for determining the ROA. However, the main downside to this method is that the approximated ROA can change significantly when analysing the deviation of states at different rates. For example, if the rates of each of the states was analysed at intervals of 1 unit per iteration, the integral states will quickly indicated instability, and since the current and voltages only reached 1A or 1V respectively, the resultant ROA will be small. In order to achieve the best possible ROA using the TS-Fuzzy method, the rates at which each of the states increase for each iteration of the analysis must be selected, or maybe best to say 'tuned' appropriately so that when an instability is identified, the other states aren't at such small values that the ROA accuracy is significantly reduced, and are in-fact closer to the point where their values become unstable themselves. Such issues are not present in SOS or Random Sample methods, which is the drawback for the possibility of attaining very accurate ROAs as a end result.

Finally, the Fast Sample method was tested which requires testing across the whole $\Re^n$ space and thus all states can be tested against every other until the Lyapunov stability criteria is met. This method too resulted in visualised ROA approximation which was also very accurate to that of the true ROA. Many points were selected about the limit cycle of the approximated system ROA are were shown to be stable, which confirmed that this ROA was a true depiction of all the stable steady state points of the closed loop system. However, the resultant robustness index $\underline{c}$ is not as direct as that received from TS-Fuzzy as it depends not only on the synthesised controller gains which form $f(x)$, but additionally is dependant on the Lyapunov function which is used. If $V(x)$ is kept constant through the optimisation, then this is not an issue, and the larger the $\underline{c}$ is computed, the more robust the system is. Although it wasn't analysed in this thesis, if the fast sample method can in addition utilise rational Lyapunov functions as shown in (8.14) using optimisation method presented in [162]. This would enable this approximation method to not to have to use elliptical approximations for the ROA and may result in even better accuracy. This particular point cannot be applied to TS-Fuzzy, and with TS-Fuzzy, an elliptical Lyapunov is generated as part of the analysis which cannot be changed.

As a conclusion, it was therefore found that both the use of TS-Fuzzy and Fast Sample Approximation can be used as a means of quantifying the robustness of a system accurately, where if visualisation of the system is also important for analysis, the either the TS-Fuzzy or the

Fast Sample method of all the methods analysed would be the preferential choice.

It is hoped in the future, that using the theory and findings presented in this chapter, that these methods can then be utilised into the H_2 controller synthesis to guarantee optimal performance, but also guarantee optimal and largest field of stability possible. In utilising these methods into the controller optimisation, a couple of ideas come to mind.

Initially, and probably the most straight forward method would be to optimise the H_2 weights Q_γ and R_γ from within a given specified range of change. A user can supply the desired controller performance by setting initial values for Q_γ and R_γ and an optimisation method can be utilised to adjust these weights, about the predetermined performance bound to enlarge the ROA as much as possible. This is the most preferred approach, but not the most elegant, and would be compatible with any of the two proposed approaches. Another method comes from an idea presented in [156] whereby an LMI optimisation based optimisation can occur which not only analyses the ROA of the system by using TS-Fuzzy, but additionally develops the controller under the same procedure. This is in-fact a very intuitive method as the H_2 optimisation can be represented as an LMI optimisation, where employing the methods shown in [169] can the desired structure of K can be imposed. Some early attempts on the latter approach have been attempted on the AFE alone. However up to now no presentable results have come to fruition. Problems so far have entailed too large a value of K being generated by the synthesis, albeit still providing a stable system, but not interfaceable with a physical system, due to the amplification of noise by the generated controller.

What has been presented is only the start of this area of research and the are many routes to be followed from this point of augmenting these approaches, including adaptation of these approaches to even high order systems, and maybe possibly a full grid instead of local system approximation.

Chapter 9

Conclusion

This chapter provides the concluding remarks on how the work achieved its goals all the proposed novelties developed shall be summarised; detailing the performance shown for each of the designs as well as where improvements could be made. In section 9.2 guidelines for future research in this area shall be addressed and the new open possibilities for the use of this controller inside and outside of MEA applications.

9.1 The Novelties Achieved

In section 1.3 of the introduction a list of novelties to be delivered in this research was presented. Based on the simulative and verified experimental results, the novelties of this thesis can be summarised as follows:

Novelty 1: Development of a globally optimal decentralised controller for hybrid DC/AC three-phase grids (Chapter 3/4)

As discussed in Section 1.2.3, it was identified that whilst fully decentralised control for grids is not an entirely novel concept and has been an idea for a number of years, the literature review has shown that there were some gaps in utilising the research for given applications. Namely, the utilisation of a fully decentralised control for DC/AC micro-girds.

With the AFE being a non-linear system, it was first investigated in Section 3.1.1 if a true non-linear controller (the feedback linearised controller) could be used as a novel approach to non-linear decentralised control. However, it was shown by the result in (3.41) that this approach could not be applied into a decentralised form due to the inability of developing a strictly diagonal controller for a two converters setup. A fundamental requirement in any decentralised controller

design. As was concluded in the literature, the popular methods of decentralisation such as MPC controls were excluded as possible solutions as such approach are not globally optimal and does not directly counteract against the problem of interaction mitigation without transforming the control architecture to a distributed form; thus requiring extra communication between sub-systems which we're trying to avoid. Investigations then moved towards looking at the popular H_2 and H_∞ methods for decentralised control, which has been applied successfully in a number of distributed control architectures.

The H_∞ based Mixed Sensitivity Control was then explored on an AFE application at first, and a stable result could be achieved. However, as was shown in papers in the literature, the H_∞ being a very conservative control synthesis can rarely, if ever, find an optimal solution to the control problem (where the constraint $\gamma \leq 1$ can be met). For a single AFE, it was far from optimal and inclusion of the VSI model, with diagonalising the controller, would add further constraints and make the solution less optimal. Therefore this approach has been excluded from consideration.

The proposed methodology for global decentralisation of the controller was then chosen to be the H_2 controller.

1. In Section 3.3 the theory behind the development and synthesis of a globally decentralised H_2 optimal controller was devised.

2. The devised formulation was then applied onto a simplified VSI-AFE grid network, which was shown from literature [49, 50] to have considerable interactive effects by itself. A diagonal matrix controller was formulated through the methods discussed in Section 3.3 and a fully global decentralised control was developed for the first time on a hybrid DC/AC network.

Simulative results presented in Section 4.1.2 shows how the proposed method of decentralised optimal control was successfully applied with stable and fast dynamic performance being achieved. The procedure was also compared against a traditional PI controller, which is the typical control choice in these applications. Although the PI controller was designed to deliver the best performance possible, whilst still guaranteeing stability of the individual converters, it was shown that applying too large a bandwidth for the current control, as observed in literature, can result in network instability due to the impedance mismatch caused by their controllers. Furthermore, simulative results in Figure 4.6 and Figure 4.7 presented how the bandwidth of the AFE terms can be increased still using the decentralised method to have dynamics much faster than that of the PI control, and still maintain stability.

Additionally to the stability being maintained, the effect of cross-converter interaction has been shown to be largely mitigated. A 1kW step constant power load was applied to the AFE in simulative tests and was observed that VSI dynamics were largely unaffected by the disturbance

occurring on the other sub-system. During testing, both the traditional and proposed control schemes were implemented onto systems where the VSI was operating close to it's maximum output voltage. When observing this system using traditional methods, the interactive effects between converters caused the grid voltages to distort and oscillate; in turn saturating the modulator severely affecting global performance. The proposed controller, on the same exact system, was able to maintain the grid voltage constant even during large disturbances on the AFE, showing the true power of the proposed method on such integrated networks.

The simulative results using the fastest H_2 controllers were then confirmed through experimental validation in Section 4.3.4 where the exact same performance on a practical setup could be achieved.

Novelty 2: Integration of PLL dynamics into a globally decentralised control architecture (Chapter 5)

It was widely known in literature about the effects the PLL has on the global stability, if improperly designed without consideration to the interactive effects between other converters. Methods which attempted to identify and solve this problem, however, required external testing of interfaced converters and manual adjustment of the PLL until instability was prevented. This is not an elegant solution to solving this problem, as if the grid was to expand including more converters, then analysis of each PLL may be required to be re-run to ensure global stability [55].

As it was shown from the results of the first novelty that was delivered, the optimised controller has the ability to ensure stability between interfaced systems, and still deliver superior performance over traditional methods. Typically in traditional approaches, the PLL is interfaced as a decentralised control with respect to its interfaced converter, and therefore can be easily implemented into the proposed decentralised controller optimisation.

In order to augment the PLL dynamics into the H_2 optimisation, a new novel model of the PLL had to be devised in state-space in order to accurately interoperate the dynamics of V_{cq} into the global model; which is in general neglected in standard state-space modelling procedures. In section 5.1.1, the new model of the SRF-PLL was formulated to properly incorporate the fundamental dynamics of V_{cq}, which would have normally been neglected through standard modelling procedures, what often leads to the dq frame imbalance causing undesired interactions.

The novel model of the PLL was augmented into the control architecture in section 5.1.2 where also, due to the fact the PLL brings the interfaced converter to its generated DQ frame instead of that of the grid, adaptations to the global model were performed to incorporate further these interactive effects of the PLL between sub-systems, with the full augmented model accounting for PLL interactions being presented in (5.33)-(5.36).

In section 5.1.4, the novel PLL control optimisation procedure was simulated in MATLAB and it

was shown that the H_2 controller can successfully design a controller for both interfaced converters, and optimise the PLL controls with respect the closed loop performances of all sub-systems on the grid. The decentralised system showed no detrimental performance between the VSI and AFE, maintaining the performance attained previously with grid voltages remaining fixed during disturbances. The PLL, when compared against the traditional methods showed great improvement in dynamic performance, and was able to keep the AFE close to the true grid angle. Be it, closer alignment is also down to the fact the overall dynamic performance to disturbances of the system was greatly improved.

The performance of this novel approach to optimised PLL controller design was then verified experimentally on a test rig in section 5.1.4, where the same performance as that shown in simulation was achieved and verifies in practice the design.

Therefore, this novelty was delivered, offering a method of PLL controller design which guarantees stability of the sub-system, and mitigates against the interactive behaviour between interfaced converters and the PLL.

Novelty 3: Developing a controller which is scalable for easy expansion of optimised power networks (Chapter 6)

One of the greatest benefits to a decentralised control structure is the ability to expand the network to interface new converters on the network with ease due to no limitation on the communication bandwidth of the control.

As it was performed when interfacing the PLL to a grid connected converter, this deliverable was able to be augmented in similar fashion, by simply expanding the network to include a new converter states.

It was presented in section 6.1 how, if an additional AFE was to be augmented onto the AC grid, then to scale the controller accordingly, it's a matter of only copying the dynamic equations and extending the A and B_2 matrices accordingly. It was shown additionally, in order to interface the converter into the optimisation accurately, accountability of the additional PLL on the new converter must be considered. When augmenting a PLL to a given converter, the interactive effects the PLL incorporates onto the grid must be attributed correctly. This is also the main consideration to be taken when scaling the controller to incorporate more decentralised systems. In section 6.2, it was shown that the VSI states V_{cd} and V_{cq} were the most important states to be considered for the the new augmentation of additional PLL dynamics of the additional converter. The new AFE dynamics can be incorporated through a largely copy and paste exercise with only minor required adaptions for each AFE and VSI to attribute the new flow of current on the grid.

Using the methodology presented in 6.2, the second AFE converter was shown to be incorporated

successfully and decentralised optimal controls for all sub-systems developed accordingly. Simulations were performed in section 6.3 confirming that, as it was observed in the simpler system, performance and cross-interactive mitigation was maintained. Both the PLLs kept both AFEs close to the angle of the true grid voltage, and again interactive elements across all converters were largely mitigated, as was to be expected from previous analysis.

Novelty 4: Proposed Controller Adaptation for Frequency Wild systems (Chapter 7)

Whilst the approach of gain scheduled control for frequency varying systems is not a novel concept in itself, applying a gain scheduled approach to the proposed controller design is considered novel in application.

Whilst the majority of micro-grid interfaced systems may be operating at fixed frequency, which is perfect for the design discussed in novelties 1-3, in the application of MEA variable frequency micro-girds are the norm and therefore the controller must be adapted for changes in operating frequency. An issue, which may have been forethought due to the non-convex nature of the optimisation method, is that with changing frequency in the state-space model, the resultant gains may have little correlation. It was shown in the case of this study how important it is to select a sufficient number of random starting points in order to locate accurately the true global minima of the optimisation of J. If an insufficient number was selected, it was shown to deliver a non-optimal results, which produced sporadically changing gains indicating true global minimums, were not located on each optimisation. By supplying enough random starting points to the optimisation procedure it was shown that the optimisation can result in a convex solution and these convex solutions can attain gains which can fit very accurately to a second order interpolated polynomial as function of grid frequency.

The H_2 controller was then adapted successfully to augment the frequency as the scheduling variable to ensure optimal performance across the full frequency range (360-800Hz) typical of MEA.

In addition this controller was augmented in a different way to how the controller was implemented in the studies before. In this study, the VSI was fixed to a given PI control structure. The AFE was therefore optimised with the closed loop dynamics of the VSI supplied to the optimisation. This was to adapt the implementation of the control to a more industrial setting, where commercially acquired converters with known propriety controls may need to be interfaced with the to-be-designed AFE converter.

The variable frequency H_2 controller, as it got to be known, was implemented onto the AFE, and was tested along side the standard PI controller, and a similarly augmented locally optimised frequency scheduled LQR controller for a performance comparison.

It was shown by simulative results in section 7.2 that, as to be expected for the proposed

decentralised H_2 control and locally optimised LQR controller outperformed the non-optimised PI controller across the board in terms of performance. However, in comparison between the proposed and LQR controls, the LQR controller suffered from the interactive effects between converters, confirming that the H_2 based global optimisation can truly mitigate against such interactive behaviours. This was later confirmed through practical experimentation in section 7.2, where the same phenomena was observed, which even led to instability of the grid due to poor bandwidths of the LQR controller.

In addition, the proposed method of adaptation to the proposed controller for variable frequency operation was shown to be very successful. Stable steady state performance could be maintained throughout the frequency transient. Additionally even exhibiting the system to a step CPL load during a frequency transient displayed how the proposed controller can mitigate against interaction between the two converters, where the VSI operated to its set closed loop dynamics with little influence due to the AFE. On the other hand the LQR control caused greater and more prolonged oscillations to occur on the VSI states for the same transients.

Therefore, the proposed H_2 controller was successfully augmented for variable frequency grid environments, where it was shown little to no performance degradation occurs. Optimal performance across the full frequency range can be guaranteed and was additionally shown that, when optimising the H_2 control with consideration to pre-designed closed loop systems, interaction between the two systems can be mitigated, and performance of pre-designed system unaltered.

Novelty 5: Region of Attraction Approximation for Optimally Controlled 3-phase converters with no simplification (Chapter 9)

As it was briefly described in the small literature review provided at the start of Chapter 8, many common approaches to the Large Signal Stability analysis for three-phase converters revolved around simplifying the model to a single phase representation and the region of attraction approximation applied. However, as it was shown when applying the TS-Fuzzy method to the three-phase converter, any state not analysed in full in the ROA approximation can lead to ever more inaccurate approximations.

The novelty in this approach was to devise (or use) a methodology by which a full 5th-order non-linear AFE could be analysed to have its Region of Attraction (ROA) mapped as accurately as possible. The end result, which unfortunately due to the time limit of the PhD was not completed. The end aim of this project was to devise and incorporate an ROA expansion algorithm into the proposed H_2 controller algorithm to provide the most optimal performance and the most robust closed loop response possible.

Several popular methods for ROA approximation were presented, and tested on standard Van

der Pol models, and then on a simple DC electrical system to highlight how the methods achieve their approximations, and adaptations required, especially so for the case of Sum of Squares Optimisation to allow approximation of non-polynomial systems.

Due to the computational complexity of a Sum of Square (SOS) optimisation which resulted in long computational times for little improvement in the ROA approximation, the most popular SOS approach was excluded as a viable candidate. The faster methods of the TS-Fuzzy, and Random Sample algorithms were explored, and the TS-Fuzzy although fast, proved to be highly inaccurate in its approximations due to the fact that the integral states could not be augmented into the algorithm. The ROA from TS-Fuzzy inaccurately portrayed the role of the AFE d-axis current, I_{ad}, and the effect it has on the system stability, predicting this current could go to hundreds of amps instead of the approximately 40A of deviation the system could tolerate.

The Random Sample Approximation was therefore utilised. With all the states tested for their maximum possible deviations, a more accurate representation of the ROA for the three-phase AFE was achieved. Through simulative testing, it was shown that this region was accurate in its approximation, with all points inside the region being shown to be stable. By use of dimensional slicing in order to attain 3-d representations of all the 5-states interacting with one another, the ROA was easily envisioned. With the quantifiable measure of robustness, given as the square of the radius of the elliptical region, it becomes easy to envision how this approximation could be augmented into the H_2 algorithm to ensure maximum robustness. This will be further discussed in the next section on future work.

9.2 Limitations and Future Work

A novel approach to the design and optimisation of decentralised controls for hybrid DC/AC grids has been proposed in this work. The majority of the novelties developed in this work were simulated to prove the mathematical concepts, and additionally verified experimentally to prove the practical implementation of the designs. However, there are still many questions that readers may consider limitations to the research conducted and must be addressed in future works. These limitations can be summarised as follows:

***Limitation 1:* The application of proposed controller design to grid sized systems**

Whilst it has been shown that the controller can be scaled up to include a number more AFEs, the research did not extend towards expansion of more sourcing VSI converters, the complex variety of loads which could be augmented onto the AFEs, or the inclusion of more exotic power electronics topologies. Questions may rise about whether an optimal solution to the decentralised H_2 problem

can be maintained for such additions to the grid. Knowing the decentralised control problem is an NP-Hard algorithm, for a grid sized system of tens of power electronic units, limitations of the proposed approach may occur, and it is not known whether optimal performance can be maintained globally. Upon application of an additional AFE, the time of computation of the optimal control, and the performance achieved suggests that increasing the size of the gird with multiple 3-phase devices will not impede the expected performance of the system. However application of newer power electronic topologies such as matrix converters, or dual active bridges is still an area which has been unexplored and would be interesting to look into in future work.

Future Work 1:

Applying the proposed decentralised controller design to greatly expanded grid with different interfaced power electronic sub-systems and loads.

Limitation 2: **Modelling of the droop controls for grids with multiple VSIs**

Referring back to some of the most recently published works in the are of decentralised control in micro-grid systems, there is particular interest these days in paralleled VSI converters sourcing a three-phase grid. In order to ensure complete synchronisation of the grid frequencies of each VSI sub-system, a decentralised droop control architecture is adopted, which ensures not only synchronous behaviour, but also good power flow in fixed frequency environments. As it was done when adopting multiple AFEs and modelling the PLL dynamics for each converter in the optimisation, it would be very beneficial for future applications of this controller design method if similar optimised droop controllers can be synthesised for additionally interfaced VSIs.

Future Work 2:

The modelling and expansion of the grid with multiple VSI converters, with their corresponding droop control dynamics augmented into the optimisation, for droop optimisation.

Limitation 3: **Inclusion of a unified global sizing and performance optimisation for aircraft power electronic embedded grids**

Design of a power grid in MEA applications is not just a matter of designing power electronic sub-systems and connecting them together. As it was pointed out, it is a balance of the sizing of the system, down to the control, and to high frequency filtering (EMC filtering) requirements. This research mainly entailed within the control of the grid in a decreased passive filter environment but an end goal would be to develop a tool which can optimise the size of the system, develop

the optimal control for said system, and interpolate the EMC requirements by specification. Joint studies conducted by the University of Nottingham with Virginia Tech [28] and G2E Labs [26] had been looking into a unified optimisation algorithm from which the sizing, control and EMC can all be automatically designed under one optimisation procedure. In the future it would be good to attempt to unify the above optimisation procedure into a global design optimisation for MEA grid applications.

Future Work 3:

Design and implementation of a unified optimisation procedure for sizing, control and EMC design for more realistic MEA power system development.

Limitation 4: **Implementation of ROA research into the controller optimisation algorithm**

The original aim of the work which was conducted in Chapter 8 regarding the ROA stability analysis of AFE converters was to devise a quantifiable approach to analysing the closed loop large signal stability for a given converter. This work was then to be included as part of the H_2 optimisation problem in order to optimise the performance of said converter to the grid, but also to ensure the maximum possible robustness given the weighting constraints set by the designer. Unfortunately due to the time limit of the PhD, this part of the work could not be completed. However, a fast viable method of ROA approximation was developed, which gave accurate results without simplification of the converter model.

Whilst the work performed may not be realisable for the application of full grid optimisation, unless performing the ROA analysis on each individual sub-system for each decentralised control, it could achieve great benefits with the system identification controller optimisation which is some on-going research utilising the proposed controller design from this thesis. Please read papers [170, 127] for more information on this. By optimising the controller for an individual converter with respect to a predefined grid, the research already performed can easily be applied to the optimisation procedure of single converter controls. This is something which is wished to be looked into in the near future beyond the PhD.

Future Work 4:

Augmentation of the ROA approximation algorithm into the H_2 optimisation. Apply to grid optimisation or the single converter optimisation through grid identification techniques to ensure expanded robustness within design constraints set by the engineer.

Appendix A

Standard Version H_2 MATLAB Scripts

A.1 Basic H_2 Controller Synthesis MATLAB Script

```
w = 2*pi*400;
C = 33e-6;
L = 230e-6;
R = 120e-6;

Vdc_source = 300;

%AFE Parameterse
Cdca = 100e-6;
La = 565e-6;
Ra = 0.8;

Ca = Cdca;
Ved = 100*sqrt(2);
Vcd = Ved;
Vcq = 0;
Vdc = 400;
Vdca = Vdc;
```

```
Rl = 96;
Pl = 1000;

Iaq = 0;

pd = (Vcd + sqrt(Vcd^2 - ((8*Pl*Ra)/3)))/(Vdc);
pq = -(La*w*(Vcd - sqrt(Vcd^2 - ((8*Pl*Ra)/3))))/(Ra*Vdc);
Iad = (Vcd - sqrt(Vcd^2 - ((8*Pl*Ra)/3)))/(2*Ra);

syms Iid Iiq Iad Vdin Vqin Vd Vq
[Iide,Iiqe,Iade,Vdine,Vqine,Vde,Vqe]=solve(...
[1/C*Iid+w*Vcq-1/C*Iad==0,...
-w*Vcd+1/C*Iiq-1/C*Iaq==0,...
w*Iiq-R/L*Iid-1/L*Vcd+Vd/L==0,...
-w*Iid-R/L*Iiq-1/L*Vcq+Vq/L==0,...
3/4/Ca*(2*Vdin/Vdca*Iad+2*Vqin/Vdca*Iaq)-Vdca/Ca/Rl==0,...
-Ra/La*Iad-Vdin/La+Vcd/La+w*Iaq==0,...
-Ra/La*Iaq-Vqin/La+Vcq/La-w*Iad==0],[Iid,Iiq,Iad,Vdin,Vqin,Vd,Vq]);

Iide=double(Iide(1));
Iiqe=double(Iiqe(1));
Iade=double(Iade(1));
Vdine=double(Vdine(1));
Vqine=double(Vqine(1));
Vde=double(Vde(1));
Vqe=double(Vqe(1));
equilibrium=[Iide,Iiqe,Iade,Vdine,Vqine,Vde,Vqe]

A = [-R/L -1/L w 0 0 0 0 0 0 0 0;
1/C 0 0 w -1/C 0 0 0 0 0 0;
-w 0 -R/L -1/L 0 0 0 0 0 0 0;
0 -w 1/C 0 0 -1/C 0 0 0 0 0;
0 1/La 0 0 -Ra/La w -pd/(2*La) 0 0 0 0;
0 0 0 1/La -w -Ra/La -pq/(2*La) 0 0 0 0;
```

```
0 0 0 0 (3*pd)/(4*Cdca) (3*pq)/(4*Cdca) Pl/(Cdca*(Vdc^2)) 0 0 0 0;
0 -1 0 0 0 0 0 0 0 0 0;
0 0 0 -1 0 0 0 0 0 0 0;
0 0 0 0 0 -1 0 0 0 0 0;
0 0 0 0 0 0 -1 0 0 0 0];


Iad = Iide;
Iaq = 0;

B2 = [Vdc_source/(2*L) 0 0 0;
0 0 0 0;
0 Vdc_source/(2*L) 0 0;
0 0 0 0;
0 0 -Vdca/(2*La) 0;
0 0 0 -Vdca/(2*La);
0 0 (3*Iad)/(4*Cdca) (3*Iaq)/(4*Cdca);
0 0 0 0;
0 0 0 0;
0 0 0 0;
0 0 0 0];

% matrix of reference signal
B1 = [0 0 0 0;
0 0 0 0;
0 0 0 0;
0 0 0 0;
0 0 0 0;
0 0 0 0;
1 0 0 0;
0 1 0 0;
0 0 1 0;
0 0 0 1];
```

```
% matrix of disturbance (only on the afe dc-bus)
Bd = [0 0 0 0 0 0 0 0 0 0 1/Cdca]';

C2 = eye(11);


Q = -1*diag([0 0 0 0 0 0 0 1 1 1 1]);
Rx = 1*diag([1 1 1 1]);

C1 = cat(1, sqrt(Q), zeros(4,11));
D12 = cat(1, zeros(11,4), sqrt(Rx));

D11 = zeros(15,11);
D21 = zeros(11,11);
D22 = zeros(11,4);

P1.A = A;
P1.B1 = eye(11);
P1.B2 = B2;
P1.C1 = C1;
P1.C2 = C2;
P1.D11 = D11;
P1.D12 = D12;
P1.D21 = D21;
P1.D22 = D22;

options.prtlevel = 0;
options.nrand = 10;

%Force feedback to provide feedback to designated states:

options.struct.d = [1 1 1 1 0 0 0 1 1 0 0;
1 1 1 1 0 0 0 1 1 0 0;
0 0 0 0 1 1 1 0 0 1 1;
0 0 0 0 1 1 1 0 0 1 1];
```

```
% lqr
P = ss(A,B2,C2,[]);
[K_lqr,S,e] = lqr(P,Q,Rx,[]);
K_lqr;

% initiazize hifoo to lqr gain
init.a = [];
init.b = zeros(0,11);
init.c = zeros(4,0);
init.d = -K_lqr.*options.struct.d;

[K,F] = hifoo(P1, 't', init, options);
K_hifoo = K.d;

s = ss(A+B2*K.d*C2, B1, Cc1, []);

K_s = [K.d(1) K.d(5) K.d(9) K.d(13) K.d(17) K.d(21) K.d(25);
K.d(2) K.d(6) K.d(10) K.d(14) K.d(18) K.d(22) K.d(26);
K.d(3) K.d(7) K.d(11) K.d(15) K.d(19) K.d(23) K.d(27);
K.d(4) K.d(8) K.d(12) K.d(16) K.d(20) K.d(24) K.d(28)];

K_s_error = [K.d(29) K.d(33) K.d(37) K.d(41);
K.d(30) K.d(34) K.d(38) K.d(42);
K.d(31) K.d(35) K.d(39) K.d(43);
K.d(32) K.d(36) K.d(40) K.d(44)];

vsi_afe_sim_v3(K_hifoo, C, R, L, Vdc_source, Ra, La, Cdca, Pl);
```

A.2 Average Model ODE45 Simple VSI and AFE System Simulation with H_2 controller implementation MATLAB Script

```
function [t,x] = vsi_afe_sim_v3(K, C, R, L, Vdc, Ra, La, Cdca, Pl)

        opt = odeset('RelTol', 1e-3);

        tspan = [0 0.1];

        x0 = [0 100*sqrt(2) 0 0 0 0 400 0 0 0 0];

        % simulate
        [t,x] = ode45(@(t,x) vsi_afe_model(t,x,K, C, R, L, Vdc, Ra,
                                ...La, Cdca, Pl), tspan, x0, opt);

        l = size(x,1);
        out = zeros(l,4);
        for(i=1:l)
                out(i,:) = K(:,8:11)*x(i,8:11)' + K(:,1:7)*x(i,1:7)';
        end

end

function [xp] = vsi_afe_model(t, x, K, C, R, L, Vdc, Ra, La, Cdca, Plx)


        w = 2*pi*400;

        C_ref = [0 1 0 0 0 0 0;
        0 0 0 1 0 0 0;
        0 0 0 0 0 1 0;
        0 0 0 0 0 0 1];
```

```
Iid = x(1);
Vcd = x(2);
Iiq = x(3);
Vcq = x(4);
Iad = x(5);
Iaq = x(6);
Vdca = x(7);
% integral states
ws = x(8:11);

% reference signals
ref = [100*sqrt(2); 0; 0; 400];

% AFE load
if(t > 0.05)
        Pl = Plx;
else
        Pl = 0;
end

% controller
err = ref - C_ref*x(1:7);

out = K(:,8:11)*ws + K(:,1:7)*x(1:7);

% integral action
wsp = err;

% saturate control
%       for(i=1:4)
%           if(abs(out(i)) > 1)
%               out(i) = sign(out(i));
%           end
%       end
```

```
        md = out(1);
        mq = out(2);
        pd = out(3);
        pq = out(4);

        % VSI equations
        Iidp = (-R/L)*Iid + w*Iiq + (-1/L)*Vcd + (Vdc/(2*L))*md;
        Vcdp = Iid/C + w*Vcq + (-1/C)*Iad;
        Iiqp = (-w)*Iid + (-R/L)*Iiq + (-1/L)*Vcq + (Vdc/(2*L))*mq;
        Vcqp = Iiq/C + (-w)*Vcd + (-1/C)*Iaq;

        % AFE equations
        Iadp = (-Ra/La)*Iad + w*Iaq + (-1/(2*La))*Vdca*pd + Vcd/La;
        Iaqp = (-w)*Iad + (-Ra/La)*Iaq + (-1/(2*La))*Vdca*pq + Vcq/La;
        Vdcap = (3/(4*Cdca))*Iad*pd + (3/(4*Cdca))*Iaq*pq + (-Pl/(Cdca*(Vdca)));

        xp = [Iidp; Vcdp; Iiqp; Vcqp; Iadp; Iaqp; Vdcap; wsp];

end
```

A.3 MATLAB Switching Model PWM Script

The resolution variable $'res'$ was set to 1000 externally from the function. The sampling time was intrinsic to the block and was set to $1/(f_s \times res \times 4)$ where f_s is equivalent to the switching frequency of the converter. In this case $10kHz$.

```
function g = fcn(t, res)

        persistent cnt inc;
        if(isempty(cnt))
                cnt = res;
                inc = -1;
        end

        cnt = cnt + inc;
        if(cnt == res)
                inc = -1;
        end
        if(cnt == -res)
                inc = 1;
        end

        t = round(t);

        g1 = 0;
        g2 = 0;
        g3 = 0;

        if(t(1) > cnt)
                g1 = 1;
        end

        if(t(2) > cnt)
                g2 = 1;
        end
```

```
        if(t(3) > cnt)
                g3 = 1;
        end

        g = [0 0 0 0 0 0];

        g(1) = g1;
        g(2) = ~g1;
        g(3) = g2;
        g(4) = ~g2;
        g(5) = g3;
        g(6) = ~g3;

end
```

A.4 Switching Model H_2 Controller Script

In this script, K_s are the gains associated directly with the states. Can also be seen as the proportional gains of the state-feedback control. K_s_error are thus the integral gains. The variables e_{int} are the internal integral states. In this case the integrals were set to zero on start-up to analyse the start-up characteristics of the system. If one wants to analyse the system at steady state condition, then the integrals can be set to their steady state values by solving the closed loop equilibrium points for each integral.

```
function [md_out, mq_out, pd_out, pq_out, e_vsi, e_afe] = ...
fcn(Iid, Vcd, Iiq, Vcq, Iad, Iaq, Vdca, Vcd_ref, Vcq_ref, Iaq_ref,...
Vdca_ref, K_s, K_s_error, C_s, K_lqr, K_hifoo, Ts)

        persistent e_int;

        if(isempty(e_int))
                e_int = [0;0;0;0];
        end


        states = [Iid; Vcd; Iiq; Vcq; Iad; Iaq; Vdca];

        input = [Vcd_ref; Vcq_ref; Iaq_ref; Vdca_ref];

        K_states = K_hifoo(:,1:7)*states;

        C_states = C_s*states;

        error = input - C_states;

        e_int = e_int + Ts*error;

        K_error_OP = K_hifoo(:,8:11)*e_int;

        output = K_error_OP + K_states;
```

```
        md_out = output(1);
        mq_out = output(2);
        pd_out = output(3);
        pq_out = output(4);

        e_vsi = [e_int(1); e_int(2)];
        e_afe = [e_int(3); e_int(4)];

end
```

Appendix B

DSP Controller C Code for Experimental Setup

B.1 DSP Interrupt Handler Code

The following code is executed on every CPU interrupt routine. It contains all the files required for sampling the input signals, running a function *compute_theta*() to condition these signals into the required dq frame terms. The switch state $fpga\_state()$ is controlled by a manual switch, where IDLE is where the controller is not running, but variables are held at their initialization states. RUN is when the control algorithm *crtl_step*() is running, and computes the required control outputs $duty\_VSI[]$; and $duty\_AFE[]$;, which are sent to the fibre-optic output modules via *set_duty*() to control the gate switching actions. On each interrupt, the fault conditions are checked via an ADC C code function (not presented here) which compares the sampled signals against pre-set limits by the designer. If a signal is sensed to be out the minimum or maximum bounds set by the ADC, a FAULT condition is established and all control actions stop. In order to run the controller, inside *main*() code of the DSP, it waits for a reset signal from the external switch controlled by the user. This received resets puts the program back into the IDLE state, for which then the RUN state can be reinitiated. The variables $lBuffer[]$ are values which store historic values of specified signals into a buffer. When a trigger has been set, and then triggered by the command $scope\_trigger = 1$, $lBuffer[]$ stops feeding values in the buffer. The buffer can then be read directly via MATLAB through a USB communications bus such that the data can be plotted and presented in the results for this thesis. The term $rmt\_cmd[]$ are variables whose value is determined by the user via MATLAB through the same USB communications bus. These values

can hold the required reference values for the controller, or allow the user to change parameters during controller operation on the fly. For instance *PL* holds the reference value for the power, *LOAD_ON* commands when the CPL is to be turned ON. *AFE_Reset* allows the user to turn the AFE controls on or off via the *crtl_step*() function, and all other terms should be self explanatory. This code is utilised for all the tests presented in this thesis, and thus some variables may only be understood after reading a given section of the thesis, for instance the PLL and the VSI frequency ramp, both of which were used in the experimentation results presented in Section 5 and Section 7 respectively. Having these functionalities of the controller being turned on or off by use of *rmt_cmd*[] allows this file to be used for all the experiments conducted as part of the work in this thesis.

```
void Ctrl_Intr_Handler(void *data){
        float d_break;

        isr_start();
        led_on();

        state = fpga_state();

        //VSI Terms

        // CURRENTS ON NEW CONVERTER :
        //IA = IB and IB = IC (changed in DQ_TRANS)

        float Ia_VSI = adc_gains[5]*get_adc(5) + adc_offs[5];
        float Ib_VSI = adc_gains[6]*get_adc(6) + adc_offs[6];
        float Vdc_source = adc_gains[7]*get_adc(7) + adc_offs[7];

        //Grid Voltages
        float Vab = adc_gains[8]*get_adc(8) + adc_offs[8];
        float Vbc = adc_gains[9]*get_adc(9) + adc_offs[9];

        //AFE Terms

        //Previous test shows simulation currents are opposite to that of rig
```

```
float Ia_AFE = -(adc_gains[0]*get_adc(0) + adc_offs[0]);
float Ib_AFE = -(adc_gains[1]*get_adc(1) + adc_offs[1]);
float Ic_AFE = -(adc_gains[2]*get_adc(2) + adc_offs[2]);
float Vdc_link = adc_gains[3]*get_adc(3) + adc_offs[3];

float LOAD_ON = rmt_cmd[6];
float PL = rmt_cmd[7];


static float Iidq[2], Iadq[2], Vcdq[2], AFE_FREQ[1];

int Angle_ramp_start = rmt_cmd[11];

int PLL_ON = rmt_cmd[5];

compute_theta(Ia_VSI, Ib_VSI, Ia_AFE, Ib_AFE, Ic_AFE,...
Vab, Vbc, Iidq, Iadq, Vcdq, PLL_ON, AFE_FREQ, Angle_ramp_start);

if (LOAD_ON == 1){
        d_break = (PL * 19.42) / (Vdc_link*Vdc_link);
        //scope_trigger = 1;
}
else {
        d_break = 0;
}

//      if (Vdc_link > 375){
//              scope_trigger = 1;
//      }


set_duty_br(d_break, 0);
set_duty_br(0, 1);
set_duty_br(0, 2);
```

```
float Vcd = Vcdq[0], Vcq = Vcdq[1], Iid = Iidq[0],...
Iiq = Iidq[1], Iad = Iadq[0], Iaq = Iadq[1];

//Controller Reference Values
float Vcd_ref = rmt_cmd[0];
float Vcq_ref = rmt_cmd[1];
float Iaq_ref = rmt_cmd[2];
float Vdca_ref = rmt_cmd[3];

if (Vcd_ref > 100){
        scope_trigger = 1;
}

int controlSelect = rmt_cmd[9];
int h2ControlType = rmt_cmd[10];

static float Vcd_r = 10;
float rate = Vcd_ref;

int AFE_Reset = rmt_cmd[4];

float duty_VSI[3], duty_AFE[3];
static float mdq[2] = {0} , pdq[2] = {0};

switch(state){

        case IDLE:

                ctrl_init(Vcd_ref);
                dq_init();
        break;

        case RUN:
```

```
                    //scope_trigger = 1;
                    Vcd_r += rate;

                    if (Vcd_r > Vcd_ref){
                            Vcd_r = Vcd_ref;
                    }

            ctrl_step(AFE_Reset, Vcd, Vcd_r, Vcq, Vcq_ref, Iid, Iiq, ...
            Vdc_link, Vdca_ref, Iad, Iaq, Iaq_ref, Vdc_source, duty_VSI,...
            duty_AFE, mdq, pdq, LOAD_ON, controlSelect, AFE_FREQ,...
            h2ControlType);
            break;

            case FAULT:
                    //scope_trigger = 1;
                    break;
    }

    set_duty(duty_VSI[0], 0 ,1);
    set_duty(duty_VSI[1], 1 ,1);
    set_duty(duty_VSI[2], 2 ,1);

    set_duty(duty_AFE[0], 0 ,0);
    set_duty(duty_AFE[1], 1 ,0);
    set_duty(duty_AFE[2], 2 ,0);


    //DQ TERMS READ/////////////////

    lBuffer[0] = Iid; lBuffer[1] = Iiq;
    lBuffer[2] = Vcd; lBuffer[3] = Vcq;
    lBuffer[4] = Iad; lBuffer[5] = Iaq;
    lBuffer[6] = Vdc_link;

    //ABC TERMS READ/////////////////
```

```
        lBuffer[7] = Ia_VSI; lBuffer[8] = Ib_VSI;
        lBuffer[9] = Ib_AFE; lBuffer[10] = Ic_AFE;
        //Va, Vb, Vc (11, 12, 13) read in DQ Trans

        //MODULATION INDEX READ//////////
        lBuffer[14] = mdq[0]; lBuffer[15] = mdq[1];
        lBuffer[16] = pdq[0]; lBuffer[17] = pdq[1];

        lBuffer[18] = duty_VSI[0]; lBuffer[19] = duty_VSI[1];
        lBuffer[20] = duty_VSI[2];
        lBuffer[21] = duty_AFE[0]; lBuffer[22] = duty_AFE[1];
        lBuffer[23] = duty_AFE[2];

        //REMAINING 24,25,26 read angles in DQ Trans

        //Source Votlage Read

        lBuffer[27] = Vdc_source;
        lBuffer[28] = Vab;
        lBuffer[29] = Vbc;
        //      lBuffer[30] = d_break;

        scope_acquire();

        isr_end();
}
```

B.2 Experimental Rig *compute_theta*() algorithm

This function performs many important operations in regards to signal conditioning. This function contains the SRF-PLL PI controller, determining θ of the grid for the AFE dq translation and controls. It conditions the voltages V_{ab} and V_{bc} so that the three-phase form can be computed. The Clarke and Park transforms to translate abc frame signals to dq and vice versa additionally occur in this function.

```
#include "dq_trans.h"
#include "scope.h"
#include <math.h>
#define M_PI 3.14159265358979323846

#define SQRT3_3          5.773502691896257e-1
#define SQRT3_2          8.660254037844386e-1

#define TS 5.0000e-05
#define freq 400

#define incr_theta 0.12566370614 //400Hz
//#define incr_theta 0.25132741228 //800Hz
#define freq_init 360

static float sine = 0.00, cosine = 0.00, th = 0;
static float sine_PLL = 0.00, cosine_PLL = 0.00, th_PLL = 0.00;
static float PLL_INT = 0.00;
static int Phase_Shift = 0;

//const float Kp = 4.24200, Ki = 900.00000;

//const float Kp = 2.96985, Ki = 636.39610;
const float Kp = 4.242000, Ki = 900.000000;

static float vsi_f = freq_init;

void dq_init(){
```

```
        vsi_f = freq_init;
}

void foc_tr_sin_cos(){
        /*sine = sinf_neon(th);*/
        sine = sin(th);
        cosine = cos(th);

        sine_PLL = sin(th_PLL);
        cosine_PLL = cos(th_PLL);
}

void foc_tr_park(float al, float be, float *d, float *q, int PLL){
        if (PLL != 1){
                *d = cosine*al + sine*be;
                *q = -sine*al + cosine*be;
        }

        if (PLL == 1){
                *d = cosine_PLL * al + sine_PLL * be;
                *q = -sine_PLL * al + cosine_PLL * be;
        }
}

void foc_tr_park_inv(float d, float q, float *al, float *be, int PLL){
        if (PLL != 1){
                *al = cosine*d - sine*q;
                *be = sine*d + cosine*q;
        }

        if (PLL == 1){
                *al = cosine_PLL * d - sine_PLL * q;
                *be = sine_PLL * d + cosine_PLL * q;
        }
```

```
}

void foc_tr_clarke(float a, float b, float c, float *al, float *be){
        *al = 0.6666*a -0.3333*b -0.3333*c;
        *be = SQRT3_3*b -SQRT3_3*c;
}

void foc_tr_clarke_inv(float al, float be, float *a, float *b, float *c){
        *a = al;
        *b = -0.5*al + SQRT3_2*be;
        *c = -0.5*al - SQRT3_2*be;
}

float theta_incr(float Angle_ramp_start){
        const int ramp_rate = 300;

        if (Angle_ramp_start == 1 && vsi_f <= rmt_cmd[12]){
                //              scope_trigger = 1;
                vsi_f += ramp_rate* TS;
        }

        return (2*M_PI*vsi_f*TS);
}

void compute_theta(float Ia_VSI, float Ib_VSI, float Ia_AFE, float Ib_AFE,...
float Ic_AFE, float Vab, float Vbc, float *Iidq, float *Iadq,...
float *Vcdq, int PLL_ON, float *AFE_FREQ, int Angle_ramp_start){

        float Va = ((2 * Vab) / 3) + (Vbc / 3);
        float Vb = (Vbc / 3) - (Vab / 3);
        float Vc = -(Vab / 3) - ((2 * Vbc) / 3);

        lBuffer[11] = Va; lBuffer[12] = Vb; lBuffer[13] = Vc;

        foc_tr_sin_cos();
```

```
float al[1], be[1], d[1], q[1];

foc_tr_clarke(Va, Vb, Vc, al, be);
foc_tr_park(al[0], be[0], d, q, 0);
Vcdq[0] = d[0];
Vcdq[1] = q[0];

foc_tr_clarke(Ia_VSI, Ib_VSI, -Ia_VSI-Ib_VSI, al, be);
foc_tr_park(al[0], be[0], d, q, 0);
Iidq[0] = d[0];
Iidq[1] = q[0];

foc_tr_clarke(Ia_AFE, Ib_AFE, Ic_AFE, al, be);
foc_tr_park(al[0], be[0], d, q, 1);
Iadq[0] = d[0];
Iadq[1] = q[0];

th += theta_incr(Angle_ramp_start);

if ((rmt_cmd[8] != 0) && Phase_Shift == 0){
        th = th - M_PI/4;
        Phase_Shift = 1;
        //scope_trigger = 1;
}

if (rmt_cmd[8] == 0){
        Phase_Shift = 0;
}


if (th > 2*M_PI) {
        th = th - 2*M_PI;
}
```

```
        foc_tr_clarke(Va, Vb, Vc, al, be);
        foc_tr_park(al[0], be[0], d, q, 1);
        float err = q[0];

        PLL_INT = PLL_INT + (err*TS);

        float output_PI = (Kp*err) + (Ki*PLL_INT) + (2.0*M_PI*freq);

        AFE_FREQ[0] = output_PI / (2*M_PI);
        lBuffer[24] = AFE_FREQ[0];

        th_PLL = th_PLL + (output_PI*TS);

        if (th_PLL >= 2*M_PI){
                th_PLL = th_PLL - 2*M_PI;
        }

        if (PLL_ON != 1){

                th_PLL = th;
                PLL_INT = 0.00;
        }

        lBuffer[25] = th_PLL;
        lBuffer[26] = th - th_PLL;

}
```

Appendix C

Variable Frequency LQR Controller Performance at Different Bandwidths

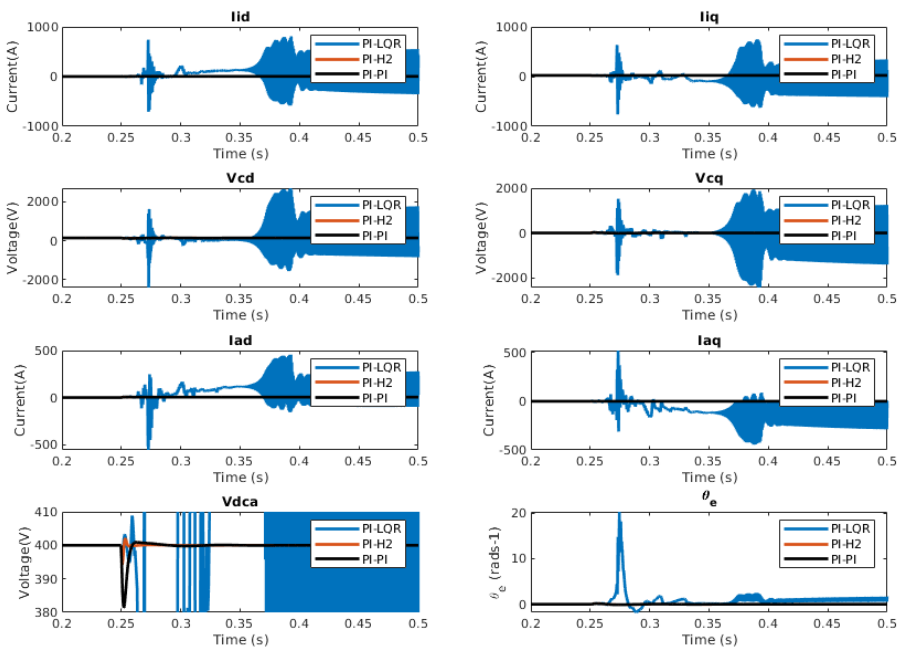

Figure C.1: LQR Performance at 400Hz operation for system described in Chapter 7 with an decreased Q_γ coefficient of 30

In figure C.1 the Q_γ coefficient has been reduced by half from the nominal value of 60 to a value of 30. The decrease in bandwidth during a loaded operation causes system instability.

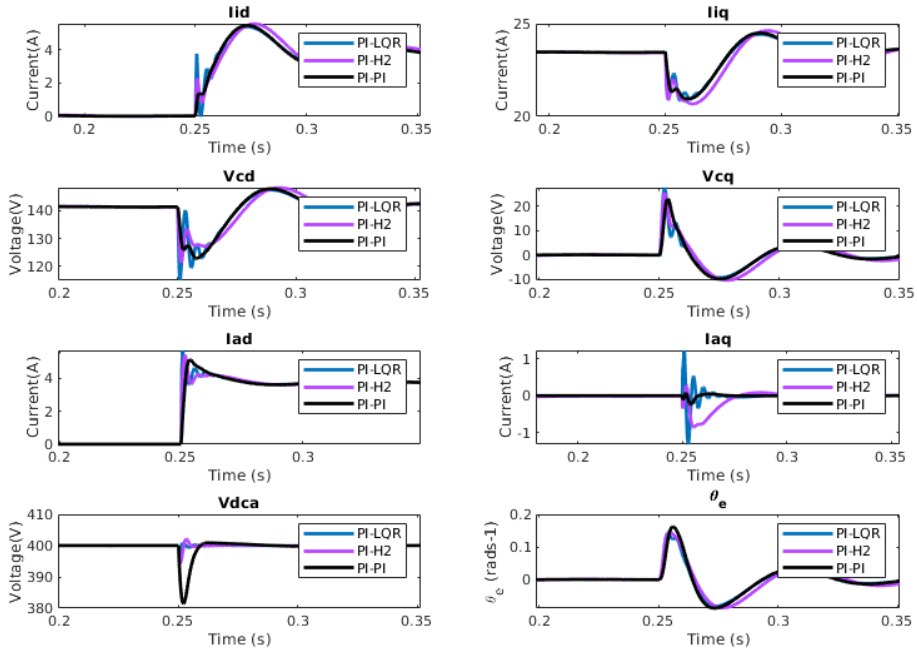

Figure C.2: LQR Performance at 400Hz operation for system described in Chapter 7 with an increased Q coefficient of 400

In figure C.2 the bandwidth is increased to $400Q_\gamma$. When compared with the default performance shown in Figure 7.13 the oscillation are somewhat smaller. However, on the implementation of the experimental rig, this controller wasn't function due to the lack of robustness as large gains in $K(\omega)$ are synthesised. Hence why $60Q_\gamma$ was selected for the test.

Appendix D

MATLAB Codes for ROA Approximations

D.1 VS Iteration for ROA Estimation of Van der Pol Oscillator

```
%STEP 0 - For reference of algorithm only. This plots the reference ROA,
%where it is aimed to find V(X) that conforms to similar shape and this
%maximimizing V(X)

% Create vector field for VDP dynamics: dx/dt = f(x)
pvar x1 x2;
x = [x1;x2];
x1dot = -x2;
x2dot = x1+(x1^2-1)*x2;
f = [x1dot; x2dot];

% Plot VDP limit cycle using backward simulation. The actual region of
% attraction is the interior of the set bounded by this limit cycle.
X0 = [0.1; 0.1];
Tf = 100;
[xtraj,isconv]=psim(-f,x,X0,Tf);
QQ = xtraj;
t = xtraj{1};
```

```
xtraj = xtraj{2};
idx = min(find(t>=Tf*0.8));

figure(1)
hold off;
ph1=plot(xtraj(idx:end,1),xtraj(idx:end,2));
set(ph1,'LineWidth',2)
xlabel('x1');
ylabel('x2');
hold on;

%STEP 1 - INITIALIZE LYAPUNOV EQUIATION FOR VS ITERATION

Alin = plinearize(f,x);
Q = eye(2);
P=lyap(Alin',Q);
V = x'*P*x;
Px = x'*x;

deg = 1;
tol = 12;
%STEP 2 - Optimize S2 and GAMMA for current V(X)

[GAM, S2] = Step2_S2_GAM_Optimize(V, x, f, deg);

% Plot ROA estimate:= countour of V associated with gamma level set.
domain = [-3 3 -3 3];
[C,ph2]=pcontour(V,GAM,domain,'r-');
set(ph2,'LineWidth',2)
hold on; grid on;

%STEP 3 - Optiimize inner approximation of ROA to expand GAM. Beta S1
%Bilinear optimization
```

```
[BETA, S1] = Step3_S1_Beta_Optimize(V, x, GAM, Px, deg, tol);

[C,ph3]=pcontour(Px,BETA,domain,'r:');
set(ph3,'LineWidth',2)
hold on; grid on;

deg = 1;

%Perform 1 more interation of steps above
[V,Vdot] = Step4_Lyapunov_Order_Search(x, f, GAM, BETA, Px, S1, S2, deg);
[GAM, S2] = Step2_S2_GAM_Optimize(V, x, f, deg);
[BETA, S1] = Step3_S1_Beta_Optimize(V, x, GAM, Px, deg, tol);

deg = 2;

[V,Vdot] = Step4_Lyapunov_Order_Search(x, f, GAM, BETA, Px, S1, S2, deg);
[GAM, S2] = Step2_S2_GAM_Optimize(V, x, f, deg);
[BETA, S1] = Step3_S1_Beta_Optimize(V, x, GAM, Px, deg, tol);

count = 0;
i = 0;

b1 = 0;
b2 = 0;
b3 = 0;
b4 = 0;

deg = 3;

[V,Vdot] = Step4_Lyapunov_Order_Search(x, f, GAM, BETA, Px, S1, S2, deg);
[GAM, S2] = Step2_S2_GAM_Optimize(V, x, f, deg);
[BETA, S1] = Step3_S1_Beta_Optimize(V, x, GAM, Px, deg, tol);

i = 0;
```

```
count = 0;

deg = 4;

while i ~= 1

        [V, Vdot] = Step4_Lyapunov_Order_Search(x, f, GAM, BETA, Px, S1,
         S2, deg);
        [GAM, S2] = Step2_S2_GAM_Optimize(V, x, f, deg);
        [BETA, S1] = Step3_S1_Beta_Optimize(V, x, GAM, Px, deg, tol);

        count = count + 1;
        fprintf('count = %4.3f\n',count);

        b4 = b3;
        b3 = b2;
        b2 = b1;
        b1 = round(BETA,3);

        if count == 10
        [C,ph23]=pcontour(V,GAM,domain,'m-');
        set(ph23,'LineWidth',2)
        hold on; grid on;

        [C,ph33]=pcontour(Px,BETA,domain,'m:');
        set(ph33,'LineWidth',2)
        hold on; grid on;
        end

        if (b1 == b3 && b2 == b3 && b3 == b4)
        i = 1;
        end

        if (count > 30)
        i = 1;
```

```
        end

end

[C,ph23]=pcontour(V,GAM,domain,'k-');
set(ph23,'LineWidth',2)
hold on; grid on;

[C,ph33]=pcontour(Px,BETA,domain,'k:');
set(ph33,'LineWidth',2)
hold on; grid on;


function [g, s] = Step2_S2_GAM_Optimize(V, x, f, deg)

        % Set options
        opts = gsosoptions;
        opts.minobj = -50;
        opts.maxobj = 0;

        % STEP 2 - Solve for maximum GAMMA and S2.

        z = monomials(x, 1:deg);

        pvar t;
        s = sosdecvar('c',z);
        Vdot = jacobian(V,x)*f;

        sosc = polyconstr;
        sosc(1) = s>=0;
        sosc(2) = Vdot <= -1e-6*(x'*x) + s*(V+t);

        % Solve with gsosopt
        [info,dopt,sossol] = gsosopt(sosc,x,t,opts);
        s = subs(s,dopt);
```

```
        g = -info.tbnds(2);
        fprintf('gamma = %4.3f\n',g);

end

function [Beta, S1] = Step3_S1_Beta_Optimize(V, x, GAM, Px, deg, tol)

        %Check variable for Convergence
        n = 0;
        test_chk = 0;
        bisection_count = 0;
        bisection_find = 0;
        Beta_U = 0;
        Beta_L = 0;
        Beta_P = 0;
        S1x_P = 0;

        % Set options
        opts = gsosoptions;
        opts.minobj = -50;
        opts.maxobj = 0;

        z = monomials(x, 1:deg);
        Beta = 2^n;
        s_h = 0;

        s = sosdecvar('c',z);

        while test_chk ~= 1

                sosc = polyconstr;
                sosc(1) = s >=0;
                sosc(2) = -((V - GAM) + s*(Beta - Px)) >= 0;
                [info,dopt,sossol] = sosopt(sosc,x,opts);
```

```
if(isempty(dopt))
if bisection_count < tol
bisection_count = bisection_count + 1;
bisection_find = 1;
else
test_chk = 1;
Beta = Beta_P;
S1 = s_h;
fprintf('Beta = %f\n',Beta);
end
end

if bisection_count == 0
        n = n+1;
        Beta_L = Beta;
        Beta = 2^n;
        if (n > 25)
        tol = 15;
        elseif (n > 30)
        tol = 20;
        elseif (n > 35)
        tol = 25;
end
else
if bisection_find == 1
        bisection_find = 0;
        Beta_U = Beta;
        elseif bisection_find == 0
        Beta_L = Beta;
end

if(~isempty(dopt))
        s_h = subs(s,dopt);
        end
        Beta_P = Beta;
```

```
                    Beta = ((Beta_U - Beta_L)/2) + Beta_L;
            end

        end
end

function [V, Vdot] = Step4_Lyapunov_Order_Search(x, f, GAM, Beta, Px,
 S1, S2, deg)

        % Set options
        opts = gsosoptions;
        opts.minobj = -20;
        opts.maxobj = 0;

        z = monomials(x, 1:deg);

        V = sosdecvar('c',z);

        Vdot = jacobian(V,x)*f;

        sosc = polyconstr;
        sosc(1) = V - 1e-6*(x'*x) >= 0;
        sosc(1) = -(Vdot + 1e-6*(x'*x) + S2*(GAM - V)) >= 0;
        sosc(2) = -((V - GAM) + S1*(Beta - Px)) >= 0;

        [info,dopt,sossol] = sosopt(sosc,x,opts);

        V = subs(V,dopt);

        V = V/GAM; %Normalize V(x) to GAM such that constraints are kept
        % for itterations.

end
```

D.2 TS-Fuzzy ROA Approximation Algorithm Script

```
clear
% define system variables
syms x1 x2;
vars = [x1; x2];



f = [-x2;
x1+(x1^2-1)*x2];

J = jacobian(f,vars);

X1_NEW = 0.0;
X1_PREV = 0;

X2_NEW = 0.0;
X2_PREV = 0;

delta = 0.01;
test_chk = 0;

count = 0;

while test_chk ~= 1

A1 = double(subs(J,[x1,x2],[X1_NEW,X2_NEW]));
A2 = double(subs(J,[x1,x2],[-X1_NEW,X2_NEW]));
A3 = double(subs(J,[x1,x2],[X1_NEW,-X2_NEW]));
A4 = double(subs(J,[x1,x2],[-X1_NEW,-X2_NEW]));

setlmis([]);
W = lmivar(1,[2 1]); % variable X, full symmetric

lmiterm([1 1 1 W],1,A1, 's');
```

```
lmiterm([2 1 1 W],1,A2, 's');
lmiterm([3 1 1 W],1,A3, 's');
lmiterm([4 1 1 W],1,A4, 's');
lmiterm([-5 1 1 W],1,1);
lmiterm([5 1 1 0],1);
lmis = getlmis;

[tmin,xfeas] = feasp(lmis);

if(tmin > 0)
test_chk = 1;
break;
end

fprintf('X1 Test = %f\n\n',X1_NEW);
fprintf('X2 Test = %f\n\n',X2_NEW);

count = count + 1;

% Slow delta for X1 due to elliptical approximation
if count > 5

X1_PREV = X1_NEW;
X1_NEW = X1_NEW + delta;

count = 0;
end

X2_PREV = X2_NEW;
X2_NEW = X2_NEW + delta;

end

A1 = double(subs(J,[x1,x2],[X1_PREV,X2_PREV]));
A2 = double(subs(J,[x1,x2],[-X1_PREV,X2_PREV]));
```

```
A3 = double(subs(J,[x1,x2],[X1_PREV,-X2_PREV]));
A4 = double(subs(J,[x1,x2],[-X1_PREV,-X2_PREV]));

setlmis([]);
W = lmivar(1,[2 1]); % variable X, full symmetric

lmiterm([1 1 1 W],1,A1, 's');
lmiterm([2 1 1 W],1,A2, 's');
lmiterm([3 1 1 W],1,A3, 's');
lmiterm([4 1 1 W],1,A4, 's');
lmiterm([-5 1 1 W],1,1);
lmiterm([5 1 1 0],1);
lmis = getlmis;

[tmin,xfeas] = feasp(lmis);

Wf = dec2mat(lmis,xfeas,W);

V = transpose(vars)*Wf*vars;

x2min = -X2_PREV;
x1min = -Wf(1,2)*(x2min/Wf(1,1));

a = double(subs(V,[x1 x2],[x1min x2min]));
b= [0,1]';
aa = (X2_PREV^2)/(b'*(Wf^-1)*b);

hv = matlabFunction(V);

V_dot = (diff(V,x1)*f(1) + diff(V,x2)*f(2));

x = linspace(-5, 5, 999);
y = linspace(-5, 5, 1000);
for(i=1:999)
for(e=1:1000)
```

```
v_plot(e,i) = hv(x(i),y(e));
end
end

figure(222)
xlabel('x1')
ylabel('x2');
grid
hold on
contour(x,y,v_plot,[a a], 'g', 'LineWidth', 2)
hold on
```

Appendix E

Papers and Publications

E.1 Conference Papers - PhD Related

1. Formentini, A., Dewar, D., Zanchetta, P., Wheeler, P., Boroyevich, D. and Schanen, J.L., 2016, June. Optimal control of three-phase embedded power grids. In 2016 IEEE 17th Workshop on Control and Modeling for Power Electronics (COMPEL) (pp. 1-6). IEEE.

2. Dewar, D., Formentini, A. and Zanchetta, P., 2017, October. Automated and scalable optimal control of three-phase embedded power grids including pll. In 2017 IEEE Energy Conversion Congress and Exposition (ECCE) (pp. 4252-4259). IEEE.

3. Dewar, D., Li, K., Formentini, A., Zanchetta, P. and Wheeler, P., 2018, September. Performance Analysis of H_2 Optimally Controlled Three-Phase Grids. In 2018 IEEE Energy Conversion Congress and Exposition (ECCE) (pp. 2258-2264). IEEE.

4. Dewar, D., Rhoten, J., Formentini, A. and Zanchetta, P., 2019, October. Fast Self-Tuning Decentralized Variable Frequency Optimal Controller Design for Three-Phase Embedded Grids. In IECON 2019-45th Annual Conference of the IEEE Industrial Electronics Society (Vol. 1, pp. 3894-3899). IEEE.

5. Czerniewski, B., Formentini, A., Dewar, D., Zanchetta, P. and Schanen, J.L., 2019, September. Impact of Converters Interactions on Control Design in a Power Electronics Dense Network: Application to More Electric Aircraft. In 2019 21st European Conference on Power Electronics and Applications (EPE'19 ECCE Europe) (pp. P-1). IEEE.

6. Li, K., Dewar, D., Formentini, A., Zanchetta, P. and Wheeler, P., 2018, September. Optimized control design for power converters in power electronics embedded networks integrating grid

model identification. In 2018 IEEE Industry Applications Society Annual Meeting (IAS) (pp. 1-6). IEEE.

7. Li, K., Dewar, D., Formentini, A., Zanchetta, P. and Wheeler, P., 2019, September. Grid Impedance Identification and Structured-h2 Optimization Based Controller Design of Active Front-end in Embedded AC Networks. In 2019 IEEE Energy Conversion Congress and Exposition (ECCE) (pp. 4840-4845). IEEE.

E.2 Conference Papers - Other topics of work

1. Morales, R., Garbarino, M., Muñoz, J., Baier, C., Rohten, J., Esparza, V. and Dewar, D., 2019, October. Grid connected PV system with new MPPT estimation method based on measuring cells. In IECON 2019-45th Annual Conference of the IEEE Industrial Electronics Society (Vol. 1, pp. 2366-2371). IEEE.

2. Xie, P., Dewar, D., Vakil, G., & Gerada, C. (2020, November). Gain-scheduled LQR control of an aerospace drive system with LC filter and long feeder cable. In 2020 23rd International Conference on Electrical Machines and Systems (ICEMS) (pp. 656-661). IEEE.

E.3 Journal Articles

1. (Accepted) Dewar, D., Formentini, A., Li, K., Zanchetta, P., & Wheeler, P. Optimal and automated decentralised converter control design in more electrical aircraft power electronics embedded grids. IET Power Electronics. 2021

2. (Accepted) Dewar, D., Rohten, J., Formentini, A., & Zanchetta, P. (2020). Decentralised Optimal Controller Design of Variable Frequency Three-Phase Power Electronic Networks Accounting for Sub-System Interactions. IEEE Open Journal of Industry Applications. 2020

3. (Accepted) Rohten, J. A., Dewar, D. N., Zanchetta, P., Formentini, A., Muñoz, J. A., Baier, C. R., & Silva, J. J. (2021). Multivariable Deadbeat Control of Power Electronics Converters with Fast Dynamic Response and Fixed Switching Frequency. Energies, 14(2), 313.

4. (Accepted) Rohten, J. A., Silva, J. J., Muñoz, J. A., Villarroel, F. A., Dewar, D. N., Rivera, M. E., & Espinoza, J. R. (2020). A Simple Self-Tuning Resonant Control Approach for Power Converters Connected to Micro-Grids With Distorted Voltage Conditions. IEEE Access, 8, 216018-216028.

5. (Under Review) Controller Design of an Active Front-End Converter Keeping in Consideration Grid Dynamic Interaction; K. Li, A. Formentini, D. Dewar, P. Zanchetta, (IEEE Transactions on Industrial Electronics)

Bibliography

[1] V. Madonna, P. Giangrande, and M. Galea, "Electrical power generation in aircraft: Review, challenges, and opportunities," *IEEE transactions on transportation electrification*, vol. 4, no. 3, pp. 646–659, 2018.

[2] M. Sinnett, "787 no-bleed systems: saving fuel and enhancing operational efficiencies," *Aero Quarterly*, vol. 18, pp. 6–11, 2007.

[3] J. Susan, "Giacc/4," 2012.

[4] T. Roinila, T. Messo, R. Luhtala, R. Scharrenberg, E. C. de Jong, A. Fabian, and Y. Sun, "Hardware-in-the-loop methods for real-time frequency-response measurements of on-board power distribution systems," *IEEE Transactions on Industrial Electronics*, vol. 66, no. 7, pp. 5769–5777, 2018.

[5] T. Morstyn, B. Hredzak, and V. G. Agelidis, "Control strategies for microgrids with distributed energy storage systems: An overview," *IEEE Transactions on Smart Grid*, vol. 9, no. 4, pp. 3652–3666, 2016.

[6] T.-S. Lee, "Input-output linearization and zero-dynamics control of three-phase ac/dc voltage-source converters," *IEEE Transactions on Power Electronics*, vol. 18, no. 1, pp. 11–22, 2003.

[7] M. Athans and P. L. Falb, *Optimal control: an introduction to the theory and its applications.* Courier Corporation, 2013.

[8] E. Najafi, R. Babu?ka, and G. A. D. Lopes, "A fast sampling method for estimating the domain of attraction," *Nonlinear Dynamics*, vol. 86, no. 2, pp. 823–834.

[9] U. Topcu, A. K. Packard, P. J. Seiler, and G. J. Balas, "Help on sos: Ask the experts," *IEEE Control Systems*, vol. 30, no. 4, pp. 18–23, 2010.

[10] J.-L. Schanen, A. Baraston, M. Delhommais, P. Zanchetta, and D. Boroyevitch, "Sizing of power electronics emc filters using design by optimization methodology," in *2016 7th Power Electronics and Drive Systems Technologies Conference (PEDSTC)*, pp. 279–284, IEEE, 2016.

[11] M. Cronin, "The all-electric aircraft," *IEE Review*, vol. 36, no. 8, pp. 309–311, 1990.

[12] R. Jones, "The more electric aircraft: the past and the future?," *IET*, 1999,.

[13] T. Holliday, "Applications of electric power in aircraft," *Electrical Engineering*, vol. 60, no. 5, pp. 218–225, 1941.

[14] G. Buticchi, S. Bozhko, M. Liserre, P. Wheeler, and K. Al-Haddad, "On-board microgrids for the more electric aircraft—technology review," *IEEE Transactions on Industrial Electronics*, vol. 66, no. 7, pp. 5588–5599, 2019.

[15] "Electrical power systems," *Aerospace Technology Institute*, 2018.

[16] F. Blaabjerg and K. Ma, "Future on power electronics for wind turbine systems," *IEEE Journal of Emerging and Selected Topics in Power Electronics*, vol. 1, no. 3, pp. 139–152, 2013.

[17] H. Wang, M. Liserre, and F. Blaabjerg, "Toward reliable power electronics: Challenges design tools and opportunities," *IEEE Industrial Electronics Magazine*, vol. 7, no. 2, pp. 17–26, 2013.

[18] T. J. Flack, B. N. Pushpakaran, and S. B. Bayne, "Gan technology for power electronic applications: a review," *Journal of Electronic Materials*, vol. 45, no. 6, pp. 2673–2682, 2016.

[19] L. Meng, Q. Shafiee, G. F. Trecate, H. Karimi, D. Fulwani, X. Lu, and J. M. Guerrero, "Review on control of dc microgrids and multiple microgrid clusters," *IEEE Journal of Emerging and Selected Topics in Power Electronics*, vol. 5, no. 3, pp. 928–948, 2017.

[20] "Facts and Figures, Aviation Industry, https://www.atag.org/facts-figures.html." Accessed: 2019-05-12.

[21] "Reducing emissions from aviation, European Commission, https://ec.europa.eu/clima/policies/transport/." Accessed: 2019-05-14.

[22] D. Dewar, "Integrated design by optimization of electrical power systems for nore electric aircraft," Master's thesis, The University of Nottingham, United Kingdom, 2016.

[23] "Clean sky 2 joint undertaking third amended bi-annual work plan and budget 2018-2019."

[24] B. Sarlioglu and C. T. Morris, "More electric aircraft: Review, challenges, and opportunities for commercial transport aircraft," *IEEE transactions on Transportation Electrification*, vol. 1, no. 1, pp. 54–64, 2015.

[25] B. Wen, D. Dong, D. Boroyevich, R. Burgos, P. Mattavelli, and Z. Shen, "Impedance-based analysis of grid-synchronization stability for three-phase paralleled converters," *IEEE Transactions on Power Electronics*, vol. 31, no. 1, pp. 26–38, 2015.

[26] B. Czerniewski, A. Formentini, D. Dewar, P. Zanchetta, and J.-L. Schanen, "Impact of converters interactions on control design in a power electronics dense network: Application to more electric aircraft," in *2019 21st European Conference on Power Electronics and Applications (EPE'19 ECCE Europe)*, pp. P–1, IEEE, 2019.

[27] A. Formentini, D. Dewar, P. Zanchetta, P. Wheeler, D. Boroyevich, and J.-L. Schanen, "Optimal control of three-phase embedded power grids," in *2016 IEEE 17th Workshop on Control and Modeling for Power Electronics (COMPEL)*, pp. 1–6, IEEE, 2016.

[28] Q. Li, A. Formentini, A. Baraston, X. Zhang, P. Zanchetta, J.-L. Schanen, and D. Boroyevich, "Taking into account interactions between converters in the design of aircraft power networks," in *2016 IEEE Energy Conversion Congress and Exposition (ECCE)*, pp. 1–7, IEEE, 2016.

[29] X. Roboam, B. Sareni, and A. De Andrade, "More electricity in the air: Toward optimized electrical networks embedded in more-electrical aircraft," *IEEE industrial electronics magazine*, vol. 6, no. 4, pp. 6–17, 2012.

[30] H. Ounis, B. Sareni, X. Roboam, and A. De Andrade, "Multi-level integrated optimal design for power systems of more electric aircraft," *Mathematics and Computers in Simulation*, vol. 130, pp. 223–235, 2016.

[31] X. Zheng, L. Xiao, Y. Lei, and Z. Wang, "Optimisation of lcl filter based on closed-loop total harmonic distortion calculation model of the grid-connected inverter," *IET Power Electronics*, vol. 8, no. 6, pp. 860–868, 2015.

[32] Y. Liu, K.-Y. See, S. Yin, R. Simanjorang, C. F. Tong, A. Nawawi, and J.-S. J. Lai, "Lcl filter design of a 50-kw 60-khz sic inverter with size and thermal considerations for aerospace applications," *IEEE transactions on Industrial Electronics*, vol. 64, no. 10, pp. 8321–8333, 2017.

[33] Z. Wu, M. Aldeen, and S. Saha, "A novel optimisation method for the design of lcl filters for three-phase grid-tied inverters," in *2016 IEEE Innovative Smart Grid Technologies-Asia (ISGT-Asia)*, pp. 214–220, IEEE, 2016.

[34] S. Jayalath and M. Hanif, "Generalized lcl-filter design algorithm for grid-connected voltage-source inverter," *IEEE Transactions on Industrial Electronics*, vol. 64, no. 3, pp. 1905–1915, 2016.

[35] Y. Huangfu, S. Pang, B. Nahid-Mobarakeh, L. Guo, A. K. Rathore, and F. Gao, "Stability analysis and active stabilization of on-board dc power converter system with input filter," *IEEE Transactions on Industrial Electronics*, vol. 65, no. 1, pp. 790–799, 2017.

[36] I. Lorzadeh, M. Savaghebi, H. A. Abyaneh, and J. M. Guerrero, "Active damping techniques for lcl-filtered inverters-based microgrids," in *2015 IEEE 10th International Symposium on Diagnostics for Electrical Machines, Power Electronics and Drives (SDEMPED)*, pp. 408–414, IEEE, 2015.

[37] D. Dong, B. Wen, D. Boroyevich, P. Mattavelli, and Y. Xue, "Analysis of phase-locked loop low-frequency stability in three-phase grid-connected power converters considering impedance interactions," *IEEE Transactions on Industrial Electronics*, vol. 62, no. 1, pp. 310–321, 2014.

[38] A. Rockhill, M. Liserre, R. Teodorescu, and P. Rodriguez, "Grid-filter design for a multimegawatt medium-voltage voltage-source inverter," *IEEE Transactions on Industrial Electronics*, vol. 58, no. 4, pp. 1205–1217, 2010.

[39] S. Pan, M. Pahlevaninezhad, and P. K. Jain, "Adaptive optimal control for parallel grid-connected inverters with lcl filters," in *2016 IEEE 7th International Symposium on Power Electronics for Distributed Generation Systems (PEDG)*, pp. 1–6, IEEE, 2016.

[40] C. Wan, M. Huang, K. T. Chi, and X. Ruan, "Effects of interaction of power converters coupled via power grid: A design-oriented study," *IEEE Transactions on Power Electronics*, vol. 30, no. 7, pp. 3589–3600, 2014.

[41] I. Cvetkovic, *Modeling and Control of Voltage-Controlling Converters for Enhanced Operation of Multi-Source Power Systems.* PhD thesis, Virginia Tech, 2018.

[42] A. A. A. Radwan and Y. A.-R. I. Mohamed, "Analysis and active suppression of ac-and dc-side instabilities in grid-connected current-source converter-based photovoltaic system," *IEEE Transactions on Sustainable Energy*, vol. 4, no. 3, pp. 630–642, 2013.

[43] B. Palethorpe, M. Sumner, and D. Thomas, "Power system impedance measurement using a power electronic converter," in *Ninth International Conference on Harmonics and Quality of Power. Proceedings (Cat. No. 00EX441)*, vol. 1, pp. 208–213, IEEE, 2000.

[44] M. Nagpal, W. Xu, and J. Sawada, "Harmonic impedance measurement using three-phase transients," *IEEE Transactions on Power Delivery*, vol. 13, no. 1, pp. 272–277, 1998.

[45] Y. A. Familiant, J. Huang, K. A. Corzine, and M. Belkhayat, "New techniques for measuring impedance characteristics of three-phase ac power systems," *IEEE Transactions on Power Electronics*, vol. 24, no. 7, pp. 1802–1810, 2009.

[46] D. Dong, *Ac-dc bus-interface bi-directional converters in renewable energy systems.* PhD thesis, Virginia Tech, 2012.

[47] D. Dong, B. Wen, P. Mattavelli, D. Boroyevich, and Y. Xue, "Grid-synchronization modeling and its stability analysis for multi-paralleled three-phase inverter systems," in *2013 Twenty-Eighth Annual IEEE Applied Power Electronics Conference and Exposition (APEC)*, pp. 439–446, IEEE, 2013.

[48] X. Wang, L. Harnefors, and F. Blaabjerg, "Unified impedance model of grid-connected voltage-source converters," *IEEE Transactions on Power Electronics*, vol. 33, no. 2, pp. 1775–1787, 2017.

[49] B. Wen, D. Boroyevich, R. Burgos, P. Mattavelli, and Z. Shen, "Analysis of dq small-signal impedance of grid-tied inverters," *IEEE Transactions on Power Electronics*, vol. 31, no. 1, pp. 675–687, 2015.

[50] B. Wen, X. Zhang, F. Effah, A. Baraston, P. Zanchetta, D. Boroyevich, J. L. Schanen, R. Burgos, P. Wheeler, and A. Tardy, "Integrated design by optimization of electrical power systems for more electric aircraft," in *MEA 2015*, pp. 3–5, 2015.

[51] B. Wen, R. Burgos, D. Boroyevich, P. Mattavelli, and Z. Shen, "Ac stability analysis and dq frame impedance specifications in power-electronics-based distributed power systems," *IEEE Journal of Emerging and Selected Topics in Power Electronics*, vol. 5, no. 4, pp. 1455–1465, 2017.

[52] M. Raza, E. Prieto-Araujo, and O. Gomis-Bellmunt, "Small-signal stability analysis of offshore ac network having multiple vsc-hvdc systems," *IEEE Transactions on Power Delivery*, vol. 33, no. 2, pp. 830–839, 2017.

[53] M. R. S. Tirtashi, O. Samuelsson, J. Svensson, and R. Pates, "Impedance matching for vsc-hvdc damping controller gain selection," *IEEE Transactions on Power Systems*, vol. 33, no. 5, pp. 5226–5235, 2018.

[54] X. Wang, F. Blaabjerg, and P. C. Loh, "An impedance-based stability analysis method for paralleled voltage source converters," in *2014 International Power Electronics Conference (IPEC-Hiroshima 2014-ECCE ASIA)*, pp. 1529–1535, IEEE, 2014.

[55] C. Li, R. Burgos, Y. Tang, and D. Boroyevich, "Impedance-based stability analysis of multiple statcoms in proximity," in *2016 IEEE 17th Workshop on Control and Modeling for Power Electronics (COMPEL)*, pp. 1–6, IEEE, 2016.

[56] C. Li, *Impedance-Based Stability Analysis in Power Systems with Multiple STATCOMs in Proximity.* PhD thesis, Virginia Tech, 2018.

[57] C. Li, R. Burgos, B. Wen, Y. Tang, and D. Boroyevich, "Stability analysis of power systems with multiple statcoms in close proximity," *IEEE Transactions on Power Electronics*, vol. 35, no. 3, pp. 2268–2283, 2019.

[58] Q. Xiao, P. Mattavelli, A. Khodamoradi, and F. Tang, "Analysis of transforming dq impedances of different converters to a common reference frame in complex converter networks," *CES Transactions on Electrical Machines and Systems*, vol. 3, no. 4, pp. 342–350, 2019.

[59] A. R. Messina, O. Begovich, J. López, and E. Reyes, "Design of multiple facts controllers for damping inter-area oscillations: a decentralised control approach," *International Journal of Electrical Power & Energy Systems*, vol. 26, no. 1, pp. 19–29, 2004.

[60] F. Gao and S. Bozhko, "Modeling and impedance analysis of a single dc bus-based multiple-source multiple-load electrical power system," *IEEE Transactions on Transportation Electrification*, vol. 2, no. 3, pp. 335–346, 2016.

[61] M. Kim, S. G. Lee, and S. Bae, "Decentralized power management for electrical power systems in more electric aircrafts," *Electronics*, vol. 7, no. 9, p. 187, 2018.

[62] J. M. Guerrero, M. Chandorkar, T.-L. Lee, and P. C. Loh, "Advanced control architectures for intelligent microgrids—part i: Decentralized and hierarchical control," *IEEE Transactions on Industrial Electronics*, vol. 60, no. 4, pp. 1254–1262, 2012.

[63] K. Ni, Y. Liu, Z. Mei, T. Wu, Y. Hu, H. Wen, and Y. Wang, "Electrical and electronic technologies in more-electric aircraft: A review," *IEEE Access*, vol. 7, pp. 76145–76166, 2019.

[64] Z. Cheng, J. Duan, and M.-Y. Chow, "To centralize or to distribute: That is the question: A comparison of advanced microgrid management systems," *IEEE Industrial Electronics Magazine*, vol. 12, no. 1, pp. 6–24, 2018.

[65] A. G. Tsikalakis and N. D. Hatziargyriou, "Centralized control for optimizing microgrids operation," in *2011 IEEE power and energy society general meeting*, pp. 1–8, IEEE, 2011.

[66] P. Shah and P. A. Parrilo, "H2-optimal decentralized control over posets: A state-space solution for state-feedback," *IEEE Transactions on Automatic Control*, vol. 58, no. 12, pp. 3084–3096, 2013.

[67] M. J. Hossain, M. A. Mahmud, F. Milano, S. Bacha, and A. Hably, "Design of robust distributed control for interconnected microgrids," *IEEE transactions on smart grid*, vol. 7, no. 6, pp. 2724–2735, 2015.

[68] N. L. Díaz, J. C. Vasquez, and J. M. Guerrero, "A communication-less distributed control architecture for islanded microgrids with renewable generation and storage," *IEEE Transactions on Power Electronics*, vol. 33, no. 3, pp. 1922–1939, 2017.

[69] Y. Wang, Y. Tang, Y. Xu, and Y. Xu, "A distributed control scheme of thermostatically controlled loads for the building-microgrid community," *IEEE Transactions on Sustainable Energy*, vol. 11, no. 1, pp. 350–360, 2019.

[70] F. Gao, S. Bozhko, A. Costabeber, G. Asher, and P. Wheeler, "Control design and voltage stability analysis of a droop-controlled electrical power system for more electric aircraft," *IEEE Transactions on Industrial Electronics*, vol. 64, no. 12, pp. 9271–9281, 2017.

[71] B. R. Vellaboyana and J. A. Taylor, "Optimal decentralized control of dc-segmented power systems," *IEEE Transactions on Automatic Control*, vol. 63, no. 10, pp. 3616–3622, 2018.

[72] X. Wu, F. Dörfler, and M. R. Jovanović, "Input-output analysis and decentralized optimal control of inter-area oscillations in power systems," *IEEE Transactions on Power Systems*, vol. 31, no. 3, pp. 2434–2444, 2015.

[73] F. Gao, *Decentralised control and stability analysis of a multi-generator based electrical power system for more electric aircraft.* PhD thesis, University of Nottingham, 2016.

[74] G. Buticchi, L. Costa, and M. Liserre, "Improving system efficiency for the more electric aircraft: A look at dc\/dc converters for the avionic onboard dc microgrid," *IEEE Industrial Electronics Magazine*, vol. 11, no. 3, pp. 26–36, 2017.

[75] L. Shu, W. Chen, and X. Jiang, "Decentralized control for fully modular input-series output-parallel (isop) inverter system based on the active power inverse-droop method," *IEEE Transactions on Power Electronics*, vol. 33, no. 9, pp. 7521–7530, 2017.

[76] M. D. Cook, E. H. Trinklein, G. G. Parker, R. D. Robinett, and W. W. Weaver, "Optimal and decentralized control strategies for inverter-based ac microgrids," *Energies*, vol. 12, no. 18, p. 3529, 2019.

[77] M. Toub, M. M. Bijaieh, W. W. Weaver, R. D. Robinett, M. Maaroufi, and G. Aniba, "Droop control in dq coordinates for fixed frequency inverter-based ac microgrids," *Electronics*, vol. 8, no. 10, p. 1168, 2019.

[78] M. Jayachandran and G. Ravi, "Decentralized model predictive hierarchical control strategy for islanded ac microgrids," *Electric Power Systems Research*, vol. 170, pp. 92–100, 2019.

[79] P. Falkowski and A. Sikorski, "Finite control set model predictive control for grid-connected ac–dc converters with lcl filter," *IEEE Transactions on Industrial Electronics*, vol. 65, no. 4, pp. 2844–2852, 2017.

[80] X. Zhang, L. Tan, J. Xian, H. Zhang, Z. Ma, and J. Kang, "Direct grid-side current model predictive control for grid-connected inverter with lcl filter," *IET Power Electronics*, vol. 11, no. 15, pp. 2450–2460, 2018.

[81] D. Xu, Y. Dai, C. Yang, and X. Yan, "Adaptive fuzzy sliding mode command-filtered backstepping control for islanded pv microgrid with energy storage system," *Journal of the Franklin Institute*, vol. 356, no. 4, pp. 1880–1898, 2019.

[82] M. Cupelli, M. Mirz, and A. Monti, "A comparison of backstepping and lqg control for stabilizing mvdc microgrids with constant power loads," in *2015 IEEE Eindhoven PowerTech*, pp. 1–6, IEEE, 2015.

[83] N. M. Dehkordi, N. Sadati, and M. Hamzeh, "A backstepping high-order sliding mode voltage control strategy for an islanded microgrid with harmonic/interharmonic loads," *Control Engineering Practice*, vol. 58, pp. 150–160, 2017.

[84] D. Dewar, A. Formentini, and P. Zanchetta, "Automated and scalable optimal control of three-phase embedded power grids including pll," in *2017 IEEE Energy Conversion Congress and Exposition (ECCE)*, pp. 4252–4259, IEEE, 2017.

[85] J. Doyle, K. Glover, P. Khargonekar, and B. Francis, "State-space solutions to standard h 2 and h-inf control problems," in *1988 American Control Conference*, pp. 1691–1696, IEEE, 1988.

[86] L. Bakule, "Decentralized control: An overview," *Annual reviews in control*, vol. 32, no. 1, pp. 87–98, 2008.

[87] C. Olalla, R. Leyva, A. El Aroudi, and I. Queinnec, "Robust lqr control for pwm converters: An lmi approach," *IEEE Transactions on industrial electronics*, vol. 56, no. 7, pp. 2548–2558, 2009.

[88] A. K. Yadav, P. Gaur, S. K. Jha, J. Gupta, and A. Mittal, "Optimal speed control of hybrid electric vehicles," *Journal of Power Electronics*, vol. 11, no. 4, pp. 393–400, 2011.

[89] N. Arab, H. Vahedi, and K. Al-Haddad, "Lqr control of single-phase grid-tied puc5 inverter with lcl filter," *IEEE Transactions on Industrial Electronics*, vol. 67, no. 1, pp. 297–307, 2019.

[90] L. Zhu, J. Liu, M. Cupelli, and A. Monti, "Decentralized linear quadratic gaussian control of multi-generator mvdc shipboard power system with constant power loads," in *2013 IEEE Electric Ship Technologies Symposium (ESTS)*, pp. 308–313, IEEE, 2013.

[91] J. Liu, D. Obradovic, and A. Monti, "Decentralized lqg control with online set-point adaptation for parallel power converter systems," in *2010 IEEE Energy Conversion Congress and Exposition*, pp. 3174–3179, IEEE, 2010.

[92] Y.-S. Wang, N. Matni, and J. C. Doyle, "Separable and localized system-level synthesis for large-scale systems," *IEEE Transactions on Automatic Control*, vol. 63, no. 12, pp. 4234–4249, 2018.

[93] Y.-S. Wang, N. Matni, and J. C. Doyle, "A system-level approach to controller synthesis," *IEEE Transactions on Automatic Control*, vol. 64, no. 10, pp. 4079–4093, 2019.

[94] K. S. Islam, M. Seyedmahmoudian, and A. Stojcevski, "Decentralized robust mixed h2/h infinity reactive power control of dfig cluster using smes," *International Journal of Electrical Power & Energy Systems*, vol. 113, pp. 176–187, 2019.

[95] M. S. Sadabadi, A. Karimi, and H. Karimi, "Fixed-order decentralized/distributed control of islanded inverter-interfaced microgrids," *Control Engineering Practice*, vol. 45, pp. 174–193, 2015.

[96] F. Ornelas-Tellez, J. J. Rico-Melgoza, E. Espinosa-Juarez, and E. N. Sanchez, "Optimal and robust control in dc microgrids," *IEEE Transactions on Smart Grid*, vol. 9, no. 6, pp. 5543–5553, 2017.

[97] G. Li, Z. Du, T. An, Y. Xia, and J. Lei, "Impact of pll and vsc control parameters on the ac/mtdc systems stability," *Electric Power Systems Research*, vol. 141, pp. 476–486, 2016.

[98] P. Zhou, X. Yuan, J. Hu, and Y. Huang, "Stability of dc-link voltage as affected by phase locked loop in vsc when attached to weak grid," in *2014 IEEE PES General Meeting—Conference & Exposition*, pp. 1–5, IEEE, 2014.

[99] X. Wang, L. Harnefors, F. Blaabjerg, and P. C. Loh, "A unified impedance model of voltage-source converters with phase-locked loop effect," in *2016 IEEE Energy Conversion Congress and Exposition (ECCE)*, pp. 1–8, IEEE, 2016.

[100] J. Z. Zhou, H. Ding, S. Fan, Y. Zhang, and A. M. Gole, "Impact of short-circuit ratio and phase-locked-loop parameters on the small-signal behavior," *IEEE Transactions on Power Delivery*, vol. 29, no. 5, pp. 2287–2296, 2014.

[101] P. Wheeler, "The more electric aircraft: Why aerospace needs power electronics?," in *Power Electronics and Applications, 2009. EPE'09. 13th European Conference on*, pp. 1–30, 2009.

[102] T. Tarczewski and L. M. Grzesiak, "State feedback control of the pmsm servo-drive with sinusoidal voltage source inverter," in *2012 15th International Power Electronics and Motion Control Conference (EPE/PEMC)*, pp. DS2a–6, IEEE, 2012.

[103] E. D. Ganev, "Electric drives for electric green taxiing systems: Examining and evaluating the electric drive system," *IEEE Electrification Magazine*, vol. 5, no. 4, pp. 10–24, 2017.

[104] M. Laterza, "Optimal control of converters in an embedded power system," 2017.

[105] S. Hiti, D. Boroyevich, and C. Cuadros, "Small-signal modeling and control of three-phase pwm converters," in *Proceedings of 1994 IEEE Industry Applications Society Annual Meeting*, vol. 2, pp. 1143–1150, IEEE, 1994.

[106] M. Dahleh, M. A. Dahleh, and G. Verghese, "Lectures on dynamic systems and control,"

[107] R. L. Williams, D. A. Lawrence, *et al.*, *Linear state-space control systems.* John Wiley & Sons, 2007.

[108] F. R. Garces, V. M. Becerra, C. Kambhampati, and K. Warwick, *Strategies for feedback linearisation: a dynamic neural network approach.* Springer Science & Business Media, 2012.

[109] S. Hiti, D. Borojevic, R. Ambatipudi, R. Zhang, and Y. Jiang, "Average current control of three-phase pwm boost rectifier," in *Proceedings of PESC'95-Power Electronics Specialist Conference*, vol. 1, pp. 131–137, IEEE, 1995.

[110] D. G. MacMartin, *cds110b Control and Dynamic Systems.* Caltech.

[111] A. A. Stoorvogel, *The H control problem: a state space approach.* Citeseer, 1990.

[112] E. Frazzoli, "6.241 dynamic systems and control," *Massachusetts Institute of Technology: MIT OpenCourseWare*, 2011.

[113] S. Skogestad and I. Postlethwaite, *Multivariable feedback control: analysis and design*, vol. 2. Wiley New York, 2007.

[114] S. Gumussoy, D. Henrion, M. Millstone, and M. L. Overton, "Multiobjective robust control with hifoo 2.0," *arXiv preprint arXiv:0905.3229*, 2009.

[115] J. V. Burke, D. Henrion, A. S. Lewis, and M. L. Overton, "Hifoo-a matlab package for fixed-order controller design and h inf optimization," *IFAC Proceedings Volumes*, vol. 39, no. 9, pp. 339–344, 2006.

[116] H. Toivonen, "Lecture notes on robust control by state-space methods," *Available at: users. abo. fi/htoivone/courses/robust/hsem. pdf*, 1995.

[117] A. Sadeghzadeh, "Fixed-structure h2 controller design: An lmi solution," *IFAC Proceedings Volumes*, vol. 45, no. 13, pp. 331–336, 2012.

[118] J. Doyle, K. Glover, P. Khargonekar, and P. Francis, "'state space solutions to standard h-2 and h-infinity," *IEEE Trans. Autom. Control, AC*, vol. 34, pp. 831–847, 1989.

[119] H. Iiduka and I. Yamada, "Computational method for solving a stochastic linear-quadratic control problem given an unsolvable stochastic algebraic riccati equation," *SIAM Journal on Control and Optimization*, vol. 50, no. 4, pp. 2173–2192, 2012.

[120] R. Hill, "Aircraft pitch control, https://uk.mathworks.com/matlabcentral/fileexchange/40798-aircraft-pitch-control."

[121] J. P. Hespanha, "Lecture notes on lqr/lqg controller design," *Knowledge creation diffusion utilization*, 2005.

[122] F. Lin, M. Fardad, and M. R. Jovanovic, "Augmented lagrangian approach to design of structured optimal state feedback gains," *IEEE Transactions on Automatic Control*, vol. 56, no. 12, pp. 2923–2929, 2011.

[123] T. Rautert and E. W. Sachs, "Computational design of optimal output feedback controllers," *SIAM Journal on Optimization*, vol. 7, no. 3, pp. 837–852, 1997.

[124] B. Wen, D. Boroyevich, R. Burgos, P. Mattavelli, and Z. Shen, "Small-signal stability analysis of three-phase ac systems in the presence of constant power loads based on measured dq frame impedances," *IEEE Transactions on Power Electronics*, vol. 30, no. 10, pp. 5952–5963, 2014.

[125] J. Rocabert, A. Luna, F. Blaabjerg, and P. Rodriguez, "Control of power converters in ac microgrids," *IEEE transactions on power electronics*, vol. 27, no. 11, pp. 4734–4749, 2012.

[126] D. Dewar, K. Li, A. Formentini, P. Zanchetta, and P. Wheeler, "Performance analysis of $h_{-}\{2\}$ optimally controlled three-phase grids," in *2018 IEEE Energy Conversion Congress and Exposition (ECCE)*, pp. 2258–2264, IEEE, 2018.

[127] K. Li, D. Dewar, A. Formentini, P. Zanchetta, and P. Wheeler, "Grid impedance identification and structured-h2 optimization based controller design of active front-end in embedded ac networks," in *2019 IEEE Energy Conversion Congress and Exposition (ECCE)*, pp. 4840–4845, IEEE.

[128] A. Galassini, G. L. Calzo, A. Formentini, C. Gerada, P. Zanchetta, and A. Costabeber, "ucube: Control platform for power electronics," in *2017 IEEE Workshop on Electrical Machines Design, Control and Diagnosis (WEMDCD)*, pp. 216–221, IEEE, 2017.

[129] B. Hoff and W. Sulkowski, "A simple dc-link pre-charging method for three-phase voltage source inverters," in *IECon 2012-38th Annual Conference on IEEE Industrial Electronics Society*, pp. 3364–3367, IEEE, 2012.

[130] B. Wen, D. Boroyevich, R. Burgos, and P. Mattavelli, "Input impedance of voltage source converter with stationary frame linear current regulators and phase-locked loop," in *2013 IEEE Energy Conversion Congress and Exposition*, pp. 4207–4213, IEEE, 2013.

[131] D. Dewar, A. Formentini, K. Li, P. Zanchetta, and P. Wheeler, "Optimal and automated decentralised converter control design in more electrical aircraft power electronics embedded grids," *IET Power Electronics*.

[132] F. Blaabjerg, R. Teodorescu, M. Liserre, and A. V. Timbus, "Overview of control and grid synchronization for distributed power generation systems," *IEEE Transactions on industrial electronics*, vol. 53, no. 5, pp. 1398–1409, 2006.

[133] B. Wen, D. Boroyevich, P. Mattavelli, Z. Shen, and R. Burgos, "Influence of phase-locked loop on input admittance of three-phase voltage-source converters," in *2013 Twenty-Eighth Annual IEEE Applied Power Electronics Conference and Exposition (APEC)*, pp. 897–904, IEEE, 2013.

[134] L. Hadjidemetriou, E. Kyriakides, and F. Blaabjerg, "A new hybrid pll for interconnecting renewable energy systems to the grid," *IEEE Transactions on industry applications*, vol. 49, no. 6, pp. 2709–2719, 2013.

[135] M. Karimi-Ghartemani, M. Mojiri, A. Safaee, J. A. Walseth, S. A. Khajehoddin, P. Jain, and A. Bakhshai, "A new phase-locked loop system for three-phase applications," *IEEE Transactions on Power Electronics*, vol. 28, no. 3, pp. 1208–1218, 2012.

[136] A. Kulkarni and V. John, "Design of synchronous reference frame phase-locked loop with the presence of dc offsets in the input voltage," *IET Power Electronics*, vol. 8, no. 12, pp. 2435–2443, 2015.

[137] D. Dewar, J. Rhoten, A. Formentini, and P. Zanchetta, "Fast self-tuning decentralized variable frequency optimal controller design for three-phase embedded grids," in *IECON 2019-45th Annual Conference of the IEEE Industrial Electronics Society*, vol. 1, pp. 3894–3899, IEEE, 2019.

[138] P. Zanchetta, M. Degano, J. Liu, and P. Mattavelli, "Iterative learning control with variable sampling frequency for current control of grid-connected converters in aircraft power systems," *IEEE Transactions on Industry Applications*, vol. 49, no. 4, pp. 1548–1555, 2013.

[139] Z. Zhang, J. Li, Y. Liu, Y. Xu, and Y. Yan, "Overview and development of variable frequency ac generators for more electric aircraft generation system," *Chinese Journal of Electrical Engineering*, vol. 3, no. 2, pp. 32–40, 2017.

[140] K. Areerak, *Modelling and stability analysis of aircraft power systems.* PhD thesis, University of Nottingham, 2009.

[141] J. Benzaquen, M. B. Shadmand, and B. Mirafzal, "Ultrafast rectifier for variable-frequency applications," *IEEE Access*, vol. 7, pp. 9903–9911, 2019.

[142] H. Xin, Z. Li, W. Dong, L. Zhang, Z. Wang, and J. Zhao, "Generalized-impedance and stability criterion for grid-connected converters," *arXiv preprint arXiv:1706.05625*, 2017.

[143] A. Adib, B. Mirafzal, X. Wang, and F. Blaabjerg, "On stability of voltage source inverters in weak grids," *IEEE Access*, vol. 6, pp. 4427–4439, 2018.

[144] V. F. Montagner, R. C. Oliveira, and P. L. Peres, "Design of h-inf gain-scheduled controllers for linear time-varying systems by means of polynomial lyapunov functions," in *Proceedings of the 45th IEEE Conference on Decision and Control*, pp. 5839–5844, IEEE, 2006.

[145] T. E. Rosa, C. F. Morais, and R. C. Oliveira, "H-inf output-feedback gain-scheduled control for discrete-time linear systems affected by time-varying parameters," *IFAC-PapersOnLine*, vol. 50, no. 1, pp. 8618–8623, 2017.

[146] D. Dewar, J. Rohten, A. Formentini, and P. Zanchetta, "Decentralised optimal controller design of variable frequency three-phase power electronic networks accounting for sub-system interactions," *IEEE Open Journal of Industry Applications*, 2020.

[147] J. C. Whitaker, *The electronics handbook*. Crc Press, 2005.

[148] M. M. Mahdi and A. Z. Ahmad, "Load frequency control in microgrid using fuzzy logic table control," in *2017 11th IEEE International Conference on Compatibility, Power Electronics and Power Engineering (CPE-POWERENG)*, pp. 318–323, IEEE, 2017.

[149] A. Egea-Alvarez, S. Fekriasl, F. Hassan, and O. Gomis-Bellmunt, "Advanced vector control for voltage source converters connected to weak grids," *IEEE Transactions on Power Systems*, vol. 30, no. 6, pp. 3072–3081, 2015.

[150] *MIL-STD-704 - DEPARTMENT OF DEFENSE INTERFACE STANDARD AIRCRAFT ELECTRIC POWER CHARACTERISTICS*, vol. F. US Department of Defence, 2004.

[151] A. Iannelli, A. Marcos, and M. Lowenberg, "Robust estimations of the region of attraction using invariant sets," *Journal of the Franklin Institute*, 2019.

[152] R. Genesio, M. Tartaglia, and A. Vicino, "On the estimation of asymptotic stability regions: State of the art and new proposals," *IEEE Transactions on Automatic Control*, vol. 30, no. 8, pp. 747–755.

[153] E. Najafi, G. A. D. Lopes, S. P. Nageshrao, and R. Babuska, "Rapid learning in sequential composition control," 2014.

[154] D. Marx, P. Magne, B. Nahid-Mobarakeh, S. Pierfederici, and B. Davat, "Large signal stability analysis tools in dc power systems with constant power loads and variable power loads—a review," *IEEE Transactions on Power Electronics*, vol. 27, no. 4, p. 1773–1787, 2012.

[155] P. Magne, D. Marx, B. Nahid-Mobarakeh, and S. Pierfederici, "Large-signal stabilization of a dc-link supplying a constant power load using a virtual capacitor: Impact on the domain of attraction," *IEEE Transactions on Industry Applications*, vol. 48, no. 3, p. 878–887, 2012.

[156] L. Herrera and W. Jin, "Stability analysis and controller design of dc microgrids with constant power loads," 2015.

[157] M. Vatani and M. Hovd, "Lyapunov stability analysis and controller design for rational polynomial systems using sum of squares programming," *2017 IEEE 56th Annual Conference on Decision and Control (CDC)*, 2017.

[158] M. Tacchi, B. Marinescu, M. Anghel, S. Kundu, S. Benahmed, and C. Cardozo, "Power system transient stability analysis using sum of squares programming," in *2018 Power Systems Computation Conference (PSCC)*, pp. 1–7, IEEE, 2018.

[159] U. Topcu, A. Packard, and P. Seiler, "Local stability analysis using simulations and sum-of-squares programming," *Automatica*, vol. 44, no. 10, pp. 2669–2675, 2008.

[160] P. Seiler, "Sosopt: a toolbox for polynomial optimization version 2.00," 2013.

[161] J. F. Sturm, "Using sedumi 1.02, a matlab toolbox for optimization over symmetric cones," *Optimization methods and software*, vol. 11, no. 1-4, pp. 625–653, 1999.

[162] A. Vannelli and M. Vidyasagar, "Maximal lyapunov functions and domains of attraction for autonomous nonlinear systems," *Automatica*, vol. 21, no. 1, pp. 69–80, 1985.

[163] S. Zhu, K. Liu, L. Qin, Q. Wang, Y. Li, Q. Pu, S. Wang, G. Li, and X. Hu, "Global asymptotic stability assessment of three-phase inverters with saturation," *IET Power Electronics*, vol. 11, no. 9, pp. 1556–1565, 2018.

[164] D. Mao, K. Potty, and J. Wang, "The impact of power-electronics-based load dynamics on large-disturbance voltage stability," in *2018 IEEE Power & Energy Society General Meeting (PESGM)*, pp. 1–5, IEEE, 2018.

[165] M. M. Rana, W. Xiang, and E. Wang, "Smart grid state estimation and stabilisation," *International Journal of Electrical Power & Energy Systems*, vol. 102, pp. 152–159, 2018.

[166] N. Kant, R. Mukherjee, D. Chowdhury, and H. K. Khalil, "Estimation of the region of attraction of underactuated systems and its enlargement using impulsive inputs," *IEEE Transactions on Robotics*, vol. 35, no. 3, pp. 618–632, 2019.

[167] A. Papachristodoulou, *Scalable analysis of nonlinear systems using convex optimization*. PhD thesis, California Institute of Technology, 2005.

[168] J. Guthrie, "Large-signal stability analysis of pulsed constant power loads via sum-of-squares optimization," in *2019 IEEE Electric Ship Technologies Symposium (ESTS)*, pp. 127–133, IEEE, 2019.

[169] D. Šiljak and D. M. Stipanovic, "Robust stabilization of nonlinear systems: The lmi approach," *Mathematical problems in Engineering*, vol. 6, no. 5, pp. 461–493, 2000.

[170] K. Li, D. Dewar, A. Formentini, P. Zanchetta, and P. Wheeler, "Optimized control design for power converters in power electronics embedded networks integrating grid model identification," in *2018 IEEE Industry Applications Society Annual Meeting (IAS)*, pp. 1–6, IEEE, 2018.